

EFFECTIVE ROLE OF CUBIC SPLINES FOR THE NUMERICAL COMPUTATIONS OF NON-LINEAR MODEL OF VISCOELASTIC FLUID

Aasma Khalid^{*}, Rubab Batool^{*}, Kashif Ali Abro^{**}, Akmal Rehan^{***}

^{*}Department of Mathematics, GC Women University Faisalabad, 38023, Faisalabad, Pakistan

^{**}Institute of Ground Water Studies, Faculty of Natural and Agricultural Sciences, University of the Free State, South Africa,
Department of Basic Science and Related Studies, Mehran University of Engineering and Technology, Jamshoro, Pakistan,
Faculty of Mathematics and Statistics, Ton Duc Thang University, Ho Chi Minh City, Vietnam

^{***} Department of Computer Science, University of Agriculture Faisalabad, 38023, Faisalabad, Pakistan

aasmakhalid@gcwuf.edu.pk, rubabbatool1272@gmail.com, kashif.abro@faculty.muft.edu.pk, akmalrehan@uaf.edu.pk

received 05 January 2024, revised 02 June 2024, accepted 25 June 2024

Abstract: The seventh-order boundary value problems (BVPs), which are important because of their complexity and prevalence in many scientific and engineering fields, are the subject of this paper's study. These high-order boundary value problems appear in fields such as fluid dynamics, where they are used to model fluid flow, and in elasticity theory, where they help describe the deformation of materials. Unfortunately, the precision and stability required to solve these high-order problems consistently are frequently lacking from current numerical techniques. Consequently, the advancement of theoretical research as well as practical applications in these disciplines depends on the development of a reliable and accurate method for solving seventh-order boundary value problems. In order to improve the accuracy and stability of solutions for these challenging issues, we propose novel numerical strategies that involves non-polynomial and polynomial cubic splines. For both methods, the domain $[0, 1]$ is divided into sub-intervals with step sizes of $h=1/10$ and $h=1/5$. This method involves initially transforming the seventh-order boundary value problems into a system of second-order. These second-order boundary value problems are then discretized using finite difference approximations, incorporating essential boundary conditions, and ultimately converted into a set of linear algebraic equations. The employed methods are rigorously assessed through experimentation on three distinct test problems. The outcomes attained showcase an exceptional level of accuracy, extending up to 7 decimal places. These commendable results are vividly depicted in both the tabulated data and accompanying graphs. Such a high degree of precision substantiates the dependability and efficiency of the proposed method. Comparisons, presented in tables and graphs, highlight the precision and reliability of our methods. These comparisons confirm that our approaches are valuable tools for addressing the challenges associated with seventh-order boundary value problems, marking a notable contribution to the field of numerical analysis. While lower-order boundary value problems have been extensively studied, applying these splines methods to seventh-order boundary value problems presents new challenges and insights. The novelty of this work involves non-polynomial and polynomial cubic spline techniques to solve seventh-order boundary value problems, offering improved accuracy and stability over existing numerical methods.

Key words: finite difference method, central difference, boundary value problems, non polynomial, spline methods, polynomial, numerical analysis

1. INTRODUCTION

Seventh-order boundary value problems are not as common as lower-order problems but can arise in specific physical and engineering contexts, particularly in areas where complex phenomena need to be described with high precision. For example, the deflection $y(x)$ of a beam might be described by a seventh-order differential equation to capture detailed physical effects:

$$EI \frac{d^7 y}{dx^7} = f(x), \quad (1)$$

where E is the modulus of elasticity, I is the moment of inertia, and $f(x)$ is the distributed load.

In fluid mechanics, seventh-order BVPs describe complex flow patterns and instabilities in boundary layers, such as those found in advanced aerodynamics or wave propagation phenomena:

$$\frac{d^7 u}{dx^7} + a \frac{d^5 u}{dx^5} + b \frac{d^3 u}{dx^3} + cu = 0, \quad (2)$$

where u represents the flow variable, and a , b , and c are coefficients representing various physical parameters. In nonlinear dynamics, these equations capture detailed interactions in systems exhibiting chaotic behavior. In quantum mechanics, higher-order differential equations appear in advanced quantum field theories and perturbation analysis, where they describe the behavior of quantum fields under complex interactions.

In computer graphics, dealing with curves is essential for drawing various objects on the screen. Cubic curves, both non-polynomial and polynomial splines, are commonly used due to their flexibility. The novelty of this study lies in the approach of utilizing both CPS and CNPS methods, to tackle nonlinear seventh-order BVPs. While previous research has explored various numerical methods for lower-order BVPs, the application of these spline techniques to seventh-order nonlinear problems is relatively unexplored.

Cubic polynomial splines are widely used due to their smoothness and computational efficiency. They ensure continuity of the first and second derivatives, which is crucial for accurately solving

high-order differential equations. The general form of a cubic spline $S(x)$ between two points x_i and x_{i+1} is:

$$S_i(x) = a_i + b_i(x - x_i) + c_i(x - x_i)^2 + d_i(x - x_i)^3, \quad (3)$$

where a_i , b_i , c_i , and d_i are coefficients determined by the spline conditions, including continuity of the first and second derivatives at the knots.

Nonpolynomial splines, such as trigonometric or exponential splines, offer flexibility in modeling functions with periodic or rapidly varying behavior, which is often encountered in physical problems. For example, a trigonometric spline $T(x)$ might be expressed as:

$$T_i(x) = a_i + b_i \sin(\omega(x - x_i)) + c_i \cos(\omega(x - x_i)), \quad (4)$$

where ω is the frequency parameter, and a_i , b_i , and c_i are coefficients. These splines are particularly useful in handling boundary conditions that exhibit periodicity or oscillatory characteristics.

Despite the advantages of CPS and CNPS methods, there are several limitations to our approach. These methods can become computationally intensive, especially for smaller step sizes, which yield more accurate results but at the cost of increased computational demand. Conversely, larger step sizes may reduce computational effort but compromise accuracy, especially for problems with steep gradients or rapid changes. Implementing cubic polynomial splines can be more complex than using simpler methods like finite differences, requiring careful construction and continuity at the knots. While cubic splines generally provide good convergence properties, certain nonlinear or stiff problems may require very fine discretization to achieve desired accuracy, increasing computational costs.

In [1], the authors conducted extensive research on the solution of parabolic Partial Differential Equations (PDEs). They introduced a novel method for calculating numerical solutions of fourth-order PDEs, building upon the foundation of the polynomial cubic spline method and the Alternating Direction Method (ADM). The ADM approach dismantled the constraints of alternate variables to achieve successive approximations. A solution to a seventh-order BVP using cubic B-spline functions was presented in [2]. The authors propose an efficient numerical algorithm based on cubic B-splines to approximate the solution to the BVP.

In [3], the focus was on trajectory planning for a robotic arm endowed with seven degrees of freedom. The primary goal was to facilitate efficient and seamless targeting of a specified point by the robotic arm. To address this challenge, cubic polynomials and seventh-degree polynomials were harnessed for joint space trajectory planning, all grounded in a foundation of kinematics analysis. The trajectory planning was subsequently simulated utilizing the MATLAB platform, enabling a comprehensive evaluation of its effectiveness and performance.

Mathematicians and engineers historically encountered challenges when attempting to solve higher-order differential equations. To address such complexities and find numerical approximations, a range of numerical techniques were employed. In [4], authors presented a distinctive numerical approach aimed at approximating tenth-order Boundary Value Problems (BVPs). The methods devised within this study were based on the innovative concept of amalgamating the decomposition process with the Non-Polynomial Cubic Spline Method (NPCSM) and the Polynomial Cubic Spline Method (PCSM).

In a research investigation employing the Kernel Hilbert technique, as outlined in [5], the study showcased the method's proficiency in solving seventh-order Boundary Value Problems (BVPs)

while adhering to boundary constraints. These findings were then contrasted with those obtained using various approaches, such as HPM, VPM, VIM, ADM, and HAM. In addition, the authors of [6] suggested using the Cubic B spline approach to deal with the numerical solutions of seventh-order BVPs. For a quantitative knowledge of seventh-order BVPs, including both linear and non-linear forms, this work especially used CB splines.

A innovative numerical method was developed in [7] by creating ninth-degree spline functions by using extended cubic splines. This method provided a special answer to challenging mathematical issues. The authors proposed a numerical method for solving linear seventh-order ordinary boundary value problems (BVPs) by utilizing the B-Spline system (BSM) in a separate work, which is described in [8]. The particular traits of seventh-order BVPs served as a foundation for the creation of this approach. In order to approximate the Septic B-Spline formulation, they invented the Collocation BSM, which they used to effectively achieve their goal.

The Homotopy Perturbation Method (HPM) was used by the author in [9] to offer a method for approximating seventh-order linear and nonlinear boundary value problems (BVPs). This approach established itself as a useful tool in this field by demonstrating its capacity to solve higher-order linear and nonlinear BVPs with little absolute error. The authors of [10] concentrated on employing quartic B-spline functions to solve seventh-order BVPs. The authors provided an efficient method for dealing with this kind of issues by proposing a numerical strategy that made use of quartic B-splines to approximate the answers.

In their research [11], the authors employed Non-Polynomial Cubic Splines of Sixth Order in conjunction with Finite Difference Approximations to solve a complex array of linear algebraic equations inherent in Boundary Value Problems (BVPs). The researchers in [12, 13, 16, 18] investigated the application of three mathematical methods, namely the homotopy perturbation method (HPM), cubic spline, spline collocation method, differential transform technique (DTT) and the modified Adomian decomposition method (MADM), for solving higher-order boundary value problems (BVPs). In [14], the author introduced an efficient numerical algorithm for solving seventh-order BVPs. The approach utilized cubic B-spline functions to approximate the solution, offering a reliable method for tackling such higher-order problems. Authors in [15] introduced quintic nonpolynomial spline algorithms specifically tailored for addressing fourth-order two-point BVPs. Importantly, this methodology extended its applicability to encompass Partial Differential Equations (PDEs) up to the fourth order, leading to enhanced approximations while demanding reduced computational effort.

In the study of induction motors [17], the behavior could be accurately described by a fifth-order differential equation (DE) model. By incorporating a torque correction factor, the full seventh-order DE structure faithfully replicated the transient torques as well as the instantaneous real and reactive power flows. Seventh-order Boundary Value Problems (BVPs) were solved using He's polynomials and the Variational Iteration Method (VIM). The solutions to these problems were approximated using a rapidly converging series.

The transformation of seventh-order Boundary Value Problems (BVPs) into a set of Integral Equations (IE) was demonstrated in [19, 20], and these equations were solvable using the Variational Element Method (VEM). It's worth noting that, at that time, there was no literature available on the numerical solutions to seventh-order BVPs and related Eigenvalue Problems (EVP). The approximate solutions of these equations were expressed in terms of overlapping series with calculable elements. By combining the Homotopy Perturbation Method (HPM) and the Adomian Decomposition Method

(ADM), [21] was able to solve seventh-order BVPs. The writers were able to solve the difficulties precisely and quickly by the use of this method. A method for solving seventh-order BVPs using cubic trigonometric B-spline functions was provided by the authors in [22]. Their approach provided an effective strategy to deal with such high-order BVPs by approximating the solutions using these customized B-splines. The author of [23] developed a numerical strategy for quickly solving linear fourth-order boundary value problems (BVPs) using the Non-Polynomial Spline (NPS) technique.

1.1. Basics of Cubic Non-Polynomial Splines

Let's break the interval $[a, b]$ into n small intervals by using node points: $\varpi_e = a + eh$, where $e = 0, 1, \dots, n$, where $a = \varpi_0$ and $b = \varpi_n$ with the step size $h = \frac{b-a}{n}$ and n is a positive integer. Let $\chi(\varpi)$ be the precise solution and χ_e be an estimate to $\chi(\varpi_e)$ attained by the CNPS $X_e(\varpi)$ between the points (ϖ_e, χ_e) and $(\varpi_{e+1}, \chi_{e+1})$. It is necessary for $X_e(\varpi)$ to fulfill the ICs at ϖ_e and ϖ_{e+1} , the BCs, and in the same way, the continuity of the initial derivative at the collective points (ϖ_e, s_e) . For every part (ϖ_e, ϖ_{e+1}) where $e = 0, 1, 2, 3, 4, \dots, n-1$, the spline $X_e(\varpi)$ makes the form:

$$X_e(\varpi) = q_e + l_e(\varpi - \varpi_e) + s_e \sin \sigma(\varpi - \varpi_e) + n_e \cos \sigma(\varpi - \varpi_e) \quad (5)$$

where q_e, l_e, s_e , and n_e are constants and σ is a free quantity.

A NP function X_{ϖ} of class $R^2[a, b]$ which includes χ_{ϖ} at the node points ϖ_e ; $e = 0, 1, 2, 3, 4, \dots, n$ is influenced by a parameter σ and decreases to a Cubic-Spline X_{ϖ} in $[a, b]$ as σ approaches 0. For the derivation of the coefficient of the equation (5) in terms of $\chi_e, \chi_{e+1}, N_e, N_{e+1}$, we first define:

$$X_e(\varpi_e) = \chi_e, \quad X_e(\varpi_{e+1}) = \chi_{e+1} \quad (6)$$

The consequent expression for the equation (5) is obtained by straightforward algebraic manipulation:

$$q_e = \chi_e + \frac{N_e}{\sigma^2}, \quad l_e = \frac{\chi_{e+1} - \chi_e}{h} + \frac{N_{e+1} - N_e}{\zeta \theta}$$

$$s_e = \frac{N_e \cos \theta - N_{e+1}}{\sigma^2 \sin \theta}, \quad n_e = -\frac{N_e}{\sigma^2}$$

where $\theta = Nh$. By the continuity equation of the first derivative at node point (ϖ_e, χ_e) , i.e., $X'_{e-1}(\varpi_e) = X'_e(\varpi_e)$ is the consistency relation for $e = 0, 1, \dots, n-1$:

$$\zeta(N_{e+1} + N_{e-1}) + 2\delta(N_e) = \frac{1}{h^2}(\chi_{e-1} + \chi_{e+1} - 2\chi_e) \quad (7)$$

where we've inserted:

$$\zeta = \frac{1}{\theta \sin \theta} - \frac{1}{\theta^2}, \quad \delta = \frac{-1}{\theta^2} - \frac{-\cos \theta}{\theta}, \quad \chi'' = N \quad (8)$$

and $\theta = Nh$

The described approach is 4th order convergent if $1-2\zeta-2\delta=0$ and $\zeta=\frac{1}{12}$ [23].

1.2. Basics of Cubic Polynomial Splines

Let's break the interval $[a, b]$ into n small intervals by using node points: $\varpi_e = a + eh$, $e = 0, 1, 2, 3, 4, \dots, n$ where $a = \varpi_0$, $b = \varpi_n$ with the step size $h = \frac{b-a}{n}$ and n a positive integer.

Let $\chi(\varpi)$ be the precise solution and χ_e be an estimate to $\chi(\varpi_e)$ attained by the NPS $X_e(\varpi)$ between the points (ϖ_e, χ_e) and $(\varpi_{e+1}, \chi_{e+1})$. It is necessary for $X_e(\varpi)$ to fulfill the interpolating conditions at ϖ_e and ϖ_{e+1} , the BCs, and in the same way, the continuity of the initial derivative at the collective points (ϖ_e, χ_e) . For every part (ϖ_e, ϖ_{e+1}) where $e = 0, 1, 2, 3, 4, \dots, n-1$ the spline $X_e(\varpi)$ makes the form where q_e, l_e, s_e , and n_e are constants and σ is a free quantity.

A NP function X_{ϖ} of class $R^2[a, b]$ which includes χ_{ϖ} at the node points ϖ_e ; $e = 0, 1, 2, 3, 4, \dots, n$ be influenced by a parameter σ and decreases to a Cubic-Spline X_{ϖ} in $[a, b]$ as σ approaches 0. We first define:

$$X_e(\varpi_e) = \chi_e, \quad X_e(\varpi_{e+1}) = \chi_{e+1}, \quad X''_e(\chi_e) = N_e, \quad X''_e(\chi_{e+1}) = N_{e+1} \quad (9)$$

By using a straightforward algebraic operation, we may get the corresponding expression:

$$q_e = \chi_e + \frac{N_e}{\sigma^2}, \quad l_e = \frac{\chi_{e+1} - \chi_e}{h} + \frac{N_{e+1} - N_e}{\zeta \theta}$$

$$s_e = \frac{N_e \cos \theta - N_{e+1}}{\sigma^2 \sin \theta}, \quad n_e = -\frac{N_e}{\sigma^2}$$

where

$$\theta = Nh$$

By the continuity equation of the first derivative at node point (ϖ_e, χ_e) , i.e., $X'_{e-1}(\varpi_e) = X'_e(\varpi_e)$ is the consistency relation for $e = 0, 1, 2, 3, 4, \dots, n-1$:

$$(N_{e+1} + N_{e-1} + 4N_e) = \frac{6}{h^2}(\chi_{e-1} + \chi_{e+1} - 2\chi_e) \quad (10)$$

where we have substituted:

$$\chi'' = N$$

The paper progresses logically from theory to application. Section 2 discusses the development of CPS and CNPS, while Section 3 evaluates their effectiveness in resolving 7th order BVPs. Section 4 concludes with a concise analysis and recommendations, providing a clear and educational reading experience.

2. SEVENTH ORDER NON-LINEAR BVPs

Using the CPS and CNPS approaches to approximatively solve a nonlinear seventh-order boundary value problem (7^{th} order BVP) is the main goal in this situation. These methods are computational tools designed to generate approximative numerical solutions to this difficult problem. By employing these techniques, we aim to effectively manage the challenges posed by the nonlinear nature of the problem and give exact numerical estimates for the desired outputs.

$$\chi^{(7)}(\varpi) = z(\varpi, \chi(\varpi), \chi^{(1)}(\varpi), \chi^{(2)}(\varpi), \chi^{(3)}(\varpi), \chi^{(4)}(\varpi), \chi^{(5)}(\varpi), \chi^{(6)}(\varpi)); \quad \varpi \in [a, b] \quad (11)$$

along with BCs:

$$\chi^{(2i)}(a) = \zeta_i, \quad \chi^{(2i)}(b) = \delta_i \quad (12)$$

where ζ_i, δ_i ; $i=0, 1, 2, 3$ are constants and $\zeta_i(0), i=1, \dots, 7$ and $z(\varpi)$ are continuous functions on $[r, s]$. To estimate CNPS and CPS choose S to BVPs with BCs, Let us distribute interval $[r, s]$ into n sub-interval $z_i = r + ih$, $i=0, 1, \dots, n-1, n$. $r = z_0$,

$$s = z_n, \quad h = \frac{s-r}{n}$$

Now for CNPS $S'_{i-1}(z_i) = S'_i(z_i)$ is relation

$$i = 0, 1, \dots, n-1,$$

$$\zeta N_{i+1} + 2\delta N_i + \zeta N_{i-1} = \frac{1}{h^2} (v_{i+1} - 2v_i + v_{i-1}) \quad (13)$$

here the substitution

$$\zeta = \frac{1}{\theta \sin \theta} - \frac{1}{\theta^2}, \quad \delta = -\frac{1}{\theta^2} - \frac{\cos \theta}{\theta}, \text{ and } \theta = \mathfrak{U} h$$

Now for CPS $S'_{i-1}(z_i) = S'_i(z_i)$ is relation

$$i = 0, 1, \dots, n-1,$$

$$N_{i+1} + 4N_i + N_{i-1} = \frac{6}{h^2} (v_{i+1} - 2v_i + v_{i-1}) \quad (14)$$

where we have replace

$$v'' = N$$

Now differentiating (11) w.r.t. χ so, the equation become $\chi^{(8)}(\varpi) = z(\varpi, \chi(\varpi), \chi^{(1)}(\varpi), \chi^{(2)}(\varpi), \chi^{(3)}(\varpi), \chi^{(4)}(\varpi), \chi^{(5)}(\varpi), \chi^{(6)}(\varpi), \chi^{(7)}(\varpi))$ (15)

Equation (15) presents an eighth-order boundary value problem. In order to manage its complexity, we proceeded to transform equation (15) into a system of second-order Boundary Value Problems (BVPs), incorporating the Boundary Conditions (BCs) from equation (12). This transformation was accomplished by substituting the equation into a specific form, resulting in a more manageable representation.

$$\chi''(\varpi) = e(\varpi) \quad (16)$$

$$e''(\varpi) = f(\varpi) \quad (17)$$

$$f''(\varpi) = g(\varpi) \quad (18)$$

in equation (15), the reduced system of 2nd order will be

$$p^{(2)}(k) = z(\varpi, \chi(\varpi), \chi^{(1)}(\varpi), e(\varpi), e^{(1)}(\varpi), f(\varpi), f^{(1)}(\varpi), g(\varpi), g^{(1)}(\varpi)); \quad \varpi \in [a, b] \quad (19)$$

Along with boundary conditions:

$$\begin{aligned} \chi(a) &= \zeta_0, \quad \chi(b) = \delta_0 \\ e(a) &= \zeta_1, \quad e(b) = \delta_1 \\ f(a) &= \zeta_2, \quad f(b) = \delta_2 \\ g(a) &= \zeta_3, \quad g(b) = \delta_3 \end{aligned} \quad (20)$$

2.1. Cubic Non-Polynomial Spline

We get relations for $\chi(\varpi), e(\varpi), f(\varpi)$ and $g(\varpi)$ by using the continuity condition of first order derivative, respectively as:

$$\zeta(R_{i+1} + R_{i-1}) + \delta 4R_i = \frac{1}{h^2} (\chi_{i+1} - 2\chi_i + \chi_{i-1}) \quad (21)$$

$$\zeta(S_{i+1} + S_{i-1}) + \delta 4S_i = \frac{1}{h^2} (e_{i+1} - 2e_i + e_{i-1}) \quad (22)$$

$$\zeta(P_{i+1} + P_{i-1}) + \delta 4P_i = \frac{1}{h^2} (g_{i+1} - 2g_i + g_{i-1}) \quad (23)$$

we have substitute

$$\begin{aligned} \chi''(\varpi) &= R(\varpi), \quad e''(\varpi) = S(\varpi), \\ f''(\varpi) &= T(\varpi), \quad g''(\varpi) = P(\varpi) \end{aligned} \quad (24)$$

Discretize equations (15)-(18) at grid points

$$(\varpi_i, g_i), (\varpi_i, \chi_i), (\varpi_i, e_i), (\varpi_i, f_i)$$

$$g^{(2)}(\varpi) = z(\varpi, \chi(\varpi), \chi^{(1)}(\varpi), e(\varpi), e^{(1)}(\varpi), f(\varpi), f^{(1)}(\varpi), g(\varpi), g^{(1)}(\varpi)) \quad (25)$$

$$\begin{aligned} \chi''(\varpi_i) &= e(\varpi_i) = e_i, \\ e''(\varpi_i) &= f(\varpi_i) = f_i, \\ f''(\varpi_i) &= g(\varpi_i) = g_i, \end{aligned} \quad (26)$$

Now after substitution we get

$$\begin{aligned} \chi''_i &= R_i, \quad e''_i = S_i, \\ f''_i &= T_i, \quad g''_i = P_i \end{aligned} \quad (27)$$

then above equation become

$$P_i = z(\varpi_i, \chi(\varpi_i), \chi^{(1)}(\varpi_i), e(\varpi_i), e^{(1)}(\varpi_i), f(\varpi_i), f^{(1)}(\varpi_i), g(\varpi_i), g^{(1)}(\varpi_i)); \quad (28)$$

$$\left. \begin{aligned} R_i &= e_i, \\ S_i &= f_i, \\ T_i &= g_i, \end{aligned} \right\} \quad (29)$$

From equation (28) and (29)

$$P_{i+1} = z(\varpi_{i+1}, \chi(\varpi_{i+1}), \chi^{(1)}(\varpi_{i+1}), e(\varpi_{i+1}), e^{(1)}(\varpi_{i+1}), f(\varpi_{i+1}), f^{(1)}(\varpi_{i+1}), g(\varpi_{i+1}), g^{(1)}(\varpi_{i+1})); \quad (30)$$

$$\left. \begin{aligned} R_{i+1} &= e_{i+1}, \\ S_{i+1} &= f_{i+1}, \\ T_{i+1} &= g_{i+1}, \end{aligned} \right\} \quad (31)$$

then similarly

$$P_{i-1} = z(\varpi_{i-1}, \chi(\varpi_{i-1}), \chi^{(1)}(\varpi_{i-1}), e(\varpi_{i-1}), e^{(1)}(\varpi_{i-1}), f(\varpi_{i-1}), f^{(1)}(\varpi_{i-1}), g(\varpi_{i-1}), g^{(1)}(\varpi_{i-1})); \quad (32)$$

$$\left. \begin{aligned} R_{i-1} &= e_{i-1}, \\ S_{i-1} &= f_{i-1}, \\ T_{i-1} &= g_{i-1}, \end{aligned} \right\} \quad (33)$$

The subsequent $O(h^2)$ approximations for the first-order derivatives l, e, f , and g in Equations (28), (30), and (33) offer a viable approach. These approximations can be effectively utilized to enhance the accuracy of the calculations.

$$\left. \begin{aligned} \chi'_i &= \frac{\chi_{i+1} - \chi_{i-1}}{2h}, \quad \chi'_{i+1} = \frac{3\chi_{i+1} - 4\chi_i + \chi_{i-1}}{2h}, \quad \chi'_{i-1} = \frac{-\chi_{i+1} + 4\chi_i - 3\chi_{i-1}}{2h}, \\ e'_i &= \frac{e_{i+1} - e_{i-1}}{2h}, \quad e'_{i+1} = \frac{3e_{i+1} - 4e_i + e_{i-1}}{2h}, \quad e'_{i-1} = \frac{-e_{i+1} + 4e_i - 3e_{i-1}}{2h}, \\ f'_i &= \frac{f_{i+1} - f_{i-1}}{2h}, \quad f'_{i+1} = \frac{3f_{i+1} - 4f_i + f_{i-1}}{2h}, \quad f'_{i-1} = \frac{-f_{i+1} + 4f_i - 3f_{i-1}}{2h}, \\ g'_i &= \frac{g_{i+1} - g_{i-1}}{2h}, \quad g'_{i+1} = \frac{3g_{i+1} - 4g_i + g_{i-1}}{2h}, \quad g'_{i-1} = \frac{-g_{i+1} + 4g_i - 3g_{i-1}}{2h}, \end{aligned} \right\} \quad (34)$$

Using equations (28)-(34) in equations (14) and (21)-(23)

$$\left. \begin{aligned} \zeta e_{i-1} + 2\delta e_i + \zeta e_{i+1} &= \frac{1}{h^2} (\chi_{i-1} - 2\chi_i + \chi_{i+1}) \\ \zeta f_{i-1} + 2\delta f_i + \zeta f_{i+1} &= \frac{1}{h^2} (e_{i-1} - 2e_i + e_{i+1}) \\ \zeta g_{i-1} + 2\delta g_i + \zeta g_{i+1} &= \frac{1}{h^2} (f_{i-1} - 2f_i + f_{i+1}) \end{aligned} \right\} \quad (35)$$

we get

$$\begin{aligned} &\zeta z(\varpi_{i+1}, \chi(\varpi_{i+1}), \chi^{(1)}(\varpi_{i+1}), e(\varpi_{i+1}), e^{(1)}(\varpi_{i+1}), f(\varpi_{i+1}), f^{(1)}(\varpi_{i+1}), g(\varpi_{i+1}), g^{(1)}(\varpi_{i+1})) + 2\delta z(\varpi_i, \chi(\varpi_i), \chi^{(1)}(\varpi_i), e^{(1)}(\varpi_i), f(\varpi_i), f^{(1)}(\varpi_i), g(\varpi_i), g^{(1)}(\varpi_i)) + \zeta z(\varpi_{i-1}, \chi(\varpi_{i-1}), \chi^{(1)}(\varpi_{i-1}), e(\varpi_{i-1}), e^{(1)}(\varpi_{i-1}), f(\varpi_{i-1}), f^{(1)}(\varpi_{i-1}), g(\varpi_{i-1}), g^{(1)}(\varpi_{i-1})) = \frac{1}{h^2} (g_{i-1} - 2g_i + g_{i+1}) \end{aligned} \quad (36)$$

we obtain

$$\begin{aligned} & \zeta z(\varpi_{i+1}, \chi(\varpi_{i+1}), \frac{3\chi_{i+1}-4\chi_i+\chi_{i-1}}{2h}, e(\varpi_{i+1}), \\ & \frac{3e_{i+1}-4e_i+e_{i-1}}{2h}, f(\varpi_{i+1}), \frac{3f_{i+1}-4f_i+f_{i-1}}{2h}, g(\varpi_{i+1}), \\ & \frac{3g_{i+1}-4g_i+g_{i-1}}{2h} + 2\delta z(\varpi_i, \chi(\varpi_i), \frac{\chi_{i+1}-\chi_{i-1}}{2h}, \\ & e(\varpi_i), \frac{e_{i+1}-e_{i-1}}{2h}, f(\varpi_i), \frac{f_{i+1}-f_{i-1}}{2h}, g(\varpi_i), \\ & \frac{g_{i+1}-g_{i-1}}{2h} + \zeta z(\varpi_{i-1}, \chi(\varpi_{i-1}), \frac{-\chi_{i+1}+4\chi_i-3\chi_{i-1}}{2h}, \\ & e(\varpi_{i-1}), \frac{-e_{i+1}+4e_i-3e_{i-1}}{2h}, f(\varpi_{i-1}), \frac{-f_{i+1}+4f_i-3f_{i-1}}{2h}, \\ & g(\varpi_{i-1}), \frac{-g_{i+1}+4g_i-3g_{i-1}}{2h} = \frac{1}{h^2} (g_{i-1} - 2g_i + g_{i+1}) \end{aligned} \quad (37)$$

Equations (36) and (37), along with the prescribed Boundary Conditions (20), come together to establish a coherent system consisting of $4(n+1)$ equations. Similarly, this system is closely linked to $4(n+1)$ unknowns, showcasing a harmonious synchronization between the equations and the set of unknown constants.

2.2. Cubic Polynomial Spline

We get relations for χ, e, f by make use of flow the surrounding of first order derivative, respectively as

$$\left. \begin{aligned} (R_{i+1} + R_{i-1}) + \delta 4R_i &= \frac{6}{h^2} (\chi_{i+1} - 2\chi_i + \chi_{i-1}) \\ (S_{i+1} + S_{i-1}) + \delta 4S_i &= \frac{6}{h^2} (e_{i+1} - 2e_i + e_{i-1}) \\ (P_{i+1} + P_{i-1}) + \delta 4P_i &= \frac{6}{h^2} (g_{i+1} - 2g_i + g_{i-1}) \end{aligned} \right\} \quad (38)$$

After substitution we get

$$\left. \begin{aligned} \zeta e_{i-1} + 2\delta e_i + \zeta e_{i+1} &= \frac{6}{h^2} (\chi_{i-1} - 2\chi_i + \chi_{i+1}) \\ \zeta f_{i-1} + 2\delta f_i + \zeta f_{i+1} &= \frac{6}{h^2} (e_{i-1} - 2e_i + e_{i+1}) \\ \zeta g_{i-1} + 2\delta g_i + \zeta g_{i+1} &= \frac{6}{h^2} (f_{i-1} - 2f_i + f_{i+1}) \end{aligned} \right\} \quad (39)$$

By considering the above data NPCS was settled in section, PCS scheme for $i = 0, 1, \dots, n-1$

Equations (40) and (41) form a system of $4(n+1)$ equations when integrated with Boundary Conditions (20). This system exhibits smooth interaction and corresponds to a set of $4(n+1)$ unknowns that are interrelated with the $4(n+1)$ equations.

$$\begin{aligned} & z(m_{i+1}, \chi(\varpi_{i+1}), \chi^{(1)}(\varpi_{i+1}), e(\varpi_{i+1}), \\ & e^{(1)}(\varpi_{i+1}), f(\varpi_{i+1}), f^{(1)}(\varpi_{i+1}), g(\varpi_{i+1}), \\ & g^{(1)}(\varpi_{i+1})) + 4z(\varpi_i, \chi(\varpi_i), \chi^{(1)}(\varpi_i), e(\varpi_i), \\ & e^{(1)}(\varpi_i), f(\varpi_i), f^{(1)}(\varpi_i), g(\varpi_i), g^{(1)}(\varpi_i)) \\ & + z(\varpi_{i-1}, \chi(\varpi_{i-1}), \chi^{(1)}(\varpi_{i-1}), e(\varpi_{i-1}), e^{(1)}(\varpi_{i-1}), \\ & f(\varpi_{i-1}), f^{(1)}(\varpi_{i-1}), g(\varpi_{i-1}), \\ & g^{(1)}(\varpi_{i-1})) = \frac{6}{h^2} (g_{i-1} - 2g_i + g_{i+1}) \end{aligned} \quad (40)$$

and

$$\begin{aligned} & z(\varpi_{i+1}, \chi(\varpi_{i+1}), \frac{3\chi_{i+1}-4\chi_i+\chi_{i-1}}{2h}, e(\varpi_{i+1}), \\ & \frac{3e_{i+1}-4e_i+e_{i-1}}{2h}, f(\varpi_{i+1}), \frac{3f_{i+1}-4f_i+f_{i-1}}{2h}, \\ & g(\varpi_{i+1}), \frac{3g_{i+1}-4g_i+g_{i-1}}{2h} + 4z(\varpi_i, \chi(\varpi_i), \\ & \frac{\chi_{i+1}-\chi_{i-1}}{2h}, e(\varpi_i), \frac{e_{i+1}-e_{i-1}}{2h}, f(\varpi_i), \\ & \frac{f_{i+1}-f_{i-1}}{2h}, g(\varpi_i), \frac{g_{i+1}-g_{i-1}}{2h} + z(\varpi_{i-1}, \\ & \chi(\varpi_{i-1}), \frac{-\chi_{i+1}+4\chi_i-3\chi_{i-1}}{2h}, e(\varpi_{i-1}), \\ & \frac{-e_{i+1}+4e_i-3e_{i-1}}{2h}, f(\varpi_{i-1}), \frac{-f_{i+1}+4f_i-3f_{i-1}}{2h}, \\ & g(\varpi_{i-1}), \frac{-g_{i+1}+4g_i-3g_{i-1}}{2h} = \frac{6}{h^2} (g_{i-1} - 2g_i + g_{i+1}) \end{aligned} \quad (41)$$

3. NUMERICAL RESULTS AND DISCUSSIONS

This section explores the outcomes of using CPS and CNPS methods to approximate solutions for a nonlinear seventh-order Boundary Value Problem (7th BVP). By choosing step sizes $h = 1/10$ and $h = 1/5$, we examine their impact on accuracy and computational efficiency. Smaller step sizes often yield more precise results but increase computational demands, highlighting the trade-off between accuracy and processing power. Comparing results across different step sizes provides insights into the convergence behavior and efficiency of both methods, demonstrating how they adapt to the complexities of the nonlinear 7th order BVP. This analysis sheds light on their convergence characteristics and offers practical guidance on balancing accuracy and computational efficiency in solving complex mathematical problems.

The solution process for the given boundary value problem involves several steps. Problem 3.1/3.2/3.3 was compared with equation (11) and boundary conditions with (12). Then, continuity conditions are defined to ensure smooth transitions across the intervals of the problem domain. Coefficients required for the numerical solution are then derived based on the given differential equation and boundary conditions by discretizing equations (15)-(18) at grid points $(\varpi_i, g_i), (\varpi_i, \chi_i), (\varpi_i, e_i), (\varpi_i, f_i)$. The subsequent $O(h^2)$ approximations for the first-order derivatives l, e, f , and g in Equations (28), (30), and (33) offer a viable approach. These approximations can be effectively utilized to enhance the accuracy of the calculations. Consistency relations prepared following the equations 34 are verified to ensure the accuracy of the numerical method. The resulting system of equations Using equations (28)-(35) in equations (14) and (21)-(23) is obtained and we get equations (36-37) then we solved numerically, and higher-order boundary value problems are transformed into a system of second-order differential equations. This transformed system is discretized, preparing it for numerical approximation and Equations (36) and (37), along with the prescribed Boundary Conditions (20), come together to establish a coherent system consisting of 44 equations for $h = 0.1$ and 24 equations for $h = 0.2$.

Similarly, this system is closely linked to 44 unknowns for $h = 0.1$ and 24 unknowns for $h = 0.2$, showcasing a harmonious synchronization between the equations and the set of unknown constants. The numerical solution is then obtained using appropriate numerical methods. Finally, the process concludes, having successfully approximated the solution to the given boundary value problem for CNPS. By considering the above data CNPS was settled in section, CPS scheme for $i = 0, 1, \dots, n-1$ will be developed using equations 38-39. Equations (40) and (41) form a system of $4(n+1)$ equations when integrated with Boundary Conditions (20). This system exhibits smooth interaction and corresponds to a set of 44 unknowns for $h = 0.1$ and 24 unknowns for $h = 0.2$ unknowns that are interrelated with the 44 equations for $h = 0.1$ and 24 equations for $h = 0.2$.

3.1 Problem 3.1

Consider the nonlinear BVP

$$\chi^{(7)}(\varpi) = -e^{\varpi} (w(\varpi))^2 \quad 0 \leq \varpi \leq 1$$

subject to

$$\chi^{(n)}(0) = 1, \quad \chi^{(n)}(1) = e^{-1}$$

for $n = 0, 2, 4, 6$.

The precise solution to the problem under consideration is

mathematically defined as $\chi(\varpi) = e^{-\varpi}$. In order to rigorously validate and assess the efficacy of the proposed method, a systematic evaluation was conducted. The interval $[0,1]$ was strategically divided into sub-intervals, employing both 10 and 5 equal segments. Subsequently, the CPS and CNPS techniques were employed to approximate the solution within each of these sub-intervals.

The outcomes obtained from the CPS and CNPS methods were meticulously compared against the analytically derived solution. For a finer granularity, the results were organized and presented in a clear tabular format. Specifically, Tab.1 was employed to present the numerical outcomes when the step size was set at $h = \frac{1}{10}$, and Tab. 2 for the case when $h = \frac{1}{5}$.

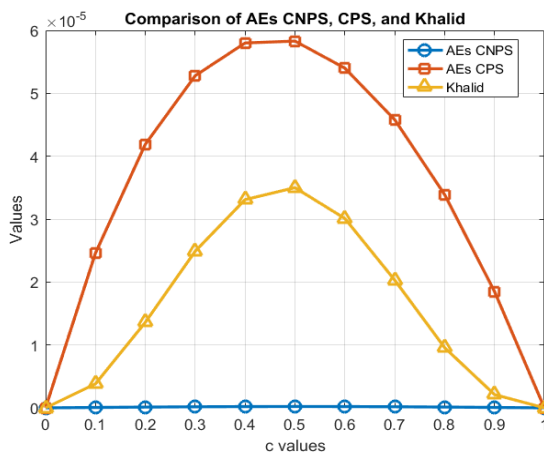


Fig.1. Comparison of AEs of CNPS and CPS with [6] of problem 3.1 at $h = \frac{1}{10}$

In addition to the numerical comparisons, visual aids were also harnessed to provide a more intuitive understanding of the precision achieved by the CPS and CNPS methods. To this end, Fig.1 and Fig.2 are crafted to illustrate the absolute errors associated with the chosen splines, specifically focusing on the scenario when the step size was $h = \frac{1}{10}$.

3.2 Problem 3.2

Consider the nonlinear BVP

$$\chi^7(\varpi) = \chi(\varpi)\chi'(\varpi) + e^{-2\varpi}(2 + e^{\varpi}(\varpi - 8) - 3\varpi + \varpi^2)0 \leq \varpi \leq 1$$

subject to

$$\chi^{(n)}(0) = (-1)^{\frac{n}{2}}(n+1), \quad \chi^{(n)}(1) = (-1)^{\frac{n}{2}}(n+1)e \text{ for } n = 0,2,4,6.$$

The precise solution is given as $\chi(\varpi) = (1 - \varpi)e^{-\varpi}$. To assess the performance of the proposed method, we conducted a systematic evaluation by segmenting the interval $[0,1]$ into 10 and 5 equal sub-intervals. Subsequently, we applied the CPS and CNPS methods to generate numerical outcomes, which were then juxtaposed with the specific analytical solution. These comparative analyses are exhaustively presented in Tab.3 for a step size of $h = \frac{1}{10}$ and in Tab.4 for $h = \frac{1}{5}$.

In order to offer a more intuitive insight into the precision achieved, Fig.3 and Fig.4 are constructed to visually depict the

absolute errors associated with the employed splines when $h = \frac{1}{10}$. These graphical representations enhance clarity by providing a visual representation of how closely the CPS and CNPS methods correspond to the analytical solution.

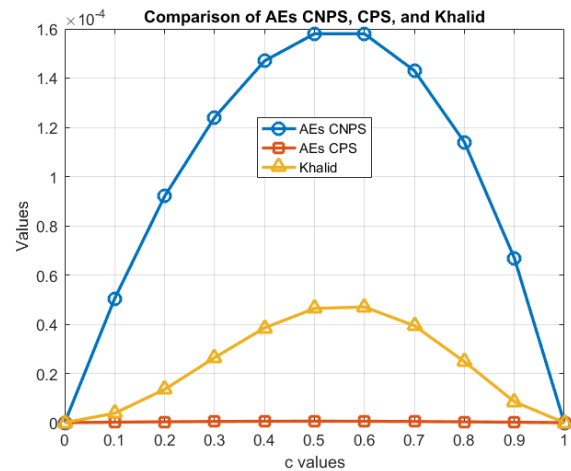


Fig.3. Comparison of AEs of CNPS and CPS with [6] of problem 3.2 at $h = \frac{1}{10}$

3.3 Problem 3.3

Consider the nonlinear BVP $\chi^{(7)} = e^{-\varpi}(w(\varpi))^2$ $0 \leq \varpi \leq 1$ subject to $\chi^{(n)}(0) = 1$, $\chi^{(n)}(1) = e^1$ for $n = 0,2,4,6$.

In pursuit of accurate approximations, the sought-after solution is $\chi(\varpi) = e^{\varpi}$. To rigorously examine the effectiveness of the proposed method, a meticulous analysis was undertaken. The interval $[0,1]$ was thoughtfully divided into 10 and 5 equal sub-intervals, setting the stage for a granular evaluation. By applying the CPS and CNPS methods, numerical results were obtained and subjected to a direct comparison with the precise analytical solution. These insightful evaluations are meticulously presented in Tab.5 for a step size of $h = \frac{1}{10}$ and in Tab.6 for $h = \frac{1}{5}$.

For an enhanced grasp of the achieved precision, Fig.5 and Fig.6 are crafted to visually encapsulate the absolute errors tied to the utilized splines, specifically when $h = \frac{1}{10}$. These graphical representations serve as a powerful tool for gauging the closeness of the CPS and CNPS methods to the established analytical solution.

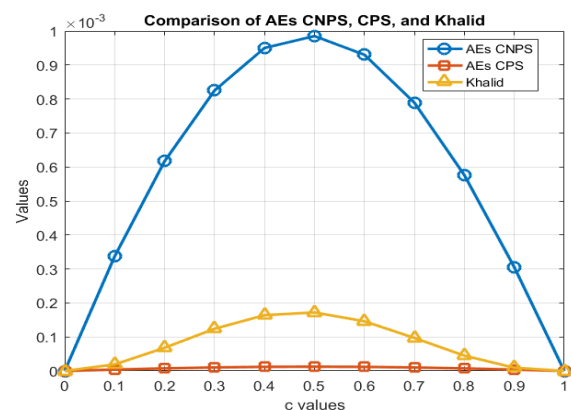


Fig.5. Comparison of AEs of CNPS and CPS with [6] of problem 3.3 at $h = \frac{1}{10}$

Tab.1. Comparison of accurate, CNPS along with CPS for problem 3.1 at $h = \frac{1}{5}$

ϖ	Accurate solution	CNPS solution	error on CNPS	CPS solution	error on CPS
0	1	1	0.00E-00	1	0.00E-00
0.2	0.818730753	0.817688874	1.04E-03	0.817618382	1.11E-03
0.4	0.670320046	0.668633087	1.69E-03	0.668558559	1.76E-03
0.6	0.548811636	0.547122919	1.69E-03	0.547064978	1.75E-03
0.8	0.449328964	0.448284237	1.04E-03	0.448246958	1.08E-03
1	0.367879441	0.367879441	0.00E-00	0.367879441	0.00E-00

Tab. 2. Comparison of accurate, CNPS along with CPS for problem 3.1 at $h = \frac{1}{10}$

ϖ	Accurate solution	CNPS solution	error on CNPS	CPS solution	error on CPS	[6]
0	1	1	0.00E-00	1	0.00E-00	0.00E-00
0.1	0.904837418	0.904837481	6.27E-08	0.904812814	2.46E-05	3.82E-06
0.2	0.818730753	0.818730875	1.22E-07	0.818688854	4.19E-05	1.36E-05
0.3	0.740818221	0.740818391	1.70E-07	0.740765438	5.28E-05	2.49E-05
0.4	0.670320046	0.670320248	2.02E-07	0.670262025	5.80E-05	3.31E-05
0.5	0.60653066	0.606530874	2.14E-07	0.606472401	5.83E-05	3.50E-05
0.6	0.548811636	0.548811841	2.05E-07	0.548757603	5.40E-05	3.01E-05
0.7	0.496585304	0.496585478	1.74E-07	0.496539521	4.58E-05	2.03E-05
0.8	0.449328964	0.44932909	1.26E-07	0.449295105	3.39E-05	9.57E-06
0.9	0.40656966	0.406569726	6.61E-08	0.406551127	1.85E-05	2.11E-06
1	0.367879441	0.367879441	0.00E-00	0.367879441	0.00E-00	0.00E-00

Tab. 3. Comparison of accurate, CNPS along with CPS for problem 3.2 at $h = \frac{1}{5}$

ϖ	Accurate solution	CNPS solution	error on CNPS	CPS solution	error on CPS
0	1	1	0.00E-00	1	0.00E-00
0.2	0.654984602	0.654548343	4.36E-04	0.653822489	1.16E-03
0.4	0.402192028	0.401485267	7.07E-04	0.400509549	1.68E-03
0.6	0.219524654	0.218816219	7.08E-04	0.217928602	1.60E-03
0.8	0.089865793	0.089426899	4.39E-04	0.088878968	9.87E-04
1	0	0	0.00E-00	0	0.00E-00

Tab. 4. Comparison of accurate, CNPS along with CPS for problem 3.2 at $h = \frac{1}{10}$

ϖ	Accurate solution	CNPS solution	error on CNPS	CPS solution	error on CPS	[6]
0	1	1	0.00E-00	1	0.00E-00	0.00E-00
0.1	0.814353676	0.814349741	0.814016517	3.37E-04	3.94E-06	1.91E-05
0.2	0.654984602	0.654977145	0.654367593	6.17E-04	7.46E-06	6.81E-05
0.3	0.518572754	0.518562529	0.517747628	8.25E-04	1.02E-05	1.24E-04
0.4	0.402192028	0.402180054	0.401241892	9.50E-04	1.20E-05	1.64E-04
0.5	0.30326533	0.303252787	0.302279968	9.85E-04	1.25E-05	1.72E-04
0.6	0.219524654	0.219512766	0.218594693	9.30E-04	1.19E-05	1.46E-04
0.7	0.148975591	0.148965506	0.148186139	7.89E-04	1.01E-05	9.70E-05
0.8	0.089865793	0.089858479	0.089290229	5.76E-04	7.31E-06	4.49E-05
0.9	0.040656966	0.040653124	0.040351558	3.05E-04	3.84E-06	9.44E-06
1	0	0	0	0.00E-00	0.00E-00	0.00E-00

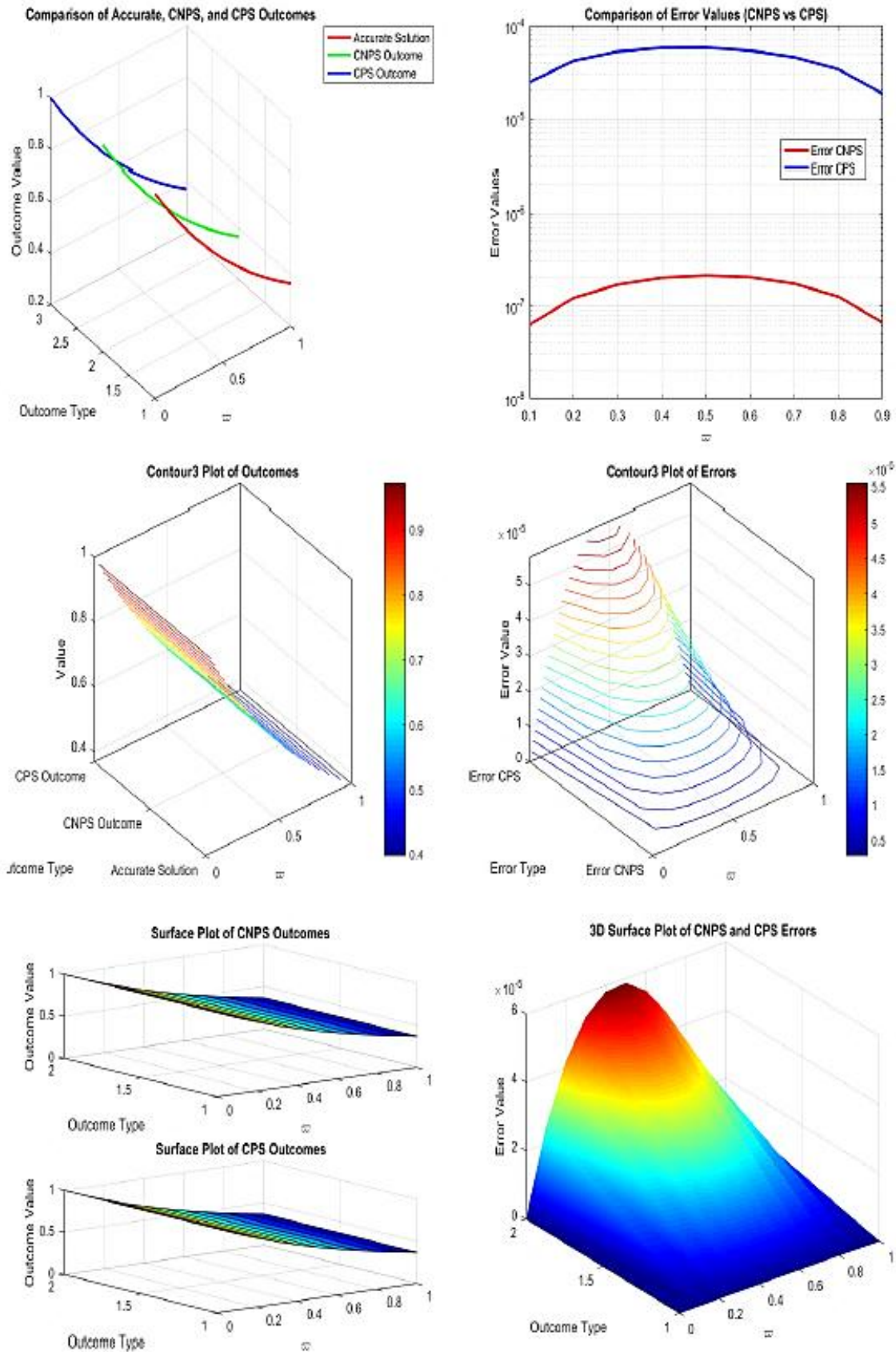


Fig. 2. Graphically representation of Accurate solution, CNPS outcome, CPS outcome and their Absolute Errors for problem 3.1 at $h = \frac{1}{10}$

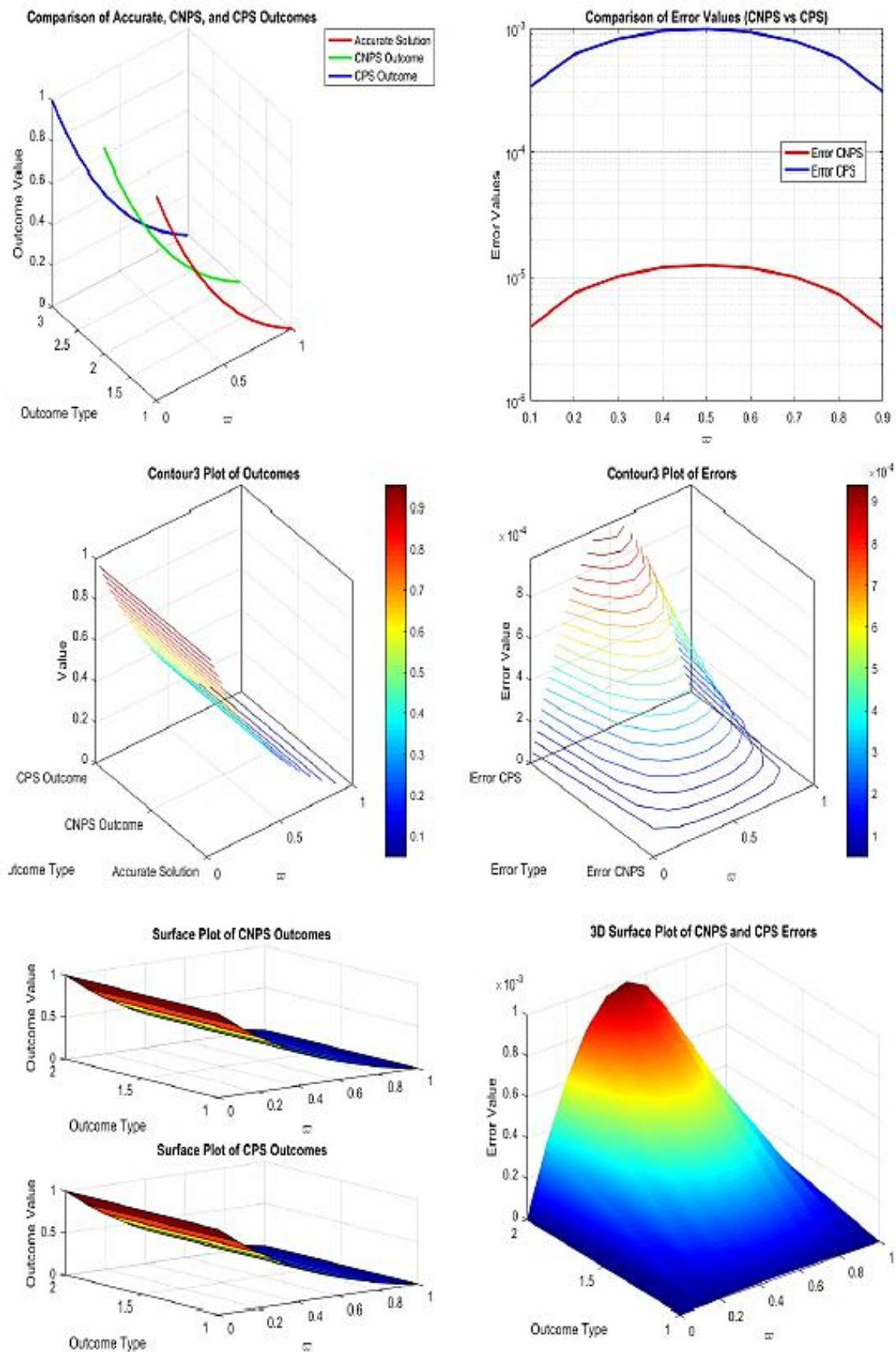


Fig. 4. Graphically representation of Accurate solution, CNPS outcome, CPS outcome and their Absolute Errors for problem 3.2 at $h = \frac{1}{10}$

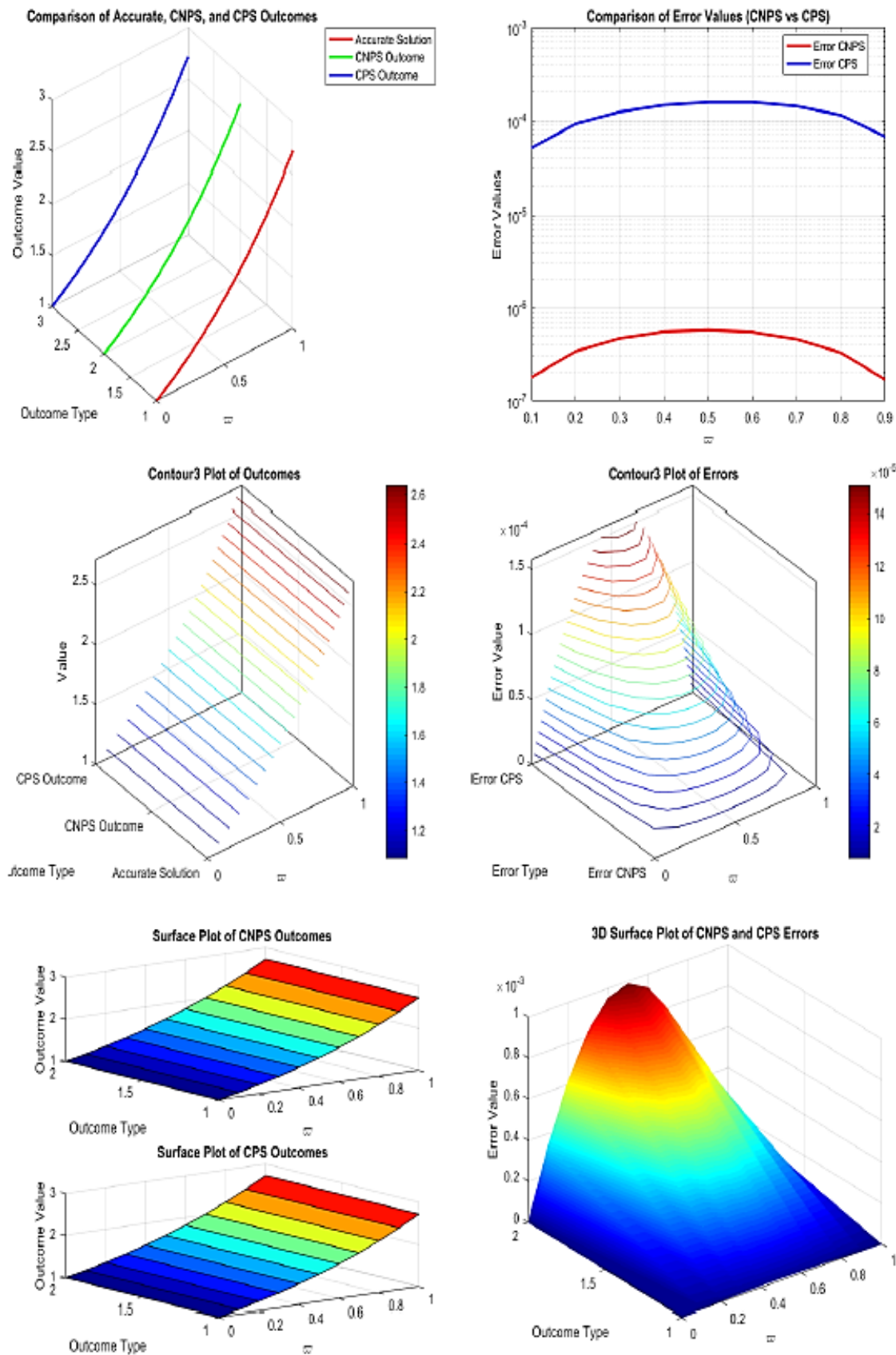


Fig. 6. Graphically representation of Accurate solution, CNPS outcome, CPS outcome and their Absolute Errors for problem 3.3 at $h = \frac{1}{10}$

Tab. 5. Comparison of accurate, CNPS along with CPS for problem 3.3 at $h = \frac{1}{10}$

ω	Accurate solution	CNPS solution	error on CNPS	CPS solution	error on CPS	[6]
0	1	1	1	0.00E-00	0.00E-00	0.00E-00
0.1	1.105170918	1.105171098	1.105120542	5.04E-05	1.80E-07	3.82E-06
0.2	1.221402758	1.221403102	1.221310719	9.20E-05	3.43E-07	1.35E-05
0.3	1.349858808	1.349859281	1.349734356	1.24E-04	4.73E-07	2.64E-05
0.4	1.491824698	1.491825254	1.49167782	1.47E-04	5.56E-07	3.85E-05
0.5	1.648721271	1.648721853	1.648562907	1.58E-04	5.82E-07	4.64E-05
0.6	1.8221188	1.82211935	1.821961083	1.58E-04	5.50E-07	4.70E-05
0.7	2.013752707	2.01375317	2.01360923	1.43E-04	4.62E-07	3.94E-05
0.8	2.225540928	2.225541259	2.225427036	1.14E-04	3.31E-07	2.48E-05
0.9	2.459603111	2.459603282	2.45953623	6.69E-05	1.70E-07	8.50E-06
1	2.718281828	2.71828	2.71828	0.00E-00	0.00E-00	0.00E-00

Tab. 6. Comparison of accurate, CNPS along with CPS for problem 3.3 at $h = \frac{1}{5}$

ω	Accurate solution	CNPS solution	error on CNPS	CPS solution	error on CPS	[6]
0	1	1	0.00E-00	1	0.00E-00	0.00E-00
0.2	1.221402758	1.221403377	6.19E-07	1.22103274	3.70E-04	5.42E-05
0.4	1.491824698	1.491825707	1.01E-06	1.491234204	5.90E-04	1.53E-04
0.6	1.8221188	1.822119714	9.13E-07	1.821484771	6.34E-04	1.95E-04
0.8	2.225540928	2.225541357	4.28E-07	2.225083141	4.58E-04	1.04E-04
1	2.718281828	2.71828	0.00E-00	2.71828	0.00E-00	0.00E-00

4. CONCLUSION

This paper addresses a gap in the existing literature by focusing on high-order nonlinear BVPs, which are less commonly explored compared to lower-order problems. this paper propose novel numerical strategies that involves non-polynomial and polynomial cubic splines to solve the nonlinear seventh order BVPs. Non-polynomial splines offer local control and are ideal for modeling intricate curves. In contrast, cubic polynomial splines excel in providing smooth interpolation. The choice between them depends on the problem's demands for local control or smoothness. The study shows that both CPS and CNPS methods can effectively solve nonlinear seventh-order BVPs, providing accurate approximations compared to exact solutions. For both methods, the domain $[0,1]$ is divided into sub-intervals with step sizes of $h = 1/10$ and $h = 1/5$.

The employed methods are rigorously assessed through experimentation on three distinct test problems. These benchmark problems encompass various nonlinear differential equations with different combinations of exponential, trigonometric, and polynomial terms, providing a diverse set of challenges for assessing the performance of the CPS and CNPS methods. The outcomes attained showcase an exceptional level of accuracy, extending up to 7 decimal places. These commendable results are vividly depicted in both the tabulated data and accompanying graphs. Such a high degree of precision substantiates the dependability and efficiency of the proposed method.

The CNPS method generally produces more accurate results than the CPS method. Smaller step sizes result in more accurate solutions for both methods, though at the cost of increased computational effort. For instance, with $h = 1/10$, the errors in both methods decrease compared to $h = 1/5$. Tab.1 shows that for Problem 3.1 with $h = 1/10$, the CNPS method achieves maximum

absolute errors as low as 1.22×10^{-7} , while the CPS method has errors up to 5.83×10^{-5} . Tab.2 for $h = 1/5$ indicates that while both methods' errors increase, CNPS still outperforms CPS in accuracy.

The graphical illustrations (Fig. 2, 4, 6) highlight the precision of both methods. CNPS shows smaller absolute errors compared to CPS, indicating better convergence to the exact solution. Figure 1 visually confirms the superior accuracy of CNPS with lower absolute errors compared to CPS. Fig. 1, 3 and 5 shows the graphical comparison on CPS and CNPS with other spline [6].

By comparing the CPS and CNPS methods, the research highlights the strengths and weaknesses of each approach, offering valuable insights for future applications. This is illustrated through various figures and numerical simulations presented in the results section, demonstrating the close agreement between the numerical and exact solutions. This comparative analysis is particularly useful for researchers and practitioners seeking efficient numerical methods for similar problems.

REFERENCES

1. Ahmad B, Perviz A, Ahmad MO, Dayan F. Solution of Parabolic Partial Differential Equations Via Non-Polynomial Cubic Spline Technique. Scientific Inquiry and Review. 2021; 5(3): 60-76.
2. Chawla MM, Chawla V. A cubic B-spline solution of a seventh-order boundary value problem. International Journal of Numerical Analysis and Modeling. 2015; 12(4): 689-703.
3. Fang S, Ma X, Qu J, Zhang S, Lu N, Zhao X. (2020). Trajectory planning for seven-DOF robotic arm based on seventh degree polynomial. In Proceedings of 2019 Chinese Intelligent Systems Conference. 2020; Volume II 15th: 286-294. Springer Singapore.
4. Iqbal MJ, Rehman S, Pervaiz A, Hakeem A. Approximations for linear tenth-order boundary value problems through polynomial and non-

- polynomial cubic spline techniques. *Proc. Pakistan Acad. Sci.* 2015; 52(4): 389-396.
5. Inc M, Akgül A. Numerical solution of seventh-order boundary value problems by a novel method. In *Abstract and Applied Analysis*; 2014; Hindawi.
 6. Khalid A, Rehan A, Nisar KS, Osman MS. Splines solutions of boundary value problems that arises in sculpturing electrical process of motors with two rotating mechanism circuit. *Physica Scripta*. 2021; 96(10): 104001.
 7. Kalyani P, Lemma MN. Solutions of seventh order boundary value problems using ninth degree spline functions and comparison with eighth degree spline solutions. *Journal of applied Mathematics and physics*. 2016; 4(02): 249.
 8. Khazaei M, Karamipour Y. Numerical Solution of the Seventh Order Boundary Value Problems Using B-Spline method; 2021. arXiv preprint: 2109.06030.
 9. Mabood F, Idrees M. Homotopy perturbation method and seventh-order boundary value problems. *International Journal of Applied Mathematical Research*. 2013; 2(1): 70-75.
 10. Nikkar A, Dehghan M. A numerical technique for solving seventh-order boundary value problems using quartic B-spline functions. *Applied Mathematics and Computation*. 2013; 219(19): 9810-9820.
 11. Pervaiz A, Ahmad A, Zafar Z, Ahmad MO. numerical solution of sixth order BVPs by applying non-polynomial spline method. *Pakistan Journal of Science*. 2014; 66(2):110.
 12. Opanuga AA, Okagbue HI, Edeki SO, Agboola OO. Differential transform technique for higher order boundary value problems. *Modern Applied Science*. 2015; 9(13): 224-230.
 13. Opanuga A, Owoloko E, Agboola O, Okagbue H. Application of homotopy perturbation and modified Adomian decomposition methods for higher order boundary value problems; 2017.
 14. Rasekh M. An efficient numerical algorithm for solving seventh-order boundary value problems using cubic B-spline functions." *Journal of Computational and Applied Mathematics*. 2016; 297: 143-154.
 15. Ramadan MA, Lashien IF, Zahra WK. Quintic nonpolynomial spline solutions for fourth order two-point boundary value problem. *Communications in Nonlinear Science and numerical Simulation*. 2009; 14(4): 1105-1114.
 16. Rashidinia J, Khazaei M, Nikmarvani H. Spline collocation method for solution of higher order linear boundary value problems. *TWMS J. Pure Appl. Math.* 2015; 6(1): 38-47.
 17. Richards G, Sarma P. (1994). Reduced order models for induction motors with two rotor circuits. *IEEE Transactions on Energy Conversion*. 1994; 9(4): 673-678.
 18. Rubin S, Khosla P. (1976). Higher-order numerical solutions using cubic splines. *AIAA Journal*. 1976;14(7): 851-858.
 19. Siddiqi SS, Iftikhar M. Variational iteration method for the solution of seventh order boundary value problems using He's polynomials. *Journal of the Association of Arab Universities for Basic and Applied Sciences*. 2015; 18: 60-65.
 20. Siddiqi SS, Akram G, Iftikhar M. Solution of seventh order boundary value problems by variational iteration technique. *Applied Mathematical Sciences*. 2012; 6(94): 4663-4672.
 21. Siddiqi SS, Iftikhar M. Solution of seventh order boundary value problems using Adomian decomposition method; 2013. arXiv preprint arXiv:1301.3603.
 22. Singh R, Pandey RK, Singh A. An efficient approach to solve seventh-order boundary value problems using cubic trigonometric B-spline. *Journal of Computational and Applied Mathematics*. 2020;367: 112418.
 23. Taiwo OA, Ogunlaran OM. A non-polynomial spline method for solving linear fourth-order boundary value problems; 2011.

Aasma Khalid and Rubab Batool are highly thankful to Government College Women University Faisalabad. Dr. Kashif Ali Abro is highly grateful to Mehran University of Engineering and Technology, Jamshoro and Mr. Akmal Rehan is highly thankful to University of Agriculture Faisalabad, Pakistan for generous support and facilities of this research work.

Aasma Khalid:  <https://orcid.org/0000-0003-4918-9732>

Rubab Batool:  <https://orcid.org/0009-0000-2073-419X>

Kashif Ali Abro:  <https://orcid.org/0000-0003-0867-642X>

Akmal Rehan:  <https://orcid.org/0000-0001-9384-0743>



This work is licensed under the Creative Commons BY-NC-ND 4.0 license.

INFLUENCE OF COMPOSITE LAY-UP ON THE LOAD-CARRYING CAPACITY OF STRUCTURES WITH CLOSED RECTANGULAR CROSS-SECTION

Kuba ROSŁANIEC^{*}, Patryk RÓŻYŁO^{*}

^{*}Faculty of Mechanical Engineering, Department of Machine Design and Mechatronics, Lublin University of Technology, Nadbystrzycka 36, 20-618 Lublin, Poland

kuba.roslaniec@pollub.edu.pl, p.rozylo@pollub.pl

received 28 November 2024, revised 29 January 2025, accepted 30 January 2025

Abstract: The purpose of this study was to carry out an experimental-numerical research of the influence of the composite layer system on the compressive strength of thin-walled eight-layer composite profiles with closed sections. The subjects of the study were thin-walled composite profiles made of carbon-epoxy composite by autoclave technique. The experimental studies utilized a universal testing machine, an optical deformation measurement system, and a digital microscope with a mobile working head. In parallel with the experimental studies, numerical simulations were conducted using the finite element method. Both the experimental studies and numerical simulations focused primarily on assessing the phenomenon of load-carrying capacity loss. The numerical simulations employed progressive damage analysis, which enabled the analysis of the obtained post-critical equilibrium paths. The research was conducted as part of a project funded by the National Science Centre, project no. 2021/41/B/ST8/00148.

Key words: failure; closed profile; experimental study; FEM; axial compression

1. INTRODUCTION

Thin-walled composite structures are widely used in many industries due to their relatively high strength and stiffness while maintaining low weight and ability to operate in harsh operating conditions [1]. These structures, especially those with closed sections, are mainly designed to carry compressive loads [2,3]. A desirable and common feature of this type of structure is the ability to carry compressive loads even after loss of stability, i.e. after buckling has occurred. In most cases, buckling does not significantly affect the ability to carry the load in the covered state (i.e., the state after buckling has occurred), since the redistribution of stresses in the loaded structure leads to a change in its deformation, which does not significantly reduce the ability to continue working under load conditions. The ability to carry higher loads than those causing buckling significantly increases the operational safety of such structures [4-7]. Some laminates with appropriately selected geometric parameters and ply arrangement are capable of carrying up to several times the buckling load. Increasing the load after buckling can lead to such phenomena as the initiation and propagation of fiber and matrix damage, delamination, and, as a further consequence, increasing the load can lead to a loss of load carrying capacity, that is, the ability of the structure to carry the load due to the development of structural damage [8,9].

The geometry of the cross-section of a composite profile has a direct impact on its strength, stiffness and load response characteristics. There are two basic varieties of composite profiles: closed cross sections [2,3,10] and open cross sections [10-12]. Studies have shown that composites with closed sections have higher strength and significantly higher stiffness compared to profiles with open sections. The higher stiffness is due to higher structural integrity, resulting in better stress distribution and higher resistance to

torsional effects. As a result, these profiles have higher structural stability [13-15].

The layer arrangement and their quantity have a significant impact on the stability and strength of the structure. These properties directly determine the behavior of the loaded structure and its resistance to damage, such as matrix and reinforcement cracking and tearing, as well as resistance to delamination. In most cases, increasing the number of layers enhances the structure's load resistance; however, as the number of layers grows, the total mass of the structure also increases [16-18]. Therefore, an important aspect is the careful selection of the number of layers and their configuration to optimize the strength properties of the profile.

This article focuses on conducting a comparative analysis of the impact of layer arrangement on the phenomenon of failure and the load-carrying capacity of three types of composite columns. These columns, made from carbon-epoxy composite, feature different layer arrangements but have identical cross-sectional geometries. The assessment of the influence of layer configuration on load-carrying capacity was performed using several independent research methods. Experimental tests were conducted using interdisciplinary techniques such as a universal testing machine, an optical deformation measurement system, and acoustic emission monitoring. Computer simulations were carried out using the finite element method in Abaqus® software. The material properties of the analyzed structures were experimentally determined in the following studies [13,19].

The novelty of this work lies in the analysis of the impact of layer arrangement on load-carrying capacity across three configurations with identical closed cross-sections. Experimentally obtained results were compared with those derived from numerical simulations. The primary aim of the study was to compare load-carrying capacities across the three different layer arrangements.

2. RESEARCH OBJECT

The thin-walled composite structures studied were made of carbon-epoxy composite CFRP by autoclave technique, using CY-COM 985-42%-HS-135-305 prepreg tape [20]. This tape is characterized by a width of 305 mm, a volume content of type 985 resin of 42% and a carbon fiber reinforcement with a density of 135 g/m². The tested structures were made by winding the prepreg onto an inner core with winding angles corresponding to the ply configuration. Curing of the composite structure in an autoclave was carried out at a temperature of 177°C and a pressure of 0.6 MPa. A detailed description of the process of manufacturing composite sections with closed sections was presented in the article [21], on the basis of which the present samples were made. Full-load tests were carried out for three different layer configurations in the composite, analyzing the following layer arrangements: 1 – [0/90/0/90]_s; 2 – [45/-45/90/0]_s; 3 – [90/-45/45/0]_s. For each layer configuration in the composite, three actual samples were produced and used in experimental studies, with the following overall dimensions (in mm):

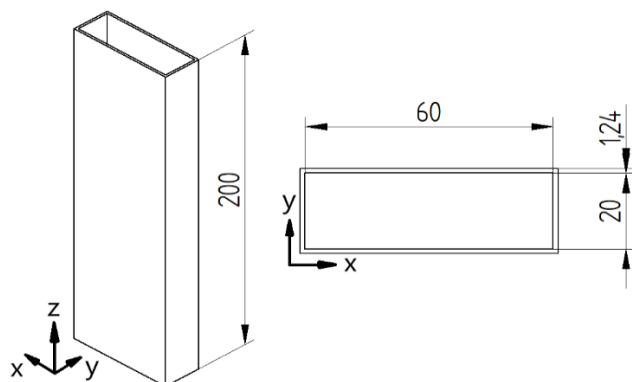


Fig. 1. Overall dimensions of test specimen

Tab. 1. Material properties of the carbon-epoxy composite: average values with standard deviation from a number of material test trials more extensively described in papers [13,19]

Mechanical properties		Strength parameters	
Young's modulus E_1 (MPa)	103014.11 (2145.73)	Tensile strength (0°) F_{tu} (MPa)	1277.41 (56.23)
Young's modulus E_2 (MPa)	7361.45 (307.97)	Compressive strength (0°) F_{cu} (MPa)	572.44 (46.20)
Poisson's ratio ν_{12} [-]	0.37 (0.17)	Tensile strength (90°) F_{tu} (MPa)	31.46 (9.64)
Kirchhoff modulus G_{12} (MPa)	4040.53 (167.35)	Compressive strength (90°) F_{cu} (MPa)	104.04 (7.34)
		Shear strength (45°) F_{su} (MPa)	134.48 (2.71)

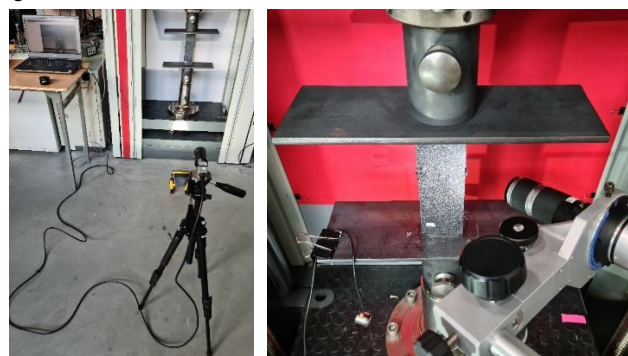
In order to develop numerical models that represented the actual structures faithfully, it was necessary to determine the mechanical and strength parameters of the material from which the test specimens were made. This allowed the analysis of the structure's load-carrying capacity and numerical simulations to be carried out in the post-buckling range up to complete failure. The material properties, shown in Table 1, were determined in accordance with current ISO standards using static strength tests. A detailed

description of the procedure for determining material parameters is presented in the article [13]. Numerical models corresponding to the actual structures were developed with a Lamin-type orthotropic model using the determined material properties, using the commercial software Abaqus. This made it possible to compare the results and behavior of the numerical models with experimental results. In the present study, the effect of mechanical couplings, such as torsion and bending of the composite structure, were not considered due to their negligible effect on the operation and behavior of the loaded real structure [22-24].

3. EXPERIMENTAL STUDIES

Experimental studies were carried out at the same time using several interdisciplinary research methods. The basic tool used in the experimental research was a Zwick Z100 universal testing machine [25], which allows recording the behavior of the structure in the covered state until it loses its load-carrying capacity, i.e. the structure's ability to carry the load. Tests carried out with a constant feed rate of the head of the strength machine of 1mm/min at room temperature. Axial compression tests were carried out by placing specimens between special working heads whose flat platforms (crossheads) maintain parallelism throughout the experimental tests. During testing with the testing machine, the Aramis 2D optical deformation measurement system was used. This system allowed non-contact recording of the deformation of the specimen under compression, which eliminates the possibility of interference and measurement inconsistencies arising from contact between the measuring tool and the test piece. The operation of this system is based on the principle of Digital Image Correlation (DIC). The use of this measurement system in the present study made it possible to record phenomena such as buckling but especially failure, which was the focus of the study. Graphical representation of deformations provided a more detailed understanding of the nature of the damage phenomenon. In order to eliminate unwanted image overexposure of the recorded composite columns, filters were used to absorb excess light that could adversely affect the quality of the obtained images. This allowed the elimination of unfavorable optical effects and reflections. In addition, LED reflectors were used to ensure uniform illumination and adequate brightness, which eliminated the problem of uneven illumination [26,27].

Fig. 2. Test stand



Also used in the research was a Keyence VHX-970F digital microscope with a movable head mounted on an articulated arm, which allows observation of defects to identify and evaluate them. This microscope included a VHX-A97FP control console, VHX-

H5M 3D measurement software, VHX-7020 camera, VH-Z20T zoom lens (magnification $20\times\div200\times$), VH-Z00T zoom lens (magnification $0\times\div50\times$) and VHX-S600E tripod. The use of this device made it possible to record high-resolution images on which various forms of damage can be observed, such as warp and fiber discontinuity and material delamination [28,29].

4. NUMERICAL SIMULATIONS

Numerical studies were carried out using the Finite Element Method (FEM). Numerical simulations were performed using the commercial software Abaqus. For each structure analyzed, dedicated numerical models were developed, faithfully reproducing actual structures and experimental tests, based on the „Lamina” type modeling method using the material data shown in Table 1. The material model used in the numerical simulations (Lamina modeling type) enabling an orthotropic approach in composite material modeling. Material properties determined experimentally (shown in Table 1) were implemented under Elastic type properties and Fail Stress type properties. The models represented an eight-layer composite made of carbon-epoxy CFRP material, with layers of equal thickness arranged in three different lay-ups: 1 - [0/90/0/90]s, 2 - [45/-45/90/0]s and 3 - [90/-45/45/0]s. In order to represent the experimental studies, the traverses of the universal testing machine, modeled as non-deformable shell elements, were modeled in the numerical model, which made it possible to incorporate boundary conditions into the numerical model. A numerical model of the composite structure was placed between the non-deformable shell elements. Discrete models of the composite structures were designed using Continuum Shell with SC8R-type finite elements (eight-node general-purpose shell elements with three degrees of freedom (translations) at each node). The traverses of the universal testing machine were modeled using Shell elements of type R3D4 (four-node elements with six degrees of freedom, i.e., three translational and three rotational). The global mesh density of the discrete composite column model was 2 mm, and the composite structure model consisted of 9200 finite elements. For the discrete model of plate elements, the global mesh density was 2.5 mm, and the model consisted of 1120 finite elements.

The FEA-based study used SC8R-type finite elements due to significantly more favorable test results than either S4R or S8R-type shell elements. Due to the high stiffness of the composite profiles, the composite modeling technique using SC8R (Continuum Shell) type elements made it possible to obtain higher convergence in terms of both structural stability and load carrying capacity.

To represent the correct interaction between the composite element and plate elements, contact relations were defined, taking into account contact interaction in the normal and tangential directions. In order to provide the correct interaction between the mating surfaces of the elements, especially in the post-buckling condition, the effect of frictional interaction in the tangential direction was taken into account. A “penalty” contact type was used, with a friction coefficient value of 0.2. Contact in the normal direction was modeled using a so-called “hard” contact of the normal-overclosure type, which allows separation of elements during the course of the numerical analysis.

To reproduce the experimental conditions, boundary conditions were defined at reference points coupled to non-deformable shell elements. For the lower plate, all degrees of freedom of the reference point were locked. On the other hand, for the upper plate, realizing axial compression of the material, the direction on the Z-axis

was left unrestrained, making it possible to introduce displacement of the reference point - thus simulating the phenomenon of axial compression of the composite structure.

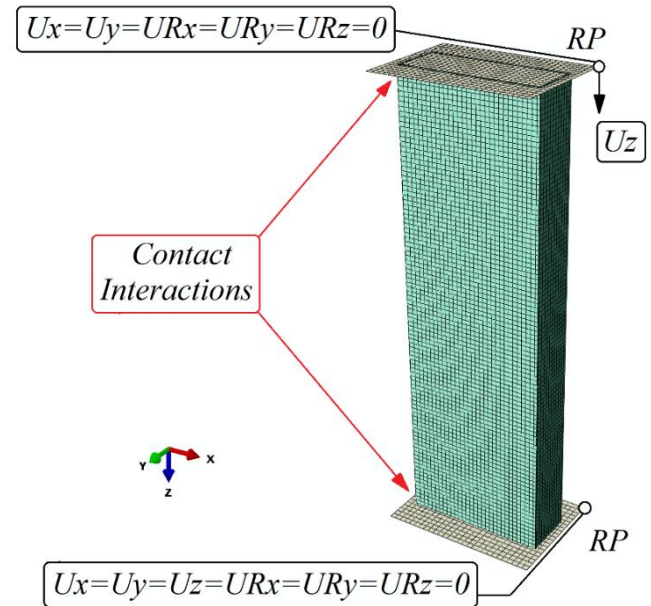


Fig. 3. Numerical model with boundary conditions

Numerical research was carried out in two stages, and in the first stage a model was developed to enable buckling state analysis, in which the force and buckling form of the structure were determined based on the minimum potential energy criterion. The solution of the linear eigenproblem is presented in Eq. (1), and its detailed description is contained in the works [2,8].

$$(K_0^{NM} + \lambda_i K_A^{NM})v_i^M = 0 \quad (1)$$

where: K_0^{NM} - structural stiffness matrix, equivalent to the initial condition, which includes the effects of preloads P^N , K_A^{NM} - the differential matrix of initial stress and load stiffness resulting from the incremental loading pattern (Q^N), λ_i - is the eigenvalues, v_i^M - represents the buckling mode, known as the eigenvectors, M and N - the degrees of freedom of the entire model, i - buckling form (mode). The critical load is represented by the equation: $P^N + \lambda_i Q^N$.

The present study didn't focus on the first stage of the research. This stage only served to correctly conduct the target nonlinear structural capacity calculations based on the obtained forms of loss of stability. The target, and the one on which the work focused, stage of numerical research was to conduct nonlinear stability analysis of the structure. In the present analysis, the obtained forms of loss of stability were used and geometric imperfections were taken into account in order to correctly carry out the nonlinear load capacity analysis. This approach makes it possible to reproduce imperfections in the shape of real structures that arise during the manufacturing process. Load simulations in the full load-carrying range were carried out using the Newton-Raphson method, an incremental-iterative method that allows analysis of the structure's behavior in the covered state, taking into account the phenomenon of degradation of the structure's stiffness due to damage initiation and evolution. The method used has enabled the use of an advanced material degradation model known as Progressive Failure Analysis (PFA). Using the Progressive Failure Analysis model [30], taking into consideration the damage initiation criterion based on the

Hashin criterion [31,32], and the damage evolution criterion based on the energy criterion [33,34]. This made it possible to carry out a numerical analysis, taking into account the adverse effects of damage caused by loading the structure on the load carrying capacity of composite structures. The damage initiation condition is achieved when any of the following equations reaches a value of 1:

$$F_f^t = \left(\frac{\hat{\sigma}_{11}}{X^T}\right)^2 + \alpha \left(\frac{\hat{\tau}_{12}}{S^L}\right)^2 = 1, (\hat{\sigma}_{11} \geq 0), \quad (2)$$

$$F_f^c = \left(\frac{\hat{\sigma}_{11}}{X^C}\right), (\hat{\sigma}_{11} < 0), \quad (3)$$

$$F_m^t = \left(\frac{\hat{\sigma}_{22}}{Y^T}\right)^2 + \left(\frac{\hat{\tau}_{12}}{S^L}\right)^2 = 1, (\hat{\sigma}_{22} \geq 0), \quad (4)$$

$$F_m^c = \left(\frac{\hat{\sigma}_{22}}{Y^C}\right)^2 + \left[\left(\frac{Y^C}{2S^T}\right)^2 - 1\right] \frac{\hat{\sigma}_{22}}{Y^C} + \left(\frac{\hat{\tau}_{12}}{S^L}\right)^2 = 1, (\hat{\sigma}_{22} < 0), \quad (5)$$

where: X^T and X^C - tensile and compressive strength in the direction along the fibers, Y^T and Y^C - tensile and compressive strength in the direction perpendicular to the fibers, S^L and S^T - shear strength in the direction along and transverse to the fibers, α - effect of shear stress, $\hat{\sigma}_{11}$, $\hat{\sigma}_{22}$, $\hat{\tau}_{12}$ - the components of the effective stress tensor.

Damage is defined as the loss of effective cross-sectional area [35], so in order to describe the phenomenon of damage, the damage coefficient d was presented in scalar form. A value of this coefficient of 0 indicates that no damage has occurred, while reaching a value of 1 indicates damage to the structure. The effective stress is defined as [36]:

$$\hat{\sigma} = M\sigma = \begin{bmatrix} \frac{1}{1-d_f} & 0 & 0 \\ 0 & \frac{1}{1-d_m} & 0 \\ 0 & 0 & \frac{1}{1-d_s} \end{bmatrix} \begin{pmatrix} \sigma_{11} \\ \sigma_{22} \\ \tau_{12} \end{pmatrix} \quad (6)$$

where: $\hat{\sigma}$ - effective tension, σ - apparent tension (Cauchy nominal), d - damage parameter: fiber, matrix and shear damage, M - damage operator, σ_{ij} - stresses on the appropriate directions.

A model accounting for the degradation of the stiffness matrix coefficients was applied for the analysis of anisotropic materials reinforced with long continuous fibers. Based on equation (6) and the quantitative analysis of the Poisson's ratio degradation [36], the compliance matrix, considering the damage, can be expressed as:

$$F = \begin{bmatrix} \frac{1}{(1-d_f)E_1} & -\frac{\nu_{12}}{E_2} & 0 \\ -\frac{\nu_{12}}{E_1} & \frac{1}{(1-d_m)E_2} & 0 \\ 0 & 0 & \frac{1}{(1-d_s)G_{12}} \end{bmatrix} \quad (7)$$

The damaged stiffness matrix can be expressed as:

$$C = \frac{1}{A} \begin{bmatrix} (1-d_f)E_1 & (1-d_f)(1-d_m)\nu_{12}E_1 & 0 \\ (1-d_f)(1-d_m)\nu_{12}E_2 & (1-d_f)E_2 & 0 \\ 0 & 0 & A(1-d_s)G_{12} \end{bmatrix} \quad (8)$$

The parameter A in the equation is expressed as:

$$A = 1 - \nu_{12}\nu_{21}(1-d_f)(1-d_m) \quad (9)$$

In the case where damage initiation has occurred in the composite material (i.e., when any of the above equations are satisfied), further loading of the composite structure results in damage evolution, leading to the gradual degradation of the composite structure's

stiffness until the loss of load-carrying capacity. Below are the parameters related to the destruction phenomenon, and a detailed description of the damage evolution phenomenon has been presented in the following articles [8,25].

$$d_f = \begin{cases} d_f^t, & \text{if } \hat{\sigma}_{11} \geq 0 \\ d_f^c, & \text{if } \hat{\sigma}_{11} < 0 \end{cases} \quad (10)$$

$$d_m = \begin{cases} d_m^t, & \text{if } \hat{\sigma}_{22} \geq 0 \\ d_m^c, & \text{if } \hat{\sigma}_{22} < 0 \end{cases} \quad (11)$$

$$d_s = 1 - (1-d_f^t)(1-d_f^c)(1-d_m^t)(1-d_m^c) \quad (12)$$

where: d_f - fiber damage parameter, d_m - matrix damage parameter, d_s - shear damage parameter.

When the damage initiation condition is realized, further loading of the thin-walled composite column will lead to degradation of the material's stiffness parameters. To allow simulation of the evolution of this phenomenon, it is necessary to introduce additional parameters of the damage energy. This process is controlled by damage variables, and its evolution is based on the fracture energy G_c , which is released during damage propagation. In the context of damage evolution, it is required to determine the energy parameters G_c^{ft} , G_c^{fc} , G_c^{mt} and G_c^{mc} , which represent the energies dissipated during damage for the tension and compression of the fiber and matrix. Damage evolution begins when the initiation criterion based on Hashin's criterion is met, which allows progressive failure analysis (PFA) to be performed, as detailed shown in the literature [8,25].

5. RESEARCH RESULTS

The application of experimental and numerical research methods enabled the assessment of the impact of layer configuration on the load-carrying capacity of thin-walled composite structures. Utilizing interdisciplinary research methods allowed for determining the maximum loads that the analyzed structures can withstand. The studies conducted with the use of a universal testing machine facilitated the determination of experimental equilibrium paths, which served as the basis for calculating maximum load capacities (P_f). Three different layer configurations were compared, with three actual structures prepared and tested for each case. The experimentally determined equilibrium paths and those calculated using the finite element method were collated and presented in Figure 4, providing a graphical representation of the differences among the results. The maximum load values obtained through experimental and numerical methods are presented in Table 2. All units of the obtained results have been presented in Newtons (N). The recorded strain results, obtained via the Aramis 2D optical deformation system and expressed as percentages, are presented with an accuracy of three decimal places.

The tests carried out showed that configuration 1 had the highest experimentally determined average limit (failure) load value, achieving about 1.30 times the load of the lowest observed average load-carrying capacity for configuration 3, and nearly 1.17 times the load of the average load-carrying capacity observed for configuration 2 (in experimental tests). Similar trends were observed in the numerical analyses, where the same samples achieved the highest and lowest load-carrying values. The numerical simulations confirmed the results of the experimental studies, indicating that the failure load for configuration 1 was 1.27 times higher than for configuration 3 and approximately 1.17 times higher than for configuration 2.

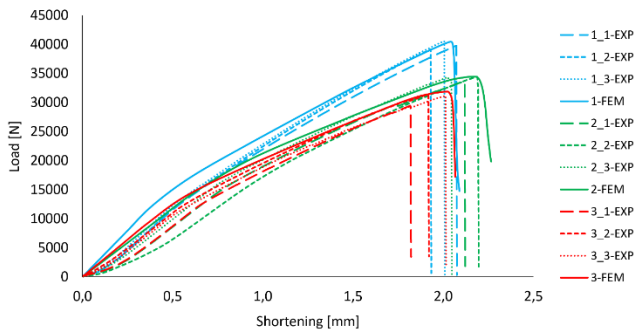


Fig. 4. Summary of post-buckling equilibrium paths

Tab. 1. Failure force values obtained experimentally and numerically

Spec. No Lay-up	1 (N)	2 (N)	3 (N)	EXP Avg.Value (N)	FEM (N)
[0/90/0/90] _s	39799.60	39150.57	40573.07	39841.08	40462.60
[45/-45/90/0] _s	33661.53	34416.62	34364.65	34147.60	34456.80
[90/-45/45/0] _s	29448.82	31415.54	31172.51	30678.96	31884.60

The conducted studies demonstrated a high level of agreement between the results obtained from experimental tests and numerical simulations, both qualitatively and quantitatively. The analysis of the equilibrium paths showed a good correlation between the characteristics obtained by experimental and numerical methods. It was observed that the loss of load-carrying capacity occurs at similar failure load values and with comparable shortening in both methods. The similarity in the behavior of the characteristics obtained through the finite element method indicates a high consistency of the numerical model with the experimental results. A quantitative analysis of the load-carrying forces obtained experimentally and numerically showed very good agreement. The failure load values obtained numerically were slightly higher than the average experimental values—about 1.016 times higher for configuration 1, approximately 1.009 times higher for configuration 2, and around 1.039 times higher for configuration 3.

The comparison of the equilibrium path progression revealed that the characteristics obtained through the finite element method display slightly higher force values compared to experimental results, especially noticeable in the early stages of structural loading. This suggests a greater stiffness in the numerical models. Discrepancies between experimental results and numerical simulations are attributed to imperfections in the sample manufacturing methods, which cause minor geometric and structural inaccuracies in the actual composite structures. Nonetheless, these differences are minimal and do not affect the overall quality of the conducted studies.

In the conducted study, it was observed that the analyzed structures failed in areas located near the midpoint of the composite column height. Additionally, it was shown that the thin-walled structures under investigation lose their load-carrying capacity due to layer cracking, matrix rupture, and interlayer delamination, as illustrated in Figure 6. Experimental studies revealed complex failure modes that exhibited varied forms of structural damage. For profiles of types 1 and 3, the predominant damage mechanism was distinct transverse cracking of the layers, perpendicular to the column

height, which results from the specific layer arrangement. This process was further associated with the occurrence of delamination. In contrast, for the second profile type, the primary damage mechanism involved layer cracking at a 45° angle relative to the longitudinal direction of the structure, resulting from the orientation of the laminate's outer layers (45°/-45°), accompanied by delamination phenomena.

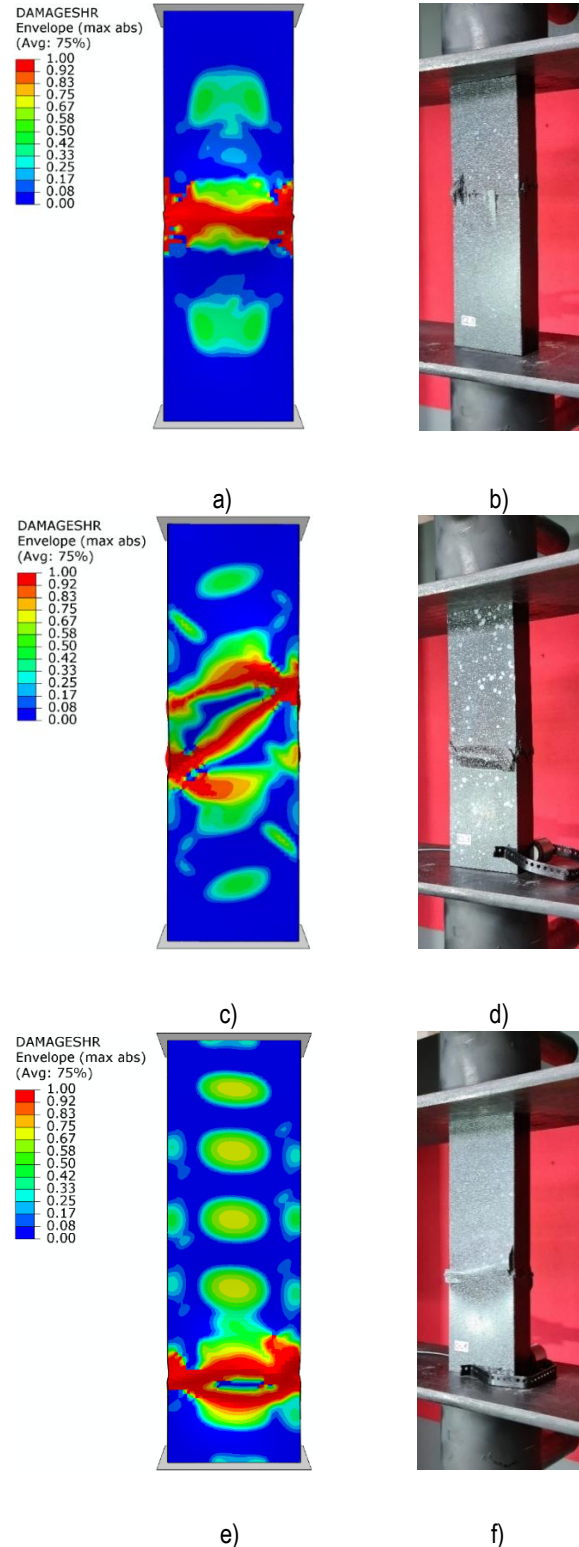


Fig. 5. Comparison of numerical-experimental failure: a) FEM – 1 lay-up, b) EXP – 1 lay-up, c) FEM – 2 lay-up, d) EXP – 2 lay-up, e) FEM – 3 lay-up, f) EXP – 3 lay-up

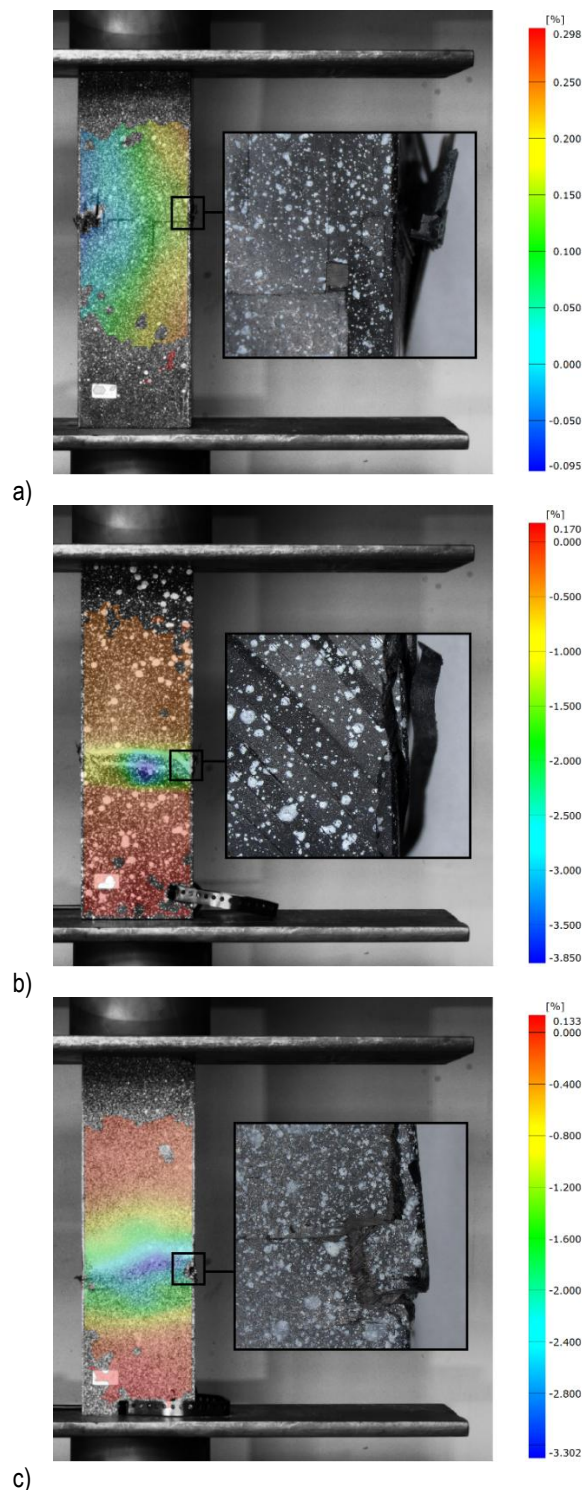


Fig. 6. Damaged structures with graphical visualization of deformations and enlarged representation of selected damage areas: a) 1 lay-up, b) 2 lay-up, c) 3 lay-up

The analysis of the damage forms in the tested profiles, as shown in the figures above, revealed a significant influence of layer arrangement on the nature of the damage. The configuration of layers determines the intensity of damage from cracking as well as the susceptibility to delamination. Despite differences in the types of damage observed, the affected areas remained similar regardless of the layer arrangement in the composite.

The numerical simulations conducted using the finite element method indicated that the outer and inner layers of the laminate are

more susceptible to damage, and consequently, to failure, compared to the central layers of the composite structure. A comparison of the damage levels is illustrated in the figure below, using the type 1 - $[0/90/0/90]_s$ profile as an example:

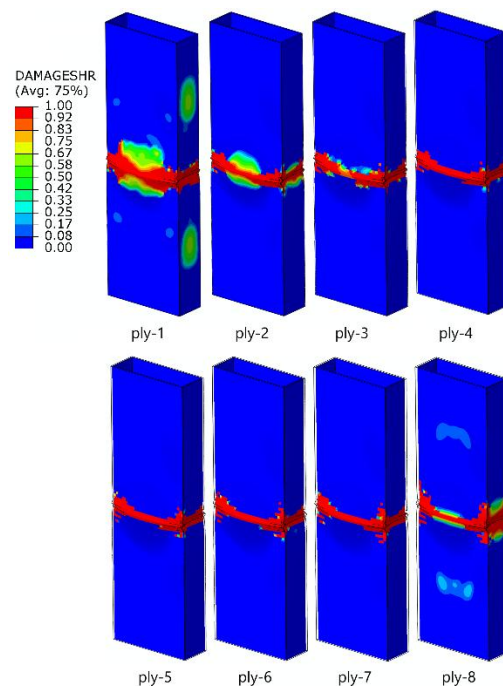


Fig. 7. Comparison of the damage level of individual layers

It was observed that the failure phenomenon is more extensive in the outer layers of the composite, which was confirmed by both numerical simulations and experimental studies. The damage forms obtained provide the basis for the development of more advanced FEM models, such as damage modeling techniques using CZM (Cohesive Zone Model) or XFEM (Extended Finite Element Method), applied to the analysis of delamination and fracture of composite material layers.

6. CONCLUSIONS

The subject of the study was an eight-layer column made of carbon-epoxy composite with a cross-sectional dimension of 60 mm x 20 mm, height of 200 mm, and thickness of 1.24 mm, with three different layer configurations: 1 - $[0/90/0/90]_s$, 2 - $[45/-45/90/0]_s$, 3 - $[90/-45/45/0]_s$. The samples were subjected to axial compression testing using a universal testing machine to determine the load-carrying capacity. The tests were conducted on nine real specimens, with three specimens produced for each layer configuration, and each specimen was tested once until failure.

Numerical simulations using the finite element method were also performed. Proprietary numerical models were developed, using the Lamin model dedicated to composite materials. The developed models reflected the conditions of the experiments carried out and the mechanical properties of the tested profiles, making it possible to analyze their behavior over the full range of loading, up to the complete failure of the structure.

The conducted studies showed that the layer arrangement significantly affects the load-carrying capacity of composite columns. Configuration 1 - $[0/90/0/90]_s$ had the highest load-carrying

capacity, while configuration 3 configuration - $[90/-45/45/0]_s$ had the lowest. Table 2 presents the detailed results of the experimental and numerical studies. The analysis of the obtained results revealed a high level of agreement between the experimentally obtained results and the numerical analysis outcomes. This indicates the high quality and accuracy of the developed numerical models. Additionally, the analysis of equilibrium paths confirms a high level of convergence between the numerical analyses and the conducted tests.

The damage analysis revealed that the most susceptible layers to failure are the outermost and innermost layers of the laminate. The middle layers exhibit less susceptibility to damage, as shown in Figure 7. It was also observed that the primary forms of failure are delamination and layer and matrix cracking, with the damage localized in the area around the midpoint of the composite column's height, as presented in Figure 6.

REFERENCES

- Różyło P, Dębski H. Stability and load-carrying capacity of short composite Z-profiles under eccentric compression. *Thin-Walled Structures*. 2020;157:107019.
- Urbaniak M, Świniarski J, Czapski P, Kubiak T. Experimental investigations of thin-walled GFRP beams subjected to pure bending. *Thin-Walled Structures*. 2016;107(1):397-404.
- Drożdź M, Podolak P, Czapski P, Zgórniak P, Jakubczak P. Failure analysis of GFRP columns subjected to axial compression manufactured under various curing-process conditions. *Composite Structures*. 2021;262:113342.
- Baker A, Dutton S, Donald KD. *Composite materials for aircraft structures*. Reston: American Institute of Aeronautics and Astronautics. 2004.
- Soutis C. Carbon fibre reinforced plastics in aircraft construction, *Materials Science and Engineering*. 2005;412 (1-2):171-176.
- Różyło P, Falkowicz K. Stability and failure analysis of compressed thin-walled composite structures with central cut-out, using three advanced independent damage models. *Composite Structures*. 2021;273:114298.
- Banat D, Mania RJ. Failure assessment of thin-walled FML profiles during buckling and postbuckling response. *Composites Part B: Engineering*. 2017;112:278-289.
- Różyło P. Stability and failure of compressed thin-walled composite columns using experimental tests and advanced numerical damage models. *International Journal For Numerical Methods In Engineering*. 2021;122(18):5076-5099.
- Li ZM, Qiao P. Buckling and postbuckling behavior of shear deformable anisotropic laminated beams with initial geometric imperfections subjected to axial compression. *Engineering Structures*. 2015;85:277-292.
- Gliszczczyński A, Kubiak T. Progressive failure analysis of thin-walled composite columns subjected to uniaxial compression. *Composite Structures*. 2017;169:52-61.
- Dębski H, Samborski S, Różyło P, Wymulski P. Stability and load-carrying capacity of thin-walled FRP composite Z-profiles under eccentric compression. *Materials*. 2020;13(13):2956.
- Różyło P. Failure phenomenon of compressed thin-walled composite columns with top-hat cross-section for three laminate lay-ups. *Composite Structures*. 2023;304(1):116381.
- Różyło P, Smagowski W, Paśnik J. Experimental Research in the Aspect of Determining the Mechanical and Strength Properties of the Composite Material Made of Carbon-Epoxy Composite. *Advances in Science and Technology Research Journal*. 2023;17(2):232-246.
- Różyło P, Rogala M, Paśnik J. Load-Carrying Capacity of Thin-Walled Composite Columns with Rectangular Cross-Section under Axial Compression. *Materials*. 2024;17(7):1615.
- Różyło P, Roslaniec K, Kuciej M. Buckling of Compressed Thin-Walled Composite Structures with Closed Sections. *Advances in Science and Technology Research Journal*. 2023;17(6):63-72.
- Podolak P, Drożdź M, Czapski P, Kubiak T, Bienias J. The failure mode variation in post-buckled GFRP columns with different stacking sequences - Experimental damage analysis and numerical prediction. *International Journal of Mechanical Sciences*. 2021;210:106747.
- Calzada KA, Kapoor SG, DeVor RE, Samuel J, Srivastava AK. Modeling and interpretation of fiber orientation-based failure mechanisms in machining of carbon fiber-reinforced polymer composites. *Journal of Manufacturing Processes*. 2012;14(2):141-149.
- Anto AD, Mia S, Hasib MA. The influence of number and orientation of ply on tensile properties of hybrid composites. *Journal of Physics*. 2019;2(2):025002.
- Różyło P. Determined Material Properties within the framework of the National Science Centre project (OPUS) No. 2021/41/B/ST8/00148. <https://doi.org/10.5281/zenodo.7606942>.
- Wymulski P. Numerical and Experimental Study of Crack Propagation in the Tensile Composite Plate with the Open Hole. *Advances in Science and Technology Research Journal*. 2023;17(4):249-261.
- Czapski P, Jakubczak P, Bienias J, Urbaniak M, Kubiak T. Influence of autoclaving process on the stability of thin-walled, composite columns with a square cross-section – Experimental and numerical studies. *Composite Structures*. 2020;250:112594.
- York CB, Almeida SFM. On Extension-Shearing Bending-Twisting coupled laminates. *Composite Structures*. 2017;164:10-22.
- York CB. Coupled quasi-homogeneous orthotropic laminates. *Mechanics of Composite Materials*. 2011;47(4):405-426.
- Rzeczkowski J, Paśnik J, Samborski S. Mode III numerical analysis of composite laminates with elastic couplings in split cantilever beam configuration. *Composite Structures*. 2021;265:113751.
- Różyło P, Dębski H. Failure study of compressed thin-walled composite columns with top-hat cross-section. *Thin-Walled Structures*. 2022;180:109869.
- Dębski H, Różyło P, Wymulski P, Falkowicz K, Ferdynus M. Experimental study on the effect of eccentric compressive load on the stability and load-carrying capacity of thin-walled composite profiles. *Composites Part B*. 2021;226:109346.
- Dębski H, Jonak J. Failure analysis of thin-walled composite channel section columns. *Composite Structures*. 2018;132:567-574.
- Roslaniec K, Różyło P. Stability of Thin-Walled Composite Structures with Closed Sections Under Compression. *Advances in Science and Technology Research Journal*. 2024;18(3):188-199.
- Różyło P. Limit states of thin-walled composite structures with closed sections under axial compression. *Composites Part B: Engineering*. 2024;287:111813.
- Lapczyk I, Hurtado JA. Progressive damage modeling in fiber-reinforced materials. *Composites Part A: Applied Science and Manufacturing*. 2007;38(11):2333-2341.
- Hashin Z, Rotem A. A Fatigue Failure Criterion for Fiber Reinforced Materials. *Journal of Composite Materials*. 1973; 7(4):448-464.
- Hashin Z. Failure Criteria for Unidirectional Fiber Composites. *Journal of Applied Mechanics*. 1980;47(2):329-334.
- Lemaitre J, Plumtree A. Application of Damage Concepts to Predict Creep-Fatigue Failures. *Journal of Engineering Material and Technology*. 1979;101(3):284-292.
- Ribeiro ML, Vandepitte D, Tita V. Damage Model and Progressive Failure Analyses for Filament Wound Composite Laminates. *Applied Composite Materials*. 2013;20:975-992.
- Kachanov L. Time of the Rupture Process under Creep Conditions, *Izv. An SSSR. Otd. Tekh. Nauk*. 1958;8:26-31.
- Laws N, Dvorak GJ, Hejazi M. Stiffness changes in unidirectional composites caused by crack systems. *Mechanics of Materials*. 1983;2(2):127-137.



The research was conducted under project No. 2021/41/B/ST8/00148, financed by the National Science Centre, Poland. This research was funded in whole or in part by National Science Centre, Poland [2021/41/B/ST8/00148]. For the purpose of Open Access, the author has applied a CC-BY public copyright license to any Author Accepted Manuscript (AAM) version arising from this submission.

Kuba Roslaniec:  <https://orcid.org/0000-0002-4093-1702>

Patryk Różyło:  <https://orcid.org/0000-0003-1997-3235>



This work is licensed under the Creative Commons BY-NC-ND 4.0 license.

HEAT CONDUCTION PROBLEMS FOR HALF-SPACES WITH TRANSVERSAL ISOTROPIC GRADIENT COATING

Roman KULCHYTSKYI-ZHYHAILO*

*Białystok University of Technology, Faculty of Mechanical Engineering, 45C Wiejska Str., Białystok 15-351, Poland

r.kulczycki@pb.edu

received 5 September 2024, revised 20 November 2024, accepted 23 March 2025

Abstract: The axisymmetric heat conduction problems of local surface heating for a FGM-coated body are considered. The following types of the coating were considered: a transversal isotropic gradient coating with continuously varying thermal properties; a coating consisting of a finite number of homogeneous transversal isotropic layers with slowly varying thermal properties; a coating consisting of a finite number of representative cells containing two homogeneous layers. The solution for a specially selected multilayer coating was compared with that for a transversal isotropic coating with exponentially varying properties. It has been shown that multilayer coatings with a step change of the thermal properties can be described using a homogenization method with microlocal parameters.

Key words: heat conduction problem, temperature, heat flux, transversal isotropic gradient coating, multi-layered structure

1. INTRODUCTION

In engineering practice, assessing the reliability of machine components or the strength of structures is closely related to the problems of heat generation and conduction. High temperature may cause an additional thermos-elastic deformation, thermal stress-induced cracking, and even a change of material properties. Therefore, the substrate is usually coated with a protective thermal barrier. The base material used in most high-temperature applications is ceramic. However, ceramics have some shortcomings, such as being brittle and susceptible to cracking. Protective coverings made of functionally graded material (FGM) are often used to alleviate these problems. Unlike a homogeneous or periodic coating, FGM-coating allows matching material properties at the interface. As a result, these coating structures are able to withstand high-temperature gradients without structural failures. Many experimental and numerical studies [1 – 3] have shown that FGMs used as coatings can effectively reduce thermal stresses, enhance interface bonding strength and improve the surface properties of materials.

Actually, FGMs are mixtures of two or more different materials. Volume fraction of each material varies along the thickness of the coating. The gradual change in material properties is adapted to meet the different requirements. The mathematical models of such materials are derived by using some averaging procedures. In the case of the gradient coating that has the properties of an isotropic solid at the macro level, classical averaging methods are still often used: the Voigt estimation [4] or the Reus's estimation [5]. However, these estimates are insufficient [6] to properly describe FGM-coating that has the anisotropic properties at the macro level, in particular the multilayer structures. Therefore, increasing usage of multi-layered coatings requires development of more accurate mathematical models for analysis of experimental results.

The anisotropic properties of the multi-layer coating are taken into account in homogenization methods. Particularly noteworthy is

the homogenization method with microlocal parameters [7, 8], which was previously used to solve problems for periodic multilayer media. In the problems of thermal conductivity for a multilayer coating with a periodic structure [9, 10], this method makes it possible to evaluate not only mean values of the analyzed state functions but also their local values in every layer of the periodicity cell.

It is usually assumed that the condition for applying the homogenization method is that a considered body consists of a periodically repeating representative unit cells. Kulchytsky-Zhyhailo et al. demonstrated [11, 12] the possibility of using the homogenization method with microlocal parameters for modeling cylindrical and spherical multilayer structures with slowly changing properties. The authors solved one-dimensional centrally-symmetric thermo-elasticity problems for a hollow multilayer cylindrical or spherical vessel. The vessel wall was made of a composite material assembled of concentric perfectly connected representative cells. A representative cell was composed of two homogeneous layers. The parameter describing the volumetric fraction of the first-kind layer in a representative cell may have been different for different representative cells. It has been shown that the solution based on the homogenization method is fully consistent with the solution for the problem in which each layer is considered separately.

In the case where a multilayer coating with a periodic structure is described by the homogenization method, the problem consists in solving the differential equations with constant coefficients. The analytical solution of obtained equations is known. A homogenized multilayer coating with slowly changing properties is described by the differential equations with variable coefficients. The analytical methods for solving such equations are known only for a few forms of a functions describing material properties. An overview of cases in which we can find analytical solutions to selected problems can be found in [13]. In this paper the problem for transversely isotropic half-space with Young's and shear moduli varying exponentially with depth was considered. In recent years, a number of the fundamental solutions to an exponentially graded transversely isotropic

medium (half-space or layer) have been obtained [14 – 22]. The analytical solution algorithm usually consists of writing the state function in integral form, which integrands contain Fourier or Hankel transforms of the forcing factor and the fundamental solution of ordinary differential equations with variable coefficients, obtained using the integral transformations.

Parallel with the application of analytic methods for the solution of partial differential equations, a gradient isotropic coatings was also modelled by using an approach [23 – 34] according to which the coating is replaced with a package of homogeneous or inhomogeneous layers. Solution in each layer was constructed analytically. This made it possible to solve problems for functionally graded isotropic coating with arbitrarily varying properties. For transversal isotropic gradient coating, this approach was not used.

In this paper, the axisymmetric thermal conduction problem of the local heating of the surface of an inhomogeneous anisotropic half-space is investigated. The considered half space consists of a homogeneous substrate and a graded transversely isotropic coating with the slowly graded structure. In the first part of the article, the effectiveness of the algorithm based on replacing the gradient coating with continuously varying thermal properties with the package of homogeneous transversally isotropic layers is verified. For this purpose, the solution for the multilayer coating was compared with that for a transversely isotropic coating with exponentially varying properties.

In the second part of the paper, a gradient coating containing a finite number of representative cells consisting of two homogeneous isotropic layers was investigated. The considered coating was described using the homogenization method with microlocal parameters. The problem for the homogenized coating was solved using the algorithm presented in the first part of the work. Good agreement was shown between the solution for the coating described by the homogenization method and the solution for the multilayer coating with a step change in thermal properties.

2. FORMULATION OF THE PROBLEM

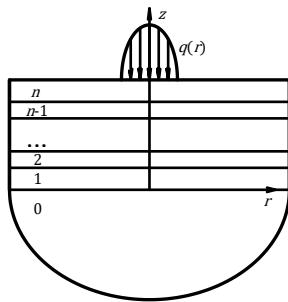


Fig. 1. The scheme of considered problem

Assume that the surface $z = h$ of the graded coated half-space is heated by a heat flux $q(r)$ on the circle of radius a , where r, z are dimensionless cylindrical coordinates referred to the linear size $a, h = H/a, H$ is thickness of the coating (Fig. 1). The remaining surface of the inhomogeneous half-space is thermally insulated.

The considered half space is formed by the homogeneous substrate with the heat conductivity coefficient K_0 and a transversal isotropic gradient layer with the heat conductivity coefficients K_r and K_z , which can vary along its thickness. Let the homogeneous substrate occupies the region $0 \leq r < \infty, -\infty < z \leq 0$. The

inhomogeneous coating occupies the region $0 \leq r < \infty, 0 \leq z \leq h$. Functions $K_r(z)$ and $K_z(z)$ are continuous in intervals (h_{i-1}, h_i) , $i = 1, \dots, n$, $h_0 = 0, h_n = h$, while points $h_i, i = 1, \dots, n-1$ are discontinuity points of the first kind. On the surfaces of the discontinuity $z = h_i, i = 1, \dots, n-1$ and on the surface $z = h_0$ between the coating and the substrate, the conditions of perfect thermal contact are satisfied.

The analysed problem reduces to a boundary problem, which involves solving the following partial differential equation

$$\frac{\partial}{\partial z} \left(K_z \frac{\partial T}{\partial z} \right) + \frac{K_r}{r} \frac{\partial}{\partial r} \left(r \frac{\partial T}{\partial r} \right) = 0, r \geq 0, z \in \cup_{i=0}^n (h_{i-1}, h_i) \quad (1)$$

and satisfying the boundary conditions:

$$K_z(h_n) \frac{\partial T}{\partial z}(r, h_n) = a q(r) H(1-r), \quad (2)$$

$$T(r, h_i - 0) = T(r, h_i + 0), i = 0, 1, \dots, n-1, \quad (3a)$$

$$K_z(h_{i-}) \frac{\partial T}{\partial z}(r, h_{i-}) = K_z(h_{i+}) \frac{\partial T}{\partial z}(r, h_{i+}), i = 0, 1, \dots, n-1, \quad (3b)$$

$$T(r, z) \rightarrow 0, r^2 + z^2 \rightarrow \infty, \quad (4)$$

where T is the temperature, $K_r(z) = K_z(z) = K_0, z < 0, h_{i+} = h_i + 0, h_{i-} = h_i - 0, h_{-1} \rightarrow -\infty, H(r)$ is Heaviside step function.

3. METHOD OF SOLUTION

The solution of the boundary value problem (1) – (4) is sought by applying the Hankel integral transformation

$$\bar{T}(s, z) = \int_0^\infty T(r, z) r J_0(sr) dr, -\infty < z \leq h, s \geq 0, \quad (5)$$

where $J_0(sr)$ is the Bessel function.

Using the technique of the Hankel integral transformation, we transform the partial differential equation (1) to the form of the ordinary linear differential equation with variable coefficients

$$\frac{d}{dz} \left(K_z \frac{d\bar{T}}{dz} \right) - K_r s^2 \bar{T} = 0, z \in \cup_{i=0}^n (h_{i-1}, h_i). \quad (6)$$

The Hankel transform of the temperature for a homogeneous substrate that satisfies the regularity conditions at infinity (4) can be written in the form:

$$\bar{T}(s, z) = t_0(s) \exp(sz), z < 0, \quad (7)$$

where $t_0(s)$ is the unknown function.

The analytical form of the solution of the differential equation with variable coefficients (6) is known only for selected forms of the function $K_r(z)$ and $K_z(z)$.

3.1. Case A

Let $n = 1$. The dependence of the thermal conductivity coefficients on the z -coordinate is described by the formulas:

$$K_r(z) = K_r^{\text{int}} \exp(\beta z), K_z(z) = K_z^{\text{int}} \exp(\beta z), \quad (8a)$$

$$\beta = \frac{1}{h} \ln \left(\frac{K_z^{\text{sur}}}{K_z^{\text{int}}} \right), \quad (8b)$$

where K_z^{sur} is the heat conductivity coefficient on the surface of the inhomogeneous half-space in a direction normal to it.

The general solution to differential equation (6) in the Hankel transform space specified in the coating can be written in the form:

$$\bar{T} = t_1(s) \exp(\gamma_1 z) + t_2(s) \exp(\gamma_2(z - h)), 0 < z < h \quad (9)$$

where $t_1(s)$ and $t_2(s)$ are the unknown functions,

$$\gamma_{1,2} = -\frac{\beta}{2} \mp \frac{1}{2} \sqrt{\beta^2 + 4\kappa^2 s^2}, \kappa^2 = \frac{K_r^{\text{int}}}{K_z^{\text{int}}}. \quad (10)$$

Satisfying boundary conditions (2)–(4), the functions $t_i(s)$, $i = 0, 1, 2$ may be written as

$$t_i(s) = \frac{\bar{q}(s)a}{s\sqrt{K_r^{\text{sur}}K_z^{\text{sur}}}} \tilde{t}_i(s), \quad (11)$$

where the functions $\tilde{t}_i(s)$, $i = 0, 1, 2$ are obtained solution of linear equations:

$$\gamma_1 \tilde{t}_1(s) \exp(\gamma_1 h) + \gamma_2 \tilde{t}_2(s) = \kappa s, \quad (12a)$$

$$\gamma_1 \tilde{t}_1(s) \exp(\gamma_1 h) + \gamma_2 \tilde{t}_2(s) = \kappa s, \quad (12b)$$

$$K_0 s \tilde{t}_0(s) - \gamma_1 K_z^{\text{int}} \tilde{t}_1(s) - \gamma_2 K_z^{\text{int}} \tilde{t}_2(s) \exp(-\gamma_2 h) = 0 \quad (12c)$$

K_r^{sur} is the heat conductivity coefficient on the surface of the inhomogeneous half-space in a plane of transverse isotropy, $\bar{q}(s)$ is Hankel transform of order 0 of function $q(r)H(1-r)$:

$$\bar{q}(s) = \int_0^1 q(r) r J_0(sr) dr \quad (13)$$

3.2. Case B

In cases where the analytical solution of the differential equation with variable coefficients (6) is not known, the inhomogeneous coating can be replaced by a multilayer system of n homogeneous transversal isotropic layers. The thermal properties of the replacement coating are described by thermal conductivity coefficients:

$$\begin{bmatrix} K_r(z) \\ K_z(z) \end{bmatrix} = \begin{bmatrix} K_r^i \\ K_z^i \end{bmatrix}, h_{i-1} < z < h_i, i = 1, \dots, n, \quad (14)$$

where the parameters K_r^i and K_z^i are means value of functions $K_r(z)$ and $K_z(z)$ in the region (h_{i-1}, h_i) respectively.

The general solution to differential equation (6) in the Hankel transform space defined in the region (h_{i-1}, h_i) , $i = 1, \dots, n$ can be written in the form:

$$\bar{T} = t_{2i-1}(s) \sinh(\kappa_i^*) + t_{2i}(s) \cosh(\kappa_i^*), h_{i-1} < z < h_i \quad (15)$$

where $\kappa_i^* = s\kappa_i(h_i - z)$, $\kappa_i^2 = K_r^i/K_z^i$, $i = 1, \dots, n$.

Satisfying boundary conditions (2)–(3), the functions $t_i(s)$, $i = 0, 1, \dots, 2n$ may be written as

$$t_i(s) = \frac{\bar{q}(s)a}{s\sqrt{K_r^i K_z^i}} \tilde{t}_i(s), \quad (16)$$

where the functions $\tilde{t}_i(s)$, $i = 0, 1, \dots, 2n$ are obtained solution of linear equations:

$$\tilde{t}_0 - S_1 \tilde{t}_1 - C_1 \tilde{t}_2 = 0, \quad (17a)$$

$$K_0 \tilde{t}_0(s) + K_1^* C_1 \tilde{t}_1 + K_1^* S_1 \tilde{t}_2 = 0, \quad (17b)$$

$$\tilde{t}_{2i-2} - S_i \tilde{t}_{2i-1} - C_i \tilde{t}_{2i} = 0, i = 2, \dots, n, \quad (17c)$$

$$K_{i-1}^* \tilde{t}_{2i-3} - K_i^* C_i \tilde{t}_{2i-1} - K_i^* S_i \tilde{t}_{2i} = 0, i = 2, \dots, n, \quad (17d)$$

$$\tilde{t}_{2n-1} = -1, \quad (17e)$$

where $S_i = \sinh(s\kappa_i(h_i - h_{i-1}))$, $C_i = \cosh(s\kappa_i(h_i - h_{i-1}))$, $K_i^* = K_z^i \kappa_i$, $i = 1, \dots, n$.

3.3 Case C

Let the investigated coating in its cross section is composed of m representative cells (Fig. 2). The representative cell contains two homogeneous layers with the thermal conductivity coefficients K_1 , K_2 , and dimensionless thickness $\delta_1 = \eta\delta$, $\delta_2 = (1 - \eta)\delta$, where $\delta = h/m$ is dimensionless cell thickness. The parameter $\eta \in (0, 1)$ describes the content of the first type material in a representative cell and can vary along the thickness of the coating.

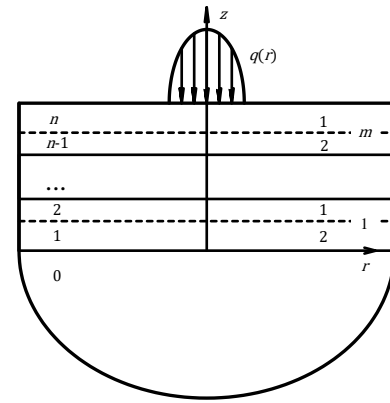


Fig. 2. The scheme of considered problem

The thermal properties of the investigated coating are described by thermal conductivity coefficients:

$$K_r(z) = K_z(z) = \begin{bmatrix} K_1, h_{2j-1} < z < h_{2j} \\ K_2, h_{2j-2} < z < h_{2j-1} \end{bmatrix}, j = 1, \dots, m. \quad (18)$$

The temperature induced in the considered inhomogeneous half-space can be evaluated through the use of two different concepts. One concept implies the analysis of the actual strata through writing the solution in the form of the formulas (15) and solving the system of equations (17) in which: $n = 2m$, $\kappa_i = 1$, $i = 1, \dots, n$, $K_z^{2j} = K_1$, $K_z^{2j-1} = K_2$, $j = 1, \dots, m$.

3.4 Case D

A large number boundary conditions on the interfaces complicates the solution of the problem. Another approach is using a homogenized model in which properties of the homogenized coating are determined on the base of properties of the components. In the latter case, the material properties across the coating depend on the continuous function $\eta(z)$ chosen so that the relationships are satisfied:

$$\eta_j = \frac{1}{h_{2j} - h_{2j-2}} \int_{h_{2j-2}}^{h_{2j}} \eta(z) dz, j = 1, \dots, m, \quad (19)$$

where the parameter η_j describes the volume fraction of the layer of the first kind in the representation cell with the number j .

According to the homogenization method with microlocal parameters [7, 8], the solution in the coating is represented by the temperature $T^{\text{hom}}(r, z)$ which is determined by the thermal properties of the two layers forming the representative cell with account for the function $\eta(z)$. The function $T^{\text{hom}}(r, z)$ is obtained from solving boundary problem (1) – (4), with $n = 1$ and the heat conductivity coefficients computed through the use of the homogenization method in the form, as follows:

$$K_r(z) = K_1\eta(z) + K_2(1 - \eta(z)), 0 < z < h, \quad (20a)$$

$$K_z(z) = \frac{K_1 K_2}{K_2 \eta(z) + K_1 (1 - \eta(z))}, 0 < z < h. \quad (20b)$$

It should be noted that solving the problem with the homogenization method leads to the differential equation with variable coefficients (6), for which the analytical solution is not known. Therefore, the homogenized coating is replaced by a multilayer array of n homogeneous transverse isotropic layers. As in the section B, the thermal properties of the layers are described by formulas (14).

As a result of solving the system of equations (12) in case A or the system of equations (17) in cases B, C or D, the Hankel transform of the temperature is found. In order to restore the found temperature in the physical domain, we employ the inverse transform:

$$T(r, z) = \int_0^\infty \bar{T}(s, z) s J_0(sr) ds, -\infty < z \leq h, r \geq 0. \quad (21)$$

The integral (21) at internal points of the considered inhomogeneous half space ($z < h$) is taken with the help of the Gaussian quadrature. On the surface $z = h$, the considered integral is computed with regard for the asymptotic behavior of the function $\bar{T}(s, h)$ as $s \rightarrow \infty$:

$$\lim_{s \rightarrow \infty} \bar{T}(s, h) = \frac{a \bar{q}(s)}{s \sqrt{K_r(h) K_z(h)}}. \quad (22)$$

The integral in which the integrand is replaced by its asymptotic is taken analytically. It should be noted that the formula (22) describes the Hankel transform of order 0 of the temperature in a homogeneous transversal isotropic half-space with the heat conductivity coefficients $K_r(h)$ and $K_z(h)$. To find the remaining integrals, we apply the Gaussian quadrature.

4. NUMERICAL EXAMPLES AND DISCUSSION

We assume that

$$q(r) = q_0 \sqrt{1 - r^2}, r < 1. \quad (23)$$

The Hankel transform of the function $q(r)H(1 - r)$ is described by equation

$$\bar{q}(s) = q_0 \sqrt{\frac{\pi}{2}} \frac{J_{3/2}(s)}{s \sqrt{s}}, \quad (24)$$

where $J_{3/2}(s)$ is the Bessel function.

Formula to calculate the temperature over the surface of the homogeneous isotropic half-space with the heat conductivity coefficient K_0 have form

$$\frac{12TK_0}{aq_0} = \begin{cases} 3\pi(1 - 0.5r^2), & r \leq 1, \\ 4r^{-1}F(0.5, 0.5; 2.5; r^{-2}), & r > 1, \end{cases} \quad (25)$$

where F is hypergeometric function.

4.1 Case AB

First, we intend to verify the effectiveness of the algorithm based on replacing the gradient coating with continuously varying thermal properties with the package of homogeneous transversal isotropic layers. To this end, the solution for a gradient coating whose thermal properties are described by formulas (8) will be obtained using two approaches. The first approach is described in the section A, and the second approach is described in the section B.

If the functions $K_r(z)$ and $K_z(z)$ are described by formula (8), then:

$$\begin{bmatrix} K_r^i \\ K_z^i \end{bmatrix} = \begin{bmatrix} K_r^{\text{int}} \\ K_z^{\text{int}} \end{bmatrix} \frac{\exp(\beta h_i) - \exp(\beta h_{i-1})}{\beta(h_i - h_{i-1})}, \quad (26a)$$

$$\kappa_i^2 = \kappa^2 = \frac{K_r^{\text{int}}}{K_z^{\text{int}}}, i = 1, \dots, n. \quad (26b)$$

The analysis of the obtained relations enables us to conclude that the solution of the posed problem of modelling of the gradient coating by a package of layers depends on five dimensionless parameters: the ratios of the heat conductivity coefficients K_z^{sur}/K_0 , K_z^{int}/K_0 and K_r^{int}/K_0 , the dimensionless thickness of the coating h and the number of layers in the package n . The solution of the problem for the inhomogeneous coating obtained with regard for the continuous dependence of the thermal properties depends on the first four indicated parameters. In order to decrease the number of parameters, it will be assumed that the gradient coating is a thermal insulator with the heat conductivity coefficients: $K_z^{\text{sur}} = 0.2K_0$, $K_z^{\text{int}} = K_0$, $K_r^{\text{int}} = K_0$ or $5K_0$. In addition, it is assumed that: $h = 0.4$ and $n = 10, 20, 40, 80$ and 160 .

Figure 3 show the distributions of the temperature over the surface of the inhomogeneous half-space $z = h$ (black lines and rhombi) and over the interface between coating and base $z = 0$ (grey lines and rhombi) for two values of the parameter κ^2 .

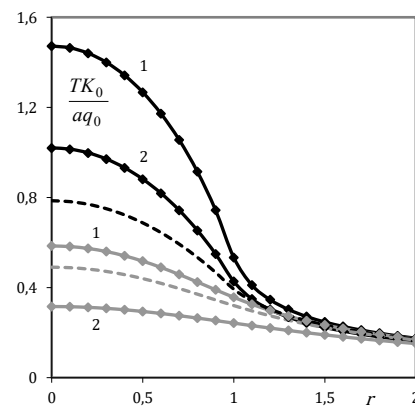


Fig. 3. Distributions of the temperature over the surface $z = h$ (black lines and rhombi) and over $z = 0$ (grey lines and rhombi), dashed lines – the distributions of the temperature for the homogeneous half-space: 1 – $\kappa^2 = 1$; 2 – $\kappa^2 = 5$; $n = 20$

Distributions of the radial heat flux along the surface $z = h$ are shown in Figure 4. In this figures, the continuous lines correspond to the solution of the problem with continuous variation of the thermal properties. The rhombi correspond to the results obtained for a package formed by 20 homogeneous transversal isotropic layers.

The dashed lines in Figures 3 and 4 describe the solution for a isotropic homogeneous half-space with the heat conductivity coefficient K_0 . The results of calculations presented in Figs. 3 and 4 show good agreement between the solutions obtained using the analysed two models of the considered coating.

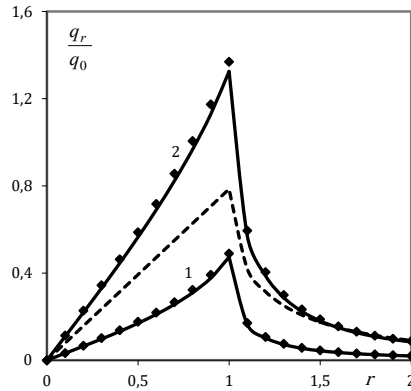


Fig. 4. Distributions of the radial heat flux along the surface $z = h$, dashed line – the distributions of the radial heat flux for the homogeneous half-space: 1 – $\kappa^2 = 1$; 2 – $\kappa^2 = 5$; $n = 20$.

As was to be expected, the highest temperature value is observed in the middle of the heating zone. At the interface between the coating and the substrate the maximum temperature occurs at the point $r = z = 0$. The maximum radial heat flux is formed on the boundary of the heating zone.

Tab. 1. Dependence of the dimensionless parameters $T_{\text{sur}}^{\text{max}} = \frac{T(0,h)K_0}{aq_0}$, $T_{\text{int}}^{\text{max}} = \frac{T(0,0)K_0}{aq_0}$, $q_{r,\text{sur}}^{\text{max}} = \frac{q_r(1,h)}{q_0}$ on the dimensionless parameter κ^2 and number of the layers n

κ^2	n	$T_{\text{sur}}^{\text{max}}$	$\varepsilon_{T_{\text{sur}}}, \%$	$T_{\text{int}}^{\text{max}}$	$\varepsilon_{T_{\text{int}}}, \%$	$q_{r,\text{sur}}^{\text{max}}$	$\varepsilon_{q_{r,\text{sur}}}, \%$
1	∞	1.4723		0.5847		0.4733	
	160	-0.0011		-0.0002		0.5103	
	80	-0.0036		-0.0007		0.9445	
	40	-0.0135		-0.0028		1.7952	
	20	-0.0537		-0.0113		3.4317	
	10	-0.2146		-0.0451		6.5039	
5	∞	1.0200		0.3158		13256	
	160	-0.0017		-0.0007		0.4731	
	80	-0.0064		-0.0017		0.9078	
	40	-0.0252		-0.0054		1.7408	
	20	-0.1005		-0.0204		3.2928	
	10	-0.4007		-0.0799		6.0922	

The dimensionless values $T(0,h)K_0/aq_0$, $T(0,0)K_0/aq_0$ and $q_r(1,h)/q_0$ for the problem with continuous variation of thermal properties for two values of parameter κ^2 , are presented in the corresponding columns of Table 1. In order to compare the difference between solutions, which is caused by an application of the two proposed approaches to solving the problem in the rows with $n = 160, 80, 40, 20$ and 10 we present the relative deviations (given in percent's) obtained for the multi-layered coating with the indicated number of the layers. As can be seen from Table 1, the double increase in the layer number cause the

fourfold decrease in the difference between the analyzed temperature values and the twofold decrease in the difference between the analyzed radial heat flux. The good agreement in temperature calculation is observed even for a relatively small number of layers in the package $n = 10$. The greatest difference between the analyzed solutions when calculating the radial heat flux at the boundary of the heating zone. It should be noted that the relative big difference occurs only in a small area around the point $r = 1, z = 0$. For 40 layers in the package this difference do not exceed 2%.

Lines 1 in Figures 3 and 4 describe an insulating coating with isotropic properties, i.e., a coating with equal heat conductivity coefficients in the plane $z = \text{const.}$ and in a direction normal to it. As can be seen from Figure 3, the temperature level in the heating zone in the half-space with such coating is much higher than the corresponding temperature level in the half-space without coating. The temperature level on the surface of the substrate is also higher. This means that in the problems, in which the quantity of the heat generated in the heating zone is the input parameter (for example in the problems with the heat generated by friction), an insulating coating does not only necessarily decrease the temperature level in the base, but even increases it. From the Figure 3 also it is shown that for the coating with the ratio of the heat conductivity coefficients $\kappa^2 = 5$ we observe a significant decrease of the temperature in the heating zone and on the interface between the coating and the base. It is caused by the increase of the radial heat flux (line 2 in Figure 4).

4.2 Case CD

In the section AB a hypothetical gradient covering whose thermal properties are described by formulas (8) was investigated. A coating structure that would make it possible to obtain a coating with assumed thermal properties was not considered. In this section the multilayer coating described in section C is analyzed.

The analysis of relations shows, the temperature in the homogenized model (section D) depends on the function $\eta(z)$ and the three dimensionless parameters: K_1/K_0 , K_2/K_0 and h . However if the coating is treated as a multilayered body (section C), one should take into account the number of a representative cells m .

To simplify, let us assume that the content of the first type material in the representative cell is described by a linear function of the coordinate z , i.e.:

$$\eta(z) = \frac{z}{h}, 0 < z < h \quad (27)$$

The parameters describing the content of the first type material in the representative cells numbered $i = 1, \dots, m$ are calculated using the following formulas

$$\eta_i = \frac{2i-1}{2m}, i = 1, \dots, m. \quad (28)$$

The coating described by the homogenization method is replaced by a multilayer coating consisting of N homogeneous transversal isotropic layers of equal thickness $h^* = h/N$. The thermal properties of layers are described by formulas:

$$K_r^l = K_2 + (K_1 - K_2) \frac{2l-1}{2N}, l = 1, \dots, N, \quad (29a)$$

$$K_z^l = \frac{K_1 K_2 N}{K_2 - K_1} \ln \frac{K_1 N + (K_2 - K_1) l}{K_1 N + (K_2 - K_1) (l-1)}, l = 1, \dots, N. \quad (29b)$$

As in the section AB, the gradient coating is a thermal insulator: $K_1/K_0 = 0.2$; $K_2/K_0 = 1$ or 5 . In addition, it is assumed that: $h = 0.4$ and $m = 5, 10, 20, 40$ and 80 .

Based on the comparison of the temperature values in the homogenized coating calculated for different values of the parameter N , it can be concluded that the calculation error will not exceed 0.2% when the homogenized coating is replaced by a package of 20 homogeneous transversal isotropic layers with a slowly changing thermal properties. If $N = 10$, the error of temperature calculation does not exceed 0.5% .

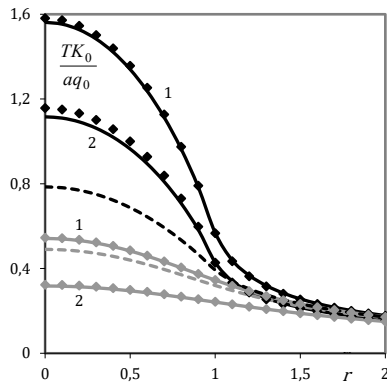


Fig. 5. Distributions of the temperature over the plane $z = h$ (black lines and rhombi) and over the plane $z = 0$ (grey lines and rhombi), dashed lines – the distributions of the temperature for the isotropic homogeneous half-space with the heat conductivity coefficient K_0 : 1 – $K_2/K_0 = 1$; 2 – $K_2/K_0 = 5$; $m = 10$

In the following analysis, we will focus on comparing solutions based on the two mathematical models of the considered coating described in sections C and D. Figure 5 shows the distributions of the temperature over the surface of the inhomogeneous half-space (black lines and rhombi) and over the interface between coating and base (grey lines and rhombi). The continuous lines describe the distributions of the temperature obtained within the framework of the homogenization method described in section D. The rhombi mark the numerical results obtained for the multilayer coating with a step change in thermal properties on the surfaces between the layers (the approach described in section C). The dashed lines describe the solution in the isotropic homogeneous half-space with the heat conductivity coefficient K_0 .

Tab. 2. Dependence of the dimensionless parameters $T_{\text{sur}}^{\text{max}} = \frac{T(0,h)K_0}{aq_0}$, $T_{\text{int}}^{\text{max}} = \frac{T(0,0)K_0}{aq_0}$ on the dimensionless parameter K_2/K_0 and number of the representative cells m

K_2/K_0	m	$T_{\text{sur}}^{\text{max}}$	$\varepsilon_{T_{\text{sur}}}, \%$	$T_{\text{int}}^{\text{max}}$	$\varepsilon_{T_{\text{int}}}, \%$
1	∞	1.5630		0.5420	
	80		0.1613		0.0992
	40		0.3173		0.1965
	20		0.6171		0.3854
	10		1.1698		0.7407
	5		2.1096		1.3661
5	∞	1.1164		0.3217	
	80		0.4999		0.2566
	40		0.9858		0.5106

20	1.9225	0.9844
10	3.6628	2.0010
5	6.6678	3.8612

The results of calculations presented in Fig. 5 show good agreement between the distributions of the temperature obtained using the analyzed two models of the considered coating. We can estimate the differences obtained when calculating the maximum temperatures in the planes $z = h$ and $z = 0$ from the calculation results shown in Table 2. The maximum temperatures for the problem described in section D are presented in the columns $T_{\text{sur}}^{\text{max}}$ and $T_{\text{int}}^{\text{max}}$ of Table 2. The relative deviations (given as percentages) that result from the two proposed approaches to solving the problem are shown in the rows with $m = 80, 40, 20, 10$ and 5 . As can be seen from Table 2, the double increase in the representative cells number in the multilayer coating with a step change in thermal properties cause the double decrease in the deviations between the analyzed temperature values. Larger differences between temperature values occur when one layer in the representative cell is a heat conductor. If $m = 20$, the error in calculating the parameters $T_{\text{sur}}^{\text{max}}$ and $T_{\text{int}}^{\text{max}}$ does not exceed 2% and 1% respectively.

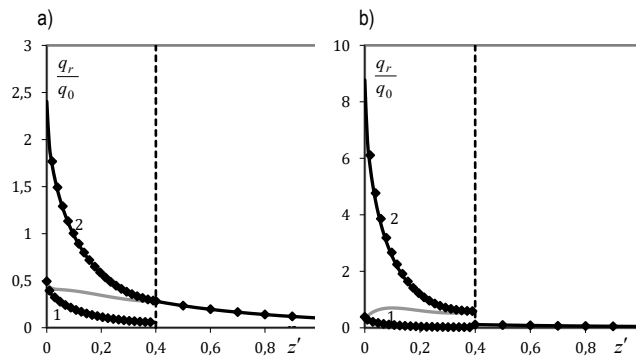


Fig. 6. Distributions of the radial heat flux on the cylindrical surface $r = 1$ (black lines and rhombi): fig. a) – $K_2/K_0 = 1$; fig. b) – $K_2/K_0 = 5$; grey line – the distribution of the average radial heat flux; vertical dashed line – the interface of the coating and base; $m = 20$; $z' = h - z$

The temperature in the considered problem can be treated as a macro-characteristic, which does not depend on the choice of component of the representative cell. An example of micro-characteristic is the radial heat flux. Figures 6 presents the distributions of the radial heat flux on the cylindrical surface $r = 1$ containing the edge of the heating zone. When the homogenization method is applied, there is no information connected with the kind of the layer in the specified point of coating. At each point of the coating we obtain two equations to calculate the radial heat flux

$$q_r^{(l)}(r, z) = -K_l \frac{\partial T^{\text{hom}}(r, z)}{\partial z}. \quad (30)$$

The equation with the index 1 allows to determine of the radial heat flux in the layer of the first kind, and the one with the index 2 – in the layer of the second kind. Two continuous lines denoted by numbers 1 and 2 (the indexes of types of layers) are appropriate for the values of radial heat flux in the layer of the representative cell numbered 1 or 2, respectively. The rhombi are adequate for the problem for the multilayer coating with a step change in thermal properties (section C). Averaged within the representational cell,

the radial heat flux values calculated according to the formula

$$q_r^*(r, z) = -K_r(z) \frac{\partial T^{\text{hom}}(r, z)}{\partial z} \quad (31)$$

are described in the figure with a gray line. The vertical dashed line indicate the interface of the coating and base.

If the radial heat flux is calculated in the layers with even numbers, the adequate rhombi are consistent with the continuous line denoted by 1, in the layers with odd numbers, with the continuous line denoted by 2. This means that the continuous lines within the homogenized model correctly determine the distribution of radial heat flux in the both layers of the representative cell.

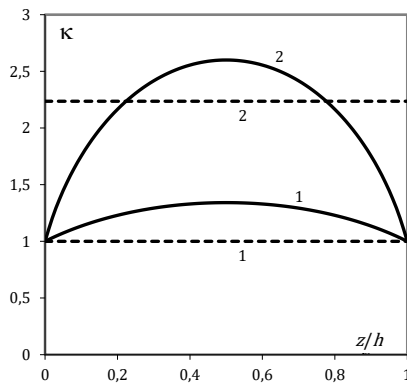


Fig. 7. Graphs of the function $\kappa(z)$: continuous lines – coatings described in section C: 1 – $K_1/K_0 = 0.2$, $K_2/K_0 = 1$; 2 – $K_1/K_0 = 0.2$, $K_2/K_0 = 5$; dashed lines – coatings described in section A: 1 – $\kappa^2 = 1$; 2 – $\kappa^2 = 5$

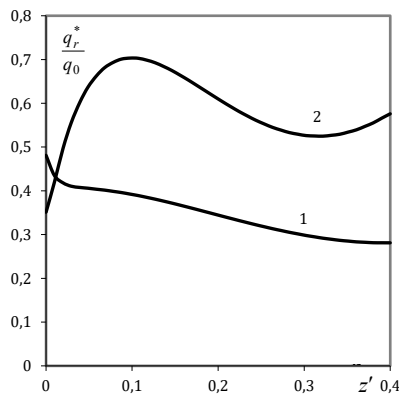


Fig. 8. Distributions of the average radial heat flux on the cylindrical surface $r = 1$ (coatings described in section C): 1 – $K_1/K_0 = 0.2$, $K_2/K_0 = 1$; 2 – $K_1/K_0 = 0.2$, $K_2/K_0 = 5$; $m = 20$; $z' = h - z$

Comparing Figures 3 and 5, we conclude that the temperature distributions in both figures are very similar. The multilayer coating with thermal conductivity coefficients $K_1 = 0.2K_0$ and $K_2 = K_0$ is not an isotropic covering. However, Figure 7 shows that the values of the function $\kappa(z)$ for this coating only slightly exceed the value of $\kappa = 1$, which describes a gradient isotropic coating. The average value of this function is about 1.238. Therefore, the curves numbered 1 in Figures 3 and 5 differ only slightly in these figures. Curve 2 in Figure 7 is a graph of the function $\kappa(z)$, which describes a multilayer coating whose representative cell consists of a thermal insulator with thermal conductivity coefficient $K_1 = 0.2K_0$ and a heat conductor with thermal conductivity coefficient $K_2 = 5K_0$. The

average value of this function is 2.2, and the second coating considered in section AB is described by a constant parameter $\kappa = \sqrt{5} \approx 2.236$. This shows that there is a high correlation between the temperature distribution and the average value of the function $\kappa(z)$.

As the average value of the function $\kappa(z)$ increases, it increases the average radial heat flux (Fig. 8). In the gradient coating considered in the CD section, this increases heat collection along layers that are heat conductors in representative cells, and their heat conduction coefficient is higher than of the base heat conduction coefficient. This results in lower temperatures in both the heating zone and the base.

5. CONCLUSIONS

In the paper the method of solving heat conduction problems for coated solids is presented. The considered body is modeled by a inhomogeneous half-space consisting of a homogeneous substrate and a transversal isotropic coating with arbitrary variations of thermal properties along the thickness. The investigated coating is replaced by a package of homogeneous transversal isotropic layers.

To verify the method, the solution for an appropriately selected multilayer coating was compared with the analytical solution of the problem in which the thermal properties of the coating are described by exponential functions. A comparison of the obtained solutions showed that a twofold increase in the number of layers cause a fourfold decrease in the difference between the analyzed temperature and a twofold decrease in the difference between the analyzed radial heat flux. Sufficient agreement for engineering applications in temperature calculations was observed with 10 layers in the package. The conducted tests allow us to suggest that the proposed method is effective for the transversely isotropic gradient coatings, whose the thermal properties are described by arbitrary piecewise continuous functions of the distance to the coating surface.

In the second part of the paper, the proposed solution method was used to analyze a multilayer coating with a step change of the thermal properties. The tested coating consisted of a finite number of a representative cells containing two homogeneous isotropic layers with different thermal conductivity coefficients. The content of the first type material in a representative cell was allowed to vary along the thickness of the coating.

For a large number of layers, the temperature and heat flux induced in the considered inhomogeneous half-space can be calculated using two different concepts. One concept implies the analysis of the actual layers. The other one is concerned with homogenization procedure leading to a FGM-coating with continuously varying thermal properties.

Previous studies [9, 10] have shown that the homogenization is effective when the content of the first type material in a representative cell is constant, i.e. the investigated coating has a periodic structure. Similar studies for a gradient coatings with slowly varying properties have been carried out only for one-dimensional problems [11, 12].

The main difficulty of the present study compared to the study of the coating with the periodic structure is that the homogenized gradient coating is described by differential equations, for which the analytical solution is not known. Therefore, the algorithm for solving the problem for the obtained homogenized coating uses the approach described in the first part of the article. This means that in

the conducted research two packages of layers are compared. The first package contains layers with step changes in thermal properties. The second consists of layers with slowly changing properties. The comparison of solutions has shown that it is possible to select the second package of layers in such a way that the difference between the obtained solutions is negligible. The main advantage of the second package of layers is that satisfactory results for engineering applications are obtained for 10 layers in the package.

It is also shown that the proposed homogenization approach allows to correctly calculate not only the temperature, which is the average characteristic in a representative cell, but also the radial heat flux, the value of which depends on the choice of the component in the representative cell.

It should be emphasized that the presented research suggests that it will allow to correctly solve a more complicated problems, in particular axisymmetric and three-dimensional thermoelasticity problems.

REFERENCES

- Guler MA, Erdogan F. Contact mechanics of graded coatings. *Int J Solids Struct.* 2004; 41:3865–3889.
- Liu J, Ke L, Zhang C. Axisymmetric thermo-elastic contact of an FGM-coated half-space under a rotating punch. *Acta Mechanica.* 2021; 232:2361–2378.
- Suresh S. Graded materials for resistance to contact deformation and damage. *Sci.* 2001; 292:2447–2451.
- Voigt W. Über die Beziehungen zwischen beiden Elastizitätskonstanten isotroper Körper. *Wied Ann.* 1889; 38: 573–587.
- Reuss A. Berechnung der Fließgrenze von Mischkristallen auf Grund der Plastizitätsbedingung für Einkristalle. *ZAMM.* 1929; 9: 49–58.
- Ganczarski A, Skrzypek J. *Mechanika nowoczesnych materiałów*, Kraków: W-wo Politechniki Krakowskiej 2013.
- Matysiak SJ, Woźniak Cz. Micromorphic effects in a modeling of periodic multilayered elastic composites. *Int J Eng Sci.* 1987; 25: 549–559.
- Woźniak Cz. A nonstandard method of modelling of thermoelastic periodic composites. *Int J Eng Sci.* 1987; 25:483–499.
- Bajkowski AS, Kulchytsky-Zhyhailo R, Matysiak SJ. The problem of a periodically two-layered coating on a homogeneous half-space heated by moving heat fluxes. *Int J Heat Mass Transf.* 2019; 103: 110–116.
- Kulchytsky-Zhyhailo R, Matysiak SJ, Bajkowski AS. Semi-analytical solution of three-dimensional thermoelastic problem for half-space with gradient coating. *J Therm Stresses.* 2018; 41(9):1169–1181.
- Kulchytsky-Zhyhailo R, Matysiak SJ, Perkowski DM. On some thermoelastic problem of a nonhomogeneous long pipe, *IJHT.* 2021; 39(5): 1430-1442.
- Kulchytsky-Zhyhailo R. Thermal stresses in a multi-layered spherical tank with a slowly graded structure. *Acta Mechanica et Automatica.* 2024; 18(2):274-281.
- Wang CD, Tzeng CS, Pan E, Liao JJ. Displacements and stresses due to a vertical point load in an inhomogeneous transversely isotropic half-space. *Int J Rock Mech Min Sci.* 2003; 40:667–685.
- Akbari F, Khojasteh A, Rahimian M. Three-Dimensional Interfacial Green's Function for Exponentially Graded Transversely Isotropic Bimaterials, *Civ Eng Infrastruct J.* 2016; 49(1):71 – 96.
- Eskandari M, Shodja HM. Green's functions of an exponentially graded transversely isotropic half-space. *Int J Solids Struct.* 2010; 47: 1537-1545.
- Guler MA, Kucuksucu A, Yilmaz KB. On the analytical and finite element solution of plane contact problem of a rigid cylindrical punch sliding over a functionally graded orthotropic medium. *Int J Mech Sci.* 2017; 120:12–29.
- Kalantari M, Khaji N, Eskandari-Ghadi M. Rocking forced displacement of a rigid disc embedded in a functionally graded transversely isotropic half-space. *MMS.* 2021; 26(7):1029-1052.
- Ning X, Lovell M, Slaughter WS. Asymptotic solutions for axisymmetric contact of a thin, transversely isotropic elastic layer. *Wear.* 2006; 260(7): 693-698.
- Wang CD, Pan E, Tzeng CS, Han F, Liao JJ. Displacements and stresses due to a uniform vertical circular load in an inhomogeneous cross-anisotropic half-space. *Int J Geomech.* 2006; 6(1):1-10.
- Wang CD, Tzeng CS. Displacements and stresses due to non-uniform circular loadings in an inhomogeneous cross-anisotropic material, *Mech Res Commun.* 2009; 36(8):921-932.
- Volkov SS, Belov AA, Litvinchuk SYu, Aizikovich SM. Indentation of a hard transversely isotropic functionally graded coating by a conical indenter, *Int J Eng Sci.* 2017; 112: 63-75.
- Yilmaz KB, Comez I, Guler MA, Yildirim B. The effect of orthotropic material gradation on the plane sliding frictional contact mechanics problem. *J Strain Anal Eng.* 2019; 54(4):254–275.
- Ke LL, Wang YS. Two-dimensional contact mechanics of functionally graded materials with arbitrary spatial variations of material properties. *Int J Solids Struct.* 2006; 43:5779-5798.
- Ke LL, Wang YS. Two-dimensional sliding frictional contact of functionally graded materials. *Eur J Mech A/Solids.* 2007; 26: 171-188.
- Kulchytsky-Zhyhailo R, Bajkowski A. Elastic half space with inhomogeneous coating under the action of tangential forces. *Mater Sci.* 2011; 46(6):735-746.
- Kulchytsky-Zhyhailo R, Bajkowski A. Analytical and numerical methods of solution of three-dimensional problem of elasticity for functionally graded coated half-space. *Int J Mech Sci.* 2012; 54:105-112.
- Kulchytsky-Zhyhailo R, Bajkowski A. Three-dimensional analytical elasticity solution for loaded functionally graded coated half-space. *Mech Res Commun.* 2015; 65:43-50.
- Kulchytsky-Zhyhailo R, Bajkowski AS. Axisymmetrical problem of thermoelasticity for half-space with gradient coating. *Int J Mech Sci.* 2016; 106:62–71.
- Kulchytsky-Zhyhailo R, Matysiak SJ, Perkowski DM. On thermal analysis of periodic composite coatings for a homogeneous conductive layer, *Int Comm Heat Mass Transfer.* 2018; 91:210–215.
- Kulchytsky-Zhyhailo R, Perkowski D, Kołodziejczyk W. On Axisymmetric Heat Conduction Problem for Multilayer Graded Coated Half-Space. *JTAM.* 2018; 56(1):147-156.
- Liu J, Ke LL, Wang YS, Yang J, Alam F. Thermoelastic frictional contact of functionally graded materials with arbitrarily varying properties. *Int J Mech Sci.* 2011; 63:86–98.
- Liu TJ, Wang YS. Reissner-Sagoci problem for functionally graded materials with arbitrary spatial variation of material properties. *Mech Res Commun.* 2009; 36:322-329.
- Liu TJ, Wang YS, Zhang C. Axisymmetric frictionless contact of functionally graded materials. *Arch Appl Mech.* 2008; 78:267–82.
- Yang J, Ke LL. Two-dimensional contact problem for a coating-graded layer– substrate structure under a rigid cylindrical punch. *Int J Mech Sci.* 2008; 50:985-994.

Roman Kulchytskyi-Zhyhailo:  <https://orcid.org/0000-0001-6390-2261>



This work is licensed under the Creative Commons BY-NC-ND 4.0 license.

CORROSION RESISTANCE OF ADDITIVE MANUFACTURED 17-4PH DMLS STEEL AFTER HEAT TREATMENT AND SHOT PEENING PROCESS

Aleksander Świetlicki*, Mariusz Walczak*, Mirosław Szala*

*Department of Materials Engineering, Faculty of Mechanical Engineering, Lublin University of Technology, Nadbystrzycka 36D, 20-618 Lublin, Poland

aleksander.swietlicki@pollub.edu.pl, m.walczak@pollub.pl, m.szala@pollub.pl

received 31 December 2024, revised 14 March 2025, accepted 23 March 2025

Abstract: Additively manufactured steel is not free of drawbacks and defects. Such disadvantages include high roughness and lower hardness compared to conventional steel. The 17-4PH steel is a grade designed for precipitation hardening. The application of 17-4PH steel ranges from turbine blades, pumps, valves, and propellers for aerospace, maritime, nuclear power plants, and medical instruments. This grade of steel is often applied where high mechanical performance and good corrosion resistance are required. Considering these factors, it was decided to use a heat treatment designed for conventional steel of this steel grade, that is, a precipitation hardening process followed by shot peening. The use of a constant supersaturation temperature of 1040°C and aging at 450°C made it possible to evaluate the mechanical properties depending only on the type of treatment used. Different peening media were also used to determine the effect of the medium on the properties of the surface layer after the peening process. To determine the surface characteristics, tests were carried out using optical profilometry, above that, hardness was tested, and corrosion resistance was examined using potentiodynamic polarization tests in a 3.5% NaCl environment. The aim of this study is to evaluate the effect of precipitation hardening combined with SP on the corrosion resistance of 17-4PH steel. Results obtained for steel produced using DMLS technology were compared with conventionally fabricated 17-4PH steel. Heat treatment contributed to a greater increase in hardness for the DMLS made steel. The corrosion resistance turned out to be dependent mainly on the roughness that increased after the Shot Peening process. The main purpose of the study was to evaluate the effects of precipitation hardening combined with shot peening on the corrosion resistance of 17-4PH steel. Results obtained for steel produced using DMLS technology were compared with conventionally produced 17-4PH steel.

Key words: corrosion resistance, additive manufacturing, stainless steel, heat treatment, shot peening, surface roughness

1. INTRODUCTION

3D fabrication is a growing field of science and industry and is finding more and more applications, especially in the context of medicine and aeronautics. However, as many studies have shown, it is important to ensure the quality of the products often even at the expense of additional labor time and increased costs. This article proposes a relatively inexpensive processing solution consisting of a combination of precipitation hardening and shot peening (SP). Using these processes separately makes it possible to control the roughness parameters, mechanical properties and corrosion resistance of the steel components. This makes it possible to quickly produce particularly cost-effective low-volume parts from material with high mechanical properties, with the possibility of selecting the appropriate mechanical parameters, roughness and corrosion resistance. However, according to the authors' knowledge, none of the current literature studies investigates the combination of shot peening and heat treatment of additively manufactured 17-4PH steel on corrosion resistance.

Additive manufacturing (AM) with Direct Metal Laser Sintering (DMLS) technology consists of successive sintering of successive thin layers of powder from a bed using a laser. This layer has the shape of a cross-section obtained from a CAD model. The use of DMLS makes it possible to obtain products with relatively high dimensional shape accuracy. In addition, DMLS achieves high strength and repeatability compared to other additive methods [1].

Steel 17-4PH (AISI630), is a material with high mechanical strength and can be classified as austenitic steel [2], semi-austenitic [3] or martensitic [4]. The phase composition depends on the treatment the steel grade is intended for, i.e. precipitation hardening, and thus, the phase composition can be modified with appropriate heat treatment [5]. The phase composition, combined with the formation of precipitates at different temperatures and times of precipitation hardening and ageing processes, determines the mechanical properties. The most commonly used treatments are those described in the ASTM standards for finished products from this steel grade, corresponding to classifications H900 to H1150M [6]. The requirements for the precipitation hardening process described above are designed for steels produced by conventional methods, although they are also employed for AM steels. However, based on previous research, more favorable processing conditions have been selected to protect the surface layer [7]. The next stage was the selection of the medium and the parameters of the SP process, which further increased the hardness and improved some of the parameters of the processed material [8]. Those multiple process parameters involved in SP have a complex and interdependent impact on the SP effects, including surface roughness and compressive residual stress distribution [9]. Finally, this paper focuses on the synergistic effect of these treatments.

In a previous study [7], under the same conditions, the following proportions of α -martensite 23% and γ -austenite 77% were obtained for the AP specimen, thus corresponding to the RD heat

treatment. Specimen ST1040, corresponding in this case to the RD specimen, contained α -martensite 49% and γ -austenite 51%, while specimen PH450, corresponding to the PHD specimen, was characterised by an α -martensite content of 46% γ -austenite 54%.

Improving corrosion properties is a problem of great interest, especially in medical applications [10]. Corrosion resistance is largely a synergy of the three components of phase composition of surface roughness and grain size [11]. As studies have also shown, the induction of residual stresses in the surface area as occurs during SP may also have a positive [12] or negative [13] effect on corrosion resistance depending upon whether the stresses are compressive or tensile.

One of the most frequently studied parameters characterising surfaces are roughness parameters [12,13]. It is also worth mentioning here that important, but not usual, surface features are structure defects, e.g. those created in the AM process or during further processing. Such defects reduce the cohesion of the structure, which may be associated with impaired resistance to fatigue and corrosion processes in the case of 17-4PH steel [14,15]. Yu investigated the corrosion resistance of 17-4PH steel after laser surface melting in a 3.5% NaCl environment. In that study, the corrosion failure model of 17-4PH material in NaCl environment was presented, and a significant effect of grain size and stress on the corrosion resistance of steel was found [16].

The aim of this study is to evaluate the effect of precipitation hardening combined with SP on the corrosion resistance of 17-4PH steel. Results obtained for steel produced using DMLS technology were compared with conventionally fabricated 17-4PH steel. After a previous literature analysis, it was found that there is no detailed comparison of the effect of heat treatment and SP on the corrosion resistance of 17-4PH steel in a 3.5 % NaCl solution environment. This type of material, due to its proven non-cytotoxicity and the aforementioned high mechanical properties, has great potential for use on medical instrumentation. But it is not only the comparison between conventional and DMLS steels that can contribute to the knowledge base, e.g. for rapid prototyping and small batch production, which has lower costs compared to conventional manufacturing and machining methods, such as turning or grinding. This also allows greater freedom with regard to the shape of the component to be produced [17]. Further novelty is the use of SP after the precipitation hardening process for 17-4PH steels, where, as far as the authors' knowledge goes, there are even descriptions of the SP process after ageing [7]. There are no descriptions in the literature so far of the effects of combining the two processes i.e. heat treatment and shot peening of 17-4PH additive manufactured steel.

2. MATERIAL AND METHODS

2.1. Material

The test object was X5CrNiCuNb16-4 (17-4PH) steel samples both conventional and additively manufactured (DMLS). The specimens of 17-4PH steel were in the shape of disks with dimensions of 30 mm in diameter and height of 6 mm. The first part was conventional, and the second part was printed from GP1 metal powder produced by EOS. The particles of the powder used are mainly spherical in shape and had an average size of 10-50 μ m. Nitrogen was used as a shielding gas for fabrication. The 3D metal printing process was carried out through DMLS technology. The EOSINT M280 device (from EOS GmbH) was used, using the optimal printing parameters from the closed license of EOS software, including

the laser power of 200 W, the laser spot size of 0.1 mm, and the sinter thickness of 0.02 mm. Scanning speed was 1000 mm/s, and hatch spacing at 0.1 mm. A parallel scanning strategy with alternate scanning direction was adopted, and for subsequent layers the scanning direction was rotated by 90° relative to the previous layer. The fabricated specimens were built horizontally orientated. Once the samples were obtained, their surface was prepared by abrading on papers of decreasing gradation. The processes listed below in in Table 1 were then applied. At the same time, however, it should be noted that precipitation hardening was applied first and the next step was peening of the prepared and cleaned surface. Cooling after the solution treatment process was carried out in oil, while after the aging process, the cooling was carried out in air.

Tab. 1. Post-manufacture heat treatment and shot peening conditions

Sample	Material	Heat treatment parameters				Shot Peening parameters		
		Solution treatment		Ageing		Working pressure [MPa]	Time [min]	Medium
		Temperature [°C]	Time [min]	Temperature [°C]	Time [min]			
RP	Conventional	-	-	-	-	-	-	-
RD	DMLS	-	-	-	-	-	-	-
STP	Conventional	1040	40	-	-	-	-	-
STD	DMLS	1040	40	-	-	-	-	-
PHP	Conventional	1040	40	450	240	-	-	-
PHD	DMLS	1040	40	450	240	-	-	-
PHPG	Conventional	1040	40	450	240	0.4	2	Glass
PHDG	DMLS	1040	40	450	240	0.4	2	Glass
PHPS	Conventional	1040	40	450	240	0.4	2	Steel
PHDS	DMLS	1040	40	450	240	0.4	2	Steel
PHPC	Conventional	1040	40	450	240	0.4	2	Ceramic
PHDC	DMLS	1040	40	450	240	0.4	2	Ceramic

Note: Solution treatment and ageing time values are given with an accuracy of about 2 min.

It should also be noted that only the top surface of the specimens was treated by SP. Three different peening media was used, namely glass, steel and ceramic. Glass beads (Marbad) with a diameter of 200-300 μ m, steel shots (Amacast 30) with a diameter of 150-500 μ m and Ceramic (Marbad, CERAM 350) (250-425 μ m). Distance from the nozzle was constant at 20 mm.

2.2. Methods

The chemical composition was tested using with a Magellan Q8 spark emission spectrometer from Bruker (Billerica, MA, USA). Five spark burns were performed for each specimen to calculate

average values. Roughness parameters were calculated thru optical profilometry on Contour Countour GT-K1 (Veeco, USA) based on the VXI technique with the 5× magnification lens. Surface microgeometry maps were examined in the area of 1,26 mm × 0,946 mm. Obtained arithmetic mean deviation (Ra), root mean square deviation (Rq), maximum peak to valley (Rt) parameters from the maps were then tabularised and mean value was calculated. For each specimen, 8 measurements were taken. Measurements were taken according to ISO 4287 standard recommendations.

Hardness tests were carried out on a Future-Tech FM-800 microhardness tester at a load of 1,961 N and a dwell time of 15 s. Ten indentations were made for each sample on the top surface.

The structural characteristics of the surface were identified using a Phenom World ProX SEM microscope. In addition, an EDS attachment was also used to determine the surface's composition after shot peening. Above this, surface images were also taken in topographic mode at 1000x magnification.

Electrochemical tests were carried out on an ATLAS 0531 potentiostat system in a 3.5% NaCl solution at 22°C. A three-electrode electrochemical tank was used; the test area was 0.5 cm². The control electrode was a platinum electrode, the saturated calomel electrode (SCE) was the reference electrode. Polarisation curves were recorded with an automatic potential shift of 1 mV/s between -500 mV and +600 mV. Corrosion current density i_{corr} and corrosion potential E_{corr} were determined from Tafel curves by analysing potentiodynamic curves in AtlasLab from -25 mV to +25 mV. The corrosion rate was calculated based on ASTM G 102-89 according to the formulas 1 and 2 given below.

$$CR = K \frac{i_{corr}}{\rho} EW \quad (1)$$

$$EW = \frac{1}{\sum \frac{n_i f_i}{M_i}} \quad (2)$$

where: $K - 3,27 \cdot 10^{-3} [\text{mm} \cdot \text{g} \cdot \mu\text{A}^{-1} \cdot \text{cm}^{-1} \cdot \text{rok}^{-1}]$, i_{corr} – corrosion current density [$\mu\text{A} \cdot \text{cm}^{-2}$], ρ – alloy density [$\text{g} \cdot \text{cm}^{-3}$], EW – equivalent weight, n_i – valence of the i-th element in the alloy, f_i – mass fraction of the i-th element in the alloy, M_i – atomic mass of the i-th element in the alloy [$\text{g} \cdot \text{mol}^{-1}$]

3. RESULTS

3.1. Chemical composition

The chemical composition did not differ from that declared by the manufacturer and was in accordance with the requirements presented in ASTM and ISO standards. It is also in line with previous results as well as other relevant literature [18,19].

Tab. 2. Chemical composition of reference 17-4PH after DMLS fabrication

Element		C	Cr	Ni	Cu	Mn	Si	Mo	Nb	Fe
RD as-manufactured		0.04	15.95	4.72	4.6	0.69	0.71	0.12	0.26	Bal.
GP1 powder (EOS declaration)	Wt.	<0.07	15-17.5	3-5	3-5	<1	<1	<0.5	0.15-0.45	Bal.
ASTM A564	[%]	<0.07	15-17.5	3-5	3-5	<1	1	<0.5	0.15-0.45	Bal.
EN10088-1		<0.07	15-17	3-5	3-5	<1.5	<0.7	<0.6	5°C-0.45	Bal.

3.2. SEM-EDS Analysis

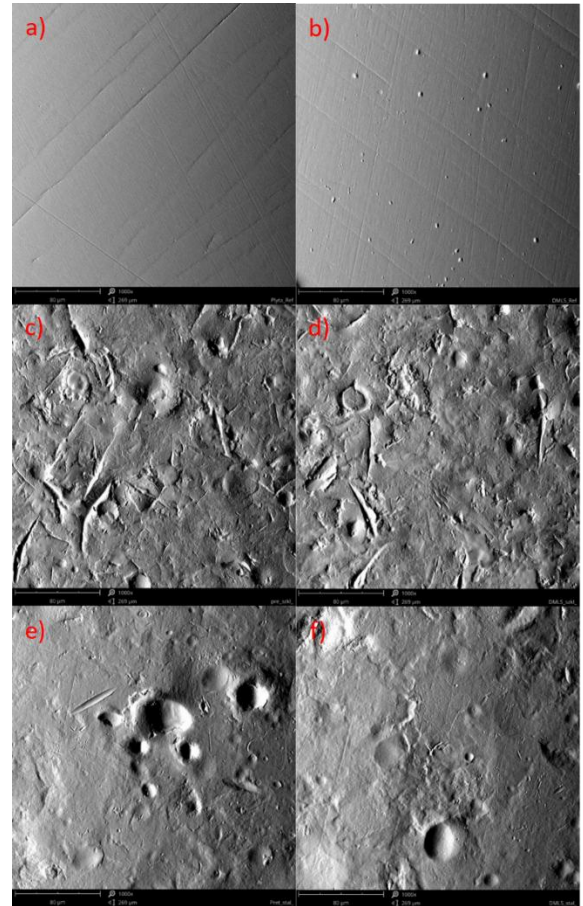


Fig. 1. a) RP topographic mode, b) RD c) PHPG, d) PHDG, e) PHPS, f) PHDS topographic mode - SEM micrographs

Surface of analysed referenced material showed visible grooves after grinding process (see Fig. 1 a, b). As can be seen in the Fig. 1 and Fig. 2, differences were evident between the groups depending on the pressing medium used. The PHPG and PHDG samples were characterised by visible grooves originating from fragmentation of the medium.

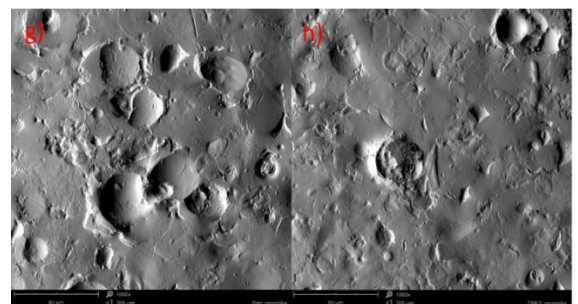


Fig. 2. g) PHPC, h) PHPC - SEM micrographs

The next group, PHPS and PHDS samples, are characterised by a smoother surface with visible, in places oval-shaped craters resulting from the impact of the spherical medium. This is also visible in the first group, but to a lesser extent. However, the greatest number of spherical craters are visible in the last group, the ceramic-impacted spherical craters (PHPC and PHDC). SEM-EDS analysis showed the presence of SP medium particles stuck on the

surface of the tested materials. The presence of both glass and ceramic ball particles was verified. The presence of steel beads has not been detected using the EDS method due to the similar composition. Comparable results are reported in the previous authors papers [20] related to the shot peening of the different types of stainless steels.

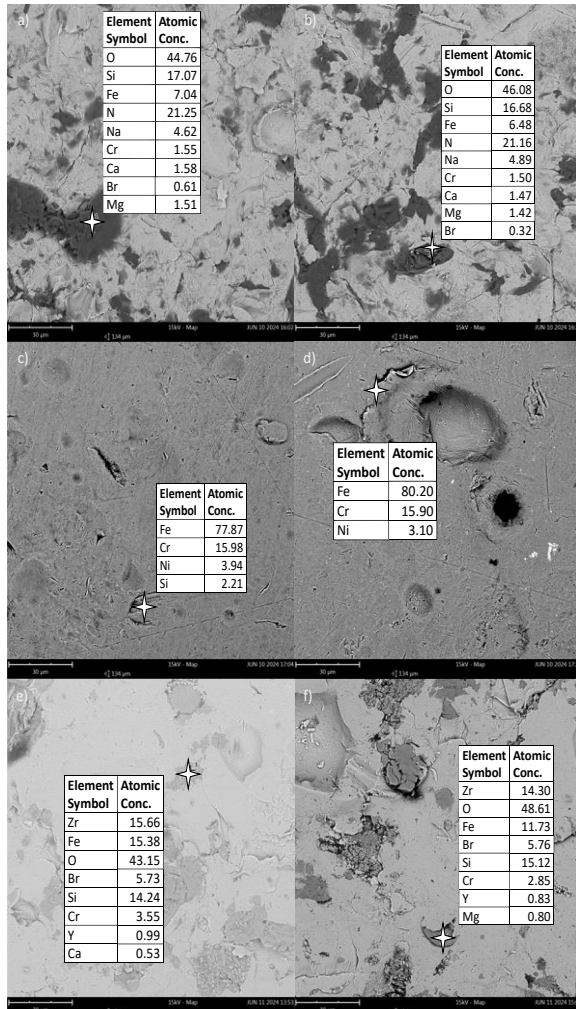


Fig. 3. SEM-EDS spot analysis after SP process a) PHPG, b) PHDG c) PHPS, d) PHDS, e) PHPC, f) PHDC

3.3. Hardness

The analysis of the hardness plots given in fig. 3 indicates that precipitation hardening process increased surface hardness for the DMLS-produced 17-4PH steel of approximately 53% from 255 HV_{0.2} for the reference material to 389 HV_{0.2}. Equally significant improvements were observed for the conventional 17-4PH steel (40%) from 322 HV_{0.2} for the reference material to 421 HV_{0.2}. Precipitation hardening combined with shot peening with glass contributed to the same increase in surface hardness in both cases (596 HV_{0.2}) corresponding to increases of 85% (PHPG) and 134% (PHDG), respectively, compared to the reference material. The use of precipitation hardening combined with steel peening increased the hardness of the conventional material by 65% and that of 17-4PH DMLS steel by 92%, while ceramic peening contributed to increases in surface hardness of 64% (PHPC) and 136% (PHDC).

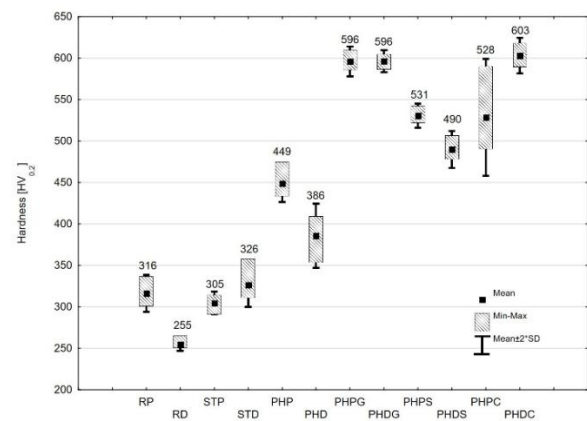


Fig. 4. Vickers hardness (HV_{0.2}) of specimen's top surfaces

In summary, the greatest increase in surface hardness was obtained for the material after additive manufacturing subjected to precipitation hardening and ceramic bead peening from 255 HV_{0.2} to 599 HV_{0.2}. After supersaturation, the hardness decreased for the conventional material, while it increased for the DMLS material, a fact that underlines the importance of research in this area. However, these results obtained are in line with other studies in this area for both 17-4PH conventional steel [21] and AM steel [22,23]. The greatest increase in hardness may have also been due to the size of the ceramic particles and their hardness because, at constant pressure and the highest density, theoretically, it is the steel shot that should provide the greatest energy during impact on the surface significantly increasing hardness through deformation and the introduction of favourable compressive residual stress (CRS) [24].

3.4. Roughness

The surface roughness increased significantly in all cases of surface peening analysed (Fig. 5-7). The smallest increase in roughness Ra was observed in the case of surface peening with steel beads. This can be explained by the higher ductility of steel compared to ceramic materials, including glass beads. By changing part of the energy into plastic deformation of the steel pellets, part of the energy that should deform the peened surface is lost.

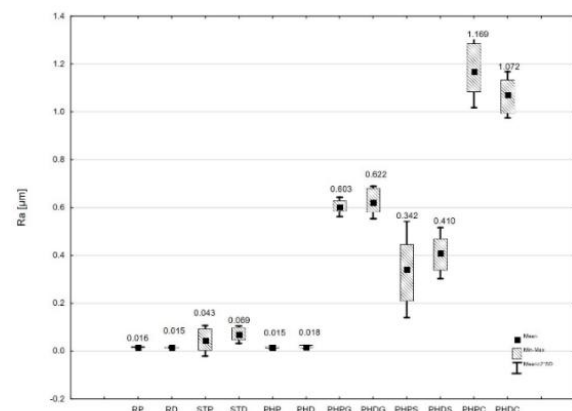


Fig. 5. Comparison of Ra roughness parameters of 17-4PH steel

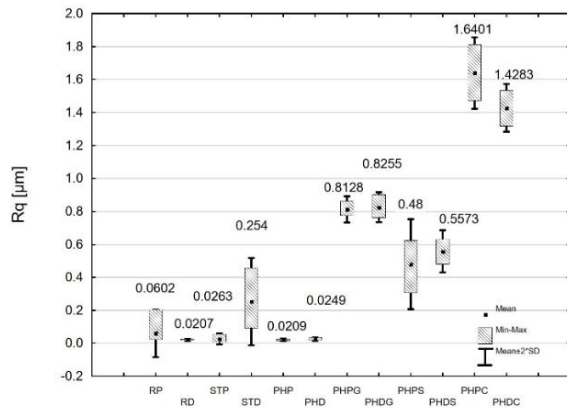


Fig. 6. Comparison of Rq roughness parameters of 17-4PH steel

This phenomenon may also explain the lower increase in hardness after peening compared to other materials. Most studies suggest that the bead material does not deform significantly. However, this is possible if only because of the high hardness of the shot peened substrate (389 HV_{0.2}, 421 HV_{0.2}) and the low hardness of the steel shots of 200 HV.

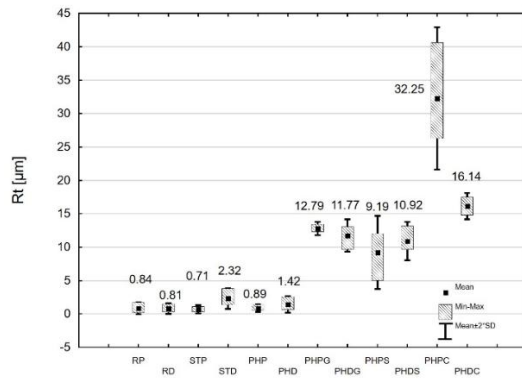


Fig. 7. Comparison of Rt roughness parameters of 17-4PH steel

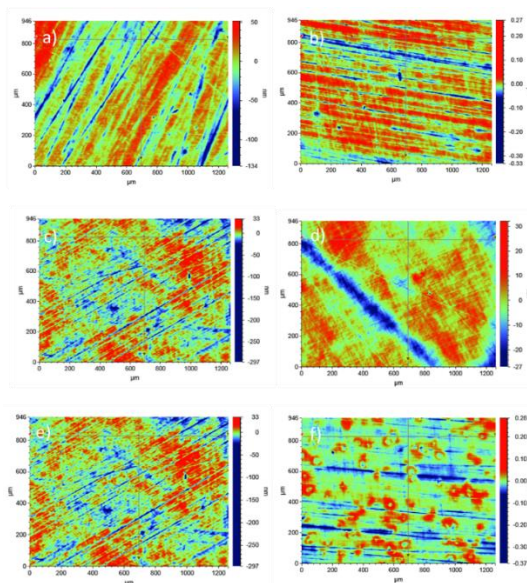


Fig. 8. Characteristic of the surface- 2D map of the surface of the investigated materials and surface features: a) RP, b) RD, c) STP, d) STD, e) PHP, f) PHD, g) PHPG, h) PHDG, i) PHPS, j) PHDS, k) PHPC, l) PHDC

Significantly lower roughness was achieved when compared to 17-4PH DMLS steel without preparation by grinding that achieved Ra 4.5-5.5 μm , Rq 5.8-7 μm , Rt 22-28 μm some differences can be noted [8]. Similar condition Ra 5.04 \pm 0.56 μm for reference material, for SP with steel shots Ra 5.71 \pm 0.26 μm and 4.39 \pm 1.43 μm for ceramic is described in [25].

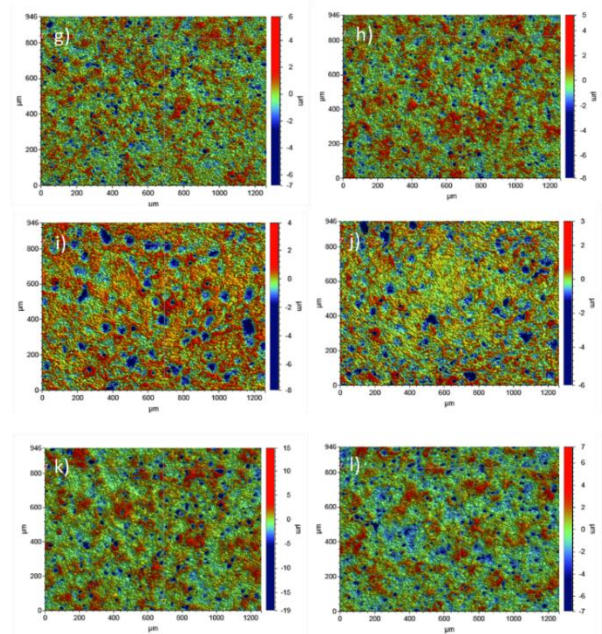


Fig. 9. Characteristic of the surface- 2D map of the surface of the investigated materials and surface features: g) PHPG, h) PHDG, i) PHPS, j) PHDS, k) PHPC, l) PHDC

3.5. Corrosion resistance

As previously noted, corrosion resistance in this case study results from the three main factors of grain size, chemical and phase composition and development, and, therefore, surface roughness. A link was noted between roughness and corrosion current density, which can be identified as a decisive parameter giving information on corrosion resistance. In the analysed case, the best coefficient for assessing corrosion resistance is CR (see Fig. 14) directly related to I_{corr} (Corrosion current density). In the case of the RP to PHD specimens, disregarding the STD with obtained a low roughness after surface grinding. However, the STD sample deviates slightly, and this translates into a significantly worse corrosion resistance. In the case of the RP sample, the influence of the microstructure is mainly visible, compared to the rest of the samples it is a material that has not been heat treated or mechanically processed.

In addition, it differs from the DMLS-made material in terms of its thermal history, as compared to the DMLS reference material it was only heated once while the RD went through a cycle of remelting and sintering successive layers while heating the material around it. The corrosion resistance of the glass-peened materials (PHRG and PHDG) is also related to the roughness. An increase in roughness resulted in a decrease in corrosion resistance in this group and a slight difference between the PHRG and PHDG samples tested was also evident in the I_{corr} parameter (see Fig. 11). Its increase led to a decrease in corrosion resistance in this group and a slight difference between the PHRG and PHDG samples tested was also seen in the I_{corr} parameter. The situation is similar for the

next group of steel specimens, but in this case, the effect of the medium on the corrosion resistance is also shown by the present and previous studies and the model proposed by Kameyama and Komotori [26]. While the presence of steel particles located on the surface is sometimes difficult to confirm using, for example, EDS, the presence of glass and ceramic particles is easy to verify. Again, however, the difference between PHRS and PHDS is apparent due to the small difference in roughness. Reference specimen made using DMLS was characterised by smallest E_{corr} on the other hand the highest E_{corr} was observed for PHDS. As can be seen corrosion potential seem to generally lower after treatment for conventional material and increase for DMLS (see Fig. 12). Discontinuities or irregularities in the surface resulting from SP indentations cause local variations in surface morphology and roughness. Differences in the E_{corr} can be correlated to spots where corrosion attack start to create usually in the top of SP induced dents [27].

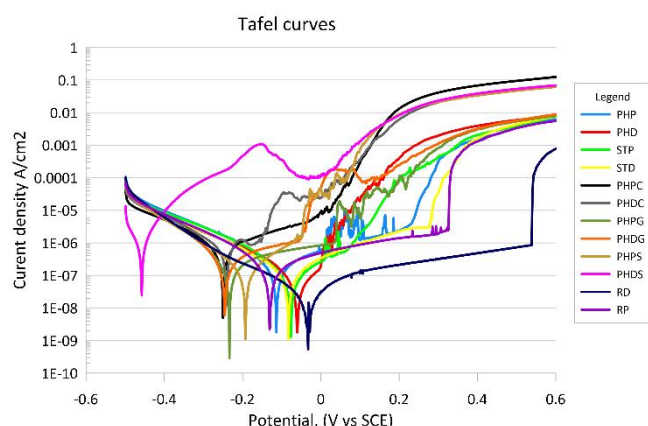


Fig. 10. Potentiodynamic polarization curves in 3.5% NaCl solution – Tafel plot

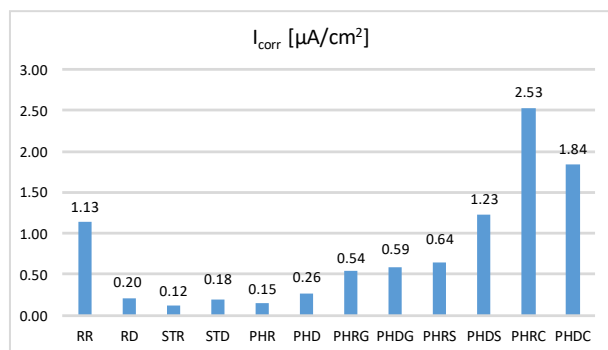


Fig. 11. Corrosion resistance parameters I_{corr} - Corrosion current density

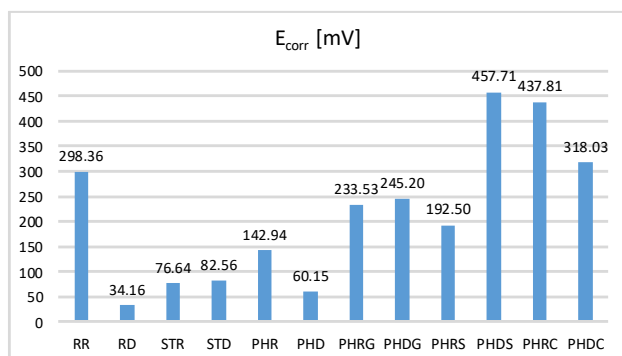


Fig. 12. Corrosion resistance parameters E_{corr} - Corrosion potential

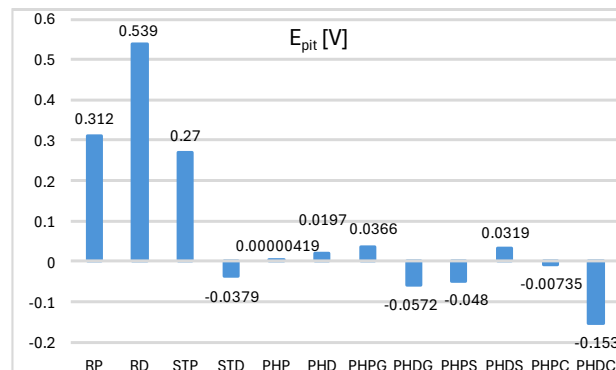


Fig. 13. Corrosion resistance parameters E_{pit} - Critical Pitting Potential

An important parameter in the context of corrosion protection is E_{pit} (see Fig. 13). The highest E_{pit} value and at the same time the most favourable one was RD (0.539 V). The lowest E_{pit} value and, at the same time, the material with the greatest potential for pitting corrosion was PHDC (-0.153 V). As can be seen in Fig. 13, there is a visible decrease in pitting corrosion resistance after the precipitation hardening process. However, it is not possible to clearly indicate whether conventional steel or DMLS is more resistant. In the group of materials that underwent SP, the highest E_{pit} value was found in PHPG (0.0366 V).

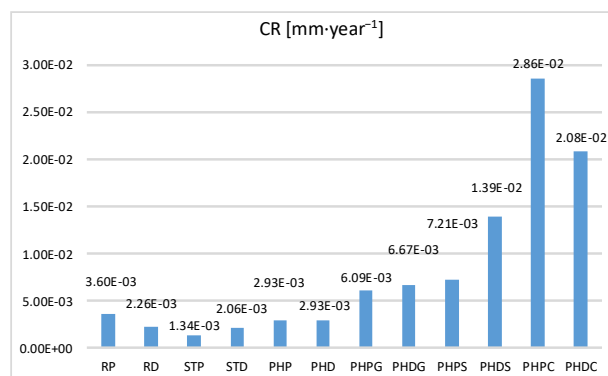


Fig. 14. Corrosion resistance parameters- Corrosion rate

4. CONCLUSIONS

The effect of precipitation hardening combined with SP on the corrosion resistance of 17-4PH steel have been evaluated. Results obtained for steel produced using DMLS technology were compared with conventionally fabricated 17-4PH steel. In conclusion, it was found that SP produced similar or sometimes even better results for 17-4PH DMLS steel compared to conventional material. Roughness has the greatest impact on the corrosion resistance proving that it the most significant factor influencing corrosion resistance. The highest corrosion resistance was obtained for STP (1.34×10^{-3}). The lowest corrosion resistance was found in PHPC (2.86×10^{-2}). Reference DMLS material (RD) has the lowest pitting corrosion potential (0.539 V). Heat treatment contributed to a greater increase in hardness for the DMLS made steel. The use of shot peening after heat treatment (precipitation hardening) appears to be effective and well-justified. The result was a significant increase in hardness for both conventional and DMLS steel from 255 HV0.2, 322 HV0.2 with increase of 40-136%. The best choice and

compromise appear to be the use of glass bead peening, which achieved high hardness in both PHPG and PHDG up to around 597 HV0.2, while maintaining average roughness (R_a at around 0.6 μm) and the best corrosion resistance in the group of peened materials. However, if hardness is the most important parameter, ceramic ball shot peening is the most suitable alternative.

REFERENCES

- Struzkiewicz G, Słodki B, Zębala W, Franczyk E. Study on Chip Breakability Index During Longitudinal Turning of Cast and DMLS Additively Manufactured AISi10Mg Aluminum Alloy. *Adv Sci Technol Res J*. 2022;16(1):28–35.
- Facchini L, Vicente N, Lonardelli I, Magalini E, Robotti P, Molinari A. Metastable Austenite in 17–4 Precipitation-Hardening Stainless Steel Produced by Selective Laser Melting. *Adv Eng Mater*. 2010;12(3):184–8.
- San Marchi C, Somerday B. Technical reference for hydrogen compatibility of materials. [Internet]. 2012 Sep [cited 2024 Dec 18] p. SAND2012-7321, 1055634. Report No: SAND2012-7321, 1055634. Available from: <https://www.osti.gov/servlets/purl/1055634/>
- Murr LE, Martinez E, Hernandez J, Collins S, Amato KN, Gaytan SM, et al. Microstructures and Properties of 17-4 PH Stainless Steel Fabricated by Selective Laser Melting. *Journal of Materials Research and Technology*. 2012;1(3):167–77.
- Eskandari H, Lashgari HR, Ye L, Eizadjou M, Wang H. Microstructural characterization and mechanical properties of additively manufactured 17-4PH stainless steel. *Materials Today Communications*. 2022;30:103075.
- ASTM E407-07(2015) Standard Practice for Microetching Metals and Alloys.
- Świetlicki A, Walczak M, Szala M, Turek M, Chocyk D. Effects of ageing heat treatment temperature on the properties of DMLS additive manufactured 17-4PH steel. *Bulletin of the Polish Academy of Sciences Technical Sciences [Internet]*. 2023 Aug 28 [cited 2023 Sep 19];(7). Available from: <https://journals.pan.pl/dlibra/publication/146237/edition/127804/content>
- Świetlicki A, Walczak M, Szala M. Effect of shot peening on corrosion resistance of additive manufactured 17-4PH steel. *Materials Science-Poland*. 2022;40(3):135–51.
- Cao Y, Niu T, Gai P, Chen Y, Pang J, Xu W. Numerical simulation for investigating the impact of shot peening process parameters via surface reconstruction. *Int J Adv Manuf Technol*. 2023;129(5–6):2721–34.
- Łępicka M, Grądzka-Dahlke M. Effect of Plasma Nitriding Process Conditions on Corrosion Resistance of 440B Martensitic Stainless Steel. *Acta Mechanica et Automatica*. 2014;8(3):156–9.
- Dillon CP. Corrosion Resistance of Stainless Steels. CRC Press; 1995; 386p.
- Macek W, Branco R, Costa JD, Pereira C. Strain sequence effect on fatigue life and fracture surface topography of 7075-T651 aluminium alloy. *Mechanics of Materials*. 2021;160:103972.
- Macek W, Branco R, Szala M, Marciniak Z, Ulewicz R, Szczygiel N, et al. Profile and Areal Surface Parameters for Fatigue Fracture Characterisation. *Materials*. 2020;13(17):3691.
- Otsuka Y, Kondo Y, Duong TT, Mitsuhashi E, Miyashita Y. Synergistic effect of defects and microstructure on fatigue strength of additively manufactured precipitation hardening 17-4PH stainless steel. *Engineering Failure Analysis*. 2024;163:108541.
- Liu G, Huang C, Zou B, Liu H, Liu Z, Liu Y, et al. The modification of corrosion resistance of 17-4PH stainless steel by cutting process. *Journal of Manufacturing Processes*. 2020;49:447–55.
- Yu DT, Wang R, Wu CL, Zhang S, Zhang CH, Chen HT, et al. Iso-Material Manufactured 17-4PH Stainless Steel to Enhance the Nano-indentation, Corrosion, and Cavitation Erosion Behavior. *J of Mater Eng and Perform [Internet]*. 2024. Available from: <https://link.springer.com/10.1007/s11665-024-10134-0>
- Singh Y, Singh NK, Ram M. *Advanced Manufacturing Processes*. CRC Press; 2022: 207p.
- Steponavičiūtė A, Stravinskas K, Selskienė A, Tretjakovas J, Petkus R, Mordas G. Mechanical properties of 17-4PH stainless-steel at various laser sintering process parameters. *physics [Internet]*. 2024 Jul 2 [cited 2025 Mar 12];64(2). Available from: <https://www.lma-leidykla.lt/ojs/index.php/physics/article/view/5350>
- Walczak M, Świetlicki A, Szala M, Turek M, Chocyk D. Shot Peening Effect on Sliding Wear in 0.9% NaCl of Additively Manufactured 17-4PH Steel. *Materials*. 2024;17(6):1383.
- Walczak M, Matijošius J, Özkan D, Pasierbiewicz K. Effect of Shot Peening Parameters on Surface Properties and Corrosion Resistance of 316L Stainless Steel. *Adv Sci Technol Res J*. 2024;18(3):296–304.
- Sowa R, Kowal A, Roga E, Arabasz S, Dziedzic A, Dul I, et al. Influence of double solution treatment on hardness in 17-4 pH steel. *Zas Mat*. 2015;56(3):261–8.
- Sun Y, Hebert RJ, Aindow M. Effect of heat treatments on microstructural evolution of additively manufactured and wrought 17-4PH stainless steel. *Materials & Design*. 2018;156:429–40.
- AlMangour B, Yang JM. Improving the surface quality and mechanical properties by shot-peening of 17-4 stainless steel fabricated by additive manufacturing. *Materials & Design*. 2016;110:914–24.
- Świetlicki A, Szala M, Walczak M. Effects of Shot Peening and Cavitation Peening on Properties of Surface Layer of Metallic Materials—A Short Review. *Materials*. 2022;15(7):2476.
- Walczak M, Szala M. Effect of shot peening on the surface properties, corrosion and wear performance of 17-4PH steel produced by DMLS additive manufacturing. *ArchivCivMechEng*. 2021;21(4):157.
- Kameyama Y, Komotori J. Effect of micro ploughing during fine particle peening process on the microstructure of metallic materials. *Journal of Materials Processing Technology*. 2009;209(20):6146–55.
- Walczak M, Szala M, Okuniewski W. Assessment of Corrosion Resistance and Hardness of Shot Peened X5CrNi18-10 Steel. *Materials*. 2022;15(24):9000.

Aleksander Świetlicki:  <https://orcid.org/0000-0002-8246-046X>

Mariusz Walczak:  <https://orcid.org/0000-0001-6728-9134>

Mirosław Szala:  <https://orcid.org/0000-0003-1059-8854>



This work is licensed under the Creative Commons BY-NC-ND 4.0 license.

FRACTIONAL DISCRETE-TIME COMPARTMENTAL LINEAR SYSTEMS

Tadeusz Kaczorek^{*}, Andrzej Ruszewski^{*}

^{*}Faculty of Electrical Engineering, Białystok University of Technology, Wiejska 45D, 15-351 Białystok, Poland

t.kaczorek@pb.edu.pl, a.ruszewski@pb.edu.pl

received 27 January 2025, revised 1 March 2025, accepted 5 March 2025

Abstract: This paper introduces a class of fractional discrete-time compartmental linear systems. The fundamental system properties, including controllability and observability, are analysed. Furthermore, the eigenvalue assignment problem related with this class of systems is addressed. Theoretical considerations are demonstrated through a numerical example.

Key words: discrete-time system, fractional, compartmental, observability, controllability

1. INTRODUCTION

Fractional calculus is an extension of classical integer-order calculus that involves derivatives and integrals of non-integer (fractional) orders. The mathematical foundations of fractional calculus are presented in various monographs, such as [12], [13], and [14]. The applications of fractional calculus across various fields of science and engineering have attracted considerable attention in recent years. It has been used in areas such as mechanics, electrical engineering, biology, chemistry, and signal processing [13, 16, 18]. The fractional-order modeling of real-world phenomena are often more accurate than classical integer-order models. The theory of fractional systems is an expanding field that explores properties of systems, including stability, controllability, observability, realisability, and more [1, 2, 4, 7, 11, 15, 17, 19]. Standard and positive fractional linear systems have been discussed in monographs [8] and [10], respectively. A dynamical system is termed positive when its state variables and outputs take nonnegative values for any nonnegative inputs. Numerous models exhibiting positive behaviour can be found across fields such as engineering, biology, medicine, and economics. A comprehensive overview of research in positive systems theory is provided in [3, 6].

In the modelling process, compartmental linear systems are frequently used. These systems consist of separate compartments that are interconnected, each representing a subsystem containing a specific material. The transfer of material between compartments is governed by linear equations [5]. The fractional continuous-time compartmental systems have been studied in [9].

In this paper, fractional discrete-time compartmental time-invariant linear systems are introduced and analysed. To the best of the authors' knowledge, the problems of controllability, observability, and eigenvalue assignment have not yet been addressed for fractional discrete-time linear systems. This paper extends the fractional-order systems theory to this concern. A key advantage of discrete-time fractional-order numerical models is their ability to describe complex dynamical systems with non-local, memory-based interactions, providing more accurate and nuanced representations. These models are suitable for real-world processes where

the future state depends not only on the current value but also on the entire history of the system.

The structure of the paper is as follows. Section 2 provides the fundamental definitions and theorems related to fractional and positive linear systems. In Section 3, the concept of fractional discrete-time compartmental linear systems is introduced. Section 4 is devoted to the analysis of controllability and observability of the proposed systems, while Section 5 addresses the eigenvalue assignment problem. Finally, concluding remarks are presented in Section 6.

The notation used in this paper is as follows: \mathfrak{R} - the set of real numbers, $\mathfrak{R}^{n \times m}$ - the set of $n \times m$ real matrices, Z_+ - the set of nonnegative integers, $\mathfrak{R}_+^{n \times m}$ - the set of $n \times m$ matrices with nonnegative entries and $\mathfrak{R}_+^n = \mathfrak{R}_+^{n \times 1}$, I_n - the $n \times n$ identity matrix.

2. STANDARD LINEAR DISCRETE-TIME SYSTEMS

Let us consider a linear discrete-time system represented by the following equations.

$$x_{i+1} = Ax_i + Bu_i, i \in Z_+ = \{0, 1, \dots\}, \quad (2.1a)$$

$$y_i = Cx_i, \quad (2.1b)$$

with the initial condition x_0 , where $x_i \in \mathfrak{R}^n$ represents the state vector, $u_i \in \mathfrak{R}^m$ the control input, and $y_i \in \mathfrak{R}^p$ the system output, while $A \in \mathfrak{R}^{n \times n}$, $B \in \mathfrak{R}^{n \times m}$ and $C \in \mathfrak{R}^{p \times n}$ are the corresponding system matrices.

Definition 2.1. [6, 8] The linear system (2.1) is called (internally) positive if $x_i \in \mathfrak{R}_+^n$ and $y_i \in \mathfrak{R}_+^p$, $i \in Z_+$ for any initial conditions $x_0 \in \mathfrak{R}_+^n$ and all inputs $u_i \in \mathfrak{R}_+^m$, $i \in Z_+$.

Theorem 2.1. [6, 8] The linear system (2.1) is positive if and only if:

$$A \in \mathfrak{R}_+^{n \times n}, B \in \mathfrak{R}_+^{n \times m}, C \in \mathfrak{R}_+^{p \times n} \quad (2.2)$$

Definition 2.2. The linear system (2.1) is called asymptotically stable if $\lim_{i \rightarrow \infty} x_i = 0$ for $u_i = 0$ and any initial $x_0 \in \mathfrak{R}^n$.

Theorem 2.2. [6, 8] The linear system (2.1) is asymptotically

stable if the matrix A is a Schur matrix.

Theorem 2.3. [6, 8] The positive linear system (2.1) is asymptotically stable if and only if:

1. all coefficients of the polynomial

$$p_A(z) = \det[I_n(z+1) - A] = z^n + a_{n-1}z^{n-1} + \dots + a_1z + a_0 \quad (2.3)$$

are positive, i.e., $a_i > 0$ for $i = 0, 1, \dots, n-1$.

2. there exists strictly positive vector

$$\lambda^T = [\lambda_1 \ \dots \ \lambda_n]^T, \lambda_k > 0, k = 1, \dots, n \text{ such that} \\ A\lambda < 0 \text{ or } \lambda^T A < 0. \quad (2.4)$$

Let us now examine a linear fractional discrete-time system given by the following equations:

$$\Delta^\alpha x_{i+1} = Ax_i + Bu_i, \quad i \in Z_+ = \{0, 1, \dots\}, \quad 0 < \alpha < 1 \quad (2.5a)$$

where $x_i \in \mathbb{R}^n$, $u_i \in \mathbb{R}^m$ and $y_i \in \mathbb{R}^p$ are the state, input and output vectors and $A \in \mathbb{R}^{n \times n}$, $B \in \mathbb{R}^{n \times m}$, $C \in \mathbb{R}^{p \times n}$ and

$$\Delta^\alpha x_i = \sum_{j=0}^i (-1)^j \binom{\alpha}{j} x_{i-j} \\ \binom{\alpha}{j} = \begin{cases} 1 & \text{for } j = 0 \\ \frac{\alpha(\alpha-1)\dots(\alpha-j+1)}{j!} & \text{for } j = 1, 2, \dots \end{cases} \quad (2.5b)$$

is the fractional α -order difference of x_i .

Substitution of (2.5b) into (2.5a) yields

$$x_{i+1} = A_\alpha x_i - \sum_{j=2}^{i+1} c_j x_{i-j+1} + Bu_i, \quad i \in Z_+, \quad (2.6a)$$

where

$$A_\alpha = A + I_n \alpha, \quad c_j = (-1)^{j+1} \binom{\alpha}{j}, \quad j = 1, 2, \dots \quad (2.6b)$$

Definition 2.3. [6, 8] The fractional system (2.5) is called (internally) positive if $x_i \in \mathbb{R}_+^n$, $i \in Z_+$ for any initial conditions $x_0 \in \mathbb{R}_+^n$.

Theorem 2.4. [6, 8] The fractional system (2.5) is positive if and only if

$$A_\alpha \in \mathbb{R}_+^{n \times n}. \quad (2.7)$$

Definition 2.4. [6, 8] The fractional positive system (2.5) is called asymptotically stable if

$$\lim_{i \rightarrow \infty} x_i = 0 \text{ for all } x_0 \in \mathbb{R}_+^n. \quad (2.8)$$

Theorem 2.5. [6, 8] The fractional positive system (2.5) is asymptotically stable if and only if one of the equivalent conditions is satisfied:

1. all coefficients of the polynomial

$$p_A(z) = \det[I_n(z+1) - A] = z^n + a_{n-1}z^{n-1} + \dots + a_1z + a_0 \quad (2.9)$$

are positive, i.e., $a_i > 0$ for $i = 0, 1, \dots, n-1$.

2. there exists strictly positive vector

$$\lambda^T = [\lambda_1 \ \dots \ \lambda_n]^T, \lambda_k > 0, k = 1, \dots, n \text{ such that} \\ [A - I_n]\lambda < 0 \text{ or } \lambda^T [A - I_n] < 0. \quad (2.10)$$

3. STATE EQUATIONS OF THE FRACTIONAL DISCRETE-TIME LINEAR COMPARTMENTAL SYSTEMS

Let us consider the compartmental discrete-time time invariant system consisting of n compartments (Fig.1).

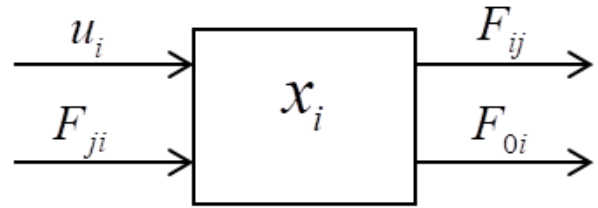


Fig. 1. The i -th subsystem of the compartmental system

Let: $x_i = x_i(k)$, $i = 1, \dots, n$ be the amount of a material of the i -th compartmental at the time instant k , $F_{ij}(k) > 0$ be the output flow of the material from the j -th to the i -th compartmental ($i \neq j$), between the k -th and $k+1$ -th time instants,

$F_{0i}(k) > 0$ be the output of the material from the i -th ($i = 1, \dots, n$) compartmental to the environment, $u_i = u_i(k)$ be the output flow of the material to the i -th compartmental from environment.

It is assumed that the input material is instantaneously mixed with the material already present in the compartment and that $F_{ij}(k)$ depends linearly on $x(k)$, i.e.,

$$F_{ij}(k) = f_{ij}x_j(k) \quad \text{for } i \neq j, \quad i = 1, \dots, n, \quad j = 1, \dots, n, \quad (3.1)$$

where f_{ij} is a coefficient depending on $x_j(k)$ and the discrete-time instant k .

The system is linear if f_{ij} is independent of $x_j(k)$ and it is additionally time-invariant if f_{ij} is independent of k .

From the balance of material of the i -th compartment we have the following fractional difference equation

$$\Delta^\alpha x_i(k+1) = \sum_{i \neq j}^n f_{ij}x_j(k) + f_{ii}x_i(k) + u_i(k) \quad \text{for } i = 1, \dots, n, \quad (3.2)$$

where $\Delta^\alpha x_i$ is defined by (2.5b) and $x_i(k)$ denotes the amount of material in the i -th compartment at time step k , i.e.,

$$f_{ii}x_i(k) = x_i(k) - f_{0i}x_i(k) - \sum_{i \neq j}^n f_{ij}x_i(k) = \left(1 - f_{0i} - \sum_{i \neq j}^n f_{ij}\right)x_i(k). \quad (3.3)$$

From equation (3.3) we have

$$f_{ii} = 1 - f_{0i} - \sum_{i \neq j}^n f_{ij} \text{ for } i = 1, \dots, n. \quad (3.4)$$

Note that if $u_j(k) = 0$, then the output flow of material from the j -th compartment at the time instant $k+1$ cannot exceed the total amount of material present in the compartment at time instant k , i.e.,

$$\sum_{i=1}^n f_{ij} \leq 1 \text{ for } j = 1, \dots, n \text{ and } f_{ij} \geq 0. \quad (3.5)$$

Definition 3.1. The matrix $F \in \mathbb{R}_+^{n \times n}$ satisfying the condition (3.5) is called the compartmental matrix of the fractional discrete-time linear system.

Using (3.3) for $i = 1, \dots, n$ we obtain the state equation of the compartmental system in the form

$$x(k+1) = Fx(k) + Bu(k), \quad i = 1, \dots, n \quad (3.6a)$$

where

$$x(k) = \begin{bmatrix} x_1(k) \\ \vdots \\ x_n(k) \end{bmatrix}, \quad u(k) = \begin{bmatrix} u_1(k) \\ \vdots \\ u_n(k) \end{bmatrix}, \quad F = \begin{bmatrix} f_{11} & \cdots & f_{1n} \\ \vdots & \cdots & \vdots \\ f_{n1} & \cdots & f_{nn} \end{bmatrix}. \quad (3.6b)$$

The output equation of the compartmental system has the form

$$y(k) = Cx(k), \quad (3.6c)$$

where $C \in \mathbb{R}_+^{p \times n}$.

From (3.6) it follows that the fractional compartmental systems are positive linear systems.

4. CONTROLLABILITY AND OBSERVABILITY OF STANDARD AND COMPARTMENTAL LINEAR SYSTEMS

Let us consider a linear discrete-time system described by the following equations:

$$x_{i+1} = Ax_i + Bu_i, \quad i \in Z_+ = \{0, 1, \dots\}, \quad (4.1a)$$

$$y_i = Cx_i, \quad (4.1b)$$

with the initial condition x_0 , where $x_i \in \mathbb{R}^n$, $u_i \in \mathbb{R}^m$ and $y_i \in \mathbb{R}^p$ are the state, input and output vectors and $A \in \mathbb{R}^{n \times n}$, $B \in \mathbb{R}^{n \times m}$ and $C \in \mathbb{R}^{p \times n}$ are system matrices.

Definition 4.1. The linear system (4.1) (or the pair (A, B)) is called controllable in the interval time $[0, i_f]$ if and only if there exists an input u_i for $i \in [0, i_f]$ which steers the state of the system from initial state $x_0 \in \mathbb{R}^n$ to the given final state x_{i_f} , i.e., $x_{i_f} = x_f$.

Theorem 4.1. The linear system (4.1) is controllable if and only if one of the following conditions is satisfied:

$$1. \text{rank}[B \quad AB \quad \dots \quad A^{n-1}B] = n \quad (4.2)$$

$$2. \text{rank}[I_n z - A \quad B] = n \text{ for all } z \in \mathbb{C}, \quad (4.3)$$

where \mathbb{C} is the field of complex numbers.

Definition 4.2. The linear system (4.1), or equivalently the pair (A, C) , is called observable if it is possible to uniquely determine the initial state x_0 based on the input u_i and output y_i for $i = 0, 1, \dots, i_f$.

Theorem 4.2. The linear system (4.1) is observable if and only if at least one of the following conditions is satisfied:

$$1. \text{rank} \begin{bmatrix} C \\ CA \\ \vdots \\ CA^{n-1} \end{bmatrix} = n, \quad (4.4)$$

$$2. \text{rank} \begin{bmatrix} I_n z - A \\ C \end{bmatrix} = n, \text{ for all } z \in \mathbb{C}, \quad (4.5)$$

Now let us consider the fractional compartmental linear system (3.6)

Definition 4.3. The fractional compartmental linear system (3.6), or equivalently the pair (F, B) , is called reachable on the time interval $[0, i_f]$ if there exists an input sequence u_i for $i \in [0, i_f]$ which steers the system state from the zero initial condition to a given final state x_f , i.e., $x_{i_f} = x_f$.

A matrix $F \in \mathbb{R}^{n \times n}$ is called monomial if each of its rows and each of its columns contains exactly one positive entry, and all other entries are zero.

Theorem 4.4. The fractional compartmental linear system (3.6)

is reachable if the matrix

$$R_f = \sum_{i=0}^{i_f-1} F^i (F^T)^i \quad (4.6)$$

is monomial. The input which steers the system state to $x_{i_f} = x_f$ is given by

$$u_i = (F^T)^{i_f-i-1} R_f^{-1} x_f \quad (4.7)$$

Proof. When matrix (4.6) is monomial, its inverse $R_f^{-1} \in \mathbb{R}_+^{n \times n}$ is nonnegative matrix. Consequently, the input (4.7) is also nonnegative. Given that $x_0 = 0$, applying (4.7) yields

$$x_f = \sum_{i=0}^{i_f-1} F^{i_f-i-1} B u_i = \sum_{i=0}^{i_f-1} F^{i_f-i-1} (F^T)^{i_f-i-1} R_f^{-1} x_f = x_f \quad (4.8)$$

since $B = I_n$.

Therefore, the input (4.7) steers the state of the system from x_0 to $x_{i_f} = x_f$. \square

Theorem 4.5. The fractional compartmental positive linear system (3.6) is reachable in time $[0, i_f]$ if and only if the matrix $F \in M_n$ is monomial.

Proof. Sufficiency. If $F \in M_n$ is monomial then $F^i \in \mathbb{R}_+^{n \times n}$ is also monomial. In this case the matrix

$$R_f = \sum_{i=0}^{i_f-1} F^{i_f-i-1} (F^T)^{i_f-i-1} = \sum_{i=0}^{i_f-1} F^i (F^T)^i \quad (4.9)$$

is monomial.

Necessity. From Cayley-Hamilton theorem [6] we have

$$F^i = \sum_{j=0}^{m-1} a_{ij} F^j, \quad i = m, m+1, \dots \quad (4.10)$$

where a_{ij} are some nonzero real coefficients.

Using (4.10) we obtain

$$x_f = [B \quad FB \quad \dots \quad F^{n-1}B] \begin{bmatrix} v_{0f} \\ v_{1f} \\ \vdots \\ v_{n-1,f} \end{bmatrix} \quad (4.11a)$$

where

$$v_{i_f} = \sum_{i=0}^{i_f} a_{ij} u_i. \quad (4.11b)$$

Therefore, for given $x_f \in \mathbb{R}_+^n$ it is possible to find the nonnegative v_{i_f} for $i = 0, 1, \dots, n-1$ if and only if $\text{rank}[B \quad FB \quad \dots \quad F^{n-1}B] = n$. \square

Observe that for the nonnegative system defined in (4.11b), a nonnegative input $u_i \in \mathbb{R}_+^m$ can be determined. Hence, the proof is complete. \square

Observability of fractional positive compartmental linear systems is defined analogously to that in standard positive linear systems. Since it is determined exclusively by the matrices A and C , and not by B . Consequently, system (2.1) is replaced by the fractional positive compartmental linear system of the following form

$$\Delta^\alpha x_{i+1} = Fx_i, \quad i \in Z_+ = 0, 1, 2, \dots, \quad 0 < \alpha < 1, \quad (4.13a)$$

$$y = Cx_i, \quad (4.13b)$$

where $x_i \in \mathbb{R}^n$, $y_i \in \mathbb{R}^p$ and $C \in \mathbb{R}_+^{p \times n}$.

The solution to the equation (4.13a) with (2.6b) has the form

$$x_i = \Phi_i x_0 + \sum_{j=0}^{i-1} \Phi_{i-j-1} B u_j, \quad (4.14a)$$

where

$$\Phi_{i+1} = (F + I_n \alpha) \Phi_i + \sum_{j=2}^{i+1} (-1)^{j+1} \binom{\alpha}{i} \Phi_{i-j+1}, \quad (4.14b)$$

with $\Phi_0 = I_n$.

Definition 4.4. The fractional positive compartmental linear system (4.13) is called observable on the interval $[0, i_f]$ if knowledge of the output y_i over the interval $[0, i_f]$ enables unique determination of the initial state x_0 .

Theorem 4.6. The fractional positive compartmental linear system (4.13) is observable on the interval $[0, i_f]$ if and only if the matrix

$$\Phi^T C^T C \Phi \in \mathfrak{R}_+^{n \times n} \quad (4.15)$$

is monomial.

Proof. Substituting (4.14a) into (4.13b) we obtain

$$y = C \Phi x_0. \quad (4.16)$$

Note that $[\Phi^T C^T C \Phi]^{-1} \in \mathfrak{R}_+^{n \times n}$ if and only if the matrix (4.15) is monomial. Consequently, equation (4.16) yields

$$x_0 = [\Phi^T C^T C \Phi]^{-1} \Phi^T C^T y \in \mathfrak{R}_+^n \quad (4.17)$$

since $\Phi^T C^T y \in \mathfrak{R}_+^{n \times n}$ for y_i .

5. EIGENVALUE ASSIGNMENT IN THE STANDARD AND FRACTIONAL COMPARTMENTAL LINEAR SYSTEMS

Let us consider the fractional compartmental system (3.3) under state feedback control

$$u = Kx, \quad (5.1)$$

where $K \in \mathfrak{R}^{n \times n}$.

Assuming $B = I_n$, it follows from equation (5.1) that

$$\Delta^\alpha x_{i+1} = F_c x_i, \quad (5.2)$$

where

$$F_c = F - K. \quad (5.3)$$

Based on the given matrix A and the desired close-loop matrix A_c from (5.3), the following expression can be derived

$$K = F - F_c. \quad (5.4)$$

Accordingly, the following theorem is established.

Theorem 5.1. Given the fractional compartmental system (3.3), there always exists a state feedback (5.1) such that the closed-loop system matrix F_c achieves a specified set of eigenvalues.

Example 5.1. The matrix F of the fractional compartmental linear system is given by

$$F = \begin{bmatrix} 0 & 1 & 0 \\ 0 & 0 & 1 \\ -4 & 0 & 3 \end{bmatrix} \quad (5.5)$$

and its eigenvalues are: $z_1 = z_2 = 2$, $z_3 = -1$, since

$$\det[I_3 z - F] = \begin{vmatrix} z & -1 & 0 \\ 0 & z & -1 \\ 4 & 0 & z-3 \end{vmatrix} = z^3 - 3z^2 + 4. \quad (5.6)$$

Determine the feedback matrix $K \in \mathfrak{R}^{3 \times 3}$ such that the closed-loop system matrix F_c has eigenvalues: $\bar{z}_1 = -0.1$, $\bar{z}_2 = -0.2$, $\bar{z}_3 = -0.5$.

It should be noted that the desired closed-loop matrix F_c is not unique. Two alternative forms of F_c are considered below.

Case 1. The matrix F_c is assumed to be in the Frobenius canonical form, as in equation (5.5)

$$F_c = \begin{bmatrix} 0 & 1 & 0 \\ 0 & 0 & 1 \\ -0.01 & -0.17 & -0.8 \end{bmatrix}. \quad (5.7)$$

In this case using (5.4), (5.5) and (5.6) we obtain

$$K = F - F_c = \begin{bmatrix} 0 & 0 & 0 \\ 0 & 0 & 0 \\ -4.01 & -0.17 & 3.8 \end{bmatrix}. \quad (5.8)$$

Case 2. The matrix F_c is assumed to be diagonal

$$F_c = \begin{bmatrix} -0.1 & 0 & 0 \\ 0 & -0.2 & 0 \\ 0 & 0 & -0.5 \end{bmatrix}. \quad (5.9)$$

In this case we have

$$K = F - F_c = \begin{bmatrix} -0.1 & 1 & 0 \\ 0 & -0.2 & 1 \\ -4 & 0 & 3.5 \end{bmatrix}. \quad (5.10)$$

Note that the presented approach can be generalized to include output feedback strategies.

6. CONCLUDING REMARKS

Fractional, compartmental, time-invariant linear systems are analyzed, with a focus on their fundamental properties. Theoretical foundations, including key definitions and theorems related to standard and positive fractional linear systems, are outlined. A class of fractional compartmental discrete-time systems is introduced and studied. The concepts of controllability and observability are discussed for both standard and compartmental systems, followed by an examination of the eigenvalue assignment problem in the compartmental case. The results obtained may also be extended to descriptor discrete-time fractional linear systems.

REFERENCES

1. Abu-Saris R, Al-Mdallal Q. On the asymptotic stability of linear system of fractional-order difference equations. *Fract. Calc. Appl. Anal.* 2013; 16: 613-629.
2. Busłowicz M. Stability analysis of continuous-time linear systems consisting of n subsystems with different fractional orders, *Bull. Pol. Acad. Sci. Tech.* 2012; 60(2): 279-284.
3. Farina L, Rinaldi S. *Positive Linear Systems: Theory and Applications*. J. Wiley & Sons, New York; 2000.
4. Goodrich C, Peterson A. *Discrete Fractional Calculus*. Springer, Cham; 2015.
5. Haddad WM, Chellaboina VS, Hui Q. *Nonnegative and compartmental dynamical systems*. Princeton University Press, Oxford; 2010.
6. Kaczorek T. *Positive 1D and 2D Systems*. Springer Verlag, London; 2002.
7. Kaczorek T. Positivity and reachability of fractional electrical circuits. *Acta Mechanica et Automatica*. 2011; 5(2): 42-51.
8. Kaczorek T. *Selected Problems of Fractional Systems Theory*. Berlin, Germany: Springer-Verlag; 2011.
9. Kaczorek T. Fractional time-invariant compartmental linear systems. *Int. J. Appl. Math. Comput. Sci.* 2023; 33(1): 97-102.
10. Kaczorek T, Rogowski K. *Fractional Linear Systems and Electrical Circuits*. Studies in Systems, Decision and Control. Springer. 2015; 13.
11. Mozyrska D, Wyrwas M. The Z-transform method and delta type fractional difference operators. *Discrete Dyn. Nat. Soc.* 2015;(2-3): 1-12.

12. Oldham K, Spanier J. The fractional calculus: integrations and differentiations of arbitrary order. New York USA. Academic Press 1974.
13. Ostalczyk P. Discrete Fractional Calculus: Applications in Control and Image Processing; Series in Computer Vision, World Scientific Publishing. Hackensack New York; 2016.
14. Podlubny I. Fractional differential equations. San Diego. USA: Academic Press; 1999.
15. Ruszewski A. Stability of discrete-time fractional linear systems with delays, Archives of Control Sciences. 2019; 29(3): 549-567.
16. Sabatier J, Agrawal OP, Machado JAT. Advances in Fractional Calculus, Theoretical Developments and Applications in Physics and Engineering. Springer. London; 2007.
17. Sajewski Ł. Stabilization of positive descriptor fractional discrete-time linear systems with two different fractional orders by decentralized controller. Bull. Pol. Acad. Sci. Techn. 2017; 65(5): 709-714.
18. Sun HG, Zhang Y, Baleanu D, Chen W, Chen YQ. A new collection of real world applications of fractional calculus in science and engineering. Commun. Nonlinear Sci. Numer. Simul. 2018; 64: 213-231.
19. Wu GC, Abdeljawad T, Liu J, Baleanu D, Wu KT. Mittag-Leffler stability analysis of fractional discrete-time neural networks via fixed point technique. Nonlinear Analysis: Model. Contr. 2019;24:919-936.

This work was supported by National Science Centre in Poland under work No. 2022/45/B/ST7/03076.

Tadeusz Kaczorek:  <https://orcid.org/0000-0002-1270-3948>

Andrzej Ruszewski:  <https://orcid.org/0000-0003-0095-6486>



This work is licensed under the Creative Commons BY-NC-ND 4.0 license.

GENERALIZED KDV EQUATION: NOVEL NATURE OCEANIC, M-LUMP AND PHYSICAL COLLISION WAVES

Hajar Farhan ISMAEL ^{*}/^{**} 

^{*}Department of Mathematics, College of Science, University of Zakho, Zakho, Iraq

^{**}Department of Computer Science, College of Science, Knowledge University, Erbil 44001, Iraq

hajar.ismael@uoz.edu.krd

received 30 November 2024, revised 8 February 2025, accepted 10 February 2025

Abstract: The main idea of this study is to explore new features for the generalized (3+1)-dimensional Korteweg-De Vries problem. This equation may be used to model various physical processes in several domains, including nonlinear optics, oceanography, acoustic waves in plasma physics, and other areas where coupled wave dynamics are essential. The Hirota method and long-wave technique to reveal various wave solutions are under consideration. Complex N-soliton solutions, M-lump waves, and hybrid solutions between some types of soliton and M-lump solutions are offered. The obtained solutions are one-, two-, and three-M-lump waves and mixed soliton-lump, soliton-two-lump, and two-soliton-lump solutions. Also, one-soliton, two-soliton, three-soliton, and four-soliton solutions in complex form are offered. To better analyse and understand the propagation characteristics of these solutions, 3D and contour plots for gained solutions are drawn. As far as we know, these solutions are novel and have not been revealed. Since the KdV equation often describes shallow water waves with weakly nonlinear restoring forces, we are interested in the features that have yet to be studied.

Key words: complex multi-soliton, hybrid wave, Hirota bilinear method, long-wave method

1. INTRODUCTION

Nonlinearity is a fascinating phenomenon in nature, and scientists believe that nonlinear study is the most promising means of gaining a deeper understanding of how nature works. Investigating a wide range of nonlinear ordinary and partial differential equations is critical for mathematically describing complicated processes that change over time. These mathematical formulas are created in various fields, including economics, optical fibers, elasticity, plasma physics, solid-state physics, population ecology, infectious disease epidemiology, physics, and natural sciences. Soliton solutions of the previously mentioned phenomenon have been a fascinating and extraordinarily active topic of study for the past several decades, with the accompanying problem being the creation of exact solutions to a large variety of nonlinear partial differential equations. As a result, mathematics and physical scientists have made significant efforts to develop exact wave solutions to certain NLPDEs and various practical and potent strategies, including Hirota's method [1][2][3][4], Backlund transformations [5], Pfaffian technique [6], the extended simplest equation approach [7], Riemann–Hilbert method [8][9], modified Sardar sub-equation method [10], physics-informed neural networks algorithm [11], a unified method [12], bilinear Bäcklund transformation [13], modified F-expansion method [14], the symbolic computation and Hirota method [15], and so on.

A soliton is a single, self-reinforcing wave that passes over a medium without ever dispersing or dissipating, preserving its shape and speed. Solitons are extremely stable and may maintain their form over long distances due to their unique nature. A lump solution is an analytical rational function solution that exists in all directions in space, and solitons are analytic solutions that are exponentially

localized in all directions in space and time. They have previously been identified for nonlinear integrable equations.

A well-known partial differential equation used to model the disturbance of the surface of shallow water in the presence of solitary waves is the Korteweg-De Vries (KdV) equation. This equation incorporates leading-order nonlinearity and dispersion and can be used to study weakly nonlinear long waves. In shallow water, it describes small-amplitude waves with long wavelengths. The KdV equations have different types, such as the fifth-order KdV equation [16], the lattice potential KdV equation [17], generalized geophysical KdV equation [18], modified KdV equation [19], seventh-order KdV equation [20], Schwarzian KdV equation [21], and many others.

Recently, the generalized Korteweg-De Vries (gKdV) equation in two dimensions became known and read as follows:

$$u_t + 6uu_x + u_{xxx} + u_x + \partial_x^{-1}u_{yt} + u_y + u_{xxy} + 3uu_y + 3u_x\partial_x^{-1}u_y = 0, \quad (1)$$

where $\partial_x^{-1} := \int_{-\infty}^x \cdot dx$. It is comparable to the following equation when accounting for the potential $u(x, y, z, t) = \theta(x, y, z, t)$

$$\theta_{xt} + 6\theta_x\theta_{xx} + \theta_{xxx} + \theta_{xx} + \theta_{yt} + \theta_{xy} + \theta_{xxy} + 3\theta_x\theta_{xy} + 3\theta_{xx}\theta_y = 0. \quad (2)$$

Lu and Chen [22] investigated this problem and found many distinct solutions in addition to integrability results. By modifying the preceding (2+1)-dimensional form (1), Ismael et al. [23], have created a new (3+1)-dimensional integrable gKdV equation.

$$u_t + 6uu_x + u_{xxx} + u_x + \partial_x^{-1}u_{yt} + u_y + u_{xxy} + 3uu_y + 3u_x\partial_x^{-1}u_y + \beta u_z + \beta_1\partial_x^{-1}u_{yz} + \gamma\partial_x^{-1}u_{yy} = 0, \quad (3)$$

where β, β_1, γ are defined as non-zero constants. The Painlevé test to reveal the integrability of the equation was used and found that when $\beta = \beta_1$, the equation becomes integrable. Therefore, we have

$$u_t + 6uu_x + u_{xxx} + u_x + \partial_x^{-1}u_{yt} + u_y + u_{xy} + 3uu_y + 3u_x\partial_x^{-1}u_y + \beta u_z + \beta\partial_x^{-1}u_{yz} + \gamma\partial_x^{-1}u_{yy} = 0. \quad (4)$$

The multiple soliton solutions to the equation (4) were reported by authors in Ref. [23]. In this paper, we use Hirota's method, which is a direct method to obtain multiple soliton solutions to integrable nonlinear evolution equations. It is also possible to determine multiple soliton solutions using other methods, such as inverse scattering transform [24] and various other techniques. The advantage of Hirota's method over the others is that it is algebraic rather than analytic. Therefore, Hirota's method provides the most efficient results when we just want to construct multiple soliton solutions. Also, applying the long-wave method on N-soliton solutions, we can offer M-lump waves. In the present study, one-, two-, and three-M-lump waves, three interaction phenomena of soliton with M-lump waves, and four types of complex multiple solutions are derived. To our knowledge, these propagation wave solutions have not been investigated before.

Following is a summary of this study: In the second section, under the corresponding N-soliton solutions, the main idea is to construct M-lump solutions for equation (4), which is made possible by using a long wave method. In the third section, we offer and analyze the characteristics of mixed solutions, a mix of lump and soliton solutions. The fourth section is about the complex N-soliton solutions for the studied equation. In the fifth section, results and discussion about constructed solutions are presented. The last part contains some discussions and conclusions from this effort.

2. MULTIPLE M-LUMP SOLUTIONS

To extract the soliton solutions to the Eq. (4), consider the relation

$$u = 2(\log(f))_{xx}. \quad (5)$$

Therefore, equation (4) could be shown to possess its bilinear form

$$\left(D_t D_x + D_y D_t + D_x D_y + D_x^4 + D_x^3 D_y + \right) f \cdot f = 0, \quad (6)$$

where $f = f(x, y, z, t)$ and D is the Hirota derivative and stated as

$$D_{x_1}^{r_1} D_{x_2}^{r_2} D_{x_3}^{r_3} D_{x_4}^{r_4} \chi_1 \cdot \chi_2 = \left(\partial_{x_1} - \partial_{x_1'} \right)^{r_2} \left(\partial_{x_2} - \partial_{x_2'} \right)^{r_4} \times \left(\partial_{x_3} - \partial_{x_3'} \right)^{r_3} \left(\partial_{x_4} - \partial_{x_4'} \right)^{r_4} \times \chi_1(x_1, x_2, x_3, x_4) \chi_2(x_1', x_2', x_3', x_4')|_{x_1=x_1', x_2=x_2', x_3=x_3', x_4=x_4'},$$

where x_1, x_2, x_3, x_4 defines as independent variables, χ_1, χ_2 are dependent variables, and constants $r_1, r_2, r_3, r_4 \geq 0$. Generally, to offer the N-soliton solutions to the PDEs, we use the following formula [25]:

$$f \equiv f_N = \sum_{\mu=0,1} \exp(\sum_{m=1}^N \Omega_m \varphi_m + \sum_{m<n}^{(N)} \mu_m \mu_n A_{mn}) \quad (7)$$

The notation $\sum_{\mu=0,1}$ represents the sum of all possible composites $\mu_m = 0, 1$, for $m = 1, 2, \dots, N$.

By taking the specific condition $m < n$, the first three solutions of Eq. (7) have the form

$$\begin{aligned} f_1 &= 1 + e^{\Omega_1}, \\ f_2 &= 1 + e^{\Omega_1} + e^{\Omega_2} + A_{12} e^{\Omega_1 + \Omega_2}, \\ f_3 &= 1 + e^{\Omega_1} + e^{\Omega_2} + e^{\Omega_3} + A_{12} e^{\Omega_1 + \Omega_2} + A_{13} e^{\Omega_1 + \Omega_3} + A_{23} e^{\Omega_2 + \Omega_3} + A_{123} e^{\Omega_1 + \Omega_2 + \Omega_3}, \end{aligned} \quad (8)$$

where

$$\Omega_m = k_m(x + l_m y + j_m z + w_m t) + \lambda_m, \quad (9)$$

with dispersion relation

$$w_m = - \left(1 + k_m^2 + j_m \beta + \frac{l_m^2 \gamma}{1 + l_m} \right), \quad (10)$$

and

$$e^{A_{mn}} = \frac{K_1}{K_2}, \quad (11)$$

where

$$\begin{aligned} K_1 &= 3(k_m - k_n)(1 + l_m)(1 + l_n)(k_m(1 + l_m) - k_n(1 + l_n)) - (l_m - l_n)^2 \gamma, \\ K_2 &= 3(k_m + k_n)(1 + l_m)(1 + l_n)(k_m + k_n + k_m l_m + k_n l_n) - (l_m - l_n)^2 \gamma. \end{aligned}$$

Here, $k_m, l_m, j_m, w_m, \lambda_m$ are constants, whereas Ω_m defines as the functions dependent on x, y, z, t . Now, to address the M-lump wave solution, we apply the long-wave method by taking $N = 2$, and assuming, $k_m \rightarrow 0$, $e^{\lambda_m} = -1$, and $\frac{k_1}{k_2} = O(1)$ in Eq. (7) give

$$f_2 = \Phi_1 \Phi_2 + B_{12}, \quad (12)$$

where

$$\Phi_m = x + l_m y + j_m z + w_m t, \quad (13)$$

$$w_m = - \left(1 + j_m \beta + \frac{l_m^2 \gamma}{1 + l_m} \right), \quad (14)$$

$$B_{mn} = \frac{6(1+l_m)(1+l_n)(2+l_m+l_n)}{(l_m-l_n)^2 \gamma}. \quad (15)$$

Taking $l_1 = a_1 + b_1 i$, $l_2 = l_1^*$ and $j_1 = c_1 + d_1 i$, $j_2 = j_1^*$. Note that $i = \sqrt{-1}$ and $*$ indicates the complex conjugation. From plugging Eqs. (12-15) into Eq. (5), we have

$$u = 2 \left(\log \left(\frac{(x' + a_1 y' + c_1 z')^2 + (b_1 y' + d_1 z')^2}{- \frac{3(1+a_1)((1+a_1)^2 + b_1^2)}{b_1^2 \gamma}} \right) \right)_{xx} \quad (16)$$

where

$$\begin{aligned} x' &= \frac{\gamma a_1 + \gamma b_1^2 + \gamma a_1^2}{a_1^2 + b_1^2 + 2a_1 + 1} t - t, \\ y' &= y - \gamma t, \\ z' &= z - \beta t. \end{aligned}$$

Equation (16) is a single M-lump wave as shown in Figure (1) for the gKdV equation with decaying as $O\left(\frac{1}{x^2}, \frac{1}{y^2}, \frac{1}{z^2}\right)$ for $|x|, |y|, |z| \rightarrow \infty$ and move with the velocity

$$\begin{aligned} v_x &= 1 - \frac{(a_1 + b_1^2 + a_1^2) \gamma}{(a_1^2 + b_1^2 + 2a_1 + 1)}, \\ v_y &= \gamma, \end{aligned}$$

$$v_z = \beta.$$

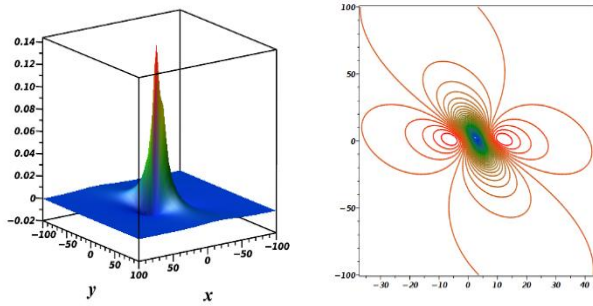


Fig. 1. Graphs of one-M-lump wave when $z = 2, t = 2, a_1 = \frac{1}{5}, b_1 = 0.5, c_1 = 0.5, d_1 = 0.5, \beta = 2, \gamma = -1$.

The path followed by this wave is denoted by the following plane:

$$y = \frac{G_1}{G_2},$$

where

$$G_1 = -((a_1 + 1)^2 + b_1^2)d_1(z - x\beta) - (a_1^2(1 + a_1) + (a_1 - 1)b_1^2)d_1z\gamma + b_1(a_1(a_1 + 2) + b_1^2)(x + c_1z)\gamma,$$

$$G_2 = ((a_1 + 1)^2 + b_1^2)(b_1 + b_1c_1\beta - a_1d_1\beta) - b_1(a_1^2 + b_1^2)\gamma.$$

The one-M-lump wave on this plane is depicted in Figure (2) at various time periods.

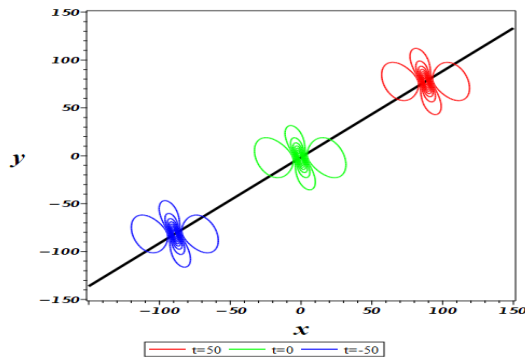


Fig. 2. Plot of Eq. (12) for $z = 2, a_1 = \frac{1}{5}, b_1 = 0.5, c_1 = 0.5, d_1 = 0.5, \beta = 2, \gamma = -1$

As part of our analysis of the equation, we want to specify the characteristics of a double-M-lump wave by considering $N = 4$ in Eq. (7), and $k_m \rightarrow 0, e^{\lambda_m} = -1$ ($m = 1, 2, 3, 4$), the outcome offers

$$f_4 = \phi_1\phi_2\phi_3\phi_4 + B_{12}\phi_3\phi_4 + b_{13}\phi_2\phi_4 + B_{14}\phi_2\phi_3 + B_{23}\phi_1\phi_4 + B_{24}\phi_1\phi_3 + B_{34}\phi_1\phi_2 + B_{12}\phi_{34} + B_{13}B_{24} + B_{14}B_{23}, \quad (17)$$

where $\phi_1, \phi_2, \phi_3, \phi_4, w_m$ and B_{mn} ($n < m$) are explained with Eqs. (13), (14), and Eq. (15), respectively. The double-lump solution is obtained by combining equation (17) with the other findings in equation (5) and demonstrated in Figure 3.

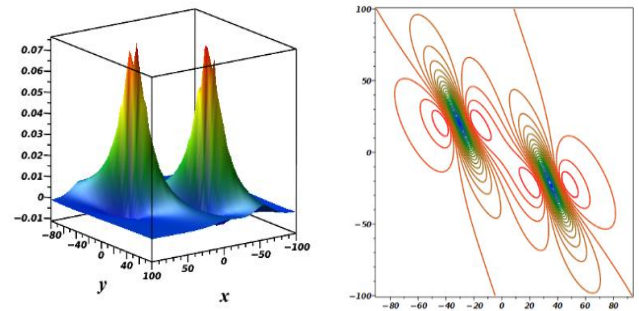


Fig. 3. Plots of 2-M-lump wave when $z = 2, t = 2, a_1 = 0.5, b_1 = 0.5, a_2 = \frac{1}{3}, b_2 = \frac{1}{3}, c_1 = \frac{1}{3}, d_1 = \frac{1}{3}, c_2 = \frac{1}{4}, d_2 = \frac{1}{4}, \beta = 2, \gamma = -1$.

For 3-M-lump of Eq. (4), we take $k_m \rightarrow 0, e^{\lambda_m} = -1$ ($m = 1, \dots, 6$) and considering $N = 6$ in Eq. (7), shows

$$f_6 = \phi_1\phi_2\phi_3\phi_4\phi_5\phi_6 + B_{12}B_{34}B_{56} + B_{12}B_{35}B_{46} + B_{12}B_{45}B_{36} + B_{13}B_{24}B_{56} + B_{13}B_{25}B_{46} + B_{13}B_{45}B_{26} + B_{23}B_{14}B_{56} + B_{14}B_{25}B_{36} + B_{14}B_{35}B_{26} + B_{24}B_{15}B_{36}B_{34}B_{15}B_{26} + B_{23}B_{15}B_{46} + B_{23}B_{45}B_{16} + B_{24}B_{35}B_{16} + B_{34}B_{25}B_{16} + \phi_2\phi_3\phi_4\phi_5B_{16} + \phi_2\phi_3\phi_5\phi_6B_{14} + \phi_2\phi_3\phi_4\phi_6B_{15} + \phi_3\phi_4\phi_5\phi_6B_{12} + \phi_2\phi_4\phi_5\phi_6B_{13} + \phi_1\phi_2\phi_4\phi_6B_{35} + \phi_1\phi_2\phi_4\phi_5B_{36} + \phi_1\phi_4\phi_5\phi_6B_{23} + \phi_1\phi_3\phi_5\phi_6B_{24} + \phi_1\phi_3\phi_4\phi_6B_{25} + \phi_1\phi_3\phi_4\phi_5B_{26} + \phi_1\phi_2\phi_3\phi_4B_{56} + \phi_1\phi_2\phi_3\phi_6B_{45} + \phi_1\phi_2\phi_3\phi_5B_{46} + \phi_1\phi_2\phi_5\phi_6B_{34} + \phi_1\phi_2\phi_3\phi_4B_{56} + \phi_1\phi_2B_{35}B_{46} + \phi_1\phi_2B_{45}B_{36} + \phi_1B_{23}\phi_5B_{46} + \phi_1B_{23}\phi_4B_{56} + \phi_1B_{23}B_{45}\phi_6 + \phi_1\phi_3B_{24}B_{56} + \phi_1\phi_6B_{24}B_{35} + \phi_1\phi_5B_{24}B_{36} + \phi_1\phi_3B_{25}B_{46} + \phi_1\phi_6B_{34}B_{25} + \phi_1\phi_4B_{25}B_{36} + \phi_1\phi_3B_{45}B_{26} + \phi_1\phi_5B_{34}B_{26} + \phi_1\phi_4B_{35}B_{26} + \phi_4\phi_5B_{12}B_{36} + \phi_3\phi_4B_{12}B_{56} + \phi_3\phi_6B_{12}B_{45} + \phi_3\phi_5B_{12}B_{46} + \phi_5\phi_6B_{12}B_{34} + \phi_4\phi_6B_{12}B_{35} + \phi_5\phi_6B_{13}B_{24} + \phi_4\phi_6B_{13}B_{25} + \phi_4\phi_5B_{13}B_{26} + \phi_2\phi_4B_{13}B_{56} + \phi_2\phi_6B_{13}B_{45} + \phi_2\phi_5B_{13}B_{46} + \phi_2\phi_3B_{14}B_{56} + \phi_2\phi_6B_{14}B_{35} + \phi_2\phi_5B_{14}B_{36} + \phi_5\phi_6B_{23}B_{14} + \phi_3\phi_6B_{14}B_{25} + \phi_3\phi_5B_{14}B_{26} + \phi_4\phi_6B_{23}B_{15} + \phi_3\phi_6B_{24}B_{15} + \phi_3\phi_4B_{15}B_{26} + \phi_2\phi_3B_{15}B_{46} + \phi_2\phi_6B_{34}B_{15} + \phi_2\phi_4B_{15}B_{36} + \phi_2\phi_4B_{35}B_{16} + \phi_4\phi_5B_{23}B_{16} + \phi_3\phi_5B_{24}B_{16} + \phi_3\phi_4B_{25}B_{16} + \phi_2\phi_3B_{45}B_{16} + \phi_2\phi_5B_{34}B_{16}. \quad (18)$$

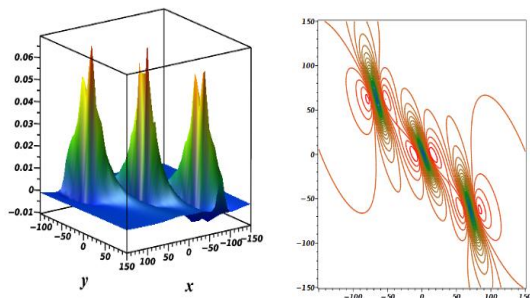


Fig. 4. Plots of 3-M-lump wave when $z = 2, t = 2, a_1 = 0.5, b_1 = 0.5, a_2 = \frac{1}{3}, b_2 = \frac{1}{3}, a_3 = \frac{1}{4}, b_3 = \frac{1}{4}, c_1 = 0.5, d_1 = 0.5, c_2 = \frac{1}{5}, d_2 = \frac{1}{5}, c_3 = \frac{1}{6}, d_3 = \frac{1}{6}, \beta = 2, \gamma = -1$

We should know that Φ_p ($p = 1, \dots, 6$), w_m , and B_{mn} are depicted in Eq. (13), Eq. (14) and Eq. (15), respectively. By introducing Eq. (18) into Eq. (5), a 3-M-lump solution is displayed in Fig. 4. It is important to understand that $l_1 = a_1 + b_1 i$, $l_2 = a_2 + b_2 i$, $l_3 = a_3 + b_3 i$, $l_4 = l_1^*$, $l_5 = l_2^*$, and $l_6 = l_3^*$.

3. COLLISION PHENOMENA

Through a long-wave approach and setting $k_m \rightarrow 0$, with $\frac{k_1}{k_2} = O(1)$, $e^{\lambda_m} = -1$ for $m = 1, 2$, and $N = 3$, therefore f_3 reads

$$f_3 = \Phi_1 \Phi_2 + B_{12} + \kappa_1 e^{\psi_3}, \quad (19)$$

where

$$\kappa_1 = \Phi_1 \Phi_2 + B_{12} + C_{23} \Phi_1 + C_{13} \Phi_2 + C_{13} C_{23}, \quad (20)$$

$$C_{mn} = -\frac{6k_n(1+l_m)(1+l_n)(2+l_m+l_n)}{3k_n^2(1+l_m)(1+l_n)^2 - (l_m - l_n)^2 \gamma}. \quad (21)$$

By combining Eq. (19) with Eq. (5), the outcome is a combination of a single-lump with a single-soliton solution (see Fig. 5).

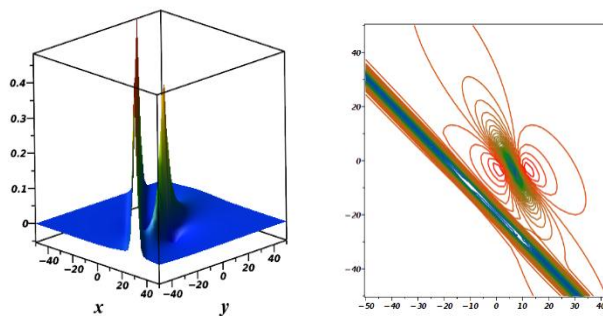


Fig. 5. Plots of M-lump with soliton solution when $z = 1$, $t = 2$, $a_1 = 0.5$, $b_1 = 0.5$, $a_2 = \frac{1}{3}$, $b_2 = \frac{1}{3}$, $k_3 = 1$, $l_3 = 1$, $j_3 = 2$, $\lambda_3 = 20$, $\beta = 2$, $\gamma = -1$

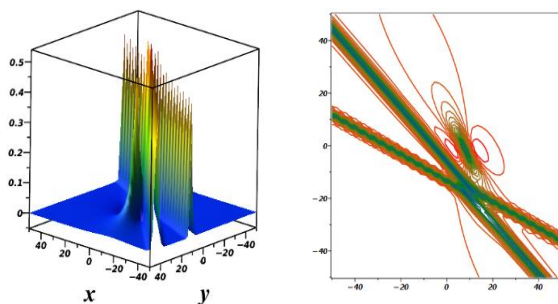


Fig. 6. Graphs of M-lump with a 2-soliton solution when $z = 1$, $t = 2$, $a_1 = 0.5$, $b_1 = 0.5$, $c_1 = \frac{1}{3}$, $d_1 = \frac{1}{3}$, $k_3 = 1$, $l_3 = 1$, $j_3 = 2$, $\lambda_3 = 10$, $k_4 = 1$, $l_4 = 2$, $j_4 = 3$, $\lambda_4 = 20$, $\beta = 1$, $\gamma = -5$

Setting $N = 4$ in Eq. (7), and $k_m \rightarrow 0$, $\frac{k_1}{k_2} = O(1)$, and $e^{\lambda_m} = -1$ for $m = 1, 2$, we set up

$$f_4 = \Phi_1 \Phi_2 + B_{12} + \kappa_1 e^{\psi_3} + \kappa_2 e^{\psi_4} + A_{34} e^{\psi_3 + \psi_4} (\kappa_1 + \kappa_2 - \Phi_1 \Phi_2 - B_{12} + C_{13} C_{24} + C_{14} C_{23}), \quad (22)$$

where

$$\kappa_2 = \Phi_1 \Phi_2 + B_{12} + C_{24} \Phi_1 + C_{14} \Phi_2 + C_{14} C_{24}. \quad (23)$$

Eq. (22) can be substituted into Eq. (5) to provide a result that combines the properties of a double-soliton solution and a single-M-lump solution (refer to Fig. 6).

If $N = 5$ and taking the limit $k_m \rightarrow 0$ and $e^{\lambda_m} = -1$ for $m = 1, 2, 3, 4$, in Eq. (7), we get

$$f_5 = \Phi_1 \Phi_2 \Phi_3 \Phi_4 + B_{34} \Phi_1 \Phi_2 + B_{24} \Phi_1 \Phi_3 + B_{23} \Phi_1 \Phi_4 + B_{14} \Phi_2 \Phi_3 + B_{13} \Phi_2 \Phi_4 + B_{12} \Phi_3 \Phi_4 + Q e^{\psi_5} + B_{14} B_{23} + B_{13} B_{24} + B_{12} B_{34} \quad (24)$$

where

$$\begin{aligned} Q = & \Phi_1 \Phi_2 \Phi_3 \Phi_4 + C_{45} \Phi_1 \Phi_2 \Phi_3 + C_{15} \Phi_2 \Phi_3 \Phi_4 \\ & + C_{25} \Phi_1 \Phi_3 \Phi_4 + C_{35} \Phi_1 \Phi_2 \Phi_4 \\ & + (B_{34} + C_{35} C_{45}) \Phi_1 \Phi_2 \\ & + (B_{24} + C_{25} C_{45}) \Phi_1 \Phi_3 \\ & + (B_{14} + C_{15} C_{45}) \Phi_2 \Phi_3 \\ & + (B_{23} + C_{25} C_{35}) \Phi_1 \Phi_4 \\ & + (B_{13} + C_{15} C_{35}) \Phi_2 \Phi_4 \\ & + (B_{12} + C_{15} C_{25}) \Phi_3 \Phi_4 \\ & + (B_{34} C_{25} + B_{24} C_{35} + B_{23} C_{45} \\ & + C_{25} C_{35} C_{45}) \Phi_1 \\ & + (B_{34} C_{15} + B_{14} C_{35} + B_{13} C_{45} \\ & + C_{15} C_{35} C_{45}) \Phi_2 \\ & + (B_{24} C_{15} + B_{14} C_{25} + B_{12} C_{45} \\ & + C_{15} C_{25} C_{45}) \Phi_3 \\ & + (B_{23} C_{15} + B_{13} C_{25} + B_{12} C_{35} \\ & + C_{15} C_{25} C_{35}) \Phi_4 + B_{14} B_{23} + B_{13} B_{24} \\ & + B_{12} B_{34} + B_{34} C_{15} C_{25} + B_{24} C_{15} C_{35} \\ & + B_{14} C_{25} C_{35} + B_{23} C_{15} C_{45} + B_{13} C_{25} C_{45} \\ & + B_{12} C_{35} C_{45} + C_{15} C_{25} C_{35} C_{45}. \end{aligned}$$

The outcome shown in Figure 7 is the observable feature, which is obtained by combining Eq. (24) and Eq. (5) to illustrate an interaction of a two-M-lump with a soliton solution. A complete list of all constants and functions can be found in this article.

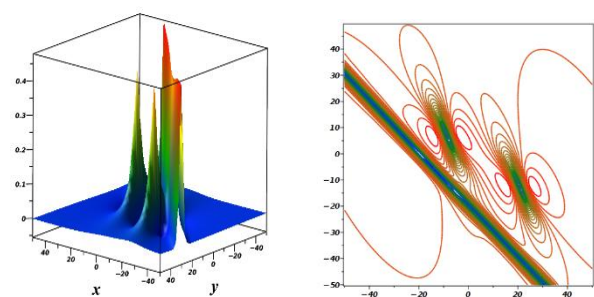


Fig. 7. Plots of 2-M-lump with soliton solution when $z = 1$, $t = 2$, $a_1 = 0.5$, $b_1 = 0.5$, $a_2 = \frac{1}{3}$, $b_2 = \frac{1}{3}$, $c_1 = \frac{1}{4}$, $d_1 = \frac{1}{4}$, $c_2 = \frac{1}{5}$, $d_2 = \frac{1}{5}$, $k_5 = 1$, $l_5 = 1$, $j_5 = 2$, $\lambda_5 = 20$, $\beta = 1$, $\gamma = -5$

4. COMPLEX MULTI-SOLITON SOLUTIONS

Here, we explore the complexity of multi-solutions to the studied equation to explore new features of solutions.

4.1. The complex one-soliton wave

First, to construct the complex one-soliton wave, the assumption is

$$g_1 = 1 + ie^{k_1(x+l_1y+j_1z-(1+k_1^2+j_1\beta+\frac{l_1^2\gamma}{1+l_1})t)+\alpha_1} \quad (25)$$

Substituting this assumption into Eq.(5), the result is

$$u = -\frac{2ik_1^2e^{\frac{\alpha_1+k_1(x+l_1y+j_1z-t(1+k_1^2+j_1\beta+\frac{l_1^2\gamma}{1+l_1}))}{2}}}{\left(e^{\frac{\alpha_1+k_1(x+l_1y+j_1z-t(1+k_1^2+j_1\beta+\frac{l_1^2\gamma}{1+l_1}))}{2}}-i\right)} \quad (26)$$

This solution is shown graphically in Fig. (8).

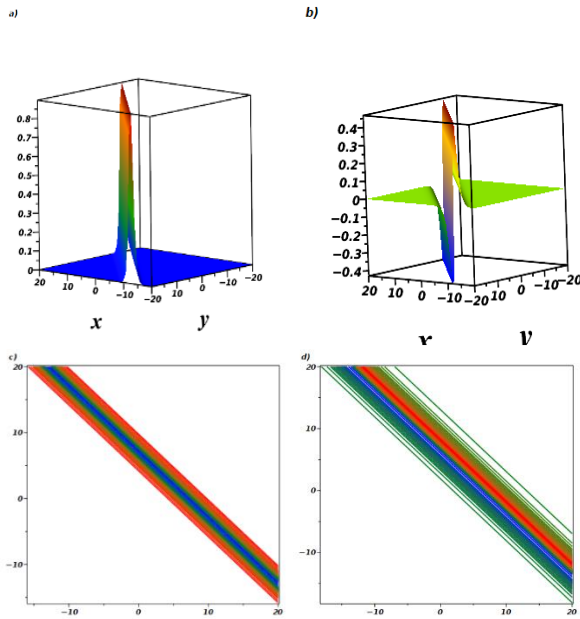


Fig. 8. Graphs of complex one-soliton wave are plotted for $z = 1, t = 2, k_1 = 1, l_1 = 1, j_1 = 2, \alpha_1 = 1, \beta = 1, \gamma = 2$: a) Real part, b) Imaginary part, c) Contour plot of real part, d) Contour plot of imaginary part

4.2. The complex two-soliton solution

Here, the objective is to drive a double-soliton solution, where the assumption is

$$g_2 = 1 + ie^{\theta_1} + ie^{\theta_2} + S_{12}e^{\theta_1+\theta_2}. \quad (27)$$

Putting this equation into Eq. (5), the result yields

$$u = \frac{2\left(g_2\frac{\partial^2 g_2}{\partial x^2}\frac{\partial g_2^2}{\partial x}\right)}{g_2^2}, \quad (28)$$

where

$$\theta_1 = k_1(x+l_1y+j_1z+\omega_1t)+\alpha_1, \theta_2 = k_2(x+l_2y+j_2z+\omega_2t)+\alpha_2, \omega_1 = -\left(1+k_1^2+j_1\beta+\frac{l_1^2\gamma}{1+l_1}\right), \omega_2 = -\left(1+k_2^2+j_2\beta+\frac{l_2^2\gamma}{1+l_2}\right)$$

and

$$S_{12} =$$

$$\frac{(l_1-l_2)^2\gamma-3(k_1-k_2)(1+l_1)(1+l_2)(k_1(1+l_1)-k_2(1+l_2))}{3(k_1+k_2)(1+l_1)(1+l_2)(k_1+k_2+k_1l_1+k_2l_2)-(l_1-l_2)^2\gamma}.$$

This solution represents a complex two-soliton solution, and it is drawn in Fig. (9).

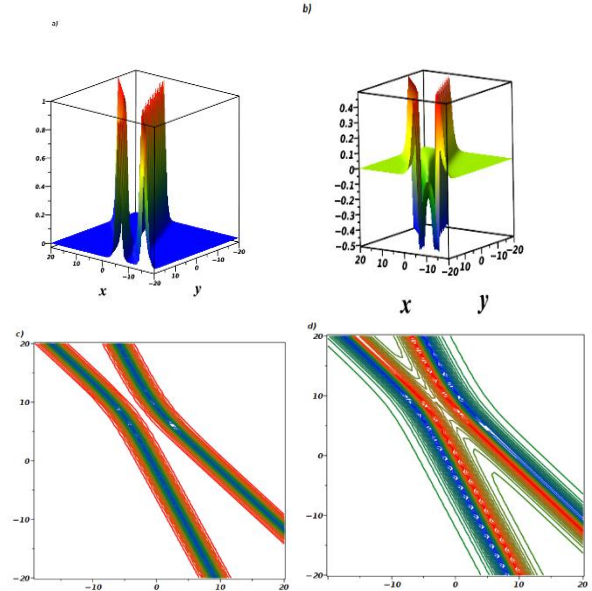


Fig. 9. Graphs of complex two-soliton wave are plotted for $z = 1, t = 2, k_1 = 1, k_2 = 1, l_1 = 1, l_2 = 0.5, j_1 = 0.5, j_2 = 0.5, \alpha_1 = 3, \alpha_2 = 6, \beta = 1, \gamma = 2$: a) Real part, b) Imaginary part, c) Contour plot of real part, d) Contour plot of imaginary part

4.3. The complex three-soliton solution

To report a three-soliton solution in complex form, let

$$g_3 = 1 + ie^{\theta_1} + ie^{\theta_2} + ie^{\theta_3} + S_{12}e^{\theta_1+\theta_2} + S_{13}e^{\theta_1+\theta_3} + S_{23}e^{\theta_2+\theta_3} + iS_{123}e^{\theta_1+\theta_2+\theta_3}. \quad (29)$$

Substituting this equation into Eq. (5), we have

$$u = \frac{2\left(g_3\frac{\partial^2 g_3}{\partial x^2}\frac{\partial g_3^2}{\partial x}\right)}{g_3^2}. \quad (30)$$

The function θ_m is defined as

$$\theta_m = k_m(x+l_my+j_mz+\omega_mt)+\alpha_m, \quad (31)$$

with dispersion relation

$$\omega_m = -\left(1+k_m^2+j_m\beta+\frac{l_m^2\gamma}{1+l_m}\right), \quad (32)$$

where the constant $S_{123} = S_{12}S_{13}S_{23}$ $S_{123} = S_{12}S_{13}S_{23}$.

The constant S_{mn} is stated as

$$S_{mn} = \frac{Z_1}{Z_2}, \quad (33)$$

where

$$Z_1 = (l_m-l_n)^2\gamma-3(k_m-k_n)(1+l_m)(1+l_n)(k_m(1+l_m)-k_n(1+l_n)),$$

$$Z_2 = 3(k_m+k_n)(1+l_m)(1+l_n)(k_m+k_n+k_ml_m+)$$

$$k_n l_n) - (l_m - l_n)^2 \gamma.$$

The result of this solution is presented in Fig. (10), which is a complex-three-soliton solution.

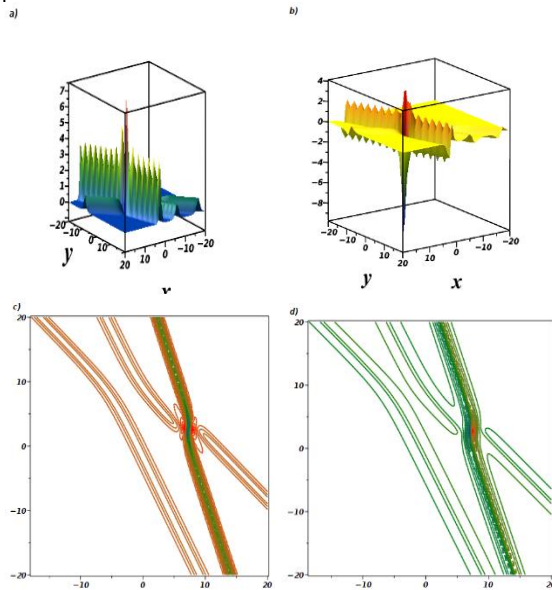


Fig. 10. Graphs of complex three-M-lump wave are plotted for $z = 1, t = 2, k_1 = 1, k_2 = 1, k_3 = 2, l_1 = 1, l_2 = 0.5, l_3 = \frac{1}{3}, j_1 = 0.5, j_2 = 0.5, j_3 = \frac{1}{3}, \alpha_1 = 3, \alpha_2 = 6, \alpha_3 = 9, \beta = 1, \gamma = 2$: a) Real part, b) Imaginary part, c) Contour plot of real part, d) Contour plot of imaginary part

4.4. The complex four-soliton solution

To report a four-soliton solution in complex form, let

$$g_4 = 1 + ie^{\varphi_1} + ie^{\varphi_2} + ie^{\varphi_3} + ie^{\varphi_4} + S_{12}e^{\varphi_1+\varphi_2} + S_{13}e^{\varphi_1+\varphi_3} + S_{14}e^{\varphi_1+\varphi_4} + S_{23}e^{\varphi_2+\varphi_3} + S_{24}e^{\varphi_2+\varphi_4} + S_{34}e^{\varphi_3+\varphi_4} + iS_{123}e^{\varphi_1+\varphi_2+\varphi_3} + iS_{124}e^{\varphi_1+\varphi_2+\varphi_4} + iS_{234}e^{\varphi_2+\varphi_3+\varphi_4} + S_{1234}e^{\varphi_1+\varphi_2+\varphi_3+\varphi_4} \quad (34)$$

where $S_{ijk} = S_{ij}S_{ik}S_{jk}$ and $S_{1234} = S_{123}S_{124}S_{234}$ are defined in Eq. (33). Substituting this equation into Eq. (5), we have

$$u = \frac{2\left(g_4 \frac{\partial^2 g_4}{\partial x^2} - \left(\frac{\partial g_4}{\partial x}\right)^2\right)}{g_4^2}. \quad (35)$$

This equation represents a complex four-soliton solution (see Fig. (11)). The research paper contains all required constants and functions.

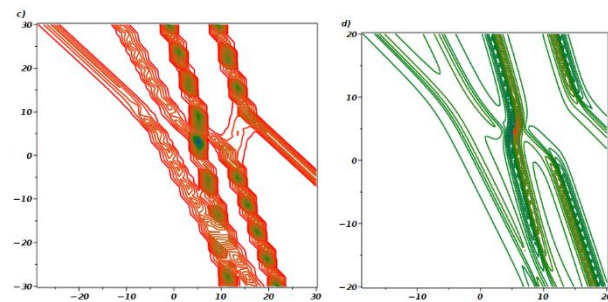
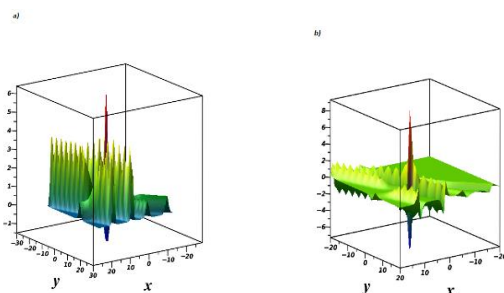


Fig. 11. Graphs of complex four-soliton wave are plotted for $z = 1, t = 2, k_1 = 1, k_2 = 1, k_3 = 2, k_4 = 2, l_1 = 1, l_2 = 0.5, l_3 = \frac{1}{3}, l_4 = \frac{1}{4}, j_1 = 0.5, j_2 = 0.5, j_3 = \frac{1}{3}, j_4 = \frac{1}{4}, \alpha_1 = 3, \alpha_2 = 6, \alpha_3 = 9, \alpha_4 = 12, \beta = 1, \gamma = 2$: a) Real part, b) Imaginary part, c) Contour plot of real part, d) Contour plot of imaginary part

5. RESULTS AND DISCUSSION

The gKdV equation has been investigated, and some novel solutions have been presented. A logarithmic variable transform is considered to transform the studied equation to the Hirota bilinear form. Via Hirota bilinear and long-wave methods, novel physical features to the considered equation are derived. The one-M-lump wave is shown in Fig. 1, and the motion of this wave, which moves on a straight line, is presented in Fig. 2. In Fig. 3 and Fig. 4, the double-, and triple-M-lump solutions have been drawn with the corresponding contour plots. Hybrid solutions are also derived. In Fig. 5 shows, mixed single soliton with a single M-lump wave, in Fig. 6 shows, mixed double soliton with a single M-lump wave, and Fig. 7 shows, mixed single soliton with a double M-lump wave with corresponding contour plots. Moreover, the complexiton soliton solutions are also constructed. In Fig. 8, the real and imaginary parts of a complex one-soliton solution are sketched. In Fig. 9, the real and imaginary parts of a complex two-soliton solution are drawn. The triple-soliton solution in complex form is derived in Fig. 10, and in Fig. 11, the behaviours of the four-soliton solution are presented.

6. CONCLUSION

We have considered the gKdV equation as a mathematical model of waves on shallow water surfaces. As far as macroscale processes and phenomena are concerned, KdV remains the most complete and arguably most useful model. First, the (3+1)-dimensional gKdV equation via variable transform is converted to the Hirota bilinear form. The M-lump wave solutions, namely one-lump, two-lump, and three-lump solutions, have been explored by applying the long-wave technique on the N-soliton solutions, which were constructed via the Hirota method. The interaction solutions via utilizing both Hirota bilinear and long-wave methods have been derived. These physical phenomena are one-soliton-lump, two-soliton-lump, and two-lump-soliton solutions. By virtue of the Hirota method, the N-complex-soliton solutions in complex form are constructed. The propagation characteristics of all gained solutions are shown graphically in 3D and contour plots. All phenomena presented in this work are verified by plugging them back into the studied equation. All presented physical phenomena are novel and have not been presented in the previously published study. In future work, these methods could be applied to more integrable NPDE and complex PDE to explore new features of solutions.

REFERENCES

1. Hirota R. The direct method in soliton theory. Cambridge University Press. 2004 (155).
2. Ismael HF, Sulaiman TA, Younas U, Nabi HR. On the autonomous multiple wave solutions and hybrid phenomena to a $(3+1)$ -dimensional Boussinesq-type equation in fluid mediums. *Chaos Solitons Fractals*. 2024;187:115374.
3. Wazwaz A-M. The simplified Hirota's method for studying three extended higher-order KdV-type equations. *Journal of Ocean Engineering and Science*. 2016;1:181–5.
4. Ismael HF, Bulut H. Nonlinear dynamics of $(2+1)$ -dimensional Bogoyavlenskii–Schieff equation arising in plasma physics. *Math Methods Appl Sci* 2021.
5. Zhao Z. Bäcklund transformations, rational solutions and soliton–cnoidal wave solutions of the modified Kadomtsev–Petviashvili equation. *Appl Math Lett*. 2019;89:103–10.
6. Hirota R. Soliton solutions to the BKP equations. I. The Pfaffian technique. *J Physical Soc Japan* 1989;58:2285–96.
7. Murad MAS, Ismael HF, Sulaiman TA. Resonant optical soliton solutions for time-fractional nonlinear Schrödinger equation in optical fibers. *Journal of Nonlinear Optical Physics & Materials*. 2024:2450024.
8. Peng W-Q, Tian S-F, Wang X-B, Zhang T-T, Fang Y. Riemann–Hilbert method and multi-soliton solutions for three-component coupled nonlinear Schrödinger equations. *Journal of Geometry and Physics*. 2019;146:103508.
9. Zhang Y, Cheng Y, He J. Riemann–Hilbert method and N-soliton for two-component Gerdjikov–Ivanov equation. *Journal of Nonlinear Mathematical Physics*. 2017;24:210–23.
10. Murad MAS, Ismael HF, Sulaiman TA. Various exact solutions to the time-fractional nonlinear Schrödinger equation via the new modified Sardar sub-equation method. *Phys Scr*. 2024;99:085252.
11. Peng W-Q, Chen Y. N-double poles solutions for nonlocal Hirota equation with nonzero boundary conditions using Riemann–Hilbert method and PINN algorithm. *Physica D*. 2022;435:133274.
12. Abdel-Gawad HI, Sulaiman TA, Ismael HF. Bright–dark envelope-optical solitons in space-time reverse generalized Fokas–Lenells equation: Modulated wave gain. *Modern Physics Letters B*. 2025;39:2450377.
13. Fan L, Bao T. The integrability and infinite conservation laws of a variable coefficient higher-order Schrödinger equation. *Chinese Journal of Physics* 2024.
14. Younas U, Muhammad J, Ismael HF, Murad MAS, Sulaiman TA. Optical fractional solitonic structures to decoupled nonlinear Schrödinger equation arising in dual-core optical fibers. *Modern Physics Letters B*. 2025;39:2450378.
15. Zhao X-H, Li S. Dark soliton solutions for a variable coefficient higher-order Schrödinger equation in the dispersion decreasing fibers. *Appl Math Lett*. 2022;132:108159.
16. Kaya D, El-Sayed SM. On a generalized fifth order KdV equations. *Phys Lett A*. 2003;310:44–51.
17. Butler S, Joshi N. An inverse scattering transform for the lattice potential KdV equation. *Inverse Probl*. 2010;26:115012.
18. Alharbi AR, Almatrafi MB. Exact solitary wave and numerical solutions for geophysical KdV equation. *Journal of King Saud University-Science*. 2022;34:102087.
19. Zhang D-J, Zhao S-L, Sun Y-Y, Zhou J. Solutions to the modified Korteweg–de Vries equation. *Reviews in Mathematical Physics*. 2014;26:1430006.
20. Salas AH, Gómez S CA. Application of the Cole–Hopf transformation for finding exact solutions to several forms of the seventh-order KdV equation. *Math Probl Eng*. 2010.
21. Ramirez J, Bruzón MS, Muriel C, Gandarias ML. The Schwarzian Korteweg–de Vries equation in $(2+1)$ dimensions. *J Phys A Math Gen*. 2003;36:1467.
22. Lü X, Chen S-J. N-soliton solutions and associated integrability for a novel $(2+1)$ -dimensional generalized KdV equation. *Chaos Solitons Fractals*. 2023;169:113291.
23. Ismaeel SME, Wazwaz A-M, El-Tantawy SA. New $(3+1)$ -dimensional integrable generalized KdV equation: Painlevé property, multiple soliton/shock solutions, and a class of lump solutions. *Rom Rep Phys*. 2024;76:102.
24. Novikov S, Manakov S V, Pitaevskii LP, Zakharov VE. Theory of solitons: the inverse scattering method. Springer Science & Business Media. 1984.
25. Satsuma J, Ablowitz MJ. Two-dimensional lumps in nonlinear dispersive systems. *J Math Phys*. 1979;20:1496–503.

Hajar Farhan Ismael:  <https://orcid.org/0000-0001-6189-9329>



This work is licensed under the Creative Commons BY-NC-ND 4.0 license.

BUOYANCY-DRIVEN FLOW AND FORCED FLOW OF COMPLEX FLUID WITHIN A TRIANGULAR CHAMBER WITH A ROTATING BODY

Youcef LAKAHAL^{*}, Houssein LAIDOU DI^{*}

^{*}Faculty of Mechanical Engineering, University of Sciences and Technology of Oran, BP 1505, El -Menaouer, Oran 31000, Algeria

houssein.laidoudi@univ-usto.dz, youcef.lakahal@univ-usto.dz

received 13 October 2024, revised 26 January 2025, accepted 10 February 2025

Abstract: This study investigates mixed convection heat transfer of a non-Newtonian fluid within a finned triangular cavity containing a horizontally oriented, rotating cylinder with a circular cross-section. The cylinder, maintained at a high temperature, rotates at a constant speed, while the cavity walls are kept at a cold temperature. This configuration is significant for applications in cooling technologies and materials processing. Unlike previous studies that primarily focused on simpler geometries, this work uniquely examines the effects of varying blockage ratios in a finned triangular cavity, a less explored configuration. The analysis considers key parameters such as cylinder rotation speed ($Re = 1, 5, \text{ and } 10$), thermal buoyancy intensity ($Ri = 0, 1, 2, \text{ and } 3$), fluid viscosity (characterized by the power-law index, $n=0.6, 1, \text{ and } 1.6$), and blockage ratio ($\beta = 0.12, 0.24, \text{ and } 0.36$). Numerical simulations were performed using the finite volume method to solve the governing equations, with Ostwald's law modeling the fluid's rheological properties. Results show that increasing the blockage ratio stabilizes the flow, suppressing counter-rotating regions around the cylinder and reducing the heat transfer rate by more than 30%. Additionally, a decrease in the fluid's power-law index enhances heat transfer from the hot cylinder. These findings provide valuable insights for optimizing thermal systems.

Key words: Complex fluid, mixed convection, blockage ratio, numerical investigation, Nusselt number, CFD

1. INTRODUCTION

Heat transfer in fluids with complex rheological properties is a growing area of research due to its critical role in industrial applications such as energy storage, cooling technologies, and material processing. Non-Newtonian fluids, particularly those with power-law characteristics, exhibit unique thermal and flow behaviors, making them essential for optimizing engineering systems. Mixed convection, which combines forced and natural convection effects, is especially significant in systems with confined geometries and rotating components.

Numerous studies have advanced our understanding of non-Newtonian fluid dynamics and heat transfer. For instance, laminar forced convection around two heated cylinders in a square duct has shown that cylinder spacing and the power-law index significantly affect flow structure [1]. Pore-scale simulations using the thermal lattice Boltzmann method have demonstrated that porosity and permeability enhance thermal conductivity in porous structures [2]. Natural convection in trapezoidal enclosures has revealed that geometry influences heat transfer, with the aspect ratio affecting temperature distribution and flow patterns [3]. Studies of magnetohydrodynamic (MHD) double-diffusive natural convection in crown enclosures have highlighted the role of magnetic fields in altering flow structure and improving heat transfer [4]. Additionally, investigations of natural convection in shallow horizontal rectangular cavities heated from below have shown that the Nusselt number increases with the power-law index as buoyancy forces dominate [5].

Research on vertical cavities subjected to horizontal temperature gradients indicates that increasing temperature differences

enhances heat transfer rates [6]. Mixed convection in lid-driven square cavities has demonstrated that thermal performance varies significantly with the interaction between fluid motion and the moving lid [7]. Similarly, studies of mixed convective heat transfer in square enclosures using higher-order finite element methods emphasize that heat transfer strongly depends on the flow regime and enclosure geometry [8]. Other work on mixed convection of non-Newtonian fluids in square chambers with discrete heating configurations highlights the impact of heating arrangements on flow and thermal performance [9].

Investigations into specific configurations have also provided valuable insights. For example, double-diffusive effects in Casson fluid flow past wavy inclined plates have shown how temperature and concentration gradients influence heat transfer [10]. Skewed lid-driven cavities have been found to enhance convective heat transfer under certain conditions [11]. Studies of power-law fluids and magnetic fields in staggered porous cavities have revealed a significant reduction in heat transfer rates when these factors are combined [12]. The arrangement of cylinders in flow fields has been shown to critically affect heat transfer efficiency [13]. Furthermore, hybrid nanofluids in 3D lid-driven chambers under magnetic fields have demonstrated improved thermal performance and reduced entropy generation [14]. Finally, research on tandem circular cylinders in cross-flow at low Reynolds numbers has indicated that proximity significantly affects flow patterns and heat transfer [15].

Nanofluids, with their enhanced thermal properties due to nanoparticle inclusion, have also been extensively studied. The role of curved fins in shaping flow patterns and analyzing entropy generation in buoyancy-driven magnetized hybrid nanofluid transport

has been investigated, offering insights into thermal management [16]. Magnetically driven hybrid nanofluid transport in micro-wave channels has demonstrated potential applications in MEMS-based drug delivery systems [17]. Studies on buoyancy-driven magnetized hybrid nanofluids in discretely heated circular chambers with fins have shown the importance of heat source configurations on hydrothermal performance [18].

Further research on natural convection and MHD effects in alumina nanofluids within triangular enclosures equipped with fins has emphasized the role of geometry in enhancing heat transfer performance [19]. Investigations into thermal modes of obstacles within triangular cavities have advanced the understanding of Al_2O_3 -water nanofluid transport mechanisms [20]. Similarly, buoyancy-driven MHD hybrid nanofluid flow in circular enclosures with fins has provided strategies for optimizing heat transfer in complex systems [21].

The development of numerical methods has further enriched this field. Studies on nanofluid convection heat transfer in renewable energy systems have highlighted its potential to improve energy efficiency [22]. The interaction of magnetic fields with heat transfer processes has been explored, shedding light on convection under MHD conditions [23]. Research on cavity design has emphasized its critical role in optimizing heat transfer performance [24]. The effects of heat source placement on natural convection in enclosures have also been examined, offering strategies to enhance thermal management [25]. Additionally, the thermal behavior of complex systems influenced by cavity design has been thoroughly investigated [26].

Despite these advances, the study of mixed convection in non-Newtonian fluids within finned triangular cavities remains underexplored, particularly in the presence of rotating cylinders. Fins are widely used in engineering systems, such as heat exchangers and cooling devices, to enhance thermal performance by increasing surface area and influencing flow behavior. Previous studies have demonstrated that fins significantly improve heat transfer and flow dynamics in buoyancy-driven and mixed convection systems [27].

Building on these insights, the current study investigates the effects of mixed convection in a finned triangular cavity containing a horizontally oriented, rotating cylinder. The analysis focuses on the effects of blockage ratio ($\beta = d/L$), Reynolds and Richardson numbers, and the rheological properties of power-law fluids on flow and heat transfer. Numerical simulations, conducted using the finite volume method, provide detailed insights into the interaction of these parameters, contributing to the optimization of energy storage systems, cooling technologies, and industrial processes. By integrating and expanding existing knowledge, this study bridges gaps in the literature and offers a novel perspective on mixed convection in power-law fluids, laying a foundation for future advancements in thermal management.

2. PHYSICAL PROBLEM AND MATHEMATICAL FORMULATIONS

Fig. 1 illustrates the computational domain used for this investigation. It consists of a rotating horizontal cylinder inside a finned triangular cavity.

The ratio of cylinder diameter d to the side length of the triangular cavity L defines the blockage ratio ($\beta = d/L$), it takes three values, $\beta = 0.12, 0.24$ and 0.36 . The cylinder has a hot temperature T_h and rotates in a counterclockwise direction (Ω), while the triangular cavity remains at a cold temperature T_c ($T_h > T_c$). The space

between the cylinder and the triangular cavity is assumed to be filled with power law fluids. Three values of the power-law index (n) were considered ($= 0.6, 1$ and 1.6).

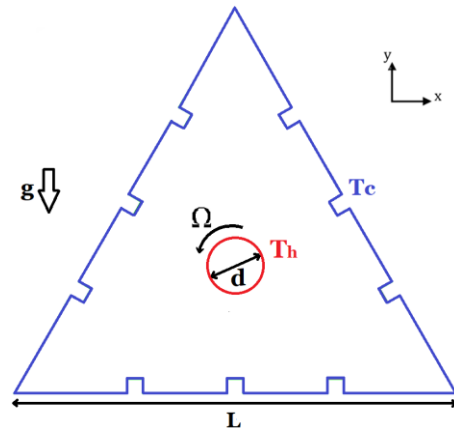


Fig. 1. Diagrammatic representation of the problem

Mixed convection occurs when both natural and forced convection mechanisms are involved in heat transfer. In this study, the rotation of the cylinder generates forced convection, while the temperature difference between the cylinder's surface and the cavity drives natural convection. The Reynolds number controls the rotational speed of the cylinder, while the Richardson number defines the relative contribution of forced versus natural convection. Four Richardson numbers are considered: 0, 1, 2, and 3.

The assumptions of laminar and non-Newtonian flow, steady-state conditions, mixed convection, and constant fluid properties are adopted in this study. The equations of continuity, momentum, and energy, subject to the Boussinesq approximation and neglecting dissipation effects, are first presented in their dimensional form as follows [1]:

The equation of continuity:

$$\frac{\partial u}{\partial x} + \frac{\partial v}{\partial y} = 0 \quad (1)$$

The equation of momentum along the x-direction:

$$\frac{\partial(uu)}{\partial x} + \frac{\partial(uv)}{\partial y} = -\frac{\partial p}{\partial x} + \left(\frac{\partial \tau_{xx}}{\partial x} + \frac{\partial \tau_{yx}}{\partial y} \right) \quad (2)$$

The equation of momentum along the y-direction:

$$\frac{\partial(uv)}{\partial x} + \frac{\partial(vv)}{\partial y} = -\frac{\partial p}{\partial y} + \left(\frac{\partial \tau_{xy}}{\partial x} + \frac{\partial \tau_{yy}}{\partial y} \right) \quad (3)$$

The equation of energy:

$$\rho c_p \left(u \frac{\partial T}{\partial x} + v \frac{\partial T}{\partial y} \right) = k \left(\frac{\partial^2 T}{\partial x^2} + \frac{\partial^2 T}{\partial y^2} \right) \quad (4)$$

To generalize the analysis, these equations are rewritten in dimensionless form using the dimensionless variables [28]:

The equation of continuity:

$$\frac{\partial u^*}{\partial x^*} + \frac{\partial v^*}{\partial y^*} = 0 \quad (5)$$

The equation of momentum along the x-direction:

$$u^* \left(\frac{\partial u^*}{\partial x^*} \right) + v^* \left(\frac{\partial u^*}{\partial y^*} \right) = -\frac{\partial p^*}{\partial x^*} + \frac{1}{Re} \left(\frac{\partial \tau_{xx}^*}{\partial x^*} + \frac{\partial \tau_{yx}^*}{\partial y^*} \right) \quad (6)$$

The equation of momentum along the y-direction:

$$u^* \left(\frac{\partial v^*}{\partial x^*} \right) + v^* \left(\frac{\partial v^*}{\partial y^*} \right) = -\frac{\partial p^*}{\partial y^*} + \frac{1}{Re} \left(\frac{\partial^2 \tau_{xy}^*}{\partial x^{*2}} + \frac{\partial^2 \tau_{yy}^*}{\partial y^{*2}} \right) + Ri \times T^* \quad (7)$$

The equation of energy:

$$u^* \left(\frac{\partial T^*}{\partial x^*} \right) + v^* \left(\frac{\partial T^*}{\partial y^*} \right) = \frac{1}{Pe} \left(\frac{\partial^2 T^*}{\partial x^{*2}} + \frac{\partial^2 T^*}{\partial y^{*2}} \right) \quad (8)$$

Re and Pe are the Reynolds and Peclet numbers, Ri is the Richardson number, and u^* and v^* are the fluid dimensionless velocities in the x^* and y^* directions. Dimensionless pressure and temperature are represented by the numbers p^* and T^* , respectively. The following represents the dimensionless variables [28]:

$$x^* = x/d, y^* = y/d, u^* = u/(\Omega \times d), \text{ and } v^* = v/(\Omega \times d) \quad (9)$$

$$p^* = p/(\rho(\Omega \times d)^2), T^* = (T - T_c)/(T_h - T_c) \quad (10)$$

$$Pe = Re \times Pr \quad (11)$$

The following equation represents the power-law fluid's behavior [28]:

$$\tau_{ij} = 2\eta \varepsilon_{ij} \quad (12)$$

where the viscous stress tensors and the rate of deformation are represented, respectively, by ε_{ij} and τ_{ij} . Furthermore, for power-law fluids, the fluid viscosity, denoted by η , is defined (in dimensional form) as follows [28]:

$$\eta = m \left(\frac{I_2}{2} \right)^{\frac{n-1}{2}} \quad (13)$$

where I_2 is the second invariant of the rate of deformation tensor, m is the consistency index, and n is the power-law index. A fluid that is shear-thinning is represented by $n < 1$, a Newtonian limit by $n = 1$, and a shear-thickening fluid by $n > 1$. The following equation gives I_2 in Cartesian coordinates [28]:

$$\left(\frac{I_2}{2} \right) = 2 \left(\frac{\partial u}{\partial x} \right)^2 + 2 \left(\frac{\partial v}{\partial y} \right)^2 + \left[\left(\frac{\partial u}{\partial y} \right) + \left(\frac{\partial v}{\partial x} \right) \right]^2 \quad (14)$$

Generally, Grashof number and Richardson number for power law fluids are computed as follows [28]:

$$Gr = g\beta_T \Delta T d^3 \left(\frac{\rho}{m} (\Omega)^{1-n} \right)^2 \quad (15)$$

$$Ri = \frac{g\beta_T \Delta T d^3}{(\Omega \times d)^2} = \frac{Gr}{Re^2} \quad (16)$$

where ρ , g , and β_T are the density of the fluid, the gravitational acceleration and volumetric expansion coefficient, respectively.

The average Nusselt number, or Nu , is calculated by integrating local values along the surface area of the inner cylinder A. The following are Nu 's average and local values [28]:

$$Nu_L = \left(\frac{\partial T^*}{\partial n} \right)_{wall}, Nu = \frac{1}{A} \int_s Nu_L dA \quad (17)$$

3. NUMERICAL PROCEDURE

The current study was conducted using ANSYS-CFX, a commercial computational fluid dynamics (CFD) software, to

numerically simulate the system. This software converts the governing equations of heat transfer and fluid dynamics into an algebraic form, which are then solved using the finite volume method. For numerical simulations, ANSYS-CFX was employed, utilizing a high-resolution scheme for the convective terms and the SIMPLEX algorithm to handle the pressure-velocity coupling. A calculation error threshold of 10^{-6} was set for both thermal and fluid dynamic equations to ensure convergence accuracy. The mesh required for the simulations was generated using Gambit. After importing the mesh into CFD-Pre, boundary conditions were defined and applied to the problem domain. For visualization and post-processing, including the generation of contour plots, CFD-Post was used to analyze and present the simulation results.

The numerical method employed in this study ensures high accuracy and reliability in solving complex heat transfer and fluid dynamics problems. Using ANSYS-CFX with a high-resolution scheme minimizes numerical diffusion, while the SIMPLEX algorithm provides efficient pressure-velocity coupling. The finite volume method and a convergence criterion of 10^{-6} guarantee solution stability. Unlike analytical methods, which are limited to simplified geometries, this approach handles complex domains and non-linear interactions with flexibility. Additionally, it is less resource-intensive than experimental approaches and allows for comprehensive analysis. The integration of Gambit for mesh generation and CFD-Post for visualization ensures efficient data processing and high-quality results, making the method suitable for diverse engineering applications.

The accuracy of the numerical simulation is strongly influenced by the number of grid elements, making the selection of an optimal mesh density crucial (Fig. 2). A grid independence test was therefore performed to determine the appropriate mesh size, as shown in Table 1. Three different mesh densities were tested, with each mesh used to calculate the Nusselt number for the heated body under conditions of $n = 1.6$, $Re = 10$, $Ri = 2$ and $\beta = 0.12$. The results confirmed that mesh M2 is optimal, as it produced Nusselt values comparable to those of the denser M3, indicating that further refinement would not significantly impact the results.

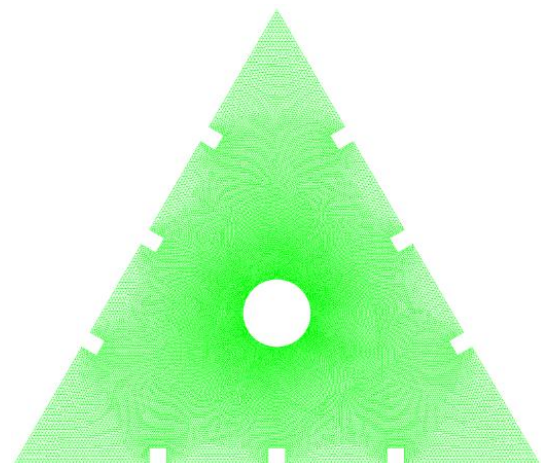


Fig. 2. The structure of the grid used for the calculations

Fig. 3 illustrates the convergence behavior of residuals for the case where $Re = 5$, $Ri = 0$, $n = 0.6$, and $\beta = 0.12$ in the numerical simulation. Fig. 3(A) presents the Root Mean Square (RMS) residuals for mass continuity and velocity components (u , v) over

accumulated time steps, while Fig. 3(B) depicts the RMS residual for energy. The residuals exhibit a consistent decrease and stabilize below the convergence threshold of 10^{-6} , confirming successful numerical convergence.

The accuracy of the numerical model has been validated through comparisons with the studies by Kuehn and Goldstein [37] and Matin and Khan [38], which investigated buoyancy-driven flow between two concentric cylinders. Fig. 4(A) illustrates the effect of Rayleigh number ($Ra = Pr \cdot Gr$) on the Nusselt number at $Pr = 0.71$ and $n = 1$, showing a strong agreement between our results and the reference data. So that the maximum value of the difference between the experimental and numerical results is less than 1%. Additionally, a second comparison was conducted to assess the influence of the non-Newtonian behavior of the fluid, specifically the effect of the power-law index n . For this purpose, results were compared with those of Matin et al. [39], as shown in Fig. 4(B) at $Pr = 100$ with a blockage ratio of 0.25. The results high-light the impact of the power-law index on the Nusselt number, again confirming good agreement. Fig. 4(C) shows a comparison test between present results and the results of [31]. The results are about the natural convection between two cylinders. Fig. 4(C) presents a good agreement.

Tab. 1. Grid independency test for $n = 1.6$, $Re = 10$, $Ri = 2$ and $\beta = 0.12$

Mesh	Elements	Nu	Difference %	CPU Se-conds
M1	130,000	3.41930	1.478	622
M2	260,000	3.36876	0.011	1021
M3	520,000	3.36913	-	-

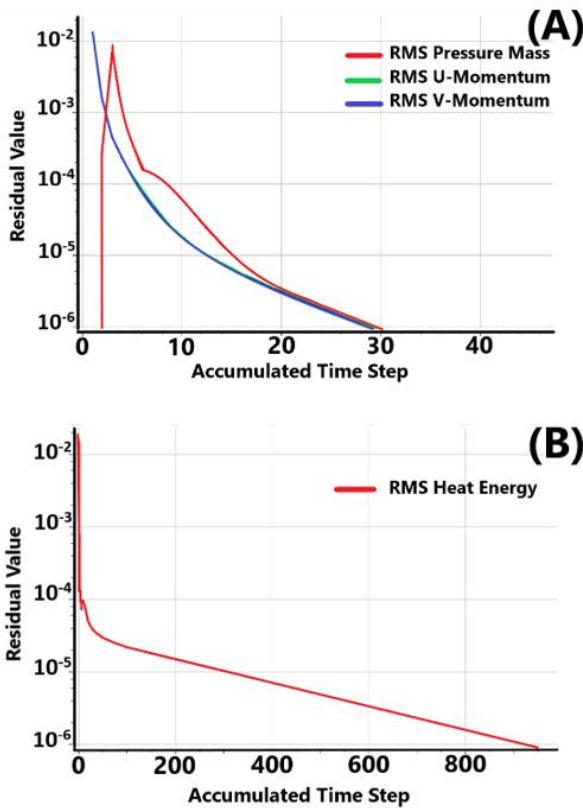


Fig. 3. Residual Convergence for $Re = 5$, $Ri = 0$, $n = 0.6$ and $\beta = 0.12$

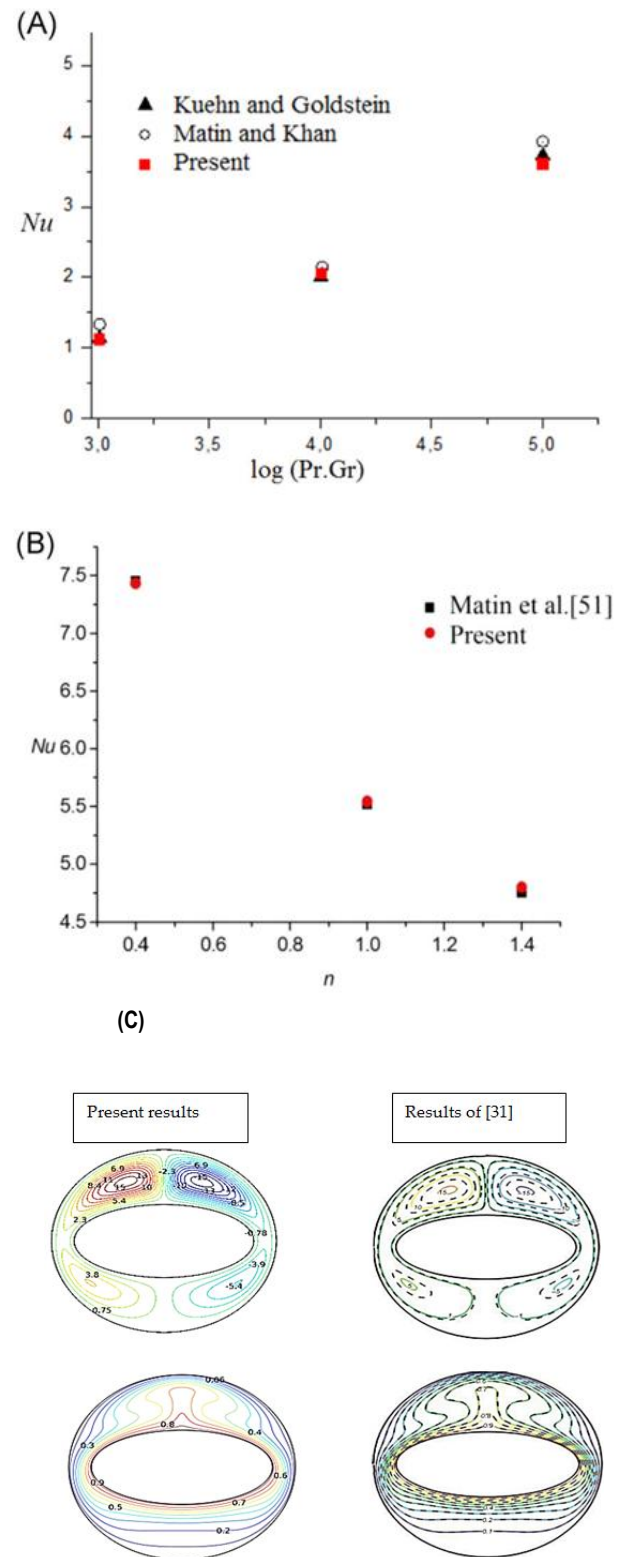


Fig. 4. Validation tests

4. RESULTS AND DISCUSSION

This section provides a detailed presentation and discussion of the streamlines, isotherm contours, and the average Nusselt number for varying values of the power-law index (n), Reynolds number (Re), and Richardson number (Ri).

Three cases are analyzed based on the blockage ratio ($\beta = d/L$): a blockage ratio of 0.12 for the first case, 0.24 for the second, and

0.36 for the third. In each scenario, streamline and isotherm contours illustrate the fluid flow and thermal patterns, respectively.

For the specified governing parameters of Ri (0, 1, 2, and 3), Re (1, 5, and 10), and n (0.6, 1.0, and 1.6) with a fixed $Pr = 50$, the Nusselt number (Nu) of the inner rotating cylinder is determined. The selected parameter values are based on a previous study [28].

Mixed convection occurs when both forced and natural convection take place simultaneously. In this study, natural convection is

driven by the temperature difference between the inner cylinder and the finned triangular cavity, while forced convection results from the cylinder's rotation. When $Ri = 0$, only forced convection is dominant. As the Ri value increases, the buoyancy force, representing the effect of natural convection, also gradually increases. Meanwhile, the rotational speed is directly related to the Reynolds number (Re).

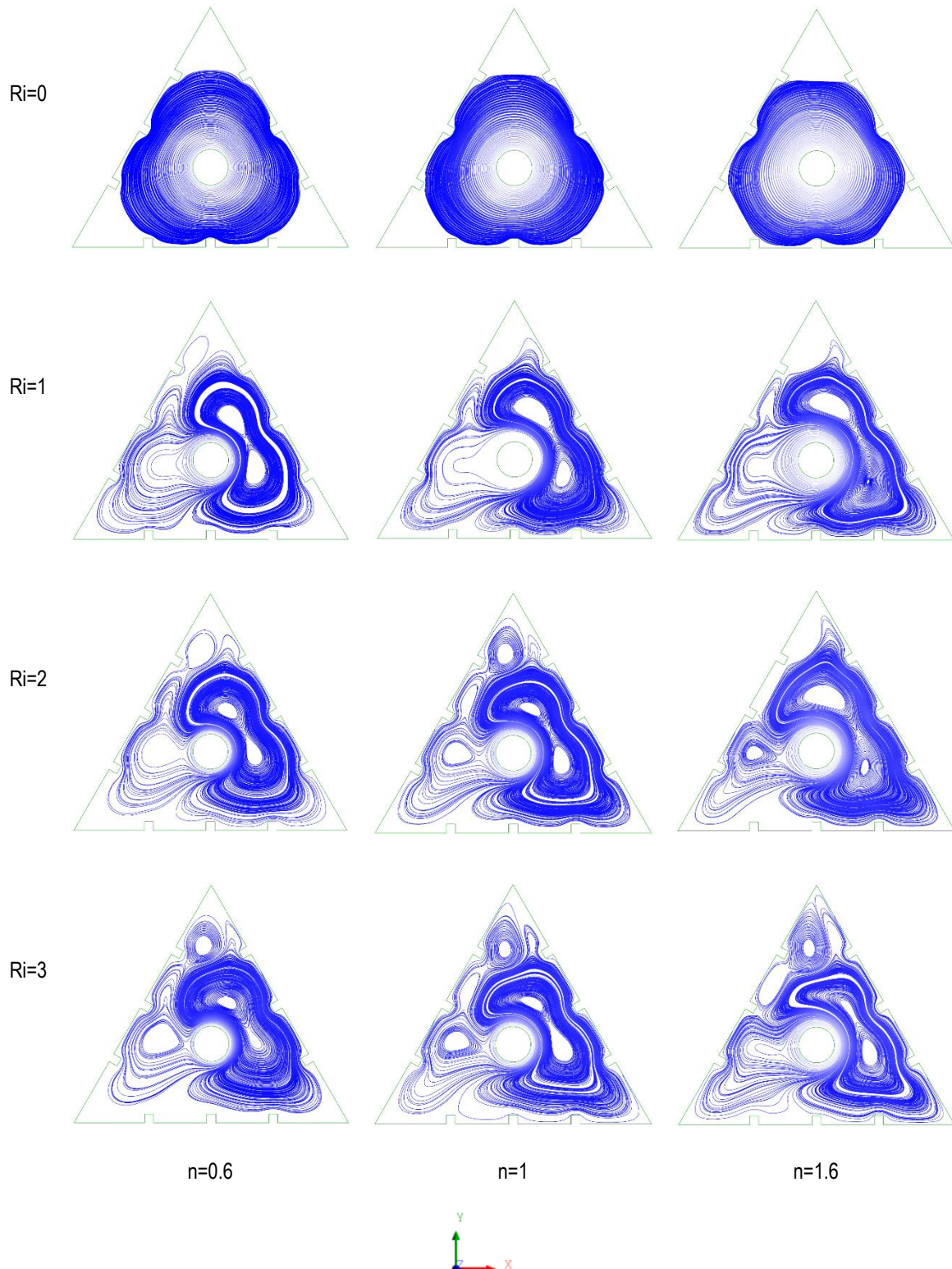


Fig. 5. Streamlines for the case of blockage ratio of 0.12 at $Re = 5$

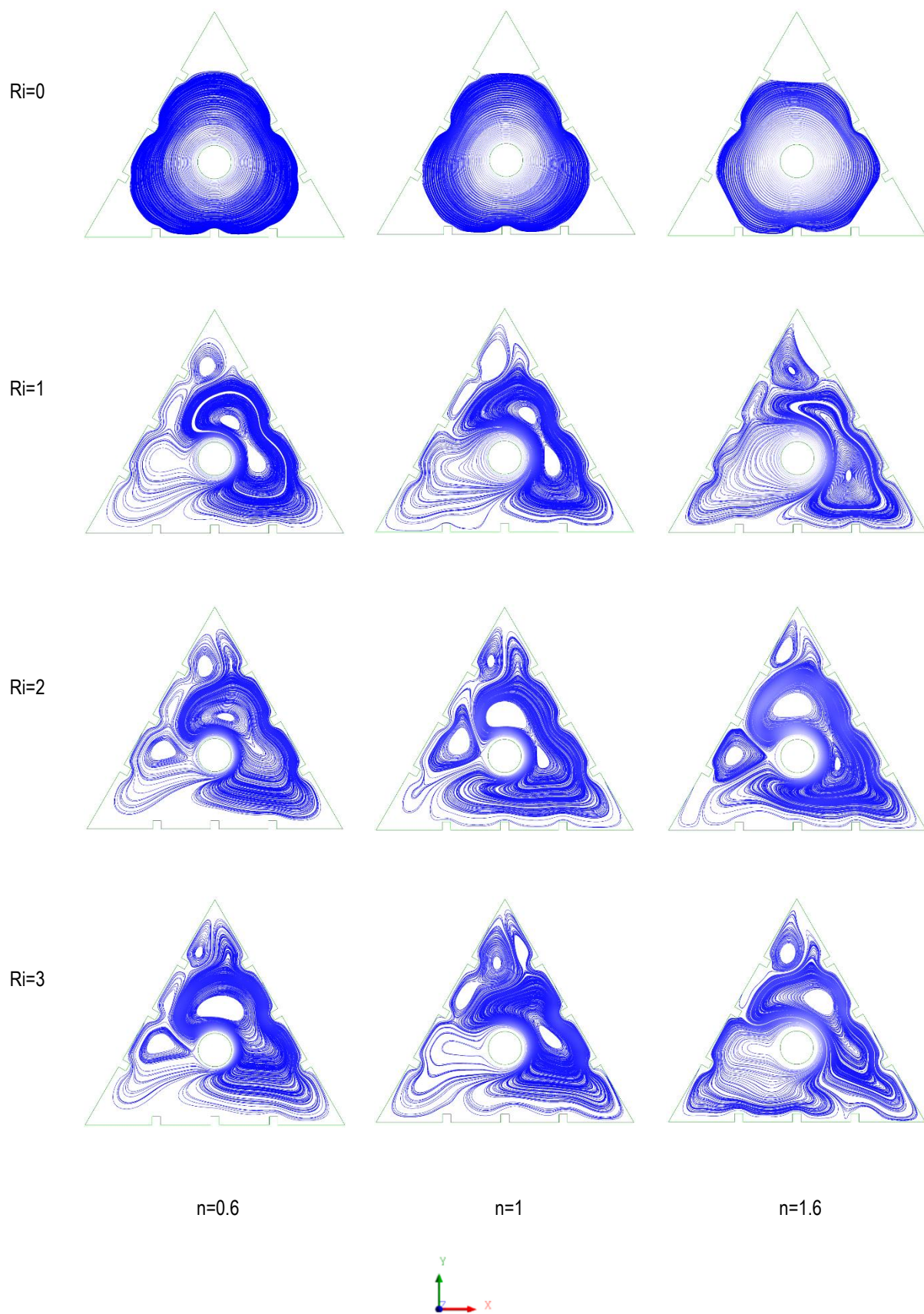


Fig. 6. Streamlines for the case of blockage ratio of 0.12 at $Re = 10$

4.1. Case No 1: a blockage ratio of 0.12

The streamlines in the area between the finned triangular cavity and the inner rotating cylinder are shown in Figs. 5 – 6. In

fact, the streamlines provide a thorough visualization of the particle trajectory and flow fields to identify stagnant and counter-rotating regions. The impact of Ri , n , and Re on the streamlines is displayed in Figs. 5 – 6.

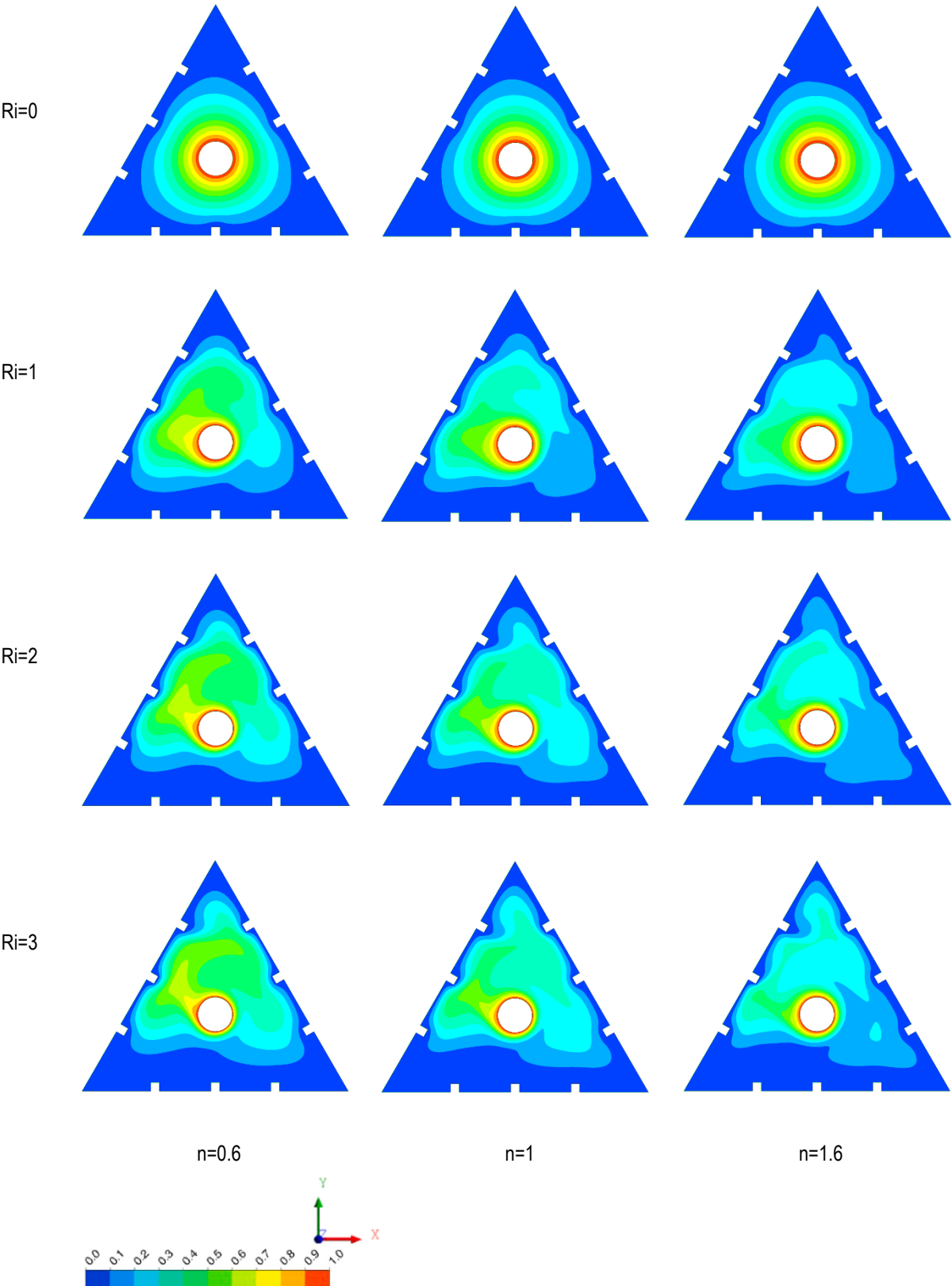


Fig. 7. Isotherms for the case of blockage ratio of 0.12 at $Re = 5$

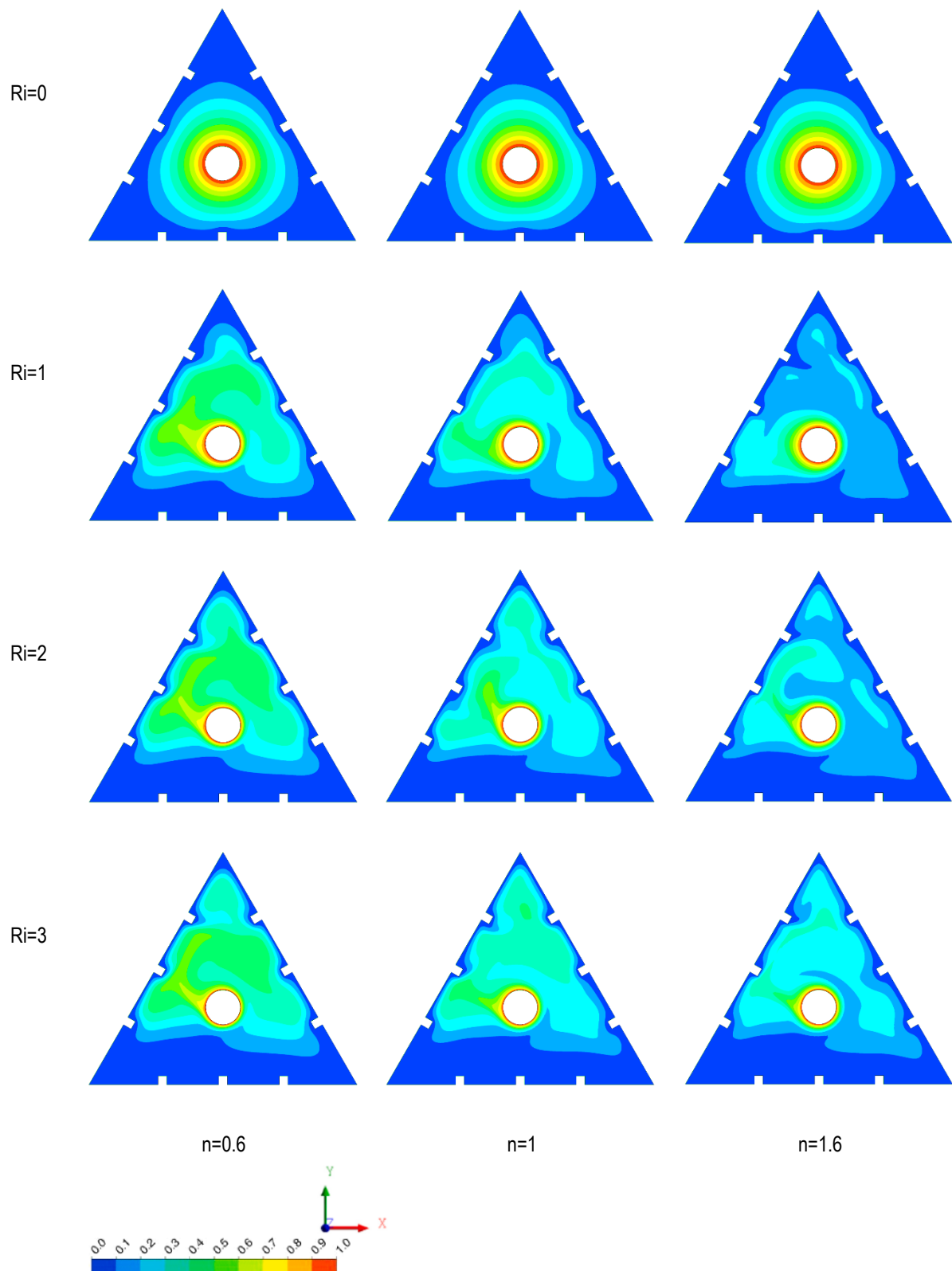


Fig. 8. Isotherms for the case of blockage ratio of 0.12 at $Re = 10$

Following the rotation of the cylinder (Ω), the flow appears to rotate steadily in the space between the cylinder and the triangular cavity for all values of Re (5 and 10) and power-law index ($n = 0.6$,

1 and 1.6) for $Ri = 0$ (pure forced convection). In the mixed convection state ($Ri \neq 0$), a closed counter-rotating region with two loops forms on the right side of the space, while a closed counter-rotating

region with a single loop appears on the left side.

As the Richardson number (Ri), representing buoyancy force, and the Reynolds number (Re), indicative of rotational speed, increase, the vortex structure on the left side of the domain expands along both the x and y axes. In contrast, the two-loop vortex on the right-side contracts with rising values of Ri and Re .

Additionally, an increase in the power-law index (n) further reduces the overall vortex size. For $n = 0.6$, the fluid is shear-thinning, meaning that as shear stress increases, the dynamic viscosity falls. As a result, the fluid particles move easily. On the other hand, when the fluid is shear-thickening ($n = 1.6$), that is, when the dynamic

viscosity increases with the shear stress, the flow becomes more stable. The rotation of the inner cylinder on the right side induces an upward flow of fluid particles, aligning with the direction of the buoyancy force, thus creating a two-loop vortex on the right side of the domain. Conversely, on the left side, the cylinder's rotation counteracts the buoyancy force's influence on fluid particles, resulting in the formation of a single-loop vortex. These observed flow characteristics in the mixed convection regime are fundamentally governed by buoyancy forces, which play a pivotal role in vortex formation.

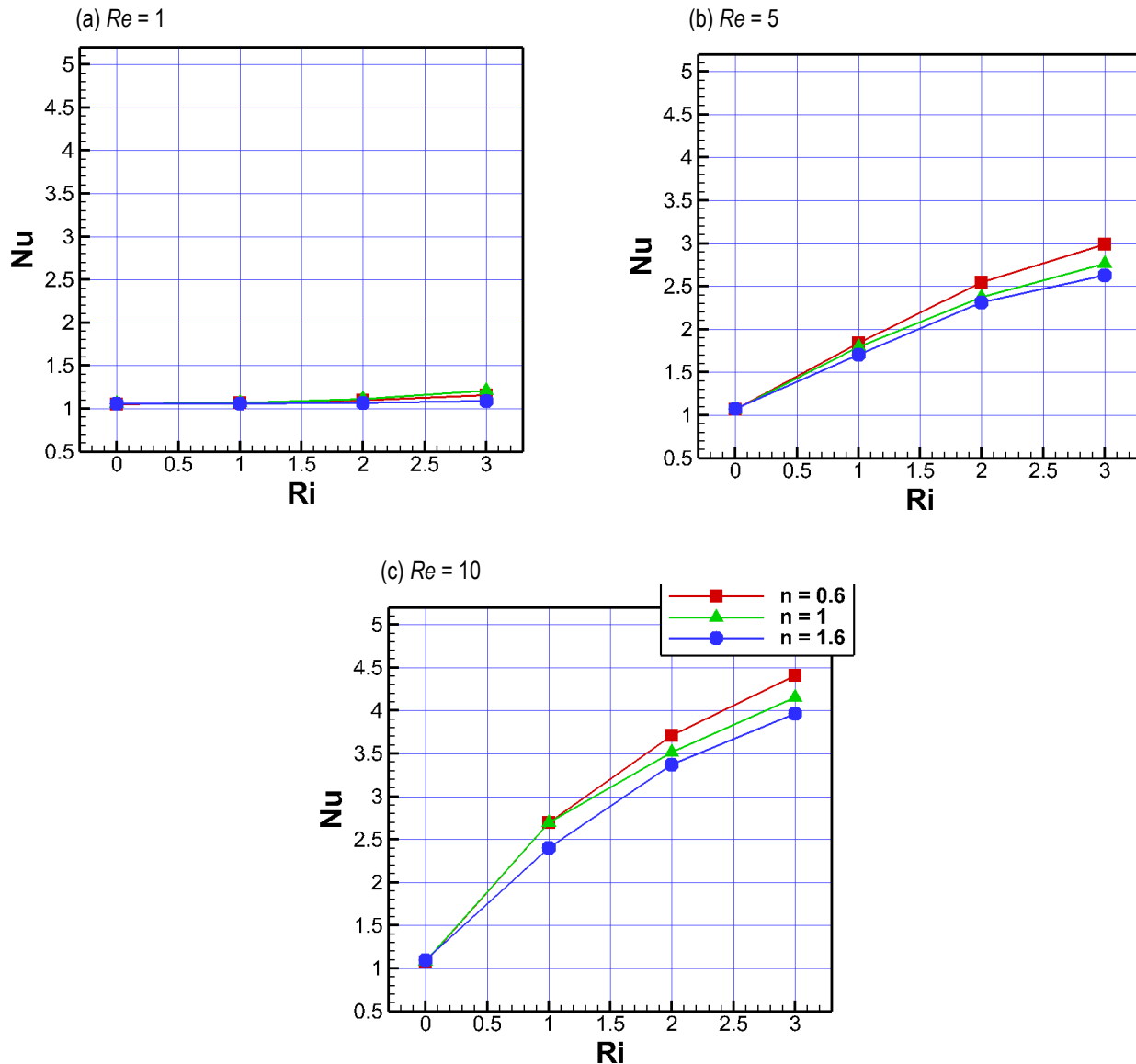


Fig. 9. Values of Nu versus Ri and n : a) for $Re = 1$; b) $Re = 5$; and c) $Re = 10$

The thermal fields in the region between the inner rotating cylinder and the finned triangular cavity are illustrated in Figs. 7 – 8, using the same parameter values for n , Ri , and Re as in the prior conditions. In the case of $Ri = 0$, Figs. 7 – 8 depict a uniform isotherm distribution in all directions. When $Ri \neq 0$, however, the thermal distribution aligns with the fluid flow pattern. On the right side,

where the two-loop vortex forms, the cylinder's rotation enhances the thermal buoyancy effect, promoting efficient heat transfer. In contrast, on the left side, fluid recirculation leads to an increase in isotherm thickness near the rotating cylinder. This increase indicates a reduction in the local temperature gradient. Overall, the dimensionless temperature gradient around the triangular block rises with increasing Re and Ri but decreases as the power-law index n increases.

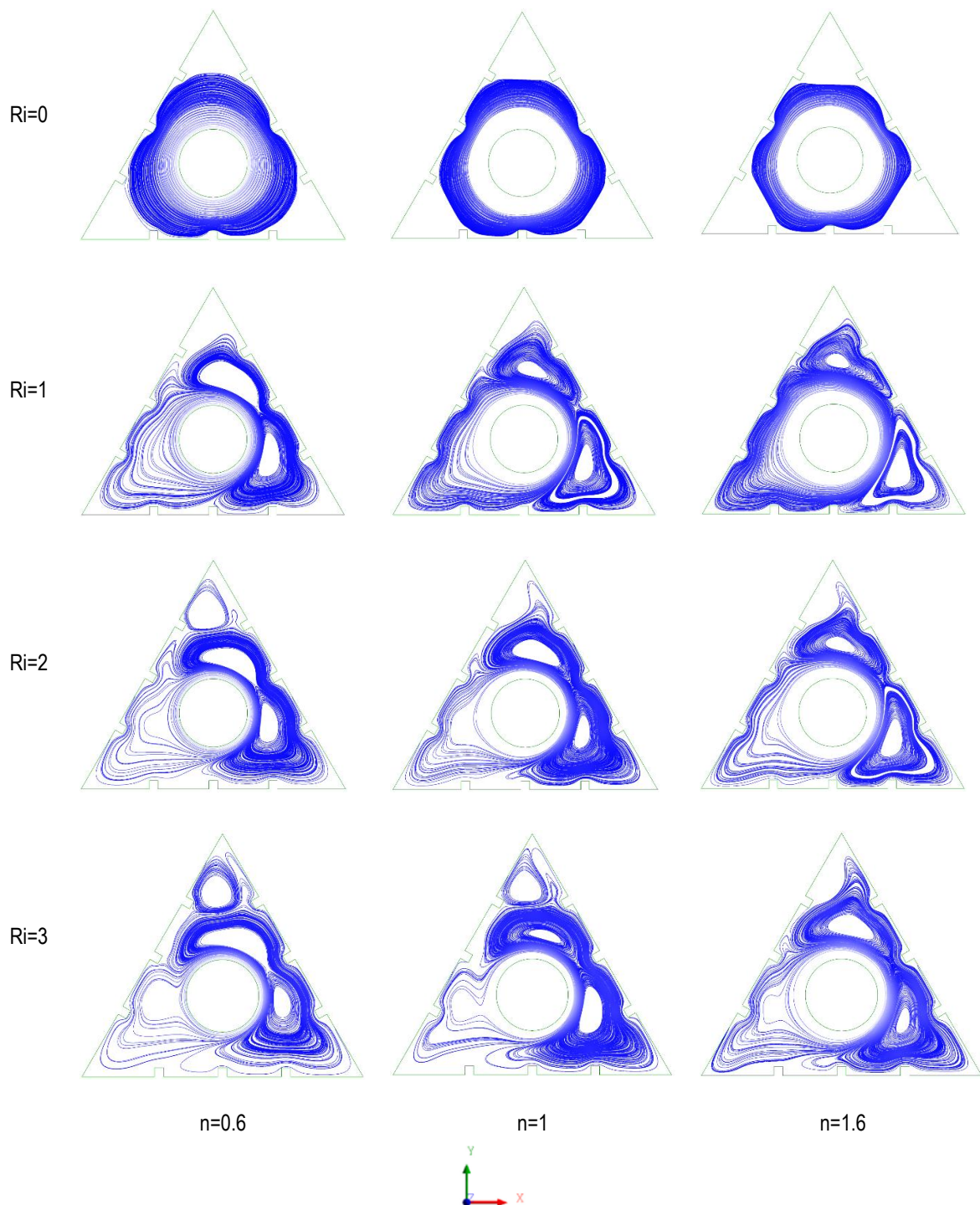


Fig. 10. Streamlines for the case of blockage ratio of 0.24 at $Re = 10$

Fig. 9 illustrates the variation in the Nusselt number (Nu) based on the parameters Ri , n , and Re . For $Re=1$, the effects of the power-law index n and Richardson number Ri on Nu remain minimal due to the low particle velocity, resulting in reduced heat transfer rates. However, at $Re=5$ and $Re=10$, the influence of n and Ri becomes more pronounced. As expected, Nu increases with rising values of Re and Ri ; however, Nu decreases significantly when the fluid behavior shifts from shear-thinning ($n=0.6$) to shear-thickening ($n=1.6$). This reduction occurs because the increased viscosity of the dilatant (shear-thickening) fluid restricts the development of the thermal boundary layer, impeding the temperature gradient,

experimental observations [30] are in agreement with our findings.

4.2. Case No 2: a blockage ratio of 0.24

In this case, the ratio of the cylinder diameter d to the side length of the triangular cavity L is set to 0.24. Fig. 10 illustrates the effects of the Richardson number Ri and the power-law index n on the streamlines at $Re = 10$. For all values of Ri and n , the streamlines closely resemble those in the initial case, with vortices growing on both the right and left sides of the domain under mixed convection conditions ($Ri \neq 0$).

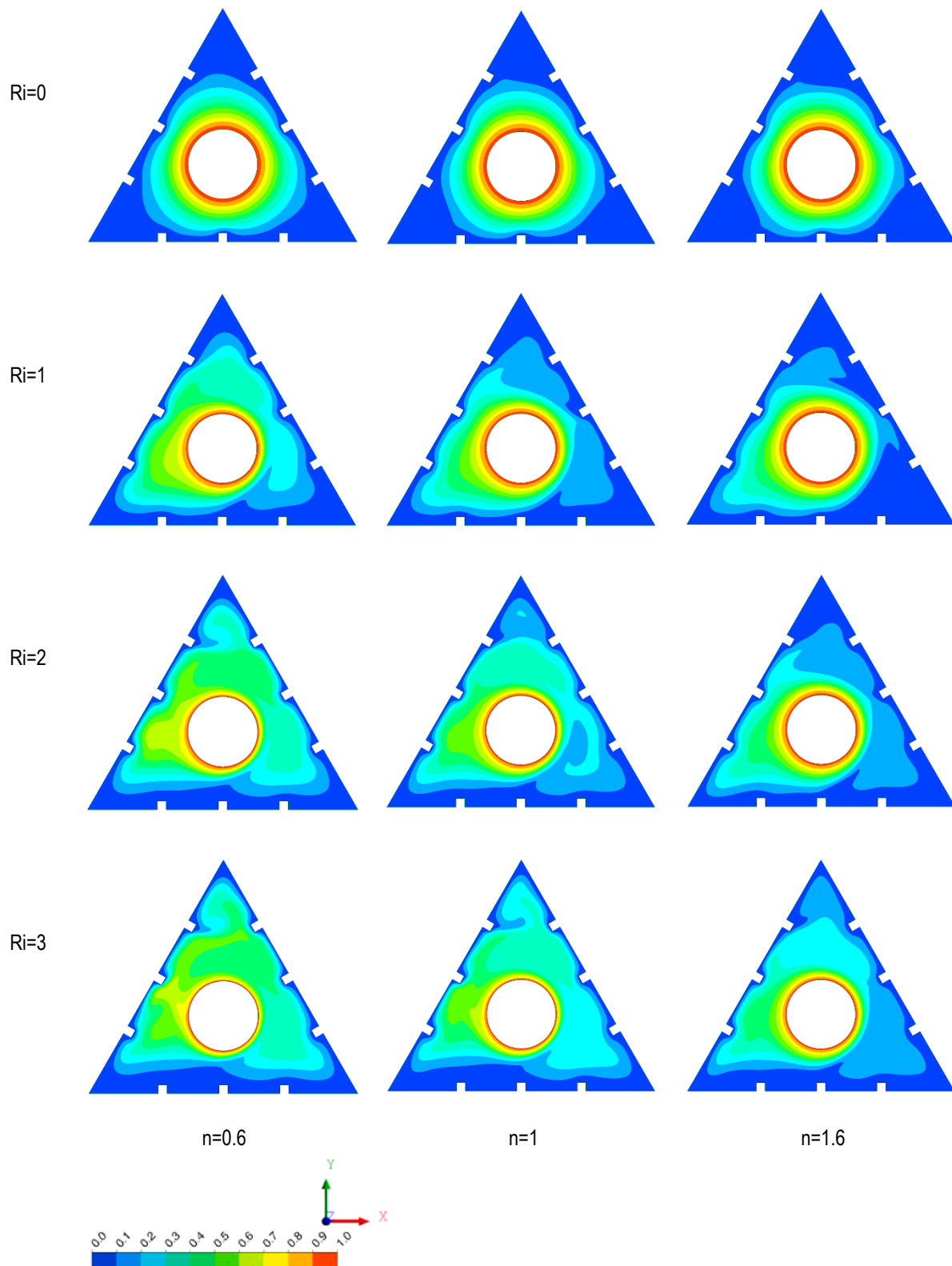


Fig. 11. Isotherms for the case of blockage ratio of 0.24 at $Re = 10$

The isotherms of the second case are shown in Fig. 11, the results indicate an increase in the isotherm thicknesses around the rotating cylinder for $Ri \neq 0$ due to the vortices growth of fluid molecules.

The estimated values of Nu versus Ri , n , and Re for the second case are shown in Fig. 12. The effects of the Richardson number (Ri) and the power law index (n) on Nu for all Re values are consistent with the findings of the first case, with Nu values reducing by approximately 30%.

4.3. Case No 3: a blockage ratio of 0.36

In this case, the blockage ratio ($\beta=d/L$) is set to 0.36. Fig. 13 illustrates the streamlines for various values of Ri and n at $Re=10$. The streamlines depicted in this figure differ from those observed in earlier cases, as spaced vortices emerge in the corners of the

triangular cavity. Additionally, the counter-rotational loops are smaller compared to those in previous cases under mixed convection conditions ($Ri \neq 0$). This reduction in size is attributed to the contraction of the fluid area resulting from the increased dimensions of the inner cylinder.

The isotherms for this case are illustrated in Fig. 14, which indicates a reduction in the thickness of the isotherms surrounding the rotating cylinder for $Ri \neq 0$ in comparison to the previous two cases. This phenomenon can be attributed to the development of the streamlines discussed earlier.

The values of the Nusselt number (Nu) for this case, considering Ri , n , and Re , are presented in Fig. 15. Both Re and Ri positively influence Nu . In the context of pseudoplastic fluids, the relationships between Nu and the parameters Re and Ri are significant, particularly when the viscosity is at its minimum. Notably, the Nu values in this case are lower than those observed in the previous cases.

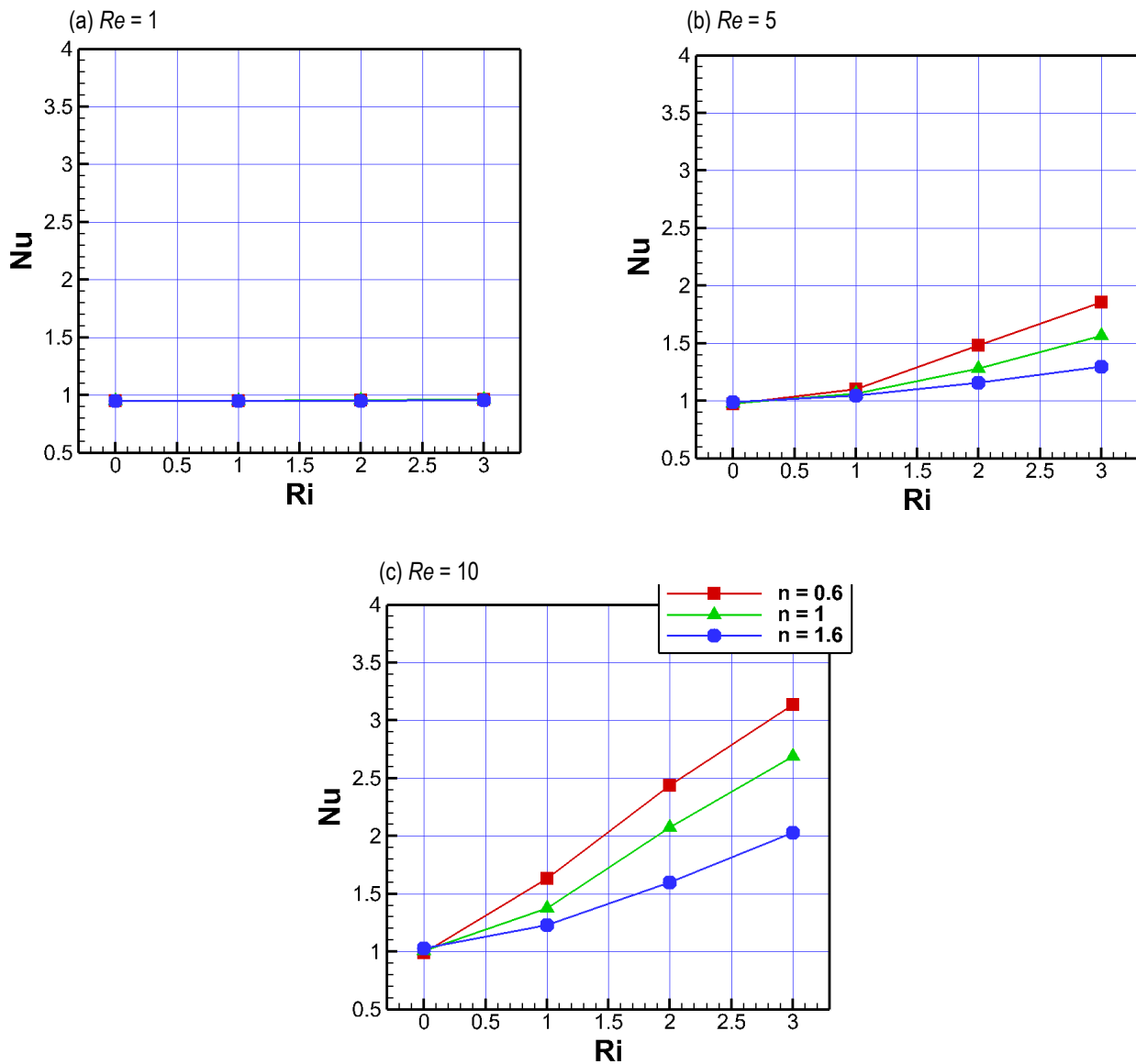


Fig. 12. Values of Nu versus Ri and n : a) for $Re = 1$; b) $Re = 5$; and c) $Re = 10$

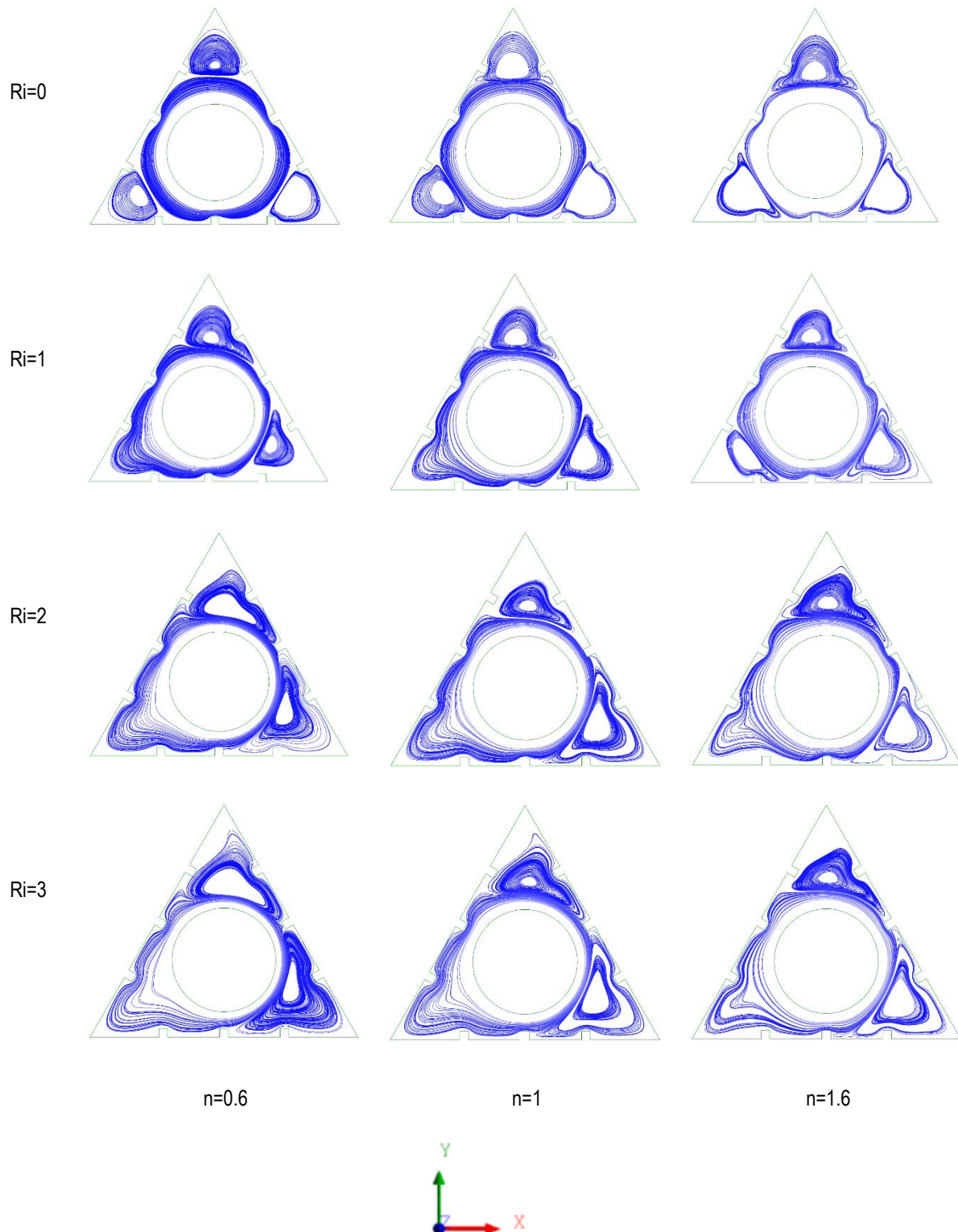
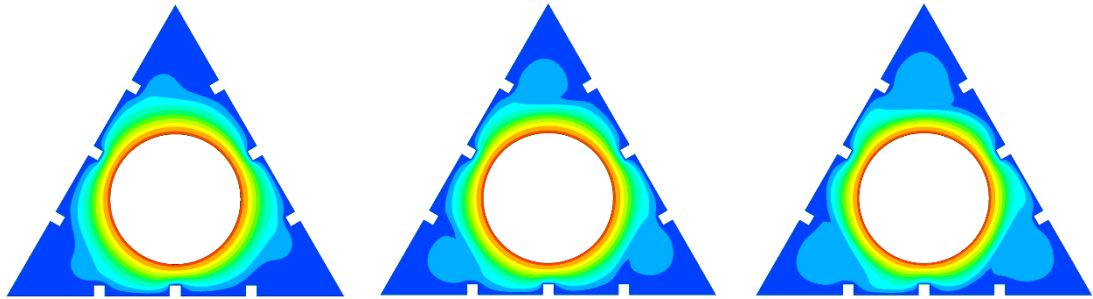


Fig. 13. Streamlines for the case of blockage ratio of 0.36 at $Re = 10$

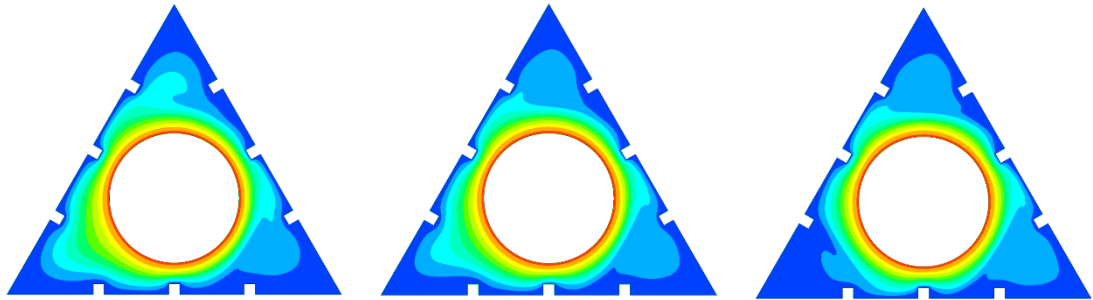
Fig. 16 presents a comparison of the Nusselt number (Nu) values for the three cases examined as a function of the Richardson number (Ri). The selected parameters are $n=0.6$ and $Re=10$. It is clear that in the mixed convection scenario involving power-law fluids, the heat transfer rate decreases significantly and progressively

from the initial state to the final state. These observations are consistent with a previous result [29], which show that higher blockage ratios stabilize the fluid flow and reduce the overall heat transfer rate.

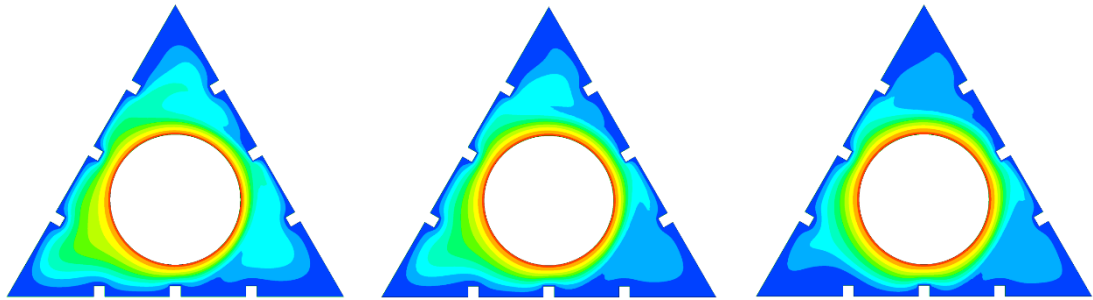
Ri=0



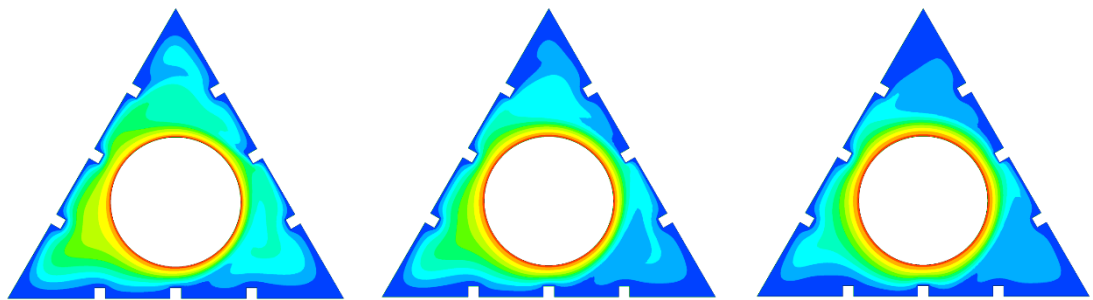
Ri=1



Ri=2



Ri=3



$n=0.6$

$n=1$

$n=1.6$

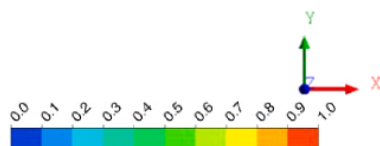


Fig. 14. Isotherms for the case of blockage ratio of 0.36 at $Re = 10$

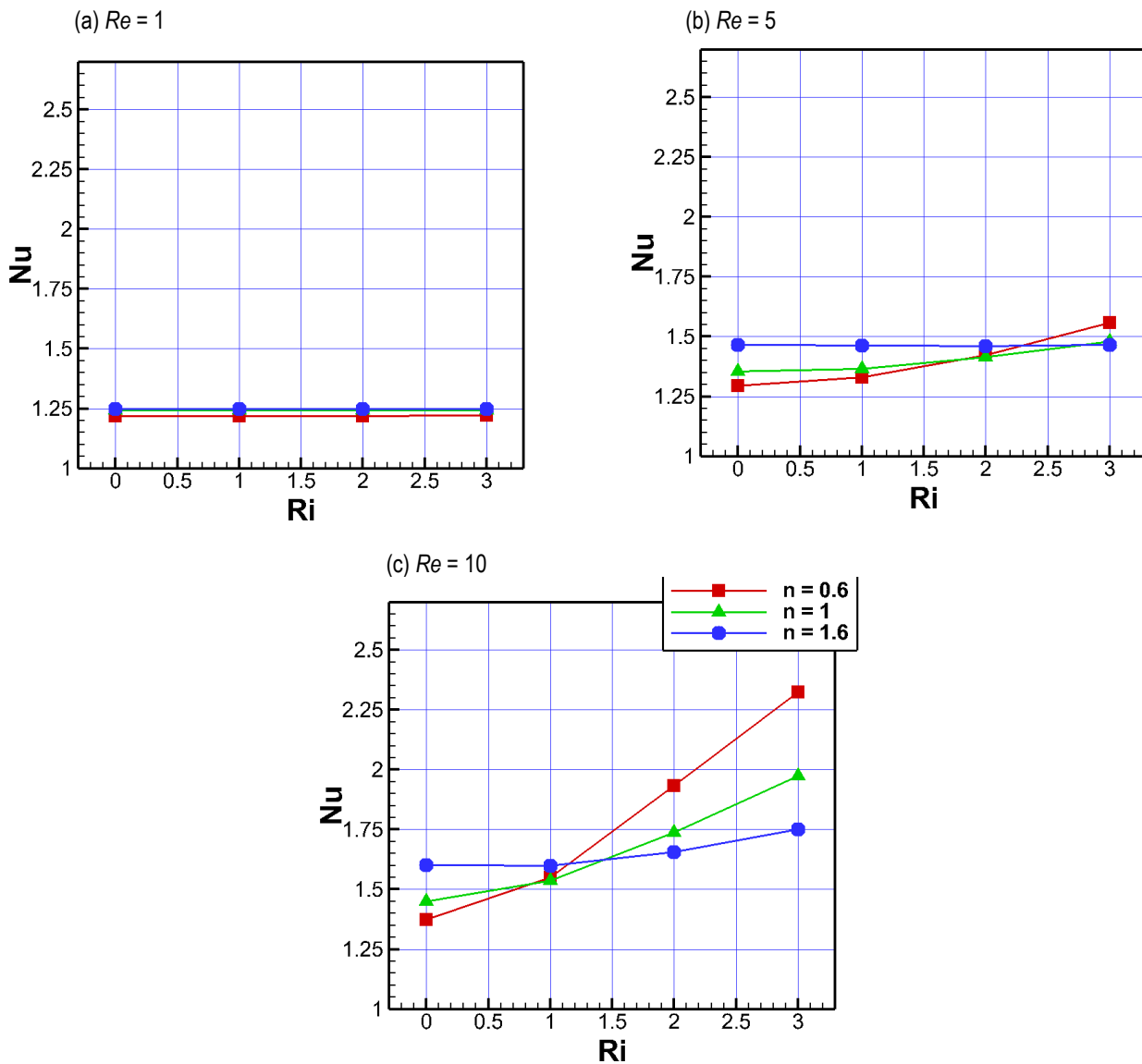


Fig. 15. Values of Nu versus Ri and n : a) for $Re = 1$; b) $Re = 5$; and c) $Re = 10$

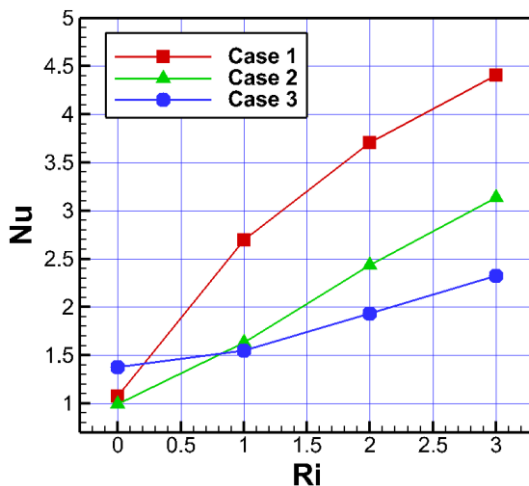


Fig. 16. Values of Nu with Ri for the three cases at $Re = 10$ and $n = 0.6$

5. CONCLUSION

This paper presents a numerical study on the behavior of a non-Newtonian fluid in a finned triangular cavity with a rotating, high-temperature horizontal cylinder. The cavity walls are maintained at a cold temperature. The study examines the effects of key parameters, including the power-law index (n), Reynolds number (Re), blockage ratio (β), and Richardson number (Ri), on fluid flow and thermal activity. The main findings are as follows:

- Increasing the blockage ratio stabilizes the flow by reducing disturbances and counter-rotating zones, but it also decreases the overall heat transfer rate;
- Higher thermal buoyancy promotes recirculation zones and vertical fluid motion, increasing the thermal activity around the heated cylinder;
- A higher Reynolds number enhances flow velocity and heat transfer due to increased rotational speed;

- A larger power-law index (n) increases fluid viscosity, reducing flow velocity and thermal activity;
- Shear-thickening fluids with a high blockage ratio are suited for thermal insulation, while shear-thinning fluids with a low blockage ratio are ideal for cooling.

Nomenclature

A	Surface area of the inner cylinder, m^2
C_p	Heat capacity of fluid, $J\ kg^{-1}\ K^{-1}$
d	Diameter of the inner cylinder, m
L	Side length of the triangular cavity, m
Gr	Grashof number
g	Gravitational acceleration, $m\ s^{-2}$
I_2	Second invariant function of strain rate tensor
K	Thermal conductivity of fluid, $W\ m^{-1}\ K^{-1}$
m	Consistency index, $Pa\ s^n$
Nu	Nusselt number (average value)
Nu_L	Nusselt number (local value)
n	Power-law index
Pr	Prandtl number
p	Pressure, Pa
Re	Reynolds number
Ri	Richardson number
T	Temperature, K
u, v	Velocity components along x and y directions, $m\ s^{-1}$
x, y	Cartesian coordinates, m

Greek symbols

β	Blockage ratio
β_T	Coefficient of volume expansion
η	Dynamic viscosity, Pa s
ρ	Density of fluid, $kg\ m^{-3}$
τ	Stress tensor, Pa
Ω	Rotation speed, $1/s$

Subscripts/Superscripts

c	Cold
h	Hot
*	dimensionless quantity

REFERENCES

1. Mishra L, Baranwal A, Chhabra R, Laminar forced convection in power-law fluids from two heated cylinders in a square duct, International Journal of Heat and Mass Transfer. 2017; 113 :589–612. <https://doi.org/10.1016/j.ijheatmasstransfer.2017.05.117>
2. Mohebbi R, Delouei A, Jamali A, Izadi M, Mohamad A, Pore-scale simulation of non-Newtonian power-law fluid flow and forced convection in partially porous media: Thermal lattice Boltzmann method, Physica A. 2019; 525 :642–656. <https://doi.org/10.1016/j.physa.2019.03.039>
3. Malkeson S, Alshaali S, Chakraborty N, Numerical investigation of steady state laminar natural convection of power-law fluids in sidecooled trapezoidal enclosures heated from the bottom, Numerical Heat Transfer, Part A: Applications. 2023; 83 :770–789. <https://doi.org/10.1080/10407782.2022.2157353>
4. Rashid U, Shahzad H, Lu D, Wang X, Majeed A, Non-Newtonian MHD double diffusive natural convection flow and heat transfer in a crown enclosure, Case Studies in Thermal Engineering. 2023; 41:102541. <https://doi.org/10.1016/j.csite.2022.102541>
5. Lamsaadi M, Naimi M, Hasnaoui M, Natural convection of non-Newtonian power law fluids in a shallow horizontal rectangular cavity uniformly heated from below, Heat Mass Transfer. 2005; 41 :239–249. <http://dx.doi.org/10.1007/s00231-004-0530-8>
6. Lamsaadi M, Naimi M, Hasnaoui M, Mamou M, Natural Convection in a Vertical Rectangular Cavity Filled with a Non-Newtonian Power Law Fluid and Subjected to a Horizontal Temperature Gradient, Numerical Heat Transfer, Part A.2006;49:969–990. <http://dx.doi.org/10.1080/10407780500324988>
7. Mahmood F, Chowdhury T, Hasan M, Fluid-structure interaction induced mixed convection characteristics in a lid-driven square cavity with non-Newtonian power law fluids, International Journal of Thermofluids. 2024; 22:100687. <https://doi.org/10.1016/j.ijft.2024.100687>
8. Bilal S, Khan N, Fatima I, Riaz A, Ansari G, Alhazmi S, Tag El-Din E, Mixed convective heat transfer in a power-law fluid in a square enclosure: Higher order finite element solutions, Frontiers in Physics.2022; 10 :1079641. <http://dx.doi.org/10.3389/fphy.2022.1079641>
9. Roy P, Chowdhury S, Raj M, Islam M, Saha S, Forced, natural and mixed convection of Non-Newtonian fluid flows in a square chamber with moving lid and discrete bottom heating, Results in Engineering. 2023; 17 :100939. <http://dx.doi.org/10.1016/j.rineng.2023.100939>
10. Prasad D, Chaitanya G, Raju R, Double diffusive effects on mixed convection Casson fluid flow past a wavy inclined plate in presence of Darcian porous medium, Results in Engineering. 2019; 3 :100019. <http://dx.doi.org/10.1016/j.rineng.2019.100019>
11. Thohura S, Molla M, Sarker M, Paul M, Study of mixed convection flow of power-law fluids in a skewed lid-driven cavity, Heat Transfer. 2021;10:1–30. <http://dx.doi.org/10.1002/htj.22174>
12. Hussain S, Jamal M, Geridonmez B, Impact of power law fluid and magnetic field on double diffusive mixed convection in staggered porous cavity considering Dufour and Soret effects, International Communications in Heat and Mass Transfer. 2021;121:105075. <http://dx.doi.org/10.1016/j.icheatmasstransfer.2020.105075>
13. Laidoudi H, Natural convection from four circular cylinders in across arrangement within horizontal annular space, Acta Mechanica et Automatica. 2020;14:98-102. <http://dx.doi.org/10.2478/ama-2020-0014>
14. Laidoudi H, Abderrahmane A, Saeed A. M, Guedri K, Weera W, Younis O, Mourad A, Marzouki R, Irreversibility interpretation and MHD mixed convection of hybrid nanofluids in a 3D heated lid-driven chamber, Nanomaterials. 2022;12:1747. <https://doi.org/10.3390/nano12101747>
15. Laidoudi H, Bouzit M, Mixed convection heat transfer from confined tandem circular cylinders in cross-flow at low Reynolds number. Mechanics. 2017; 23: 522-527. <https://doi.org/10.5755/j01.mech.23.4.15258>
16. Acharya N, Framing the effect of fitted curved fins' curvature on the flow patterns and entropy analysis of buoyancy-driven magnetized hybrid nanofluidic transport within an annular enclosure, Journal of Energy Storage.2024; 100: 113638. <https://doi.org/10.1016/j.est.2024.113638>
17. Acharya N, Magnetically driven MWCNT-Fe3O4-water hybrid nanofluidic transport through a micro-wavy channel: a novel MEMS design for drug delivery application. Materials Today Communications. 2024; 38:107844. <https://doi.org/10.1016/j.mtcomm.2023.107844>
18. Acharya N, Hydrothermal scenario of buoyancy-driven magnetized multi-walled carbon nanotube-Fe3O4-water hybrid nanofluid flow within a discretely heated circular chamber fitted with fins. Journal of Magnetism and Magnetic Materials. 2024; 589:171612. <https://doi.org/10.1016/j.jmmm.2023.171612>
19. Acharya N, On the magnetohydrodynamic natural convective alumina nanofluidic transport inside a triangular enclosure fitted with fins. Journal of the Indian Chemical Society. 2022; 99(12): 100784. <https://doi.org/10.1016/j.jics.2022.100784>
20. Acharya N, Effects of different thermal modes of obstacles on the natural convective Al2O3-water nanofluidic transport inside a triangular

- cavity. Proceedings of the Institution of Mechanical Engineers, Part C: Journal of Mechanical Engineering Science. 2022; 236(10): 5282-99.
<http://dx.doi.org/10.1177/09544062211061484>
21. Acharya N, Buoyancy driven magnetohydrodynamic hybrid nanofluid flow within a circular enclosure fitted with fins. International Communications in Heat and Mass Transfer. 2022; 133: 105980.
<https://doi.org/10.1016/j.icheatmasstransfer.2022.105980>
 22. Tayebi T, Dogonchi AS, Karimi N, Ge-JiLe H, Chamkha AJ, Elmasry Y. Thermo-economic and entropy generation analyses of magnetic natural convective flow in a nanofluid-filled annular enclosure fitted with fins, Sustain. Energy Technol. Assess. 2021; 46:1–30.
<https://doi.org/10.1016/j.seta.2021.101274>
 23. Chamkha AJ, Dogonchi AS, Ganji DD. Magnetohydrodynamic nanofluid natural convection in a cavity under thermal radiation and shape factor of nanoparticles impacts: a numerical study using CVFEM. Applied Sciences. 2018 Nov 26;8(12):2396.
<https://doi.org/10.3390/app8122396>
 24. Seyyedi SM, Dogonchi AS, Hashemi-Tilehnoee M, Ganji DD, Chamkha AJ. Second law analysis of magneto-natural convection in a nanofluid filled wavy-hexagonal porous enclosure. International Journal of Numerical Methods for Heat & Fluid Flow. 2020; 30: 4811-36.
<https://doi.org/10.1108/HFF-11-2019-0845>
 25. Dogonchi AS, Waqas M, Afshar SR, Seyyedi SM, Hashemi-Tilehnoee M, Chamkha AJ, Ganji DD. Investigation of magnetohydrodynamic fluid squeezed between two parallel disks by considering Joule heating, thermal radiation, and adding different nanoparticles. International Journal of Numerical Methods for Heat & Fluid Flow. 2020; 30:659-80. <https://doi.org/10.1108/HFF-05-2019-0390>
 26. Eshaghi S, Izadpanah F, Dogonchi AS, Chamkha AJ, Hamida MB, Alhumade H. The optimum double diffusive natural convection heat transfer in H-Shaped cavity with a baffle inside and a corrugated wall. Case Studies in Thermal Engineering. 2021; 28: 101541.
<https://doi.org/10.1016/j.csite.2021.101541>
 27. Abu-Ghurban M, Al-Farhany K. Mixed convective heat transfer in an open cavity with fins. Heat Transfer. 2024; 53(8): 4169-96.
<https://doi.org/10.1002/htj.23128>
 28. Laidoudi H, Ameur H, Investigation of the mixed convection of power-law fluids between two horizontal concentric cylinders: Effect of various operating conditions, New Journal and we have not received input yet. 2020; 20:100731.
<http://dx.doi.org/10.1016/j.tsep.2020.100731>
 29. Salman Z, Aiss F, Almudhaffar M. Experimental study of mixed convection in a cavity with a rotating cylinder. Journal of Advanced Research in Fluid Mechanics and Thermal Sciences. 2020; 74:16-26.
<https://doi.org/10.37934/arfmts.74.2.1626>
 30. Chun S, Ji B, Yang Z, Malik VK, Feng J. Experimental observation of a confined bubble moving in shear-thinning fluids. Journal of Fluid Mechanics. 2022; 953: A12.
<https://doi.org/10.1017/jfm.2022.926>
 31. Sheikholeslami M. CuO-water nanofluid free convection in a porous cavity considering Darcy law. European Physical Journal Plus. 2017; 132: 55.
<https://doi.org/10.1140/epjp/i2017-11330-3>

Youcef Lakahal:  <https://orcid.org/0009-0005-7444-4880>

Houssein Laidoudi:  <https://orcid.org/0000-0001-8700-7077>



This work is licensed under the Creative Commons BY-NC-ND 4.0 license.

THE ELZAKI TRANSFORM METHOD FOR ADDRESSING CAUCHY PROBLEMS IN HIGHER ORDER NONLINEAR PDES

Tarig M. ELZAKI^{*✉}, Mohamed Ali LATRACH^{**✉}

^{*}Department of Mathematics, University of Jeddah, College of Science and Arts El Kamel, Jeddah, Saudi Arabia
^{**}University of Tunis El Manar, National Engineering School at Tunis, Lamsin, B.P. 37, 1002, Tunis-Belvédère, Tunisia

tarig.alzaki@gmail.com, mohamedali.latrach@enit.utm.tn

received 7 December 2024, revised 1 February 2025, accepted 3 March 2025

Abstract: In this work, the new integral transform called the Elzaki transform (ET) is used to investigate and solve nonlinear higher-order partial differential equations (NHOPDEs), which serve as mathematical models in a range of practically significant disciplines of applied research. The NHOPDE solutions converge to exact solutions rather easily, were derived in a simple and easy-to-understand manner using ET. In addition, examples are given to illustrate how this method can be applied and how valid it is for the problem-solving form. There is a strong correlation between the analytical and exact solutions for the tested problems. This paper also covers the convergence of the ET technique to the exact solution of NHOPDEs. Numerical problems involving fourth and sixth order nonlinear hyperbolic equations and nonlinear wave-like equations with variable coefficients are solved to illustrate how the ET technique may efficiently yield accurate solutions for nonlinear PDEs of higher order with initial conditions. The results demonstrate the remarkable accuracy, efficiency, and dependability of the ET technique, which can be applied to a broad variety of nonlinear higher-order PDEs. This method greatly simplifies numerical calculations. The two primary goals of using this approach are to establish a fair frequency relationship and select an appropriate starting estimate. The precise, analytical, and numerical solutions to the examined problems show a high association with one another, further validating the robustness of this approach. Its unique properties, including its ability to simplify convolution operations and its close connection to the Laplace transform, also contribute to its effectiveness.

Key words: cauchy problem, nonlinear higher order partial differential equations, Elzaki transform, hyperbolic equation, wave-like equation, convergence analysis

1. INTRODUCTION

Numerous application disciplines, such as information theory, research, and engineering, depend heavily on NHOPDEs. This is especially important for applied sciences and entropy. Moreover, they have been used for a long time to explain a variety of natural phenomena, such as temperature fluctuations, growth of populations, earthquakes, and atomic structure. In literatures, there are numerous applications of the integral transform in mathematics. Integro-differential equations, integral equations, and linear DEs can all be solved with ET. This method is not appropriate for solving nonlinear DEs due to the nonlinear variables. Nonlinear DEs can be solved using ET support for the homotopy perturbation approach, differential transform method, and any other methods.

These days, nonlinear equations are very important. Applications of nonlinear phenomena are significant in engineering, physics, and applied math. Finding new exact or approximate solutions to nonlinear PDEs requires creative thinking, which is challenging even in fields like applied math and physics, where precise solutions are crucial. Many writers have focused on applying various methods to the investigation of solutions to nonlinear PDEs in the last few years. Numerous methods have been proposed, such as the homotopy perturbation, differential transform, Elzaki transform, Laplace, and double Laplace transforms, variational iteration, Adomian decomposition method and Laplace variational iteration [1–17].

Over the past few years, numerous researchers have devoted considerable effort to exploring various methods for solving nonlinear PDEs. Techniques such as the homotopy perturbation method (HPM), differential transform method (DTM), Elzaki transform, Laplace and double Laplace transforms, and the variational iteration method (VIM) have been widely employed to address these challenges. For instance, Abdulazeez et al. in [18] utilized the homotopy analysis method (HAM) and VIM to solve nonlinear pseudo-hyperbolic equations, demonstrating that HAM provides results that are more accurate and closely aligned with exact solutions compared to VIM. Similarly, the residual power series method (RPSM), as proposed by Abdulazeez et al. [19], has shown the ability to solve nonlinear pseudo-hyperbolic PDEs with non-local conditions, while providing fast convergence and accurate results. The explicit finite difference method (EFDM) was applied by Abdulazeez et al. [20] to solve fractional-order pseudo-hyperbolic telegraph PDEs using Caputo derivatives, while the Crank–Nicholson difference scheme has been successfully utilized for mobile–immobile advection–dispersion models [21]. Furthermore, Abdulla et al. [22] extended this approach by comparing the solutions of third-order fractional PDEs using Caputo and Atangana–Baleanu Caputo (ABC) fractional derivatives.

To overcome and relax the inherent difficulties of nonlinear problems, hybrid methods that combine two or more techniques have been increasingly explored. For example, Ahsan et al. in [23] present a hybrid scheme of finite-difference and Haar wavelet distribution for the ill-posed nonlinear inverse Cauchy problem.

Advanced computational techniques have also found applications in specialized areas such as signal processing and electromagnetic wave modeling. For instance, Prewitt operators combined with fractional-order telegraph PDEs have been proposed by Tenekci et al. [24] for edge detection, demonstrating the potential of fractional operators in enhancing image processing techniques. Similarly, Modanli et al. [25] introduced a computational method based on integral transforms for solving time-fractional equations arising in electromagnetic waves, highlighting the importance of fractional calculus in addressing wave propagation problems.

The new technique, which is based on a novel integral transform (ET), will be introduced and used in an accessible manner in this study [6]. We also explore the potential applications of this new transform side by side with the recently developed approach to solving NHOPDEs in this work. This method works well with standard impulse functions and functions along with discontinuities.

This document is organized as follows: Section 2 presents a new integral transform called the Elzaki transform (ET). Section 3 presents a convergence study and analytical methodology for solving NHOPDEs. Section 4 presents a several numerical example. Discussion and conclusion brought under Section 5 to a close

2. ELZAKI TRANSFORM

Integral equations, systems of PDEs, ODEs, and PDEs may all be solved with the ET, as demonstrated by Tarig M. Elzaki in [2–5, 29–33]. Effective application of ET is possible when Sumudu and Laplace transforms are unable to solve DEs with variable coefficients [11]. In engineering and applied mathematics, ET is a potent instrument.

The primary ideas behind this modification in presentation are as follows, ET of $B(\varepsilon)$ is :

$$E[B(\varepsilon)] = \xi \int_0^{+\infty} B(\varepsilon) e^{-\frac{\varepsilon}{\xi}} d\varepsilon, \quad \varepsilon > 0. \quad (1)$$

Definition 1 Let $T'(\xi)$ be the ET of the derivative of $B(\varepsilon)$, then:

$$(a) \quad T'(\xi) = \frac{T(\xi)}{\xi} - \xi B(0),$$

$$(b) \quad T^{(n)}(\xi) = \frac{T(\xi)}{\xi^n} - \sum_{k=0}^{n-1} \xi^{2-n+k} B^{(k)}(0), \quad n \geq 1,$$

where $T^{(n)}(\xi)$ is ET of the n^{th} derivative of $B(\varepsilon)$.

The following helpful ETs have been established in this study: Let $E[B(\varepsilon)] = T(\xi)$ and $E[a(\varepsilon)] = A(\xi)$, then:

1. $E[B(\varepsilon) \pm a(\varepsilon)] = E[B(\varepsilon)] \pm E[a(\varepsilon)] = T(\xi) \pm A(\xi),$
2. $E[\varepsilon^n] = \xi^{\alpha+2} \Gamma(\alpha + 1), \quad \alpha > -1,$
3. $E[B^{(n)}(\varepsilon)] = \frac{T(\xi)}{\xi^n} - \frac{B(0)}{\xi^{n-2}} - \frac{B'(0)}{\xi^{n-3}} - \dots - \xi B^{n-1}(0).$

Let $E[B(\varepsilon, \zeta)] = T(\varepsilon, \xi)$ then the ET of partial derivatives of $B(\varepsilon, \zeta)$ are,

$$E\left[\frac{\partial B(\varepsilon, \zeta)}{\partial \zeta}\right] = \frac{1}{\xi} T(\varepsilon, \xi) - \xi B(\varepsilon, 0),$$

$$E\left[\frac{\partial^2 B(\varepsilon, \zeta)}{\partial \zeta^2}\right] = \frac{1}{\xi^2} T(\varepsilon, \xi) - B(\varepsilon, 0) - \xi \frac{\partial B(\varepsilon, 0)}{\partial \zeta},$$

$$E\left[\frac{\partial B(\varepsilon, \zeta)}{\partial \varepsilon}\right] = \frac{d}{d\varepsilon} [T(\varepsilon, \xi)], \quad E\left[\frac{\partial^2 B(\varepsilon, \zeta)}{\partial \varepsilon^2}\right] = \frac{d^2}{d\varepsilon^2} [T(\varepsilon, \xi)],$$

$$E\left[\frac{\partial^n B(\varepsilon, \zeta)}{\partial \zeta^n}\right] = \frac{1}{\xi^n} T(\varepsilon, \xi) - \sum_{k=0}^{n-1} \xi^{2-n+k} B^{(k)}(\varepsilon, 0), \quad n \geq 1.$$

3. ANALYSIS OF PROPOSED SCHEME

We use the following initial conditions and NHOPDEs Cauchy problem to demonstrate the basic idea in this method:

$$\left(\frac{\partial^2}{\partial \zeta^2} - a \frac{\partial^2}{\partial \varepsilon^2}\right)^k B(\varepsilon, \zeta) = NB(\varepsilon, \zeta) + g(\varepsilon, \zeta), \quad k \geq 1, \quad (2)$$

$$\frac{\partial^i}{\partial \varepsilon^i} B(\varepsilon, 0) = g(\varepsilon), \quad i = 1, 2, \dots, 2k-1.$$

Where, $B(\varepsilon, \zeta)$ is the unknown function, $NB(\varepsilon, \zeta)$ nonlinear operator, $g(\varepsilon, \zeta)$ is the in-homogeneous or source term and $a = a(\varepsilon, \zeta)$ may be a constant or function of ε or ζ .

When $k > 1$, Eq. (2) turns into a nonlinear hyperbolic equation of greater order [26], while for $k = 1$, an equation (2) was reduced to a wave shape [27, 28].

Equation (2) can be written as follows:

$$\frac{\partial^{2k} B}{\partial \zeta^{2k}} + \sum_{r=0}^{k-1} (-a)^{k-r} \binom{k}{r} \frac{\partial^{2k} B}{\partial \zeta^{2r} \partial \varepsilon^{2k-2r}} = NB(\varepsilon, \zeta) + g(\varepsilon, \zeta),$$

$$0 \leq r \leq k, \text{ and } \binom{k}{r} = \frac{k!}{r!(k-r)!}.$$

or

$$\frac{\partial^{2k} B}{\partial \zeta^{2k}} = NB(\varepsilon, \zeta) + g(\varepsilon, \zeta) - \sum_{r=0}^{k-1} (-a)^{k-r} \binom{k}{r} \frac{\partial^{2k} B}{\partial \zeta^{2r} \partial \varepsilon^{2k-2r}}. \quad (3)$$

Using ET to obtain:

$$E\left[\frac{\partial^{2k} B}{\partial \zeta^{2k}}\right] = E\left[NB(\varepsilon, \zeta) + g(\varepsilon, \zeta) - \sum_{r=0}^{k-1} (-a)^{k-r} \binom{k}{r} \frac{\partial^{2k} B}{\partial \zeta^{2r} \partial \varepsilon^{2k-2r}}\right],$$

$$\begin{aligned} & \frac{1}{\xi^{2k}} E[B] - \sum_{r=0}^{2k-1} \frac{\partial^r B(\varepsilon, 0)}{\partial \zeta^r} \xi^{2-2k+r} \\ &= E\left[NB(\varepsilon, \zeta) + g(\varepsilon, \zeta) - \sum_{r=0}^{k-1} (-a)^{k-r} \binom{k}{r} \frac{\partial^{2k} B}{\partial \zeta^{2r} \partial \varepsilon^{2k-2r}}\right], \\ &\Rightarrow E[B] = \sum_{r=0}^{2k-1} \frac{\partial^r B(\varepsilon, 0)}{\partial \zeta^r} \xi^{2+r} \\ &+ \xi^{2k} E\left[NB(\varepsilon, \zeta) + g(\varepsilon, \zeta) - \sum_{r=0}^{k-1} (-a)^{k-r} \binom{k}{r} \frac{\partial^{2k} B}{\partial \zeta^{2r} \partial \varepsilon^{2k-2r}}\right]. \end{aligned}$$

Applying Elzaki inverse to get:

$$B(\varepsilon, \zeta) = G(\varepsilon, \zeta) + E^{-1} \left\{ \xi^{2k} E \left[NB(\varepsilon, \zeta) - \sum_{r=0}^{k-1} (-a)^{k-r} \binom{k}{r} \frac{\partial^{2k} B}{\partial \zeta^{2r} \partial \varepsilon^{2k-2r}} \right] \right\}.$$

Where $G(\varepsilon, \zeta)$ denotes the term that arises from all or some of the function $g(\varepsilon, \zeta)$ and the stipulated initial conditions.

This method's efficacy hinges on how we choose the initial iteration $B_0(\varepsilon, \zeta)$ that yields the most precise result in the fewest stages. To get a solution iteratively, we use the following relations:

$$\begin{aligned} B_{n+1}(\varepsilon, \zeta) &= E^{-1} \left\{ \xi^{2k} E \left[NB_n - \sum_{r=0}^{k-1} (-a)^{k-r} \binom{k}{r} \frac{\partial^{2k} B_n}{\partial \zeta^{2r} \partial \varepsilon^{2k-2r}} \right] \right\}, \\ B_0(\varepsilon, \zeta) &= G(\varepsilon, \zeta). \end{aligned} \quad (4)$$

It looks that the following is the series form for the solution to Eq. (2):

$$B(\varepsilon, \zeta) = \sum_{n=0}^{\infty} B_n(\varepsilon, \zeta). \quad (5)$$

According to System. (4), we are able to determine the following $B_0(\varepsilon, \zeta)$, $B_1(\varepsilon, \zeta)$, $B_2(\varepsilon, \zeta)$, \dots , Eq. (5) can then be used to find the solution.

3.1. Convergence analysis

The convergence of the ET approach to the exact solution for NHOPDEs is covered in this section.

Theorem 1. If B is a Banach space, $\sum_{n=0}^{\infty} B_n(\varepsilon, \zeta)$ in Eq. (5) is convergence, if $\exists (0 \leq \beta < 1)$, s.t. $\forall \tau \in \mathbb{N} \Rightarrow \|B_\tau\| \leq \beta \|B_{\tau-1}\|$, to $\eta \in B$.

Proof. Partially sum sequence is described as follows: $\{\eta_\tau\}_{\tau=0}^{\infty}$,

$$\eta_0 = B_0$$

$$\eta_1 = B_0 + B_1$$

$$\eta_2 = B_0 + B_1 + B_2$$

\vdots

$$\eta_\tau = B_0 + B_1 + \dots + B_\tau$$

It is now necessary to demonstrate that: $\{\eta_\tau\}_{\tau=0}^{\infty}$ is a Cauchy series in Banach space,

$$\|\eta_{\tau+1} - \eta_\tau\| = \|\sum_{n=0}^{\tau+1} B_n - \sum_{n=0}^{\tau} B_n\| = \|B_{\tau+1}\| \leq \beta \|B_\tau\| \leq \dots \leq \beta^{\tau+1} \|B_0\|.$$

For all $(\tau, \lambda) \in \mathbb{N}^2$ as $\tau \geq \lambda$

$$\begin{aligned} \|\eta_\tau - \eta_\lambda\| &= \|(\eta_\tau - \eta_{\tau-1}) + (\eta_{\tau-1} - \eta_{\tau-2}) + \dots + (\eta_{\lambda+1} - \eta_\lambda)\| \\ &\leq \|\eta_\tau - \eta_{\tau-1}\| + \|\eta_{\tau-1} - \eta_{\tau-2}\| + \dots + \|\eta_{\lambda+1} - \eta_\lambda\| \\ &\leq \beta^\tau \|B_0\| + \beta^{\tau-1} \|B_0\| + \dots + \beta^{\lambda+1} \|B_0\| \\ &\leq \beta^{\lambda+1} \|B_0\| (\beta^{\tau-\lambda-1} + \beta^{\tau-\lambda-2} + \dots + \beta) \\ &= \frac{1-\beta^{\tau-\lambda}}{1-\beta} \beta^{\lambda+1} \|B_0\|. \end{aligned}$$

Since $(\beta^{\tau-\lambda-1} + \beta^{\tau-\lambda-2} + \dots + \beta)$ is a geometric series and $0 \leq \beta < 1$ then, $\lim_{\tau, \lambda \rightarrow +\infty} (\eta_\tau - \eta_\lambda) = 0$ then $\{\eta_\tau\}_{\tau=0}^{\infty}$ is the Cauchy sequence in Banach space B then $B = \sum_{n=0}^{\infty} B_n(\varepsilon, \zeta)$ defined in Eq. (5) converges.

4. NUMERICAL APPLICATIONS

This section applies the suggested method to the solution of three numerical examples of nonlinear higher-order hyperbolic equations and two nonlinear wave-like equations with variable coefficients.

4.1. Nonlinear Higher Order Hyperbolic Equations

Numerous physical phenomena, such as vibrating strings and membranes, the motion of an inviscid compressible flow, and the motion of a compressible fluid like air, are all explained by nonlinear hyperbolic PDEs. Numerous disciplines have utilized these formulas, such as electromagnetic theory, astrophysics, hypoelastic solids, and heat wave propagation.

Example 1.

Let, $k = 2$, $a = 1$, $NB = B - \frac{\partial B}{\partial \zeta}$ and $g(\varepsilon, \zeta) = 0$,

then Eq. (2) becomes,

$$\frac{\partial^4 B}{\partial \zeta^4} - 2 \frac{\partial^4 B}{\partial \zeta^2 \partial \varepsilon^2} + \frac{\partial^4 B}{\partial \varepsilon^4} = B - \frac{\partial B}{\partial \zeta}, \quad (6)$$

$$B(\varepsilon, 0) = \frac{\partial B(\varepsilon, 0)}{\partial \zeta} = \frac{\partial^2 B(\varepsilon, 0)}{\partial \zeta^2} = \frac{\partial^3 B(\varepsilon, 0)}{\partial \zeta^3} = e^\varepsilon.$$

This is a Cauchy problem with a fourth-order hyperbolic equation [13]. Using ET in Eq. (6) to obtain,

$$\begin{aligned} \frac{1}{\xi^4} E[B(\varepsilon, \zeta)] - \sum_{k=0}^3 \frac{\partial^k B(\varepsilon, 0)}{\partial \zeta^k} \xi^{-2+k} - E[B(\varepsilon, \zeta)] \\ = E \left[2 \frac{\partial^4 B}{\partial \zeta^2 \partial \varepsilon^2} - \frac{\partial^4 B}{\partial \varepsilon^4} - \frac{\partial B}{\partial \zeta} \right], \\ (1 - \xi^4) E[B(\varepsilon, \zeta)] = (\xi^5 + \xi^4 + \xi^3 + \xi^2) e^\varepsilon \\ + \xi^4 E \left[2 \frac{\partial^4 B}{\partial \zeta^2 \partial \varepsilon^2} - \frac{\partial^4 B}{\partial \varepsilon^4} - \frac{\partial B}{\partial \zeta} \right], \\ E[B(\varepsilon, \zeta)] = \frac{\xi^2}{1-\xi} e^\varepsilon + \frac{\xi^2}{1-\xi^4} E \left[2 \frac{\partial^4 B}{\partial \zeta^2 \partial \varepsilon^2} - \frac{\partial^4 B}{\partial \varepsilon^4} - \frac{\partial B}{\partial \zeta} \right]. \end{aligned}$$

Inverse ET states that:

$$\begin{aligned} E^{-1}[E[B(\varepsilon, \zeta)]] &= E^{-1} \left[\frac{\xi^2}{1-\xi} e^\varepsilon \right] \\ &+ E^{-1} \left[\frac{\xi^4}{1-\xi^4} E \left[2 \frac{\partial^4 B}{\partial \zeta^2 \partial \varepsilon^2} - \frac{\partial^4 B}{\partial \varepsilon^4} - \frac{\partial B}{\partial \zeta} \right] \right]. \end{aligned}$$

The following diagram illustrates the iteration formula using a first approximation.

$$\begin{aligned} B_{n+1}(\varepsilon, \zeta) &= E^{-1} \left[\frac{\xi^4}{1-\xi^4} E \left[2 \frac{\partial^4 B_n}{\partial \zeta^2 \partial \varepsilon^2} - \frac{\partial^4 B_n}{\partial \varepsilon^4} - \frac{\partial B_n}{\partial \zeta} \right] \right], \\ B_0(\varepsilon, \zeta) &= e^{\varepsilon+\zeta}. \end{aligned} \quad (7)$$

Eq. (7), gives:

$$\begin{aligned} B_1(\varepsilon, \zeta) &= E^{-1} \left[\frac{\xi^4}{1-\xi^4} E \left[2 \frac{\partial^4 B_0}{\partial \zeta^2 \partial \varepsilon^2} - \frac{\partial^4 B_0}{\partial \varepsilon^4} - \frac{\partial B_0}{\partial \zeta} \right] \right] = \\ E^{-1} \left[\frac{\xi^4}{1-\xi^4} E[2e^{\varepsilon+\zeta} - e^{\varepsilon+\zeta} - e^{\varepsilon+\zeta}] \right] &= 0, \end{aligned}$$

and $B_2(\varepsilon, \zeta) = 0$, $B_3(\varepsilon, \zeta) = 0, \dots$

Hence, the solution is $B(\varepsilon, \zeta) = e^{\varepsilon+\zeta}$. The ETM gives this exact solution after only one iteration. Fig. 1 illustrates the graphical representation of the numerical solution via ETM, which is identical to the exact solution and therefore confirms higher the effectiveness and the accuracy of this method. In this example, the relative error is zero because we found the exact solution using only one step.

Let, $k = 2$, $a = 1$, $NB = \left(\frac{\partial^2 B}{\partial \zeta^2}\right)^2 - \left(\frac{\partial^2 B}{\partial \varepsilon^2}\right)^2 - 144B$ and $g(\varepsilon, \zeta) = 0$, then Eq. (2) becomes,

$$\begin{aligned} \frac{\partial^4 B}{\partial \zeta^4} - 2 \frac{\partial^4 B}{\partial \zeta^2 \partial \varepsilon^2} + \frac{\partial^4 B}{\partial \varepsilon^4} &= \left(\frac{\partial^2 B}{\partial \zeta^2}\right)^2 - \left(\frac{\partial^2 B}{\partial \varepsilon^2}\right)^2 - 144B \\ B(\varepsilon, 0) &= -\varepsilon^4, \quad \frac{\partial^i B(\varepsilon, 0)}{\partial \zeta^i} = 0, \quad i = 1, 2, 3. \end{aligned} \quad (8)$$

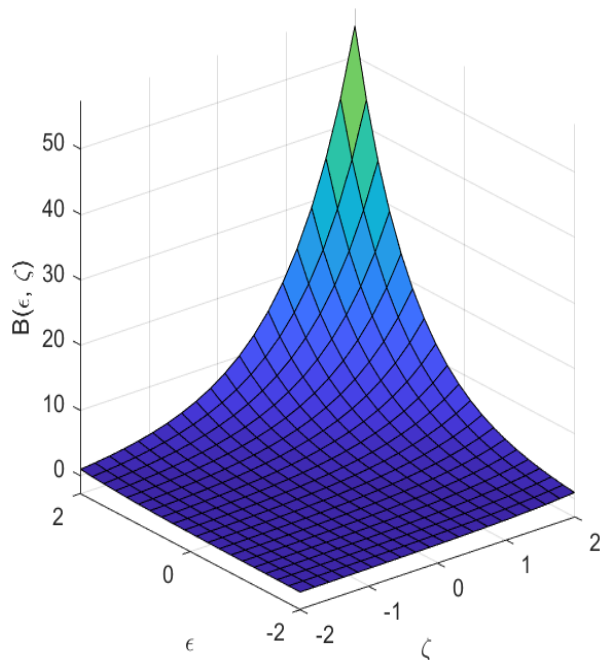


Fig. 1. Graphical representation of the ETM solution to example 1 after only one iteration

Example 2.

It is the Cauchy problem of the fourth order hyperbolic equation [13]. Using ET from Eq. (8) the following results are obtained:

$$\begin{aligned} \frac{1}{\xi^4} E[B(\varepsilon, \zeta)] - \sum_{k=0}^3 \frac{\partial^k B(\varepsilon, 0)}{\partial \zeta^k} \xi^{-2+k} \\ = E \left[2 \frac{\partial^4 B}{\partial \zeta^2 \partial \varepsilon^2} - \frac{\partial^4 B}{\partial \varepsilon^4} + \left(\frac{\partial^2 B}{\partial \zeta^2} \right)^2 - \left(\frac{\partial^2 B}{\partial \varepsilon^2} \right)^2 - 144B \right], \\ E[B(\varepsilon, \zeta)] = -\varepsilon^4 \xi^2 \\ + \xi^4 E \left[2 \frac{\partial^4 B}{\partial \zeta^2 \partial \varepsilon^2} - \frac{\partial^4 B}{\partial \varepsilon^4} + \left(\frac{\partial^2 B}{\partial \zeta^2} \right)^2 - \left(\frac{\partial^2 B}{\partial \varepsilon^2} \right)^2 - 144B \right]. \end{aligned}$$

Following Example 1, the following recurring connection can be obtained by following the same procedure:

$$\begin{aligned} B_{n+1}(\varepsilon, \zeta) = E^{-1} \left[\xi^4 E \left[2 \frac{\partial^4 B_n}{\partial \zeta^2 \partial \varepsilon^2} - \frac{\partial^4 B_n}{\partial \varepsilon^4} + \left(\frac{\partial^2 B_n}{\partial \zeta^2} \right)^2 - \left(\frac{\partial^2 B_n}{\partial \varepsilon^2} \right)^2 - 144B_n \right] \right], \\ B_0(\varepsilon, \zeta) = -\varepsilon^4. \end{aligned} \quad (9)$$

Later on, we are able to discover:

$$\begin{aligned} B_1(\varepsilon, \zeta) = E^{-1}[\xi^4 E[24]] = E^{-1}[24\xi^6] = \zeta^4, \quad B_2(\varepsilon, \zeta) = \\ E^{-1}[\xi^4 E[144\zeta^4 - 144\zeta^4]] = 0, \quad B_3(\varepsilon, \zeta) = 0, \text{ and,} \\ B_4(\varepsilon, \zeta) = 0, \dots \end{aligned}$$

Thus: $B(\varepsilon, \zeta) = \zeta^4 - \varepsilon^4$. As the example 1, Fig. 2 shows the graphical representation of the exact solution obtained by ETM to this example, where the relative error is zero because we found the exact solution using only one step.

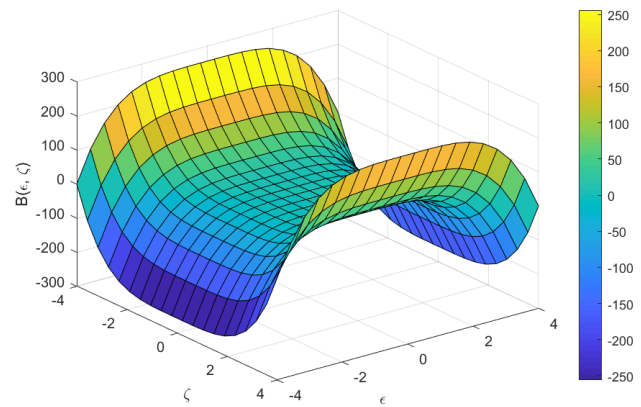


Fig. 2. Graphical representation of the exact solution to example 2 via ETM after only one step

Example 3.

Let, $k = 3$, $a = 1$, $NB = B \frac{\partial^2 B}{\partial \zeta^2} - B \frac{\partial^2 B}{\partial \varepsilon^2}$ and $g(\varepsilon, \zeta) = 0$, then Eq. (2) becomes,

$$\frac{\partial^6 B}{\partial \zeta^6} - 3 \frac{\partial^6 B}{\partial \zeta^4 \partial \varepsilon^2} + 3 \frac{\partial^6 B}{\partial \zeta^2 \partial \varepsilon^4} - \frac{\partial^6 B}{\partial \varepsilon^6} = B \frac{\partial^2 B}{\partial \zeta^2} - B \frac{\partial^2 B}{\partial \varepsilon^2}, \quad (10)$$

$$\begin{aligned} B(\varepsilon, 0) = \frac{\partial^2 B(\varepsilon, 0)}{\partial \zeta^2} = \frac{\partial^4 B(\varepsilon, 0)}{\partial \zeta^4} \\ = 0, \end{aligned}$$

$$\begin{aligned} \frac{\partial B(\varepsilon, 0)}{\partial \zeta} = \cos \varepsilon, \quad \frac{\partial^3 B(\varepsilon, 0)}{\partial \zeta^3} = -\cos \varepsilon, \\ \frac{\partial^5 B(\varepsilon, 0)}{\partial \zeta^5} = \cos \varepsilon, \end{aligned}$$

This is the Cauchy problem for the hyperbolic equation of sixth order [13]. The expression for Eq. (10) is as follows:

$$\begin{aligned} \frac{\partial^6 B}{\partial \zeta^6} + B = 3 \frac{\partial^6 B}{\partial \zeta^4 \partial \varepsilon^2} - 3 \frac{\partial^6 B}{\partial \zeta^2 \partial \varepsilon^4} + \frac{\partial^6 B}{\partial \varepsilon^6} + B \left(\frac{\partial^2 B}{\partial \zeta^2} - \frac{\partial^2 B}{\partial \varepsilon^2} \right) + B, \\ B(\varepsilon, 0) = \frac{\partial^2 B(\varepsilon, 0)}{\partial \zeta^2} = \frac{\partial^4 B(\varepsilon, 0)}{\partial \zeta^4} = 0, \\ \frac{\partial B(\varepsilon, 0)}{\partial \zeta} = \cos \varepsilon, \quad \frac{\partial^3 B(\varepsilon, 0)}{\partial \zeta^3} = -\cos \varepsilon, \quad \frac{\partial^5 B(\varepsilon, 0)}{\partial \zeta^5} = \cos \varepsilon, \end{aligned}$$

Using ET to get:

$$\begin{aligned} \frac{1}{\xi^6} E[B(\varepsilon, \zeta)] - \sum_{k=0}^5 \frac{\partial^k B(\varepsilon, 0)}{\partial \zeta^k} \xi^{-4+k} + E[B(\varepsilon, \zeta)] \\ = E \left[3 \left(\frac{\partial^6 B}{\partial \zeta^4 \partial \varepsilon^2} - \frac{\partial^6 B}{\partial \zeta^2 \partial \varepsilon^4} \right) + \frac{\partial^6 B}{\partial \varepsilon^6} + B \left(\frac{\partial^2 B}{\partial \zeta^2} - \frac{\partial^2 B}{\partial \varepsilon^2} \right) + B \right], \\ \frac{1 + \xi^6}{\xi^6} E[B(\varepsilon, \zeta)] = (\xi^7 - \xi^5 + \xi^3) \cos \varepsilon \\ + E \left[3 \left(\frac{\partial^6 B}{\partial \zeta^4 \partial \varepsilon^2} - \frac{\partial^6 B}{\partial \zeta^2 \partial \varepsilon^4} \right) + \frac{\partial^6 B}{\partial \varepsilon^6} + B \left(\frac{\partial^2 B}{\partial \zeta^2} - \frac{\partial^2 B}{\partial \varepsilon^2} \right) + B \right], \\ E[B(\varepsilon, \zeta)] = \frac{\xi^3}{1 + \xi^2} \cos \varepsilon \\ + \frac{\xi^6}{1 + \xi^6} E \left[3 \left(\frac{\partial^6 B}{\partial \zeta^4 \partial \varepsilon^2} - \frac{\partial^6 B}{\partial \zeta^2 \partial \varepsilon^4} \right) + \frac{\partial^6 B}{\partial \varepsilon^6} + B \left(\frac{\partial^2 B}{\partial \zeta^2} - \frac{\partial^2 B}{\partial \varepsilon^2} \right) + B \right], \end{aligned}$$

$$B(\varepsilon, \zeta) = \cos \varepsilon E^{-1} \left[\frac{\xi^3}{1+\xi^2} \right] + E^{-1} \left[\frac{\xi^6}{1+\xi^6} E \left[3 \left(\frac{\partial^6 B}{\partial \zeta^4 \partial \varepsilon^2} - \frac{\partial^6 B}{\partial \zeta^2 \partial \varepsilon^4} \right) + \frac{\partial^6 B}{\partial \varepsilon^6} + B \left(\frac{\partial^2 B}{\partial \zeta^2} - \frac{\partial^2 B}{\partial \varepsilon^2} \right) + B \right] \right].$$

Using the same method as in Example 1, one may find the recurrence relation in the following.

$$B_{n+1}(\varepsilon, \zeta) = E^{-1} \left[\frac{\xi^6}{1+\xi^6} E \left[3 \left(\frac{\partial^6 B}{\partial \zeta^4 \partial \varepsilon^2} - \frac{\partial^6 B}{\partial \zeta^2 \partial \varepsilon^4} \right) + \frac{\partial^6 B}{\partial \varepsilon^6} + B \left(\frac{\partial^2 B}{\partial \zeta^2} - \frac{\partial^2 B}{\partial \varepsilon^2} \right) + B \right] \right],$$

$$B_0(\varepsilon, \zeta) = \cos \varepsilon E^{-1} \left[\frac{\xi^3}{1+\xi^2} \right] = \cos \varepsilon \sin \zeta.$$

Next, we have $B_1(\varepsilon, \zeta) = 0$, $B_2(\varepsilon, \zeta) = 0$, $B_3(\varepsilon, \zeta) = 0, \dots$. Then $B(\varepsilon, \zeta) = \cos \varepsilon \sin \zeta$, this is the exact solution of this example and, is also obtained using ETM depicted graphically in Fig. 3. In this example, the relative error is zero because we found the exact solution using only one step.

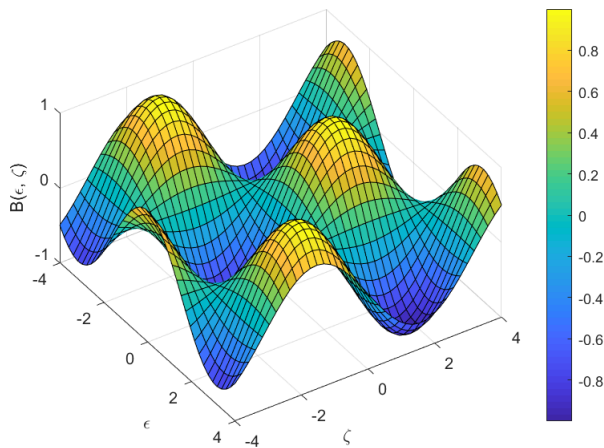


Fig. 3. Graphical representation of the exact solution to example 3 via ETM after only one iteration

4.2. Nonlinear Wave-Like Equations with Variable Coefficients

For explaining the growth of stochastic systems, one of the most widely used wave models is the wave-like equation. The stochastic behavior of exchange rates, fluctuations in laser light intensity, and the random movements of microscopic particles immersed in fluids are a few examples of such systems.

The situation in which $a = a(\varepsilon, \zeta)$ may be a constant or function of ε or ζ , will now be examined.

Example 4

Let, $k = 1$, $a = \varepsilon^2$, $NB = B - \left(\frac{\partial B}{\partial \varepsilon} \right)^2$ and $g(\varepsilon, \zeta) = e^{2\zeta}$ then Eq. (2) becomes,

$$\frac{\partial^2 B}{\partial \zeta^2} - \varepsilon^2 \frac{\partial^2 B}{\partial \varepsilon^2} = B - \left(\frac{\partial B}{\partial \varepsilon} \right)^2 + e^{2\zeta}, \quad (11)$$

$$B(\varepsilon, 0) = \frac{\partial B(\varepsilon, 0)}{\partial \zeta} = \varepsilon.$$

It is the Cauchy problem related to nonlinear wave-like equation with variable coefficients [14, 26]. Using ET to get:

$$\frac{1}{\xi^2} E[B(\varepsilon, \zeta)] - \sum_{k=0}^1 \frac{\partial^k B(\varepsilon, 0)}{\partial \zeta^k} \xi^k$$

$$= E \left[\varepsilon^2 \frac{\partial^2 B(\varepsilon, \zeta)}{\partial \varepsilon^2} - \left(\frac{\partial B(\varepsilon, \zeta)}{\partial \varepsilon} \right)^2 + B(\varepsilon, \zeta) + e^{2\zeta} \right],$$

$$\frac{1-\xi^2}{\xi^2} E[B(\varepsilon, \zeta)] = \varepsilon + \varepsilon \xi + E[e^{2\zeta}] + E \left[\varepsilon^2 \frac{\partial^2 B(\varepsilon, \zeta)}{\partial \varepsilon^2} - \left(\frac{\partial B(\varepsilon, \zeta)}{\partial \varepsilon} \right)^2 \right],$$

$$B(\varepsilon, \zeta) = E^{-1} \left[\frac{\varepsilon(\xi^2 + \xi^3)}{1-\xi^2} + \frac{\xi^4}{(1-\xi^2)(1-2\xi)} \right] + E^{-1} \left[\frac{\xi^2}{1-\xi^2} E \left[\varepsilon^2 \frac{\partial^2 B(\varepsilon, \zeta)}{\partial \varepsilon^2} - \left(\frac{\partial B(\varepsilon, \zeta)}{\partial \varepsilon} \right)^2 \right] \right].$$

Using the same method as in Example 1, one may find the recurrence relation in the following.

$$B_{n+1}(\varepsilon, \zeta) = E^{-1} \left[\frac{\xi^2}{1-\xi^2} E \left[\varepsilon^2 \frac{\partial^2 B_n}{\partial \varepsilon^2} - \left(\frac{\partial B_n}{\partial \varepsilon} \right)^2 \right] \right],$$

$$B_0(\varepsilon, \zeta) = E^{-1} \left[\frac{\varepsilon(\xi^2 + \xi^3)}{1-\xi^2} + \frac{\xi^4}{(1-\xi^2)(1-2\xi)} \right].$$

Next, we have:

$$B_0(\varepsilon, \zeta) = \varepsilon e^\zeta + \frac{e^{-\zeta}(e^\zeta - 1)^2(2e^\zeta + 1)}{6},$$

$$B_1(\varepsilon, \zeta) = \frac{e^\zeta}{2} - \frac{e^{2\zeta}}{3} - \frac{e^{-\zeta}}{6},$$

$$B_2(\varepsilon, \zeta) = 0, \quad B_3(\varepsilon, \zeta) = 0, \quad B_4(\varepsilon, \zeta) = 0 \dots$$

Then $B(\varepsilon, \zeta) = \varepsilon e^\zeta$. This is the exact solution to Eq. (11), however the HAA provided in [26] does not yield the exact solution. Fig. 4 shows the graphical representation of this solution, where the relative maximum error does not exceed 2×10^{-15} (see Tab.1). This result, achieved after just two iterations, highlights the efficiency of this method and its rapid convergence.

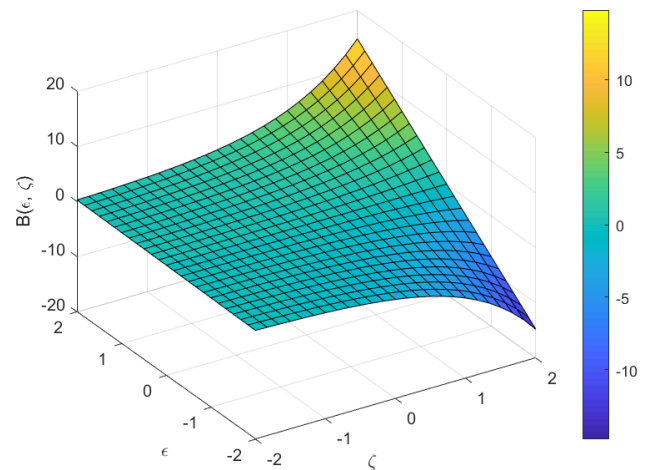


Fig. 4. Graphical representation of the exact solution to example 4 via ETM after only two iterations

Tab. 1. Relative errors concerning example 4

Point	Elzaki relative error
(0,0)	0
(-2,-2)	0
(2,2)	2.4040×10^{-16}
(0.5, 1.8333)	0

(0.5, -1.8333)	1.7360×10^{-15}
(1.5, 1.5)	2.6424×10^{-16}
(-1.5, -1.5)	3.3171×10^{-16}
(1.1667, 0.6667)	1.8535×10^{-16}

Example 5.

Let, $k = 1$, $a = \zeta$, $NB = \frac{-2}{(\varepsilon + \varepsilon^2)^2} B^2$ and $g(\varepsilon, \zeta) = 0$, then Eq. (2) becomes,

$$\frac{\partial^2 B}{\partial \zeta^2} - \zeta \frac{\partial^2 B}{\partial \varepsilon^2} = \frac{-2}{(\varepsilon + \varepsilon^2)^2} B^2, \quad (13)$$

$$B(\varepsilon, 0) = 0, \quad \frac{\partial B(\varepsilon, 0)}{\partial \zeta} = \varepsilon + \varepsilon^2.$$

This is the Cauchy problem for nonlinear wave-like equation with variable coefficients [26].

The method used in Example 1 can be adopted to find the recurrent relationship in the following.

$$B_{n+1}(\varepsilon, \zeta) = E^{-1} \left[\zeta^2 E \left[\zeta \frac{\partial^2 B_n}{\partial \varepsilon^2} - \frac{2}{(\varepsilon + \varepsilon^2)^2} (B_n)^2 \right] \right],$$

$$B_0(\varepsilon, \zeta) = (\varepsilon + \varepsilon^2) \zeta.$$

Then:

$$B_1(\varepsilon, \zeta) = 0, \quad B_2(\varepsilon, \zeta) = 0, \quad B_3(\varepsilon, \zeta) = 0, \dots,$$

therefore $B(\varepsilon, \zeta) = (\varepsilon + \varepsilon^2) \zeta$. Again, this is the exact solution to Eq.(13), while HAA in [26] will not yield the exact solution. Fig. 5 shows the graphical representation of this solution, where the relative error is zero because we found the exact solution using only one step.

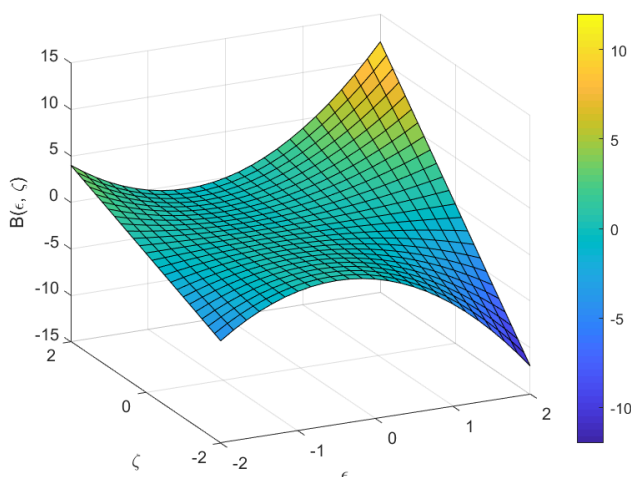


Fig. 5. Graphical representation of the exact solution to example 5 via ETM after only one iteration

5. DISCUSSION AND CONCLUSION

This article has discussed the derivation, convergence, and application of the ET technique to higher-order nonlinear PDEs. Five numerical issues were analyzed: three nonlinear higher-order hyperbolic equations and two nonlinear wave-like equations with variable coefficient types. The ET method produces infinite power series solutions under suitable initial conditions, which nearly invariably spontaneously converge to the exact solution of the DEs. The

obtained outcomes demonstrate the efficacy of the ET technique as mathematical tools for solving higher order nonlinear PDEs.

These problems can be easily solved using the ET approach, as the findings of the nonlinear wave-like equations show, but they cannot be solved exactly with HAA [26]. The ET approach has advantages over MDM, HPM, and HAA due to its efficiency, ease of use, little computational footprint, and proven lightning-fast convergence to an exact solution. Because of its efficiency and ease of use, we also want to extend its application to higher order fractional PDEs in subsequent work. Lastly, we believe that those who work in the modern technology and other areas will find this essay useful. Finally, we think this article will be helpful to people who operate in current technology and other fields. However, Elzaki transform and/or other transforms remain incapable of solving certain differential equations, especially when dealing with unsuitable initial conditions or strongly nonlinear problems.

REFERENCES

- Wu GC. Laplace transform Overcoming Principle Drawbacks in Application of the Variational Iteration Method to Fractional Heat Equations. *Thermal Science*. 2012;16(4):1257-1261. <https://doi.org/10.2298/TSC1204257W>
- Elzaki MT. Application of Projected Differential Transform Method on Nonlinear Partial Differential Equations with Proportional Delay in One Variable, *World Applied Sciences Journal*. 2014;30(3):345-349. 10.5829/idosi.wasj.2014.30.03.1841
- Elzaki MT, Biazar J. Homotopy Perturbation Method and Elzaki Transform for Solving System of Nonlinear Partial Differential Equations, *World Applied Sciences Journal*. 2013;24(4):944-948. 10.5829/idosi.wasj.2013.24.07.1041
- Elzaki MT, Elzaki MS, Elsayed A. Elnour. On the New Integral Transform "Elzaki Transform" Fundamental Properties Investigations and Applications, *Global Journal of Mathematical Sciences: Theory and Practical*. 2012;4(1):1-13. ISSN 0974-3200.
- Elzaki MT, Elzaki MS. On the Connections Between Laplace and Elzaki Transforms, *Advances in Theoretical and Applied Mathematics*. 2011;6(1):1-10. ISSN 0973-4554.
- Elzaki MT, Hilal EMA. Solution of Telegraph Equation by Modified of Double Sumudu Transform "Elzaki Transform". *Mathematical Theory and Modeling*. 2012;2(4):95-103. ISSN 2224-5804.
- Elzaki MT. Double Laplace Variational Iteration Method for Solution of Nonlinear Convolution Partial Differential Equations. *Archives Des Sciences*. 2012;65(12):588-593.
- Ahmed SA, Elzaki MT, Mohamed. A. Solving Partial Differential Equations of Fractional Order by Using a Novel Double Integral Transform. *Mathematical Problems in Engineering*. ID 9971083, 2023;12 pages. <https://doi.org/10.1155/2023/9971083>
- Elzaki MT, Chamekh M, Ahmed SA. Convergence and application of a modified double Laplace transform (MDLT) in some equations of mathematical physics. *Advances in Differential Equations and Control Processes*. 2023;30(2):151-168. <http://dx.doi.org/10.17654/0974324323010>
- Biazar J, Eslami M. A new technique for non-linear two-dimensional wave equations. *Scientia Iranica. Transactions B: Mechanical Engineering*. 2013;20(2):359-363. <https://doi.org/10.1016/j.scient.2013.02.012>
- Elzaki MT, Ishag AA. Modified Laplace Transform and Ordinary Differential Equations with Variable Coefficients. *World Engineering & Applied Sciences Journal*. 2019;10(3):79-84. 10.5829/idosi.weasj.2019.79.84
- He JH. A coupling method of homotopy technique and perturbation technique for nonlinear problems. *International Journal of Non-Linear Mechanics*. 2000;35(1):37-43.

- [https://doi.org/10.1016/S0020-7462\(98\)00085-7](https://doi.org/10.1016/S0020-7462(98)00085-7)
13. Mohamed M, Amjad H, Elzaki MT, Mohamed A, Shiraz. E. Solution of Fractional Heat-Like and Fractional Wave-Like Equation by Using Modern Strategy. *Acta Mechanica et Automatica*. 2023;17(3):372-380. <https://doi.org/10.2478/ama-2023-0042>
 14. Elzaki MT, Chamekh M, Ahmed SA. Modified integral transform for solving benney-luke and singular pseudo-hyperbolic equations. *Acta Mechanica et Automatica*. 2024;18(1). <https://doi.org/10.2478/ama-2024-0018>
 15. Chamekh M, Latrach MA, Elzaki MT. Approximate analytical solutions for some obstacle problems. *Journal of King Saud University – Science*. 2021;33(2). <https://doi.org/10.1016/j.jksus.2020.101259>
 16. Chamekh M, Latrach MA, Abed Y. Multi-step Adomian decomposition method for solving a delayed Chikungunya virus system. *Journal of Mathematics and Computer Science*. 2025;37(4):361–372. <https://doi.org/10.22436/jmcs.037.04.01>
 17. Chamekh M, Latrach MA, Jday F. Multi-step semi-analytical solutions for a chikungunya virus system. *J.Umm Al-Qura Univ. Appl. Sci*. 2023;9:123–131. <https://doi.org/10.1007/s43994-023-00027-8>
 18. Abdulazeez TS, Modanli M, Muhamad Husien A. Numerical scheme methods for solving nonlinear pseudo hyperbolic partial differential equations. *Journal of Applied Mathematics and Computational Mechanics*. 2022;21(4):5-15. <https://doi.org/10.17512/jamcm.2022.4.01>
 19. Abdulazeez TS, Modanli M, Husien MA. Solutions to nonlinear pseudo hyperbolic partial differential equations with nonlocal conditions by using residual power series method. *Sigma J. Eng. Nat. Sci*. 2023;41(3):488–492. <https://doi.org/10.14744/sigma.2023.00055>
 20. Abdulazeez TS, Modanli M. Solutions of fractional order pseudo-hyperbolic telegraph partial differential equations using finite difference method. *Alexandria Engineering Journal*. 2022;61. <https://doi.org/10.1016/j.aej.2022.06.027>
 21. Modanli M, Karadag K, Abdulazeez TS. Solutions of the mobile–immobile advection–dispersion model based on the fractional operators using the Crank–Nicholson difference scheme. *Chaos, Solitons & Fractals*. 2023;167. ISSN0960-0779. <https://doi.org/10.1016/j.chaos.2023.113114>
 22. Abdulla SO, Abdulazeez TS, Modanli M. Comparison of third-order fractional partial differential equation based on the fractional operators using the explicit finite difference method. *Alexandria Engineering Journal*. 2023;70: 37-44. ISSN 1110-0168. <https://doi.org/10.1016/j.aej.2023.02.032>
 23. Ahsana M, Hussainb I, Ahmad M. A finite-difference and Haar wavelets hybrid collocation technique for non-linear inverse Cauchy problems. *Applied Mathematics in Science and Engineering*. 2022;30(1):121–140. <https://doi.org/10.1080/17415977.2022.2026350>
 24. Tenekeci ME, Abdulazeez ST, Karadağ K, Modanli M. Edge detection using the Prewitt operator with fractional order telegraph partial differential equations (PreFOTPDE). *Multimed Tools Appl*. 2024. <https://doi.org/10.1007/s11042-024-19440-0>
 25. <https://doi.org/10.1007/s11042-024-19440-0>
 26. Modanli M, Sadiq Murad MA, Abdulazeez ST. A new computational method-based integral transform for solving time-fractional equation arises in electromagnetic waves. *Zeitschrift für angewandte Mathematik und Physik*. 2023;74(5). <https://doi.org/10.1007/s00033-023-02076-9>
 27. Bougoffa L. The Cauchy problem for nonlinear hyperbolic equations of higher order using modified decomposition method. *Journal of Mathematical Control Science and Applications (JMCSA)*. 2017;1(1):1–9.
 28. Aslanov A. Homotopy perturbation method for solving wave-like nonlinear equations with initial-boundary conditions. *Discrete Dynamics in Nature and Society*. 2011; 10 pages. ID 534165. <https://doi.org/10.1155/2011/534165>
 29. Aslanov A. A homotopy-analysis approach for nonlinear wave-like equations with variable coefficients. In *Abstract and Applied Analysis*. Hindawi; 2015. <http://dx.doi.org/10.1155/2015/628310>
 30. Elzaki MT, Chamekh M, Ahmed SA. Modified Integral Transform for Solving Benney-Luke and Singular Pseudo-Hyperbolic Equations. *Acta Mechanica et Automatica*. 2024;18(1). <http://dx.doi.org/10.2478/ama-2024-0018>
 31. Ahmed SA, Saade R, Qazza A, Elzaki MT. Applying Conformable Double Sumudu – Elzaki Approach to Solve Nonlinear Fractional Problems. *Progr. Fract. Differ. Appl*. 2024;10(2):271-286. <http://dx.doi.org/10.18576/pfda/100208>
 32. Elzaki MT, Mohamed MZ. A novel analytical method for the exact solution of the fractional-order biological population model. *Acta Mechanica et Automatica*. 2024;18(3):564-570. <http://dx.doi.org/10.2478/ama-2024-0059>
 33. Chamekh M, Latrach MA, Elzaki MT. Novel integral transform treating some Ψ -fractional derivative equations. *Acta Mechanica et Automatica*. 2024;18(3). <https://doi.org/10.2478/ama-2024-0060>
 34. Elzaki MT, Ahmed SA. Novel approach for solving fractional partial differential equations using conformable Elzaki Transform. *J.Umm Al-Qura Univ. Appl. Sci*. 2024. <https://doi.org/10.1007/s43994-024-00188-0>

The authors extend their appreciation to the Deputyship for Research & Innovation, Ministry of Education in Saudi Arabia for funding this research work through the project number MoE-IF-UJ-R2-22-04220133-1.

Tarig M. Elzaki:  <https://orcid.org/0000-0002-6946-9267>

Mohamed Ali Latrach:  <https://orcid.org/0000-0001-9274-1014>



This work is licensed under the Creative Commons BY-NC-ND 4.0 license.

NUMERICAL STUDY OF MHD MIXED CONVECTION OF NANOFUID FLOW IN A DOUBLE LID CONVERGENT CAVITY

Bouchmel MLIKI^{1*}, Mokhtar FERHI^{2***}, Mohamed Ammar ABBASSI¹

^{*}Research Lab, Technology Energy and Innovative Materials, Faculty of Sciences, University of Gafsa, Tunisia

^{**}CORIA, Normandie Université, INSA de Rouen, Technopôle du Madrillet, BP 8, Saint-Etienne-du-Rouvray 76801, France

^{***}Research Lab, Modeling, Optimization and Augmented Engineering, ISLAIB, University of Jendouba, Béja 9000, Tunisia

bouchmel.mliki@insa-rouen.fr, mokhtar.ferhi@gmail.com, abbassima@gmail.com

received 19 October 2024, revised 18 March 2025, accepted 24 March 2025

Abstract: This article presents a numerical analysis of mixed convection of a magnetic nanofluid in a double-lid driven convergent cavity. The Lattice Boltzmann Method (LBM) was used to solve the discretized system. The numerical results are illustrated through the flow, temperature, and local entropy generation fields. The study highlights the impact of several parameters, such as the Reynolds number (Re) (ranging from 1 to 100) for a Richardson number (Ri= 20), the Hartmann number (Ha) (ranging from 0 to 80), and the solid volume fraction (ϕ) (ranging from 0 to 0.04). The results show that both the total entropy generation and the average Nusselt number increases with the Reynolds number but decrease with increasing Hartmann number. Moreover, the numerical results show a significant increase in both the average Nusselt number and the total entropy generation with increasing nanoparticle volume fraction and Rayleigh number. Conversely, the Hartmann number exhibits an opposing effect, reducing both heat transfer and total entropy generation, with reductions of 30.18% and 32.15%, respectively, when Ha increases from 0 to 80. The findings of this study have significant applications in optimizing thermal management systems, such as cooling of electronic devices, energy-efficient HVAC systems, and industrial processes involving heat transfer enhancement.

Key words: mixed convection, entropy generation, nanofluid, magnetic field, LBM, convergent cavity

1. INTRODUCTION

In recent years, the mixed convection of magnetic nanofluids in various geometries has garnered increasing attention. Several studies have highlighted the diverse applications of this innovative class of nanofluids, including the works of Nandy and Yanuar [1], Soheli et al. [2], and Heris et al. [3]. Ahmed et al. [4] investigated the mixed convection of micropolar nanoliquids in a double lid-driven cavity. They reported an increase in the Nusselt number (Num) as the volume fraction (ϕ) increases, while it decreases as the length of the heat source increases.

Teamah et al. [5] investigated mixed convection in a square cavity filled with nanofluids. They observed that the mean Nusselt number (Num) increases with Reynolds (Re) and Rayleigh (Ra) numbers, but decreases as the volume fraction (ϕ) increases. In another innovative study, Garoosi et al. [6] numerically examined the mixed convection of nanoliquids. The effects of Re and Ra on heat transfer, fluid movement, and entropy generation in a nanoliquid-filled square cavity were studied by Mirmasoumi and Behzadmehr [7]. They found that Num increases with Re, Ra, and ϕ . Raisi et al. [8] studied the heat transfer by mixed convection of a Cu-water nanofluid in a vertical parallel plate channel. They found that an increase in the solid volume fraction leads to an enhancement in the heat transfer rate, particularly at low Richardson numbers. A numerical simulation of mixed convection in

inclined horizontal tubes with a uniform heat flux, using a nanofluid, was conducted by Akbari et al. [9]. The results showed that the Al₂O₃ concentration had no significant effect on the hydrodynamic parameters, and the heat transfer coefficient was maximal when the inclination angle was 45°.

In the presence of magnetic field effects, a numerical study on mixed convection in different geometries was conducted by Ali et al. [10, 11]. They suggest that the heat transfer rate depends on various physical parameters and geometric configurations. Furthermore, the heat transfer rate decreases with an increase in the magnetic field intensity. In another study, Kefayati [12] conducted a numerical examination of magnetic mixed convection. The analysis indicates that heat transfer decreases as the Hartmann number (Ha) increases. Akram et al. [13] studied MHD mixed convection in a chamfered square enclosure filled with water, analyzing the impact of magnetic field orientation on flow and heat transfer. Their results showed that both the intensity of the magnetic field and the inclination angle significantly influence heat transfer, with Nusselt numbers generally decreasing as the Hartmann number increases. Maya et al. [14] examined a lid-driven cavity with a rectangular heat source under the influence of a magnetic field, highlighting the importance of the Hartmann number in altering flow patterns and heat transfer rates.

Additionally, Mliki et al. [15, 16] studied mixed convection under the influence of the Lorentz force. They observed that in the presence of a magnetic field, the average Nusselt number along

the hot wall shows a significant dependence on several parameters. Specifically, this number increases with the Reynolds number (Re), which is generally associated with higher fluid velocity and flow intensity. On the other hand, the Nusselt number decreases with an increase in the Hartmann number (Ha). These results underscore the complex effect of the magnetic field on the mixed convection process and highlight the need to consider the interaction between these different parameters for more accurate modeling of thermal phenomena in conducting fluids. Also, Mliki et al. [17, 19] used LBM to examine the effect of nanoparticles Brownian motion on fluid movement in different geometries. Prosenjit et al. [20] used a commercial finite element solver "COMSOL Multiphysics 6.0 to examine the MHD mixed convection in a semicircular cavity with hybrid nanofluids. They found that the heat transfer increases with an increase in Ri but decreases with the rise of the Hartmann number (Ha). In another innovative study, Falah et al. [21] investigated the mixed convection phenomenon of a hybrid nanofluid flowing within a horizontally oriented channel, featuring a triangular cavity attached to the lower channel wall. They found that the average Nusselt number increases with higher Reynolds number, angular rotation speed, cylinder position, and Richardson number.

Mliki et al. [22] investigated the influence of a horizontal periodic magnetic field within a double-lid U-shaped enclosure. By comparing scenarios that included and excluded the effect of Brownian motion, they demonstrated that Brownian motion significantly enhances heat transfer under all defined conditions. In a related context, Ighris et al. [23, 24] explored the application of the Lattice Boltzmann Method (LBM) to model natural convection in hybrid nanofluids. Their work emphasized the advantages of this approach, particularly in terms of numerical stability and accuracy. Additionally, Hadoui et al. [30] studied natural double-diffusive convection in a square cavity filled with an Al_2O_3 -water-based nanofluid. Their findings revealed that the heat transfer rate increased with the nanoparticle volume fraction, while the mass transfer rate decreased. Recently, Thilagavathi et al. [25] conducted a study on heat transfer enhancement in a magnetic ternary hybrid nanofluid within a hexagonal cavity containing a square obstacle. The findings of this research demonstrate that the appropriate incorporation of nanoparticles significantly enhances the heat transfer properties of base fluids.

In recent years, magnetohydrodynamic (MHD) mixed convection of nanofluids in porous systems has attracted considerable attention due to its industrial and energy-related applications. For instance, Mandal et al. [26] investigated the MHD mixed convection of a hybrid nanofluid in a W-shaped porous system, emphasizing the influence of geometry and nanofluid properties on thermal and hydrodynamic transfer processes. Their findings demonstrated that thermal energy transfer significantly depends on the length of the heating and cooling surfaces, the fluid volume within the cavity, and the amplitude of the bottom undulation height in the W-shaped cavity. Additionally, Mandal et al. [27] examined the role of surface undulations during mixed bioconvective flow of a nanofluid in the presence of oxytactic bacteria and magnetic fields. Their study revealed that the complex interactions between magnetic forces, bioconvection, and the properties of the porous medium play a critical role in enhancing heat and mass transfer. In addition, Alomari et al. [28] performed a numerical analysis to examine the effect of a porous block on MHD mixed convection in a split lid-driven cavity containing a nanofluid. Their study demonstrated the significant impact of the porous block on thermal and hydrodynamic performance, particularly in complex configurations

such as split lid-driven cavities.

This study distinguishes itself through its innovative numerical analysis of mixed convection in a nanoliquid (CuO/water) within a double-lid driven convergent cavity featuring discrete heating, under the influence of a horizontal magnetic field. Unlike previous studies, this research simultaneously investigates the combined effects of convergent cavity geometry, discrete heating, and a horizontal magnetic field on the thermal and dynamic characteristics of the flow.

2. PROBLEM DEFINITION

We consider the magnetic nanoliquid mixed convection in a heated thermal convergent cavity. The configuration of the physical model is shown in Fig. 1. Two heat sources are situated at the left wall at constant temperature. The aspect ratio of the enclosure is defined as $AR = L/L = 0.3$. As visible from the graphical view, the superior and bottom walls of the cavity are cold and moving with a constant velocity (\vec{u}_0). The effect of periodic magnetic field (\vec{B}) is depicted in this figure. The thermal convergent is filled with CuO-Water Nanofluid (Tab. 1).

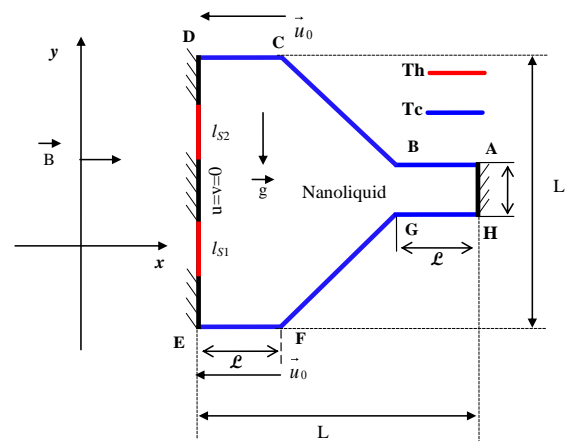


Fig. 1. Geometry of the problem

Tab. 1. Thermophysical properties of fluid and nanoparticles

Physical Properties	Fluid phase (H ₂ O)	Nanoparticle (CuO)
C_p (J/kg.K)	4179	385
ρ (kg/m ³)	997.1	8933
k (W/m.K)	0.631	401
$\beta \times 10^{-5}$ (1/K)	21	1.67
σ (Ω/m)-1	0.05	5.69 10 ⁻⁷

3. MATHEMATICAL FORMULATION

To investigate the mixed convection flow, certain assumptions are made to simplify the analysis.

3.1. Key Assumptions in the Study

Steady-State Flow: The study assumes that the flow is steady, meaning that the fluid properties (velocity, pressure, temperature, etc.) do not change with time.

Incompressible Flow: The fluid is assumed to be incompressible, implying that the density remains constant throughout the flow field. This assumption is valid for liquids and for gases at low Mach numbers (typically < 0.3).

Laminar Flow: The flow is assumed to be laminar, meaning that the fluid moves in smooth layers or streams without significant mixing. This assumption is reasonable for flows with low Reynolds numbers.

Negligible viscous dissipation: The study assumes that the energy generated by viscous dissipation is negligible. This means that the heat produced by internal friction within the fluid is insignificant compared to the other energy terms in the system.

Negligible Heat Generation: The study assumes that there is no significant heat generation within the fluid, either from chemical reactions, electrical heating, or other sources. This simplifies the energy equation by removing the heat generation term.

Constant Fluid Properties: The fluid properties such as viscosity, thermal conductivity, and specific heat are assumed to be constant. This assumption is valid for small temperature variations within the flow.

No Radiation Heat Transfer: The study assumes that heat transfer due to radiation is negligible compared to conduction and convection. This is reasonable for many engineering applications where temperatures are not extremely high.

3.2. Governing equations

By applying the Boussinesq approximation, the governing equations for this investigation are as follows [29]:

$$\frac{\partial u}{\partial x} + \frac{\partial v}{\partial y} = 0 \quad (1)$$

$$\rho_{nf} \left(u \frac{\partial u}{\partial x} + v \frac{\partial u}{\partial y} \right) = -\frac{\partial p}{\partial x} + \mu_{nf} \left(\frac{\partial^2 u}{\partial x^2} + \frac{\partial^2 u}{\partial y^2} \right) + F_x + f_{Lx} \quad (2)$$

$$\rho_{nf} \left(u \frac{\partial v}{\partial x} + v \frac{\partial v}{\partial y} \right) = -\frac{\partial p}{\partial y} + \mu_{nf} \left(\frac{\partial^2 v}{\partial x^2} + \frac{\partial^2 v}{\partial y^2} \right) + F_y + f_{Ly} \quad (3)$$

$$u \frac{\partial T}{\partial x} + v \frac{\partial T}{\partial y} = \alpha_{nf} \left(\frac{\partial^2 T}{\partial x^2} + \frac{\partial^2 T}{\partial y^2} \right) \quad (4)$$

For this problem, the fluid flow is subjected to gravitational force:

$$F_x = 0, \quad F_y = (\rho\beta)_{nf} g_y (T - T_c) \quad (5)$$

In addition to the gravitational force, the flow of the nanohybrid is subjected to the volumetric Laplace force:

$$f_{Lx} = 0, \quad f_{Ly} = -B^2 \cdot \sigma_{nf} v \quad (6)$$

To calculate this volumetric Laplace force, it is more appropriate to use the dimensionless Hartmann number, defined by:

$$Ha = LB \sqrt{\frac{\sigma_{nf}}{\mu_{nf}}} \quad (7)$$

This number is used in fluid dynamics, particularly in the study of conducting fluids in the presence of a magnetic field. It characterizes the influence of magnetic forces in relation to viscous forces within a fluid.

Where σ_{nf} is the electrical conductivity, B is the magnetic field intensity, L is the characteristic length of the cavity, and μ_{nf} is the dynamic viscosity of the nanofluid.

For Magneto-Hydro-Dynamic (MHD) nanoliquid mixed con-

vection flow, the expression for local entropy generation, S_{gen} , can be formulated as follows [30]:

$$S_{gen} = \frac{k_{nf}}{T_0^2} \left[\left(\frac{\partial T}{\partial x} \right)^2 + \left(\frac{\partial T}{\partial y} \right)^2 \right] + \frac{\mu_{nf}}{T_0} \left[2 \left(\frac{\partial u}{\partial x} \right)^2 + 2 \left(\frac{\partial v}{\partial y} \right)^2 + \left(\frac{\partial u}{\partial y} + \frac{\partial v}{\partial x} \right)^2 \right] + \frac{\sigma_{nf} B^2}{T_0} v^2 = S_{gen,h} + S_{gen,v} + S_{gen,m} \quad (8)$$

The effective density, heat capacitance, thermal expansion coefficient, thermal diffusivity, and electrical conductivity of the nanoliquid are defined as follows [31]:

$$\rho_{nf} = (1 - \phi) \rho_f + \phi \rho_p \quad (9)$$

$$(\rho C_p)_{nf} = (1 - \phi) (\rho C_p)_f + \phi (\rho C_p)_p \quad (10)$$

$$(\rho\beta)_{nf} = (1 - \phi) (\rho\beta)_f + \phi (\rho\beta)_p \quad (11)$$

$$\alpha_{nf} = \frac{k_{nf}}{(\rho C_p)_{nf}} \quad (12)$$

$$\frac{\sigma_{nf}}{\sigma_f} = 1 + \frac{3 \left(\frac{\sigma_s}{\sigma_f} - 1 \right) \phi}{\left(\frac{\sigma_s}{\sigma_f} + 2 \right) - \left(\frac{\sigma_s}{\sigma_f} - 1 \right) \phi} \quad (13)$$

The thermal conductivity of the nanoliquid is determined using the following equation [32]:

$$k_{static} = k_f \frac{k_p + 2k_f - 2\phi(k_f - k_p)}{k_p + 2k_f + \phi(k_f - k_p)} \quad (14)$$

The effective dynamic viscosity of the nanofluid is determined using the Brinkman model [33]:

$$\mu_{static} = \frac{\mu_f}{(1 - \phi)^{2.5}} \quad (15)$$

A numerical investigation of mixed convection was carried out using the following dimensionless variables:

$$X = \frac{x}{L}, \quad Y = \frac{y}{L}, \quad U = \frac{u}{U_0}, \quad V = \frac{v}{U_0}, \quad \theta = \frac{T - T_c}{T_h - T_c}, \quad Pr = \frac{\nu_{nf}}{\alpha_{nf}}, \quad P = \frac{p}{\rho_{nf} U_0^2}, \quad Gr = \frac{g\beta(T_h - T_c)L^3}{\nu_{nf}^2}, \quad Re = \frac{U_0 L}{\nu_{nf}}, \quad Ri = \frac{Gr}{Re^2}, \quad Ha = LB \sqrt{\frac{\sigma_{nf}}{\mu_{nf}}}, \quad S_T = \frac{T_0^2 L^2}{k_{nf} (T_h - T_c)^2} \quad (16)$$

The Reynolds number (Re) is one of the most important dimensionless parameters in fluid mechanics. It is used to characterize the flow regime of a fluid, whether it is laminar, transitional, or turbulent. It is defined as the ratio of inertial forces to viscous forces in a fluid flow.

By introducing the dimensionless variables mentioned above, the governing equations (1-4) are transformed into their non-dimensional forms, which can be expressed as follows:

$$\frac{\partial U}{\partial X} + \frac{\partial V}{\partial Y} = 0 \quad (17)$$

$$U \frac{\partial U}{\partial X} + V \frac{\partial U}{\partial Y} = -\frac{\partial P}{\partial X} + \frac{1}{Re} \frac{\rho_f}{\rho_{nf}} \frac{1}{(1 - \phi)^{2.5}} \left(\frac{\partial^2 U}{\partial X^2} + \frac{\partial^2 U}{\partial Y^2} \right) \quad (18)$$

$$U \frac{\partial V}{\partial X} + V \frac{\partial V}{\partial Y} = -\frac{\partial P}{\partial Y} + \frac{1}{Re} \frac{\rho_f}{\rho_{nf}} \frac{1}{(1 - \phi)^{2.5}} \left(\frac{\partial^2 V}{\partial X^2} + \frac{\partial^2 V}{\partial Y^2} \right) \quad (19)$$

$$+ Ri \frac{\rho_f}{\rho_{nf}} \left(1 - \phi + \frac{(\rho\beta)_p}{(\rho\beta)_f} \right) \theta - \frac{\rho_f}{\rho_{nf}} \frac{\sigma_{nf}}{\sigma_f} \frac{Ha^2}{Re} V$$

$$U \frac{\partial \theta}{\partial X} + V \frac{\partial \theta}{\partial Y} = \frac{\alpha_{nf}}{\alpha_f} \frac{1}{Re Pr} \left(\frac{\partial^2 \theta}{\partial X^2} + \frac{\partial^2 \theta}{\partial Y^2} \right) \quad (20)$$

Dimensionless entropy generation S_{gen} can be obtained as:

$$S_T = \frac{k_{nf}}{k_f} \left[\left(\frac{\partial \theta}{\partial X} \right)^2 + \left(\frac{\partial \theta}{\partial Y} \right)^2 \right] + \chi \frac{\mu_{nf}}{\mu_f} \left[2 \left(\frac{\partial U}{\partial X} \right)^2 + 2 \left(\frac{\partial V}{\partial Y} \right)^2 + \left(\frac{\partial U}{\partial Y} + \frac{\partial V}{\partial X} \right)^2 \right] - \chi_{nf} Ha^2 \frac{\sigma_{nf}}{\sigma_f} V^2 \quad (21)$$

where χ is the irreversibility factor. It is defined by:

$$\chi_{nf} = \frac{\mu_f T_0}{k_f} \left(\frac{U_0}{T_h - T_c} \right)^2 \quad (22)$$

The average entropy generation is calculated by:

$$S_{avr} = \frac{1}{V} \int_V S_T dV \quad (23)$$

where V is the total volume of the physical domain.

The local and average Nusselt numbers along the two heat sources (IS1, IS2) can be calculated using the following expressions:

$$Nu = - \frac{k_{nf}}{k_f} \left(\frac{\partial \theta}{\partial X} \right) \Big|_{X=0} \quad (24)$$

$$\overline{Nu}_{IS1} = \int_{0.2}^{0.4} Nu dY, \quad (25)$$

$$Nu_{IS2} = \int_{0.6}^{0.8} Nu dY$$

4. NUMERICAL METHOD AND VALIDATION

The given equations have been numerically solved using the lattice Boltzmann method (LBM), as detailed in Mliki et al. [31]. This approach was based on Ludwig Boltzmann's kinetic theory of gases. Employing the Bhatnagar-Gross-Krook approximation, the lattice Boltzmann method involves two distribution functions, denoted as g and f , representing the temperature and the flow field, respectively, Eqs. (26) and (27):

$$f_i(\mathbf{x} + \mathbf{c}_i \Delta t, t + \Delta t) = f_i(\mathbf{x}, t) - \frac{1}{\tau_v} \left(f_i(\mathbf{x}, t) - f_i^{eq}(\mathbf{x}, t) \right) + \Delta t \mathbf{c}_i F_i \quad (26)$$

$$g_i(\mathbf{x} + \mathbf{c}_i \Delta t, t + \Delta t) = g_i(\mathbf{x}, t) - \frac{1}{\tau_\alpha} \left(g_i(\mathbf{x}, t) - g_i^{eq}(\mathbf{x}, t) \right) \quad (27)$$

Here, Δt represents the lattice time, and τ_v and τ_α denote the lattice relaxation times for the flow and temperature fields, respectively.

Two local equilibrium distribution functions for the temperature and flow fields g_i^{eq} and f_i^{eq} are calculated with Eqs. (28) and (29):

$$f_i^{eq} = \omega_i \rho \left[1 + \frac{3(\mathbf{c}_i \cdot \mathbf{u})}{c^2} + \frac{9(\mathbf{c}_i \cdot \mathbf{u})^2}{2c^4} - \frac{3u^2}{2c^2} \right] \quad (28)$$

$$g_i^{eq} = \omega'_i T \left[1 + 3 \frac{\mathbf{c}_i \cdot \mathbf{u}}{c^2} \right] \quad (29)$$

The variables u and \mathbf{p} represent the macroscopic velocity and

density, respectively. The lattice speed c is defined as $c = \Delta x / \Delta t$, where Δx is the lattice spacing and Δt is the lattice time step, both of which are set to unity. Furthermore, ω_i denotes the weighting factor for the flow field, while ω'_i represents the weighting factor for the temperature field. The D2Q9 model is used for the flow field, while the D2Q4 model is applied to the temperature field.

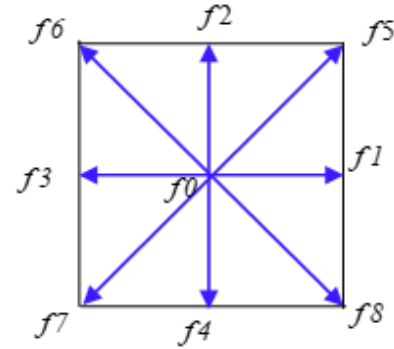


Fig. 2. Direction of streaming velocities, D2Q9

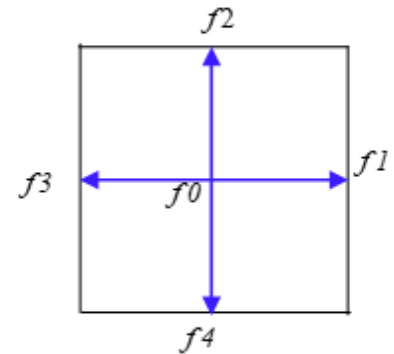


Fig. 3. Direction of streaming velocities, D2Q4

Consequently, the weighting factors and discrete particle velocity vectors differ between these two models and are calculated using Eqs. (30-33) as follows:

For D2Q9:

$$\omega_0 = \frac{4}{9}, \omega_i = \frac{1}{9} \text{ for } i = 1, 2, 3, 4 \text{ and } \omega_i = \frac{1}{36} \text{ for } i = 5, 6, 7, 8 \quad (30)$$

The discrete velocities for the D2Q9 (Fig. 2) are defined as follows:

$$\mathbf{c}_i = \begin{cases} 0 & i = 0 \\ (\cos[(i-1)\pi/2], \sin[(i-1)\pi/2])c & i = 1, 2, 3, 4 \\ \sqrt{2}(\cos[(i-5)\pi/2 + \pi/4], \sin[(i-5)\pi/2 + \pi/4])c & i = 5, 6, 7, 8 \end{cases} \quad (31)$$

For D2Q4:

The weighting factor for temperature in each direction is:

$$\omega'_i = \frac{1}{4} \quad (32)$$

The discrete velocities for the D2Q4 (Fig. 3) are defined as follows:

$$\mathbf{c}_i = (\cos[(i-1)\pi/2], \sin[(i-1)\pi/2])c \quad i = 1, 2, 3, 4 \quad (33)$$

The relationship between the kinematic viscosity ν and ther-

mal diffusivity α with the relaxation time is expressed by Eq. (34):

$$\nu = \left[\tau_v - \frac{1}{2} \right] c_s^2 \Delta t; \quad \alpha = \left[\tau_\alpha - \frac{1}{2} \right] c_s^2 \Delta t \quad (34)$$

Where c_s is the lattice speed of sound, equal to $c_s = c/\sqrt{3}$. In the simulation of natural convection, the external force term F_i is determined by Eq. (35):

$$F_i = \frac{\omega_i}{c_s^2} F \cdot c_i \quad (35)$$

With F_i is the total external body force.

The macroscopic quantities ρ , u , and T can be calculated by Eq. (36):

$$\rho = \sum_i f_i; \quad \rho u = \sum_i f_i c_i; \quad T = \sum_i g_i \quad (36)$$

5. SOLUTION METHOD

To ensure the applicability of the code in a nearly incompressible regime, the characteristic velocity must be significantly lower than the speed of sound in the fluid. Therefore, in the simulations, the Mach number is set to less than $Ma=0.3$. In this study, the Mach number is fixed at $Ma=0.1$ for all considered cases. Viscosity and thermal diffusivity are determined based on the definitions of the corresponding dimensionless parameters, while maintaining constant values for the Rayleigh number, Prandtl number, and Mach number.

$$\nu_f = NMac_s \sqrt{\frac{Pr}{Ra}} \quad (37)$$

With N indicating the total number of lattices positioned in the y -direction.

The stream function and vorticity are defined as:

$$\frac{\partial^2 \psi}{\partial x^2} + \frac{\partial^2 \psi}{\partial y^2} = -\left(\frac{\partial v}{\partial x} - \frac{\partial u}{\partial y} \right) = -\omega \quad (38)$$

where ω and ψ are vorticity and stream function, respectively.

6. MESH VERIFICATION AND VALIDATION

For the grid sensitivity analysis, Tab. 2 presents the results obtained using four different mesh sizes. The simulations revealed that the difference in results between the grid sizes of 100×100 and 150×150 was minimal. Based on these findings, the grid size of 100×100 was selected for the analysis.

Tab 2. Grid independence test for \overline{Nu}_m at $\phi=4.10^{-2}$; $Ha=0$

Lattice size	Average Nusselt number \overline{Nu}_m	
	Re=1	Re=100
50x50	1.7632	7.3423
75x75	2.1482	8.8753
100x100	2.5483	9.6128
120x120	2.5502 (0.07%)	9.6412 (0.2%)

For data validation, the present results are compared with the numerical results from Lai and Yang [34] for the case of nanoliquid natural convection in a square enclosure (Fig. 4).

Additionally, the temperature distribution along the axial mid-

line is compared between the present results and those obtained by Ghassemi et al. [35] for magnetic nanoliquid mixed convection in a square enclosure (Fig. 5). Another validation test is performed for the case of mixed convection (Fig. 6), where the current numerical results are compared with the results from Talebi et al. [36]. Based on these comparisons, the developed code is demonstrated to be reliable for studying MHD mixed convection of a nanoliquid in a double-lid driven thermally convergent cavity.

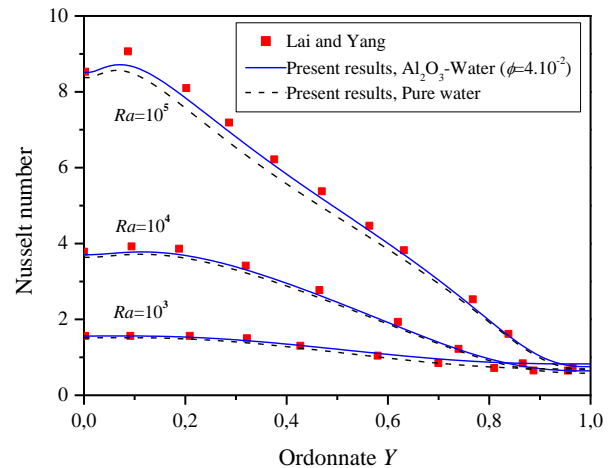


Fig. 4. Comparison of the local Nusselt number along the hot wall between the present results and numerical results by Lai and Yang [34]

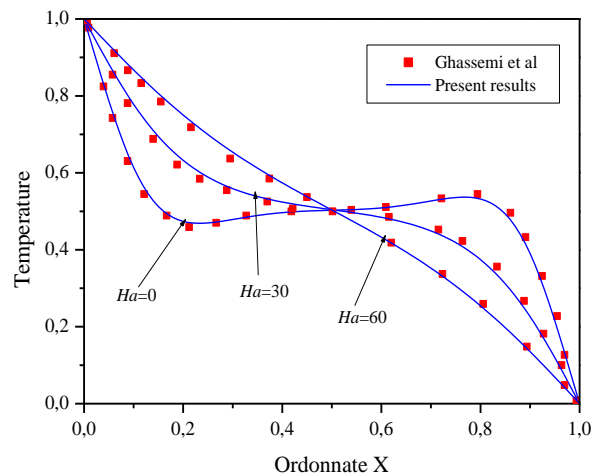
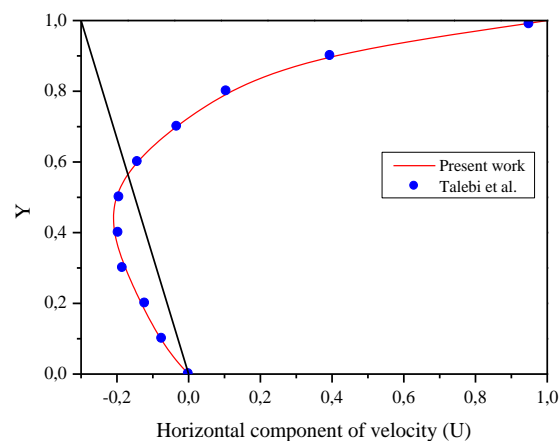
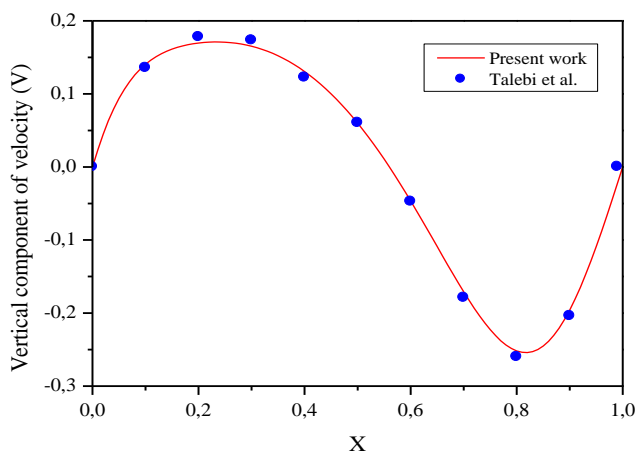


Fig. 5. Comparison of the temperature on axial midline between the present results and numerical results by Ghassemi et al. [35] ($\phi=3.10^{-2}$, $Ra=10^5$)



(a)



(b)
Fig. 6. a) Horizontal component of velocity b) vertical component of velocity with those of Talebi et al. [36]

7. RESULTS AND DISCUSSION

A numerical analysis of two-dimensional magnetohydrodynamic (MHD) mixed convection is conducted for a CuO–water nanofluid within a double lid-driven thermally convergent cavity. The study investigates the fluid flow and heat transfer characteristics under the influence of magnetic fields, focusing on the behavior of the nanofluid in this specific configuration.

7.1. Effects of Reynolds number

The main objective of this numerical study is to evaluate the effects of the Reynolds number (Re) on isotherms, local entropy generation, and streamlines inside the cavity saturated with CuO–water nanofluid, for $Ri = 20$, $\phi = 4 \cdot 10^{-2}$, and $Ha = 0$. For $Re = 1$, the flow, local entropy generation, and temperature contours are nearly symmetric about the horizontal centerline ($Y = 0.5$) of the cavity and are concentrated along the two heated sources (IS1 and IS2) due to the enhanced fluid movement in these regions. In this case, the flow is characterized by the presence of two symmetric counterclockwise vortices, rotating in opposite directions with intensities ($|\psi|_{max} = 7.16 \times 10^{-2}$ and 6.91×10^{-2}), respectively (Fig. 7). As the Reynolds number increases, the influence of the moving walls (CD and EF) becomes increasingly significant, leading to substantial changes in the flow dynamics within the cavity. These walls, moving relative to the fluid, introduce a forced convection component that enhances fluid circulation in the surrounding regions. This effect is especially prominent in the lower part of the cavity, where the largest circulation cell develops.

In this figure, at low Reynolds numbers ($Re = 1$), heat transfer within the cavity is primarily dominated by conduction, with isotherms appearing nearly parallel to the isothermal walls. As the Reynolds number increases ($Re = 10, 50$, and 100), the cold nanofluid penetrates deeper into the corners (D and E), intensifying the temperature gradients around the discrete heat sources (IS1 and IS2). Additionally, enhanced circulation of the nanofluid is observed on the left side of the cavity (zone ABGH), resulting in a more efficient heat transfer process. The effect of increasing the Reynolds number on entropy generation is also illustrated in Fig. 7. It is observed that an increase in the Reynolds number enhances fluid motion, resulting in a higher concentration of entropy genera-

tion contours near the discrete heat sources. This leads to the formation of active regions of entropy generation, which are particularly pronounced at higher Reynolds numbers ($Re = 10, 50$, and 100).

In summary, an increase in the Reynolds number significantly modifies the distribution and intensity of entropy generation within the cavity. These changes are primarily driven by the intensification of forced convection, which enhances temperature and velocity gradients, leading to the formation of active entropy generation zones near the heat sources and in regions of increased fluid circulation. These findings underscore the importance of accounting for the effects of the Reynolds number in the design and optimization of heat transfer systems that utilize nanofluids.

The effect of solid nanoparticle concentration on the Nusselt number (Num) along the discrete heat sources (IS1 and IS2) is illustrated in Fig. 8. A detailed analysis of Equation (14) shows that increasing the concentration of solid nanoparticles in the nanofluid directly enhances its effective thermal conductivity. This enhancement is critical, as it improves heat transfer through the fluid, particularly in the regions near the heat sources where the heat transfer intensity is highest. As a result, the fluid becomes more effective in transferring heat, leading to an increase in the Nusselt number. In Fig. 9, the total entropy generation (S_{gen}) exhibits a trend similar to that of the Nusselt number (Num). This correlation can be explained by the fact that the enhancement of heat transfer, driven by the increase in nanoparticle concentration, is accompanied with an increase in thermodynamic irreversibilities, as measured by entropy generation.

Figs 10 and 11 illustrate the temperature profile within the cavity at two specific positions: $x/L = 0.5$ and $y/L = 0.75$, for different Reynolds numbers (Re). These graphs provide a detailed analysis of how temperature evolves within the cavity as Re changes. It is clearly observed that the temperature in the ABGH region of the cavity increases with higher Re . This trend can be attributed to the increasing influence of mixed convection heat transfer, which becomes more dominant as Re rises. At low Reynolds numbers, heat transfer is mainly governed by thermal conduction, a slower and less efficient mechanism for heat transfer. However, as Re increases, mixed convection enhances heat transfer, leading to a more significant temperature rise in regions close to the heated walls of the cavity, particularly in the ABGH area. This behavior underscores the importance of fluid velocity and the convection regime in optimizing heat transfer within confined systems such as the one studied. These findings highlight the critical role of Reynolds number in controlling heat transfer dynamics and suggest that optimizing fluid flow conditions can significantly improve the efficiency and reliability of thermal management systems in practical applications.

7.2. Effects of Hartmann number

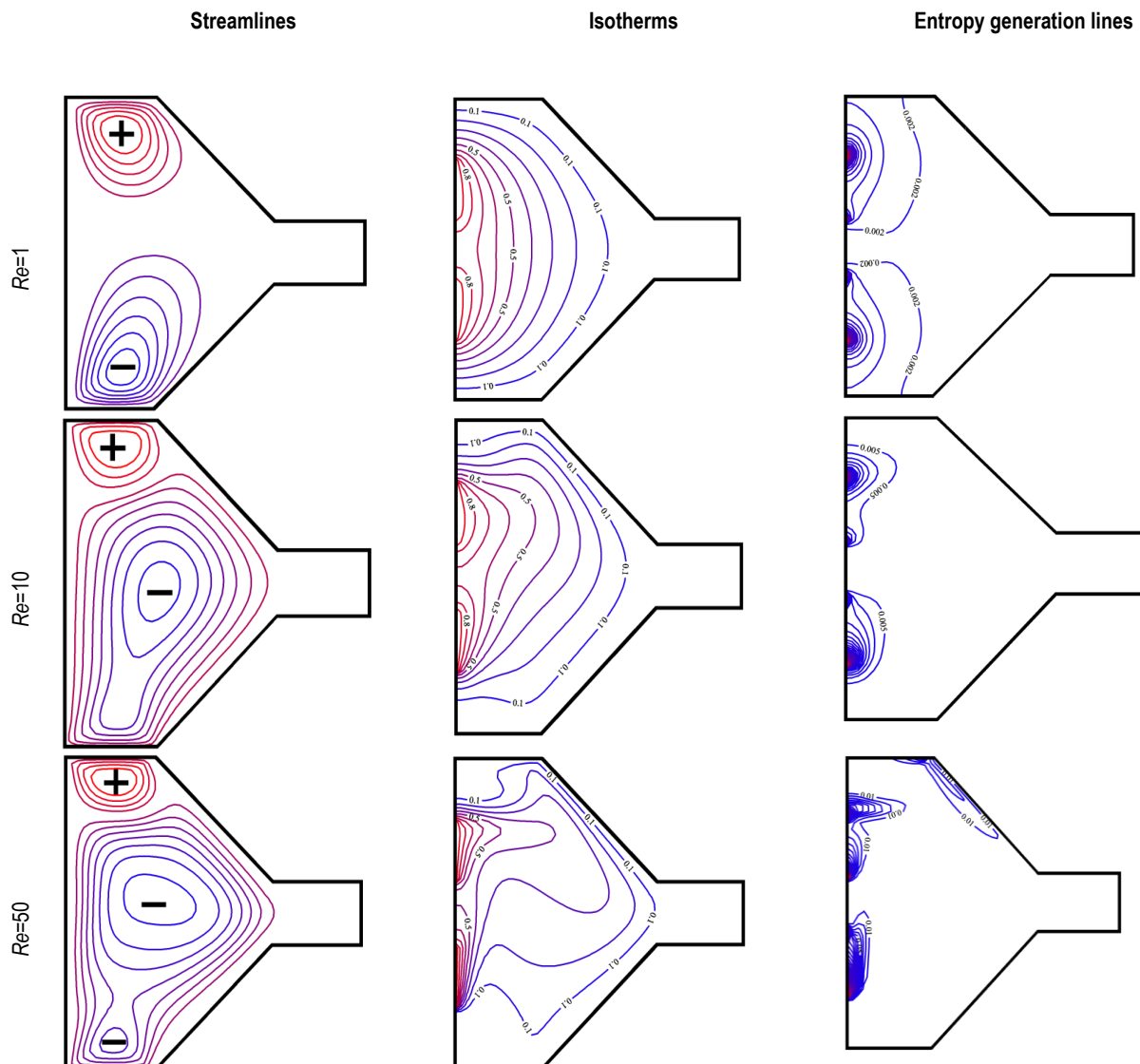
The effects of the Hartmann number (Ha) on the streamlines and entropy generation contours for $Re = 100$, $Ri = 20$, and $\phi = 4 \cdot 10^{-2}$ are shown in Fig. 12. The presence of a magnetic field leads to a significant reduction in mixed convection, resulting in an unfavorable impact on heat transfer. While buoyancy enhances heat transfer, the Lorentz force induced by the magnetic field counteracts this effect, reducing thermal transfer efficiency and minimizing entropy generation, making the process less favorable for optimizing heat transfer. As observed, an increase in the Hartmann number results in a reduction in flow intensity, with the

minimum value occurring at the highest Hartmann number. The maximum value of the stream function is 3.68×10^{-1} for $Ha = 0$, 2.94×10^{-1} for $Ha = 20$, and 1.5×10^{-1} for $Ha = 80$, which explains the stagnation of the stream function at $Ha = 80$. This flow stagnation at high Hartmann numbers has significant implications for heat transfer dynamics. Specifically, the reduction in mixed convection results in a greater dominance of thermal conduction. As a consequence, while entropy generation is reduced due to the decrease in irreversibilities associated with fluid motion, the overall heat transfer efficiency is diminished.

Fig. 13. illustrates the effect of the Lorentz force on the variation of the average Nusselt number and total entropy generation for different Hartmann numbers ($Ha = 0, 20, 40, 60$ and 80) at a solid particle concentration of $\phi = 0.04$. It can generally be observed that the average Nusselt number decreases as the Hartmann number (Ha) increases. This decrease is primarily attributed to the inhibitory effect of the Lorentz force, which opposes fluid motion and reduces the intensity of mixed convection. In the absence of a magnetic field ($Ha = 0$), the average Nusselt number reaches its maximum value, reflecting optimal mixed convection and efficient heat transfer. However, as Ha increases, the Lorentz force becomes more dominant, slowing

down the flow and thereby reducing the contribution of convection to heat transfer. Consequently, heat transfer becomes increasingly dominated by conduction, a less efficient mechanism compared to convection. The variation in entropy generation follows a trend similar to that of the Nusselt number. At low Hartmann numbers ($Ha = 0$), entropy generation is relatively high due to the irreversibilities associated with intense fluid motion and pronounced temperature gradients. However, as Ha increases, the reduction in flow intensity decreases these irreversibilities, leading to a gradual decline in entropy generation.

Figs. 14 and 15 show the temperature profile within the cavity at two specific positions: $x/L = 0.5$ and $y/L = 0.75$, for different Hartmann numbers (Ha). These graphs provide a detailed analysis of how the temperature evolves within the cavity as Ha changes. It is clearly observed that the temperature in the ABGH region of the cavity decreases as Ha increases. This trend can be attributed to the reduced influence of mixed convection heat transfer, which becomes less significant as Ha increases. At high Hartmann numbers, heat transfer is primarily governed by thermal conduction. This results in a more significant decrease in temperature in the ABGH region.



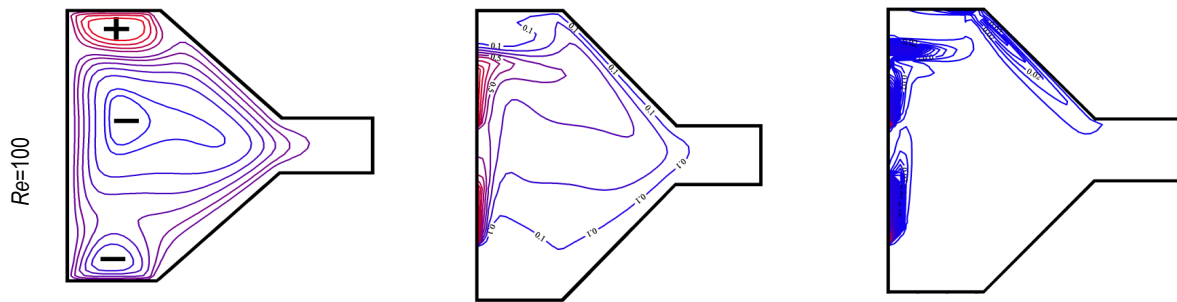


Fig.7. Streamlines, Isotherms and Entropy generation lines for different Re at $Ri=20$, $Ha=0$, and $\phi= 4 \cdot 10^{-2}$

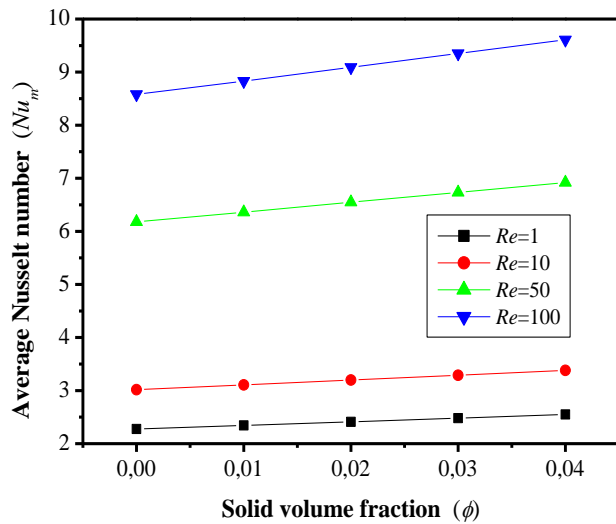


Fig.8. Average Nusselt number for different values of the Reynolds numbers and volumetric fraction of nanoparticles (ϕ) at $Ri=20$, $Re=100$ and $Ha=0$

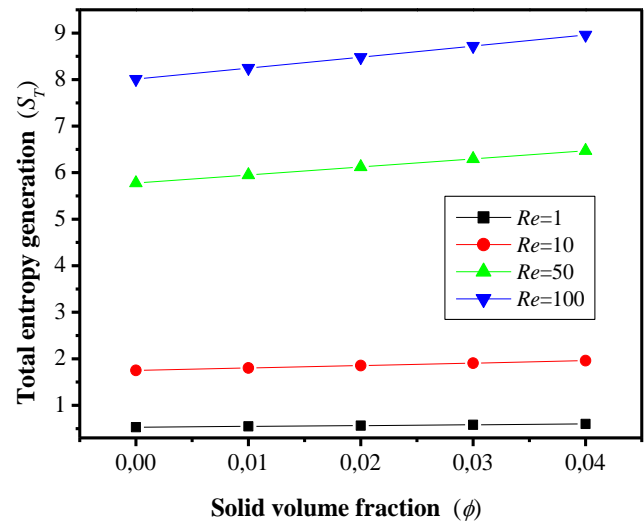


Fig.9. Total entropy generation for different values of the Reynolds numbers and volumetric fraction of nanoparticles (ϕ) at $Ri=20$, $Re=100$ and $Ha=0$

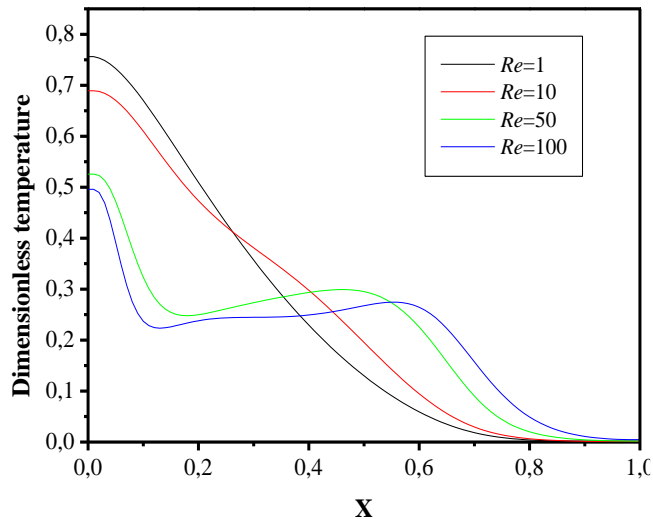


Fig.10. Profiles of the dimensionless temperature in the middle of the thermally convergent cavity $y/L = 0.5$ for different Reynolds numbers at $Ri=20$, $Ha=0$ and $\phi= 4 \cdot 10^{-2}$

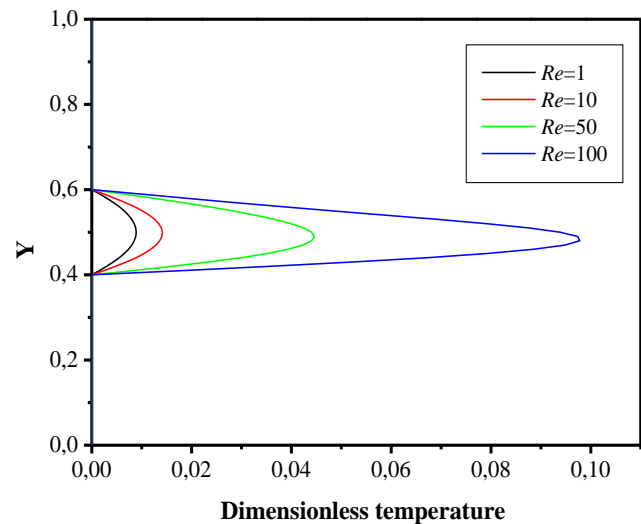


Fig.11. Profiles of the dimensionless temperature in the middle of the thermally convergent cavity $x/L = 0.75$ for different Reynolds numbers at $Ri=20$, $Ha=0$ and $\phi= 4 \cdot 10^{-2}$

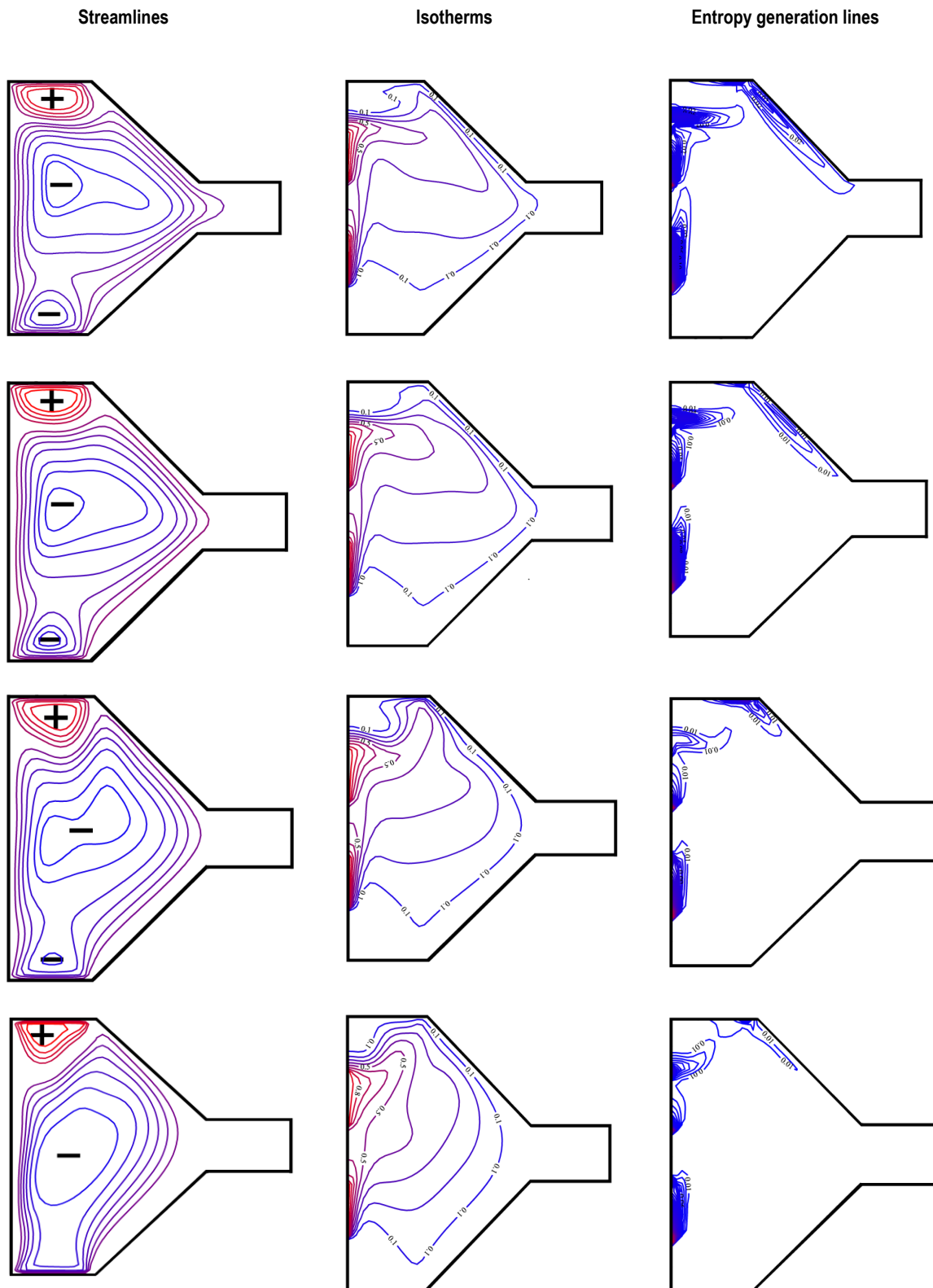


Fig. 12. Streamlines, Isotherms and Entropy generation lines for different Ha at $Re=100$, $Ri=20$ and $\phi=4.10^{-2}$

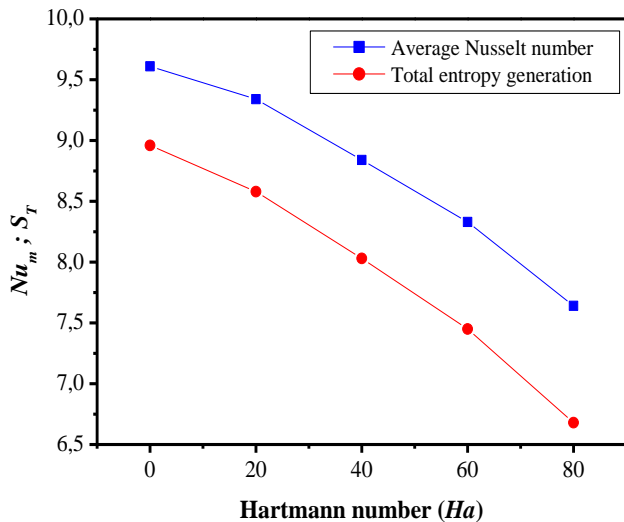


Fig. 13. Effect of Hartmann number on average Nusselt number and on total entropy generation for different Hartmann numbers at $Ri = 20$, $Re = 100$ and $\phi = 4.10^{-2}$

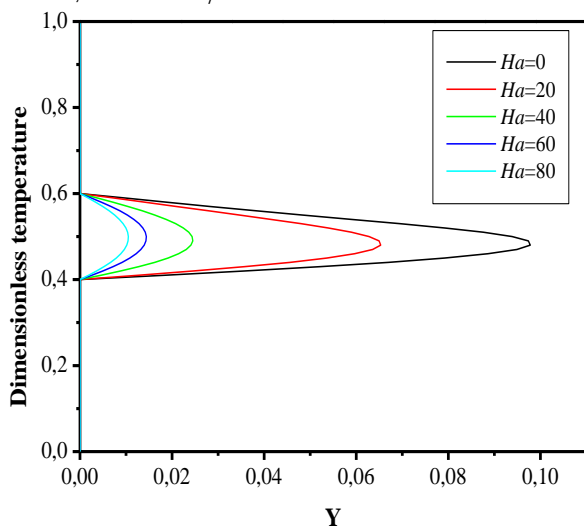


Fig.14. Profiles of the dimensionless temperature in the middle of the thermally convergent cavity $x/L = 0.75$ for different Hartmann numbers at $Ri = 20$, $Re = 100$ and $\phi = 4.10^{-2}$

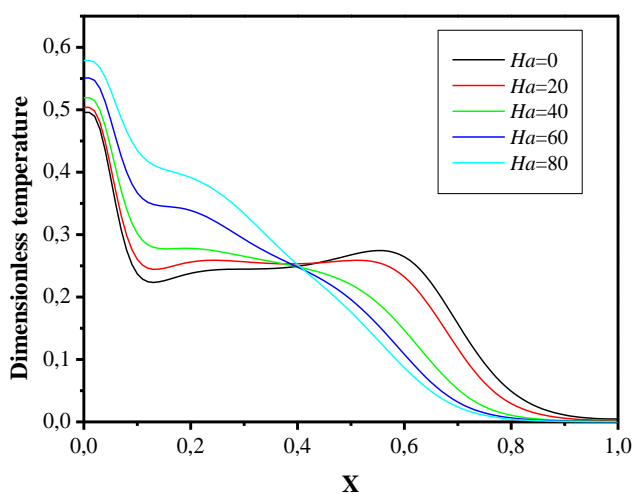


Fig. 15. Profiles of the dimensionless temperature in the middle of the thermally convergent cavity $y/L = 0.5$ for different Hartmann numbers at $Ri = 20$, $Re = 100$ and $\phi = 4.10^{-2}$

8. CONCLUSION

This study introduces an innovative approach to investigate mixed convection heat transfer by analyzing the influence of a magnetic field on heat transfer and flow characteristics in a convergent double-lid-driven cavity with discrete heating. The effects of the Reynolds number (Re), Hartmann number (Ha), and nanoparticle volume fraction (ϕ) on flow dynamics and heat transfer performance were systematically examined. The primary conclusions derived from the numerical results are as follows:

- For all considered values of Re and Ha , increasing the nanoparticle volume fraction leads to an increase in the average Nusselt number and total entropy generation.
- As the Reynolds number (Re) the values of the Nusselt number (Num) also increase.
- The maximum value of the stream function ($|\psi|_{max}$) is achieved at $Re = 100$.
- When a magnetic field is applied, the velocity of the nanoliquid decreases, which in turn leads to a reduction in the maximum value of $|\psi|_{max}$.
- Both the Nusselt number (Num) and entropy generation are inversely related to the Hartmann number (Ha).
- The temperature in convergent cavity increases with an increase in Re , whereas the opposite effect is observed when Ha increases.
- The influence of Ha on Num and entropy generation is more pronounced at higher Reynolds numbers ($Re = 50$ and 100).


Based on the results presented in this article, it is recommended to use a combination of $Re = 100$, $Ha = 0$ (absence of a magnetic field), and $\phi = 0.04$ to maximize heat transfer. However, if entropy generation must be minimized, a compromise with $Ha = 80$ is suggested. This higher Hartmann number value will improve flow control and reduce entropy generation while maintaining acceptable heat transfer performance. This approach is particularly beneficial in applications where energy efficiency and loss minimization are top priorities.

REFERENCES

1. Nandy P, Iskandar F N. Application of nanofluid to a heat pipe liquid-block and the thermoelectric cooling of electronic equipment. *Exp Therm Fluid Sci.* 2011; 5:1274–1281.
2. Sohel MR, Saidur R, Mohd S M, Ijam A. Investigating the heat transfer performance and thermophysical properties of nanofluid in a circular micro-channel. *Int Commun Heat Mass Transf.* 2013; 42:75–81.
3. Heris SZ, Esfahany MN, Etemad SG. Experimental investigation of convective heat transfer of AL2O3/H2O nanofluid in circular tube. *Int J Heat Fluid Flow.* 2007; 28:203–10.
4. Ahmed S E, Mansour M A, Hussein, A K and Sivasankaran S. Mixed convection from a discrete heat source. *Engineering Science and Technology, an International Journal*, 2016; 19: 364-376.
5. Teamah MA, Sorour M M, El-Maghlany W M and Afifi A. Numerical simulation of double diffusive laminar mixed convection. *Alexandria Engineering Journal.* 2013; 52: 227-239.
6. Garoosi F, Rohani B, Rashidi MM. Two-phase mixture modeling of mixed convection of nanofluids in a square cavity. *Powder Technology.* (2015), 275: 304–321.
7. Mirmasoumi S, Behzadmehr A. Effect of nanoparticles mean diameter on mixed convection heat transfer of a nanofluid in a horizontal tube. *Int. J. Heat Fluid.* 2008; 29: 557–56.
8. Raisi A, Aminossadati S M and Ghasemi B. Magnetohydrodynamic mixed convection of a cu-water nanofluid in a vertical channel. *Journal of Heat Transfer.* 2013; 135.

9. Akbari M, Behzadmehr A and Shahraki F. Fully developed mixed convection in horizontal and inclined tubes with uniform heat flux using Nanofluid. *International Journal of Heat and Fluid Flow*. 2008; 29: 545-556.
10. Ali MM, Alim MA, Ahmed SS. Oriented magnetic field effect on mixed convective flow of nanofluid in a grooved channel with internal rotating cylindrical heat source. *International Journal of Mechanical Sciences*. 2019; 151: 385-409.
11. Ali MM, Alim MA, Ahmed SS, et al. Magneto hydrodynamic mixed convection flow in a hexagonal enclosure. *Procedia engineering*. 2017;(194):479-486.
12. Kefayati G R. Magnetic field effect on heat and mass transfer of mixed convection of shear-thinning fluids in a lid-driven enclosure with non-uniform boundary conditions. *Journal of the Taiwan Institute of Chemical Engineers*. 2015; 51: 20-33.
13. Akram B, Ullah N, Nadeem S, Eldin SM. Simulations for MHD mixed convection in a partially heated lid-driven chamfered enclosure. *Numer. Heat. Transf. A Appl*. 2023: 1-21.
14. Maya U M, Alam Md N, Refaie Ali A. Influence of magnetic field on MHD mixed convection in lid-driven cavity with heated wavy bottom surface. *Sci. Rep*. 2023;13 (1):18959.
15. Mliki B, Abbassi MA and Ridha D. CUO-water MHD Mixed Convection Analysis and Entropy Generation Minimisation In Double-Lid-Driven U-Shaped Enclosure with Discrete Heating. *Acta Mechanica et Automatica*. 2023; 17(1): 112-123.
16. Mliki B and Abbassi MA. LBM Analysis of Magneto-Hydrodynamic Mixed Convection of Nanofluid in a Double Lid Driven Heated Incinerator Shaped Cavity with Discrete Heating. *Mathematical Modelling of Fluid Dynamics and Nanofluids*. 2023: 264-282
17. Mliki B and Abbassi MA. Simulation of Magnetic Hybrid Nanofluid (Al₂O₃-Cu/ H₂O) Effect on Natural Convection and Entropy Generation in a Square Enclosure with a Hot Obstacle. *Mathematical Modelling of Fluid Dynamics and Nanofluids*. 2023: 511-525
18. Mliki B, Abbassi MA, Omri A and Belkacem Z. Lattice Boltzmann analysis of MHD natural convection of CuO-water nanofluid in inclined C-shaped enclosures under the effect of nanoparticles Brownian motion. *Powder Technology*. 2017; 308: 70-83.
19. Mliki, B., Abbassi, M. A., Omri, A. Lattice Boltzmann Simulation of Magneto-Hydrodynamics Natural Convection in an L-Shaped Enclosure. *International Journal of Heat And Technology*. 2016; 34 (4).
20. Prosenjit D , Mohammad AH. Predicting MHD mixed convection in a semicircular cavity with hybrid nanofluids using AI. *Heliyon*. 2024; 10:38303.
21. Falah A, Zainab K, Ali K, Raad Z, Hayder I. MHD mixed convection of nanofluid flow Ag- Mgo/water in a channel contain a rotational cylinder. *International Journal of Thermofluids*. 2024; 22: 100713.
22. Mliki B, Abbassi, MA. Analysis of Natural Convection Under the Effect of Nanoparticles Brownian Motion and a Periodic Magnetic Field Utilizing CuO-Water Nanofluid. *J. Nanofluids*. 2024; 13:1123-1133.
23. Ighris Y, Qaffou M, Baliti J, Elguennouni Y, Hssikou M, Thermal management optimization of natural convection in a triangular chamber: Role of heating positions and ternary hybrid Nanofluid. *Physics of Fluids*. 2024; 36: 092002.
24. Ighris Y, BouhouchiY, Baliti J, Hssikou M, Boumezzough A. Numerical study of natural convection in an inclined cavity filled with Al₂O₃/Cu-H₂O nanofluids. *Numerical Heat Transfer, Part A: Applications*. 2024: 1-25. <https://doi.org/10.1080/10407782.2024.2314230>
25. Thilagavathi A, Prasad V R. Thermal Heat Transfer Enhancement Analysis of Magnetic Ternary Hybrid Nanofluid in a Hexagonal Cavity with Square Obstacle. *J. Appl. Comput. Mech*. 2025; 11(1): 239-252.
26. Dipak K M, Nirmalendu B, Nirmal K. M, Rama Subba R G, Chamkha Ali J. Hybrid nanofluid magnetohydrodynamic mixed convection in a novel W-shaped porous system. *International Journal of Numerical Methods for Heat & Fluid*. 2022; 33(10).
27. Dipak K M. Nirmalendu B. Nirmal K M, Rama Subba R G, Chamkha Ali J. Role of surface undulation during mixed bioconvective nanofluid flow in porous media in presence of oxytactic bacteria and magnetic fields. *International Journal of Mechanical Sciences*. 2021; 211: 106778.
28. Mohammed A A, Khaled A F, Qusay H. Al-Salami, Ali I R, Biswas N, Mohamed H, Faris A. Numerical analysis to investigate the effect of a porous block on MHD mixed convection in a split lid-driven cavity with Nanofluid. *International Journal of Thermofluids*. 2024; 22: 100621.
29. Aniket H, Arabdha B, Biswas N, Nirmal K Manna, Dipak K M. MHD nanofluidic mixed convection and entropy generation in a butterfly-shaped cavity. *Sādhanā*. 2024; 49:80.
30. Mliki B, Abbassi MA, Omri A. Lattice Boltzmann Simulation of MHD Double Dispersion Natural Convection in a C-shaped Enclosure in the Presence of a Nanofluid. *Fluid Dynamic and Material Processing*. 2015; 11(1): 87-114.
31. Mliki B, Abbassi MA, Omri A and Belkacem Z. Effects of nanoparticles Brownian motion in a linearly/sinusoidally heated cavity with MHD natural convection in the presence of uniform heat generation/absorption. *Powder Technol*. 2016; 295: 69-83.
32. Maxwell J C. A treatise on electricity and magnetism. Oxford University. Press Cambridge. UK. 1873; 2.
33. Bhatnagar PL, Gross EP and Krook M. A model for collision processes in gases, I: small amplitude processes in charged and neutral one-component systems. *Physical Review*. 1954; 94 (3): 511.
34. Lai FH, Yang YT. Lattice Boltzmann simulation of natural convection heat transfer of Al₂O₃/Water nanofluids in a square enclosure. *Int J of Therm Sci*. 2011; 50: 1930-1941.
35. Ghasemi B, Aminossadati SM, Raisi A. Magnetic field effect on natural convection in a nanofluid-filled square enclosure. *Int J Therm Sci*. 2011; 50:1748-1756.
36. Talebi F, Mahmoudi A H and Shahi M. Numerical study of mixed convection flows in a square lid-driven cavity utilizing Nanofluid. *International Communications in Heat and Mass Transfer*. 2010; 37: 79-90.

Bouchmel Mliki  <https://orcid.org/0000-0002-0200-8060>

Mokhtar Ferhi  <https://orcid.org/0000-0002-6677-3335>

Mohamed A. Abbassi  <https://orcid.org/0000-0002-1915-0944>



This work is licensed under the Creative Commons BY-NC-ND 4.0 license.

THE IMPACT OF MULTIFUNCTIONAL POLYSILOXANES ON ENHANCING THE PROPERTIES OF POLYETHYLENE TEREPHTHALATE GLYCOL (PET-G) FOR FDM/FFF 3D-PRINTING

Bogna SZTORCH^{*}, Julia GŁOWACKA^{*/**}, Miłosz FRYDRYCH^{*}, Daria PAKUŁA^{*},
Eliza ROMANČZUK-RUSZUK^{***}, Natalia KUBIAK^{*/**}, Robert E. PRZEKOP^{*}

^{*}Centre for Advanced Technologies, Adam Mickiewicz University in Poznań,
10 Uniwersytetu Poznańskiego, 61-614 Poznań, Poland

^{**}Faculty of Chemistry, Adam Mickiewicz University in Poznań,
8 Uniwersytetu Poznańskiego, 61-614 Poznań, Poland

^{***}Institute of Biomedical Engineering, Faculty of Mechanical Engineering,
Białystok University of Technology, Wiejska 45C Street, 15-351 Białystok, Poland

bogna.sztorch@amu.edu.pl, julia.glowacka@amu.edu.pl, frzydrych@amu.edu.pl, darapak@amu.edu.pl,
e.romanczuk@pb.edu.pl, natalia.kubiak@amu.edu.pl, rprzekop@amu.edu.pl

received 27 December 2023, revised 03 April 2024, accepted 27 November 2024

Abstract: The use of incremental technologies in various biomedical fields requires the development of new materials that can meet the needs of new applications. This article delves into the impact of modifying PETG with multifunctional polysiloxanes (0.10 wt.% to 2.5 wt.%) on the properties of composite materials produced for 3D printing in bioengineering applications. The article covers the effects on strength (tensile, flexural), rheological (MFR), thermal (DSC), and surface (WCA) properties. The results obtained in this study indicate that polysiloxane additives have a positive effect on the material's elasticity and bending strength. Moreover, the results presented are a great example of interdisciplinary research combining chemical knowledge to develop specialized material applications.

Key words: PETG, polysiloxanes, 3D-printing, FDM/FFF, mechanical properties

1. INTRODUCTION

FDM/FFF 3D printing is gaining popularity and becoming more widely available as a tool for professional 3D printing facilities and home applications. It allows for fast and precise manufacturing and the creation of multipolymer-component systems with a wide range of materials. Obtaining physical prototypes through 3D FDM/FFF printing is quicker and more cost-effective than traditional manufacturing methods. In the event of failure of machine components, it allows the rapid manufacture of replacement parts, so that production does not have to be halted until replacement parts are made. 3D printing is also a tool that allows the development of creativity, which is why it is increasingly used by artists, clothing designers [1], and in education introduced as an element that shapes a new approach to shaping reality (giving non-obvious shapes) and exercising spatial imagination. This technology and other additive techniques will grow significantly in the coming years. However, additive techniques have limitations, including the current availability of printing materials on the market, which may not always meet the growing expectations of end users [2].

Currently, FDM/FFF 3D printing is one of the most popular additive techniques that are used in various fields, such as automotive, submarines, aviation, and biomedical engineering. The increasing use of 3D printing in various fields is related to the possibility of creating elements with complex geometry and at the

same time with good properties (low density, high mechanical properties) [3,4].

PETG (Polyethylene Terephthalate Glycol-Modified), where glycol-modified means that during the polymerization reaction, glycol was added but it is not included in the final product, is a popular 3D printing filament material stands out for its good mechanical properties, chemical stability, excellent aesthetic properties, and biocompatibility [5]. In addition, PET has high resistance to radiation and degradation in the presence of body fluids, which is why it is the most commonly used biomaterial [6]. Some of its uses include materials for orthodontic use, antibacterial films, scaffolds (tissue engineering), drugs, delivery, surgical models, etc [7-9]. However, like any material, it does have some weaknesses that users should be aware of: warping, stringing (tendency to produce thin strands or strings of filament between non-contiguous parts of the print), and hygroscopic. The flexibility of PET-G is good, but it may not be sufficient for more complex applications [10].

Polysiloxanes are a class of polymers that are also commonly known as silicones. They are made up of repeating units of siloxane ($-R_2Si-O-$) where R represents various organic groups or hydrogen atoms. The general chemical formula for polysiloxanes is $[(R_2SiO)_n]$, where "n" represents the number of repeating units in the polymer chain. Silicones are unique among polymers because they contain alternating silicon and oxygen atoms in their backbone, which gives them their distinctive properties. The organic groups attached to the silicon atoms determine the specific

characteristics of the silicone polymer. Polysiloxanes/silicones have several notable properties, making them useful in various applications: high-temperature stability, flexibility and elasticity, water repellency, and transparency and optical clarity [11].

The literature contains publications on 3D printing of PETG filaments, but many of them focus on research on PETG-based composite materials. The analysis of the literature shows that there are no studies on the properties of PETG composites with polysiloxane modifiers. The most commonly used additives are carbon fibers or graphite and natural fiber [12,13,14]. Additives in the form of carbon fiber particles are added to improve the mechanical properties of the material [15,16]. In the work of Vijayasankar et al. [14] the properties of a 3D printed PETG composite with a natural filler were tested. Different percentages (2%, 5%, 10% by weight) of silk fibers were used. The research shows that the material with 2 % wt. silk increased the elastic modulus and compressive modulus compared to neat PETG. A printed prosthetic socket for the lower limb was presented as a possibility of using the material in biomedical engineering.

This study aimed to investigate how multifunctional polysiloxanes affect the properties of PETG for its suitability in FDM/FFF 3D printing technology. New polymer systems have been developed to address the limitations of 3D printing technology using PETG material. This system includes multifunctional polysiloxanes and PETG as the polymer matrix. The materials were modified with a series of polysiloxane-based derivatives obtained by a hydrosilylation reaction.

2. MATERIALS AND METHODS

2.1. Materials

Polyethylene terephthalate glycol-modified (PET-G) copolyester type SELENIS SELEKT™ BD 110 (SELENIC NORTH AMERICA, LLC) The chemicals were purchased from the following sources: Polymethylhydrosiloxane, Trimethylsilyl Terminated (PWS) from Gelest, vinyl(trimetoxy)silane (VTMOS) (97%) from UNISIL; hexene (HEX), octene (OCT), allyl-glycidyl ether (AGE)) from Linegal Chemicals Warsaw, Poland, toluene from Avantor Performance Materials Poland S.A. Gliwice, Poland, and chloroform-d, Karstedt catalyst from Merck Group. In the process, toluene was dried and purified with MB SPS 800 Solvent Drying System and stored under an argon atmosphere in Rotaflo Schlenk flasks.

2.2. Synthesis of modifiers

Following the procedure described in the literature a 500 ml three-necked round bottom flask was filled with 30 g of PWS, 250 ml of toluene, and the appropriate amounts of olefins based on the number of moles of the Si-H moiety (see Tab. 1). A magnetic stirrer was then added to the flask. The reaction mixture was heated to 70°C and Karstedt's catalyst solution (8 x 10⁻⁵ eq. Pt/mol SiH) was added. The reaction mixture was kept at reflux and samples were taken for FT-IR control until the Si-H signal disappeared completely (at 2141 and 889 cm⁻¹). The solvent was removed under reduced pressure, resulting in an analytically pure sample.

Tab. 1. Polysiloxane derivatives

Core	Olefin 1	Olefin 2	Molar ratio
PWS	HEX	TMOS	2:1
PWS	OCT	TMOS	4:1
PWS	HEX	AGE	2:1
PWS	OCT	AGE	2:1

2.3. Filaments fabrication steps

For the masterbatch preparation, the polymer and the chosen additive were homogenized using a laboratory two-roll mill ZAMAK MERCATOR WG 150/280. A portion of 500 g PET-G was molten on the rolls, and then the additive was added in portions, until the final concentration of 5.0 wt.% (with respect to the whole system mass). The mixing was performed at the roll temperature of 225°C for 15 min, getting to full homogeneity of the composition. The resulting polymer system was then granulated using a SHINI SG-1417-CE grinding mill and dried at 55°C/24 h. After that, all of the prepared masterbatches were extruded using a twin-screw extruder machine to obtain final granulates. The granulates were diluted with neat PLA up to the final additive loading of 0.10, 0.25, 0.50, 1.0, 1.5, 2.5 wt.% upon screw extrusion with subsequent cold granulation on the extrusion setup HAAKE Rheomex OS in the processing temperature range 215-230°C, and then dried for 24 h at 55°C. The granulates obtained as above were used for the extrusion of filaments of 1.75 mm diameter by a single-screw extrusion setup FILABOT EX6. Extrusion temperatures were sequentially from the nozzle to the feed zone respectively: 190°C, 220°C, 220°C, and 80°C.

2.4. process by FDM/FFF technique

Using a 3D printer Prusa i3 MK3S+ two types of samples were printed: dumbbells and bars, according to PN-EN ISO 527. The parameters of printing are given in Table 2.

Tab. 2. 3D Printing process parameters

Parameter name	Parameter value
Layer height	0.18 mm
Top layer height	0.27 mm
Shells	2
Top and bottom layers number	3
Infill density	100%
Fill angle	45°
Infill pattern	Rectlinear grid
Printing speed	60 mm/s
Idle speed	80 mm/s
Extruder temp.	230°C
Table temp.	75°C

2.5. Methods and analyses

¹H, ¹³C, and ²⁹Si Nuclear Magnetic Resonance (NMR) spectra were recorded at 25°C on Bruker Ascend 400 and Ultra Shield 300 spectrometers using CDCl₃ as a solvent. Chemical shifts are

reported in ppm concerning the residual solvent (CHCl_3) peaks for ^1H and ^{13}C .

Differential scanning calorimetry (DSC) was performed using a NETZSCH 204 F1 Phoenix (NETZSCH, Selb, Germany). Calorimeter samples of 5 ± 0.2 mg were cut and placed in an aluminum crucible with a punctured lid. The measurements were performed under nitrogen in the temperature range of -20 – 300°C and at a $20^\circ\text{C}/\text{min}$ heating rate.

The effect of the modifier addition on the mass flow rate (MFR) was determined. The measurements were made using an Instron plastometer, model Ceast MF20 according to the applicable standard ISO 1133. The measurement temperature was $230 \pm 0.5^\circ\text{C}$, while the piston loading was 2.16 kg.

Static tensile and three-point bending tests were used to evaluate the mechanical behavior of PET-G composite 3D-printed samples. For flexural and tensile strength tests, the obtained materials were printed into type 1B and 1BA specimens by PN-EN ISO 527 and PN-EN ISO 178. Tests of the obtained specimens were performed on a universal testing machine INSTRON 5969 with a maximum load force of 50 kN. The traverse speed for tensile and flexural measurements was set at 2 mm/min. For all the series, 7 measurements were performed for each material.

Contact angle analyses were performed by the sessile drop technique at room temperature and atmospheric pressure, with a Krüss DSA100 goniometer. Three independent measurements were performed for each sample, each with a 5 μl water drop, and the obtained results were averaged to reduce the impact of surface nonuniformity.

Light microscopy images of the printed samples were taken using a KEYENCE VHX-7000 digital microscope (Keyence International, Mechelen, Belgium, NV/SA) with a VH-Z100R wide-angle zoom lens at $\times 100$ – 200 magnification.

3. RESULTS AND DISCUSSION

3.1. Characterization of synthesis products – NMR analysis

The synthesis procedure outlined in section 2.2 was followed to prepare the modifiers. In order to monitor the substrate conversion throughout the process, FT-IR analysis was employed. The reaction was carried out until the disappearance of the characteristic band (at 2141 and 889 cm^{-1}) originating from the Si-H group of the precursor. In order to ascertain purity and determine the exact conversion, ^1H NMR, ^{13}C NMR, and ^{29}Si NMR spectroscopy were also conducted. Based on ^1H NMR analysis, the degree of conversion for all compounds was determined to be greater than 94%.

The product structures were confirmed by NMR spectroscopy, the following signals were assigned:

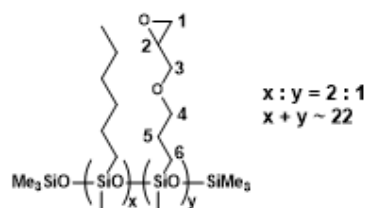


Fig. 1. PWS-2HEX-1AGE, Poly((hexylmethylsiloxane)-co-(3-propylglycidyl), trimethylsilyl terminated

^1H NMR (400 MHz, CDCl_3): δ (ppm) = 3.71–3.68 (m, position 3), 3.47–3.41 (m, position 3 and 4), 3.14 (m, position 2), 2.80–2.78 (m, position 1), 2.61 (m, position 1), 1.64–1.61 (m, position 5), 1.32–1.28 (m, hexyl $-\text{CH}_2-$), 0.90–0.88 (m, hexyl $-\text{CH}_3$), 0.54–0.53 (m, SiCH_2-), 0.13–0.06 (s, SiMe , SiMe_3)

^{13}C NMR (101 MHz, CDCl_3): δ (ppm) = 74.23, 72.15, 71.53, 69.69, 50.95, 44.42 (AGE), 33.17, 31.77 (HEX), 23.35, 23.01 (AGE), 22.76, 17.70, 17.61, 17.46, 14.25 (HEX), 13.63, 13.51 (AGE), 1.98–1.51, -0.22(–0.58) (SiMe , SiMe_3)

^{29}Si NMR (79.5 MHz, CDCl_3): δ (ppm) = -20.98(–22.88) (SiMe , SiMe_3).

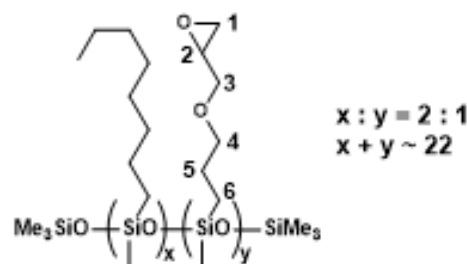
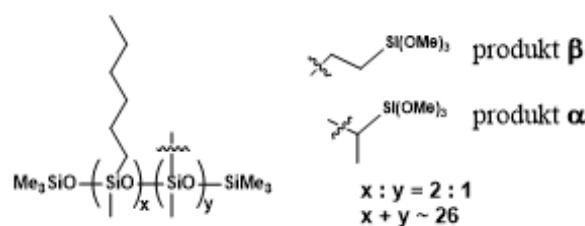


Fig. 2. PWS-2OKT-1AGE, Poly((methyloctylsiloxane)-co-(3-propylglycidyl), trimethylsilyl terminated

^1H NMR (400 MHz, CDCl_3): δ (ppm) = 3.72–3.68 (m, position 3), 3.50–3.40 (m, position 3 and 4), 3.17–3.13 (m, position 2), 2.82–2.79 (m, position 1), 2.63–2.60 (m, position 1), 1.69–1.62 (m, position 5), 1.34–1.30 (m, octyl $-\text{CH}_2-$), 0.93–0.89 (m, octyl $-\text{CH}_3$), 0.57–0.51 (m, SiCH_2-), 0.12–0.08 (SiMe_2)

^{13}C NMR (101 MHz, CDCl_3): δ (ppm) = 74.30, 71.53, 50.94, 44.39 (AGE), 33.63, 33.55, 32.11, 29.57, 29.50 (OCT), 23.37, 23.21 (AGE), 22.83, 17.65, 17.54, 14.22 (OCT), 13.54, 13.44 (AGE), 1.98, 1.60, -0.19, -0.29, -0.47 (SiMe , SiMe_3);

^{29}Si NMR (79.5 MHz, CDCl_3): δ (ppm) = -21.28(–23.45) (SiMe , SiMe_3).



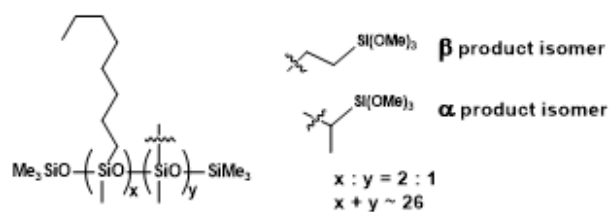
α and β - 31:69

Fig. 3. PWS-2HEX-1TMOS, Poly((hexylmethylsiloxane)-co-(methyl(trimethoxyethyl)siloxane)), trimethylsilyl terminated (94% conversion)

^1H NMR (400 MHz, CDCl_3): δ (ppm) = 3.55 (s, OMe), 1.30–1.27 (m, hexyl $-\text{CH}_2-$), 1.09 (d, $J=7.4\text{Hz}$, α trimethylsiloxy), 0.87 (t, $J=6.3\text{Hz}$, hexyl $-\text{CH}_3$), 0.61–0.50 (m, SiCH_2- , $\text{SiCH}(\text{CH}_3)\text{Si}$), 0.14, 0.08, 0.06, 0.04 (s, SiMe_2 , SiMe_3);

^{13}C NMR (101 MHz, CDCl_3): δ (ppm) = 50.67, 50.61 (OMe), 33.28, 31.81, 23.19, 23.06, 22.80, 17.85, 14.24 (hexyl), 8.45 ($\text{Si-CH}_2\text{CH}_2\text{-Si}$), 7.60, 5.11 ($\text{SiCH}(\text{CH}_3)\text{Si}$), 1.98, 1.59, 0.67, -0.21, -1.14 ($\text{Si-CH}_2\text{CH}_2\text{-Si}$, SiMe_2 , SiMe_3);

^{29}Si NMR (79.5 MHz, CDCl_3): δ (ppm) = -21.24(–22.64) (SiMe , SiMe_3), -41.51(–41.65) ($\text{Si}(\text{OMe})_3$).



α and β - 34:66

Fig. 4. PWS-2OCT-1TMOS, Poly((methyloctylsiloxane)-co-(methyl(trimethoxyethyl)siloxane)), trimethylsilyl terminated (94% conversion)

^1H NMR (400 MHz, CDCl_3): δ (ppm) = 3.56 (s, OMe), 1.30-1.27 (m, octyl $-\text{CH}_2-$), 1.09 (d, $J=7.5\text{Hz}$, α trimethylsiloxy), 0.88 (t, $J=6.2\text{Hz}$, octyl $-\text{CH}_3$), 0.61-0.50 (m, SiCH_2- , $\text{SiCH}(\text{CH}_3)\text{Si}$), 0.14, 0.08, 0.07, 0.04 (s, SiMe_2 , SiMe_3);

^{13}C NMR (101 MHz, CDCl_3): δ (ppm) = 50.65 (OMe), 33.31, 31.83, 23.18, 23.06, 22.80, 17.84, 14.25 (octyl), 8.42 ($\text{Si}-\text{CH}_2\text{CH}_2-\text{Si}$), 1.98, 1.58, 0.64, -0.22, -1.14 ($\text{Si}-\text{CH}_2\text{CH}_2-\text{Si}$, SiMe_2 , SiMe_3);

^{29}Si NMR (79.5 MHz, CDCl_3): δ (ppm) = -21.22, -22.37 (-22.82) (SiMe , SiMe_3), -38.00, -41.54 ($\text{OSi}(\text{OMe})_3$).

3.2. Mechanical behavior evaluation

To understand how additives affect the mechanical properties of composite materials, static mechanical tests on 3D FDM/FFF printed samples were conducted. The polysiloxane-based additives used strongly influenced the change in the mechanical characteristics of PET-G, because of their high plastification impact on polymeric materials similar to silsesquioxanes [17].

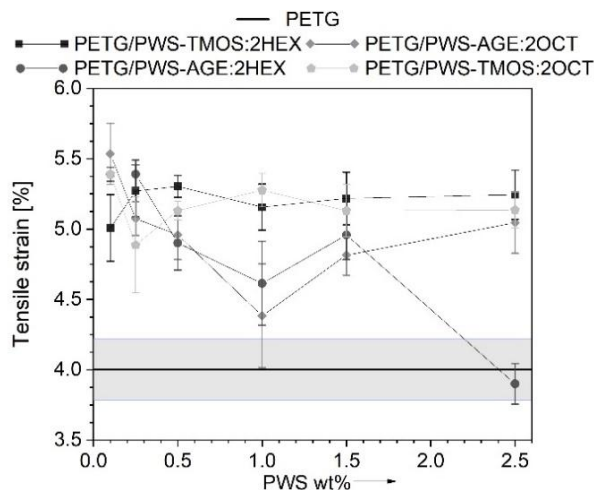


Fig. 5. Tensile strain (elongation at tensile strength) of PET-G and its composites as a function of polysiloxane-based modifier share

The mechanical results obtained from testing objects made with additive technology are not as straightforward as those produced through traditional methods of processing polymeric materials. This is due to the complexity of the additives used and the anisotropic nature of the objects' properties and defective structure resulting from their implementation, because of it all the results show a non-

linear trend. Results derived from static tensile tests are represented in Fig. 5-7. In Figure 5, it can be seen that materials with polysiloxane additions have higher tensile strain compared to neat PET-G. The exception is the material PETG/PWS-AGE:2HEX with 2.5% wt. modifier, that tensile strain is similar to neat PETG. The additives cause a strong plasticizing effect on the polymer matrix, as a result of which an increase in deformation of 35% compared to neat PET-G is observed. The presence of polysiloxanes in the polymer matrix indicates an increase in elastic properties which is attributed to their chemical structure. Polysiloxane's main chain is built with Si-O-Si, which is less restrictive and more flexible than the carbon-carbon C-C bonds found in carbon polymers. Side groups of polysiloxanes may also rotate around Si-O-Si bonds, contributing to their flexibility. In carbon polymers, such movements are typically more limited due to the less flexible carbon-carbon bonds [18]. The force-extension curve illustrates three distinct steps that correspond to the debonding of various sample layers and their deformation under axial tensile force (Fig. 6). The tensile strength (Fig. 7) of all tested materials with modifiers is worse compared to neat PET-G. The modifier particles penetrated the PET-G molecular chains, which reduced the intramolecular interactions between them and decreased their ability to resist tensile force. The addition of modifiers enhances the flexibility of the polymer matrix and negatively influences the tensile strength of the tested samples [19]. Only in the PETG/PWS-AGE:2HEX system, there is a slight improvement in tensile strength. This improvement may be due to the increased miscibility of the additive with the polymer matrix. The higher tensile strength could be attributed to the existence of epoxy groups in the glycidyl allyl. These groups potentially enhance the bonding between the different layers of the printed sample. Casarano et al. discussed the beneficial impact of allyl glycidyl ether on the properties of LMDPE/cellulose composites. They observed that the inclusion of AGE reduced the degree of crystallinity in the blends, acting as a plasticizer, and also enhanced interfacial interactions within the composites. Although there was a minor decrease in strength, the addition of AGE resulted in a noteworthy increase in elongation at break and improved adhesion between the two phases [20]. This phenomenon can be enhanced by the presence of hexane functional alkyl groups, which can also improve intermolecular adhesion.

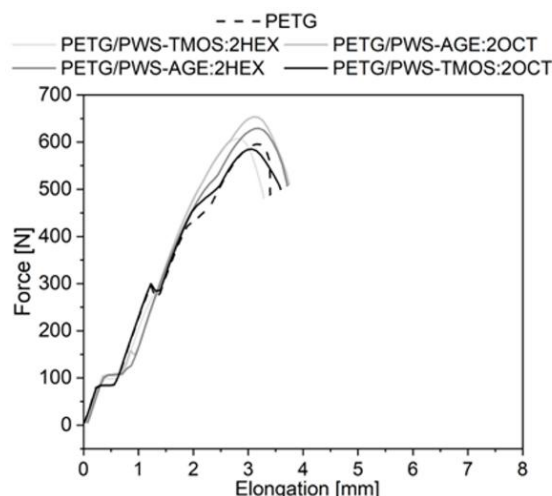


Fig. 6. Force vs elongation curves of PET-G and its composites

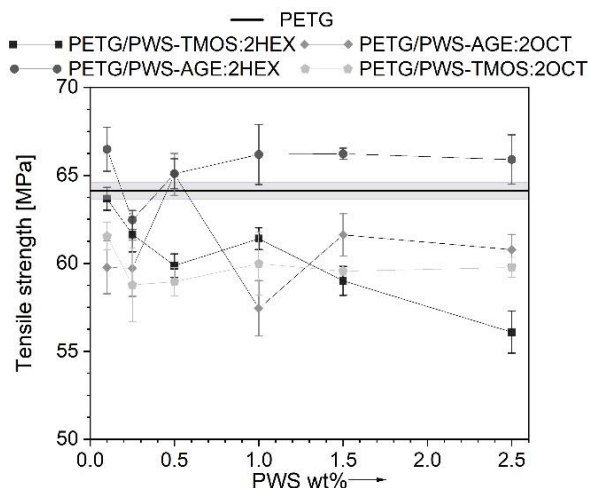


Fig. 7. Tensile strength of PET-G and its composites as a function of polysiloxane-based modifier share

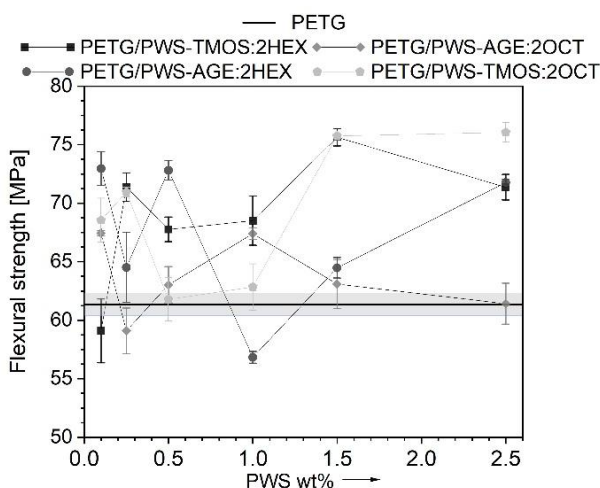


Fig. 8. Flexural strength of PET-G and its composites as a function of polysiloxane-based modifier share

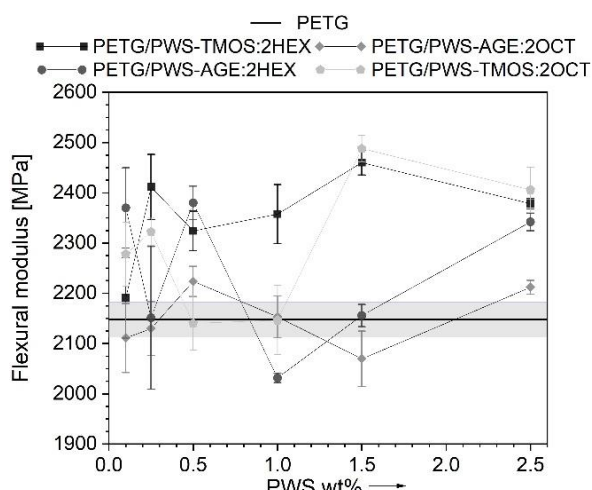


Fig. 9. Flexural modulus of PET-G and its composites as a function of polysiloxane-based modifier share

To assess the mechanical characteristics of the obtained composite materials and their ability to transfer bending loads, three-point bending mechanical tests were also carried out. The use of additives has notably enhanced the strength and bending

stiffness of the composites (Fig. 8-9). Glycidyl and trimethoxysilane groups can cause the formation of additional cross-links in the PET-G polymer structure, which can improve the material's flexural strength and stiffness [21]. Interactions between PET-G and polysiloxane additives' functional side groups can lead to a local increase in molecular entanglement and the formation of an interwoven network [22]. The change in flexural strength is greater than that in tensile strength, due to the different directions of load application and stress distribution resulting from the alignment of the print paths.

3.3. Rheological analysis

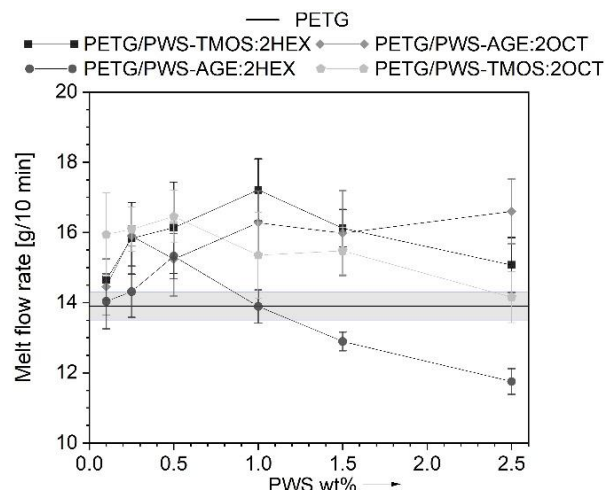


Fig. 10. Melt flow rate of PET-G and its composites as a function of polysiloxane-based modifier share

To evaluate the basic processing properties of PETG/PWS composites, mass flow rate (MFR) measurements were carried out. The results obtained are shown in Fig. 10. The additives used in small contents of up to 1% by weight have a positive effect on the change in the melt flow rate, which is due to the presence of alkylated substituents in the modifier molecule derived from hexene and octene allowing increased mobility of PET-G polymer chains. It promotes an increase in the MFR. Thus, these additives have the character of slip agents. Above 1% by weight of the additive, the lubricating character of the additives used arranges in a downward trend affecting the reduction of MFR, in the PETG/PWS-AGE:2HEX system, the MFR values are lower than the reference material (PET-G). It is related to the increasing proportion of glycidyl and trimethoxysilyl groups in the total volume of the composite, which, due to their similar polarity to the polymer matrix, can affect the stronger interaction of the modifier with the PET-G matrix.

3.4. Microscopic analysis

Microscopic images of sample fractures allow for a visual assessment of the adhesion level of the layers of the printed object. In the reference sample Fig. 11. 1A-1B, air gaps and clearly outlined layer boundaries can be seen. At the lowest concentration of 0.1%, no significant changes are visible compared to the reference sample (Fig. 11. series of images 1). This suggests that at this concentration, the material properties remain relatively consistent with the unmodified material. The modifiers PWS-

AGE:2OCT and PWS-TMOS:2HEX had a positive effect on the processability of materials (Section 3.3), increasing the MFR. Images Fig. 11. 2C and 2E exhibit smaller air gaps and improved interlayer adhesion, resulting in the disappearance of layer boundaries, which were visible in the reference sample.

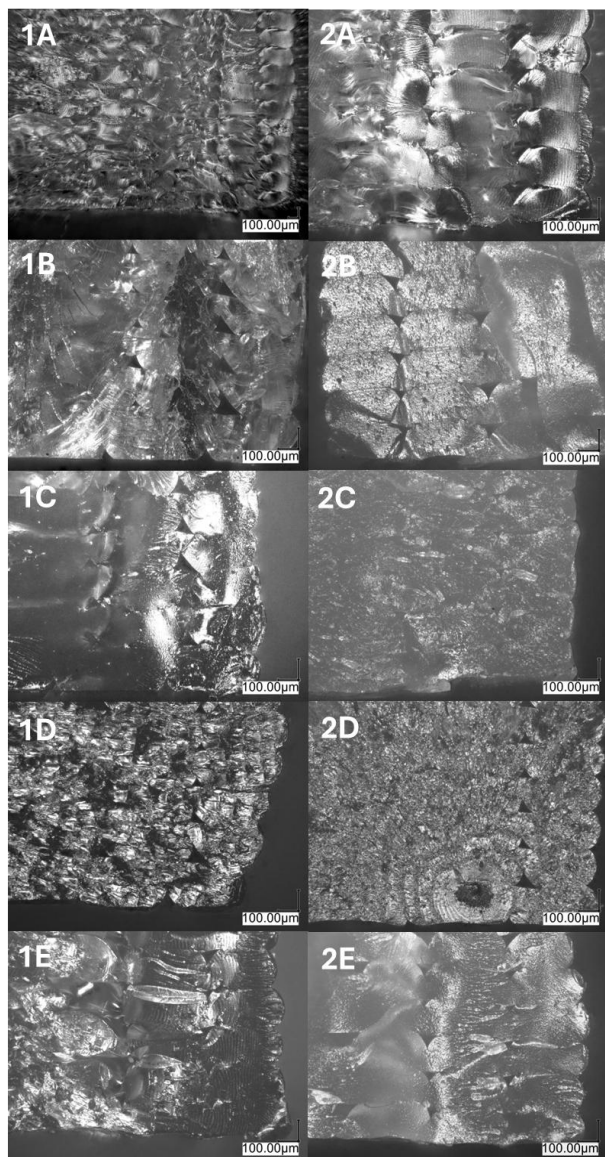


Fig. 11. Microscopic photos of sample fractures: 1A-2A Reference; 1B-0.1%, 2B- 2.5% - PETG/PWS-AGE:2HEX; 1C- 0.1%, 2C- 2.5% - PETG/PWS-AGE:2OCT; 1D- 0.1%, 2D- 2.5% - PETG/PWS-TMOS:2OCT; 1E- 0.1%, 2E- 2.5% PETG/PWS-TMOS:2HEX

3.5. Water contact angle measurements (WCA)

In order to assess the impact of the polysiloxane-based additives with a concentration of 2.5% by weight in the composite systems on the surface properties of the 3D-printed samples, a test to measure the water contact angle on the surface was conducted. The measurement results are shown in Tab. 3. The value of the contact angle of the neat PET-G is 70.6°. It was observed that the addition of a modifier containing non-polar alkyl groups increases the degree of hydrophobicity of the tested samples. Visible effects are observed for the modifier using longer chain olefins, i.e. octene.

The contact angle increases by 14% and 25% for PETG/PWS-TMOS:4OCT composites with a longer alkyl chain and PETG/PWS-AGE:2OCT. For composites modified with polysiloxanes containing hexene substituents, the changes are insignificant.

Tab. 3. Contact angle measurement results for PET-G systems containing 2.5% polysiloxane-based additive

Name of the sample	Contact angle[°]
PET-G neat	70.6
PETG/PWS-TMOS:2HEX	73.4
PETG/PWS-TMOS:4OCT	80.6
PETG/PWS-AGE:2HEX	75.8
PETG/PWS-AGE:2OCT	88.2

3.6. Differential scanning calorimetry (DSC)

Figure 12 shows the results of differential scanning calorimetry (DSC) in inert gas flow. Neat PET-G and composite samples containing 2.5% modifier content were analyzed. The DSC curves (seen in Fig. 12) show only one endothermic peak in each sample, which corresponds to the glass transition temperature (T_g). PET-G belongs to amorphous polymers, therefore other transitions such as crystallization or melting are not observed. The unmodified sample has the highest glass transition temperature $T_g = 86.3^\circ\text{C}$ (Tab. 4). Organosilicon modifiers may have a plasticizing effect in polymer systems, which results in a lower glass transition temperature. The PETG/PWS-AGE:2OCT sample has the lowest T_g value. Glycidyl groups present in the modifier molecule affect the amorphization of the matrix material, which is also visible by changing the course of the DSC curve, for both PETG/PWS-AGE:2OCT and PETG/PWS-AGE:2HEX composite systems [23].

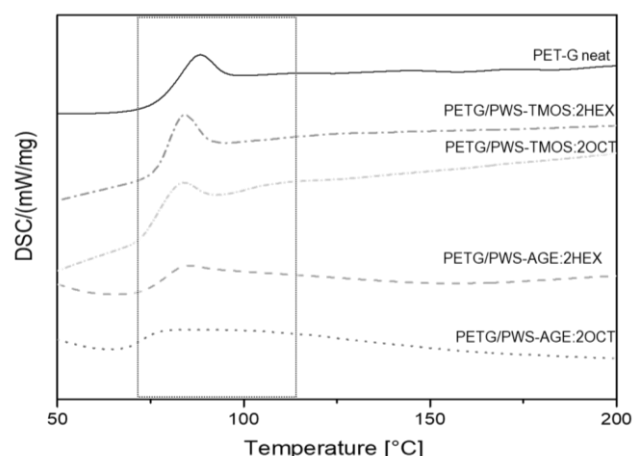


Fig. 12. DSC curves recorded for samples

Tab. 4. Results of DSC analysis

Name of the sample	T_g [°C]
PET-G neat	86.3
PETG/PWS-TMOS:2HEX	82.1
PETG/PWS-TMOS:2OCT	80.4
PETG/PWS-AGE:2HEX	84.3
PETG/PWS-AGE:2OCT	78.2

4. CONCLUSIONS

The field of biomedical engineering is constantly evolving, which calls for new solutions to meet the requirements for therapy, device construction, and materials. Additive technologies offer engineers design freedom due to the virtually unlimited spatial shaping possibilities, but materials and their properties can pose limitations. This study examines the impact of multifunctional polysiloxanes (ranging from 0.10 wt.% to 2.5 wt.%) on the properties of PETG for biomedical applications. Results show that the polysiloxane additives affect the plasticization of the polymer matrix, resulting in increased tensile flexibility of the composite materials. The addition of glycidic and trimethoxysilyl functional groups into the polysiloxane molecule also improves the bending strength properties. However, changes in strength properties were not clearly correlated with the concentration of the organosilicon modifier due to the anisotropic nature of 3D printed structures and the potential for internal defects. The analysis of the melt flow rate shows improved rheological properties of the composites, making them easier to process. Microscopic observations confirmed improvement in interlayer adhesion with increasing MFR. The hydrophobic nature of the polysiloxanes with octene groups increases the water contact angle of the print surface, reducing the negative impact of moisture on printed objects made from these composite materials.

REFERENCES

- Yap YL, Yeong WY. Additive manufacture of fashion and jewellery products: a mini review. *Virtual Phys Prototyp*. 2014;9(3):195–201.
- Shahrudin N, Lee TC, Ramlan RJPM. An overview on 3D printing technology: Technological, materials, and applications. *Procedia Manuf*. 2019;35:1286–96.
- Cali M, Pascoletti G, Gaeta M, Milazzo G, Ambu R. New filaments with natural fillers for FDM 3D printing and their applications in biomedical field. *Procedia Manuf*. 2020;51:698–703.
- Pu'ad NM, Haq RA, Noh HM, Abdullah HZ, Idris MI, Lee TC. Review on the fabrication of fused deposition modelling (FDM) composite filament for biomedical applications. *Mater Today Proc*. 2020; 29:228–32.
- Hsueh MH, Lai CJ, Wang SH, Zeng YS, Hsieh CH, Pan CY, et al. Effect of printing parameters on the thermal and mechanical properties of 3D-printed PLA and PETG, using fused deposition modeling. *Polymers (Basel)*. 2021;13(11).
- Gün Gök Z, İnal M, Bozkaya O, Yiğitoğlu M, Vargel İ. Production of 2-hydroxyethyl methacrylate-g-poly(ethylene terephthalate) nanofibers by electrospinning and evaluation of the properties of the obtained nanofibers. *J Appl Polym Sci*. 2020;137(41).
- Szymczyk-Ziółkowska P, Łabowska MB, Detyna J, Michalak I, Gruber P. A review of fabrication polymer scaffolds for biomedical applications using additive manufacturing techniques. *Biocybern Biomed Eng*. 2020;40:624–38.
- Ping X, Wang M, Xuewu G. Surface modification of poly(ethylene terephthalate) (PET) film by gamma-ray induced grafting of poly(acrylic acid) and its application in antibacterial hybrid film. *Radiat Phys Chem*. 2011;80(4):567–72.
- Nicita F, D'Amico C, Filardi V, Spadaro D, Aquilio E, Mancini M, et al. Chemical-Physical Characterization of PET-G-Based Material for Orthodontic Use: Preliminary Evaluation of micro-Raman Analysis. *Eur J Dent*. 2023.
- Holcomb G, Caldon EB, Cheng X, et al. On the optimized 3D printing and post-processing of PETG materials. *MRS Commun*. 2022;12:381–7.
- Zaman Q, Zia KM, Zuber M, et al. A comprehensive review on synthesis, characterization, and applications of polydimethylsiloxane and copolymers. *Int J Plast Technol*. 2019;23:261–82.
- García E, Núñez PJ, Caminero MA, Chacón JM, Kamarthi S. Effects of carbon fibre reinforcement on the geometric properties of PETG-based filament using FFF additive manufacturing. *Compos B Eng*. 2022;235.
- Kováčová M, Kozakovičová J, Procházka M, Janigová I, Vysopal M, Černíková I, et al. Novel Hybrid PETG Composites for 3D Printing. *Appl Sci*. 2020;10.
- Vijayasankar KN, Bonthu D, Doddamani M, Pati F. Additive Manufacturing of Short Silk Fiber Reinforced PETG Composites. *Mater Today Commun*. 2022;33:104772.
- Guessasma S, Belhabib S, Nouri H. Printability and Tensile Performance of 3D Printed Polyethylene Terephthalate Glycol Using Fused Deposition Modelling. *Polymers (Basel)*. 2019;11(7).
- Alarifi IM. PETG/carbon fiber composites with different structures produced by 3D printing. *Polym Test*. 2023;120:107949.
- Brząkański D, Sztorch B, Frydrych M, Pakula D, Dydek K, Kozera R, et al. Limonene Derivative of Spherosilicate as a Polylactide Modifier for Applications in 3D Printing Technology. *Molecules*. 2020;25(24):5882.
- Dvornic PR. Thermal properties of polysiloxanes. In: *Silicon-containing polymers: the science and technology of their synthesis and applications*. Dordrecht: Springer Netherlands; 2000. p. 185–212.
- Safandowska M, Rozanski A, Galeski A. Plasticization of Polylactide after Solidification: An Effectiveness and Utilization for Correct Interpretation of Thermal Properties. *Polymers (Basel)*. 2020;12(3):561.
- Casasano R, Matos JDR, Fantini MCDA, Petri DFS. Composites of allyl glycidyl ether modified polyethylene and cellulose. *Polymer (Guildf)*. 2005;46(10):3289–99.
- Przekop RE, Gabriel E, Pakula D, Sztorch B. Liquid to Fused Deposition Modeling (L-FDM)—A Revolution in Application Chemicals to 3D Printing Technology—Mechanical and Functional Properties. *Appl Sci*. 2023;13(14):8462.
- Pakula D, Sztorch B, Romańczuk-Ruszk E, Marciniec B, Przekop RE. High impact polylactide based on organosilicon nucleation agent. *Chin J Polym Sci*. 2024;1–11.
- Obermeier B, Frey H. Poly(ethylene glycol-co-allyl glycidyl ether)s: A PEG-based modular synthetic platform for multiple bioconjugation. *Bioconjug Chem*. 2011;22(3):436–44.

Scientific research in the field of designing organosilicon modifiers of thermoplastic properties for the incremental FDM technique financed from the sources of the National Center for Research and Development under the LIDER X project (LIDER/01/0001 /L-10/18/NCBR/2019).

Bogna Sztorch:  <https://orcid.org/0000-0001-5166-8391>

Julia Glowacka:  <https://orcid.org/0000-0003-1082-6714>

Miłosz Frydrych:  <https://orcid.org/0000-0003-4196-5522>

Daria Pakula:  <https://orcid.org/0000-0001-6741-3019>

Eliza Romańczuk-Ruszk  <https://orcid.org/0000-0001-5228-4920>

Natalia Kubiak:  <https://orcid.org/0009-0009-0536-4990>

Robert E. Przekop:  <https://orcid.org/0000-0002-7355-5803>



This work is licensed under the Creative Commons BY-NC-ND 4.0 license.

HARDWARE IMPLEMENTATION OF FRACTIONAL-ORDER CALCULUS IN CONTROL SYSTEMS

Paweł KIECZMERSKI*

*Department of Automation and Robotics, Białystok University of Technology, Wiejska 45A, 15-351 Białystok, Poland

pawel.kieczmerski@pb.edu.pl

received 10 September 2024, revised 18 April 2025, accepted 2 May 2025

Abstract: This article analyzes the implementation process of a fractional-order control system using available toolboxes, software, and hardware. The main objective is to showcase the current state-of-the-art hardware implementation of fractional-order control, comparing its potential to classical counterparts, and emphasizing the benefits of its utilization in industry. The article covers theoretical aspects of fractional-order calculus and provides an example implementation of a Fractional-order PID controller with a NI MyRIO-1900 measurement board with FPGA module, comparing it with simulations for a given control plant.

Key words: fractional calculus, fractional-order systems, fractance; domino ladder, fractional integrator, Simulink, implementation, control

1. INTRODUCTION

In recent years, fractional calculus has gained considerable attention among researchers in various fields of science and technology. This calculus deals with the general extension of the concept of differentiation and integration to non-integer orders, which makes it possible to analyze and model complex phenomena that are not fully described by classical equations [1, 2, 3, 4, 5]. However, the greatest potential of fractional calculus lies in its application to systems modeling and control, where the possibility of designing much more robust and accurate control systems emerges. Current research indicates that fractional-order controllers can achieve much better values of control quality indicators and are more resistant to changes in model parameters than the commonly used classical PID controller [2, 6, 7, 8, 9, 10, 11, 12, 13], but most industrial solutions available on the market use PI/PID-type controllers without achieving optimal performance. This fact is due to the difficulty of understanding the complexity of non-integer order controllers by the personnel operating the system and the complexity of implementing control algorithms in classical microcontrollers or other commercial devices. With the coming of Industry 4.0 [14] the automation industry is looking for new solutions to increase overall efficiency; that is why this paper will present both the recent available tools and implementation options for non-integer controllers.

The purpose of this article is to compile key theoretical foundations of fractional-order calculus, provide an overview of current trends in its practical applications, and demonstrate an example implementation of Fractional-order PID controller on myRIO-1900 measurement board.

In this paper, all necessary theoretical aspects related to fractional-order calculus and its application in automatic control systems will be presented. The most popular types of fractional-order controllers, methods for approximating fractional order, and current tuning methods for such controllers will be discussed. This will be followed by an analysis of current trends in hardware implementation of fractional-order controllers, along with an indication and

comparison of available hardware and software tools. These tools were used to obtain models, the responses of which were compared with the response of a model of an object with fractional-order dynamics, called fractance, in order to determine the best one. The best tool will be used to develop an automatic control system with both a classical PID controller and a fractional-order controller, both in simulation and in the laboratory, and their results will eventually be compared. Both types of controllers will be tuned using the Modified Grey Wolf optimization algorithm.

2. FRACTIONAL CALCULUS

The fractional calculus is a form of generalization of the operations of integration and differentiation, through a new operator ${}_a D_t^q$ combining the functionality of both, where q - the order of the operator, such that q is a real number $q \in \mathbb{R}$ and a and t are the limits of the operation. Depending on the sign of the order of the operator, it can be treated as a differentiation or integration operator [2] according to the following formula:

$${}_a D_t^q = \begin{cases} \frac{d^q}{dt^q} & \text{dla } q > 0, \\ 1 & \text{dla } q = 0, \\ \int_a^t (d\tau)^q & \text{dla } q < 0. \end{cases} \quad (2.1)$$

There are many definitions of fractional operator, but they are used in different fields, making it easier to analyze the relevant functions. Currently, the most popular definitions found in modern books describing fractional calculus are the Riemann-Liouville definition RL, the Grünwald-Letnikov definition GL and the Caputo definition C.

Definition 2.1. A function given by the integral [1]

$$\Gamma(x) = \int_0^\infty t^{x-1} e^{-t} dt, \quad R(x) > 0 \quad (2.2)$$

is called the Euler gamma function and satisfies the equality

$$\Gamma(x + 1) = x\Gamma(x)$$

where $R(x)$ is real part of complex number x . (2.3)

Definition 2.2. Riemann-Liouville fractional-order derivative is defined as [1]

$${}^{RL}_a D_t^q f(t) = \frac{1}{\Gamma(N-q)} \frac{d^N}{dt^N} \int_a^t (t-\tau)^{N-q-1} f(\tau) d\tau. \quad (2.4)$$

Definition 2.3. Grünwald-Letnikov fractional-order derivative is defined as [4]

$${}^{GL}_a D_t^q f(t) = \lim_{h \rightarrow 0} h^{-q} \sum_{k=0}^{\lfloor \frac{t-a}{h} \rfloor} (-1)^k \binom{q}{k} f(t - kh). \quad (2.5)$$

Definition 2.4. Caputo fractional-order derivative is defined as [1]

$${}^C D_t^q f(t) = \frac{1}{\Gamma(N-q)} \int_a^t \frac{f^{(N)}(\tau)}{(t-\tau)^{q+1-N}} d\tau, \quad (n-1 \leq q < n). \quad (2.6)$$

Due to its form, the Riemann-Liouville definition is used for relatively simple functions (xa, ex, sin(x), etc.), while Grünwald-Letnikov definition found its use in numerical evaluation. On the other hand, because of its ability to consider time delays, memory effects, and the possibility of using the same form of initial conditions as for the integer-order case, the Caputo definition has found wide application in control theory and automation. In this paper, the Caputo definition will be used precisely because of the aforementioned properties.

Definition 2.5. The formula for the Laplace transform of the q -th order Caputo derivative eq. (2.6), when $(N-1 \leq q < N)$ has the form [1]:

$$\mathcal{L}[{}^C_0 D_t^q f(t)] = s^q F(s) - \sum_{k=1}^N s^{(q-k)} f^{(k-1)}(0^+). \quad (2.7)$$

Given that the function $f(t)$ and all its derivatives have zero initial conditions $f(0) = 0$ when $t = 0$, then transform of the q -th order Caputo derivative can be simplified to $s^q F(s)$.

3. FRACTIONAL-ORDER CONTROLLERS

Controllers are an integral part of systems that provide process control using feedback loops. Fractional-order controllers, which are a generalization of classical integer-order controllers, are becoming increasingly popular. The leading types of Fractional-order controllers [4] today are CRONE Controller developed by Oustaloup in 1995, Fractional-order PID controller proposed by Igor Podlubny, and a number of lesser used controllers; Fractional lead-lag compensator (Raynaud and Zegaïnoh, 2000), non-integer integral (Manabe, 1961) and TID compensator (Lurie, 1994). In this paper only FOPID controller will be considered due to its relative simplicity.

3.1. FOPID Controller

Fractional-order $PI^{\lambda}D^{\mu}$ controller (FOPID) [3, 4] was first introduced in 1999 by Igor Podlubny as generalization of the classical PID controller with integrator of real order λ and differentiator of real order μ .

Definition 3.1. The FOPID Controller [4, 15] transfer function can be defined in time domain as:

$$C(s) = k_p + \frac{k_i}{s^{\lambda}} + k_d s^{\mu}, \quad (\lambda, \mu \geq 0) \quad (3.1)$$

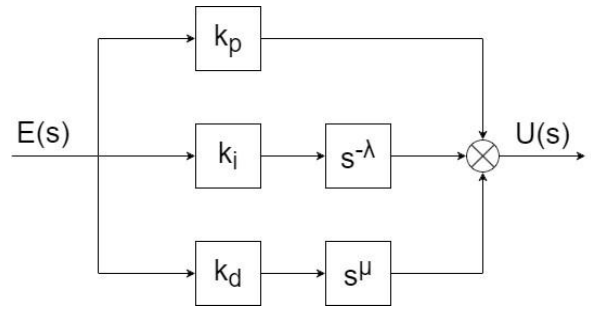


Fig. 3.1. General structure of FOPID Controller

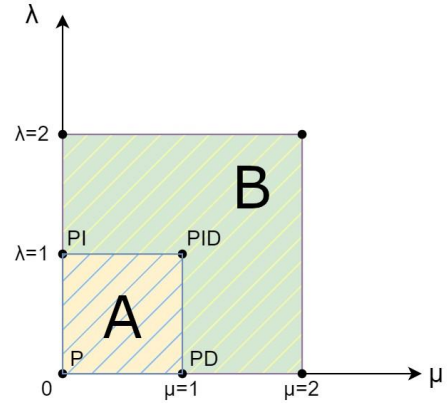


Fig. 3.2. The FOPID controller plane

where, k_p , k_i , k_d are proportional constant, integration constant and differentiation constant respectively.

The general structure of FOPID Controller corresponding to eq. (3.1) is shown on Figure 3.1, where $E(s)$ is control error and $U(s)$ is controller output. In special circumstances $PI^{\lambda}D^{\mu}$ controller can be equal to the classic PID Controller, for example if $\lambda = 1$ and $\mu = 0$, then eq. (3.1) will describe PI controller as shown in Figure 3.2. The controller plane for FOPID has to be divided into two areas: A when $0 < \lambda, \mu \leq 1$ and B when $1 < \lambda, \mu \leq 2$. This is due to the stability conditions [16] of the system depending on the value of the controller order. In Figure 3.3, where q corresponds to fractional operator order, stability regions are depicted for the controller order corresponding to the zones separated in Figure 3.2. It is worth mentioning that using $\lambda, \mu > 2$ will result in controllers instability.

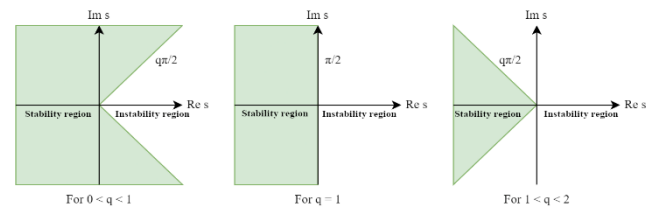


Fig. 3.3. Stability region of fractional order system

3.2. Approximation

For practical implementation of fractional integro-differentiator of order α it is necessary to use conventional transfer function approximation. One of such approximation methods is Oustaloup recursive filter [2,3], which provides very good results in specified frequency range (ω_b ; ω_h) using the following equations:

$$s^\alpha \approx K \prod_{k=1}^N \frac{s + \omega_k'}{s + \omega_k} \quad (3.2)$$

$$\omega_k' = \omega_b \cdot \omega_u^{\frac{2k-1-\alpha}{N}}, \quad (3.3)$$

$$\omega_k = \omega_b \cdot \omega_u^{\frac{2k-1+\alpha}{N}}, \quad (3.4)$$

$$K = \omega_h^\alpha, \quad \omega_u = \sqrt{\omega_h/\omega_b}. \quad (3.5)$$

where, N - order of approximation, ω_h - higher bound of frequency fitness, ω_b - bottom bound of frequency fitness.

For digital implementation it is possible to use any suitable method for conversion to discrete-time equivalent.

3.3. Controller tuning methods

The most challenging part of working with FOPID controllers arises when tuning them with the addition of two parameters related to the orders of integration and differentiation. The authors of the book [3] state that the known principles of the Ziegler-Nichols tuning method for the classical PID, can be applied to FOPID controllers for the values of constants k_p , k_i , k_d , while the orders of λ and μ must be selected experimentally. However, this creates a difficulty in obtaining optimal system performance, as well as requiring the selection of the appropriate type of controller before the tuning process begins, as each controller (P , P^λ , PD^μ , $P^\lambda D^\mu$) provided significantly different results. They also proposed an analytical tuning method which is as follows:

Consider the mathematical model of a given plant

$$G(s) = \frac{K}{Ts+1}. \quad (3.6)$$

Since open-loop transfer function $L(s) = C(s)G(s)$, the controller transfer function $C(s)$, that gives the Bode's ideal loop transfer function

$$L(s) = \left(\frac{\omega_c}{s}\right)^\alpha, \quad (3.7)$$

takes the form:

$$C(s) = K_p \frac{Ts+1}{s^\alpha}, \quad (3.8)$$

which can be expressed as

$$C(s) = K_p \left(\frac{1}{s^\alpha} + Ts^{1-\alpha}\right). \quad (3.9)$$

The transfer function eq. (3.9) is basically a $IaD\mu$ controller (where $\mu = 1-\alpha$). The time-domain equation of the controller $C(s)$ is:

$$u(t) = K_p ({}_0D_t^{-\alpha} e(t) + T {}_0D_t^{1-\alpha} e(t)). \quad (3.10)$$

The open-loop transfer function $L(s) = C(s)G(s)$ can then be described as

$$L(s) = \frac{K_p K}{s^\alpha}, \quad 1 < \alpha < 2. \quad (3.11)$$

To obtain α and K_p the following procedure has to be used:

1. Find the fractional order α by using formula:

$$\varphi_m = \pi + \arg L(j\omega_c) = \pi \left(1 - \frac{\alpha}{2}\right) \quad (3.12)$$

from the desired phase margin φ_m .

2. Calculate the proportional gain K_p by using formula:

$$|L(j\omega_c)| = 1 \rightarrow K_p = \frac{\omega_c^\alpha}{K}, \quad (3.13)$$

from the gain-crossover frequency ω_{cg} and nominal gain of the system K . This method was verified by experiment conducted by the authors which proved that the system behaved according to designed specifications.

In [17] the extension of Z-N tuning rules was presented, in which the authors pointed out new more complex rules. They stated that by formulating five design criteria—target gain crossover frequency ω_{cg} , desired phase margin φ_m , high-frequency noise attenuation, disturbance rejection, and robustness to plant gain variations—the parameters of a FOPID controller can be systematically computed.

The first criterion is posed as the objective function, while the remaining four are treated as constraints, resulting in a constrained optimization problem. This solution can provide good results in most cases but tends to reach local minima. However those results strongly depend on initial estimates of parameters provided, which is an important drawback, because in some cases finding the solution without well-chosen initial estimates can be difficult. The Authors tested those tuning rules on three different theoretical plants; first-order, second order and fractional-order. The experiment proved the usefulness of these rules and at the same time showed that, as in the case of the classical Z-N method, the resulting settings offer inferior performance to the one sought but can be applied even without knowledge of the plant model.

The last approach presented in [18] focuses on solely optimization algorithms. The authors considered BLDC (brushless direct-current) motor as a control plant and used PID and FOPID controller tuned with multiple different methods to test the performance of such system. They used genetic algorithm, fuzzy logic, Grey Wolf Algorithm, Artificial bee colony algorithm, Neural-networks and more, with all of them using the same conditions and cost functions. The most popular cost functions are defined with integral indexes, for example, Integral Absolute Error (IAE), Integral of Time Multiplied Squared Error (ITSE), Integral of Time Multiplied Absolute Error (ITAE). Each algorithm generated a certain controller set vector and then determined the value of the cost function, which it minimized at the next iteration. The main difference between the aforementioned solutions was the difference in the operation of the algorithm's core, which handled the generation and updating of new set vectors. According to the results obtained by the authors, all of the considered methods can be successfully applied to determine optimal setting for controller, which proved that optimization algorithms are viable option as tuning method.

4. IMPLEMENTATION FEASIBILITY STUDY

Theoretical analyses of algorithms using non-integer-order controllers for process control purposes are becoming an increasingly common phenomenon and indicate the superiority of such controllers over classical solutions [19, 20, 21, 22, 23]. However, the part related to hardware implementation is currently at an early stage, and publications related to it, as well as available tools, are few. Delving into the currently occurring attempts to implement the aforementioned algorithms, it can be seen that they are mostly focused on problems related to electric motors, in particular DC motors [10, 24], PMSM motors [25] and servo motors [11, 26]. There

have also been attempts to control such objects as a PEM Fuel Cell [6], a heater [7], an Industrial boiler burning system [8], a water tank [9], as well as a simulation model of plant-coupled fluid tanks tested using a microcontroller [27]. The main software used to create and operate the algorithms were MATLAB/Simulink and Labview. On the other hand, the hardware part was mainly implemented using DAQ boards, PCI board or PLC, with the addition of real-time control libraries.

4.1. Available toolboxes

Compared to Labview, MATLAB has a wider range of available tools. In MATLAB's add-ons library there are some easy-to-use toolboxes, which provide complete structures and functions for fractional calculus and control, based on different definitions or approximations. Among them, the most extensive can be distinguished: the FOMCON toolbox [28, 29, 30, 31], FOTF toolbox [32] and Ninteger toolbox [33]. The FOMCON toolbox is the most complex available tools as of today, it includes many useful easy-to-use blocks such as complete FOPID Controller, fractional integrator/derivative, fractional transfer function both in continuous and discrete-time domain and many more. FOMCON can be used for design, analysis, simulation and control of fractional-order systems. The fractional-order elements are approximated using Oustaloup's recursive filters, described in Section 3.2. It also comes with controller tuning under performance and robustness specifications. However, its most significant advantage lies in providing a comprehensive, end-to-end framework that facilitates the seamless transition from fractional-order system model to a fully implementable control solution. FOTF toolbox is less complex than FOMCON but still provides all the basic blocks; fractional operator, Caputo operator, Riemann-Liouville operator, FOPID Controller and FOTF Model.

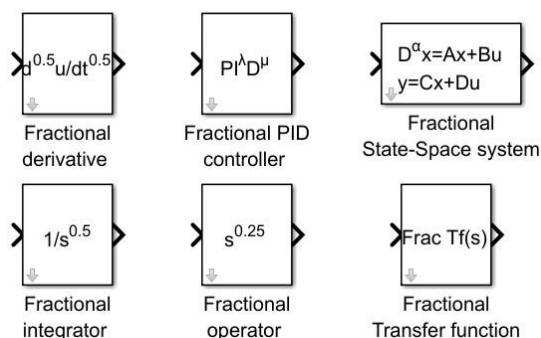


Fig. 4.1. Example of universal blocks from FOMCON toolbox

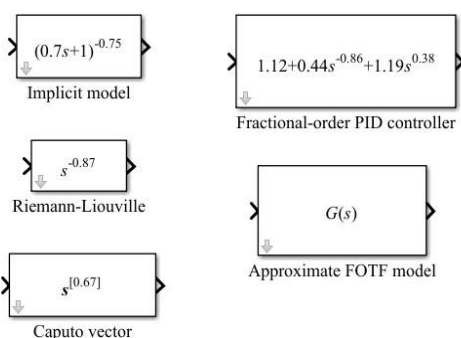


Fig. 4.2. Example of universal blocks from FOTF toolbox

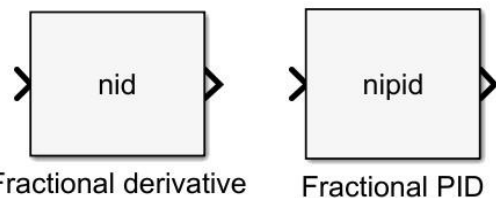


Fig. 4.3. Example of universal blocks from Ninteger toolbox

The Ninteger toolbox has a wide range of available functions with focus on CRONE Controllers and approximations but comes with only two universal block structures: Fractional derivative and FOPID controller. Figures 4.1, 4.2 and 4.3 show examples of universal blocks from the mentioned toolboxes. Those toolboxes are also suitable for hardware implementation.

4.2. Real-Time implementation

For real-time implementation of fractional-order algorithms, a number of tools can be highlighted. There are MATLAB libraries such as HDL Coder for DAQ boards with FPGA modules or FPGA and ASIC standalone systems and PLC Coder for PLC controllers. Both of those libraries are toolsets to automatically generate code from the simulink graphical interface for a particular target, for example, VHDL/Verilog for FPGAs and ST and Ladder Logic for PLCs, and allow verification of code operation, as well as providing support for external interfaces. However, these libraries support a limited number of hardware platforms, so one must verify compatibility with specific hardware before deciding to use them.

There is also third-party software interfacing with MATLAB available commercially, such as QUARC and dSPACE real-time software. These software solve the problem of handling embedded systems as a target and support the design and implementation of complex algorithms. Together with the software, it is possible to use dedicated measurement boards so that all control and measurements can be performed by a single unit fully compatible with Simulink. Within the scope of this work, the QUARC software kit was used together with a measurement board with an FPGA module, acting as an external target in the form of NI-myRIO-1900. Most of the measurement boards from National Instruments are compatible with the QUARC software; hence, the NI-PCI-6221 card could also be used. It is worth mentioning that the previously presented equation describing the FOPID controller (eq. (3.1)) in the case of practical implementation often requires consideration of saturation and anti-windup algorithms.

5. FRACTANCE DEVICES

A device demonstrating behavior governed by fractional-order dynamics is termed a fractance [34, 35]. The fractance devices can be classified by three basic types: domino ladder circuit network, a tree structure of electrical elements and net-grid network. Each is built with infinitely many resistors R and capacitors C connected in series or parallel. As part of the study, it was decided to consider the case of a domino ladder system described as a Cauer type I structure, shown in Figure 5.1. Since there is no phenomenon of infinity in reality, a fractance with dynamics corresponding to a non-integer order α system, can be approximated by finite number of

elements using truncated continued fraction expansion (CFE). Using the aforementioned CFE method, the impedance of domino ladder system can be described as: [34]

$$Z_{DL}(s) = R_0 + \frac{1}{C_1 s + \frac{1}{R_1 + \frac{1}{C_2 s + \frac{1}{R_{n-1} + \frac{1}{C_n s + \frac{1}{R_n}}}}} \approx \frac{1}{C_\alpha s^\alpha} \quad (5.1)$$

where, C_α - is pseudo-capacity of the system, R_n is resistance value and C_n is capacitance value. The circuit RC_α in Figure 5.1, can be described using Kirchhoff's second law as:

$$u_{in}(t) = u_r(t) + u_{out}(t), \quad t \geq 0, \quad (5.2)$$

where $u_r(t)$ is voltage of resistor R , $u_{in}(t)$ is source voltage e and $u_{out}(t) = V_0 - V_-$ is voltage on the fractional-order element.

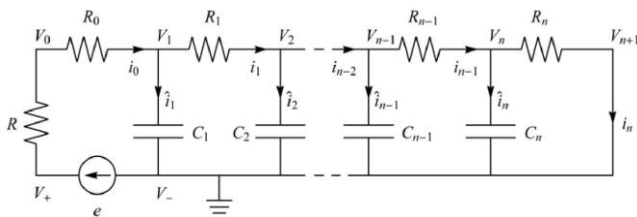


Fig. 5.1. Distribution of potentials and currents in the ladder system [34]

Considering that

$$i_0(t) = C_\alpha D_t^\alpha u(t), \quad (5.3)$$

equation eq. (5.2) can be expressed as

$$u_{in}(t) = RC_\alpha D_t^\alpha u_{out}(t) + u_{out}(t), \quad t \geq 0, \quad (5.4)$$

which can then be converted to

$$C_\alpha D_t^\alpha u_{out}(t) = -\frac{u_{out}(t)}{RC_\alpha} + \frac{u_{in}(t)}{RC_\alpha}, \quad t \geq 0, \quad (5.5)$$

after applying the Laplace transform, the following was obtained

$$Z(s) = \frac{U_{out}(s)}{U_{in}(s)} = \frac{1}{RC_\alpha s^{\alpha+1}} \quad (5.6)$$

6. SIMULATION ANALYSIS

6.1. Toolbox comparison

The domino ladder system from Figure 5.1 was recreated in Simulink using values specified in [34] for $\alpha = 0.60$ with Simscape electrical library as shown in Figure 6.1. That is because such system can effectively be used as a base sample for comparison with models created with considered toolboxes.

Using eq. (5.6) and FOMCON, FOTF and NINTEGER Toolboxes several models were created with approximation order of 5 and frequency range [0.001;1000]. All of the considered models were then supplied with a voltage step signal of 10 V and their response was compared with domino ladder system response. This step is essential to verify that all fractional integrators provided by the toolboxes perform as expected and to identify the most suitable implementation before applying them in control scenarios. The responses of those models are shown in Figure 6.2, where the difference between them is apparent, but appears to be insignificant.

Hence, in addition, a correlation showing the relative error between the responses of the models and the domino ladder system over time was determined, which can be seen in Figure 6.3.

Analyzing the results shown in Figure 6.3, it turns out that the best approximation of the non-integer-order element was obtained for the FOMCON toolbox. Therefore, FOMCON Toolbox will be used for simulation and practical implementation.

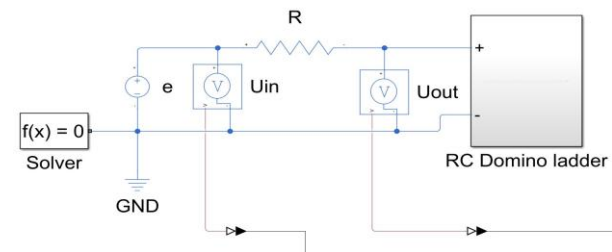


Fig. 6.1. Domino ladder system created in Simulink for $\alpha = 0.60$

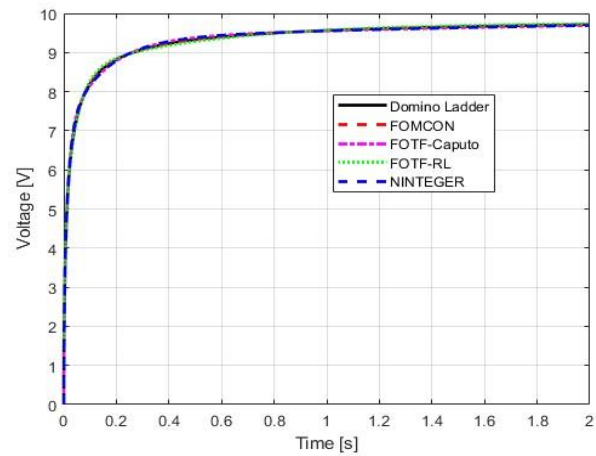


Fig. 6.2. Comparison of the responses of the considered fractional-order models

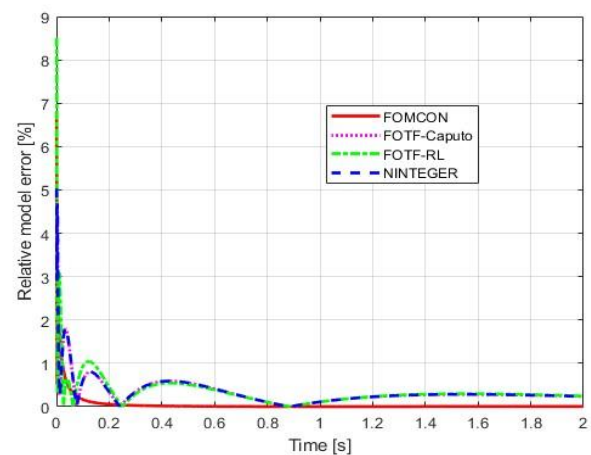


Fig. 6.3. Relative error of the considered fractional-order models

6.2. Second order system

Now an example implementation of a fractional-order algorithm using the aforementioned tools will be presented, where a very simple system without delays will be taken as the control plant in order

to show the required operations. Note, however, that in reality many systems have delays, but the approach will remain the same. Now let's consider second-order control plant which can be described as

$$G(s) = \frac{U_{out}(s)}{U_{in}(s)} = \frac{K}{(sT_1+1)(sT_2+1)}. \quad (6.1)$$

When $K = 1$, $T_1 = 1.5$ and $T_2 = 2.5$ the transfer function eq. (6.1) of plant takes form

$$G(s) = \frac{1}{3.75s^2 + 4s + 1}. \quad (6.2)$$

Based on equation (6.2), a simulation was carried out using both PID and FOPID controllers, where each controller was implemented according to equation (3.1). For the PID controller, the parameters were set to $\lambda = 1$ and $\mu = 1$, while for the FOPID controller, the values were selected within the fractional ranges $\lambda \in (0,1)$ and $\mu \in (0,1)$.

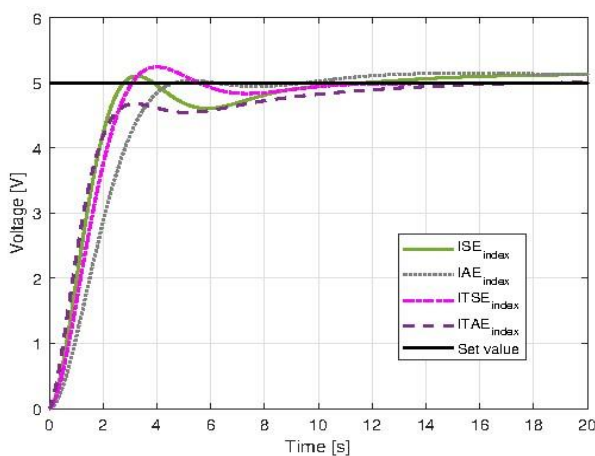


Fig. 6.4. Comparison of the response of the system with a FOPID controller tuned by considering different integral indices

As for the tuning method, Modified Grey Wolf Optimization algorithm [18, 36] was implemented and both controllers were tuned with the same conditions and constraints. The key distinction lies in the number of optimized parameters: the PID controller required tuning of three parameters (k_p , k_i , k_d), whereas the FOPID controller involved five parameters (k_p , k_i , k_d , λ , μ). The cost function eq. (6.3) consisted of the cost of deviation (CF_E) and the cost of control (CF_U) with weights of 400:20. Considering the control effort in the optimization process helps to obtain controller settings that can be realistically implemented in hardware, as the resulting control signal stays within the limits supported by the measurement card, e.g. $\pm 10V$. The cost of deviation can be determined using different integral indices: ISE, IAE, ITSE or ITAE, while the cost of control was determined as the square of the error. Depending on the selected performance index, the optimization algorithm emphasizes different characteristics of the system response. Therefore, a separate controller tuning procedure was performed for each of the specified indices to examine how the choice of a particular criterion influences the final outcome of the algorithm. The algorithm yielded four sets of settings for the PID and FOPID controller, using the aforementioned indices, 40 iterations and 20 searching agents. It is important that the optimization process is carried out for a higher setpoint than the one envisaged in the target implementation. The closed-loop response of the system (6.2) with FOPID control is shown in Figure 6.4. The ITSE criterion provided the best performance, and thus its associated controller settings were adopted for

implementation. The cycle execution time was 0.002 s for both controllers.

$$Cost\ function = 400 \cdot CF_E + 20 \cdot CF_U \quad (6.3)$$

7. HARDWARE IMPLEMENTATION

7.1. Implementation procedure

The hardware unit supporting the control algorithm is a measurement board NI-myRIO-1900. Its operation and control have been implemented using QUARC software, which provides the blocks shown in Figure 7.1. The first of these (HIL Initialize) is the hardware configuration block, where all the parameters of the system are specified, including the number of inputs/outputs and their channel numbers, measurement ranges, encoder inputs, etc. Further on, you can see the analog input and output blocks of the card, as well as the block that allows you to save data to a file (To Host File). Analog laboratory model was used to simulate the operation of the system eq. (6.2).

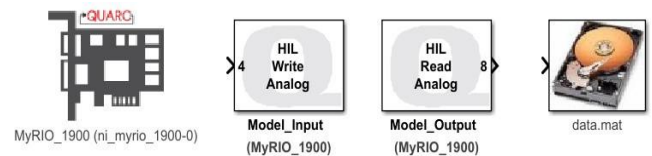


Fig. 7.1. Example of QUARC blocks for real-time implementation

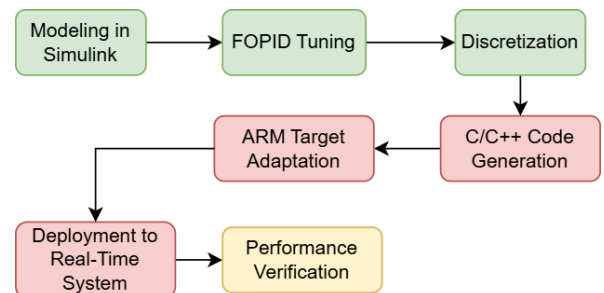


Fig. 7.2. A flow chart of the procedure for implementing the control algorithm

The process of implementing the algorithm from Section 6.2. into a real system is shown in Figure 7.2. The first three steps are associated with Matlab Simulink software, while the next four are implemented by the QUARC add-on.

1. Modeling in Simulink – design the chosen control algorithm, in this case a PID/FOPID controller in Simulink. It is important to use blocks from the QUARC library, from Figure 4.1 and Figure 7.1. Remember to define the I/O along with the board configuration via the HIL Initialize block.
2. FOPID Tuning – input the designated controller settings – k_p , k_i , k_d , λ , μ .
3. Discretization – as the algorithm is ultimately intended for a real system, it should be discretized with sample time T_s . In this case, T_s was taken as 0.002s.
4. C/C++ Code Generation – compile the discretized model to C/C++ using QUARC's auto-code tools.
5. ARM Target Adaptation – modify generated code for ARM architecture compatibility (e.g., myRIO-1900).

6. Deployment to Real-Time System – upload the executable to the myRIO-1900 real-time target.
7. Performance Verification – validate real-time operation against design requirements (e.g., step response, stability).

It is critical to select the correct target type in the QUARC compiler options during the initial model preparation stage (Step 1), as Steps 4–6 are automatically executed by QUARC during compilation based on the specified target. For this implementation, the `quarc_linux_rt_armv7` target was chosen, as it provides a generic real-time framework for ARM-based systems, including the myRIO-1900 board.

Due to the interferences introduced by the control plant, a low-pass filter described as eq. (7.1), was applied to its output to negate its effect on system operation.

$$G(s) = \frac{75}{s+75} \quad (7.1)$$

7.2. Experimental Results

The system from section 6.2 has been implemented with a procedure from Figure 7.2. into myRIO-1900 using the PID and FOPID controller parameters optimized for the ITSE criterion. Figure 7.3 presents the closed-loop responses of both the physical plant and simulated system, while Figure 7.4 displays their corresponding control signals.

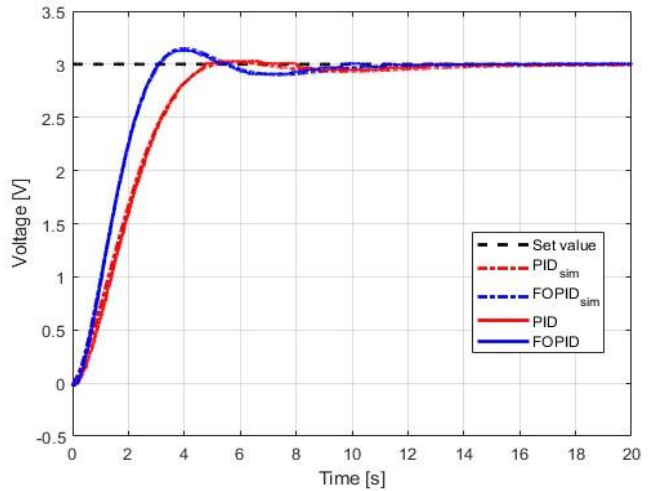


Fig. 7.3. Comparison of the simulation and real control plant responses for PID and FOPID controller

Analyzing the results shown in Figures 7.3 and 7.4, it is evident that the experimental results coincided with the simulation results. The values of the cost function obtained in both the simulation and the experiment, along with the selected values of the controller settings, are summarized in Table 1. Clearly the FOPID controller scored about 30% better in terms of control deviation and about 6% better in terms of control cost than the PID controller in both the simulations and the experiment. The FOPID controller demonstrated superior performance with a 16% lower RMSE (Root Mean Square Error) value compared to the conventional PID controller, further validating its effectiveness for the given control application. The experimental results also yielded better results in terms of control deviation than the simulation with comparable value of control

signal. In addition, in the waveform of the control signal in Figure 7.4, it can be seen that the FOPID Controller handled the control signal better. It is also worth mentioning that control signal from FOPID controller was more resistant to interference than PID controller, which is visible in Figure 7.4.

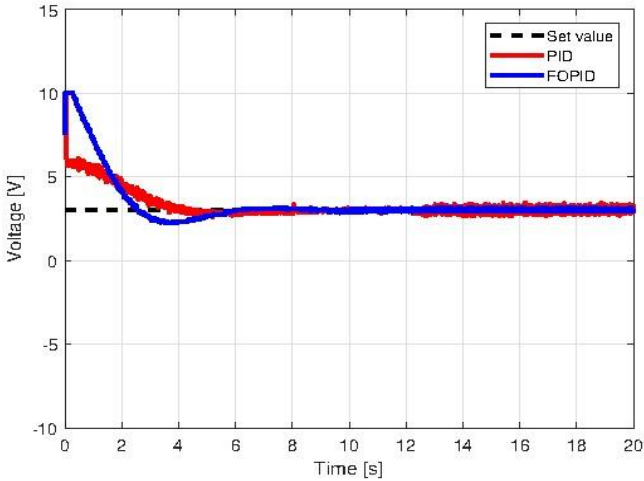


Fig. 7.4. Comparison of control signals from PID and FOPID controller from the experiment

Tab. 1. Controller parameters and cost function for the system

	<i>PID Controller</i>	<i>FOPID Controller</i>
K_p	1,8902	2,5043
K_i	0,4785	0,6644
λ	1,0000	1,0060
K_d	0,4370	0,7156
μ	1,0000	0,5027
$CF_{E_{SIM}}$	12,4389	8,0557
$CF_{E_{REAL}}$	11,0435	7,5231
$CF_{U_{SIM}}$	318,4723	300,3850
$CF_{U_{REAL}}$	328,7697	306,1467
$RMSE$	0,7948	0,6858

8. CONCLUDING REMARKS

In this paper, a method for design and implementation of fractional-order controller for both simulation and experiment were presented. The analysis of currently existing solutions made it possible to identify current trends in the tuning of FO controllers and showed the superiority and potential of FOPID controllers over their classical counterparts. The available tools for working with fractional-order calculus were presented, and the FOMCON Toolbox was clearly identified as the current best solution. Then the physical implementation of the fractional-order element is shown, along with an example implementation procedure for a given model of a control object. It turns out that the process of tuning FOPID controllers is relatively lengthy and requires appropriate definition of search ranges and cost functions to enable a smooth transition from the simulation environment to the real one. The solution shown can

also be easily applied to other control objects and hardware platforms. Further research will focus on switched systems, which will eventually be enriched with fractional-order controllers.

REFERENCES

- Kaczorek T, Rogowski K. Fractional Linear Systems and Electrical Circuits. Białystok Poland. Springer; 2015.
- Tepljakov A. Fractional-order Modeling and Control of Dynamic Systems. Tallinn Estonia. Springer; 2017.
- Luo A, Sun J. Complex Systems – Fractionality. Time delay and Synchronization. Springer; 2012.
- Petras I. Fractional-Order Nonlinear Systems - modeling, analysis and simulation. Springer; 2011.
- Das S, Pan I. Fractional Order Signal Processing: Introductory Concepts and Applications. Springer; 2012.
- Lu X, Miao X, Xue Y, Deng L, Wang M, GU D, et al. Dynamic modeling and fractional order PIAD μ control of PEM fuel cell. Int J Electrochem Sci. 2017;12(8):7518–36. doi:10.20964/2017.08.12
- Zamojski M. Implementation of fractional order pid controller based on recursive Oustaloup's filter. In: 2018 International Interdisciplinary PhD Workshop (IIPHDW). Świnoujście Poland. 2018; 414–7. doi:10.1109/I-IPHDW.2018.8388402
- He Y, Gong R. Application of fractional-order model reference adaptive control on industry boiler burning system. In: 2010 Int Conf Intell Comput Technol Autom. Changsha China. 2010; 750–3. doi:10.1109/ICICTA.2010.59
- Bhambhani V, Chen Y. Experimental study of fractional order proportional integral (FOPI) controller for water level control. In: 2008 47th IEEE Conf Decision Control. Cancun, Mexico. 2008; 1791–6. doi:10.1109/CDC.2008.4739341
- Tepljakov A, Gonzalez E, Petlenkov E, Belikov J, Monje C, Petráš I. Incorporation of fractional-order dynamics into an existing PI/PID DC motor control loop. ISA Trans. 2016;60:262–73. doi:10.1016/j.isatra.2015.11.012
- Tepljakov A, Petlenkov E, Belikov J, Astapov S. Tuning and digital implementation of a fractional-order PD controller for a position servo. Int J Microelectron Comput Sci. 2013;4(3):116–23.
- Sun J, Wang C, Xin R. Design of fractional order proportional differentiation controller for second order position servo system. In: 2018 Chinese Control And Decision Conf (CCDC). Shenyang China. 2018; 5939–44. doi:10.1109/CCDC.2018.8408171
- Kadiyala V, Jatoth R, Pothalaiah S. Design and implementation of fractional order PID controller for aerofin control system. In: 2009 World Congr Nature Biol Inspired Comput (NaBIC). Coimbatore India. 2009; 696–701. doi:10.1109/NABIC.2009.5393470
- Xu X, Lu Y, Vogel-Heuser B, Wang L. Industry 4.0 and industry 5.0— inception, conception and perception. J Manuf Syst. 2021;61:530–5. doi:10.1016/j.jmsy.2021.10.006
- Shah P, Agashe S. Review of fractional PID controller. Mechatronics. 2016;38:29–41. doi:10.1016/j.mechatronics.2016.06.005
- Kaczorek T. Fractional descriptor observers for fractional descriptor continuous-time linear system. Arch Control Sci. 2014;24:27–37. doi:10.2478/acsc-2014-0002
- Valerio D, Costa J. Ziegler-Nichols type tuning rules for fractional PID controllers. In: ASME 2005 Int Des Eng Tech Conf Comput Inf Eng Conf; 2005. doi:10.1115/DETC2005-84344
- Kumarasamy V, Ramasamy VKT, Chandrasekaran G, et al. A review of integer order PID and fractional order PID controllers using optimization techniques for speed control of brushless DC motor drive. Int J Syst Assur Eng Manag. 2023;14:1139–50. doi:10.1007/s13198-023-01952-x
- Rastogi P, Chatterji S, Karanjkar D. Performance analysis of fractional-order controller for pH neutralization process. In: 2012 2nd Int Conf Power Control Embedded Syst (ICPES). Allahabad, India. 2012; 1–6. doi:10.1109/ICPES.2012.6508116
- Petras I. Modeling and numerical analysis of fractional-order Bloch equations. Comput Math Appl. 2011;61(2):341–56. doi:10.1016/j.camwa.2010.11.009
- Bai L, Xue D. Universal block diagram-based modeling and simulation schemes for fractional-order control systems. ISA Trans. 2018;82:153–62. doi:10.1016/j.isatra.2017.04.018
- Sun X, Yan G, Zhang B. The simulation analysis for a kind of fractional order Kalman estimator. Procedia Comput Sci. 2017;111:308–14. doi:10.1016/j.procs.2017.06.028
- Dzielinski A, Sierociuk D. Simulation and experimental tools for fractional order control education. IFAC Proc. 2008;41(2):11654–9. doi:10.3182/20080706-5-KR-1001.01975
- Kanzari B, Taieb A, Chaari A. Fractional modeling of the speed of a DC motor and control with FOPID controller. In: 2023 9th Int Conf Control, Decision Inf Technol (CoDIT). Rome Italy. 2023; 2085–90. doi:10.1109/CoDIT58514.2023.10284258
- Thakar U, Joshi V, Vyawahare V. Design of fractional-order PI controllers and comparative analysis of these controllers with linearized, nonlinear integer-order and nonlinear fractional-order representations of PMSM. Int J Dyn Control. 2017;5:187–97. doi:10.1007/s40435-016-0243-0
- Barbosa R, Machado J, Jesus I. On the fractional PID control of a laboratory servo system. IFAC Proc. 2008;41(2):15273–8. doi:10.3182/20080706-5-KR-1001.02583
- Tepljakov A, Petlenkov E, Belikov J. Embedded system implementation of digital fractional filter approximations for control applications. In: 2014 Proc 21st Int Conf Mixed Des Integr Circuits Syst (MIXDES). Lublin Poland. 2014; 441–5. doi:10.1109/MIXDES.2014.6872237
- Tepljakov A, Petlenkov E, Belikov J. FOMCON: A MATLAB toolbox for fractional-order system identification and control. Int J Microelectron Comput Sci. 2011;2:51–62.
- Tepljakov A, Petlenkov E, Belikov J. Closed-loop identification of fractional-order models using FOMCON toolbox for MATLAB. In: 2014 14th Biennial Baltic Electron Conf (BEC). Tallinn Estonia. 2014; 213–6. doi:10.1109/BEC.2014.7320594
- Tepljakov A, Petlenkov E, Belikov J. A flexible MATLAB tool for optimal fractional-order PID controller design subject to specifications. In: Proc 31st Chinese Control Conf. Hefei China. 2012; 4698–703.
- Tepljakov A, Petlenkov E, Belikov J. FOMCON: Fractional-order modeling and control toolbox for MATLAB. In: Proc 18th Int Conf Mixed Des Integr Circuits Syst (MIXDES). Gliwice Poland. 2011; 684–9.
- Li T, Xue D, Cui X. A tutorial on a universal blockset for fractional-order systems. In: 2021 33rd Chinese Control and Decision Conf (CCDC). Kunming China. 2021; 1210–6. doi:10.1109/CCDC52312.2021.9602256
- Valerio D, Costa J. Ninteger: A non-integer control toolbox for MATLAB. In: Proc 1st IFAC Workshop Fractional Differentiation Appl; 2004.
- Piotrowska E. Analiza obwodów elektrycznych zawierających elementy opisane pochodną o różnych rzędach niecałkowitych [PhD dissertation]. Białystok Poland: Politechnika Białostocka; 2021.
- Petras I, Sierociuk D, Podlubny I. Identification of parameters of a half-order system. IEEE Trans Signal Process. 2012;60(10):5561–6. doi:10.1109/TSP.2012.2205920
- Yazici I, Yaylaci E. Modified grey wolf optimizer based MPPT design and experimentally performance evaluations for wind energy systems. Eng Sci Technol Int J. 2023;46. doi:10.1016/j.jestch.2023.101520

This research was carried out in the framework of the grant no. 2022/45/B/ST7/03076 financed by the National Science Center in Poland.

Paweł Kieczmerski:  <https://orcid.org/0009-0008-5029-3792>



This work is licensed under the Creative Commons BY-NC-ND 4.0 license.

EVALUATING THE STATIC AND DYNAMIC IMPACT PROPERTIES OF LDPE FILM: INSIGHTS INTO MECHANICAL ENERGY CONSUMPTION

Maciej OBST^{*}

^{*}Institute of Applied Mechanics, Poznan University of Technology, ul. Jana Pawła II 24, 60-965 Poznań, Poland

maciej.obst@put.poznan.pl

received 04 November 2024, revised 31 March 2025, accepted 14 April 2025

Abstract: Plastics, or more precisely, polymers, have been utilized as construction materials for numerous decades. The broad range of plastic types results in a vast array of physical properties, consequently yielding a wide spectrum of practical applications. Significant advancements in materials engineering, manufacturing technology, and structural design call for the continuous enhancement of experimental research methods and the exploration of domains that are often regarded as conventional or standardized. The prevailing method for evaluating the mechanical properties of plastics is the static tensile test, which is conducted in accordance with established standards that meticulously delineate the test conditions and specimen preparation methodologies. While static tensile test results furnish valuable information, integrating them with dynamic test results facilitates a more precise evaluation of the structural material under examination. The objective of this study was to conduct a comprehensive investigation of the mechanical properties of film made of low-density polyethylene (LDPE) subjected to static and dynamic loads, thereby enabling the formulation of more comprehensive conclusions about the tested plastic. The methodology entailed conducting experimental static and dynamic tests on samples of recycled LDPE film from this plastic. The experimental results obtained were used to develop a series of mechanical characteristics based on energy relationships. The integration of the outcomes from static tests with impact tests at varying strain rates and impact energies resulted in the identification of several pivotal indices and characteristics. The developed material and structure diagnostic indicators are imperative for future endeavors involving the utilization of LDPE and other unconventional materials as structural materials, particularly in structures designed for controlled mechanical energy dissipation. In summary, a comprehensive understanding of the mechanical properties of materials such as plastics is essential for optimizing their use in specific engineering applications. One critical area where static and dynamic material properties are essential is human safety. Protective measures, including helmets, harnesses, safety belts, and energy-absorbing mats, depend on precise knowledge of material properties.

Key words: LDPE polymer, Low Density Polyethylene, static mechanical properties, force pulse, LDPE dynamic properties, mechanical energy dissipation, LDPE mechanical properties, mechanical state of the LDPE

1. INTRODUCTION

From the perspective of their applications in mechanical structures, polymers exhibit a broad spectrum of mechanical properties, which undoubtedly contributes to their widespread use in engineering practice. A plethora of standards exist that specify mechanical testing methods for polymers. These include standards for foil testing (PN-EN ISO 527-3:2019-01), static testing of polymers (PN-EN ISO 527-1:2020-01), bending tests (PN-EN ISO 178:2019-06), and impact testing of thermoplastic pipes (PN-EN ISO 3127:2017-12). These standards detail the preparation of specimens and the procedures for conducting tests under various loading, deformation, and environmental conditions. Notwithstanding substantial progress in the domain of testing apparatus and methodologies, the pursuit of novel quantitative indicators remains imperative to facilitate a more objective evaluation of a material's mechanical properties. The present study offers the results of tests conducted on films fabricated from Low-Density Polyethylene (LDPE), a material derived from recycled resources. LDPE boasts a wide range of applications and is frequently utilized in various products, particularly in the food industry and transportation sectors. Examples of such products include bags, containers, pipes, hoses, ropes, bottles,

tools, and toys. A notable advantage of LDPE is its recyclability, although it should be noted that indefinite reprocessing is not feasible. Moreover, LDPE's capacity for energy absorption, which is a consequence of its mechanical properties, renders it a valuable material in the design and manufacture of equipment intended to safeguard health and safety from shock loads (Drane et al. [22]). Such equipment includes bumpers, impact absorbers, helmet linings, and energy-absorbing mats, to name a few. LDPE polymer is extensively utilized in the packaging industry, where its impact-resistance is crucial for safeguarding fragile products during storage. Additionally, LDPE polymer is a plastic that can be efficiently processed via automated methods, making it well-suited for high-volume production scenarios. This characteristic contributes to a reduction in unit production costs. LDPE Polymer is distinguished by its favorable elastic properties and capacity for energy storage. The advantages of LDPE also include favorable properties related to the release of strain energy stored during deformation. However, it is important to note that the LDPE polymer exhibits a lack of resistance to high temperatures and shear loads. A substantial body of literature exists that details the modification of LDPE plastics through the addition of various substances, aiming to tailor the final product's properties. Research is ongoing into the development of composites with LDPE and their mechanical properties. In a related

study, Sailaja et al. [10] examined the mechanical properties of biodegradable blends of LDPE and cellulose acetate phthalate. The researchers conducted a series of fundamental mechanical property tests to assess parameters such as tensile strength and longitudinal modulus of elasticity.

Barbosa and Catelli de Souza [1] performed tests on plastic formed from Surlyn® industrial waste ionomer mixed with LDPE, evaluating mixtures with varying percentages of the two components. The researchers assessed the melt flow index (MFI) and morphology (SEM), in addition to mechanical properties through tensile, bending, and impact tests. Furthermore, thermal tests of the prepared mixtures were conducted, encompassing DSC, TGA, and HDT analyses. It was observed that the incorporation of ionomer, in conjunction with LDPE, led to an enhancement in tensile and flexural strength, as well as tensile and flexural modulus values and strain at break. Conversely, an increase in ionomer concentration has been observed to result in a decline in impact strength.

It is evident that plastic waste management is a pressing issue. The potential for creating new plastics from recycled materials presents a promising avenue. However, it is imperative to conduct extensive testing to ascertain the properties of these novel materials, as they have the potential to fulfill a wide range of applications. A more profound comprehension of the mechanical properties of these materials can facilitate more precise material selection for specific operational conditions.

In a study by Kismet et al. [2], three distinct electrostatic waste thermosetting powder coatings were utilized as fillers in low-density polyethylene (LDPE). Subsequent to the fabrication of the composite material, a series of evaluations were conducted to ascertain its mechanical, thermal, and morphological properties. The composite compositions included powder waste coatings in the proportions of 10%, 20%, and 30%, respectively. The injection molding method was employed to create rod specimens for tensile tests, with plate-shaped specimens also utilized. An energy intensity study of the prepared composite specimens was conducted, and the results were compared with those of pure LDPE specimens. For pure LDPE, the highest energy absorption occurred during low-speed impacts. Efforts were made to enhance the impact and flexural strength of LDPE composites containing deactivated powder paint waste.

Sirin et al. [3] investigated the effects of various organic peroxides on selected types of LDPE, including F2-21T, F5-21T, and I22-19T, mixed in varying percentages with dialkyl, dibenzoyl, and dilauroyl peroxides. The experimental tests conducted in this study yielded critical insights into the mechanical properties of the resulting plastics, encompassing stress-strain characteristics, tensile strength at break, and elongation at break.

Peršić et al. [4] prepared composites of LDPE with iron oxide hematite particles, demonstrating superior physical properties compared to pure LDPE. Mechanical property tests were conducted under static conditions to evaluate tensile strength and elongation at break. Dwivedi et al. [5] proposed a composite with sisal fiber coated in LDPE. The coated fibers were utilized as the material for composites with varying weight percentages of sisal fibers. Significant increases in strength and abrasion resistance were observed based on strength tests. Dynamic properties were assessed through three-point bending tests, revealing that the elastic modulus (E') and loss modulus (E'') values were lower for the tested composites compared to pure LDPE and sisal fibers alone.

Barabaszová et al. [6] presented results on an LDPE nanocomposite with ZnO/V and ZnO/V₂CH nanofillers, indicating its potential application as a medical material. Mechanical properties such

as hardness and Vickers microhardness were determined, alongside friction coefficient tests that demonstrated reduced wear. Antimicrobial tests further suggested beneficial medical properties of both fillers used.

In preparation for the extrusion process, Janik [7] developed a composite of polymer blends of poly(butylene terephthalate) (PBT) and LDPE. Subsequent testing on the mechanical properties of the PBT/LDPE composite demonstrated enhancements in tensile strength, flexural strength, and alterations in both Young's tensile modulus and flexural modulus when compared to unmodified LDPE. Additionally, an enhancement in elongation ranging from 10% to 20% was observed in comparison to unmodified LDPE.

Ono and Yamaguchi [9] conducted research on the effects of the extrusion process on the structure and mechanical properties of low-density polyethylene (LDPE). Their analysis focused on the outcomes of rheological tests, which revealed that linear viscoelastic properties exhibit reduced sensitivity to alterations in polyethylene structure. However, an enhanced sensitivity was observed in specimens subjected to extrusion temperatures of 350°C. Czarnecka-Komorowska et al. [8] presented the findings of a study on the thermomechanical, rheological, and structural properties of films made from recycled polyethylene. The authors observed that recycled rLDPE/rLDPE blends possess qualities that render them suitable for thin film production. Mechanical property tests demonstrated enhancements in tensile strength and elongation values. Furthermore, it was observed that films derived from rLDPE/rLDPE blends demonstrated superior puncture resistance in comparison to films fabricated from virgin materials.

Yao et al. [11] investigated the mechanical properties of LDPE composites with colored CBF filler, highlighting concerns about heavy metal contamination in plastics used to manufacture children's toys. The CBF-filled composite is posited as a potential solution to this issue. Preliminary investigations into the mechanical properties of the composite have indicated that the integration of CBF with LDPE can result in a substantial enhancement of tensile strength, Young's modulus, flexural strength, and the modulus of elasticity of the composite under consideration. Rana et al. [14] presented the results of an LDPE composite reinforced with jute. The fabrication of the composite involved the compression of LDPE film and jute into slab form. A series of fundamental mechanical property tests were conducted, encompassing bending, tensile, impact, DMA, and SEM analyses. The outcomes of these tests indicated that the LDPE-jute composite demonstrated enhanced impact strength in comparison to the pure polymer.

Yazdani et al. [15] investigated the mechanical properties of low-density (LDPE) and high-density polyethylene (HDPE) and their composites with carbon nanotubes (CNTs). The study identified four stages of deformation: linear elasticity, plasticity, softening deformation, and strengthening. The strain rate was found to have a significant impact on the mechanical properties of the polymers and their composites studied.

In a related study, Sahraeian et al. [16] examined the mechanical properties of nanocomposites based on low-density polyethylene (LDPE) with varying contents of nanoperlite. The researchers performed rheological tests, dynamic mechanical thermal analysis (DMTA), and thermogravimetric analysis (TGA).

In addition to static tests on various materials, including LDPE, dynamic tests at different impact speeds were also carried out. Kofi et al. [12] conducted impact resistance tests on birch fiber-reinforced HDPE composites obtained through injection molding. The authors noted that the dynamic properties of these composites are not fully characterized, and there is a paucity of studies on their

impact resistance. The composite material that was the subject of this study was submitted to impact tests, hardness tests, tensile strength evaluations, and elastic modulus assessments. Impact tests were conducted at speeds of 1 m/s and 1.25 m/s using a system based on an inertially falling mass with a semicircular head for composite specimens with varying birch fiber content. The authors observed the tup bouncing after striking the test specimen and noted the minimal energy absorbed by the composite material.

Karthikeyan et al. [13] conducted a series of experiments on laminated beams composed of monolithic carbon-fiber-reinforced plastic (CFRP) and ultra-high molecular weight polyethylene (UHMWPE). The experimental design encompassed three-point bending of composite beams, with dynamic tests involving the use of a metal foam beater to simulate an explosion by striking the mid-span of the beam. The authors of the study examined the impact of the support method on the beam's response to the applied load, with a particular focus on the movement of so-called moving or shear hinges from the impact point toward the beam supports. Fiber cracking of the composite was observed in the proximity of the supports.

Xu et al. [17] subjected low-density polyethylene (LDPE) and ultra-high molecular weight polyethylene (UHMWPE) to static and dynamic tests, thereby determining the relationship between yield strength and strain rate. A comparison was made between the mechanical properties of the two polymers, with particular attention given to the impact of molecular structure on the tensile fracture behavior of polyethylene specimens.

Zhu et al. [18] developed experimental stress-strain characteristics for four types of polyethylene: low-density polyethylene (LDPE), linear low-density polyethylene (LLDPE), medium-density polyethylene (MDPE), and high-density polyethylene (HDPE), across strain rates ranging from 0.001 to 1000 s⁻¹. It was observed that the fracture characteristics of the specimens varied with the strain rate, as did the strain rate-dependent changes during yield stress analysis.

In a related study, Mohagheghian et al. [19] investigated the fracture characteristics of low-density polyethylene (LDPE), high-density polyethylene (HDPE), and ultra-high molecular weight polyethylene (UHMWPE) specimens, focusing on their capacity to absorb impact energy. The researchers explored the relationship between the shape of the bullet's contact surface and the energy absorbed by the polymer material. Plates fabricated from the materials under consideration were subjected to static loads and bullet impacts at a velocity of 100 meters per second. The increased strain rate resulted in softening, which in turn led to the destabilization of neck propagation during stretching in LDPE and HDPE. In contrast, UHMWPE exhibited notable stability. The study underscored discrepancies in energy absorption intensity among the materials under scrutiny, contingent on the morphology of the bullet contact surface. The findings for the examined polymers were then juxtaposed with those garnered from an aluminum alloy specimen, here designated as 6082.

Sandeep and Murali [20] conducted experimental tests on low-density polyethylene (LDPE) foams of five different densities under compressive loading at various strain rates. It was observed that the compressive strength of LDPE foam is more favorable at higher strain rates.

It is also imperative to acknowledge the prevalence of other composite materials that currently garner significant interest among researchers, particularly within the domains of aerospace and au-

tomotive engineering. In contemporary composite structures, natural fibers, including wool, silk, kenaf, and others, are frequently utilized as base materials. Additionally, composites incorporating carbon nanotubes have garnered significant attention. Sahu et al. [28] examined the mechanical and electrical properties of multi-walled carbon nanotubes (MWCNTs) filled with pineapple fibers and hybrid laminated composite structures based on kenaf fibers. The study highlighted the benefits of the electrical and mechanical properties of the composites to the aerospace industry. Similarly, Das et al. [27] conducted extensive research on a KF/epoxy composite whose electrical and mechanical properties are ideal for the automotive and aerospace industries. Antony et al. [26] evaluated composite structures designed to absorb radar waves. The composites tested utilized various fibers, including wool, silk, E-glass, aramid, and wave-absorbing foams such as balsa wood, PVC, and PM. The experimental and simulation methods are employed in the study of composite structures. Modal analysis and finite element simulation are popular methods [24,25]. Sahu et al. [23] conducted simulation and experimental tests of polymeric composite plates reinforced with natural fibers and polyethylene terephthalate (PET) foam cores for impact bending of polymeric composite plates reinforced with natural fibers.

This article presents the results of experimental static and impact tests on specimens made of low-density polyethylene (LDPE) in film form. The author observed the effects of strain rate and impact energy on the mechanical properties of the test material.

It was observed that the manufacturing process of the film appeared to induce anisotropy in its mechanical properties. This observation was based on a visual assessment of the examined material. The failure mechanism observed visually exhibited a dependence on the direction of the applied load; however, this variation had a negligible impact on the overall performance of the film, based solely on data obtained from static tests. The author also presents indices based on strain energy, the interpretation of which aids in a more precise evaluation of the plastic tested. The proposed methodology can be applied to evaluate and diagnose the mechanical properties of various materials and structures.

The study of the mechanical dynamic properties of polymers and composites is a vital and contemporary field of scientific inquiry. The findings from this research are directly applicable in engineering practice, particularly in the comprehensive analysis of polymeric materials, their composites, and structures made from them. Obst et al. [21] conducted experimental and analytical studies of the dynamic mechanical properties of pneumatic absorbers made from LDPE polymer. The tests results of pneumatic impact absorbers made of LDPE polymer [21] and the research results of LDPE film presented in this article are a continuation of dynamic tests aimed at the safety of people exposed to impact loads.

2. EXPERIMENTAL RESEARCH METHODOLOGY

LDPE film, precisely cut into strips measuring 210 millimeters in length, 25 millimeters in width, and with a thickness ranging from 0.36 to 0.39 millimeters, was utilized for the experimental procedure. The observed variation in foil thickness is attributable to the manufacturing process. Micrometric measurements were conducted at several points on the foil, and the thickness measurements obtained were within the specified dimensional range. The initial material used was a sheet of LDPE film, which was fabricated

from a polymer blend of recycled materials. Strips were meticulously cut from this film in three distinct orientations relative to the manufacturing traces that were visible to the naked eye: parallel to the traces, perpendicular, and at a 45-degree angle. As previously mentioned in the introduction, the objective was to conduct a diagnostic study of the material's mechanical properties in relation to these manufacturing traces. To mitigate the risk of damage from flat test grips, the gripping sections of the test specimens were fortified. The section between grips measured 110 mm in length. The LDPE strip specimens, as illustrated in Figures 1-2 and 7, were subjected to static loading on a Zwick Z100 testing machine at a loading rate of 300 mm/s. Identical belt specimens were also subjected to impact tests using a drop tower. In this experiment, a 3.3-kilogram steel striker, falling freely under the influence of gravity, impacted a steel bumper, thereby generating an impact load on the LDPE film specimen. The striker was released from heights of 0.5 m, 1 m, and 1.5 m, resulting in varying velocities and kinetic energies at impact. The configuration of the impact test apparatus is illustrated in Figure 8. LDPE film specimens were meticulously extracted from a sheet in three distinct orientations, designated as 0°, 45°, and 90° relative to the visible structural lines of the film. The tested specimens are displayed in Figure 7. During the impact testing procedure, the LDPE film strips underwent tensile loading as the striker made contact with the rigid reversing plate. A Chronos 2.1-HD high-speed camera was employed to record the movement of the LDPE strip under dynamic stretching conditions. All tests were conducted at ambient temperature (23°C).

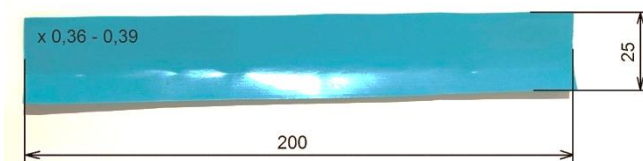


Fig. 1. Strip cut from a sheet of tested LDPE film

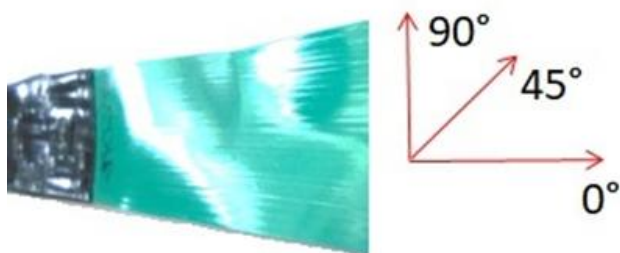


Fig. 2. Tested LDPE film. Visible technological straight lines and coordinates of cutting directions

2.1. Static testing of LDPE film

The findings from the static tensile test of LDPE film strips under uniaxial tension provided the foundation for the subsequent development of additional mechanical characteristics. Tensile plots for the three angular orientations of the strip specimens are shown in Figure 3a, b, and c. Upon examination of both LDPE film samples and pneumatic absorbers made of this plastic, some peculiarities were noted for some measurement results. The author attributes this phenomenon to the internal structure of plastics and the sensitivity of deformation mechanisms to the velocity of loading and other factors. The author intentionally left the measurement result labeled

as specimen No. 6 to indicate that despite providing the same boundary conditions, plastics do not necessarily guarantee perfect repeatability of results.

The Young's modulus and the static strain energy density, expressed as the specific energy of deformation, were determined. The strain energy density was calculated using the following formula:

$$E_c \left[\frac{mJ}{mm^3} \right] = \int_{l_0}^{l_0+\Delta l} \frac{F}{V_0} dl = \int_0^\varepsilon \sigma d\varepsilon \quad (1)$$

where F and V_0 are respectively the current value of tension force, and the initial value of sample volume.

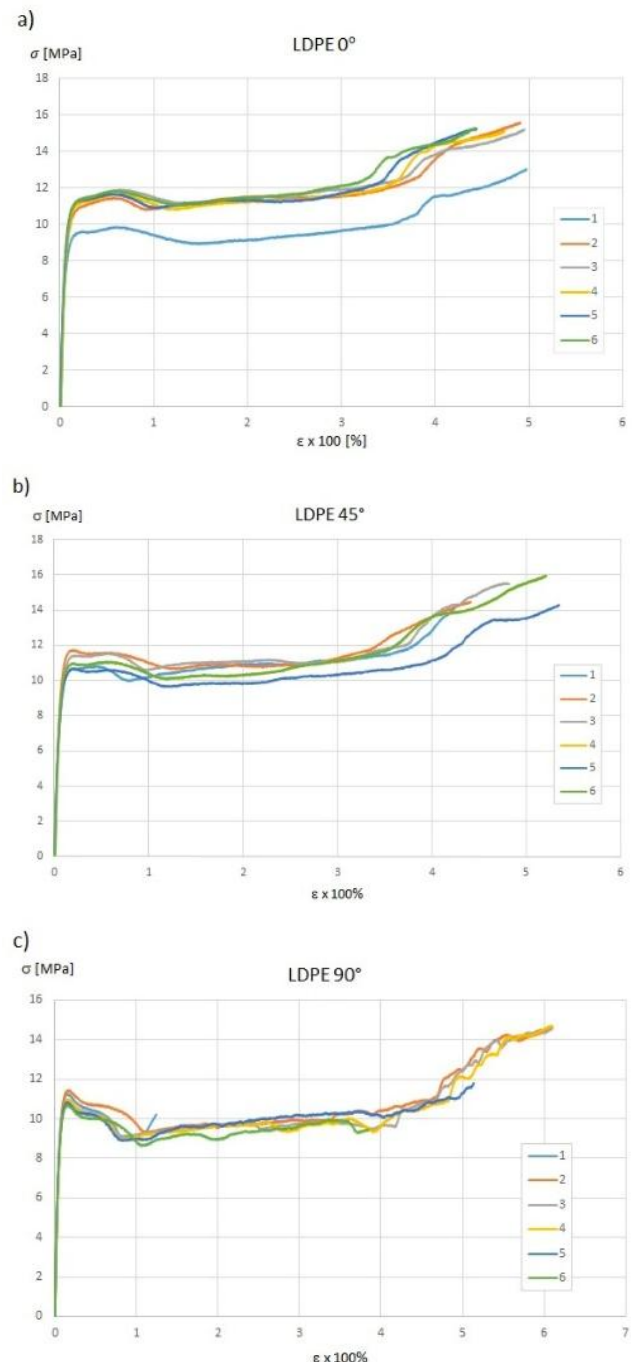


Fig. 3. Static stress σ on relative strain ε for angles: 0°, 45° and 90°

As demonstrated in Figure 3, the fundamental mechanical characteristics, denoted by $\sigma(\epsilon)$, derived from tensile testing of LDPE film strips, reveal no substantial disparities among the selected angular orientations. However, it is noteworthy that substantial strain values for the 90° orientation (where the load is applied perpendicular to the lines visible to the naked eye in the film structure) are accompanied by local fluctuations in both load and strain.

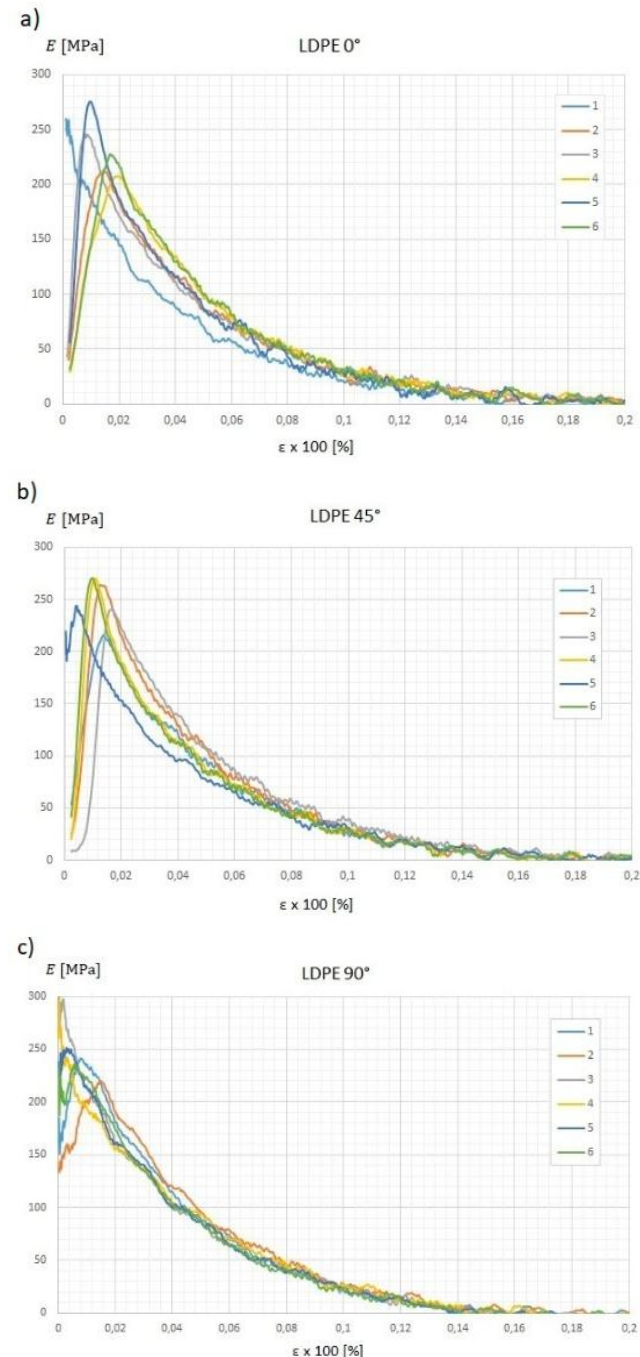


Fig. 4. Static Young's modulus E on relative strain ϵ for angles: 0°, 45° and 90°

The estimated value of the instantaneous Young's modulus suggests a degree of dependence on the loading directions of the samples. However, the observed differences are of negligible practical significance. The total work expended in deforming the

tested LDPE film specimens was calculated and is denoted as the total energy consumed in the deformation work, related to the unit volume of the tested material. The total strain energy index possesses the dimension of specific energy, otherwise known as strain energy density, a quantity frequently utilized in materials science. A thorough examination of the energy characteristics (Fig. 6) reveals that the energy intensity exhibited by the tested LDPE film displays a modest dependence on the selected loading directions. For the 90° orientation, the range varies from approximately 38 mJ/mm³ to approximately 65 mJ/mm³, indicating that the film in the 90° orientation relative to the load exhibits greater variability in specific energy limits.

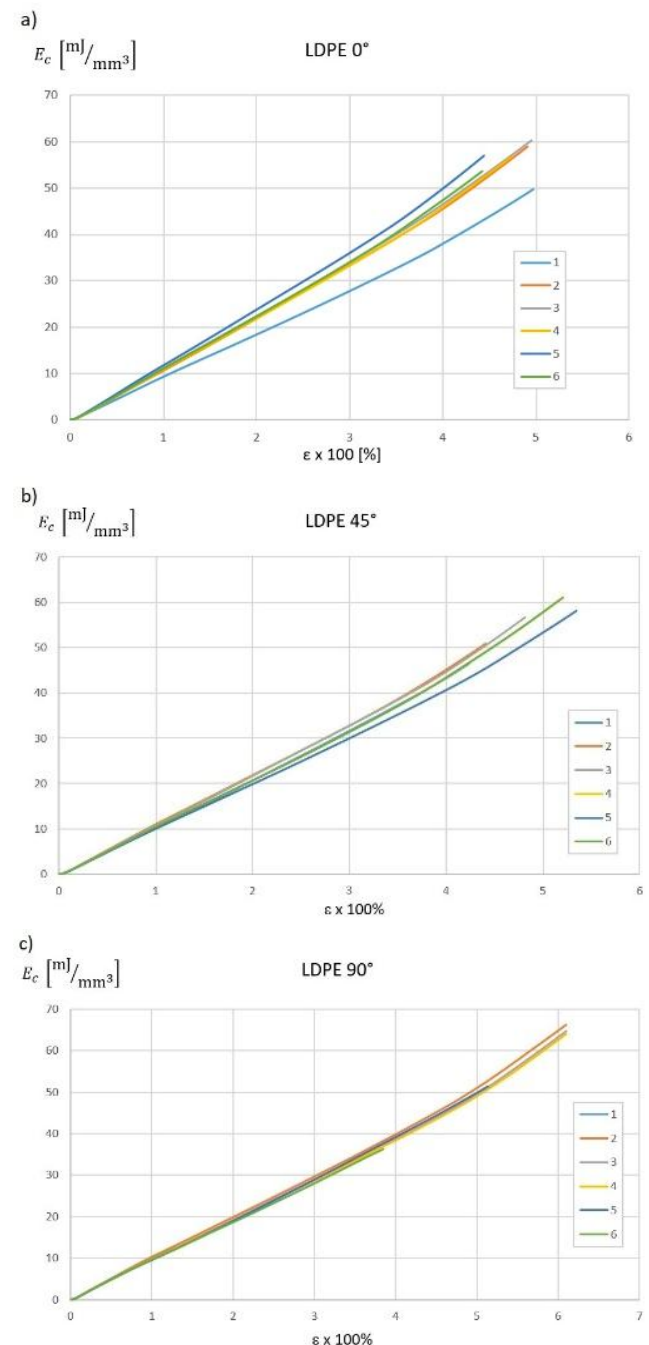


Fig. 5. Static energy density E_c [mJ/mm³] on relative strain ϵ for angles: 0°, 45° and 90°

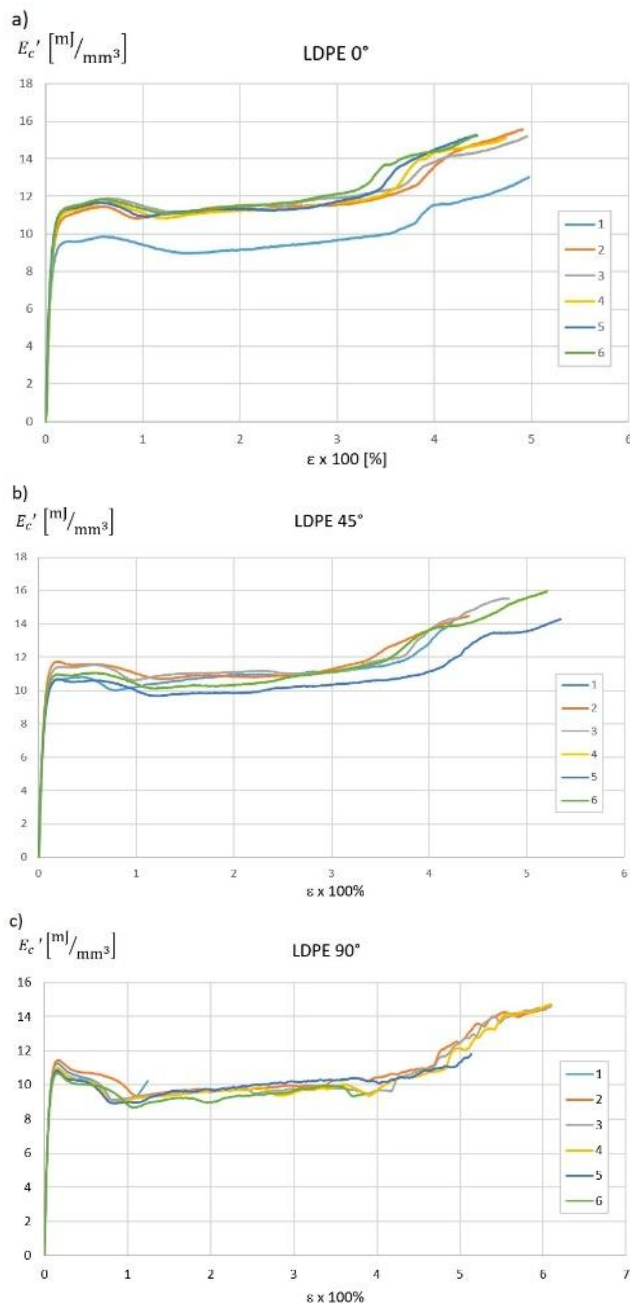


Fig. 6. Volumetric Energy change intensity E_c' [mJ/mm^3] on relative strain ε for angles: 0° , 45° and 90°

2.2. Dynamic impact testing of LDPE film

The dynamic mechanical properties of the tested foil specimens were determined based on the displacement of markers applied to the foil specimens (Fig. 7). The schematic of the test stand designed for impact load testing is shown in Fig. 8.

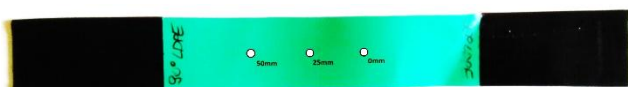


Fig. 7. Strip specimen with three displacement markers of the tested LDPE film

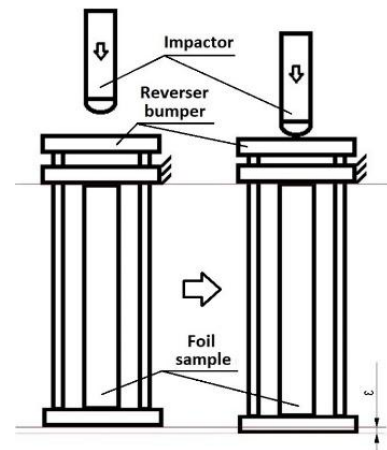


Fig. 8. Schematic of the impact load acting on the LDPE film strip specimen

The test stand employed during the impulse load tests, in conjunction with the drop tower, comprised two masses: the mass of the beater (3.3 kg) descending inertly from heights of 0.5 m, 1 m, and 1.5 m, as well as the mass of the bumper (the mass of the reverser), incorporating the guide rods and jaws that secure the specimen. It was hypothesized that the collision of the steel striker with the steel plate of the reversing bumper would be purely elastic. The kinetic energy of the beater was hypothesized to be transferred to the mass of the reverser, resulting in work done in deforming the tested LDPE tape specimens. The displacements of three markers along the survey section, labeled sequentially as 0 mm, 25 mm, and 50 mm, were recorded with a Chronos 2.1 HD high-speed camera. Subsequent to the aforementioned, a thorough deformation analysis was conducted, and mechanical characteristics were determined in relation to the previously mentioned reference points.

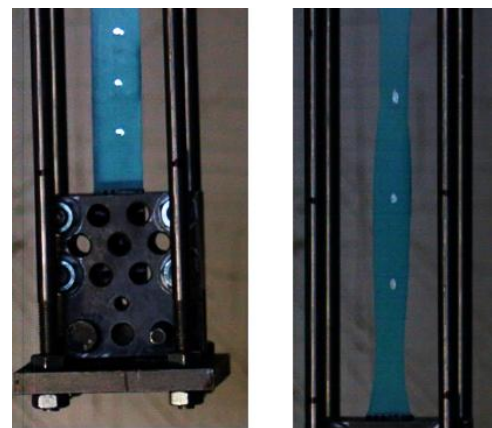


Fig. 9. LDPE film strip specimen under impact load. Initial and final elongation phase for angle 0° and flail drop height equal 1m

The characteristics of $\Delta l(t)$ (see Figures 10-12) were developed for experimental data, and their approximation by a family of modified sinusoidal functions (2.1) was determined.

$$\Delta l(t) = a \cdot \sin^n(bt) \quad (2)$$

where a, b, n are approximation coefficients.

The objective of the approximation was twofold: first, to minimize measurement errors, and second, to provide an analytical representation of the collected results using a function that met the following conditions:

- smoothness,
- differentiability up to the fourth order,
- simple analytical form.

The modified sine function meets these requirements, and the graphs resulting from the approximation are superimposed on those based on the experimental data. The legends on the graphs indicate the measurement segments between the reference points, with the subscript "A" denoting results obtained from the approximation using the modified sine function.

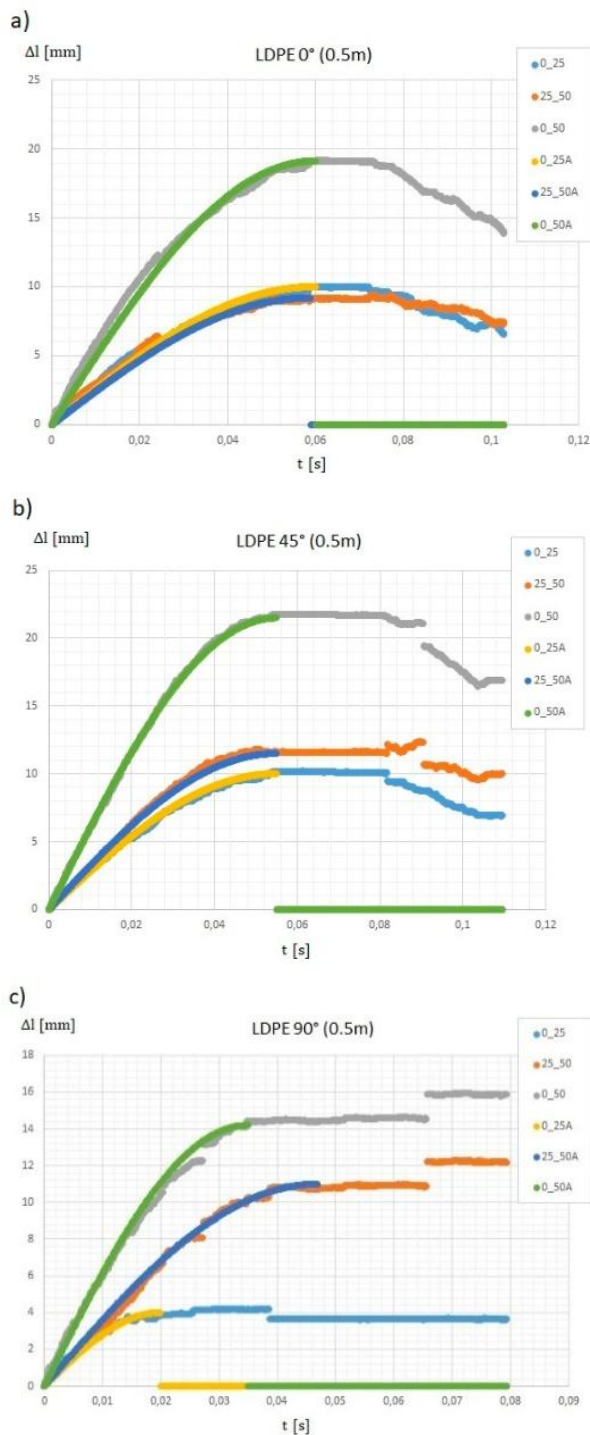


Fig. 10. Dynamic elongation Δl [mm] as a function of time for angles: 0°, 45° and 90° and 0.5m drop height

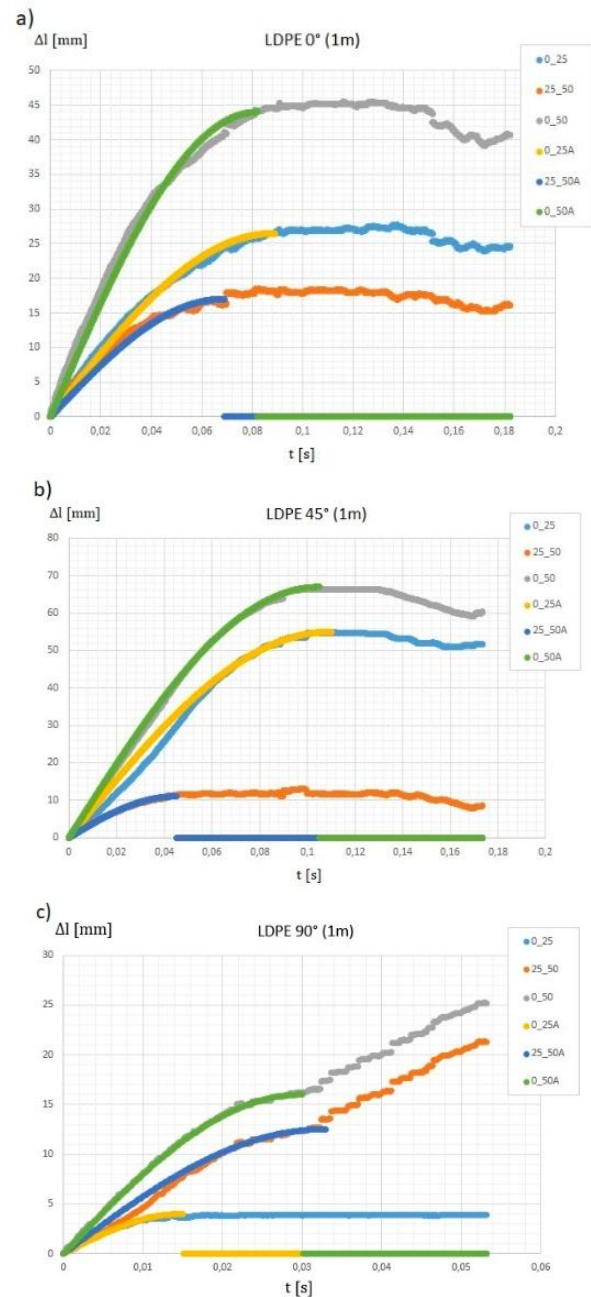
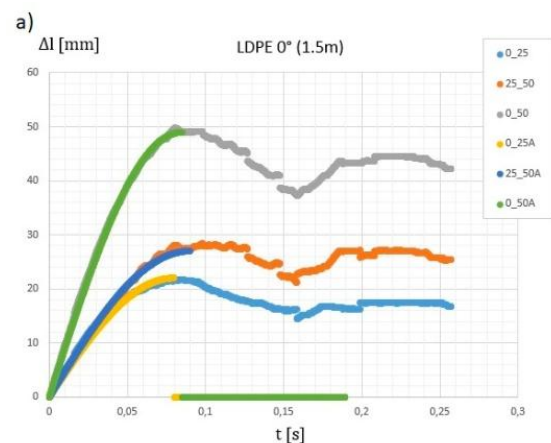


Fig. 11. Dynamic elongation Δl [mm] as a function of time for angles: 0°, 45° and 90° and 1m drop height



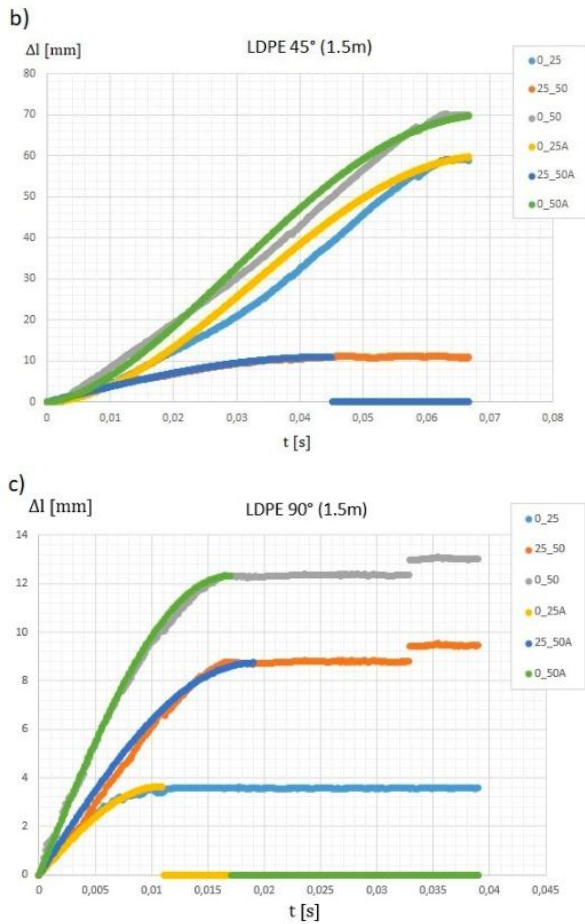


Fig. 12. Dynamic elongation Δl [mm] as a function of time for angles: 0°, 45° and 90° and 1.5m drop height

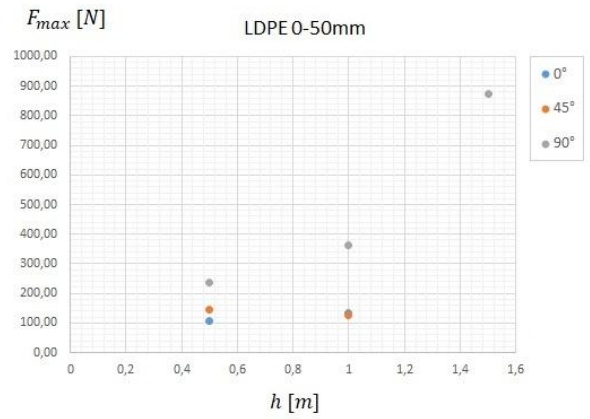


Fig. 13. Impact tension force F [N] as a function of flail drop heights h [m]. Results for angles: 0°, 45° and 90° and three measuring sections 0-25mm, 25-50mm and 0-50mm

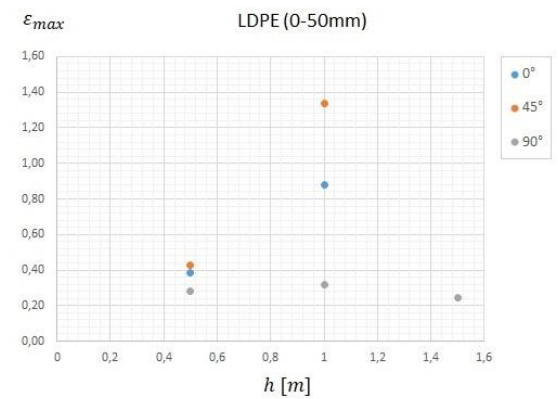
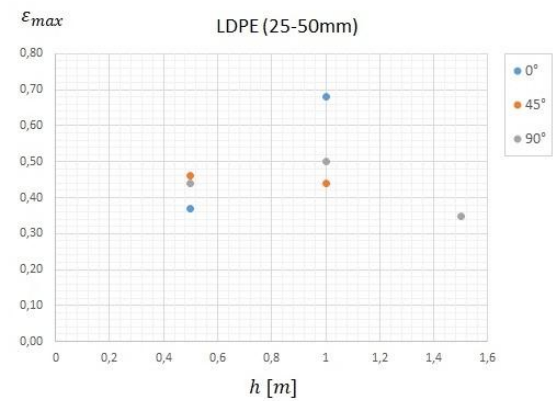
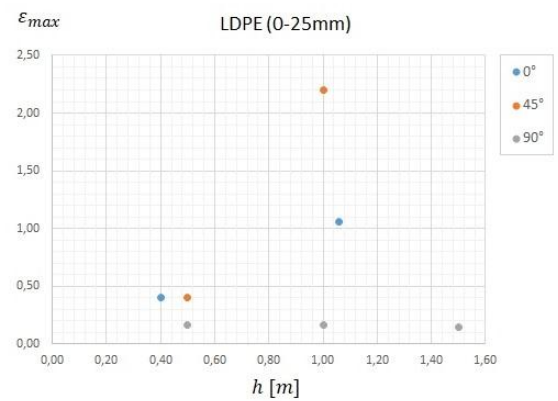


Fig. 14. Relative strain ε as a function of flail drop heights h [m]. Results for angles: 0°, 45° and 90° and three measuring sections 0-25mm, 25-50mm and 0-50mm

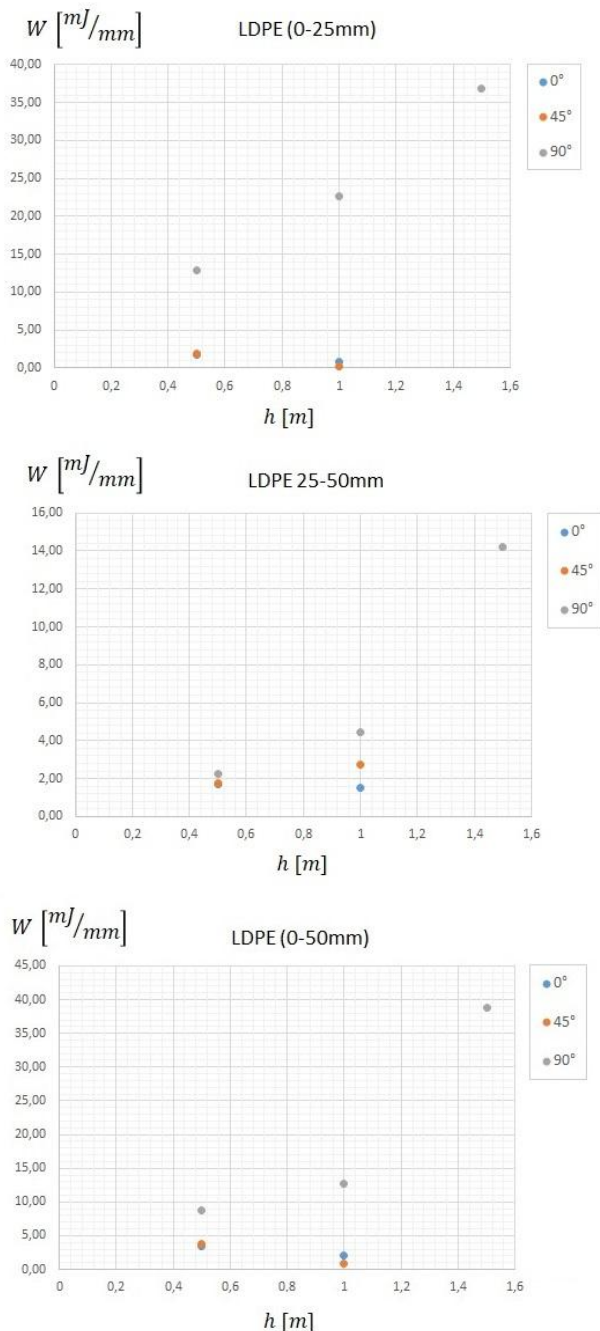


Fig. 15. Work of deformation per unit length W [mJ/mm] as a function of flail drop heights h [m] calculated for $\varepsilon = 0.15$. Results for angles: 0° , 45° and 90° and three measuring sections 0-25mm, 25-50mm and 0-50mm

3. CONCLUSIONS

An investigation was conducted into the static and dynamic characteristics of the mechanical properties of LDPE plastic. The mechanical properties of the tested LDPE film demonstrate a high capacity for deformation and energy absorption, which are used to permanently deform the material. During the static tensile testing of LDPE strips, a discernible local constriction shifted position as the load increased, and multiple zones of plastic flow appeared along the gauge length of the specimen. In impulse-loaded tensile tests, two to three zones of plastic deformation were also observed along

the gauge length of the strip specimen.

In both static and impulse loading cases, the production process of the LDPE film influences its mechanical properties, as evidenced by the dynamic test results. Tests conducted in different orientations revealed differences in deformation mechanisms.

In summary, the following conclusions were derived:


- The production processes employed for plastic films have the capacity to exert an influence on both their static and dynamic properties.
- Testing the mechanical properties of LDPE film in different orientations, influenced by the production processes, can reveal discrepancies in the measured properties.
- A more precise assessment of the material can be achieved through the integration of static tests with impact tests.
- The dynamic properties of LDPE film are contingent upon orientation and impact velocity.
- The deformation work per unit length of the LDPE film varies based on these factors.

The impact strength of the tested LDPE film strips was also found to be relatively high. The obtained results of the mechanical properties of the tested material testify to its advantages and applicability in the area of protection of human security or transportation of sensitive goods. The proposed mechanical characteristics for static and impact loads can be used as diagnostic tools when testing materials and structures. Furthermore, the proposed experimental characterizations can facilitate more precise assessments of the suitability of the tested material or structure for specific practical applications. The author is currently investigating pneumatic absorbers, which are made of LDPE plastic, exhibit exceptional impact energy absorption properties. Research is currently underway on the use of LDPE pneumatic shock absorbers with controlled air flow as inserts for protective helmets. The objective of the present study is to develop a methodology that enables quantitative assessment of the mechanical response of the protective helmet and the human head to impact, with consideration for the mechanical properties of the neck. That is to say, the elements of the system that are in a cause-and-effect correlation with each other. Additionally, the results of rheological tests on both LDPE plastic in the form of films and LDPE pneumatic absorbers are of interest. Rheological studies employing LDPE film samples are currently underway.

REFERENCES

1. Barbosa MF, Souza AMCD. Reusing Surllyn® Ionomer Scraps in LDPE Blends: Mechanical and Thermal Properties. *Mater Res.* 2023; 26 (suppl1): e20230019. DOI:10.1590/1980-5373-mr-2023-0019
2. Kismet Y, Dogan A, Wagner MH. Thermoset powder coating wastes as filler in LDPE – Characterization of mechanical, thermal and morphological properties. *Polym Test.* 2021 Jan;93:106897.
3. Sirin K, Cengel Ö, Canli M. Thermal and mechanical properties of LDPE by the effects of organic peroxides: Mechanical Properties of LDPE. *Polym Adv Technol.* 2017 Jul;28(7):876–85.
4. Peršić A, Popov N, Kratošil Krehula L, Krehula S. The Influence of Different Hematite (α -Fe $2O_3$) Particles on the Thermal, Optical, Mechanical, and Barrier Properties of LDPE/Hematite Composites. *Materials.* 2023 Jan 11;16(2):706
5. Dwivedi UK, Hashmi SAR, Naik A, Joshi R, Chand N. Development and physico-mechanical behavior of LDPE–sisal prepreg-based composites. *Polym Compos.* 2013 May;34(5):650–5.
6. Čech Barabaszová K, Holešová S, Hundáková M, Kalendová A. Tribo-Mechanical Properties of the Antimicrobial Low-Density Polyethylene

- (LDPE) Nanocomposite with Hybrid ZnO–Vermiculite–Chlorhexidine Nanofillers. *Polymers*. 2020 Nov 27;12(12):2811.
7. Janik J. Właściwości mieszanin polimerów termoplastycznych PBT/LDPE. *Przetw Tworzyw*. 2015;21(6 (168)):451–5.
 8. Czarnecka-Komorowska D, Wiszumirska K, Garbacz T. FILMS LDPE/LLDPE MADE FROM POST - CONSUMER PLASTICS: PROCESSING, STRUCTURE, MECHANICAL PROPERTIES. *Adv Sci Technol Res J*. 2018 Sep 1;12(3):134–42.
 9. Ono K, Yamaguchi M. Thermal and mechanical modification of LDPE in single-screw extruder. *J Appl Polym Sci*. 2009 Aug 5;113(3):1462–70.
 10. Sailaja RRN, Seetharamu S. Mechanical and thermal properties of LDPE-cellulose acetate phthalate blends—Effect of maleic anhydride-grafted LDPE compatibilizer. *J Appl Polym Sci*. 2009 Apr 15;112(2):649–59.
 11. Yao Z, Heng JYY, Lanceros-Méndez S, Pegoretti A, Xia M, Tang J, et al. Surface free energy and mechanical performance of LDPE/CBF composites containing toxic-metal free filler. *Int J Adhes Adhes*. 2017 Sep;77:58–62.
 12. Koffi A, Koffi D, Toubal L. Mechanical properties and drop-weight impact performance of injection-molded HDPE/birch fiber composites. *Polym Test*. 2021 Jan;93:106956.
 13. Karthikeyan K, Russell BP, Fleck NA, O'Masta M, Wadley HNG, Deshpande VS. The soft impact response of composite laminate beams. *Int J Impact Eng*. 2013 Oct;60:24–36.
 14. Rana AK, Mandal A, Banerjee AN. Jute sliver-LDPE composites: Effect of aqueous consolidation on mechanical and dynamic properties. *J Appl Polym Sci*. 2000 May 2;76(5):684–9.
 15. Yazdani H, Ghasemi H, Wallace C, Hatami K. Mechanical properties of carbon nanotube-filled polyethylene composites: A molecular dynamics simulation study. *Polym Compos [Internet]*. 2019 Mar [cited 2024 Oct 24];40(S2). Available from: <https://4spepublications.onlinelibrary.wiley.com/doi/10.1002/pc.25175>
 16. Sahraeian R, Esfandeh M, Hashemi SA. Rheological, Thermal and Dynamic Mechanical Studies of the Ldpe/Perlite Nanocomposites. *Polym Polym Compos*. 2013 May;21(4):243–50.
 17. Xu M ming, Huang G yan, Feng S shan, McShane G, Stronge W. Static and Dynamic Properties of Semi-Crystalline Polyethylene. *Polymers*. 2016 Mar 28;8(4):77.
 18. Zhu T, Li X, Zhao X, Zhang X, Lu Y, Zhang L. Stress-strain behavior and corresponding crystalline structures of four types of polyethylene under a wide range of strain rates. *Polym Test*. 2022 Feb;106:107460.
 19. Mohagheghian I, McShane GJ, Stronge WJ. Impact perforation of monolithic polyethylene plates: Projectile nose shape dependence. *Int J Impact Eng*. 2015 Jun;80:162–76.
 20. Sandeep J, Murali V. Low Density Polyethylene/Polymeric Microballon Syntactic Foam: Strain Rate Dependent Compressive Response. *J Polym Mater*. 2017;34(2).
 21. Obst M, Kurpisz D, Jakubowski M. Experimental and Analytical Approaches on Air Spring Absorbers Made of LDPE Polymer. *Acta Mech Autom*. 2024 Jun 1;18(2):314–22.
 22. Drane P, De Jesus-Vega M, Inalpolat M, Sherwood J, Orbey N. Inductive quantification of energy absorption of high-density polyethylene foam for repeated blunt impact. *Proc Inst Mech Eng Part J Mater Des Appl*. 2020 Mar;234(3):531–45.
 23. Sahu DP, Mohanty SC. Static and dynamic analysis of polyethylene terephthalate foam core and different natural fiber-reinforced laminated composite-based sandwich plates through experimental and numerical simulation. *Mechanics of Advanced Materials and Structures*. 2024 Aug 8;1–20.
 24. Sahu DP, Das R, Prusty JK, Mohanty SC. Frequency analysis of skew sandwich plates with polyethylene terephthalate foam-core and carbon/basalt fiber-reinforced hybrid face layers using ANFIS model and experimental validation. *Mechanics of Advanced Materials and Structures*. 2024 Dec 11;1–23.
 25. Sahu DP, Das R, Prusty JK, Mohanty SC. Flexural and dynamic characterization of carbon/basalt hybrid laminated composite sandwich plates with PET foam core: A numerical and experimental approach. *Structures*. 2025 Feb;72:108204.
 26. Antony Vincent V, Kailasanathan C, Ramesh G, Maridurai T, Arun Prakash VR. Fabrication and Characterization of Hybrid Natural Fibre-Reinforced Sandwich Composite Radar Wave Absorbing Structure for Stealth Radomes. *Trans Electr Electron Mater*. 2021 Dec;22(6):794–802.
 27. Das R, Sahu DP, Bisoyi DK. Silane-treated kapok fiber/epoxy composites for aerospace cabin interiors: Synthesis and characterization. *Polymer Composites*. 2024 Dec 6;pc.29359.
 28. Sahu DP, Das R, Mohanty SC. Multiwalled carbon nanotubes filled pineapple/kenaf hybrid laminated composites structures for electromagnetic interface shielding applications. *Polymer Composites*. 2024 Dec 26;pc.29428.

Maciej Obst:  <https://orcid.org/0000-0001-6555-6198>



This work is licensed under the Creative Commons BY-NC-ND 4.0 license.

METAMODEL-BASED INVERSE DESIGN OF A COMPOSITE MATERIAL WITH PRESCRIBED INTERVAL EFFECTIVE ELASTIC PROPERTIES

Witold BELUCH^{*}, Jacek PTASZNY^{*}, Marcin HATŁAS^{*}

^{*}Faculty of Mechanical Engineering,
 Department of Computational Mechanics and Engineering,
 Silesian University of Technology, Konarskiego 18A, 44-100, Gliwice, Poland

witold.beluch@polsl.pl, jacek.ptaszny@polsl.pl, marcin.hatlas@mechadevs.com

received 17 December 2024, revised 17 March 2025, accepted 14 April 2025

Abstract: A problem of inverse design of a composite material with prescribed (desired) interval effective elastic constants is formulated and solved. The identified parameters are the interval parameters of the constituent geometry and material properties on the microscale. Such uncertainty falls into the category of epistemic uncertainty, which is frequent in engineering practice and is caused by incomplete knowledge, not allowing for the stochastic description of quantities of interest. Commercial finite element code Ansys is applied to the computational homogenisation with representative volume element (RVE) analysis. The high-fidelity model is replaced by a finely adjusted polynomial response surface to minimise overall computation time. The response surface is used for the interval computations involved in the identification problem. Directed interval arithmetic is applied. It includes cancellation laws for addition and multiplication and is the preferred method in engineering problems. Objective functions also involve differences between the desired and actual effective interval properties and widths of the identified microstructure parameters. The single- and multi-objective evolutionary algorithms are applied to solve the optimisation tasks. In the identification problem, the interval variables are represented as pairs of real numbers (components of the directed intervals). As numerical examples, two problems concerning a unidirectional fibre-reinforced composite with linear-elastic properties are formulated and solved. The first one employs scalarization by combining the objectives with presumed weights. In the second, a more extensive Pareto-frontier approach is considered. The proposed approaches provide feasible solutions to identification problems and provide perspectives for their extension to efficient solutions of more complex ones with epistemic uncertainty: fuzzy representation of uncertain parameters, nonlinear inhomogeneous materials, and others.

Key words: inverse design, computational homogenisation, directed interval arithmetic, response surface, evolutionary algorithm

1. INTRODUCTION

The design of new engineering materials allows for filling holes in the macroscopic property-space maps. These new materials include particulate and fibrous composites, sandwich structures, foams, lattice structures and others [1]. The components of these new materials are described by their properties and shape on a lower (e.g. micro) scale. One can evaluate the macroscopic properties, mechanical or other, of non-homogeneous materials using homogenisation methods. Computational methods, mainly finite and boundary element methods, have gained increasing attention from engineers and researchers due to their versatility also in the problems of multiscale modelling and homogenization [2,3,4,5]. The homogenisation problems consist of the evaluation of effective properties (e.g. elastic) of non-homogeneous materials on the macro scale. The problem involves a solution to the boundary value problem (BVP) at the microscale: simulation of a representative volume element (RVE) with given microstructural topology and parameters. On the other hand, one can formulate and solve an inverse problem to identify the microstructure topology and parameters, based on the macroscopic properties of homogenized material [6,7]. Among the crucial factors related to the analysis of heterogeneous engineering materials, uncertainties are currently of interest due to their impact on the precise design and manufacturing of such

structures. Therefore, the development of computational approaches capable of dealing with uncertainties is crucial for the successful design and manufacturing of new materials.

Observed uncertainty falls into one of two categories: aleatoric or epistemic [8,9]. Aleatoric uncertainty is natural, random, and irreducible. Epistemic uncertainty is due to incomplete scientific knowledge and can be reduced by new insights. From the probability point of view, the uncertainty of engineering quantities can be grouped into stochastic uncertainty (known probability), incertitude (unknown probability) or ignorance (fixed values). A very common in engineering problems, including up-to-date experimental material characterisation methods, e.g. [10], is the second category (incertitude) which includes cases of intervals and fuzzy numbers. From the point of view of information processing, this representation of quantities is also known as information granularity [11,12,13]. In engineering practice, this representation is useful in the situation of insufficient data availability that does not allow the engineer to describe the process as stochastic. In the context of modelling, another classification of uncertainty can be introduced: uncertainty induced by data, component (model uncertainty), and structure (structural uncertainty) [9,14]. In general, incertitude uncertainties in geometry, material properties, loading, and boundary conditions significantly affect structural analysis, introducing variability in performance estimations, leading to potential inaccuracies [15]. By including imperfect data in the quantification of uncertainty,

more reliable and relevant results can be obtained that better reflect the complexity and uncertainty present in real-world conditions. Note that in the case of metamodel-based computational homogenization preparation stage, the boundary conditions or loading for the RVE with uncertain parameters (geometry, material parameters and phase bonding conditions) can be precise as they are driven by the homogenization procedure that imposes macro strains (or stresses) and their increments for non-linear structures. However, at the possible latter stage of analysing a macro-structure, that is beyond the scope of the present work, the transferred macro strains or stresses to the RVE as boundary conditions can be uncertain due to all macro-structure uncertainties under consideration.

Recently, researchers have considered the incertitude uncertainty to be of practical importance in engineering problems, including homogenisation and multi-scale modelling. One of the basic approaches applied to numerical modelling of mechanical and micro-mechanical structures with incertitude properties is the interval and fuzzy finite element method. Note that its efficiency is deteriorated by an amount of conservatism (overestimation of the uncertainty in the output) due to the interval matrix assembly phase [16]. In [17], 2D composite structures were analysed, with the application of Taylor expansions of effective elasticity matrices, with sensitivity analysis. In [18], stochastic FEM was applied to the analysis of the random RVE, to determine the respective limits and evaluate fuzzy Young's modulus of a composite material. The modulus was applied to the dynamic simulation of multi-body structures to obtain fuzzy response curves. In [19], a fuzzy RVE was introduced that allows one to consider the spatial variability of the ply level of the ply level in laminates. Fuzzy FEM is coupled with the radial basis functions metamodel. Global responses in dynamics and stability problems were solved. In [20] fuzzy numbers were applied to the computational homogenisation of composite materials with fuzzy microstructure parameters.

One can observe that the recent approach to the solution of the BVP on a micro scale in complex problems involving homogenisation and multi-scale modelling, becomes the shift of the RVE numerical modelling to the offline stage, outside the main loop of the procedure under consideration: multiscale simulation, optimisation or identification. This preliminary stage prepares data and creates model for metamodeling or a data-driven approach. Such an approach employs metamodels (surrogates) built based on observations computed by high-fidelity numerical models, usually analysed by the FEM. The metamodels include polynomial response surfaces [20], radial-basis functions [19,21], Kriging [22,23], artificial neural networks [24], combined analytical-numerical metamodels [25], and possibly others. Such an approach leads to a substantial reduction in the overall computation time compared to the traditional approach based on in-loop time-consuming simulations of the RVE. The approach with offline metamodel-based RVE simulations also has potential advantages in the inverse problems involving incertitude uncertainties, due to the substantial number of calculations related to the interval arithmetic.

The goal of the present work is to formulate and solve a novel problem of inverse design of composite materials with desired incertitude (interval) macroscopic properties and incertitude micro-structure unknown data. To solve the problem efficiently, the metamodeling approach is applied with appropriate design of experiment (DoE) for numerical calculations based on a high-fidelity finite element method model built in Ansys software. The DoE takes into account the admissible ranges of geometry and material parameters of the microstructure of the composite. The minimised objective function is dependent on the desired bounds of the

macroscopic elastic properties of the designed material. In some situations, e.g. manufacturing, it may be more convenient to have wider ranges of input microstructure parameters. Therefore, these ranges are also incorporated into objectives. For interval analysis, directed interval arithmetic is applied, which is considered efficient in solving engineering problems due to its feature of including cancellation laws for both addition and multiplication [26,27,28,29,30]. In identification problems, the interval parameters are represented as pairs of real numbers (components of the directed intervals). Such an approach allows for the application of regular evolutionary algorithms for real variables. The inverse problem is solved by both approaches of scalarization with presumed weights for objective functions, and the Pareto frontier approach as well. A problem concerning unidirectional fibre-reinforced composite is solved and results are presented. While similar methodologies for computational homogenization are documented in the literature, we believe that no corresponding solutions of inverse design problems for inhomogeneous materials with epistemic incertitude structural parameters, including the multi-objective identification (optimization) approach, have been reported.

The paper is organised as follows: Section 2 contains an introduction to computational homogenisation and related inverse problem as well as the design of the experiment and the description of applied metamodels. Section 3 introduces the notation and operators of interval arithmetic and directed interval arithmetic. In Section 4 the idea and formulation of the inverse problem involving computational homogenisation with incertitude input parameters of the microstructure and desired incertitude of the effective elastic constants are presented. In Section 5, numerical examples are solved with the approaches of weighted objective functions and the Pareto frontier. Section 6 contains conclusions.

2. COMPUTATIONAL HOMOGENISATION AND INVERSE DESIGN USING METAMODELS

Multiscale modelling allows the structure to be modelled at different length scales. One of the elements of multiscale modelling that enables the analysis of heterogeneous materials, such as composites or porous materials, at the microscale is homogenisation. Among the different homogenisation methods, computational homogenisation is the most versatile [2].

Computational homogenisation [31] allows equivalent macroscopic material properties to be calculated from microscopic data. The basic idea of computational homogenisation is to represent the microstructure of a material by a statistically representative piece of its geometry, called a representative volume element (RVE). Stress analysis for RVE provides detailed information about the material's macro-scale behaviour. The analysis can be carried out using numerical methods such as the finite element method (FEM) [32] or the boundary element method (BEM) [33].

The RVE represents the structure of the entire medium (or a portion of it in the case of local periodicity) and thus contains all the information required to fully describe both the structure and properties of that medium. The RVE must satisfy the scale separation condition, the Hill Mandel condition, and the imposed boundary conditions [34].

The separation of scales condition assumes that the RVE geometry must be of an appropriate size:

$$l_{micro} \ll l_{RVE} \ll l_{macro} \quad (1)$$

where l_{micro} , l_{RVE} and l_{macro} are characteristic microscale, RVE

scale and macroscale dimensions, respectively.

The Hill-Mandel condition describes the equality of the average energy density at the microscale and the macroscopic energy density at the macrostructure point corresponding to the RVE location:

$$\langle \sigma_{ij} \varepsilon_{ij} \rangle = \langle \sigma_{ij} \rangle \langle \varepsilon_{ij} \rangle, \quad (2)$$

where: σ_{ij} , ε_{ij} are the components of the stress and strain tensors respectively, $\langle \cdot \rangle$ is the averaged value of the considered field:

$$\langle \cdot \rangle = \frac{1}{|V|} \int_V (\cdot) dV, \quad (3)$$

where V is the RVE volume.

Boundary conditions have to satisfy the Hill-Mandel condition, e.g. in the form of periodic, linear displacement, or uniform traction boundary conditions. In this paper, the periodic boundary conditions are used:

$$\begin{aligned} u_i^+ - u_i^- &= \langle \varepsilon_{ij} \rangle \cdot (x_i^+ - x_i^-), \quad \forall x \in \Gamma: n_i^+ = -n_i^- \\ t_i^+ &= -t_i^-, \quad \forall x \in \Gamma: n_i^+ = -n_i^- \end{aligned}, \quad (4)$$

where u_i^+ , u_i^- are displacements of the corresponding points at the opposite RVE boundaries, x_i^+ , x_i^- represent locations of the corresponding points at the opposite RVE boundaries, t_i^+ , t_i^- are tractions on the corresponding points at the opposite RVE boundaries, Γ is the external boundary of RVE, n_i^+ , n_i^- are normal vectors at the opposite RVE boundaries.

Periodic boundary conditions allow for the determination of equivalent material properties with greater accuracy and with fewer internal inclusions or voids in the RVE than displacement and traction boundary conditions [35].

A heterogeneous material is usually assumed to consist of two or more homogeneous phases that obey the laws of continuum mechanics. In this paper, it is assumed that there is an ideal contact between the phases. The behaviour of an elastic body made of a linear isotropic material (single phase) under external loads is described by [36]:

– geometrical relations:

$$\varepsilon_{ij} = \frac{1}{2} (u_{i,j} + u_{j,i}), \quad (5)$$

– constitutive law (Hooke's law):

$$\sigma_{ij} = \lambda \delta_{ij} \varepsilon_{kk} + 2G \varepsilon_{ij}, \quad (6)$$

– equilibrium equations:

$$\sigma_{i,j,j} + b_i = 0, \quad i, j = 1, 2, 3, \quad (7)$$

where u_i represents the components of the displacement tensor, λ is the Lamé's parameter, δ_{ij} is the Kronecker's delta, G is the Kirchhoff modulus and b_i denotes the volume forces.

Using Equations (5) and (6), the equilibrium equations expressed by displacements (Navier-Lamé equations) are obtained:

$$G u_{i,j,j} + (G + \lambda) \lambda u_{j,j,i} + b_i = 0. \quad (8)$$

For linear elastic materials, there is no need to analyse the RVE for each point in the macrostructure, and equivalent material properties can be calculated prior to analysing the macroscopic model. In order to obtain equivalent properties, described by a fourth-order material tensor, a series of RVE analyses must be performed with specific boundary conditions.

For a homogenised orthotropic material, 6 analyses allow the calculation of 9 stiffness coefficients C representing stress-strain relationship. In this case, Eq. (6) can be written using the Voigt

notation as [37]:

$$\begin{bmatrix} \langle \sigma_{11} \rangle \\ \langle \sigma_{22} \rangle \\ \langle \sigma_{33} \rangle \\ \langle \sigma_{23} \rangle \\ \langle \sigma_{13} \rangle \\ \langle \sigma_{12} \rangle \end{bmatrix} = \begin{bmatrix} C_{11} & C_{12} & C_{13} & 0 & 0 & 0 \\ & C_{22} & C_{23} & 0 & 0 & 0 \\ & & C_{33} & 0 & 0 & 0 \\ & & & C_{44} & 0 & 0 \\ & sym & & & C_{55} & 0 \\ & & & & & C_{66} \end{bmatrix} \begin{bmatrix} \langle \varepsilon_{11} \rangle \\ \langle \varepsilon_{22} \rangle \\ \langle \varepsilon_{33} \rangle \\ 2\langle \varepsilon_{23} \rangle \\ 2\langle \varepsilon_{13} \rangle \\ 2\langle \varepsilon_{12} \rangle \end{bmatrix}. \quad (9)$$

The problem of determining the values of microscopic properties for given macroscopic data is known as the inverse design [6,7]. The inverse design belongs to a group of ill-posed problems as different sets of microscopic parameters can fulfil the assumed macroscopic values. One of the techniques for solving common inverse design problems is the use of optimisation methods. Due to the presence of a large number of local extremes of the objective functions, global optimisation methods, such as evolutionary algorithms, artificial immune systems, particle swarm, and ant colony algorithms, are recommended [38]. In this paper, evolutionary algorithms (EAs) are applied to solve the inverse design problem [39].

The inverse design problem can be described as a constrained optimisation task:

$$g(\mathbf{p}) = \|C_{ij}(\mathbf{p}) - C_{ij}^*\| \rightarrow \min, \quad (10)$$

where \mathbf{p} is a vector of design variables, $g(\mathbf{p})$ is an objective function, $C_{ij}(\mathbf{p})$ are elastic constants dependent on the design variables, C_{ij}^* denotes required stiffness coefficients and $\|\cdot\|$ is a matrix Euclidean norm.

Due to manufacturing and material property constraints, optimisation constraints are related to design variables:

$$b_i^L \leq p_i^{-,+} \leq b_i^U, \quad i = 1, 2, \dots, n, \quad (11)$$

where n is the number of design variables, \mathbf{b}^L and \mathbf{b}^U are vectors of lower and upper design variable constraints, respectively:

$$\mathbf{b}^{LU} = [\mathbf{b}^L \ \mathbf{b}^U] = \begin{bmatrix} b_1^L & b_1^U \\ b_2^L & b_2^U \\ \vdots & \vdots \\ b_n^L & b_n^U \end{bmatrix}. \quad (12)$$

Solving an inverse design problem requires multiple calculations of the objective function(s) value. This is particularly time-consuming when FEM is used to solve the boundary value problem. A way to reduce computational costs may be to use response surfaces (RS) as the metamodel [40].

The use of RS allows the highly nonlinear behaviour of the structure to be modelled, without the need to perform complex mathematical operations on the system matrices. RS is generated from precomputed sets of output parameters. The RS constitutes an approximate parametric model of the original system created from a precomputed set of models with different input parameter values. The quality of RS strongly depends on the shape of the exact response function being approximated, the number of data points, and the volume of the design space in which the model is built. To reduce the number of cases required for evaluation, an appropriate design of experiment (DoE) based on the type of expected response and the proposed RS should be used [41].

Then, the calculated values of the output parameters are used to compute RS.

This paper adopts the 2nd order polynomial method as RS. This method uses an enhanced quadratic form to represent the relationship between inputs and outputs and is suitable for optimisation

problems because of the generation of smooth functions with a single extremum.

The work assumes a very exact fit of the metamodel, and the uncertainty of its parameters is ignored. As a result, only the uncertainty associated with the design variables is considered.

Once the RS has been created, an assessment of its quality should be carried out to ensure that the values of the output parameters are correctly represented. In the paper the coefficient of determination R^2 , the predicted residual error sum of squares $PRESS$ and the standard error of the estimate σ_{est} quality metrics are used to assess the quality of RS.

3. DIRECTED INTERVALS AND DIRECTED INTERVAL ARITHMETIC

If the parameters of the system are not precisely determinable, they may be treated as uncertain and modelled as information granules [13]. In mechanical systems, uncertainties typically arise from both design and manufacturing processes. The most widely used granularity models for such uncertainties are rough sets, interval numbers, fuzzy numbers, and random variables.

GrC can be introduced into both the numerical homogenisation and inverse design procedures considered in the paper. Uncertainties that can be used as model parameters can relate to geometry, material properties, loads, or boundary conditions. As a result of the analysis, ranges of estimated quantity values can be obtained. When a specific range of parameter values is known, the interval numbers allow the representation of uncertainty.

Interval arithmetic is based on the interval representation of a single number [42]:

$$\bar{a} = [a^-, a^+] = \{a \in \mathbb{R} : a^- \leq a \leq a^+\}, \quad (13)$$

where a^- and $a^+ \in \mathbb{R}$ are left and right ends of the interval \bar{a} . The central value of the interval is calculated as follows:

$$c_w(\bar{a}) = \text{mean}(a^-, a^+). \quad (14)$$

In the case where $a^- = a^+$, the interval is called degenerate. Classical interval arithmetic is based on simple arithmetic for real numbers, which is extended to interval numbers. This results in the following operations on interval numbers: addition, subtraction, multiplication, division, multiplication by a scalar, and the inverse of an interval [43].

The main drawback of classical interval arithmetic is the lack of operations opposite to addition and inverse to multiplication [44]. As a result, e.g. when solving interval systems of equations, a widening of the intervals occurs. This effect can be significantly reduced by using directed interval numbers and directed interval arithmetic.

A directed interval number is defined as an ordered pair of real numbers:

$$\bar{a} = [a^-, a^+] = \{a \in \mathbb{D} : a^-, a^+ \in \mathbb{R}\}, \quad (15)$$

where $\mathbb{D} = \mathbb{P} \cup \mathbb{I}$ is a set of all proper \mathbb{P} and all improper \mathbb{I} interval numbers with real ends [27].

The directed interval numbers are proper if $a^- < a^+$ and improper if $a^- \geq a^+$. Additionally, the set $\mathbb{Z} = \mathbb{Z}_{\mathbb{P}} \cup \mathbb{Z}_{\mathbb{I}}$ contains all directed intervals with element 0:

$$\begin{aligned} \mathbb{Z}_{\mathbb{P}} &= \{\bar{a} \in \mathbb{P} : a^- \leq 0 \leq a^+\} \\ \mathbb{Z}_{\mathbb{I}} &= \{\bar{a} \in \mathbb{I} : a^+ \leq 0 \leq a^-\} \end{aligned} \quad (16)$$

Each interval in set \mathbb{D} has two functionals [40]:

– the 'direction' functional:

$$\tau(\bar{a}) = \begin{cases} +, & \text{if } a^- \leq a^+ \\ -, & \text{if } a^- > a^+ \end{cases}, \quad (17)$$

– the 'sign' functional:

$$\forall \bar{a} \in \mathbb{D} \setminus \mathbb{Z} \quad \sigma(\bar{a}) = \begin{cases} +, & \text{if } a^-, a^+ > 0 \\ -, & \text{if } a^-, a^+ < 0 \end{cases}. \quad (18)$$

These functionals determine the result of an arithmetic operation performed on two directed intervals. Based on these, basic operations in directed interval arithmetic are defined as:

– addition:

$$\forall \bar{a} \in \mathbb{D} \quad \bar{a} + \bar{b} = [a^- + b^-, a^+ + b^+], \quad (19)$$

– subtraction:

$$\forall \bar{a} \in \mathbb{D} \quad \bar{a} - \bar{b} = [a^- - b^+, a^+ - b^-], \quad (20)$$

– multiplication:

$$\bar{a} \cdot \bar{b} = \begin{cases} [a^{-\sigma(\bar{b})} \cdot b^{-\sigma(\bar{a})}, a^{\sigma(\bar{b})} \cdot b^{\sigma(\bar{a})}], & \bar{a}, \bar{b} \in \mathbb{D} \setminus \mathbb{Z} \\ [a^{\sigma(\bar{a})\tau(\bar{b})} \cdot b^{-\sigma(\bar{a})}, a^{\sigma(\bar{a})\tau(\bar{b})} \cdot b^{\sigma(\bar{a})}], & \bar{a} \in \mathbb{D} \setminus \mathbb{Z}, \bar{b} \in \mathbb{Z} \\ [a^{-\sigma(\bar{b})} \cdot b^{\sigma(\bar{b})\tau(\bar{a})}, a^{\sigma(\bar{b})} \cdot b^{\sigma(\bar{b})\tau(\bar{a})}], & \bar{a} \in \mathbb{Z}, \bar{b} \in \mathbb{D} \setminus \mathbb{Z} \\ [\min\{a^- \cdot b^+, a^+ \cdot b^-\}, \max\{a^- \cdot b^-, a^+ \cdot b^+\}], & \bar{a}, \bar{b} \in \mathbb{Z}_{\mathbb{P}} \\ [\max\{a^- \cdot b^-, a^+ \cdot b^+\}, \min\{a^- \cdot b^+, a^+ \cdot b^-\}], & \bar{a}, \bar{b} \in \mathbb{Z}_{\mathbb{I}} \\ \bar{0}, & (\bar{a} \in \mathbb{Z}_{\mathbb{P}}, \bar{b} \in \mathbb{Z}_{\mathbb{I}}) \cup (\bar{a} \in \mathbb{Z}_{\mathbb{I}}, \bar{b} \in \mathbb{Z}_{\mathbb{P}}) \end{cases}, \quad (21)$$

– division ($0 \notin [b^-, b^+]$):

$$\frac{\bar{a}}{\bar{b}} = \begin{cases} [a^{-\sigma(\bar{b})}/b^{\sigma(\bar{a})}, a^{\sigma(\bar{b})}/b^{-\sigma(\bar{a})}], & \bar{a}, \bar{b} \in \mathbb{D} \setminus \mathbb{Z} \\ [a^{-\sigma(\bar{b})}/b^{-\sigma(\bar{b})\tau(\bar{a})}, a^{\sigma(\bar{b})}/b^{-\sigma(\bar{b})\tau(\bar{a})}], & \bar{a} \in \mathbb{Z}, \bar{b} \in \mathbb{D} \setminus \mathbb{Z} \end{cases}. \quad (22)$$

The symbols σ and $-\sigma$ occurring in the superscript determine which end of the interval appears in the formula depending on whether it is a proper or improper number. Specifically, $-\sigma$ changes the particular end from left to right or vice versa.

The directed interval arithmetic defines two additional operators:

– opposite of addition:

$$\forall \bar{a} \in \mathbb{D} \quad -_{\mathbb{D}} \bar{a} = [-a^-, -a^+], \quad (23)$$

– inverse of multiplication:

$$\forall \bar{a} \in \mathbb{D} \setminus \mathbb{Z} \quad 1/_{\mathbb{D}} \bar{a} = [1/a^-, -1/a^+], \quad (24)$$

which allow determining two additional directed operations:

– directed subtraction:

$$\forall \bar{a}, \bar{b} \in \mathbb{D} \quad \bar{a} -_{\mathbb{D}} \bar{b} = [a^- - b^-, a^+ - b^+], \quad (25)$$

– directed division:

$$\bar{a}/_{\mathbb{D}} \bar{b} = \begin{cases} [a^{-\sigma(\bar{b})}/b^{-\sigma(\bar{a})}, a^{\sigma(\bar{b})}/b^{\sigma(\bar{a})}], & \bar{a}, \bar{b} \in \mathbb{D} \setminus \mathbb{Z} \\ [a^{-\sigma(\bar{b})}/b^{\sigma(\bar{b})}, a^{\sigma(\bar{b})}/b^{\sigma(\bar{b})}], & \bar{a} \in \mathbb{Z}, \bar{b} \in \mathbb{D} \setminus \mathbb{Z} \end{cases}. \quad (26)$$

As a result, the $\bar{a} -_{\mathbb{D}} \bar{a} = \bar{0}$ and $\bar{a}/_{\mathbb{D}} \bar{a} = \bar{1}$ operations can be obtained. These operations allow the efficient application of arithmetic operations of subtraction and division with a significant decrease in unwanted interval widening [44]. Moreover, the difference of the interval numbers appearing in the objective function can take a value close to or equal to 0, which is advantageous in optimisation problems where the width of this difference can be minimised.

4. GRANULAR COMPUTATIONAL INVERSE DESIGN

In this paper, a granular approach is proposed to perform homogenisation and inverse design for inhomogeneous materials with uncertainties of their microstructure parameters. The Granular Computational Homogenisation (GCH) procedure is applied to perform the inverse design. The first step of GCH is related to the analysis of the material structure and available property data. On the basis of the microstructure of the material, a geometrical model of the structure (RVE) is prepared which is transferred to the FEM software. Material property data are used to create a numerical model of the microstructure, including the constitutive relationships. The decision about the geometry and the treatment of individual material properties as certain or uncertain results in input parameters for the GCH procedure. The number of identified parameters affects the number of sample calculations in the DoE phase. The GCH procedure, together with numerical examples showing homogenisation results for granular linear and nonlinear heterogeneous materials, is described in detail in the previous publication [20].

The Granular Computational Inverse Design (GCID) problem is related to the search for ranges of properties of the model on the micro scale that result in a specific material behaviour on the macro scale. The problem is formulated as an optimisation task using granular computing and can be described as:

$$\begin{cases} \text{minimise } f_g(\bar{\mathbf{p}}) \\ \text{subject to: } b_i^- \leq p_i^- \leq b_i^+, i = 1, 2, \dots, n \end{cases} \quad (27)$$

To create the objective function for the optimisation algorithm, the resulting interval stiffness coefficients are used to assess the consistency with the assumed uncertain values of the material properties. The measure of mismatch (distance) between two interval numbers is described by the norm:

$$D([a^-, a^+], [b^-, b^+]) = \sqrt{(a^- - b^-)^2 + (a^+ - b^+)^2}. \quad (28)$$

This representation allows for a continuous and smooth objective function. The objective function for linear-elastic material properties is described by:

$$f_k(\bar{\mathbf{p}}) = f[D(\bar{C}_{ij}(\bar{\mathbf{p}}) - \bar{C}_{ij}^*)], \quad (29)$$

where $\bar{C}_{ij}(\bar{\mathbf{p}})$ is an interval function of stiffness coefficient based on RS, \bar{C}_{ij}^* is an assumed output interval of stiffness coefficient, $f_k(\bar{\mathbf{p}})$ is a function describing the k -th optimisation objective in multi-objective problems.

An additional objective of material optimisation is related to the current width of the design variables:

$$w(\bar{p}_i) = |p_i^+ - p_i^-|. \quad (30)$$

A larger uncertainty width of the optimised design variables makes it easier to find a material with properties that meet the specified values. For multiple design variables, the widths of the parameters can vary considerably. To provide an equivalent treatment of the parameters, width normalisation is introduced. The normalized width $w'(\bar{p}_i)$ of interval parameter \bar{p}_i is described as:

$$w'(\bar{p}_i) = \frac{w(\bar{p}_i)}{b_i^+ - b_i^-}, \quad (31)$$

In the optimisation process, the minimum normalized width of all parameters is maximized:

$$f_k(\bar{\mathbf{p}}) = \min_{p_i} w'(\bar{p}_i) \rightarrow \max, i = 1, \dots, n, \quad (32)$$

where n is a number of design variables.

To solve optimisation tasks, global optimisation algorithms in the form of evolutionary algorithms are employed. For a single-objective optimisation task, the distributed evolutionary algorithm (DEA) is applied [45]. DEA is based on the concept of coevolutionary algorithms, where an entire population of individuals is divided into two or more subpopulations, usually with an identical number of individuals in each. Each subpopulation evolves almost independently, exchanging information with other subpopulations during the migration phase. DEA has been shown to be highly efficient and effective in many optimisation problems [38].

To solve a multi-objective optimisation problem, the MOOPTIM (MultiObjective OPTIMization tool) algorithm [46] is used. The algorithm is based on Pareto concept, and it allows one to obtain a set on non-dominated solutions. MOOPTIM is an improved version of NSGA-II [47] with different selection and new as well as modified mutation and crossover operators. As presented in [48], MOOPTIM outperforms NSGA-II in some benchmark and engineering problems, especially for functions difficult to optimise, that is, strongly multimodal, with a non-convex or discontinuous Pareto front. To assess the quality of the resulting Pareto front, a weighted hypervolume indicator [49] is used.

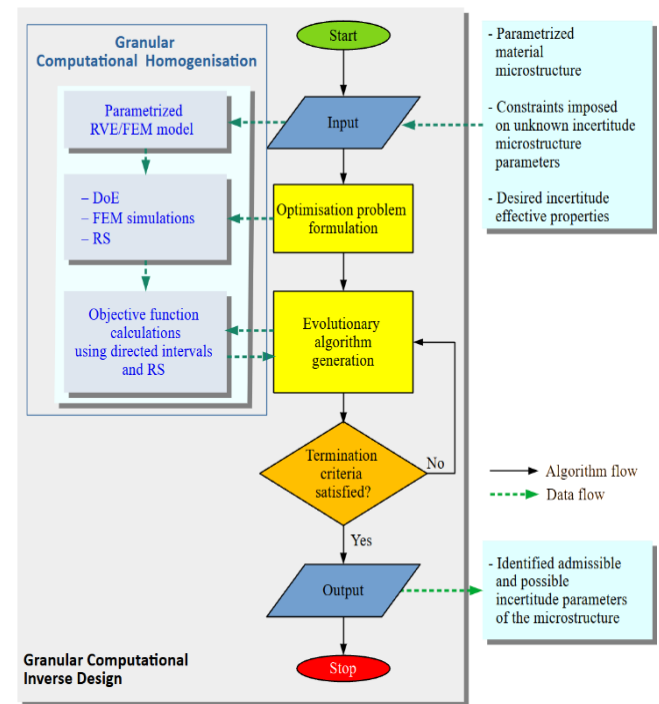


Fig. 1. Granular Computational Inverse Design scheme

The concept of GCID is illustrated in Fig. 1. In the first step, the optimisation problem is formulated (number of design variables, number of stiffness coefficients considered, constraints on the variables, number of criteria). Based on this information, an optimisation approach (use of a single- or multi-objective algorithm) is selected. The next step involves the Granular Computational Homogenisation procedure to calculate the output interval stiffness coefficients based on the interval variables. The output values are used to compute the values of the objective functions. These operations are performed until the stopping criterion of the optimisation algorithm is met.

A multi-criteria optimisation problem can be solved using multi-

objective algorithms or single-criteria algorithms with additional assumptions, such as the use of a weighting method or changing objectives into optimisation constraints. The use of a multi-objective algorithm may require the use of additional nonlinear constraints related to the values of the objective function. As the result of the multi-objective algorithm is a Pareto front, the search area can be reduced by limiting the maximum distance between the required values of the stiffness coefficients and the values given by the optimisation algorithm. As a result of the optimisation, it is possible to obtain maximum ranges of uncertain microscopic properties of the homogeneous materials of which the final material is composed.

The GCID procedure assumes the use of regular optimisation algorithms (based on classic arithmetic) to solve the problem described by granular data. An application of EA for problems with imprecise data is done by converting the design variables. It is performed by introducing two design variables as α^- and α^+ values of each proper interval input parameter. In order to ensure the proper intervals are maintained, the correct sequence of end values is verified and adjusted as needed.

5. NUMERICAL RESULTS

A fibre-reinforced composite with uniform distribution of unidirectional fibres is considered. RVE contains 9 uniformly distributed parallel fibres. The dimensions of the RVE are assumed as $30 \times 30 \times 30 \mu\text{m}$ (Fig. 2). The volume fraction of the reinforcement f depends on the diameter of the fibre d_f . The geometry is discretised into 29 484 high-quality hexahedral elements with quadratic shape functions (Hex20), resulting in 124 531 nodes and 373 593 DoFs.

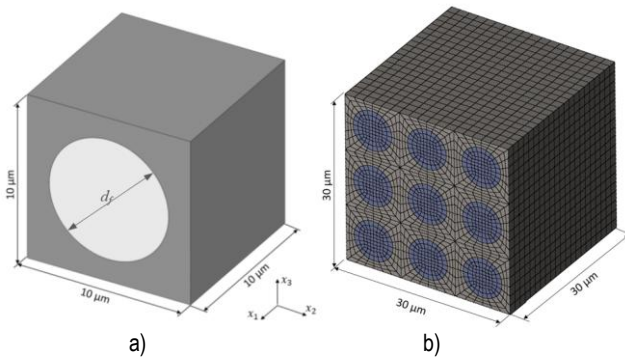


Fig. 2. The RVE model of the fibre-reinforced composite material: a) unit cell geometry, b) FEM mesh

Since a uniform fibre distribution is assumed, the material can be treated as orthotropic with two equivalent perpendicular directions (x_2 and x_3). As a result, the number of independent stiffness coefficients in Eq. 9 reduces to six due to the following equalities:

$$C_{12} = C_{13}, C_{22} = C_{33}, C_{55} = C_{66}.$$

The aim of the inverse design is to optimise the possible ranges of input parameters at the microscale in order to obtain the presumed equivalent macroscopic linear material properties due to normal strain loading in one direction. Microscopic material models are assumed to be isotropic ones.

The first objective is to obtain an uncertain value of the C_{22} coefficient of the stiffness matrix: $\bar{C}_{22}^* = [15.2, 16.8]$ GPa. This factor is related to the stress response to the load in the direction perpendicular to the fibre orientation and is crucial to determining the

mechanical properties of the laminate. The second objective is to obtain the width of the identified parameters' ranges in assumed intervals.

The interval values of elastic moduli, Poisson's ratios of fibre and matrix materials, as well as the volume fraction of the reinforcement are used as the design variables:

$$\bar{p}_1 = \bar{E}_m [\text{GPa}], \bar{p}_2 = \bar{\nu}_m [-], \bar{p}_3 = \bar{E}_f [\text{GPa}], \bar{p}_4 = \bar{\nu}_f [-], \bar{p}_5 = \bar{f} [-].$$

It is assumed that reinforcement volume fraction range is $f \in [0.2, 0.4]$ while assumed linearly-elastic material properties' ranges (variable constrains) are:

- matrix Young's modulus $E_m \in [2, 8]$ GPa,
- matrix Poisson's ratio $\nu_m \in [0.3, 0.4]$,
- fibre Young's modulus $E_f \in [50, 450]$ GPa,
- fibre Poisson's ratio $\nu_f \in [0.2, 0.35]$.

As the introduced objectives are potentially contradictory, two approaches to the optimisation problem are applied. The first approach involves a single-objective evolutionary algorithm using a weighting method to combine both optimisation goals. In the second approach, a multi-objective evolutionary algorithm is used to determine the Pareto front for the two objective functions. To solve the inverse design problem, computational homogenisation based on the material microstructure representation, 2nd order polynomial RS for interval variables and evolutionary algorithms are used.

To solve the optimisation problem, the RS, describing material behaviour for a wide range of identified parameters, is created. To create the RS in terms of the 2nd order polynomial, the DoE is performed. The CCF variant of Central Composite Design is used, resulting in 43 design points [41]. The output values are calculated using periodic boundary conditions. Numerical homogenisation is performed for each design point.

All calculations were performed on a workstation notebook with an Intel Core i7-8750H 6-core 2.2GHz processor and 32GB of RAM. The computational time for homogenisation for each design point was approximately 60 s, and the total computation time for all design points to obtain the response surface was approximately 45 min. The optimisation algorithms used within the methodology (populational algorithms, here the Evolutionary Algorithm) require a very large number of calculations of the objective function. The use of a response surface, once constructed, provides almost instantaneous information about the value of the objective function.

After the design points calculation, the coefficients of 2nd order polynomial RS are calculated utilising the least squares method for each output parameter. The number of variable input parameters is equal to 5, resulting in 21 polynomial coefficients. The RS is described by:

$$C_{22}^{RS} = \beta_0 + \sum_{k=1}^5 \beta_k p_k + \sum_{k,l} \beta_{kl} p_k p_l, \quad (33)$$

where

$$k, l \in \left\{ (1,1), (1,2), (1,3), (1,4), (1,5), (2,2), (2,3), (2,4), (2,5), (3,3), (3,4), (3,5), (4,4), (4,5), (5,5) \right\},$$

p_ξ is the ξ -th design variable value ($p_1 = E_m$, $p_2 = \nu_m$, $p_3 = E_f$, $p_4 = \nu_f$, $p_5 = f$).

The values of the polynomial coefficients β and quality metrics for C_{22}^{RS} are collected in Tab. 1.

Independent datasets were used to create and test the models. An additional 47 sets of combinations of random parameters were used to calculate the PRESS metric values. Quality metrics indicate very good match between the samples and the RS.

Tab. 1. Polynomial coefficients for C_{22}^{RS} and quality metrics

β_0	2.663E+01
β_k	$\beta_1 = -8.969\text{E-}01$; $\beta_2 = -1.410\text{E+}02$; $\beta_3 = -3.450\text{E-}04$; $\beta_4 = -3.622\text{E-}01$; $\beta_5 = -4.214\text{E+}01$
β_{kl}	$\beta_{11} = 6.144\text{E+}00$; $\beta_{12} = 5.427\text{E-}04$; $\beta_{13} = 1.586\text{E-}01$; $\beta_{14} = 4.170\text{E+}00$; $\beta_{15} = 6.277\text{E-}03$; $\beta_{22} = 2.490\text{E+}00$; $\beta_{23} = 5.768\text{E+}01$; $\beta_{24} = 4.311\text{E-}03$; $\beta_{25} = 1.405\text{E-}02$; $\beta_{33} = 3.669\text{E+}00$; $\beta_{34} = -1.067\text{E-}02$; $\beta_{35} = 2.056\text{E+}02$; $\beta_{44} = -1.086\text{E-}05$; $\beta_{45} = -8.753\text{E-}01$; $\beta_{55} = 3.672\text{E+}01$
R^2	0.99586
PRESS	23.23325
σ_{est}	0.35107

5.1. Weighted sum approach

To solve the optimisation problem using a single-objective algorithm, a single objective function describing three optimisation goals was proposed: matching the obtained values of the stiffness coefficients with the expected ones (minimisation of $g_1(\bar{\mathbf{p}})$) and widening the normalised widths of the design parameters (maximisation of $g_2(\bar{\mathbf{p}})$). The optimisation problem is formulated as follows:

$$\left\{ \begin{array}{l} \text{minimise } f_g(\bar{\mathbf{p}}) = \varphi_1 g_1(\bar{\mathbf{p}}) - \varphi_2 g_2(\bar{\mathbf{p}}) \\ \left\{ \begin{array}{l} g_1(\bar{\mathbf{p}}) = D(\bar{C}_{22}(\bar{\mathbf{p}}) - \bar{C}_{22}^*) \\ g_2(\bar{\mathbf{p}}) = \min_{p_i} w'(\bar{p}_i), i = 1, 2, \dots, 5 \\ b_{Li} \leq p_i^{\pm} \leq b_{Ui}, i = 1, 2, \dots, 5 \end{array} \right. \\ \text{subject to: } \mathbf{b}^{LU} = \begin{bmatrix} 2.0 & 8.0 \\ 0.3 & 0.4 \\ 50.0 & 450.0 \\ 0.2 & 0.35 \\ 0.2 & 0.4 \end{bmatrix} \end{array} \right. \quad (34)$$

where $w(\bar{p}_i)$ is a width of design parameter \bar{p}_i , φ_1 and φ_2 are weighting coefficients. Three sets of weighting coefficients are considered: A: $\varphi_1 = 0.5, \varphi_2 = 0.5$; B: $\varphi_1 = 0.25, \varphi_2 = 0.75$; C: $\varphi_1 = 0.75, \varphi_2 = 0.25$. In order to be able to apply the regular (non-interval) optimisation algorithm, both ends of each design parameter are treated as design variables, resulting in 10 design variables.

The optimisation is performed by the DEA algorithm. The DEA parameters were set on initial DEA runs and the authors' previous experience. The parameters of the DEA are:

- number of subpopulations: $sp_n = 2$,
- number of individuals in each subpopulation $sp_size = 100$,
- simple crossover and Gaussian mutation probability $p_{SG} = 1$,
- uniform mutation probability $p_{im} = 0.1$,
- rank selection pressure: $ps = 0.8$,
- number of generations (stopping criterion) $gen_no = 100$.

The results in the form of the best solution for 30 independent runs of DPEA for each set of weighting coefficients with information about the average objective function value $avg[f_g(\bar{\mathbf{p}})]$ and its standard deviation $\sigma[f_g(\bar{\mathbf{p}})]$, the relative difference δ_w between \bar{C}_{22}^* and $\bar{C}_{22}(\bar{\mathbf{p}})$ widths:

$$\delta_w = \frac{|w(\bar{C}_{22}(\bar{\mathbf{p}})) - w(\bar{C}_{22}^*)|}{w(\bar{C}_{22}^*)} \quad (35)$$

and the relative difference δ_c between \bar{C}_{22}^* and $\bar{C}_{22}(\bar{\mathbf{p}})$ central values:

$$\delta_c = \frac{|c_w(\bar{C}_{22}(\bar{\mathbf{p}})) - c_w(\bar{C}_{22}^*)|}{c_w(\bar{C}_{22}^*)} \quad (36)$$

are collected in Tab. 2.

The values of the relative differences between \bar{C}_{22}^* and $\bar{C}_{22}(\bar{\mathbf{p}})$, summarised in Tab. 2, indicate very good agreement with the assumed values of \bar{C}_{22}^* . It can be seen that the weighting coefficients affect the $g_1(\bar{\mathbf{p}})$ and $g_2(\bar{\mathbf{p}})$ in such a way that a higher φ_1 value results in lower (better) values of $g_1(\bar{\mathbf{p}})$ and lower (worse) values of $g_2(\bar{\mathbf{p}})$ and vice versa. Standard deviation values for all combinations of φ_1 and φ_2 show the high repeatability of $f_g(\bar{\mathbf{p}})$ results for all 30 DPEA runs in each case.

Tab. 2. The best results of the single-objective optimisation for different weighting coefficients

Variant	A	B	C
Weighting coefficients	$\varphi_1 = 0.25$, $\varphi_2 = 0.75$	$\varphi_1 = 0.5$, $\varphi_2 = 0.5$	$\varphi_1 = 0.75$, $\varphi_2 = 0.25$
$\bar{p}_1 = E_m$ [GPa]	[6.05064, 6.46002]	[4.91259, 5.15732]	[5.29892, 5.54251]
$\bar{p}_2 = v_m$ [-]	[0.37837, 0.38391]	[0.34833, 0.35504]	[0.36931, 0.37214]
$\bar{p}_3 = E_f$ [GPa]	[443.933, 354.949]	[298.173, 331.484]	[303.429, 370.799]
$\bar{p}_4 = v_f$ [-]	[0.30482, 0.31628]	[0.24757, 0.27883]	[0.26779, 0.34706]
$\bar{p}_5 = f$ [-]	[0.20564, 0.21752]	[0.37770, 0.38936]	[0.29828, 0.31968]
$g_1(\bar{\mathbf{p}})$ [GPa]	1.0987E-02	1.6975E-03	7.7079E-04
$g_2(\bar{\mathbf{p}})$ [-]	5.5390E-02	4.0799E-02	2.8280E-02
$f_g(\bar{\mathbf{p}})$	-3.8796E-02	-1.9551E-02	-6.4919E-03
$avg[f_g(\bar{\mathbf{p}})]$	-1.6084E-02	-5.5497E-03	1.6779E-02
$\sigma[f_g(\bar{\mathbf{p}})]$	9.9484E-03	1.1636E-02	5.7618E-02
$\bar{C}_{22}(\bar{\mathbf{p}})$ [GPa]	[15.210668, 16.797376]	[15.200626, 16.801578]	[15.200105, 16.800763]
δ_w [%]	2.5140E-02	6.8900E-03	2.7100E-03
δ_c [%]	8.3075E-01	5.9500E-02	4.1120E-02

Exemplary optimisation results for the first five best results and the worst one for $\varphi_1 = 0.75$ and $\varphi_2 = 0.25$ are collected in Tab. 3. The results indicate that the objective function is multimodal, as different sets of design variables result in similar objective function values. In particular, the expected proportional effect of the value of parameter \bar{p}_3 on $\bar{C}_{22}(\bar{\mathbf{p}})$ is compensated for by the values of the other interval parameters.

The values of δ_w and δ_c indicate that there are very low discrepancies between the assumed and obtained widths and central values of interval stiffness coefficients.

5.2. Pareto approach

The optimisation problem for the Pareto approach is described as:

$$\left\{ \begin{array}{l} \text{minimise } f_1(\bar{\mathbf{p}}) \\ \text{maximise } f_2(\bar{\mathbf{p}}) \\ f_1(\bar{\mathbf{p}}) = D(\bar{C}_{22}(\bar{\mathbf{p}}) - \bar{C}_{22}^*) \\ f_2(\bar{\mathbf{p}}) = \min_{p_i} w'(\bar{p}_i), i = 1, 2, \dots, 5 \\ \text{subject to: } \left\{ \begin{array}{l} b_{Li} \leq p_i^{-,+} \leq b_{Ui}, i = 1, \dots, 5 \\ \mathbf{b}^{LU} = \begin{bmatrix} 2.0 & 8.0 \\ 0.3 & 0.4 \\ 50.0 & 450.0 \\ 0.2 & 0.35 \\ 0.2 & 0.4 \end{bmatrix} \end{array} \right. \end{array} \right. \quad (37)$$

Nonlinear constraints in the form of are introduced to limit the search area of the Pareto front: $f_1(\bar{\mathbf{p}}) < 2.5$ [GPa] and $f_2(\bar{\mathbf{p}}) < 0.2$. This has been implemented by means of an exterior penalty method [50].

Optimisation is performed by the MOOPTIM algorithm. The MOOPTIM parameters were set on initial MOOPTIM runs and the authors' previous experience as:

- number of individuals $pop_size = 100$,
- Gaussian mutation probability $p_{mG} = 0.7$,
- Gaussian mutation range $r_{mG} = 0.2$,
- uniform mutation probability $p_{mu} = 0.1$,
- simple crossover probability $p_{sG} = 0.1$,
- arithmetic crossover probability $p_{sG} = 0.1$,
- number of generations (stopping criterion) $gen_no = 200$.

The results of the optimisation in the form of Pareto fronts for 10 executions of MOOPTIM are shown in Fig. 3. To compare the results with the weighted sum approach, DPEA results are also presented. Selected results for the Pareto approach are summarised in Tab. 4.

These include the minimum values of $f_1(\bar{\mathbf{p}})$ the maximum values of $f_2(\bar{\mathbf{p}})$, the values of the resulting design variables and the values of the hyper-volume indicators I_H for ideal point (0.0, 0.2) and nadir point (2.5, 0.0). As negative hypervolume values are generated by the algorithm described in [49], a lower I_H value denotes a better approximation set.

The results show that the objective functions are contradictory; hence, an increase in the uncertainty of the design variables causes a drift beyond the assumed value of the stiffness coefficient. However, the Pareto fronts show that there exists an individual with $f_1(\bar{\mathbf{p}})$ value close to 0 with specific non-zero value of $f_2(\bar{\mathbf{p}})$. The best results for the first objective function ($f_1(\bar{\mathbf{p}}) = 6.2008\text{E-}04$) has been obtained for the 5th run of the MOOPTIM algorithm while the best results for the second objective function ($f_2(\bar{\mathbf{p}}) = 1.8884\text{E-}01$) has been obtained for the 6th run of the algorithm.

The average value of I_H is equal to -0.288657, while its standard deviation is 0.01291, indicating a high similarity of hypervolume indicators for the different MOOPTIM runs. The best I_H value has been obtained for the 6th run of the algorithm – purple triangles in Fig. 3, while the worst I_H value has been achieved for the 1st run (red diamonds). The values of δ_w and δ_c for the Pareto points representing the best results for $f_1(\bar{\mathbf{p}})$ show a very low difference between the assumed and obtained widths and central values of interval stiffness coefficients, not exceeding 0.9% in the worst case.

The multi-objective algorithm also explores the possible stiffness coefficient matching for large uncertainties of the identified parameters. The highest values of $f_2(\bar{\mathbf{p}})$ (limited to 0.2 by a non-linear constraint) are from the range of 0.14-0.19.

As in the case of the single-objective algorithm, the multi-objective algorithm calculates similar values of $f_1(\bar{\mathbf{p}})$ and $f_2(\bar{\mathbf{p}})$ for different sets of design parameters. The solved optimisation problem is multimodal, indicating that different materials can satisfy the optimisation objectives. This may be due to a relatively large number of design variables that describe the mechanical properties of the structure.

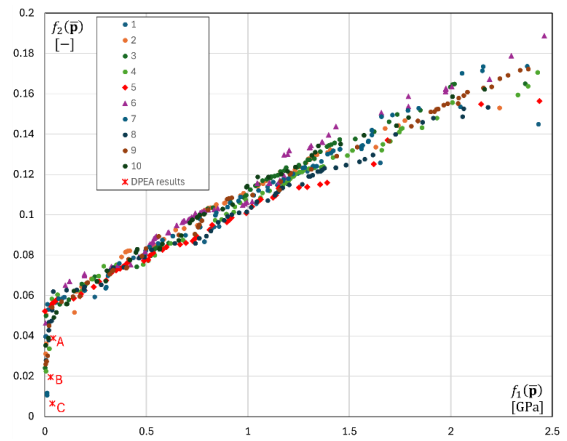


Fig. 3. Pareto fronts and DPEA results

The presented approach belongs to a-posteriori multi-criteria optimisation methods, in which a second phase is necessary to select a single solution. Since all solutions on the Pareto front are equivalent, additional criteria can be used, such as cost, manufacturability or material availability. Moreover, additional non-linear constraints may limit the search area and should be considered in the decision-making process

Tab. 3. Exemplary results of the single-objective optimisation for $\varphi_1 = 0.75$, $\varphi_2 = 0.25$

Rank	$\bar{p}_1 = E_m$ [GPa]	$\bar{p}_2 = v_m$ [-]	$\bar{p}_3 = E_f$ [GPa]	$\bar{p}_4 = v_f$ [-]	$\bar{p}_5 = f$ [-]	$g_1(\bar{\mathbf{p}})$ [GPa]	$g_2(\bar{\mathbf{p}})$ [-]	$f_g(\bar{\mathbf{p}})$	$\bar{C}_{22}(\bar{\mathbf{p}})$ [GPa]	δ_w, δ_c [%]
1	[5.29892, 5.54251]	[0.36931, 0.37214]	[303.429, 370.799]	[0.26779, 0.34706]	[0.29828, 0.31968]	7.7079E-04	2.8280E-02	-6.4919E-03	[15.200105, 16.800763]	2.7100E-03 4.1120E-02
2	[6.58579, 6.84576]	[0.31106, 0.31661]	[179.078, 257.930]	[0.23188, 0.34675]	[0.31161, 0.32033]	1.0045E-02	4.3329E-02	-3.2986E-03	[15.195634, 16.790953]	4.1916E-02 2.9256E-01
3	[6.02565, 6.17328]	[0.32825, 0.33579]	[260.926, 321.946]	[0.26363, 0.25501]	[0.33863, 0.31755]	4.2133E-03	2.4606E-02	-2.9916E-03	[15.202722, 16.803215]	1.8553E-02 3.0813E-02
4	[5.75597, 6.09119]	[0.37103, 0.36848]	[80.847, 99.605]	[0.22293, 0.29563]	[0.29018, 0.30173]	4.9521E-03	2.5470E-02	-2.6534E-03	[15.204895, 16.800749]	1.7638E-02 2.5913E-01
5	[5.79374, 6.38056]	[0.37613, 0.37806]	[317.142, 421.272]	[0.33603, 0.34437]	[0.23377, 0.23645]	2.3205E-03	1.3425E-02	-1.6159E-03	[15.199783, 16.802310]	6.5406E-03 1.5794E-01
30	[7.34717, 7.41631]	[0.34548, 0.34419]	[98.303, 450.000]	[0.28926, 0.29484]	[0.20000, 0.22936]	5.8223E-02	1.1523E-02	4.0787E-02	[15.194355, 16.857949]	1.6345E-01 3.9746E+00

Tab. 4. Results of the multi-objective optimisation

Run	I_H	Pareto point	$\bar{p}_1 = E_m$ [GPa]	$\bar{p}_2 = \nu_m$ [-]	$\bar{p}_3 = E_f$ [GPa]	$\bar{p}_4 = \nu_f$ [-]	$\bar{p}_5 = f$ [-]	$f_1(\bar{\mathbf{p}})$ [GPa]	$f_2(\bar{\mathbf{p}})$ [-]	$\bar{c}_{22}(\bar{\mathbf{p}})$ [GPa]	δ_w, δ_c [%]
1	-0.26058	min $f_1(\bar{\mathbf{p}})$	[6.21597, 6.45371]	[0.32362, 0.32760]	[149.183, 180.177]	[0.21958, 0.30889]	[0.32641, 0.34275]	2.9865E-03	3.9623E-02	[15.197072, 16.799410]	1.0994E-02 1.4612E-01
		max $f_2(\bar{\mathbf{p}})$	[5.65513, 6.52451]	[0.30761, 0.32362]	[377.437, 450.000]	[0.31219, 0.33490]	[0.30399, 0.36323]	2.4308E+00	1.4490E-01	[13.106417, 18.035232]	2.6823E+00 2.0805E+02
2	-0.28839	min $f_1(\bar{\mathbf{p}})$	[6.64138, 6.87106]	[0.36113, 0.36698]	[71.940, 162.432]	[0.26203, 0.31893]	[0.22596, 0.23219]	2.9716E-03	3.1145E-02	[15.201644, 16.802470]	1.2856E-02 5.1625E-02
		max $f_2(\bar{\mathbf{p}})$	[5.78269, 6.87106]	[0.32687, 0.34218]	[334.408, 450.000]	[0.29318, 0.35000]	[0.25825, 0.28928]	2.2397E+00	1.5310E-01	[13.032410, 17.363930]	5.0114E+00 1.7072E+02
3	-0.29693	min $f_1(\bar{\mathbf{p}})$	[6.02157, 6.24235]	[0.30924, 0.32460]	[313.892, 323.541]	[0.20476, 0.23224]	[0.34545, 0.35226]	9.1474E-04	2.4120E-02	[15.199641, 16.799159]	3.7500E-03 3.0125E-02
		max $f_2(\bar{\mathbf{p}})$	[5.94323, 6.93317]	[0.30700, 0.32460]	[357.547, 450.000]	[0.28208, 0.35000]	[0.27794, 0.32512]	2.3664E+00	1.6499E-01	[13.038762, 17.763848]	3.7418E+00 1.9532E+02
4	-0.28615	min $f_1(\bar{\mathbf{p}})$	[5.67805, 5.81318]	[0.30305, 0.32223]	[318.653, 450.000]	[0.21592, 0.30478]	[0.38134, 0.38597]	4.6047E-03	2.2522E-02	[15.201917, 16.795817]	7.0812E-03 3.8125E-01
		max $f_2(\bar{\mathbf{p}})$	[5.26435, 6.37166]	[0.34681, 0.36387]	[345.252, 450.000]	[0.31243, 0.35000]	[0.28161, 0.31635]	2.4268E+00	1.7065E-01	[13.389715, 18.416232]	6.0642E-01 2.1416E+02
5	-0.27313	min $f_1(\bar{\mathbf{p}})$	[5.49730, 5.83237]	[0.33979, 0.34532]	[377.152, 450.000]	[0.20000, 0.24683]	[0.33794, 0.34838]	6.2008E-04	5.2240E-02	[15.200134, 16.799395]	1.4719E-03 4.6188E-02
		max $f_2(\bar{\mathbf{p}})$	[5.20406, 6.14267]	[0.31508, 0.33451]	[359.835, 450.000]	[0.30955, 0.33613]	[0.33212, 0.37497]	2.4372E+00	1.5643E-01	[13.098494, 18.034225]	2.7103E+00 2.0848E+02
6	-0.30318	min $f_1(\bar{\mathbf{p}})$	[6.74116, 7.13123]	[0.34609, 0.35073]	[326.580, 388.616]	[0.22717, 0.31078]	[0.22181, 0.23521]	2.8838E-03	4.6350E-02	[15.201307, 16.802570]	1.2116E-02 7.8937E-02
		max $f_2(\bar{\mathbf{p}})$	[6.84060, 8.00000]	[0.31912, 0.34471]	[313.585, 450.000]	[0.28905, 0.35000]	[0.20547, 0.24324]	2.4610E+00	1.8884E-01	[13.588805, 18.660209]	7.7817E-01 2.1696E+02
7	-0.29861	min $f_1(\bar{\mathbf{p}})$	[6.07599, 6.13976]	[0.35545, 0.36251]	[66.934, 103.602]	[0.23487, 0.27334]	[0.29319, 0.31667]	1.0141E-02	1.0628E-02	[15.204597, 16.790961]	1.3881E-02 8.5225E-01
		max $f_2(\bar{\mathbf{p}})$	[6.16085, 7.23273]	[0.30000, 0.31959]	[311.748, 381.206]	[0.24644, 0.27261]	[0.28919, 0.33169]	2.3757E+00	1.7365E-01	[13.514604, 18.474349]	3.4522E-02 2.0998E+02
8	-0.28615	min $f_1(\bar{\mathbf{p}})$	[7.06127, 7.38220]	[0.30000, 0.30279]	[357.869, 392.536]	[0.28429, 0.32087]	[0.27701, 0.29914]	3.8161E-03	-2.796E-02	[15.201885, 16.803318]	1.6259E-02 8.9562E-02
		max $f_2(\bar{\mathbf{p}})$	[5.11271, 6.11818]	[0.37069, 0.38602]	[326.957, 450.000]	[0.32087, 0.35000]	[0.24097, 0.27701]	2.1827E+00	1.5331E-01	[13.333662, 17.931799]	2.2954E+00 1.8738E+02
9	-0.29202	min $f_1(\bar{\mathbf{p}})$	[6.98408, 7.14029]	[0.32483, 0.33341]	[89.1451, 110.587]	[0.27858, 0.34763]	[0.27141, 0.28943]	2.6195E-03	2.6035E-02	[15.202586, 16.799585]	6.7844E-03 1.8756E-01
		max $f_2(\bar{\mathbf{p}})$	[5.12698, 6.16768]	[0.36979, 0.38819]	[293.851, 450.000]	[0.30270, 0.33132]	[0.25029, 0.28474]	2.3811E+00	1.7227E-01	[13.529283, 18.496622]	8.0953E-02 2.1046E+02
10	-0.29388	min $f_1(\bar{\mathbf{p}})$	[6.41585, 6.79624]	[0.37605, 0.37959]	[50.000, 71.4883]	[0.20603, 0.24717]	[0.21665, 0.22781]	2.9710E-03	3.5399E-02	[15.199480, 16.802953]	7.6031E-03 2.1706E-01
		max $f_2(\bar{\mathbf{p}})$	[6.41585, 7.39224]	[0.34290, 0.36104]	[346.451, 450.000]	[0.30325, 0.34305]	[0.22490, 0.25735]	2.1655E+00	1.6221E-01	[14.412384, 18.817226]	3.8425E+00 1.7530E+02

6. CONCLUSIONS

The paper presents the Granular Computational Inverse Design procedure as a novel approach to the problems of identification of interval microstructure parameters of inhomogeneous materials for desired uncertainty macroscopic properties. As a result of the identification, interval parameters of the constituent geometry and the material properties on the microscale are obtained. Directed interval arithmetic is applied instead of the classical one to reduce the undesirable effect of interval widening as a result of arithmetical operations. To speed up the calculations, response surfaces has been applied to build the metamodel. The Central Composite Design method has been used as the Design of Experiment method because of the high precision of the mesh. The quality of the RS obtained has been using several quality metrics.

The GCID procedure has been verified on a fibre-reinforced composite with a uniform distribution of unidirectional fibres. Two approaches to the multi-objective optimisation are presented. A-priori methods (here the weighted sum approach) combine objectives using predefined weights and transform a multi-criteria problem into a single-criteria problem, which is solved here using a DEA

algorithm. This method targets a specific region of the solution space, generating fewer candidate solutions. The second approach uses the MOOPTIM algorithm to generate Pareto optimal solutions without taking preferences into account. The decision maker can analyse different post-optimisation scenarios.

Single-criteria optimisation usually produces specific solutions that may not be optimal in different scenarios, whereas multi-criteria optimisation reveals a range of viable solutions. Multi-criteria algorithms like MOOPTIM explore a wider design space, resulting in a multimodal optimisation problem where different sets of design variables can achieve similar values of the objective function. The choice of approach depends on the researcher.

The results obtained show the high efficiency of the GCID procedure in both cases.

The presented methodology can be applied to parameter identification problems in material design and manufacturing processes with epistemic uncertainties. It is planned to extend the proposed attitude to diverse types of information granularity (fuzzy numbers), novel hybrid materials including e.g. auxetics, and different material models (nonlinear materials), and others. The extension may require application of more sophisticated and accurate metamodels.

REFERENCES

- Ashby M, Bréchet Y. Designing hybrid materials. *Acta Materialia*. 2003; 51(19): 5801–5821. [https://doi.org/10.1016/S1359-6454\(03\)00441-5](https://doi.org/10.1016/S1359-6454(03)00441-5)
- Zohdi T, Wriggers P. An introduction to computational micromechanics. Berlin Heidelberg: Springer-Verlag; 2005.
- Burczyński T, Pietrzyk M, Kuś W, Madej Ł, Mrozek A, Rauch Ł. Multiscale Modelling and Optimisation of Materials and Structures, Hoboken: Wiley, 2022.
- Ptaszny J, Hatlas M. Evaluation of the FMBEM efficiency in the analysis of porous structures. *Engineering Computations*. 2018;35(2): 843–866. <https://doi.org/10.1108/EC-12-2016-0436>
- Ptaszny J. A fast multipole BEM with higher-order elements for 3-D composite materials. *Computers & Mathematics with Applications*. 2021;82: 148–160. <https://doi.org/10.1016/j.camwa.2020.10.024>
- Sigmund O. Materials with prescribed constitutive parameters: An inverse homogenization problem, *International Journal of Solids and Structures*. 1994, 31(17): 2313–2329. [https://doi.org/10.1016/0020-7683\(94\)90154-6](https://doi.org/10.1016/0020-7683(94)90154-6)
- Trofimov A, Abaimov S, Sevostianov I. Inverse homogenization problem: Evaluation of elastic and electrical (thermal) properties of composite constituents. *International Journal of Engineering Science*. 2018;129: 34–46. <https://doi.org/10.1016/j.ijengsci.2018.04.001>
- Hoffman FO, Hammonds JS. Propagation of Uncertainty in Risk Assessments: The Need to Distinguish Between Uncertainty Due to Lack of Knowledge and Uncertainty Due to Variability. *Risk Analysis*. 1994;14(5). <https://doi.org/10.1111/J.1539-6924.1994.TB00281.X>
- Pelz PF, Groche P, Pfetsch ME, Schaeffner M (Eds). *Mastering Uncertainty in Mechanical Engineering*, Cham: Springer; 2021.
- Araque L, Wang L, Mal A, Schaal C. Advanced fuzzy arithmetic for material characterization of composites using guided ultrasonic waves. *Mechanical Systems and Signal Processing*. 2022; 171, 108856. <https://doi.org/10.1016/j.ymssp.2022.108856>
- Yao JT. A ten-year review of granular computing. *Proceeding of 2007 IEEE International Conference on Granular Computing, Silicon Valley, USA*. 2007; 734–739. <https://doi.org/10.1109/GrC.2007.11>
- Pedrycz W. *Granular computing: analysis and design of intelligent systems*. Boca Raton: CRC Press; 2018.
- Ramli AA, Watada J, Pedrycz W. Information Granules Problem: An Efficient Solution of Real-Time Fuzzy Regression Analysis. In: Pedrycz, W., Chen, SM. (eds) *Information Granularity, Big Data, and Computational Intelligence. Studies in Big Data*, vol 8. Cham: Springer, 2015. https://doi.org/10.1007/978-3-319-08254-7_3
- Möller B, Beer M. *Fuzzy Randomness. Uncertainty in Civil Engineering and Computational Mechanics*. Berlin-Heidelberg: Springer-Verlag; 2004.
- Wang L., Qiu Z., Zheng Y. State-of-the-Art Nonprobabilistic Finite Element Analyses. Jan Peter Hessler (ed.), *Uncertainty Quantification and Model Calibration*, IntechOpen; 2017.
- Moens D, Vandepitte D. A survey of non-probabilistic uncertainty treatment in finite element analysis. *Computer Methods in Applied Mechanics and Engineering*. 2005; 194: 1527–1555. <https://doi.org/10.1016/j.cma.2004.03.019>
- Chen N, Yu D, Xia B, Li J, Ma Z. Interval and subinterval homogenization-based method for determining the effective elastic properties of periodic microstructure with interval parameters, *International Journal of Solids and Structures*. 2017; 106–107: 174–182. <https://doi.org/10.1016/j.jisols.2016.11.022>
- Pivovarov D, Hahn V, Steinmann P, Willner K, Leyendecker S. Fuzzy dynamics of multibody systems with polymorphic uncertainty in the material microstructure. *Computational Mechanics*. 2019; 64: 1601–1619. <https://doi.org/10.1007/s00466-019-01737-9>
- Naskar S, Mukhopadhyay T, Sriramula S. Spatially varying fuzzy multi-scale uncertainty propagation in unidirectional fibre reinforced composites. *Composite Structures*. 2019; 209: 940–967. <https://doi.org/10.1016/j.compstruct.2018.09.090>
- Beluch W, Hatlas M, Ptaszny J. Granular Computational Homogenization of Composite Structures with Imprecise Parameters, *Archives of Mechanics*. 2023; 75(3): 271–300. <https://doi.org/10.24423/aom.4186>
- Yamanaka Y, Matsubara S, Hirayama N, Moriguchi S, Terada K. Surrogate modeling for the homogenization of elastoplastic composites based on RBF interpolation, *Computer Methods in Applied Mechanics and Engineering*. 2023; 415, 116282. <https://doi.org/10.1016/j.cma.2023.116282>
- Fuhg JN, Böhm C, Bouklas N, Fau A, Wriggers P, Marino M. Model-data-driven constitutive responses: Application to a multiscale computational framework. *International Journal of Engineering Science*. 2021; 167, 103522. <https://doi.org/10.1016/j.ijengsci.2021.103522>
- Rodríguez-Romero R, Compán V, Sáez A, García-Macias E. Hierarchical meta-modelling for fast prediction of the elastic properties of stone injected with CNT/cement mortar. *Construction and Building Materials*. 2023; 408. <https://doi.org/10.1016/j.conbuildmat.2023.133725>
- Le BA, Yvonnet J, He QC. Computational homogenization of nonlinear elastic materials using neural networks. *International Journal for Numerical Methods in Engineering*. 2015; 104: 1061–1084. <https://doi.org/10.1002/nme.4953>
- Ogierman W. A data-driven model based on the numerical solution of the equivalent inclusion problem for the analysis of nonlinear short-fibre composites. *Composites Science and Technology*. 2024; 250, 110516. <https://doi.org/10.1016/j.compscitech.2024.110516>
- Kaucher E. Interval Analysis in the Extended Interval Space IR. In: Alefeld, G., Grigorieff, R.D. (eds), *Fundamentals of Numerical Computation (Computer-Oriented Numerical Analysis)*. Computing Supplementum. 1980; 2: 33–49. https://doi.org/10.1007/978-3-7091-8577-3_3
- Markov SM. On direct interval arithmetic and its applications, *Journal of Universal Computer Science*. 1995; 1(7): 514–526. https://doi.org/10.1007/978-3-642-80350-5_43
- Popova ED. Multiplication distributivity of proper and improper intervals. *Reliable Computing*. 2001; 7: 129–140. <https://doi.org/10.1023/A:1011470131086>
- Piasecka-Belkhat A. Interval boundary element method for imprecisely defined unsteady heat transfer problems (in Polish). *Monographs*, 321. Gliwice: Publishing House of Silesian University of Technology, 2011.
- Shary SP. Non-Traditional Intervals and Their Use. Which Ones Really Make Sense? *Numerical Analysis and Applications*. 2023; 16(2): 179–191. <https://doi.org/10.1134/S1995423923020088>
- Kouznetsova V. Computational homogenization for the multi-scale analysis of multi-phase materials. PhD. thesis, Technische Universiteit Eindhoven; 2002.
- Zienkiewicz OC, Taylor RL, Zhu JZ. *The finite element method: its basis and fundamentals*. Butterworth-Heinemann; 2013.
- Brebbia J, Dominguez J. *Boundary Elements: An Introductory Course*. New York: McGraw-Hill; 1992.
- Hill R. Elastic properties of reinforced solids: some theoretical principles. *Journal of the Mechanics and Physics of Solids*. 1963; 11: 357–372. [https://doi.org/10.1016/0022-5096\(63\)90036-X](https://doi.org/10.1016/0022-5096(63)90036-X)
- Nguyen V, Béchet E, Geuzaine C, Noels L. Imposing periodic boundary condition on arbitrary meshes by polynomial interpolation. *Computational Materials Science*. 2012;55: 390–406. <https://doi.org/10.1016/j.commatsci.2011.10.017>
- Botsis J, Deville M. *Mechanics of Continuous Media: an Introduction*. EPFL Press; 2018.
- Bos L, Gibson P, Kotchetov M, Slawinski M. *Classes of Anisotropic Media: A Tutorial*. *Studia Geophysica et Geodaetica*. 2004;48: 265–287. <https://doi.org/10.1023/B:SGEG.0000015596.68104.31>
- Burczyński T, Kuś W, Beluch W, Długosz A, Poteralski A, Szczepanik M. *Intelligent computing in optimal design*. Springer International Publishing; 2020.

39. Michalewicz Z, Fogel DB., How to Solve It: Modern Heuristics. Berlin, Heidelberg: Springer; 2004.
40. Nelson PR, Coffin M, Copeland KAF. Response surface methods, In: Nelson PR, Coffin M, Copeland KAF (eds) Introductory Statistics for Engineering Experimentation. Academic Press, 395–423, 2003.
41. Montgomery D. Design and analysis of experiments. New York: John Wiley & Sons; 2012.
42. Halmos PR. Naive set theory. New York: Springer-Verlag; 1974.
43. Jaulin L, Kieffer M, Didrit O, Water E. Applied interval analysis, London: Springer; 2001.
44. Hayes B. A lucid interval. American Scientist, 2003;91(6): 484–488.
45. Burczyński T., Kuś W. Optimization of structures using distributed and parallel evolutionary algorithms, Parallel Processing and Applied Mathematics, Lecture Notes on Computational Sciences 3019, Springer, 572–579, 2004.
46. Długosz A. Optimization in multiscale thermoelastic problems, Computer Methods in Materials Science, 2014;14(1): 86–93. <https://doi.org/10.7494/cmms.2014.1.0478>
47. Deb K. Multi-objective optimization using evolutionary algorithms. New York: John Wiley & Sons; 2001.
48. Długosz, A. Multiobjective Evolutionary Optimization of MEMS Structures, Computer Assisted Mechanics and Engineering Sciences, 2010;17(1): 41–50.
49. Zitzler, E., Brockhoff, D., Thiele, L. The Hypervolume Indicator Revisited: On the Design of Pareto-compliant Indicators Via Weighted Integration. In: Obayashi, S., Deb, K., Poloni, C., Hiroyasu, T., Murata, T. (eds) Evolutionary Multi-Criterion Optimization. EMO 2007. Lecture

Notes in Computer Science. Springer, Berlin, Heidelberg, 2007; 4403: 862–876. https://doi.org/10.1007/978-3-540-70928-2_64

50. Rothwell, A. Optimization Methods in Structural Design. Springer International Publishing; 2017.

The scientific research was funded from the statutory subsidy of the Faculty of Mechanical Engineering, Silesian University of Technology, Poland.

Witold Beluch:  <https://orcid.org/0000-0002-6406-3719>

Jacek Ptaszny:  <https://orcid.org/0000-0001-6298-8331>

Marcin Hatlas:  <https://orcid.org/0000-0001-8917-6691>



This work is licensed under the Creative Commons BY-NC-ND 4.0 license.

MODELLING OF CREEP CRACK GROWTH USING FRACTURE MECHANICS AND DAMAGE MECHANICS METHODS

Krzysztof NOWAK^{*✉}

^{*}Tadeusz Kosciuszko Cracow University of Technology,
Faculty of Civil Engineering, 30-409 Kraków, ul. Warszawska 24

krzysztof.nowak@pk.edu.pl

received 16 July 2024., revised 21 December 2024, accepted 23 March 2025

Abstract: Methods for modelling of crack growth and prediction of the lifetime of structure operated at creep conditions are presented in the paper. Analyses were performed at fracture mechanics (FM) and damage mechanics (DM). In the case of FM, the C^* -integral and $C(t)$ -integral were used. Two models were considered: without and with damage development in the vicinity of crack tip. For DM models, the Kachanov equation was chosen as the basic one. To avoid the strain and damage concentration and thus the mesh-dependence of the solution, the non-local integral method was applied. Since the damage model is stress-dependent, strains cannot be used as an averaged parameter; nevertheless, damage increment was used. The simulations of creep crack growth were performed for a compact tension specimen made of 316 stainless steel at a temperature of 550°C and their results were compared with experimental results. The FM method in a damaged environment and the non-local DM method were identified as the most promising. As the results for time to failure were ambiguous, the safety margin and critical crack length were recognised as parameters that are useful in safety analysis in the case of creep crack growth.

Keywords: creep crack growth, life prediction, C^* -integral, $C(t)$ -integral, non-local damage mechanics method

1. INTRODUCTION

Nowadays, there remains a growing demand for greater accuracy and reliability of the models used for predicting the lifetime of structures working at elevated temperatures. Not only can the absolute lifetime be evaluated, but relative parameters like safety margins also contain important information. They enable the prediction of the remaining time after the first symptoms of damage are noticed.

In order to assess the safety margin, the lifetime of a component working in creep conditions is divided into two stages. The first stage is characterised by the development of internal damage. This stage, called the pre-cracking process, is terminated when the first macroscopically observed damage occurs, this time is denoted by t_i . In the second stage, the defects spread to form a single crack or a field of cracks or voids (cf. [1]). This is called post-cracking. The mode of this development depends on the material properties as well as on the geometry of the specimen and the environmental conditions. At the beginning of this stage, the crack develops in a stationary manner. The strain rate is almost constant and the stress distribution around the crack tip follows the crack tip position, i.e. it is constant in time as a function of position relative to the current crack tip. At the end of the process, one can observe the acceleration of the crack growth. In this stage, the length of the crack reaches its critical size, i.e. the final fracture occurs. The total time to failure is denoted by t_f . The safety margin is defined by ratio t_f/t_i .

The first stage can be described by damage mechanics (DM) methods. The second one is the domain of fracture mechanics (FM), but the DM approach can also be involved. The FM methods give a much more relevant solution of the problem of crack growth,

but DM allows for a better understanding of the crack propagation process, especially for complex geometrical and material configurations.

In the current work, the stress-based model of damage development originally proposed by Kachanov [2] and then developed by Rabotnov [3] was examined. Its description of the crack growth process in creep conditions was compared with the results of FM analysis. As a basic tool, the finite element method (FEM) was used. The non-local integral method was applied in order to regularise the solution. Many other models of damage development exist, such as the stress-based Murakami-Liu model (e.g. [4]), strain-based models (e.g. [5]), the micromechanical model (e.g. [6]). There are also many methods of numerical solution, like XFEM (e.g. [7]), the eikonal non-local method (e.g. [8]) and gradient methods of regularisation (e.g. [9]). However, they usually require very specialised tools. Additionally some stress-based DM methods, to accurately describe the crack growth process introduce several damage parameters [10, 11, 12]. This, in turn, requires the identification of many material parameters, which is not straightforward due to the time-consuming nature of damage testing under creep conditions.

The aim of the current paper is to show the capabilities of the application of a relatively simple Kachanov equation in order to solve a given problem. The $C(t)$ -integral, as well as the time to failure were determined for a material with developing damage using the numerical method proposed by the author. Additionally, a non-local method already proposed in [13] has been developed using the DM approach, where averaging is performed with a weighting function over an area limited by the interaction radius.

The main goal of the present work is to compare the mentioned methods and their applicability to studying various stages of crack development under creep conditions. This will allow for the

establishment of a safety margin, i.e., a parameter that enables the estimation of the lifetime of structural elements based on the observed first signs of damage.

To illustrate the problem, the cracking of a specimen made of 316 stainless steel at a temperature of 550°C was analysed. The 316SS is widely used, e.g. in pressure vessels in nuclear reactors, especially at elevated temperatures where creep and creep-fatigue resistance are of primary importance.

There are numerous items of experimental data available in the literature for this material, both for the tension of initially undamaged specimens and for compact tension (CT) specimens (e.g. [14,15,16,17,18]). The typical operating temperature for pressure vessels made of 316 steel is about 0.4 T_m, where T_m is the melting temperature approximately 1680 K (cf. [19]). Most of the available experimental data pertains to the temperature range of 0.5 to 0.6 T_m, as tests at lower temperatures are more time-consuming. The chosen temperature also falls into this range, as 550°C corresponds to 0.49 T_m. Therefore, the extension of the obtained results to other temperature ranges should be done with great caution, taking into account the changes in creep and damage mechanisms observed on the corresponding maps (cf. [19,20]).

2. THE FRACTURE MECHANICS APPROACH

2.1. FM models of creep crack growth (CCG)

The FM approach uses the energy needed for crack development as the main source of information about the process. For a given crack length, it is possible to calculate the critical loading or alternatively the critical crack length for a given loading.

In the first stage of failure development, there is no observable crack, so it is impossible to describe this stage in terms of FM. However, it is possible to correlate this period with FM parameters and determine the time of crack initiation (cf. [21,22]).

In the second stage, FM is mainly used in the case of a single crack. If the stress field around the crack tip is known, the J-integral or its creep equivalents C^* or $C(t)$ can be calculated. The definition of the C^* contour integral is similar to the J-integral but strains and displacements are replaced by their rates (cf. [22,23]):

$$C^* = \int_{\Gamma} (W_s^* dy - T_k \frac{\partial \dot{u}_k}{\partial x} ds), \quad (1)$$

where $W_s^* = \int_0^{\varepsilon_{ij}^c} \sigma_{ij} d\varepsilon_{ij}^c$ is the strain energy rate density, T_k is the traction vector, \dot{u}_k is the displacement rate vector in stationary creep state, Γ is a contour around the crack tip. The C^* -integral is path independent if the elastic strain rates are small in comparison to creep strain rates. In these conditions, C^* describes the stress distribution near the crack tip [23].

When the stationary creep does not occur, the stress field around the crack tip can be described by the $C(t)$ parameter [24]:

$$C(t) = \int_{\Gamma \rightarrow 0} (W_s^* dy - T_k \frac{\partial \dot{u}_k}{\partial x} ds). \quad (2)$$

This integral is not path independent, it has to be evaluated near the crack tip. For a large t , when creep becomes stationary, $C(t)$ approaches the C^* -integral, for any t : $C(t) > C^*$. It was shown that in stationary creep conditions, the C^* -integral can be correlated with the crack growth rate (cf. e.g. [21,25,26]).

2.2. FM estimation of lifetime

The time for crack initiation t_i is not directly described by FM models. There are some estimations, and the proposition of Tan, Celard et al. [21] is applied in the current work. They defined a lower and upper approximation. The first formula uses the typical relation between the C^* parameter and crack growth rate:

$$\dot{a} = DC^{*\varphi}, \quad (3)$$

where a is the current crack length, and D and φ are material parameters. To calculate the time t_i , the initial crack increment da is assumed. This increment is assessed as the minimum crack length which can be measured. This approach gives the lower approximation of the crack initiation time:

$$t_{iL} = \frac{da}{DC^{*\varphi}}. \quad (4)$$

The upper approximation t_{iU} is achieved under assumption that the initial crack growth rate is $(n+1)$ times smaller than the rate in a stationary state, where n is creep index in the Norton creep eq. (8):

$$t_{iU} = \frac{(n+1)da}{DC^{*\varphi}}. \quad (5)$$

The comparison of the results of experiments for different steels with the approximations defined above indicated that the crack initiation times fall within the expected range. The lower approximation was closer to the experimental results in most of the examined cases (cf. [21]).

The next step in the determination of the safety margin is the estimation of the crack growth time period $t_f - t_i$. This is usually determined through the integration of eq. (3), starting from the initial crack length $a_i = da$ up to the final crack length a_f which is equal to the total width of the element (cf. [27]). To perform this integration, the relationship between the value of the C^* parameter and the current crack length has to be established. This relationship can either be obtained analytically (cf. [22]) or numerically. This approach is limited by the assumption that the crack grows in a stationary environment, i.e. the stress distribution in the vicinity of the crack tip is described by stationary creep equations. This is possible only when the rate of stress redistribution is faster than the rate of crack growth. If this assumption is not satisfied, the C^* -integral cannot be used and instead, other parameters, specific to the transition creep period, like $C(t)$ or C_t , can be applied (cf. [28]).

The material parameters D , φ (eq. (3)) can be found experimentally or determined by some analytical formulas (see [22]). There is also an approximate solution which describes the creep crack growth quite well for most of the cases (cf. [5]):

$$\dot{a} = \frac{3C^{*0.85}}{\varepsilon_f^*}, \quad (6)$$

while $\varepsilon_f^* = \varepsilon_f$ in plane stress, where ε_f is equal to the ductility at the uniaxial tension probe, in plane strain, it is assumed that

$$\varepsilon_f^* = \varepsilon_f / 50$$

or

$$\varepsilon_f^* = \varepsilon_f / 30, \varepsilon_f^*$$

is in a dimensionless unit, \dot{a} is in mm/h, and C^* is in MPam/h (cf. [5,21]).

3. THE DAMAGE MECHANICS APPROACH

3.1. Uniaxial tension creep damage model

All of the formulas of *FM* are valid only in situations where an initial crack exists. Parameters like C^* , $C(t)$ are undefined for uncracked specimens. There is no such limitation in the case of damage mechanics models. The damage develops in material that is initially undamaged, which leads to the initiation of a microcrack. Therefore, *DM* can be used for determination of the time t_i . It is also possible to model the flaws or microcrack systems in original material by setting an appropriate initial damage field.

When the crack starts to develop, the application of *DM* is more troublesome. However, attempts to describe the crack development by growth of the damage field up to its critical value and further development are often made (cf. e.g. [5,25,29,30,31]).

This approach, known as the local approach to fracture (*LAF*) encounters a series of problems [32]. Applications of continuous equations in the solving of *DM* problems (named continuous damage mechanics [33]) are limited by the size of the smallest element in which system variables can be considered continuous, called representative volume element (*RVE*). The requirements for *RVE* are contradictory. *RVE* should be large enough to contain the representative number of defects and sufficiently small that the variations of stress and strain values are relatively small. These requirements can be more or less satisfied for a problem with undamaged or randomly distributed damage to the material (cf. [34]). The damage distribution is usually correlated with the microstructure of the material and the size of *RVE* is then adopted to the characteristic dimensions of this microstructure.

In the original Kachanov model [2] and in its successors (e.g. [4,18,35]), the development of damage is dependent upon the stress state. There are also strain-based damage models (e.g. [15,36,37]) in which the critical value of the damage parameter is achieved when the ductility of material is exhausted. The current work is mainly based on the Kachanov proposition of creep damage development. Additionally, it is assumed that the creep strains are associated with damage (cf. [3]). The uniaxial constitutive equations are as follows:

$$\dot{\omega} = C \left(\frac{\sigma}{1-\omega} \right)^m, \quad (7)$$

$$\dot{\varepsilon}_c = B \left(\frac{\sigma}{1-\omega} \right)^n, \quad (8)$$

where σ is uniaxial stress, $\dot{\varepsilon}_c$ is the creep strain rate, ω is the damage parameter, and C , m , B and n are material parameters. The time to failure and the stationary creep rate obtained as a solution of the Kachanov model show a good agreement with experimental results for a very large spectrum of materials. However, the strain values and the shape of the creep curve are not well predicted by the eqs. (7-8). This is so because the primary creep stage is not considered in these equations. To compensate, the effect of primary creep, the instantaneous strain ε_0 which is equal to sum of elastic, plastic and the equivalent of primary strain is introduced. The total strain is then the sum of instantaneous and creep strain:

$$\varepsilon = \varepsilon_0 + \varepsilon_c. \quad (9)$$

3.2. Influence of stress triaxiality

The equations of the development of creep damage are fitted to experimental results in the uniaxial tension creep test. While the

triaxial stress state is achieved in the vicinity of the crack tip (cf. e.g. [15,18,35,38]). Hayhurst, who analysed the growth of damage in the multiaxial state, assumed that effective stress σ_{eff} is responsible for damage development and it takes the form [39]:

$$\sigma_{eff} = \alpha \sigma_{max} + 3\beta \sigma_m + \gamma \sigma_e, \quad \alpha + \beta + \gamma = 1, \quad (10)$$

where α , β , γ are material parameters, σ_{max} is maximum principal stress, σ_m is mean stress and σ_e is Huber-von Mises-Hencky equivalent stress. The influence of σ_m is negligible for metallic materials as it is responsible for the volumetric growth of voids and creep deformation is regarded as incompressible. Then eq. (10) reduces to:

$$\sigma_{eff} = \alpha \sigma_{max} + (1 - \alpha) \sigma_e, \quad (11)$$

and the effect of stress triaxiality is solely described by parameter α . This approach is widely used in many stress-based damage models (cf. e.g. [4,25,35]).

In models where the damage parameter is based on strain, the ductility is described by the Manjoine equation (cf. e.g. [4,15,40]):

$$\varepsilon_f^* = \varepsilon_f 2^{1 - \frac{3\sigma_m}{\sigma_e}}. \quad (12)$$

Here, the ductility is a function of the triaxiality coefficient defined as ratio σ_m/σ_e . In the vicinity of the crack tip, the value of this coefficient is large, so the strain at failure is small (cf. [18]). In Fig. 1 it can be seen that the strain at failure calculated from the Kachanov model (eqs. (7-8, 11)) is close to the Manjoine model in this range.

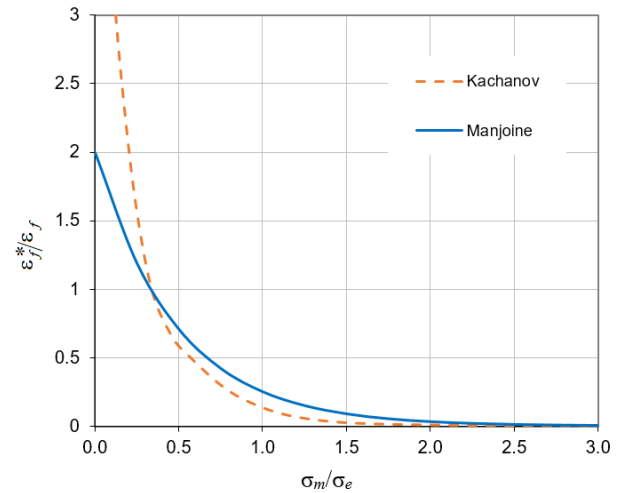


Fig. 1. Comparison of the ductility obtained on the basis of the Kachanov and Manjoine models

3.3. Non-local damage model

The main problem in the application of continuous *DM* equations is strong localised damage and strain occurring in the numerical solution of crack problems. It results in the spurious mesh dependence of the solution (cf. [41]).

There are many possibilities to prevent excessive damage localisation, such as the mesh-dependent softening modulus, the limitation of mesh size, artificial viscosity, the Cosserat continuum, the gradient method and the non-local integral method (see [42] for review). The non-local damage theory seems to be one of the most popular theories. The idea is that the constitutive equation contains

not only local values but also some non-local parameters obtained by averaging the chosen value in a particular volume. The motivation for the use of non-local theory is the observation that the growth of the crack does not depend on the state at a given point but on energy release in its vicinity (cf. [43]). This method is also used in the current work.

The definition of the non-local value of the state variable ξ is:

$$\bar{\xi}(x) = \frac{1}{V_r} \int_{V(x)} w(x,r) \xi(r) dv, \quad r \in V(x), \quad (13)$$

where $V(x)$ is the neighbourhood of point x , $w(x,r)$ is the weighted function, and

$$V_r = \int_{V(x)} w(x,r) dv, \quad r \in V(x), \quad (14)$$

is the characteristic volume (cf. [44]).

The value of weighted function depends on the relative position of points x and r . The most popular version of it is Gaussian distribution:

$$w(x,r) = \exp\left(-\left(\frac{d(x,r)}{d^*}\right)^2\right), \quad (15)$$

where $d(x,r)$ is the distance between points x , r , and d^* is the characteristic length. The characteristic length becomes a new method parameter. Usually, it is a material parameter, depended on the internal structure of the material. For crystalline materials, it has to be associated with grain size (cf. e.g. [13,45]). According to some authors, it is not a pure material parameter as it is also dependent on the used solution method (cf. e.g. [46,47]).

Theoretically, the size of the neighbourhood $V(x)$ can be unlimited, but for practical reason, it is limited to some extension of characteristic length. The smallest distance between points x and r , at which the weighted function vanishes or becomes negligible, is called the non-local interaction radius (cf. [43]). There are also methods for which the interaction radius is exactly equal to the characteristic length (e.g. grid method [13,48]).

4. CREEP CRACK GROWTH SIMULATION OF CT SPECIMEN

4.1. Experiment description

The analysis was performed for a compact tension (CT) specimen made of 316 stainless steel creeping at a temperature of 550°C. Its results were compared with experimental data [18]. The dimensions of the specimen are presented in Fig. 2 and Table 1. The CT specimen was prepared according to the standard procedure given in ASTM E-399. The loading was 19,620 N which gives a time to rupture of about 40 200 hours at a temperature of 550°C. The reference stress level calculated according to [18] is 164 MPa. The fracture toughness of 316 stainless steel is about 240 MPa^{0.5} at room temperature and it is reduced by about half at 550°C (cf. [49]). A similar reduction can also be found in [50].

The specimen was modelled in the Abaqus Finite Element system in plane strain. Due to symmetry, only half of each specimen was modelled. The example of the mesh with symmetric boundary conditions is presented in Fig. 3.

The material parameters were determined on the basis of uniaxial creep tests at a temperature of 550°C (cf. [14,18]). They are as follows: elasticity modulus $E=169617$ MPa, Poisson ratio $\nu=0.3$, creep deformation parameters: $B=6.561E-24$ (MPa)^{- n} h⁻¹, $n=7.778$, damage development parameters: $A=3.983E-23$ (MPa)^{- m} h⁻¹, $m=7.622$. Additionally, the dependency of instantaneous strain ε_0

was modelled on the basis of plastic deformation and primary creep.

It can be observed in Fig. 4 that the Kachanov eqs. (7-8) assure a good approximation of strains in the secondary creep period but exceed the experimental values for tertiary creep. It affects the strain at failure but does not change the time to failure which is the main target of the analysis.

To model the influence of stress triaxiality, equation (11) is used. Parameter α was determined by Hayhurst et al. [14] in the notched bar tension experiments and the value of $\alpha=0.75$ was used in the current paper.

Tab. 1. Parameters of CT test [18]

T [°C]	W [cm]	B (width) [cm]	a [cm]	P [kN]	tr [h]
550	50	25	16.67	19.620	40 200

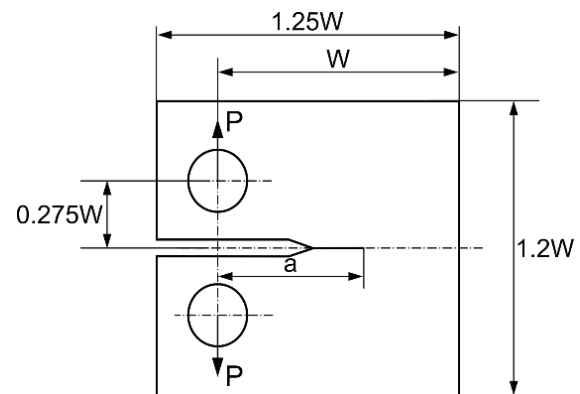


Fig. 2. Compact tension specimen

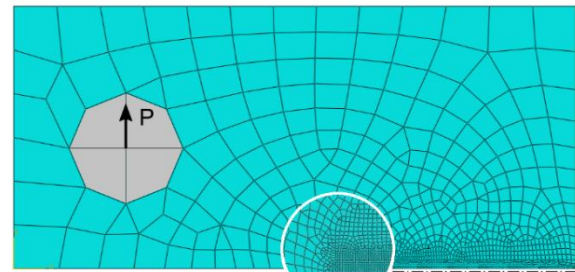


Fig. 3. Finite element mesh with symmetric boundary conditions

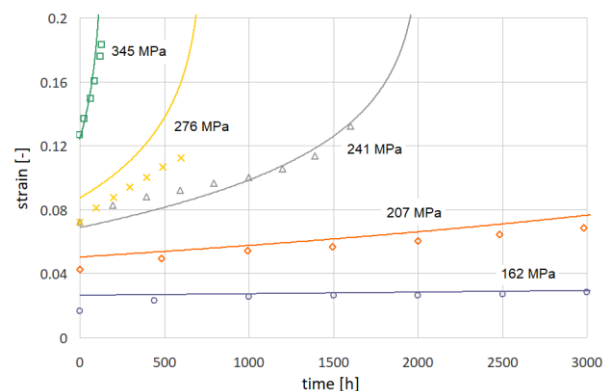


Fig. 4. Comparison of results of the Kachanov model with chosen experimental points of uniaxial tension creep of 316 steel at a temperature of 550°C [14]

4.2. FM crack growth simulation for stationary creep

In order to simulate the crack growth, the C^* -integral was used. The dependency of C^* on crack length was found using finite element analysis. The built-in procedure of Abaqus system (cf. [51]) was used for the determination of the $C(t)$ parameter and then the limit value of it in the stationary state was established as the C^* value. The Norton creep model – eq. (8) – without damage development ($\omega=0$) was used as a constitutive equation. The results of this analysis are presented in Fig. 5 (blue line).

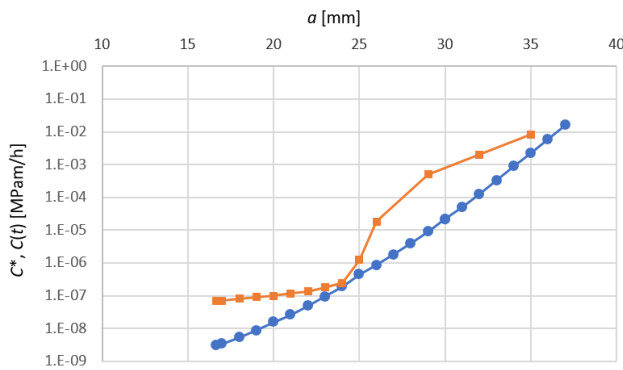


Fig. 5. C^* -integral for stationary creep (blue circles), and $C(t)$ for a model with damage (orange squares) as a function of crack length

Next, the value of t_i (crack initiation) was established. Eqs. (4-5) require knowledge of material parameters D and φ . The approximate values of these parameters are defined in eq. (6). The index φ is equal to 0.85 and the value of parameter D is equal to 692.3, assuming a plane strain state and ductility of $\varepsilon_f=0.13$ (cf. [14]). Using these values, the lower estimation of initiation time is 12.6E3 h and the upper estimation is 110.8E3 h for $da=0.5$ mm. The upper estimation is much larger than the experimental value of the time of final failure; therefore, the lower estimation was chosen for future analysis. Such an approach also corresponds to the results presented in [22].

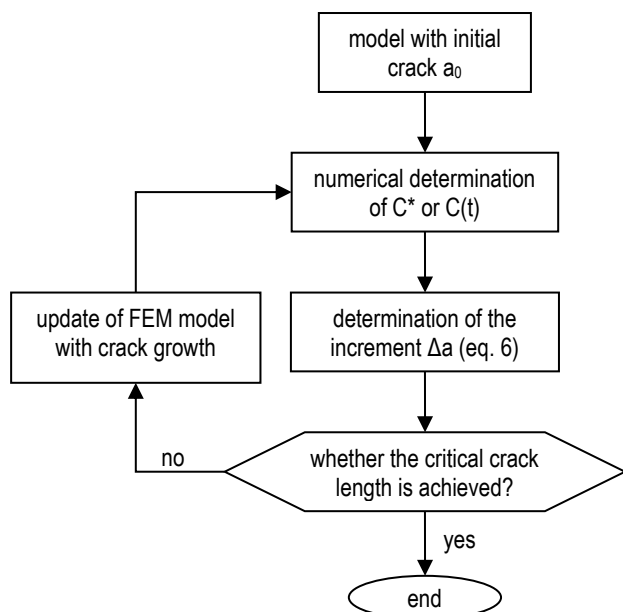


Fig. 6. Flowchart of numerical simulation of crack growth

The simulation of crack growth was obtained by the integration of eq. (6). The simplified flowchart of the applied procedure is presented in Fig. 6. The result is presented in Fig. 7 – solid blue line. The time to failure t_f obtained in this method (sum of the initiation time and crack growth time) is 84.7E3 h, which is two times greater than the experimental value. The safety margin according to this method is $t_f/t_i=84.7/12.6=6.7$.

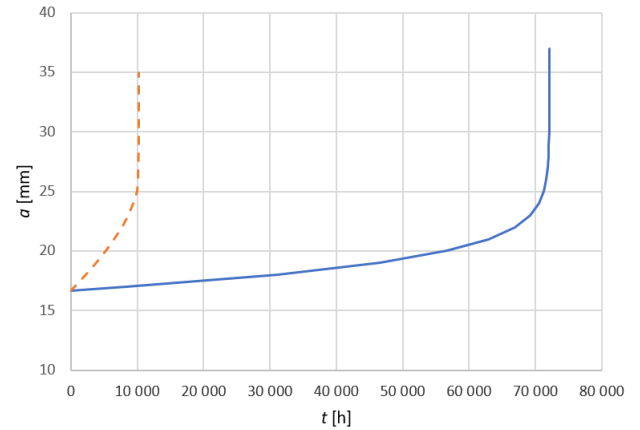


Fig. 7. Crack growth simulation for stationary creep (solid blue line) and for the creep damage model (dashed orange line) obtained on the basis of FM equations

4.3. FM crack growth simulation for the creep damage model

The method described above can be applied when in the vicinity of the crack tip, the stress distribution reflects the stationary state. This is the case when stress redistribution is faster than crack growth. The duration of stress redistribution can be calculated from the formula (cf. [1]):

$$t_{red} = \frac{J}{(1+n)C^*}, \quad (16)$$

where the J -integral describes the initial plastic distribution. This time for the examined case is equal to 124E3 h, so it is much greater than the expected time of crack growth. This is the reason that the stationary creep model does not describe the case well.

The second model considers the damage field developing prior to the crack formation. As a consequence, the crack growth is faster and the time to failure shorter. The full set of eqs. (7-9) is used in this case. When the damage parameter reaches its critical value (0.99) at an integration point, this point is marked as damaged and excluded from the problem domain. The cluster of such points forms a crack or a void ahead of the crack tip.

In these conditions, it is impossible to reach the stationary distribution and determine the C^* parameter. The $C(t)$ defined by eq. (2) can be used instead (cf. [1,22]). There are not many works using this approach (cf. [52,53]); therefore, a custom procedure based on the scheme presented in Fig. 6 was used. The value of $C(t)$ integral is determined at the moment just before the damage parameter reaches its critical value. The obtained results for different crack lengths are presented in Fig. 5 (orange line). These values are greater than the corresponding C^* values, but for small crack lengths, the increment of $C(t)$ is smaller, which generates a more stable rate of crack growth of order 1E-3 mm/h. The change of dependency function can be observed when the crack length

achieves about 25 mm, which can be considered as the critical length.

The parameters of eq. (3) are the same as in the previous model. The index φ in the damaged environment is often equal to (cf. [54]):

$$\varphi = \frac{m}{1+n}. \quad (17)$$

However, in the examined case, this expression gives a value very close to the approximate value given by eq. (6), which was finally chosen (0.868 vs. 0.85).

The curve of crack growth obtained on the basis of the above assumptions is presented in Fig. 7 (dashed orange line). The time of crack growth up to failure is 10.2E3 h, and total time including the initiation time is 22.8E3 h. This value is about two times smaller than the experimental time and the safety margin obtained in this model is $t/t_i=1.8$. It is much smaller than predicted by the previous analysis and can be used as its lower approximation.

4.4. DM local model

In the next step, the local Kachanov model described by eqs. (7-9) was used. The material parameters were listed in Section 4.1. As the solution is strongly mesh-dependent, the simulations were performed for four meshes with a minimum mesh size from 0.5 to 0.05 mm. The times t_i and t_f obtained in these simulations are presented in Fig. 8. Despite the large spread of results, it can be noticed that the safety margin t_f/t_i is more repetitive and it falls between 2.0 and 2.6, except for one case (a very rare mesh). The lower bound of this range can be used as an appropriate approximation of the ratio t_f/t_i .

For the examined model, the value of time to failure parameter t_f is within the range of 160 h to 11E3 h, indicating a very large spread. All calculated values are smaller than the experimental value. The crack was developing in a plane of initial crack, as it was expected. Its growth rate is initially stationary at the level of 2E-2 mm/h (see Fig. 9). From Fig. 9, the approximate value of critical crack length can also be determined. Its value depends on the mesh density and varies from 20 to 32 mm.

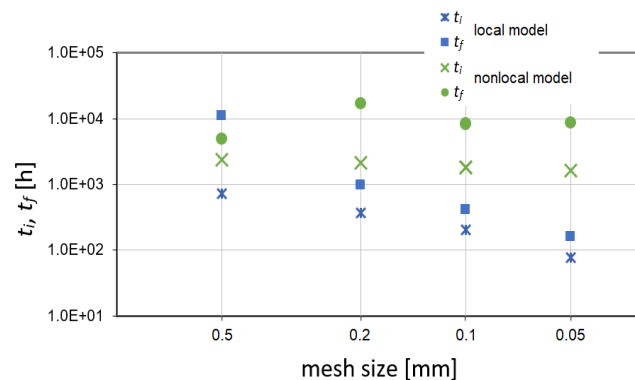


Fig. 8. Crack initiation time t_i and the time to failure t_f as a function of minimum mesh size for local and non-local damage models

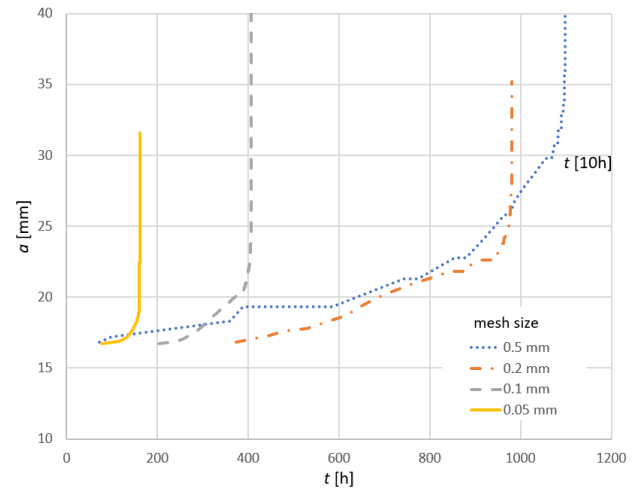


Fig. 9. Simulation of crack growth by local damage model for different mesh sizes (the time scale for mesh size 0.5 mm is ten times greater than for the other meshes)

4.5. DM non-local model

In the non-local model, the state of point depends not only on the previous state of the point but also on the state of neighbouring points. This causes the time to rupture of the cracked specimen to be greater than that obtained in the local method as the factors influencing the damage growth are volume averaged.

Different state variables can be averaged (see [43] for review). The most popular formulation assumes that the damage variable depends on averaged strains (cf. e.g. [45,55,56,57,58]). In the current work, damage development is a function of stress and the damage increment was chosen as the averaged parameter. Such an approach was proposed by Chaboche (cf. e.g. [13,44,59]). First, the local damage increment is calculated:

$$\dot{\omega}_{loc} = C \left(\frac{\sigma}{1-\omega} \right)^m. \quad (18)$$

In the next stage, the equation of damage growth is formulated in terms of the average value of damage growth. It is calculated with use a formula derived from eq. (13):

$$\bar{\omega}(x) = \frac{1}{V_r} \int_{V(x)} w(x,r) \dot{\omega}_{loc}(r) dv, \quad r \in V(x), \quad (19)$$

where the weighted function $w(x,r)$ and the volume V_r are determined according to formulas (14-15). In these equations, the characteristic length parameter d^* plays the key role. In the present work, it is assumed to be equal to parameter da used in *FM* model, i.e. 0.5 mm. The volume $V(x)$ was bounded and the interaction radius was assumed to be equal to $3d^*$.

The application of the non-local method enabled the obtaining of the time to crack initiation t_i which is much less dependent on mesh size than in the local model. Its dispersion was from 1.6E3 to 2.3E3 h. The value of the t_f parameter was much more scattered, from 5E3 to 17E3 h, but it was still more stable than in case of the local method. According to the performed simulations, the estimation of the safety margin is between 2 and 4, which is slightly more than that obtained from previous methods.

By comparison of the growth curves for different mesh sizes, one can notice that they are close to each other in the initial period. Thus, the goal of the application of the non-local method was achieved. Further development of the crack follows by step increments and the differences between individual solutions are observed. This indicates that an unambiguous solution cannot be achieved for time t_f using the presented method. Despite it can be noticed that all solutions give a common starting point for fast crack development, this point can be approximated as 25 mm of crack length. This result aligns very well with the previously obtained solution using *FM* in the damaged environment.

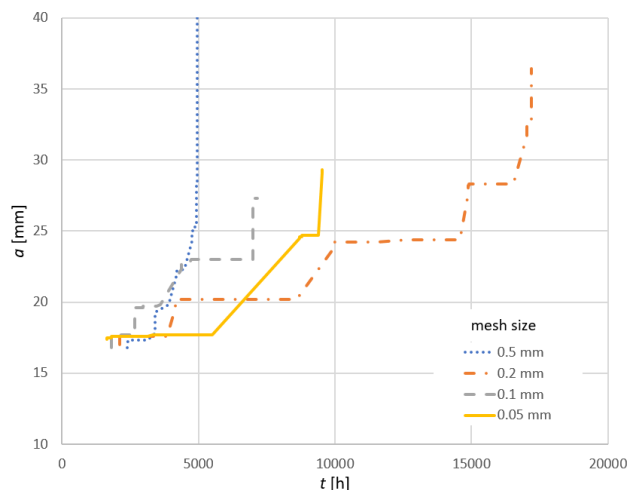


Fig. 10. Simulation of crack growth by the non-local damage model for different mesh sizes

5. SUMMARY

The presented solutions to the crack growth problem under creep conditions did not yield fully satisfactory results. The obtained times exhibit significant variability. In the case of the *FM* methods, the time to crack initiation depends primarily on the parameter d_a . Its role is similar to the mesh size in the finite element method (*FEM*) or the characteristic length for non-local methods. The shortest time to failure was achieved in the local model, but it strongly depends on the mesh size. The non-local method provides a prediction of crack initiation time independent of mesh size, thus achieving the intended goal. However, this approximation is significantly smaller than the lower bound estimate obtained using the method proposed by Tan, Celard et al. [21]. Obtaining larger times to failure in simulations is possible by adjusting the parameter α (see discussion below).

A significant spread of results was also obtained for the time to failure. *FM*-based methods yield longer times than the empirical ones, while *DM*-based methods yield shorter times. The longest time of crack growth was determined using the C^* parameter. However, this method assumes the stationary stress distribution in the vicinity of the crack tip, which is unattainable. Other methods based on damage mechanics yield more realistic results, although these are lower than the experimental values. Nevertheless, they are on the safe side, making them suitable for estimating time to failure in situations where initial signs of damage are observed.

Despite the discrepancy in specific times, the comparison of safety margin estimates t_f/t_i presented in this paper yields very similar results. Especially, the local *DM* method provides a relatively constant value of safety margin, meaning that the time to rupture is

proportional to the time of initiation, regardless of the element size. On the other hand, the non-local method exhibits a larger spread in safety margin due to the variability in time to rupture, while maintaining a constant initiation time. The non-local method also clearly indicates a critical crack length, which is the value at which a rapid increase in crack growth velocity occurs. Its value is also consistent with the result obtained using the $C(t)$ integral.

The key problem of these predictions is also the availability and reliability of material parameters. There is large dispersion of material data for examined steel (cf. [16]). Additionally, they are mainly determined in uniaxial creep tension experiments, but are used in situations in which the multiaxial stress state dominates. Only the parameters of eq. (10) are responsible for this behaviour, so their proper determination is crucial. To solve this problem, Hyde proposed calibration of the value of parameter α by fitting the time to rupture in the *CT* experiment [35]. They obtained value $\alpha=0.48$ for similar material at a temperature of 600°C. The smaller value of parameter α gives larger time to failure, so closer to experimental value. However, the application of this approach raises many doubts. It should be used only when the numerical simulations produce unambiguous results. Since this is not the case here, applying this method is not possible.


The solutions obtained by the author enables drawing the conclusion that the most reliable results are obtained from the $C(t)$ method and the non-local *DM* model, which are very close to each other. These methods, despite some limitations, are relatively simple and they can therefore be used in the estimation of lifetimes to fracture and safety margins for structures undergoing cracking in creep conditions.

REFERENCES

1. Riedel H. Fracture at High Temperatures. Berlin: Springer-Verlag; 1987. <https://doi.org/10.1007/978-3-642-82961-1>
2. Kachanov LM. On the time of the rupture in creep conditions (Russian). Izv AN SSSR. 1958;8: 26-31.
3. Rabotnov YuN. Creep Problems of Structural Members. Amsterdam: North-Holland; 1969.
4. Liu Y, Murakami S. Damage localization of conventional creep damage models and proposition of a new model for creep damage analysis. JSME Int J. 1998;41A: 57-65. <https://doi.org/10.1299/jsmea.41.57>
5. Nishida K, Nikbin KM, Webster GA. Influence of net section damage on creep crack growth. J Strain Anal Eng. 1989;24:75-82. <https://doi.org/10.1243/03093247V242075>
6. Tvergaard V. Analysis of creep crack growth by grain boundary cavitation. Int J Fract. 1986;31: 183-209. <https://doi.org/10.1007/BF00018927>
7. Pandey VB, Singh V, Mishra BK, Ahmad S, Rao AV. Creep crack simulations using continuum damage mechanics and extended finite element method. Int J of Damage Mech. 2019;28: 3-34. <https://doi.org/10.1177/1056789517737593>
8. Rastello G, Giry C, Gatuingt F, Desmorat R. From diffuse damage to strain localization from an Eikonal Non-Local (ENL) Continuum Damage model with evolving internal length. Comput Methods Appl Mech Engng. 2018;331: 650-674. <https://doi.org/10.1016/j.cma.2017.12.006>
9. Peerlings RHJ, de Borst R, Brekelmans WAM, de Vree JHP. Gradient-enhanced damage for quasi-brittle materials. Int J Numer Meth Engng. 1996;39: 3391-3403. [https://doi.org/10.1002/\(SICI\)1097-0207\(19961015\)39:19<3391::AID-NME7>3.0.CO;2-D](https://doi.org/10.1002/(SICI)1097-0207(19961015)39:19<3391::AID-NME7>3.0.CO;2-D)
10. McLean M, Dyson BF. Modeling the Effects of Damage and Microstructural Evolution on the Creep Behavior of Engineering Alloys. ASME J Eng Mater Tech. 2000;122: 273-278. <https://doi.org/10.1115/1.482798>
11. Hayhurst DR. CDM mechanisms-based modelling of tertiary creep:

- ability to predict the life of engineering components. Arch Mech. 2005;57: 71-100.
<https://am.ippt.pan.pl/index.php/am/article/view/v57p103>
12. Mustata R, Hayhurst DR. Creep constitutive equations for a 0.5Cr 0.5 Mo 0.25V ferritic steel in the temperature range 565 C–675 C. Int J Pres Ves & Piping. 2005;82: 363-372.
<https://doi.org/10.1016/j.ijpvp.2004.11.002>
13. Hall FR, Hayhurst DR. Modelling of Grain Size Effects in Creep Crack Growth Using a Non-Local Continuum Damage Approach. Proc. R. Soc. London A. 1991;433: 405-421.
<https://doi.org/10.1098/rspa.1991.0055>
14. Hayhurst DR, Dimmer PR, Morrison CJ. Development of Continuum Damage in the Creep Rupture of Notched Bars. Phil Trans R Soc Lond A. 1984;311: 103-129. <https://doi.org/10.1098/rsta.1984.0021>
15. Wen JF, Tu ST, Gao XL, Reddy JN. Simulations of creep crack growth in 316 stainless steel using a novel creep-damage model. Eng Fract Mech. 2013;98: 169-184.
<https://doi.org/10.1016/j.engfracmech.2012.12.014>
16. Hayhurst DR, Vakili-Tahami F, Zhou JQ. Constitutive equations for time independent plasticity and creep of 316 stainless steel at 550°C. Int J Pres Ves & Piping. 2003;80: 97-109.
[https://doi.org/10.1016/S0308-0161\(03\)00027-9](https://doi.org/10.1016/S0308-0161(03)00027-9)
17. Kelly DA, Morrison CJ. Creep life of AISI 316 stainless steel loaded at constant strain rate. J Strain Anal Eng. 1983; 18:189-193.
<https://doi.org/10.1243/03093247V183189>
18. Hall FR, Hayhurst DR, Brown PR. Prediction of Plane-Strain Creep-Crack Growth Using Continuum Damage Mechanics. Int J of Damage Mech. 1996;5: 353-383.
<https://doi.org/10.1177/105678959600500402>
19. Miller DA, Langdon TG. Creep fracture maps for 316 stainless steel. Metall Mater Trans A. 1979;10:1635-1641.
<https://doi.org/10.1007/BF02811696>
20. Petkov MP, Juan PA. Revised creep fracture maps of Type 316 stainless steel and their mechanistic perspective. Engineering Failure Analysis. 2024;159:108094.
<https://doi.org/10.1016/j.engfailanal.2024.108094>
21. Tan M, Celard NJC, Nikbin KM, Webster GA. Comparison of creep crack initiation and growth in four steels tested in HIDA. Int J Pres Ves & Piping. 2001;78: 737-747.
[http://dx.doi.org/10.1016/S0308-0161\(01\)00085-0](http://dx.doi.org/10.1016/S0308-0161(01)00085-0)
22. Webster GA, Ainsworth RA. High temperature component life assessment. London: Chapman and Hall; 1994.
23. Landes JD, Begley JA. A fracture mechanics approach to creep crack growth. In: Rice JR, Paris PC, editors. Mechanics of crack growth. STP590: Proc. of the 8th National Symposium on Fracture Mechanics; 1974 Aug 26-28; ASTM 1976. p. 128-148.
<http://dx.doi.org/10.1520/STP33943S>
24. Riedel H, Rice JR. Tensile cracks in creeping solids. In: Paris PC, editor. Fracture mechanics. STP700. West Conshohocken: ASTM; 1980. p. 112-130. <http://dx.doi.org/10.1520/STP36967S>
25. Hayhurst DR, Brown PR, Morrison CJ. The Role of Continuum Damage in Creep Crack Growth. Phil Trans R Soc Lond A. 1984;311: 131-158. <https://doi.org/10.1098/rsta.1984.0022>
26. Harper MP, Ellison EG. The use of the C* parameter in predicting creep crack propagation rates. J Strain Anal Eng. 1977;12: 167-179.
<https://doi.org/10.1243/03093247V123167>
27. Hyde TH, Sun W, Hyde CJ. Applied Creep Mechanics. New York: McGraw Hill; 2013.
28. Saxena A. Creep and creep-fatigue crack growth. Int J Fract. 2015;191: 31-51. <https://doi.org/10.1007/s10704-015-9994-4>
29. Hayhurst DR, Dimmer PR, Chernuka MW. Estimates of the creep rupture lifetime of structures using the finite element method. J Mech Phys Solids. 1975;23: 335-350.
[https://doi.org/10.1016/0022-5096\(75\)90032-0](https://doi.org/10.1016/0022-5096(75)90032-0)
30. Murakami S, Hirano T, Liu Y. Asymptotic fields of stress and damage of a mode I creep crack in steady-state growth. Int J Sol Struct. 2000;37: 6203-6220.
[https://doi.org/10.1016/S0020-7683\(99\)00267-X](https://doi.org/10.1016/S0020-7683(99)00267-X)
31. Bodnar A, Chrzanowski M, Nowak K. Brittle failure lines in creeping plates. Int J Pres Ves & Piping. 1996;66: 253-261.
[https://doi.org/10.1016/0308-0161\(95\)00100-X](https://doi.org/10.1016/0308-0161(95)00100-X)
32. Skrzypek J, Ganczarski A. Modeling of Material Damage and Failure of Structures. Berlin, Heidelberg: Springer; 1999.
<https://doi.org/10.1007/978-3-540-69637-7>
33. Janson J, Hult J. Fracture mechanics and damage mechanics, a combined approach. J. de Mec. Appliquee. 1977;1: 69-84.
34. Lemaître J. A Course on Damage Mechanics. Berlin, Heidelberg: Springer; 1996.
35. Hyde CJ, Hyde TH, Sun W, Becker AA. Damage mechanics based predictions of creep crack growth in 316 stainless steel. Eng Fract Mech. 2010;77: 2385-2402.
<https://doi.org/10.1016/j.engfracmech.2010.06.011>
36. Spindler MW. The multiaxial creep ductility of austenitic stainless steels. Fatigue Fract Engng Mater Struct. 2004;27: 273-281.
<https://doi.org/10.1111/j.1460-2695.2004.00732.x>
37. Oh CS, Kim NH, Kim YJ, Davies C, Nikbin K, Dean D. Creep failure simulations of 316H at 550°C: Part I – A method and validation. Eng Fract Mech. 2011;78:2966-2977. <https://doi.org/10.1016/j.engfracmech.2011.08.015>
38. Wen JF, Tu ST. A multiaxial creep-damage model for creep crack growth considering cavity growth and microcrack interaction. Eng Fract Mech. 2014;123: 197-210. <https://doi.org/10.1016/j.engfracmech.2014.03.001>
39. Hayhurst DR. Creep rupture under multi-axial states of stress. J Mech Phys Solids. 1972;20: 381-390.
[https://doi.org/10.1016/0022-5096\(72\)90015-4](https://doi.org/10.1016/0022-5096(72)90015-4)
40. Manjoine MJ. Creep-rupture behavior of weldments. Weld J. 1982;61: S50-7.
41. Pijaudier-Cabot G, Bazant ZP. Nonlocal damage theory. J Eng Mech. 1987;113: 1512-1533.
[https://doi.org/10.1061/\(ASCE\)0733-9399\(1987\)113:10\(1512\)](https://doi.org/10.1061/(ASCE)0733-9399(1987)113:10(1512))
42. Murakami S. Continuum Damage Mechanics. Dordrecht: Springer; 2012. <https://doi.org/10.1007/978-94-007-2666-6>
43. Bazant ZP, Jirasek M. Nonlocal integral formulations of plasticity and damage: survey of progress. J Eng Mech. 2002;128: 1119-1149.
[https://doi.org/10.1061/\(ASCE\)0733-9399\(2002\)128:11\(1119\)](https://doi.org/10.1061/(ASCE)0733-9399(2002)128:11(1119))
44. Chaboche JL. Phenomenological aspects of continuum damage mechanics. In: Germain P, Piau M, Caillerie D, editors. Theoretical and Applied Mechanics. Proc. XVII Int. Cong. Theor. Appl. Mech; 1988 Aug 21-27; Grenoble, France. Elsevier; 1989. p. 41-56.
<https://doi.org/10.1016/B978-0-444-87302-6.50011-9>
45. de Vree JHP, Brekelmans WAM, van Gils MAJ. Comparison of non-local approaches in continuum damage mechanics. Comp and Struct. 1995;55:581-8. [https://doi.org/10.1016/0045-7949\(94\)00501-S](https://doi.org/10.1016/0045-7949(94)00501-S)
46. Bazant ZP. Nonlocal Damage Theory Based on Micromechanics of Crack Interactions. J Eng Mech. 1994;120:593-617.
[https://doi.org/10.1061/\(ASCE\)0733-9399\(1994\)120:3\(593\)](https://doi.org/10.1061/(ASCE)0733-9399(1994)120:3(593))
47. Murakami S, Liu Y. Mesh-Dependence in Local Approach to Creep Fracture. Int J of Damage Mech. 1995;4:230-250.
<https://doi.org/10.1177/105678959500400303>
48. Nowak K. Application of a nonlocal grid model for analysis of the creep damage of metals. Int J of Damage Mech. 2020;29: 780-797.
<https://doi.org/10.1177/1056789519883668>
49. Picker C. The fracture toughness of Type 316 steel and weld metal. Report No. IWGFR-49(V.2). 1983;16:915-93.
50. Gao W, Chen K, Guo X, Zhang L. Fracture toughness of type 316LN stainless steel welded joints. Mater Sci Eng A. 2017;685:107-114.
<https://doi.org/10.1016/j.msea.2016.12.128>
51. Abaqus 2021 Documentation. Dassault Systèmes Simulia Corp. 2021.
52. Webster GA. Fracture Mechanics in the creep range. J Strain Anal Eng. 1994;29:215-223.
<http://journals.sagepub.com/doi/10.1243/03093247V293215>
53. Kumar M, Singh IV. Numerical investigation of creep crack growth in plastically graded materials using C(t) and XFEM. Eng Fract Mech. 2020; 226:106820.
<https://doi.org/10.1016/j.engfracmech.2019.106820>

54. Webster GA, Nikbin KM, Chorlton MR, Cellard NJC, Ober M. A comparison of high temperature defect assessment methods. *J Mater High Temp.* 1998;15:337-346. <https://doi.org/10.1080/09603409.1998.11689620>
55. Garcia R, Flórez-López J, Cerrolaza M. A boundary element formulation for a class of non-local damage models. *Int J Sol Struct.* 1999;36:3617-3638. [https://doi.org/10.1016/S0020-7683\(98\)00159-0](https://doi.org/10.1016/S0020-7683(98)00159-0)
56. Broz P. Regularization procedures for damage problems. *Transactions on Modelling and Simulation.* 2003;35:103-111. <https://doi.org/10.2495/BE030111>
57. Simone A, Wells GN, Sluys LJ. From continuous to discontinuous failure in a gradient-enhanced continuum damage model. *Comput Methods Appl Mech Engng.* 2003;192:4581-4607. [https://doi.org/10.1016/S0045-7825\(03\)00428-6](https://doi.org/10.1016/S0045-7825(03)00428-6)
58. De-Pouplana I, Onate E. Combination of a non-local damage model for quasi-brittle materials with a mesh-adaptive finite element technique. *Finite Elements in Analysis and Design.* 2016;112:26-39. <https://doi.org/10.1016/j.finel.2015.12.011>
59. Duddu R, Waisman H. A nonlocal continuum damage mechanics approach to simulation of creep fracture in ice sheets. *Comput Mech.* 2013;51:961–974. <https://doi.org/10.1007/s00466-012-0778-7>

Krzysztof Nowak:  <https://orcid.org/0000-0001-8892-3050>



This work is licensed under the Creative Commons BY-NC-ND 4.0 license.

POINTWISE COMPLETENESS AND POINTWISE DEGENERACY OF DESCRIPTOR LINEAR DISCRETE-TIME SYSTEMS WITH DIFFERENT FRACTIONAL ORDERS

Tadeusz KACZOREK*

*Faculty of Electrical Engineering, Bialystok University of Technology, Wiejska 45D, 15-351 Bialystok

t.kaczorek@pb.edu.pl

received 13 July 2024, revised 23 May 2025, accepted 06 June 2025

Abstract: The solution to the system of equations of the descriptor linear discrete-time with different fractional orders is derived by the use of the Drazin inverse of matrices. This solution is applied to analysis of the pointwise completeness and the pointwise degeneracy of the descriptor discrete-time linear systems with different fractional orders. Necessary and sufficient conditions for the pointwise completeness and the pointwise degeneracy of the descriptor discrete –time linear systems with different fractional orders are established. The proposed methods are illustrated by numerical examples.

Key words: drazin inverse, descriptor, discrete-time, linear, system, pointwise completeness, pointwise degeneracy, fractional, different orders

1. INTRODUCTION

Descriptor (singular) linear systems have been considered in [3,5,7,15,19]. The fundamentals of fractional calculus have been given in [22, 23, 13]. The linear systems with fractional orders have been analyzed in [4, 6, 9, 10] and with different fractional orders in [1, 12, 15, 23, 24]. The analysis of differential algebraic equations and its numerical solutions have been analyzed in [20] and the numerical and symbolic computations of generalized inverses in [29]. The T-Jordan canonical form and the T-Drazin inverse based on the T-product have been addressed in [23]. In [21] The multilinear time-invariant descriptor systems have been analyzed in [21]. The descriptor and standard positive linear systems by the use of Drazin inverse has been addressed in [2, 8, 15]. The pointwise degeneracy of autonomous control systems have been considered in [20] and of linear delay-differential systems with nonnilpotent passive matrices in [16]. The pointwise completeness and degeneracy of fractional descriptor discrete-time linear systems by the use of the Drazin inverse matrices have been addressed in [9, 11, 12] and of fractional different orders in [14, 15, 26]. Analysis of the differential-algebraic equations has been analyzed in [19] and the numerical and symbolic computations of the generalized inverses in [27]. The T-Jordan canonical form and T-Drazin inverse based on the T-Jordan canonical form and T-Drazin inverse based on the T-product has been investigated in [21, 22]. The numerical and symbolic computation of the generalized inverses have been analyzed in [27].

In this paper the pointwise completeness and the pointwise degeneracy of descriptor linear discrete-time systems with different orders will be analyzed.

The paper is organized as follows. In Section 2 the Drazin inverse of matrices is applied to find the solution to descriptor linear discrete-time systems with different fractional orders. Necessary and sufficient conditions for the pointwise completeness of the

systems with fractional orders are established in Section 3 and the pointwise degeneracy of the systems in Section 4. Concluding remarks are given in Section 5.

The following notation will be used: \mathfrak{R} - the set of real numbers, $\mathfrak{R}^{n \times m}$ - the set of $n \times m$ real matrices and $\mathfrak{R}^n = \mathfrak{R}^{n \times 1}$, Z_+ - the set of nonnegative integers, I_n - the $n \times n$ identity matrix, $imgP$ - the image of the matrix P .

2. SOLUTION OF THE STATE EQUATIONS OF FRACTIONAL DESCRIPTOR DISCRETE-TIME LINEAR SYSTEMS

Consider the descriptor fractional discrete-time linear system with two different fractional orders

$$\begin{aligned} E \begin{bmatrix} \Delta^\alpha x_1(i+1) \\ \Delta^\beta x_2(i+1) \end{bmatrix} &= A \begin{bmatrix} x_1(i) \\ x_2(i) \end{bmatrix} \text{ and} \\ E &= \begin{bmatrix} E_1 & 0 \\ 0 & E_2 \end{bmatrix}, A = \begin{bmatrix} A_{11} & A_{12} \\ A_{21} & A_{22} \end{bmatrix}, \end{aligned} \quad (1)$$

where

$$0 < \alpha, \beta < 2, \quad i \in Z_+ = \{0, 1, 2, \dots\}, \quad x_1(i) \in \mathfrak{R}^{n_1} \text{ and}$$

$$x_2(i) \in \mathfrak{R}^{n_2}$$

are the state vectors and

$$E_k, A_{kj} \in \mathfrak{R}^{n_k \times n_j}; k, j = 1, 2.$$

The fractional difference of α (β) order is defined by [11, 13]

$$\begin{aligned} \Delta^\alpha x(i) &= \sum_{j=0}^i c_\alpha(j) x(i-j), \\ c_\alpha(j) &= (-1)^j \binom{\alpha}{j} = (-1)^j \frac{\alpha(\alpha-1)\dots(\alpha-j+1)}{j!}, c_\alpha(0) = 1, j = 1, 2, \dots \end{aligned} \quad (2)$$

In descriptor systems it is assumed that $\det E = 0$ and the pencil is regular, i.e.

$$\det \left[\begin{bmatrix} E_1 z_1 & 0 \\ 0 & E_2 z_2 \end{bmatrix} - \begin{bmatrix} A_{11} & A_{12} \\ A_{21} & A_{22} \end{bmatrix} \right] \neq 0 \text{ for some } z_1, z_2 \in C \quad (3)$$

where C is the field of complex numbers.

Premultiplying (1) by the matrix

$$[E \operatorname{diag}(I_{n_1} c_1, I_{n_2} c_2) - A]^{-1}$$

we obtain

$$\bar{E} \begin{bmatrix} \Delta^\alpha x_1(i+1) \\ \Delta^\beta x_2(i+1) \end{bmatrix} = \bar{A} \begin{bmatrix} x_1(i) \\ x_2(i) \end{bmatrix}, i \in Z_+ \quad (4)$$

where

$$\bar{E} = [E \operatorname{diag}(I_{n_1} c_1, I_{n_2} c_2) - A]^{-1} E = \begin{bmatrix} \bar{E}_{11} & \bar{E}_{12} \\ \bar{E}_{21} & \bar{E}_{22} \end{bmatrix},$$

$$\bar{A} = [E \operatorname{diag}(I_{n_1} c_1, I_{n_2} c_2) - A]^{-1} A = \begin{bmatrix} \bar{A}_{11} & \bar{A}_{12} \\ \bar{A}_{21} & \bar{A}_{22} \end{bmatrix}. \quad (5)$$

The equation (1) and (4) have the same solution

$$x(i) = \begin{bmatrix} x_1(i) \\ x_2(i) \end{bmatrix}.$$

Lemma 1. If there exist $c_1, c_2 \in C$ such that

$$\bar{E} [\operatorname{diag}(I_{n_1} c_1, I_{n_2} c_2)] \bar{E} = \bar{E}^2 [\operatorname{diag}(I_{n_1} c_1, I_{n_2} c_2)] \quad (6)$$

then

$$\bar{E} \bar{A} = \bar{A} \bar{E}. \quad (7)$$

Proof. From (5) we have

$$\bar{E} \operatorname{diag}(I_{n_1} c_1, I_{n_2} c_2) - \bar{A} = [E \operatorname{diag}(I_{n_1} c_1, I_{n_2} c_2) - A]^{-1} \times [E \operatorname{diag}(I_{n_1} c_1, I_{n_2} c_2) - A]^{-1} A = I_n \quad (8)$$

and

$$\bar{A} = \bar{E} \operatorname{diag}(I_{n_1} c_1, I_{n_2} c_2) - I_n. \quad (9)$$

Using (9) we obtain

$$\bar{E} \bar{A} = \bar{E} \{ \bar{E} \operatorname{diag}(I_{n_1} c_1, I_{n_2} c_2) - I_n \} = \bar{E}^2 \operatorname{diag}(I_{n_1} c_1, I_{n_2} c_2) - \bar{E} \quad (10)$$

and

$$\bar{A} \bar{E} = \{ \bar{E} \operatorname{diag}(I_{n_1} c_1, I_{n_2} c_2) - I_n \} \bar{E} = \bar{E} \operatorname{diag}(I_{n_1} c_1, I_{n_2} c_2) \bar{E} - \bar{E}. \quad (11)$$

Therefore, if the condition (6) is satisfied then the equation (7) holds.

Remark 1. If $c_1 = c_2 \in C$ then the equality (6) is always satisfied

$$\bar{E} [\operatorname{diag}(I_{n_1} c_1, I_{n_2} c_2)] = \bar{E} c = c \bar{E}. \quad (12)$$

Lemma 2. If the condition (7) is satisfied then

$$\bar{E} \bar{A}^D = \bar{A}^D \bar{E}, \quad (13)$$

$$\bar{E}^D \bar{A} = \bar{A} \bar{E}^D, \quad (14)$$

$$\bar{E}^D \bar{A}^D = \bar{A}^D \bar{E}^D. \quad (15)$$

Proof is given in [13].

Remark 2. If $\det A \neq 0$ and we assume $c_1 = c_2 = 0$ then

$$\bar{E} = [-A]^{-1} E, \bar{A} = -I_n \quad (16)$$

in this case the condition (7) is satisfied.

Substituting (2) into (4) we obtain

$$\bar{E} \begin{bmatrix} \Delta^\alpha x_1(i+1) \\ \Delta^\beta x_2(i+1) \end{bmatrix} = \begin{bmatrix} \bar{A}_{1\alpha} & \bar{A}_{12} \\ \bar{A}_{21} & \bar{A}_{2\beta} \end{bmatrix} \begin{bmatrix} x_1(i) \\ x_2(i) \end{bmatrix} + \sum_{j=2}^{i+1} \begin{bmatrix} I_{n_1} c_\alpha(j+1) & 0 \\ 0 & I_{n_2} c_\beta(j+1) \end{bmatrix} \begin{bmatrix} x_1(i-j+1) \\ x_2(i-j+1) \end{bmatrix}, \quad (17)$$

where $\bar{A}_{1\alpha} = \bar{A}_{11} + \alpha I_{n_1}, \bar{A}_{2\beta} = \bar{A}_{22} + \beta I_{n_2}$.

In particular case when $\bar{E} = I_n$ we have the following theorem.

Theorem 1. The fractional discrete-time linear system (4) with $\bar{E} = I_n$ and initial conditions

$$x(0) = \begin{bmatrix} x_1(0) \\ x_2(0) \end{bmatrix}$$

has the solution

$$x(i) = \Phi_i \begin{bmatrix} x_1(0) \\ x_2(0) \end{bmatrix}, \quad (18)$$

where

$$\Phi_i = \begin{cases} I_n & \text{for } i = 0 \\ \bar{A} \Phi_{i-1} - D_1 \Phi_{i-2} - \dots - D_{i-1} \Phi_0 & \text{for } i = 1, 2, \dots \end{cases} \quad (19a)$$

$$\bar{A} = \begin{bmatrix} \bar{A}_{11} & \bar{A}_{12} \\ \bar{A}_{21} & \bar{A}_{22} \end{bmatrix}, D_k = \begin{bmatrix} I_{n_1} c_\alpha(k+1) & 0 \\ 0 & I_{n_2} c_\beta(k+1) \end{bmatrix}, \quad k = 1, 2, \dots \quad (19b)$$

Proof is given in [13].

If $\bar{E} \neq I_n$ then the Drazin inverse of matrix \bar{E} will be applied to find the solution to the equation (4).

Definition 1. A matrix \bar{E}^D is called the Drazin inverse of $\bar{E} \in \mathfrak{R}^{n \times n}$ if it satisfies the conditions

$$\bar{E} \bar{E}^D = \bar{E}^D \bar{E}, \quad (20a)$$

$$\bar{E}^D \bar{E} \bar{E}^D = \bar{E}^D, \quad (20b)$$

$$\bar{E}^D \bar{E}^{q+1} = \bar{E}^q, \quad (20c)$$

where q is the smallest nonnegative integer (called index of \bar{E}), satisfying the condition $\operatorname{rank} \bar{E}^q = \operatorname{rank} \bar{E}^{q+1}$.

The Drazin inverse \bar{E}^D of a square matrix \bar{E} always exists and is unique. If $\det \bar{E} \neq 0$ then $\bar{E}^D = \bar{E}^{-1}$. The Drazin inverse matrix \bar{E}^D can be computer by the one of known methods [2, 3, 13].

Theorem 2. The descriptor fractional discrete-time linear system (4) with initial conditions $x(0) = \begin{bmatrix} x_1(i) \\ x_2(i) \end{bmatrix} \in \operatorname{Im}(\bar{E}^D \bar{E}) = \bar{E}^D \bar{E} v, x \in \mathfrak{R}^n$ has the solution

$$x(i) = \begin{bmatrix} x_1(i) \\ x_2(i) \end{bmatrix} = \hat{\Phi}_i \bar{E}^D \bar{E} v, \quad (21)$$

where

$$\hat{\Phi}_i = \begin{cases} I_n & \text{for } i = 0 \\ \hat{A} \hat{\Phi}_{i-1} - \hat{D}_1 \hat{\Phi}_{i-2} - \dots - \hat{D}_{i-1} \hat{\Phi}_0 & \text{for } i = 1, 2, \dots \end{cases} \quad (22a)$$

$$\hat{A} = \bar{E}^D \bar{A} = \begin{bmatrix} \hat{A}_{11} & \hat{A}_{12} \\ \hat{A}_{21} & \hat{A}_{22} \end{bmatrix},$$

$$\widehat{D}_k = \bar{E}^D \begin{bmatrix} I_{n_1} c_\alpha (k+1) & 0 \\ 0 & I_{n_2} c_\beta (k+1) \end{bmatrix}, k = 1, 2, \dots \quad (22b)$$

Proof. Taking into account that the equations (1) and (4) have the same solution the proof will be accomplished by showing that the solution (21) satisfies the equation (4).

Using (21) and (22) we obtain

$$\begin{aligned} \bar{E} \widehat{\Phi}_{i+1} \bar{E}^D \bar{E} v &= \bar{E} (\widehat{A} \widehat{\Phi}_i - \widehat{D}_1 \widehat{\Phi}_{i-1} - \dots - \widehat{D}_i \widehat{\Phi}_0) \bar{E}^D \bar{E} v = \\ &= \bar{E} \bar{E}^D \widehat{A} (\widehat{A} \widehat{\Phi}_{i-1} - \widehat{D}_1 \widehat{\Phi}_{i-2} - \dots - \widehat{D}_{i-1} \widehat{\Phi}_0) \bar{E}^D \bar{E} v \\ &= \widehat{A} (\widehat{A} \widehat{\Phi}_{i-1} - \widehat{D}_1 \widehat{\Phi}_{i-2} - \dots - \widehat{D}_{i-1} \widehat{\Phi}_0) (\bar{E}^D \bar{E})^2 v = \widehat{A} \widehat{\Phi}_i \bar{E}^D \bar{E} v \end{aligned} \quad (23)$$

since (14) and $(\bar{E}^D \bar{E})^2 = \bar{E}^D \bar{E}$. Therefore, the solution of the equation (1) has the form (21).

3. THE POINTWISE COMPLETENESS OF DESCRIPTOR FRACTIONAL DISCRETE-TIME LINEAR SYSTEMS WITH DIFFERENT FRACTIONAL ORDERS

In this section necessary and sufficient conditions for the pointwise completeness of the descriptor discrete-time linear systems with different fractional orders will be established.

Definition 2. The descriptor fractional discrete-time linear system (1) is called pointwise complete at the point $i = q$ if for every final state $x_f \in \mathfrak{R}^n$, there exists an boundary condition $x(0) \in Im \bar{E} \bar{E}^D$ such that

$$x(q) = x_f \in Im \bar{E} \bar{E}^D. \quad (24)$$

Theorem 3. The descriptor fractional discrete-time linear system (1) is pointwise complete for $i = q$ and every $x_f \in \mathfrak{R}^n \in Im \bar{E} \bar{E}^D$ if and only if

$$\det \widehat{\Phi}_q \neq 0 \quad (25a)$$

where

$$\widehat{\Phi}_q = \widehat{A} \widehat{\Phi}_{q-1} - \widehat{D}_1 \widehat{\Phi}_{q-2} - \dots - \widehat{D}_{q-1} \widehat{\Phi}_0 \quad (25b)$$

and \widehat{A} , \widehat{D}_k are defined by (22b).

Proof. From (21) for $i = q$ we obtain

$$x_f = x(q) = \widehat{\Phi}_q \bar{E}^D \bar{E} x(0). \quad (26)$$

For given $x_f \in \mathfrak{R}^n \in Im \bar{E} \bar{E}^D$ we may find $x(0) \in Im \bar{E} \bar{E}^D$ if and only if the condition (25) is satisfied. Therefore, the descriptor fractional system (1) is pointwise complete at the point $i = q$ if and only if the condition (25) is satisfied.

Example 1. Consider the descriptor fractional system (1) for $\alpha = 0.6, \beta = 0.8$ with the matrices

$$\begin{aligned} E = \begin{bmatrix} E_1 & 0 \\ 0 & E_2 \end{bmatrix} = \begin{bmatrix} 1 & 0 & 0 \\ 0 & 0 & 1 \\ 0 & 0 & 0 \end{bmatrix}, A = \begin{bmatrix} A_{11} & A_{12} \\ A_{21} & A_{22} \end{bmatrix} = \\ = \begin{bmatrix} 0 & 1 & 1 \\ 0 & 0 & 0 \\ 0 & 1 & 0 \end{bmatrix}, \\ n_1 = 1, n_2 = 2. \end{aligned} \quad (27)$$

We choose $c_1 = c_2 = 1$ and using (5), (27) we obtain

$$\begin{aligned} \bar{E} &= [E \operatorname{diag}(c_1, c_2) - A]^{-1} E = \begin{bmatrix} \bar{E}_{11} & \bar{E}_{12} \\ \bar{E}_{21} & \bar{E}_{22} \end{bmatrix} = \begin{bmatrix} 1 & 0 & 1 \\ 0 & 0 & 0 \\ 0 & 0 & 1 \end{bmatrix}, \\ \bar{A} &= [E \operatorname{diag}(c_1, c_2) - A]^{-1} A = \begin{bmatrix} \bar{A}_{11} & \bar{A}_{12} \\ \bar{A}_{21} & \bar{A}_{22} \end{bmatrix} = \end{aligned}$$

$$\begin{bmatrix} 0 & 0 & 1 \\ 0 & -1 & 0 \\ 0 & 0 & 0 \end{bmatrix} \quad (28)$$

The Drazin inverse matrix of \bar{E} has the form

$$\bar{E}^D = \begin{bmatrix} 1 & 0 & -1 \\ 0 & 0 & 0 \\ 0 & 0 & 1 \end{bmatrix} \text{ and } \bar{E} \bar{E}^D = \begin{bmatrix} 1 & 0 & 0 \\ 0 & 0 & 0 \\ 0 & 0 & 1 \end{bmatrix}. \quad (29)$$

In this case

$$\begin{aligned} \widehat{\Phi}_1 &= \widehat{A} = \bar{E}^D \bar{A} = \begin{bmatrix} 1 & 0 & -1 \\ 0 & 0 & 0 \\ 0 & 0 & 1 \end{bmatrix} \begin{bmatrix} 0 & 0 & 1 \\ 0 & -1 & 0 \\ 0 & 0 & 0 \end{bmatrix} = \\ &= \begin{bmatrix} 0 & 0 & 1 \\ 0 & 0 & 0 \\ 0 & 0 & 0 \end{bmatrix}. \end{aligned} \quad (30)$$

$$\text{And } x(0) \in Im \bar{E} \bar{E}^D = \begin{bmatrix} x_{11}(0) \\ 0 \\ x_{21}(0) \end{bmatrix} \text{ and } x_{11}(0), x_{21}(0)$$

are arbitrary.

Note that the matrix $\widehat{\Phi}_1$ is singular and by Theorem 2 the descriptor fractional system with (27) is not pointwise complete

$$\text{for } q = 1 \text{ and every } x_f \in \mathfrak{R}^3 \text{ of the form } x_f = \begin{bmatrix} x_{11}(t_f) \\ 0 \\ x_{21}(t_f) \end{bmatrix}$$

and $x_{11}(t_f), x_{21}(t_f)$ are arbitrary.

Using (25b) for $q = 2$ we obtain

$$\begin{aligned} \widehat{\Phi}_2 &= \widehat{A}^2 - \widehat{D}_1 = \begin{bmatrix} 0 & 0 & 1 \\ 0 & -1 & 0 \\ 0 & 0 & 0 \end{bmatrix}^2 - \begin{bmatrix} I_2 c_\alpha(2) & 0 \\ 0 & c_\beta(2) \end{bmatrix} = \\ &= \begin{bmatrix} 0.12 & 0 & 0 \\ 0 & 0.88 & 0 \\ 0 & 0 & 0.08 \end{bmatrix} \end{aligned} \quad (31)$$

and

$$\widehat{\det} \widehat{\Phi}_2 = 8.448 * 10^{-3} \neq 0. \quad (32)$$

Therefore, by Theorem 2 the descriptor fractional system with (27) is pointwise complete for $q = 2$.

4. THE POINTWISE DEGENERACY OF FRACTIONAL DESCRIPTOR LINEAR DISCRETE-TIME SYSTEMS

In this section necessary and sufficient conditions for the pointwise degeneracy of the descriptor discrete-time linear systems with different fractional orders will be established.

Definition 4.1. The descriptor fractional discrete-time linear system (1) is called pointwise degenerated in the direction v for $q = q_f$ if there exists a vector $v \in \mathfrak{R}^n$ such that for all initial conditions $x(0) \in Im \bar{E} \bar{E}^D$ the solution of (1) for $q = q_f$ satisfy the condition

$$v^T x_f = 0. \quad (33)$$

Theorem 3. The descriptor fractional continuous-time linear system (1) is pointwise degenerated in the direction $v \in \mathfrak{R}^n$ for $q = q_f$ if and only if

$$\det \widehat{\Phi}_q = 0, \quad (34)$$

where $\widehat{\Phi}_q$ is defined by (25b).

Proof. From (4.1) and (26) for $q = q_f$ we have

$$v^T \hat{\Phi}_q x(0) = 0. \quad (35)$$

There exists a nonzero vector $v \in \mathbb{R}^n$ such that (35) holds for all $x(0) \in \text{Im } E \tilde{E}^D$ if and only if the condition (34) is satisfied. Therefore, the descriptor fractional system (1) is pointwise degenerated in the direction $v \in \mathbb{R}^n$ for $q = q_f$ if the condition (34) is satisfied. \square

Remark 2. The vector $v \in \mathbb{R}^n$ in which the descriptor fractional discrete-time linear system (1) is pointwise degenerated can be computed from the equation

$$v^T \hat{\Phi}_q = 0. \quad (36)$$

Example 2. (Continuation of Example 1) Consider the system (1) for $\alpha = 0.6, \beta = 0.8$ with the matrices (27). In Example 1 it was shown that the matrix $\hat{\Phi}_q$ for $q = 1$ is nonsingular. Therefore, the descriptor fractional system (1) with (27) is pointwise degenerated for $q = 1$ and any direction v .

From (31) and Theorem 3 it follows that the matrix $\hat{\Phi}_2$ is nonsingular. Therefore, by Theorem 3 the system (1) with (27) is not pointwise degenerated for $i = q = 2$.

5. CONCLUDING REMARKS

The Drazin inverse of matrices has been applied to investigation of the pointwise completeness and the pointwise degeneracy of the descriptor linear discrete-time systems with different fractional orders. Necessary and sufficient conditions for the pointwise completeness (Theorem 2) and for the pointwise degeneracy (Theorem 3) of the fractional linear discrete-time systems have been established. The considerations have been illustrated by numerical examples. The presented methods can be extended to the descriptor linear systems with many different fractional orders.

REFERENCES

- Buslowicz M. Stability analysis of continuous-time linear systems consisting of n subsystem with different fractional orders. Bull. Pol. Ac.: Tech. 2012; 60(2): 279-284.
- Campbell SL, Meyer CD and Rose NJ. Applications of the Drazin inverse to linear systems of differential equations with singular constant coefficients. SIAMJ Appl. Math. 1976; 31(3): 411-425.
- Dai L. Singular control systems. Lectures Notes in Control and Information Sciences. Springer-Verlag. Berlin; 1989.
- Dzieliński A, Sierociuk D, Sarwas G. Ultracapacitor parameters identification based on fractional order model. Proc ECC. Budapest; 2009.
- Fahmy MM, O'Reill J. Matrix pencil of closed-loop descriptor systems: infinite-eigenvalues assignment, Int. J. Control. 1989; 49(4): 1421-1431.
- Ferreira NMF, Machado JAT. Fractional-order hybrid control of robotic manipulators, Proc. 11th Int. Conf. Advanced Robotics. ICAR Coimbra. Portugal; 2003: 393-398.
- Guang-Ren D. Analysis and Design of Descriptor Linear Systems. Springer. New York; 2010.
- Kaczorek T. Pointwise Completeness and Pointwise Degeneracy of Linear Systems. In: Selected Problems of Fractional Systems Theory. Lecture Notes in Control and Information Sciences. Springer, Berlin Heidelberg. 2011;411: 81-101.
- Kaczorek T. Pointwise completeness and pointwise degeneracy of fractional descriptor continuous-time linear systems with regular pencils, Bulletin of the Polish Academy of Sciences Technical Sciences. 2015;63(1): 169-172, 2015.
- Kaczorek, T. Positive linear systems with different fractional orders. Bull. Pol. Ac.: Tech. 2010;58(3): 453-458.
- Kaczorek, T. Selected Problems in Fractional Systems Theory. Springer-Verlag. Berlin; 2011.
- Kaczorek T, Busłowicz M. Pointwise completeness and pointwise degeneracy of linear continuous-time fractional order systems. Journal of Automation. Mobile Robotics and Intelligent Systems. 2009; 3(1): 8-11.
- Kaczorek T, Rogowski K. Fractional Linear Systems and Electrical Circuits. Springer; 2015.
- Kaczorek T, Sajewski Ł. The pointwise completeness and the pointwise degeneracy of linear discrete-time different fractional orders systems, Bulletin of the Polish Academy of Sciences: Technical Sciences. 2020; 68 (6); 1513-1516.
- Kaczorek T, Sajewski Ł. Pointwise completeness and the pointwise degeneracy of fractional standard and descriptor linear continuous-time systems with different fractional, International Journal of Applied Mathematics & Computer Science. 2020; 30(4).
- Korobov AA. On pointwise degenerate linear delay-differential systems with nonnilpotent passive matrices, J. Appl. Industr. Math. 2017; 11(3): 369-380.
- Kucera V, Zagalak P. Fundamental theorem of state feedback for singular systems. Automatica. 1988; 24 (5): 653-658.
- Kundel P, Mehrmann V. Differential algebraic equations. Analysis and numerical solution 2nd edition. EMS Textboobs in Mathematics. Berlin; 2024.
- Metel'skii AV, Karpuk VV. On properties of pointwise degenerate linear autonomous control systems. I. Autom. Remote Control. 2009; 70(10): 1613-1625.
- Kundel P, Mehrmann V. Differential-algebraic equations. Analysis and numerical solution 2nd edition. EMS Textbooks in Mathematics. Berlin Mathematical Society (EMS); 2024.
- Liu Ma W, Wei Y. Multilinear time-invariant descriptor system. Computational and Applied Mathematics; 2025.
- Weia IY, Liu W, Wei C. T-Jordan canonical form and T-Drazin inverse based on the T-product. Commun.Appl.Math.Comput. 2021; 3(2):201-220.
- Miao Y, Qi Y. Wei, T-Jordan canonical form and T-Drazin inverse based on the T-product. Commun. Appl. Math. Comput. 2021; 3(2):201-220.
- Miller KS, Ross B. An Introduction to the Fractional Calculus and Fractional Differential Equations. Wiley New York; 1993.
- Podlubny I, Fractional Differential Equations. Academic Press. San Diego;1999.
- Sajewski Ł. Reachability, observability and minimum energy control of fractional positive continuous-time linear systems with two different fractional orders. Multidim. Syst. Sign. Process. 25.
- Sajewski Ł. Minimum energy control of fractional positive continuous-time linear systems with two different fractional orders and bounded inputs, Advances in Modelling and Control of Non-integer-Order Systems. Lecture Notes in Electrical Engineering. 2015; 320:171-181.
- Trzasko W. Pointwise Completeness and Pointwise Degeneracy of Linear Continuous-Time Systems with Different Fractional Orders. In: Szewczyk R, Zieliński C, Kaliczyńska M. (eds) Recent Advances in Automation, Robotics and Measuring Techniques. Advances in Intelligent Systems and Computing. Springer Cham. 2014; 267: 307-316.
- Wei Y, Stanimirovic P. Petkovic M. Numerical and symbolic computations of generalized inverses. Hackensack NJ World Scientific; 2018.

The work has been accomplished under the research project WZ/WE-IA/5/2023 financed from the funds for science by the Polish Ministry of Science and Higher Education.

Tadeusz Kaczorek:  <https://orcid.org/0000-0002-1270-3948>



This work is licensed under the Creative Commons BY-NC-ND 4.0 license.

EVALUATION OF TENSILE STRESS RELAXATION OF SELECTIVE LASER SINTERING OF PA2200 MATERIAL USING THE MAXWELL-WIECHERT MODEL

Wiktor SZOT^{*,}, Mateusz RUDNIK^{*,}, Paweł SZCZYGIEL^{*,}, Natalia KOWALSKA^{*,}

^{*,} Faculty of Mechatronics and Mechanical Engineering,
Department of Metrology and Unconventional Manufacturing Methods,
Kielce University of Technology, al. Tysiąclecia Państwa Polskiego 7 25-314 Kielce, Poland

^{*,} Faculty of Mechatronics and Mechanical Engineering,
Department of Fundamentals of Mechanical Engineering and Mechanical Technology,
Kielce University of Technology, al. Tysiąclecia Państwa Polskiego 7 25-314 Kielce, Poland

wszot@tu.kielce.pl, mrudnik@tu.kielce.pl, pszczygiel@tu.kielce.pl, nkowalska@tu.kielce.pl

received 16 December 2024, revised 26 March 2025, accepted 14 April 2025

Abstract: The use of 3D printing for the manufacture of functional components has led to a demand for research into the mechanical properties, including rheological properties, of additive manufactured models. In this article, the results of a study to evaluate the relaxation of tensile stress of samples made by selective laser sintering (SLS) of PA2200 material are presented. The evaluation of tensile stress relaxation was performed using the five-parameter Maxwell-Wiechert model. With the model used, elastic moduli and dynamic viscosity coefficients were calculated. The samples were made in three print orientations (0°, 45°, 90°) and two types of energy density ($E_d = 0.056 \text{ J/mm}^2$, $E_d = 0.076 \text{ J/mm}^2$). The results indicate that increasing the applied energy density leads to higher values of elastic moduli and dynamic viscosity coefficients. A strong fit of the model to the experimental curves was obtained, as confirmed by the obtained coefficients χ^2 and R^2 . This research comprehensively addresses the evaluation of the applicability of selective laser sintering technology, which is increasingly used in various areas of industry, as well as the influence of the process on the relaxation of tensile stress.

Key words: 3D printing, stress relaxation, Maxwell-Wiechert model, SLS

1. INTRODUCTION

Additive technology is one of the elements of Industry 4.0 [1]. Industry 4.0 also includes the process of testing technological and functional prototypes using 3D printing [1]. The testing of prototypes helps speed up the process of preparing the technological process for mass production [1]. In turn, testing of functional prototypes with properties similar to those of finished products enables a rapid and almost simultaneous refinement of the product at the prototype stage [1,2]. Testing involves, among other things, geometric analysis of the object through, for example, 3D scanning, and testing the mechanical properties (including rheological properties) of the functional prototype [3,4].

Studying the rheological properties of 3D printed parts is very important, if only because these parts can be subjected to long-term deformation or stress [5]. In the case of parts subjected to long-term deformation, one can speak of the phenomenon of stress relaxation [5,6]. Stress relaxation can be described using Maxwell's model as presented in several articles [7–14]. Maxwell models have different forms: simple and complex models, for example, models based on Prony series or models described by fractional calculus [13,14]. The stress relaxation of additively manufactured parts can vary depending on the print material used or the technological parameters of 3D printing, as confirmed in the articles [15,16].

In the article [7], the author conducted a study of stress

relaxation of samples made by selective powder sintering (SLS) technology from PA 2200 material. Samples were produced setting values for two technological parameters: layer height (0.1 mm – 0.4 mm) and print orientation (0°, 90°). Stress relaxation was determined during uniaxial compression testing. The Maxwell-Wiechert model was used to describe the stress relaxation curves. The results showed a clear influence of layer height on stress relaxation. Additionally, it was shown that the orientation of the print affects stress relaxation.

In [17], the authors conducted stress relaxation tests on PLA material using fused deposition technology (FDM). The samples were produced using two technological parameters of the print: the orientation of the print (0°, 45°, 90°) and the presence of a contour. In addition, the samples were subjected to different values of deformation and exposure to different temperatures during the tensile stress relaxation tests. To describe the stress-relaxation curves, 3 models were used: Maxwell, Findley and Linear solid. The results showed that Findley's law was the most appropriate empirical expression to predict the PLA tested. Stress distributions ranging from 11% to 14% were obtained. Both cooled and heated samples provided degradation of the quasistatic and long-term material properties. The presented results show the importance of stress relaxation effects in AM PLA structures.

In the article [11], the authors investigated, among other things, the stress relaxations of samples made of G6-Impact

nanocomposite using MEX material extrusion technology. The samples were made using the parameter of variable printing direction (0/45/-45/90/90/-45/45/0). The following were carried out: tensile stress relaxations, bending stress relaxations and compressive stress relaxations. On the basis of the results, it was found that the bending mode had the lowest relaxation, while the highest relaxation was observed for the tensile mode.

The viscoelastic behaviour of the materials strongly influences their application area [18,19]. The literature review presented above shows that the viscoelastic behaviour of 3D printed polymers depends on factors such as material type, 3D printing process, and type of load [2,10,20,21]. However, due to the limited number of studies in the field of stress relaxation of 3D printed materials, there is a need for continuous expansion to better understand this phenomenon.

Consequently, the purpose of the article was to determine the elastic moduli and dynamic viscosity coefficients of the PA 2200 polymer material. This material is well suited for medical devices such as orthoses or biomodels. The calculations used the five-parameter Maxwell-Wiechert model to determine the stress relaxation in the material. This research is very important because the calculated coefficients and modulus can be used in engineering calculations.

2. MATERIAL AND METHODS

2.1. Material PA2200

The test samples were made from PA 2200. This material is a powdered whitish fine polyamide. Prints made from polyamide powder have good mechanical properties, stiffness, and chemical resistance, similar to those of other materials used in industrial applications [20,22]. Table 1 focusses on the properties of PA 2200 as given by the manufacturer (EOS GmbH, Krailling, Germany) [23].

Tab. 1. Properties of PA 2200 powder [23]

Powder properties		Value	Unit	Test Standard
Medium grain size		60	μm	-
Density of ubound powder		0.435 – 0.445	g/cm^3	DIN 53466
Density of sintered powder		0.9 – 0.95	g/cm^3	EOS - Method
Mechanical Properties		Value	Unit	Test Standard
Flexural modulus, 23°C		1500	MPa	ISO 178
Flexural strength		58		ISO 178
Izod impact notched, 23°C		4.4	kJ/m^2	ISO 180/1A
Izod impact unnotched, 23°C		32.8		ISO 180/1U
Shore D hardness (15 s)		75	-----	ISO 868
Ball indentation hardness		78	MPa	ISO 2039-1
3D Data		Value	Unit	Test Standard
Tensile modulus	X-direction	700	MPa	ISO 527-1/-2
	Y-direction	1700		
	Z-direction	1650		
	X-direction	48		

Tensile strength	Y-direction	48		
	Z-direction	47		
Strain at break	X-direction	24	%	ISO 527-1/-2
Charpy impact strength (+23°C)	X-direction	53	kJ/m^2	ISO 179/1eU
Charpy notched impact strength (+23°C)	X-direction	4.8		ISO 179/1eA
Thermal conductivity	X-direction	0.144	$\text{W}/(\text{mK})$	DIN 52616
	Y-direction	0.144		
	Z-direction	0.127		

The PA 2200 material is biocompatible according to EN ISO 10993-1 and is USP / level VI / 121°C and approved for food contact according to the European Directive 2002/72/EC (except for alcoholic products) [23]. This polyamide can be used to manufacture consumer parts, medical devices, and functional plastic parts [2].

2.2. SLS technology

In the presented research, the well-known Formiga P100 machine (EOS GmbH, Krailling, Germany), which realises selective laser sintering - SLS technology, was used to build models. This machine makes it possible to produce physical plastic-based models with dimensions that do not exceed the dimensions of the working chamber of 250 mm x 200 mm x 330 mm. In the mentioned technology, a CO_2 laser is very often used to sinter the input material in the form of powder. The entire technological process is performed in an inert gas. The production scheme using SLS technology is shown in Figure 1 [2,24,25].

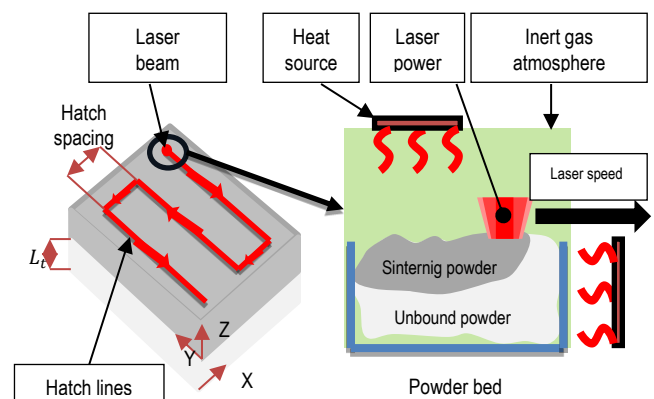


Fig. 1. Principle of SLS technology [2]

Fig. 1 also provides an explanation of the technological parameters in SLS technology such as layer thickness L_t , hatch spacing, laserpower and laser speed.

2.3. Samples Preparation

The test samples were designed in SolidWorks according to ISO 527. The shape of the samples are paddles with the dimensions in millimeters shown in Figure 2(a).

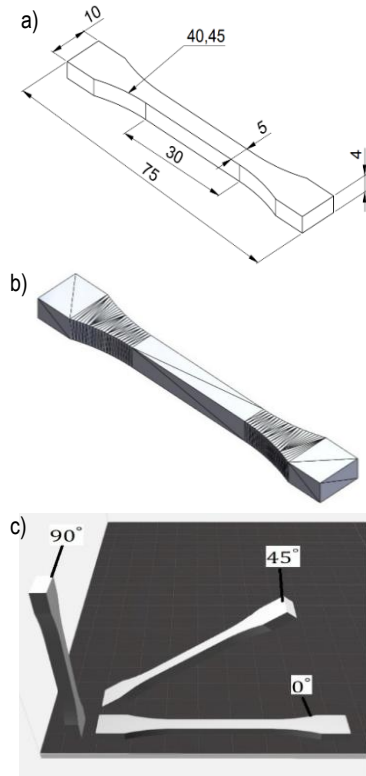


Fig. 2. Test specimens: a) dimensions, b) STL saving, c) print orientation

The STL files of the samples were saved with the following approximation parameters: linear tolerance of 0.007 mm and angular tolerance of 5°. The appearance of the sample in the STL record is shown in Figure 2(b). Six types of samples were produced with different 3D printing technological parameters, each variant was parted 10 times to account for statistical calculations.

The analysed technological parameters of 3D printing were energy density E_d , print orientation P_d and layer height L_t whose values are shown in Table 2. Interpretations of the positioning of the samples on the work platform are shown in Figure 2(c).

Tab. 2. Values of technological parameters

E_d		P_d	L_t
0.056 J/mm ²	0.076 J/mm ²	0°, 45°, 90°	0.1 mm
P = 21 W	P = 22 W		
v = 2500 mm/s	v = 1970 mm/s		

The energy density E_d transferred to the sintered layer was calculated using Equation 1 [5,24]:

$$E_d = \frac{P}{v \cdot h} \chi \quad (1)$$

where: P – laser power, W; v – laser beam speed, mm/s.; h = 0.25 mm (distance between successive laser beams); d = 0.42 mm (diameter of focused beam); χ = 1.68 (overlap factor).

Each individual sample was labelled according to the formula: $E_d^{56} - P_d^0 - 1$, which means E_d^{56} – energy density, P_d^0 – print orientations, 1 – sample number.

2.4. The Maxwell-Wiechert model

A complex five-parameter Maxwell-Wiechert model was used to describe the stress relaxation curves obtained from the stress relaxation tests. Approximations of this model to experimental curves were carried out with the OriginPro software using the Levenberg-Marquardt algorithm. The mechanical analogy of the Maxwell-Wiechert five-parameter model is shown in Figure 3 [5,13].

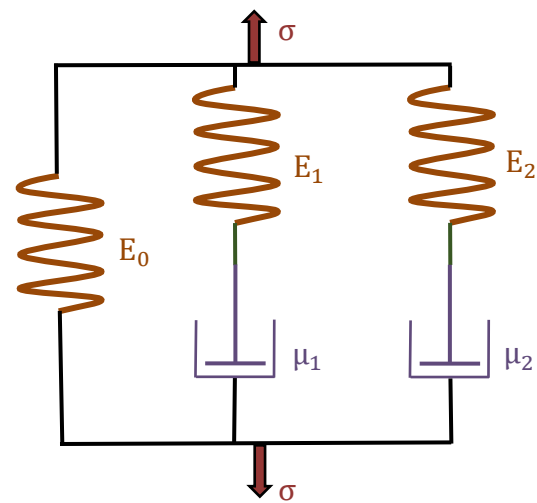


Fig. 3. Mechanical analogy of the Maxwell-Wiechert model [5,13]

The equation describing the Maxwell-Wiechert model consisting of five parameters is as follows [5,13]:

$$\sigma(t) = \sigma_0 + \sigma_1 e^{-\frac{t}{t_1}} + \sigma_2 e^{-\frac{t}{t_2}} \quad (2)$$

where t_1, t_2 are there relaxation times (s) of each model:

$$t_1 = \frac{\mu_1}{E_1}, \quad t_2 = \frac{\mu_2}{E_2} \quad (3)$$

After transforming equations (2) and (3), an equation was obtained describing the five-parameter Maxwell-Wiechert model, including all the parameters of this model [5,13].

$$\sigma(t) = \varepsilon_0 \left(E_0 + E_1 e^{-\frac{E_1 t}{\mu_1}} + E_2 e^{-\frac{E_2 t}{\mu_2}} \right) \quad (4)$$

where: ε_0 – unit initial strain; E_0, E_1, E_2 – moduli of elasticity, MPa; μ_1, μ_2 – coefficients of dynamic viscosity, MPa; t – time, s.

The equivalent modulus was also calculated using the following formula [5,13]:

$$E_s = E_0 + E_1 + E_2 \quad (5)$$

where: E_0, E_1, E_2 – moduli of elasticity, MPa.

The decrease in stress after time t was calculated using the formula [5,13]:

$$R_{\sigma} = \frac{\sigma_0 - \sigma_t}{\sigma_0} \cdot 100\% \quad (6)$$

where: σ_0 – initial stress, MPa; σ_t – stress after time t , MPa.

2.5. Measurement technologies

Stress relaxation tests were conducted using a Hegewald & Peschke Inspekt 3kN testing machine. The test parameters used to conduct the stress relaxation tests were: preload $F_p = 100 \text{ N}$, speed of displacement of the machine crossbar to achieve the set strain $v_{mm} = 10 \text{ mm/s}$, permanent strain $\varepsilon_0 = 0.02$, test duration $t = 600 \text{ s}$. The test specimens were subjected to tensile stress, as can be seen in Figure 4.



Fig. 4. Appearance of samples during stress relaxation tests

The test samples were exposed to tensile stresses.

3. RESULTS

Stress relaxation tests were performed, resulting in stress relaxation curves. These curves are shown in Figures 5 and 6.

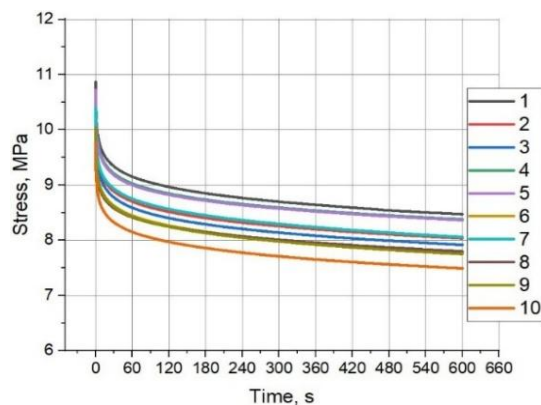
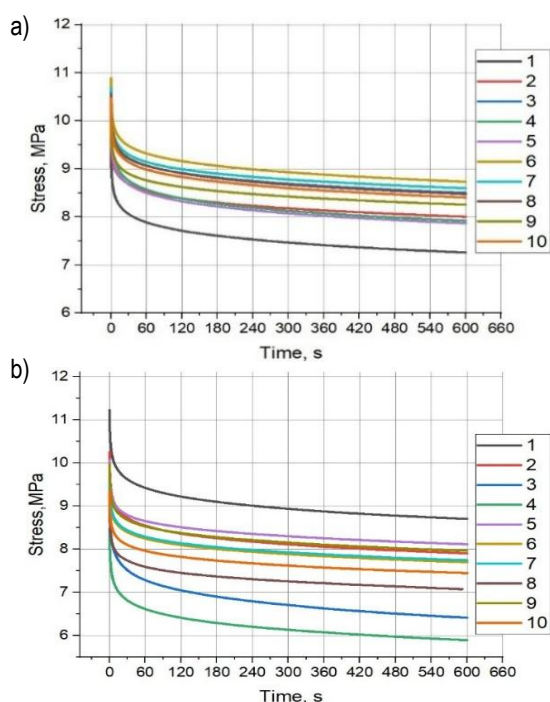


Fig. 5. Stress relaxation curves for PA2200 material; E_d^{56} : a) $E_d^{56} - P_d^0$, b) $E_d^{56} - P_d^{45}$, c) $E_d^{56} - P_d^{90}$

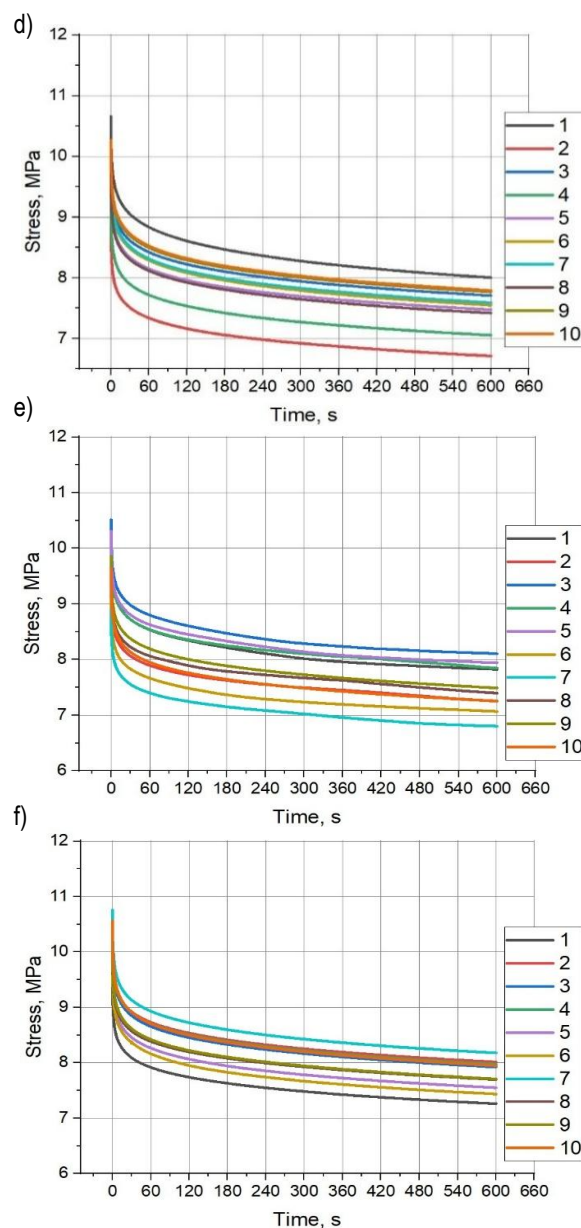


Fig. 6. Stress relaxation curves for PA2200 material: d) $E_d^{76} - P_d^0$, e) $E_d^{76} - P_d^{45}$, f) $E_d^{76} - P_d^{90}$

For each individual curve, a five-parameter Maxwell-Wiechert model was approximated using the Levenberg-Marquardt algorithm. An example of the appearance of these fits for selected relaxation curves is shown in Figure 7.

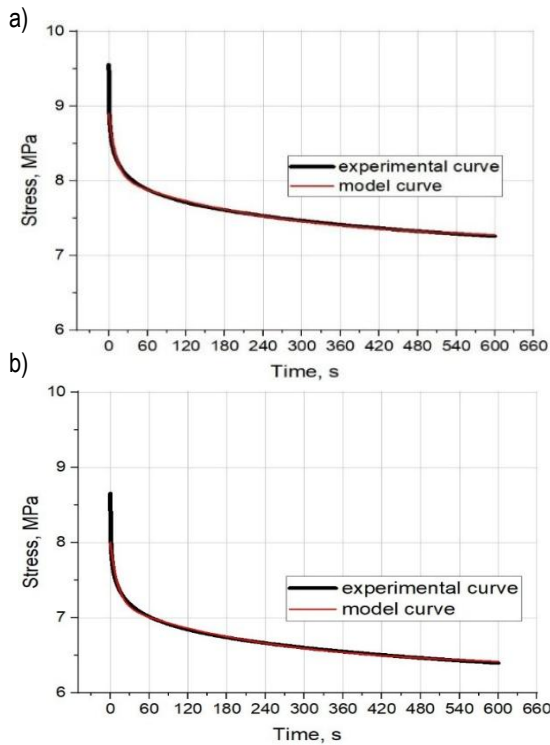


Fig. 7. Example of a Maxwell-Wiechert model fit to experimental curves: a) $E_d^{56} - P_d^0 - 1$, b) $E_d^{76} - P_d^0 - 1$

As a result of fitting of the five-parameter Maxwell-Wiechert model with five parameters to the stress relaxation curves, the values of model parameters σ_0 , σ_1 , σ_2 , t_1 , t_2 and fitting coefficients Chi^2 , R^2 were obtained. The values of these parameters and welding coefficients were separated into two tables 3, 4 due to the energy density of the technological 3D printing parameter energy density occurring in two values $E_d = 0.056 \text{ J/mm}^2$ and $E_d = 0.076 \text{ J/mm}^2$.

Tab. 3. Maxwell-Wiechert model parameters and fit coefficients; E_d^{56}

Lp.	σ_0 , MPa	σ_1 , MPa	σ_2 , MPa	t_1 , s	t_2 , s	Chi^2	R^2
P_d^0							
1	7.8	0.9	0.8	11	232	0.000390	0.9942
2	8.4	0.7	0.8	10	252	0.000299	0.9945
3	8.4	0.7	0.8	10	239	0.000314	0.9947
4	7.9	0.9	0.9	11	233	0.000403	0.9947
5	7.8	0.8	0.9	11	241	0.000369	0.9948
6	8.7	0.8	0.8	11	252	0.000348	0.9942
7	8.5	0.8	0.7	11	247	0.000337	0.9937

8	8.2	0.7	0.7	11	251	0.000267	0.9941
9	8.3	0.7	0.8	11	255	0.000299	0.9949
10	8.0	0.7	0.7	11	240	0.000309	0.9938
\bar{x}	8.2	0.8	0.8	11	244	0.000334	0.9944
SD	0.3	0.1	0.1	0.3	8	0.000044	0.0004
P_d^{45}							
1	8.6	0.9	1.0	12	243	0.000445	0.9951
2	7.9	0.9	0.9	11	241	0.000410	0.9944
3	6.3	1.0	1.2	12	263	0.000544	0.9958
4	5.8	1.0	1.0	12	249	0.000512	0.9944
5	8.1	0.7	0.7	11	267	0.000279	0.9943
6	7.6	0.7	0.7	11	259	0.000304	0.9941
7	7.7	0.7	0.7	11	252	0.000332	0.9936
8	7.0	0.7	0.7	10	264	0.000326	0.9930
9	7.9	0.7	0.8	11	258	0.000292	0.9947
10	7.4	0.7	0.7	10	249	0.000264	0.9943
\bar{x}	7.4	0.8	0.8	11	255	0.000371	0.9944
SD	0.8	0.1	0.2	1	9	0.000101	0.0008
P_d^{90}							
1	8.4	0.9	0.9	12	257	0.000421	0.9948
2	8.0	0.9	0.9	11	245	0.000424	0.9945
3	7.9	0.9	0.9	11	245	0.000433	0.9945
4	8.3	0.9	0.9	12	242	0.000393	0.9947
5	8.3	0.9	0.9	11	245	0.000408	0.9944
6	7.7	0.8	0.9	12	262	0.000367	0.9952
7	7.9	0.8	0.9	12	253	0.000369	0.9954
8	7.7	0.8	0.8	11	260	0.000364	0.9944
9	7.7	0.8	0.9	12	262	0.000353	0.9954
10	8.0	0.8	0.9	12	268	0.000391	0.9952
\bar{x}	8.0	0.8	0.9	12	254	0.000392	0.9948
SD	0.3	0.04	0.03	0.3	9	0.000028	0.0004

Based on Table 3, high standard deviation values of standard deviations can be seen for t_2 relaxation times. Low standard

deviation values were obtained for the other parameters of the Maxwell-Wiechert model and the fit coefficients Chi^2 , R^2 .

Tab. 4. Maxwell-Wichert model parameters and fit coefficients; E_d^{76}

Lp.	σ_0 , MPa	σ_1 , MPa	σ_2 , MPa	t_1 , s	t_2 , s	Chi^2	R^2
P_d^0							
1	7.9	0.9	1.1	13	255	0.000464	0.9960
2	6.7	0.8	0.8	12	251	0.000377	0.9945
3	7.6	0.9	1.0	12	249	0.000404	0.9954
4	7.0	0.8	0.9	11	242	0.000382	0.9950
5	7.4	0.9	0.9	12	243	0.000425	0.9947
6	7.5	0.9	1.0	12	248	0.000412	0.9956
7	7.5	0.9	1.0	12	251	0.000439	0.9952
8	7.7	0.9	1.0	12	245	0.000434	0.9953
9	7.4	0.9	1.0	11	244	0.000402	0.9952
10	7.7	0.9	1.0	13	246	0.000434	0.9953
\bar{x}	7.4	0.9	1.0	12	247	0.000418	0.9952
SD	0.4	0.03	0.1	1	4	0.000027	0.0004
P_d^{45}							
1	7.8	0.9	1.0	9	209	0.000264	0.9971
2	7.1	0.8	0.9	14	337	0.000558	0.9917
3	8.1	0.9	1.0	8	193	0.000226	0.9974
4	7.7	0.9	0.9	14	314	0.000579	0.9925
5	7.9	0.9	1.0	9	224	0.000252	0.9970
6	7.1	0.8	0.8	9	182	0.000303	0.9953
7	6.7	0.8	0.9	13	330	0.000343	0.9945
8	7.1	0.8	1.0	17	464	0.000635	0.9908
9	7.4	0.8	1.0	12	264	0.000395	0.9953
10	7.2	0.8	1.0	12	257	0.000394	0.9952
\bar{x}	7.4	0.8	0.9	12	277	0.000395	0.9947
SD	0.4	0.04	0.1	3	86	0.000147	0.0023
P_d^{90}							
1	7.2	0.8	0.9	12	258	0.000373	0.9949
2	7.9	0.9	1.0	11	252	0.000415	0.9953
3	7.9	0.9	1.0	12	253	0.000446	0.9952

4	7.9	0.9	1.0	12	253	0.000430	0.9954
5	7.5	0.9	1.0	12	244	0.000415	0.9953
6	7.4	0.9	1.0	13	239	0.000444	0.9951
7	8.1	0.9	1.0	12	250	0.000458	0.9953
8	7.6	0.9	0.9	11	251	0.000414	0.9949
9	7.6	0.9	1.0	12	253	0.000430	0.9951
10	7.9	1.0	1.0	12	248	0.000482	0.9951
\bar{x}	7.7	0.9	1.0	12	250	0.000431	0.9952
SD	0.3	0.04	0.04	0.4	5	0.000029	0.0001

Analysing the data collected in Table 4, high values of standard deviations can be observed for the t_2 relaxation times. Low standard deviation values were obtained for the other parameters of the Maxwell-Wiechert model and fit coefficients Chi^2 , R^2 .

Based on the average values of the Maxwell-Wiechert model parameters $\bar{\sigma}_0$, $\bar{\sigma}_1$, $\bar{\sigma}_2$, \bar{t}_1 , \bar{t}_2 and the values of the constant strain $\varepsilon_0 = 1 \text{ mm}$, using formulas (2), (3) and (4), the elastic moduli E_0 , E_1 , E_2 and the dynamic viscosity coefficients μ_1 , μ_2 were calculated. The values of these moduli and coefficients are shown in Figures 8, 9. Furthermore, using formula (5), the equivalent modulus E_s was calculated, which is also shown in Figure 8.

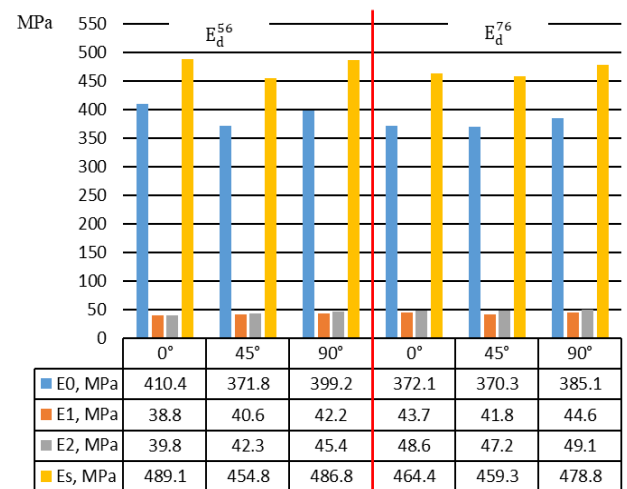
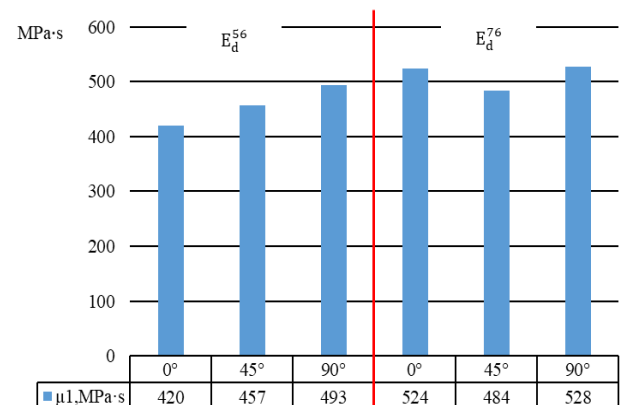


Fig. 8. Moduli of elasticity for PA 2200 material



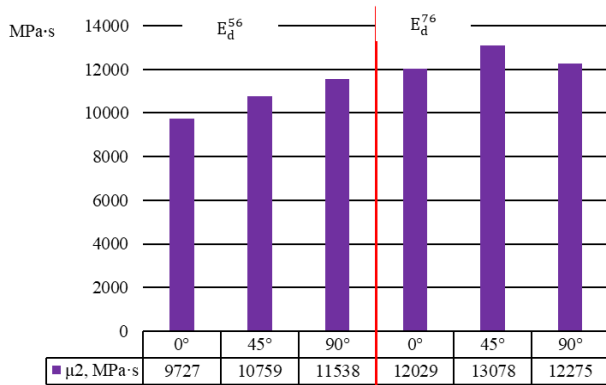


Fig. 9. Dynamic viscosity coefficients for PA 2200 material

The stress relaxation curves obtained from the tests were used to calculate, according to Equation (6), the percentage decrease in stress R_σ after time t . The values of the percentage decrease in stress R_σ are shown in Table 5.

In the data in the table above, it is evident that the highest decrease in stress occurred for E_d^{56} and P_d^{45} . While the lowest decrease in stress was for E_d^{56} and P_d^0 .

Tab. 5. Percentage of stress drop in PA2200 material

$R_{\sigma}, \%$			
E_d^{56}			
P_d	0°	45°	90°
\bar{x}	20.98	23.85	22.61
SD	1.86	4.86	0.56
E_d^{76}			
\bar{x}	24.5	23.6	24.1
SD	0.4	0.5	0.4

In the data in the table above, it is evident that the highest decrease in stress occurred for E_d^{56} and P_d^{45} . While the lowest decrease in stress was for E_d^{56} and P_d^0 .

4. DISCUSSION

The translation of stress relaxation curves seen in Figures 5 and 6, and particularly noticeable for samples printed according to technological parameters $E_d^{56} - P_d^{45}$ may be due to the difficulty of realising a unit stress stroke. The unit stress stroke is performed at the highest possible speed, which is difficult to perform under laboratory conditions. Also, the difficulty of setting a pre-stress for each individual specimen, can cause an apparent translation of test results. Too high values of pre-stress will cause the specimen to begin relaxing stresses even before the test begins, while too low values will lead to a stress stroke that is not correct to achieve the set strain.

Based on Figure 7, the Maxwell-Wiechert fit of the five-parameter model to the stress relaxation curves is strong. This can be concluded not only from a visual assessment of Figure 7 (the red line overlaps with the black line), but also by turning our attention to the values of the χ^2 fit test coefficients and R^2 determination coefficients shown in Tables 3 and 4. It should be mentioned here that the R^2 determination coefficient always varies between '0' and '1' and is a measure of the fit of the regression equation R^2 values

close to "1", i.e. those shown in Tables 3 and 4, indicate that the regression equation is very useful to predict the value of the dependent variable Y with the independent variable X . For the χ^2 concordance test, values close to '0' indicate a strong model fit.

The high standard deviation values for the stress relaxation time t_2 (Table 3 and 4) may be related to dynamic viscosity. The dynamic viscosity, on the other hand, depends on the structure at the molecular level of the material in this case PA 2200, which is a polymer. Polymers are made up of long polymer chains that form numerous intermolecular interactions.

When analysing the data in Figures 8 and 9, that is, the elastic moduli E_0, E_1, E_2 and the dynamic viscosity coefficients μ_1, μ_2 , one can see a slight anisotropy of the stress relaxation properties due to the orientations of the print.

Analysing the elastic moduli E_0, E_1, E_2 p shown in Figure 8, it can be concluded that, there are differences within the same direction, e.g. the modulus of E_0 is many times greater than the moduli of E_1, E_2 . This regularity informs that in terms of viscoelastic properties the material produced by selective laser sintering technology can be quasi-isotropic.

Analysing the different print orientations $0^\circ, 45^\circ, 90^\circ$ for the equivalent moduli E_s and dynamic viscosity coefficients μ_1, μ_2 shown in Figures 8 and 9, it can be seen that there is a difference in values between the applied energy densities $E_d = 0.056 \text{ J/mm}^2$ and $E_d = 0.076 \text{ J/mm}^2$. The equivalent moduli of E_s for print orientations $0^\circ, 90^\circ$ and energy density E_d^{56} are 5% and 2% larger, respectively, than the same equivalent moduli and print orientation, but for energy density E_d^{76} . The value of the equivalent modulus E_s with print orientation 45° and E_d^{56} was 1% smaller than the same modulus for the same print orientation but energy density E_d^{76} . For dynamic viscosity coefficient μ_1 the differences between the energy densities for print orientations $0^\circ, 45^\circ, 90^\circ$ were 20%, 6%, 7%, respectively, in favor of energy density E_d^{76} or dynamic viscosity coefficient $0^\circ, 45^\circ, 90^\circ$ the differences between energy densities for print orientations E_d^{76} .

However, for energy density E_d^{76} and print orientations $0^\circ, 90^\circ$ the values of percentage stress drop values are higher by 14%, 6%, respectively, compared to the same orientations but for lower energy density E_d^{56} . In contrast, for print orientation 45° , the value of percentage stress drop for energy density E_d^{56} was 1% higher than the same value but for energy density E_d^{76} .

5. CONCLUSIONS

On the basis of the results of the stress relaxation tests, the following general conclusions can be drawn:

- A strong fit of the Maxwell-Wiechert model to the stress relaxation curves, confirmed by the values of the χ^2 consistency and R^2 determination test coefficients.
- A small anisotropy of rheological properties was detected due to the orientation of the print.
- Increasing the energy density from 0.056 J/mm^2 to 0.076 J/mm^2 , or the equivalent modulus E_s , it increases in $0^\circ, 90^\circ$ orientations. The opposite is true for this modulus in the case of 45° print orientation.
- Increasing the energy densities from 0.056 J/mm^2 to 0.076 J/mm^2 also increases the values of dynamic viscosity coefficients μ_1, μ_2 in the 0° ($9727 \text{ MPa} \cdot \text{s} \uparrow 12029 \text{ MPa} \cdot \text{s}$), 45° ($10759 \text{ MPa} \cdot \text{s} \uparrow 13078 \text{ MPa} \cdot \text{s}$).

s), 90° ($11539 \text{ MPa} \cdot \text{s} \uparrow 12275 \text{ MPa} \cdot \text{s}$) print orientations.

- Increasing the energy densities from 0.056 J/mm^2 to 0.076 J/mm^2 also increases the values of the percentage stress drop R_σ in the 0° ($20.98\% \uparrow 24.5\%$), 90° ($22.61\% \uparrow 24.1\%$) print orientations. In the case of 45° ($23.85\% \downarrow 23.6\%$) print orientation, the trend is reversed.

The calculated values of the elastic moduli E_0 , E_1 , E_2 and dynamic viscosity coefficients μ_1 , μ_2 can be used to model components produced by selective powder sintering (SLS) technology from PA2200 material. In particular, the application of these moduli and dynamic viscosity coefficients can be found in engineering calculations.

REFERENCES

- Oleksy M, Budzik G, Sanocka-Zajdel A, Paszkiewicz A, Bolanowski M, Oliwa R, et al. Industry 4.0 Part I. Selected applications in processing of polymer materials. *Polimery/Polymers*. 2018;63(7–8):531–5.
- Dincă (Shamieh) LL, Popa NM, Milodin NL, Stanca C, Gheorghiu D. Influence of the process parameters on mechanical properties of the final parts obtained by selective laser sintering from PA2200 powder. *MATEC Web of Conferences*. 2019;299:01001.
- Malashin I, Martysyuk D, Tynchenko V, Nelyub V, Borodulin A, Galinovsky A. Mechanical Testing of Selective-Laser-Sintered Polyamide PA2200 Details: Analysis of Tensile Properties via Finite Element Method and Machine Learning Approaches. *Polymers (Basel)*. 2024 Mar 1;16(6).
- Eftekhari M, Fatemi A. On the strengthening effect of increasing cycling frequency on fatigue behavior of some polymers and their composites: Experiments and modeling. *Int J Fatigue*. 2016 Jun 1;87:153–66.
- Szot W, Bochnia J, Zmarzły P. Effect of selective laser sintering on stress relaxation in PA12. In: *Polimery/Polymers*. Industrial Chemistry Research Institute; 2024. p. 179–85.
- Szot W, Rudnik M. Effect of the Number of Shells on Selected Mechanical Properties of Parts Manufactured by FDM/FFF Technology. *Advances in Materials Science*. 2024 Mar 1;24(1):86–103.
- Kozior T. Rheological properties of polyamide pa 2200 in sls technology. *Tehnicky Vjesnik*. 2020 Aug 1;27(4):1092–100.
- Nam TH, Petriková I, Marvalová B. Stress relaxation behavior of isotropic and anisotropic magnetorheological elastomers. *Continuum Mechanics and Thermodynamics*. 2024 Mar 1;36(2):299–315.
- Obaid N, Kortschot MT, Sain M. Understanding the stress relaxation behavior of polymers reinforced with short elastic fibers. *Materials*. 2017;10(5).
- Ye J, Yao T, Deng Z, Zhang K, Dai S, Liu X. A modified creep model of polylactic acid (PLA-max) materials with different printing angles processed by fused filament fabrication. *J Appl Polym Sci*. 2021 May 5;138(17).
- Reis PNB, Valvez S, Ferreira JAM. Creep and stress relaxation behaviour of 3D printed nanocomposites. In: *Procedia Structural Integrity*. Elsevier B.V.; 2022. p. 934–40.
- Kozior T, Kundera C. Rheological properties of cellular structures manufactured by additive PJM technology. *Tehnicky Vjesnik*. 2021;28(1):82–7.
- Bochnia J. Evaluation of relaxation properties of digital materials obtained by means of PolyJet Matrix technology. *Bulletin of the Polish Academy of Sciences: Technical Sciences*. 2018;66(6):891–7.
- Bochnia J, Blasiak S. Stress relaxation and creep of a polymer-aluminum composite produced through selective laser sintering. *Polymers (Basel)*. 2020 Apr 1;12(4).
- Aberoumand M, Rahmatabadi D, Soltanmohammadi K, Soleyman E, Ghasemi I, Baniassadi M, et al. Stress recovery and stress relaxation behaviors of PVC 4D printed by FDM technology for high-performance actuation applications. *Sens Actuators A Phys*. 2023 Oct 16;361.
- Jang JW, Min KE, Kim C, Wern C, Yi S. Rheological Properties and 3D Printing Behavior of PCL and DMSO2 Composites for Bio-Scaffold. *Materials*. 2024 May 1;17(10).
- Bertocco A, Bruno M, Armentani E, Esposito L, Perrella M. Stress Relaxation Behavior of Additively Manufactured Polylactic Acid (PLA). *Materials*. 2022 May 1;15(10).
- Wang X, Zhou M, Bai J, Liao Y, Li D, Zhang B. Research on the Rheological Properties and Diffusion Law of Coal-Based Solid Waste Geopolymer Grouting Material. *Materials [Internet]*. 2024 Nov 7;17(22):5433. Available from: <https://www.mdpi.com/1996-1944/17/22/5433>
- Tüfekci K, Çakan BG, Küçükakarsu VM. Stress relaxation of 3D printed PLA of various infill orientations under tensile and bending loadings. *J Appl Polym Sci*. 2023 Oct 15;140(39).
- Singh S, Kaur D, Singh M, Balu R, Mehta A, Vasudev H. Challenges and issues in manufacturing of components using polymer-based selective laser sintering (SLS): a review. *International Journal on Interactive Design and Manufacturing*. 2024;
- Chen J, Kong Y, Lu K, Huang Q. A Computational Solid Mechanics analysis on the supportability of 3D 2 printing surimi depended on creep and stress relaxation [Internet]. Available from: <https://ssrn.com/abstract=4956847>
- Jabri FE, Oubalouch A, Lasri L, Alajji R El. A comprehensive review of polymer materials and selective laser sintering technology for 3D printing. Vol. 118, *Journal of Achievements in Materials and Manufacturing Engineering*. International OCSCO World Press; 2023. p. 5–17.
- EOS GmbH. Material data sheet PA 2200 [Internet]. Krailing: EOS GmbH Electro Optical Systems; [cited 2025 May 14]. Available from: <https://www.eos.info/polymer-solutions/polymer-materials/data-sheets/mds-pa-2200-balance>
- Liu K. Effect of process parameters on the temperature field of laser sintering of nylon PA2200 powder. In: *Journal of Physics: Conference Series*. Institute of Physics; 2024.
- Faes M, Wang Y, Lava P, Moens D. Variability, heterogeneity, and anisotropy in the quasi-static response of laser sintered PA12 components. *Strain*. 2017 Apr 1;53(2).

Wiktor Szot:  <https://orcid.org/0000-0001-9512-9680>

Mateusz Rudnik:  <https://orcid.org/0000-0001-5096-608X>

Paweł Szczygieł:  <https://orcid.org/0000-0002-3113-3557>

Natalia Kowalska:  <https://orcid.org/0000-0003-3043-7812>



This work is licensed under the Creative Commons BY-NC-ND 4.0 license.

MACHINABILITY ASSESSMENT OF ALUMINIUM ALLOY EN AW-7075 T651 UNDER VARYING MACHINING CONDITIONS

Jarosław KORPYSA^{*}, Magdalena ZAWADA-MICHAŁOWSKA^{*}, Paweł PIEŚKO^{*},
 Witold HABRAT^{**}, Joanna LISOWICZ^{**}

^{*} Faculty of Mechanical Engineering, Department of Production Engineering,
 Lublin University of Technology, Nadbystrzycka 36, 20-618 Lublin, Poland

^{**} Faculty of Mechanical Engineering and Aeronautics, Department of Manufacturing Techniques and Automation,
 Rzeszów University of Technology, Powstańców Warszawy 12, 35-959 Rzeszów, Poland

j.korpysa@pollub.pl, m.michalowska@pollub.pl, p.piesko@pollub.pl, witekhab@prz.edu.pl, j.lisowicz@prz.edu.pl

received 07 February 2025, revised 22 April 2025, accepted 02 May 2025

Abstract: This paper presents the experimental results of a study investigating the milling process of aluminium alloy EN AW-7075 T651. The main objective of the study was to establish the relationship between machining conditions, such as cutting parameters and cutting tool type, and selected machinability indicators, i.e. cutting force components and surface roughness parameters. The milling process was conducted using two different tools: a solid carbide cutter and a cutter with PCD (polycrystalline diamond) inserts. Obtained results showed that the use of the PCD tool led to a significant improvement of surface quality. In particular, the surface roughness parameter Ra was reduced, but changes are also visible for the other roughness parameters. Despite a similar trend of variations in surface roughness parameters observed for both tools, the values of these parameters obtained with the PCD tool were significantly lower. Similar values of the cutting force components were obtained with both cutting tools, these values being lower only in some cases for the carbide cutter. The effect of varying the cutting speed and feed per tooth on these indicators was also determined. The obtained results indicate that the selection of cutting parameters depends primarily on the expected results. Considering the surface roughness, it is better to use high cutting speeds, while in terms of cutting force, low speeds are more beneficial. In both cases, it is recommended to use the lowest possible feed.

Key words: milling, aluminium alloy, surface roughness, cutting force, cutting tools

1. INTRODUCTION

Aluminium alloys are widely used in the aerospace and automotive industries, among others [1,2]. This is primarily owing to their low density, high corrosion resistance and good strength properties. However, the peculiarities of these industries require high quality of manufactured components, which implies a need for continuous improvement of machining processes. The selection of appropriate cutting conditions is therefore crucial for ensuring optimum machining results, and hence research must be conducted in this area [3–5].

The machining result depends on numerous factors such as the machine tool, cutting tool and cutting parameters. The dynamics of this process, which is significantly related to the cutting force, is of importance, too. The selection of optimum machining conditions has been of interest to researchers from all over the world. By varying technological parameters, it is possible to exert a significant impact on the cutting process and its effects. The machining of alloy EN-AW 7075 conducted with variable cutting parameters was investigated in [6]. The study showed that the spindle speed and feed rate had the primary impact on surface roughness. Increasing the values of these parameters resulted in improved surface quality. The depth of cut, on the other hand, showed no specific effect on surface condition. Similar conclusions were included in the paper [7], also concerning EN-AW 7075 alloy. It was shown that cutting speed had an approx. 85% effect on surface roughness and chip

segmentation. However, this applied to high speed machining, because when standard cutting speeds were used, the significance of cutting speed decreased, while the influence of feed and depth of cut increased. A study [8] investigated the milling process of pure EN-AW 7075 alloy, EN-AW 7075 alloy with Sc and Li additives, as well as of EN-AW 7075 after different heat treatments. The applied feed rate was found to have the greatest effect on cutting forces. A reduction in the feed value had a positive effect on the cutting force. This observation was especially important when machining high-hardness alloys, for which it was recommended using a cutting fluid in order to reduce the cutting force. It was also more advantageous to use higher cutting speeds. A study investigating the machining of EN-AW 7050 conducted by Ping et al. [9] showed that the cutting force components remained constant despite an increase in the cutting speed and a higher cutting temperature. The depth of cut was found to have the greatest effect on the cutting force, as increasing the depth of cut value resulted in a several-fold increase in the components of this force. The effect of tool geometry was also investigated. It was observed that as the rake angle was increased, the cutting force components and the cutting temperature decreased. In contrast, an increase in the tool tip radius produced the opposite effect. This implies that the cutting tool geometry, too, has impact on the machining process.

The effect of rake angle and clearance angle was investigated in [10] for the EN-AW 7075 alloy. It was shown that the “sharper” cutting edge caused the cutting temperature to decrease and the

cutting force to increase at the same time. Other tools caused the cutting temperature to increase, which probably led to plasticization of the material and a decrease in the cutting force. The study [11] focused on rake angle and nose radius. Choosing the right rake angle proved to be a difficult task, as increasing the rake angle results in a reduction of the infeed force, while at the same time the crossfeed and thrust forces increase intensively. However, by increasing the nose radius, the cutting forces were reduced by up to several times. A study [12] showed that the cutting tool's helix angle had a significant impact on the cutting process. The cutting temperature was reduced when using a small helix angle tool. This angle had a greater effect on the cutting temperature than the spindle speed and feed. The use of a large helix angle, on the other hand, had a positive effect on surface roughness and was more significant than a variable feed. Ikhries et al. [13] compared the results of a machining process conducted with a flat and a ball tool. The use of the flat tool resulted in enhanced surface quality and a higher material removal rate. In the machining process conducted with the flat tool, the feed rate had the dominant effect on surface roughness, while for the ball tool – the depth of cut had the greatest effect on surface roughness.

Not only does the overall geometry of the tool matter, but the cutting edge microgeometry is of significance too, as demonstrated in [14]. The results showed the margin width to be of the greatest significance, as any increase in this parameter led to reduced surface quality. The corner radius was found to have a nonlinear impact, as the best effect was obtained using intermediate radius values. In contrast, the relief angle did not have any significant effect on surface roughness. Schönecker et al. [15] developed HSS end mills with structure elements on the flank face. The research showed that the proposed tool geometry reduced the cutting force and the susceptibility to chatter vibration, which, in turn, allowed the depth of cut to be increased. This effect became more powerful with increasing the size of structure elements.

The material of a cutting tool is of vital importance, too. Kuczmazewski et al. [16] conducted a comparative analysis of the results of an HSM (High Speed Milling) process for EN-AW 2024 that was conducted using a carbide and a PCD tool. Lower values of the roughness parameter R_a over the entire length of the machined surface were obtained with the PCD tool, regardless of the rolling direction. However, the differences were relatively small. The use of the diamond tool resulted in lower deflection along the longitudinal rolling direction. A comparison of carbide and PCD tools was also undertaken in [17]. The use of the PCD tool for milling EN-AW 5754 and EN-AW 6082 alloys resulted in several-fold lower values of the surface roughness parameter R_a . The tool was also found to be less sensitive to changes in cutting parameters. The dependence of high surface quality on the use of diamond tools was also confirmed in [18]. The best results were obtained using low cutting speeds, feeds and cutting depths. The diamond tool also had a positive effect on the shape of formed chips, which promoted improved surface quality. O'Toole et al. [19] compared the use of a PCD tool and a CBN (Cubic Boron Nitride) tool in the micromilling of pure aluminium. The PCD tool produced better surface quality and several-fold lower cutting force components. The tool also exhibited lower wear. Similar results were obtained in the simulation of a milling process for the EN-AW 7075-0 alloy [20]. The use of the PCD tool resulted in lower cutting forces and feed forces than those obtained in the milling process conducted with a tool made of carbide K10. This also meant lower cutting temperatures. The favourable properties of polycrystalline diamond were also found to promote reduced burr formation [21]. The benefits of using diamond tools

were confirmed not only by research on milling, but also by studies devoted to turning [22–26].

The machining effect can also be enhanced via tool coatings. The benefits of using coatings in micromilling were confirmed in a study [27]. It was demonstrated that compared to an uncoated tool, the use of DLC (Diamond-Like Carbon) and NCD (Nano-Crystalline Diamond) coatings reduced the cutting forces by up to 20-30%. The use of the DLC-coated tool also produced the best surface quality. Similar observations were made in a study [28] which investigated the machining process of EN-AW 6082-T6. The use of the DLC-coated tool produced significantly better results than when using uncoated and AlCrN-coated tools. The obtained surfaces had higher quality and better properties. The DLC-coated tool also generated lower vibration. It should be emphasized that the coating material selection depends on the specific application, as the use of a wrong coating can even deteriorate the machining process and its results [29].

The selection of a suitable machining strategy is also important. In [30], conventional and plunge milling strategies were considered. Plunge milling was shown to improve productivity and reduce tool wear, but at the same time generated more vibration and poorer surface quality. This machining strategy can therefore be an interesting option for rough machining. The type of milling can also affect the machining effect. Burhanudin et al. [31] compared climb and conventional milling using an HSS end mill. The results showed that climb milling produced better surface quality, with significantly greater differences obtained for EN-AW 5052 than for EN-AW 7075. The study also demonstrated that increasing the cutting allowance promoted improved surface roughness. A similar investigation of the EN-AW 7075-T6 alloy was made in [32]. In this study, however, no clear differences were observed between the two types of treatment. This could be due to the fact that the carbide tool had a different geometry or that the aluminium alloy was subjected to a different heat treatment condition.

Sivalingam et al. [33] showed that the machining effects for aluminium alloy EN-AW 7075 can also be improved by using lubricants. They investigated several cooling methods: MQL (Minimum Quantity Lubrication), cryogenic, and a combination of MQL and cryogenic. The use of lubrication led to reduced friction, which resulted in lower cutting forces and tool wear. Surface quality was also improved, with fewer defects occurring. The most benefits were achieved using a combination of MQL and cryogenic. The positive effect of cooling on surface roughness was also confirmed in a study [34]. The use of cooling led to a more than half reduction in the surface roughness parameter R_a . Nevertheless, the spindle speed was found to have a much greater effect on surface roughness. Yapan et al. [35] conducted a study on EN-AW 6082 using MQL with graphene nanoparticles. The use of nanofluid resulted in significant improvements in cutting force, surface roughness, temperature and carbon emission. A study [36] compared dry machining and SQL (Small Quantity Lubrication) with sunflower oil. The application of SQL reduced the cutting force by up to 35% and the surface roughness by even up to 45%. The effect of using SQL in milling was much better than that achieved in turning. Innovative solutions were also proposed for cutting force reduction, such as vibration assisted milling [37,38], which could additionally be implemented over helical paths [39].

Based on the literature review, it can be seen that the milling process depends on many factors. In order to obtain an optimal machining effect, it is necessary to determine the influence of individual machining conditions. The objective of this study is to determine the effect of variable cutting parameters and different cutting

tool types on surface quality and cutting force. For improving surface quality, one of the first steps to be taken is to change the cutting parameters, as this does not require additional tooling and equipment. Therefore, an attempt is made to determine the extent to which varying the machining conditions will affect the milling effect. The impact of the cutting tool is also considered, since the end mills used in this study are made of different materials and have different geometries.

The novelty of the research consists in a comprehensive analysis of the influence of various cutting parameters on the machinability of the EN AW-7075 T651 aluminum alloy, considering two different cutting tools. This provides new information on the optimization of the milling process of this aluminum alloy, which can contribute to improving the quality and efficiency of manufactured parts. A wide range of cutting parameters corresponding to conventional and High Speed Cutting allows for better representation of real manufacturing conditions.

2. MATERIALS AND METHODS

The study involved investigating the stability and effects of a milling process for aluminium alloy EN AW-7075 T651. Owing to its high strength and corrosion resistance combined with low specific weight, this material is widely used in the aerospace and automotive industries. Test specimens came in the form of cuboids with the dimensions of 160x70x33 mm. The milling process was performed on an AVIA VMC 800HS milling centre – Figure 1.

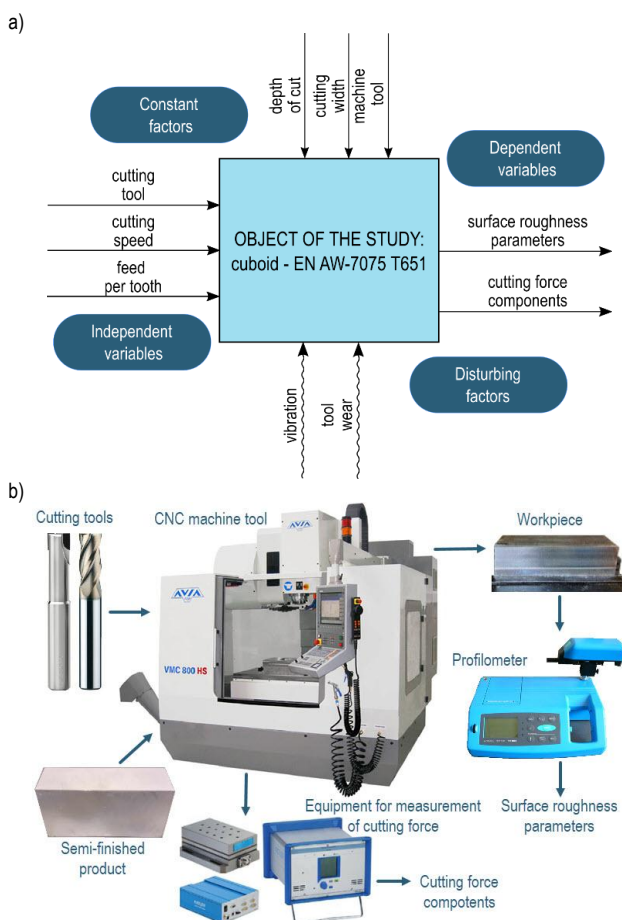


Fig. 1. Experimental setup: a) schematic diagram; b) experimental procedure

The milling process was conducted using variable cutting parameters, as shown in Table 1. The variable parameters were the cutting speed v_c and the feed per tooth f_z , while the constant parameters were the depth of cut equal to 1 mm and the width of cut equal to 12 mm.

Tab. 1. Parameters of milling process

v_c (m/min)	f_z (mm/tooth)	n (rpm)	v_f (mm/min)
100	0.100	2 654	796
300		7 962	2 389
500		13 270	3 981
700		18 577	5 573
900		23 885	7 166
300	0.050	7 962	1 194
	0.075		1 791
	0.100		2 389
	0.125		2 986
	0.150		3 583
900	0.050	23 885	3 583
	0.075		5 374
	0.100		7 166
	0.125		8 957
	0.150		10 748

The selection of technological parameters was based on the recommendations of the cutting tool manufacturers, as well as the authors' experience in machining aluminium alloys. The tests were carried out on the basis of one pass for one configuration of technological parameters for two tools. The milling process was carried out using two 12 mm diameter milling cutters:

- a cutter with three PCD inserts (Bryk D10.1210), each having a length of 25 mm, with an overall length of 82 mm and a tooth angle of 0°;
- a four-teeth solid carbide cutter (Engram 4HCEG 120 260 S12), with a tooth length of 26 mm, having an overall length of 75 mm and a tooth angle of 35°, provided with Nano-X coating.

During the tests, no significant wear on the cutting tools was found to affect the results.

Cutting forces were measured during the milling process using a Kistler 9257B piezoelectric force gauge connected to a 5070A amplifier, from which the signal was sent to a DAQ 5697A module. The maximum values of the cutting force components F_x , F_y and F_z were analysed.

The study also included an evaluation of surface roughness parameters R_a , R_z and RS_m . The measurements were made using a Hommel Tester T1000 contact profilometer in accordance with the PN-EN ISO 4287 standard.

3. RESULTS

3.1. Surface roughness

Results of the investigated surface roughness parameters are given in Figures 2-4.

Regardless of the cutting tool type, a similar trend of changes in the values of all surface roughness parameters can be observed for the milling process conducted with a variable cutting speed. However, significantly lower values of all parameters were obtained for the PCD tool. The differences are as high as $0.79 \mu\text{m}$ for the R_a parameter, $1.3 \mu\text{m}$ for R_z and 0.045 mm for R_{Sm} . Comparing the results obtained for both tools, the greatest differences in the values of the surface roughness parameters can be observed for the milling process conducted with the lowest cutting speed. These differences decrease as the cutting speed is increased.

Similar relationships can also be observed for the milling process conducted with variable feed per tooth. Lower values of the surface roughness parameters were again obtained for the tool with PCD inserts, and the trend of changes is similar for all roughness parameters regardless of the tool; this time, however, the values increase with increasing the feed per tooth. At the same time, the tool with PCD inserts was more sensitive to the variations in feed, because the values of the roughness parameters increase faster with increasing the feed value. This is particularly true for the parameters R_z and R_{Sm} , for which the differences between the results obtained with both tools gradually decrease as the feed is increased. On the other hand, for the lowest feed value, the differences in the values of R_a , R_z and R_{Sm} obtained with the two tools are $1.16 \mu\text{m}$, $2.1 \mu\text{m}$ and 0.09 mm , respectively.

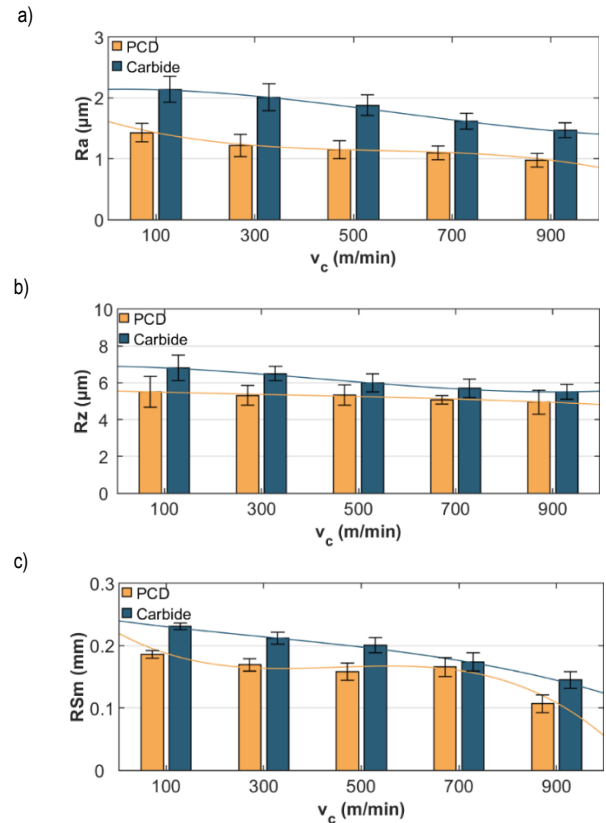


Fig. 2. Cutting speed vs surface roughness parameters:
a) R_a ; b) R_z ; c) R_{Sm} ($f_z = 0.1 \text{ mm/tooth}$)

Tab. 2. Regression equations for surface roughness parameters

Parameter	PCD	Carbide
v_c		
R_a	$y = -2.2396 \times 10^{-9}x^3 + 3.7195 \times 10^{-6}x^2 - 0.0022461x + 1.6193$ $R^2 = 0.99992$	$y = 1.1458 \times 10^{-9}x^3 - 2.0223 \times 10^{-6}x^2 + 0.00014211x + 2.1396$ $R^2 = 0.99358$
R_z	$y = -5.2083 \times 10^{-10}x^3 + 5.1339 \times 10^{-7}x^2 - 0.00072693x + 5.555$ $R^2 = 0.93879$	$y = 3.125 \times 10^{-9}x^3 - 3.9732 \times 10^{-6}x^2 - 0.00049554x + 6.8933$ $R^2 = 0.99697$
R_{Sm}	$y = -7.5521 \times 10^{-10}x^3 + 1.0158 \times 10^{-6}x^2 - 0.00042798x + 0.22112$ $R^2 = 0.96237$	$y = -1.0417 \times 10^{-10}x^3 + 9.1964 \times 10^{-8}x^2 - 0.00010467x + 0.24011$ $R^2 = 0.99545$
$f_z (v_c = 300 \text{ m/min})$		
R_a	$y = 8.8889x^3 - 43.2381x^2 + 16.6754x + 0.001$ $R^2 = 0.99686$	$y = 1493.3333x^3 - 416x^2 + 44.2667x + 0.39$ $R^2 = 1$
R_z	$y = -4800x^3 + 1228.5714x^2 - 73.7143x + 5.23$ $R^2 = 0.99256$	$y = 533.3333x^3 - 148.5714x^2 + 23.381x + 5.24$ $R^2 = 0.99824$
R_{Sm}	$y = -57.7778x^3 + 9.1619x^2 + 1.4737x + 0.0045667$ $R^2 = 0.97841$	$y = 5.3333x^3 - 2.0571x^2 + 0.8481x + 0.15$ $R^2 = 0.99985$
$f_z (v_c = 900 \text{ m/min})$		
R_a	$y = -1395.5556x^3 + 396.381x^2 - 23.104x + 0.88433$ $R^2 = 0.93968$	$y = -320x^3 + 137.1429x^2 - 8.8286x + 1.42$ $R^2 = 0.97975$
R_z	$y = -1244.4444x^3 + 161.9048x^2 + 38.0635x + 0.73333$ $R^2 = 0.99764$	$y = 1.1446 \times 10^{-11}x^3 + 11.4286x^2 + 11.7143x + 4.4$ $R^2 = 0.98848$
R_{Sm}	$y = -268.4444x^3 + 88.0571x^2 - 7.6403x + 0.28237$ $R^2 = 0.9568$	$y = 21.3333x^3 - 5.8286x^2 + 1.1324x + 0.077$ $R^2 = 0.99786$

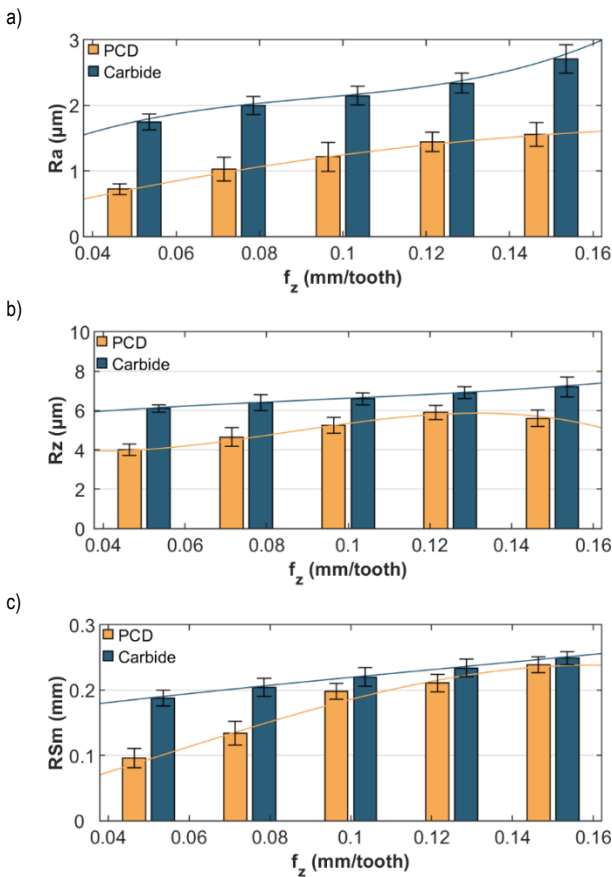


Fig. 3. Feed per tooth vs surface roughness parameters:
a) Ra ; b) Rz ; c) RSm ($v_c = 300$ m/min)

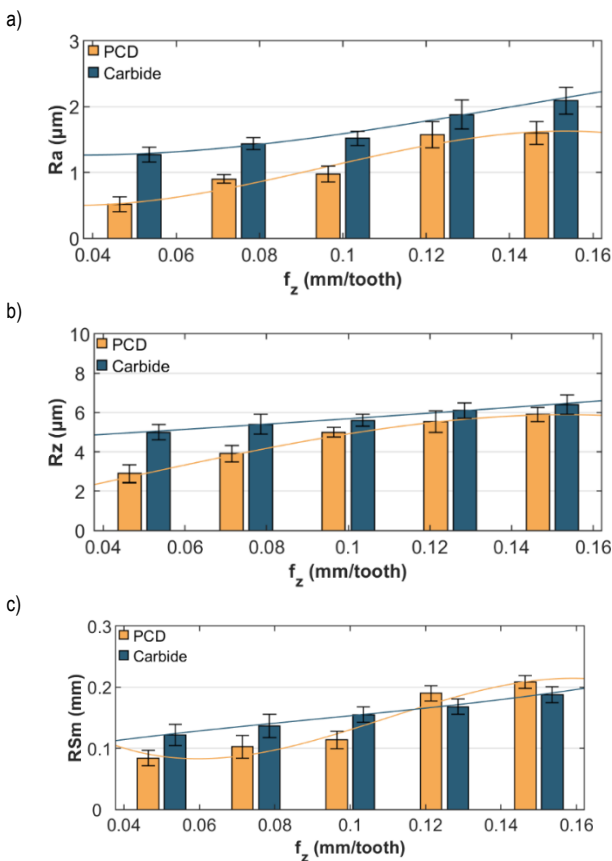


Fig. 4. Variable feed per tooth vs surface roughness parameters:
a) Ra ; b) Rz ; c) RSm ($v_c = 900$ m/min)

In a milling process conducted with the cutting speed $v_c = 900$ m/min similar relationships can be observed as in that conducted with $v_c = 300$ m/min. The surface roughness parameters increase with increasing the feed per tooth and they are lower by as much as 0.75μ m for Ra , 2.1μ m for Rz and 0.038 mm for RSm for the milling process performed using the tool with PCD inserts. The use of the highest feed values, however, resulted in a significant increase in the RSm value, exceeding that obtained with the carbide tool.

In addition, the use of higher cutting speeds resulted in lower values of the surface roughness parameters than those obtained with $v_c = 300$ m/min. For the tool with PCD inserts, the differences are 0.24μ m for Ra , 1.1μ m for Rz and 0.084 mm for RSm . At the highest feed per tooth, however, the parameters are comparable for both cutting speeds. For the carbide tool, an increase in the cutting speed is beneficial over the entire tested feed per tooth range as the differences are as high as 0.62μ m for Ra , 1.1μ m for Rz and 0.067 mm for RSm .

Regression equations were also determined for the obtained surface roughness parameters – Table 2.

3.2. Cutting force

The study also involved measuring the cutting force components during machining. Figures 5-7 give examples of signals of the cutting force component F_x for the extreme values of the analysed cutting parameters. The signals are characterized by high stability, with no sudden jumps in their values, which indicates that the milling process proceeded in a stable manner. On the other hand, their characteristics change with varying the machining parameters.

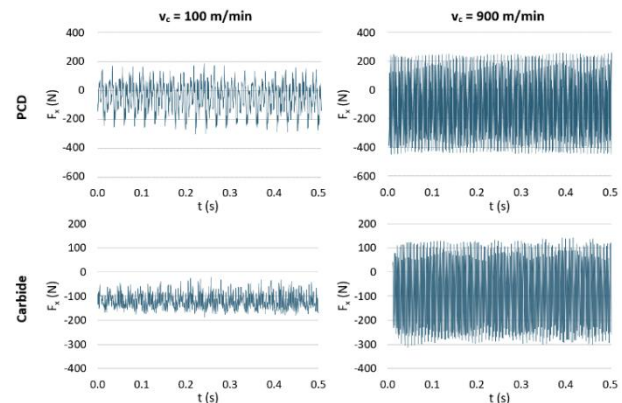


Fig. 5. Variations in the cutting force component F_x during a milling process conducted with variable v_c

Based on the obtained signals, the maximum values of the cutting force components were determined and analysed. A similar trend of changes in the values of these components can be observed in the milling process conducted with a variable cutting speed, for both cutting tools – Figures 8-10. The F_z component values increase with the cutting speed, while the values of F_x and F_y decrease first and then begin to increase again when the process is conducted with the high cutting speed values. The exception is milling conducted using the diamond tool and $v_c = 300$ m/min where all cutting force components increase. The highest values were obtained for the F_x , F_y and F_z components,

respectively for both tools. Significantly higher values were obtained using a diamond tool, which is due to its geometry. No correlation is observed between the changes in the values of the cutting force components and the surface roughness parameters, as the latter decrease steadily with increasing the cutting speed.

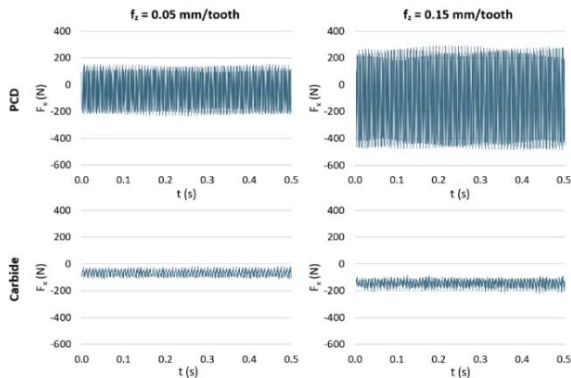


Fig. 6. Variations in the cutting force component F_x during a milling process conducted with variable f_z ($v_c = 300$ m/min)

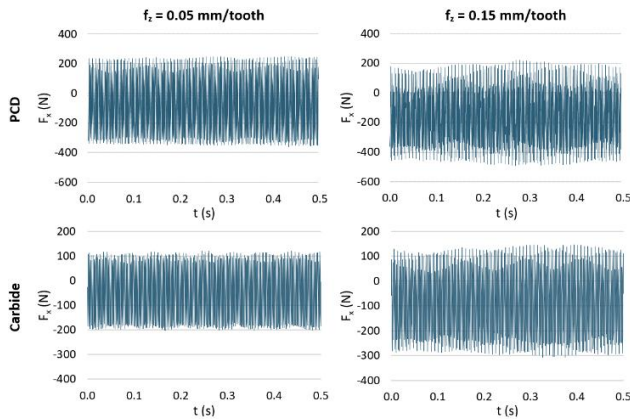


Fig. 7. Variations in the cutting force component F_x during a milling process conducted with variable f_z ($v_c = 900$ m/min)

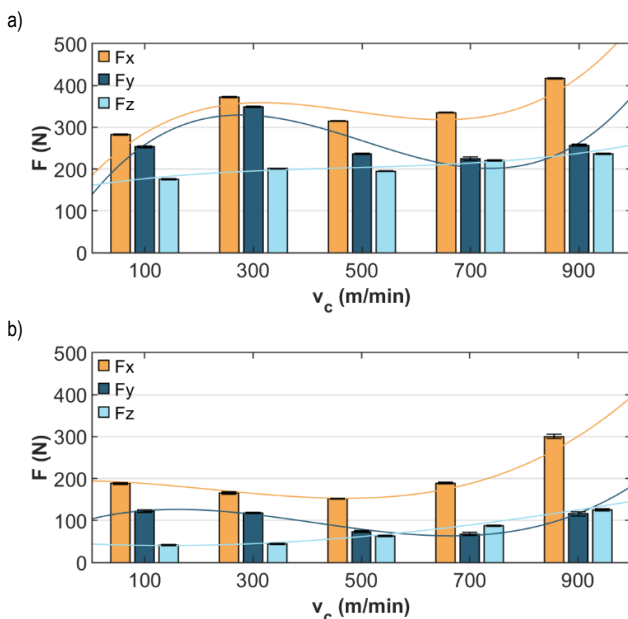


Fig. 8. Variable cutting speed vs cutting force for: a) PCD; b) carbide tool ($f_z = 0.1$ mm/tooth)

The relationship between a variable feed and the cutting force components is rather unambiguous for the milling process conducted using the diamond tool. All components successively increase their value over the entire feed range. The highest values are observed for the F_x component. The F_y component values are lower, with an increasing difference between them. In contrast, the values of the F_z component are about half lower than those of the F_x component. This trend of changes in the cutting force components corresponds to the changes observed for the surface texture, where the values of the surface roughness parameters would gradually increase with increasing the feed per tooth.

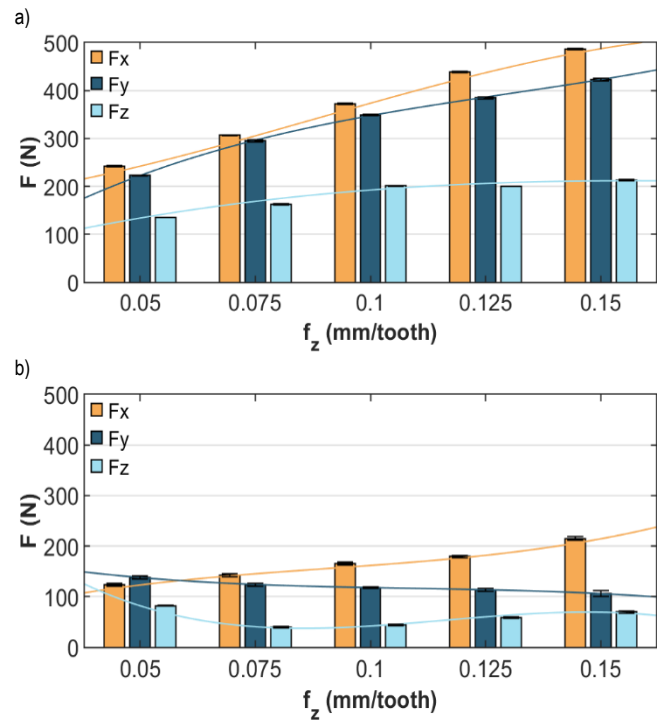


Fig. 9. Feed per tooth vs cutting force for: a) PCD; b) carbide tool ($v_c = 300$ m/min)

Regarding the carbide tool, each cutting force component shows a different trend. The F_x component increases over the entire tested feed range, while the F_y component decreases. The F_z component decreases first and then increases starting from $f_z = 0.075$ mm/tooth. The distribution of the cutting force components is similar to that obtained for the diamond tool, i.e. the highest values are achieved by the F_x component whereas the lowest by the F_z component.

Significant differences can be observed in the values of the cutting force components depending on the type of tool. In addition, these differences increase with increasing the feed per tooth. In a milling process conducted with the carbide tool, the values are lower by as much as 271 N for the F_x component, by 316 N for the F_y component and by 143 N for the F_z component. These significant differences may be due to a larger helix angle, leading to a reduction in the generated cutting force. The increase in the cutting force components is accompanied by higher surface roughness parameters.

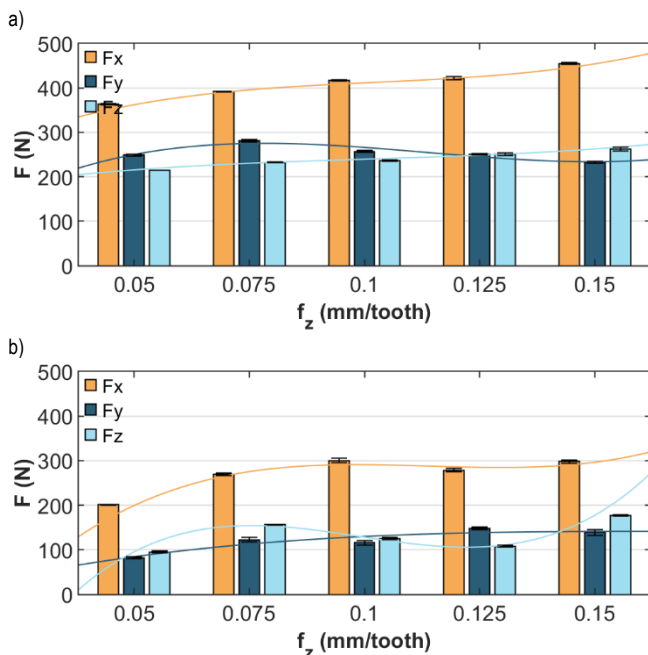


Fig. 10. Feed per tooth vs cutting force for: a) PCD; b) carbide tool
($v_c = 900$ m/min)

Completely different results were obtained from a milling process conducted with a variable feed per tooth and the cutting speed $v_c = 900$ m/min. When using the diamond tool, the values of the Fx and Fz components increase with increasing the feed per tooth, which – to some extent – is due to changes in the surface texture and reduced surface quality with the feed increase. In contrast, the value of the Fy component begins to decrease starting from $f_z = 0.075$ mm/tooth. For the carbide tool, on the other hand, the values of the cutting force components vary in a non-linear manner, as they fluctuate when the feed per tooth is changed. The values of the cutting force components are again lower for the carbide tool. The highest values are again achieved by the Fx component, while the values of Fy and Fz are about half as high.

The milling process conducted using the diamond tool and the cutting speed $v_c = 900$ m/min had no clear impact on the cutting force components when compared to the milling process conducted with $v_c = 300$ m/min. Mainly higher values of the Fx and Fz components were obtained, while the values for the Fy component were lower. The values differ by 121 N for Fx, 190 N for Fy and 79 N for Fz. As for the carbide tool, the high cutting speed has proved to be undesirable because the cutting force increases with the cutting speed. The obtained maximum values are higher by 134 N for Fx, by 34 N for Fy and by 117 N for Fz compared to the machining process conducted with $v_c = 300$ m/min.

Regression equations were also determined for the obtained results – Table 3.

Tab. 3. Regression equations for the cutting force components

Component	PCD	Carbide
v_c		
F_x	$y = 2.1734 \times 10^{-6}x^3 - 0.0031486x^2 + 1.3387x - 181.5044$ $R^2 = 0.92574$	$y = 6.8696 \times 10^{-7}x^3 - 0.00046211x^2 - 0.022684x + 194.5068$ $R^2 = 0.99967$
F_y	$y = 2.6357 \times 10^{-6}x^3 - 0.0040011x^2 + 1.6079x - 134.8438$ $R^2 = 0.80254$	$y = 9.7847 \times 10^{-7}x^3 - 0.0012124x^2 + 0.31351x + 103.4101$ $R^2 = 0.97897$
F_z	$y = 2.3882 \times 10^{-7}x^3 - 0.00033649x^2 + 0.19507x - 160.758$ $R^2 = 0.92635$	$y = -4.3391 \times 10^{-8}x^3 + 0.00019882x^2 - 0.053533x + 44.2173$ $R^2 = 0.9991$
$f_z (v_c = 300 \text{ m/min})$		
F_x	$y = -96682.6667x^3 + 25468.1943x^2 + 496.6658x + 165.8101$ $R^2 = 0.99988$	$y = 97571.7333x^3 - 26474.3086x^2 + 3036.7114x + 25.412$ $R^2 = 0.99437$
F_y	$y = 109699.2x^3 - 42818.3886x^2 + 6999.1857x - 33.956$ $R^2 = 0.99976$	$y = -58838.9333x^3 + 19257.8057x^2 - 2257.4428x + 210.1391$ $R^2 = 0.99969$
F_z	$y = 15057.0667x^3 - 12366.2514x^2 + 2759.5016x + 25.1968$ $R^2 = 0.96265$	$y = -275146.5067x^3 + 96013.5394x^2 - 10386.9419x + 395.9015$ $R^2 = 0.99571$
$f_z (v_c = 900 \text{ m/min})$		
F_x	$y = 170491.7333x^3 - 52457.1543x^2 + 5869.7915x + 178.4637$ $R^2 = 0.98706$	$y = 413898.1333x^3 - 141383.1543x^2 + 15794.7885x - 288.4818$ $R^2 = 0.9745$
F_y	$y = 232014.1333x^3 - 79230.3303x^2 + 8143.1002x + 12.1011$ $R^2 = 0.87723$	$y = 29947.2x^3 - 15807.84x^2 + 2755.607x - 17.3301$ $R^2 = 0.84802$
F_z	$y = 57291.3067x^3 - 17403.6217x^2 + 2089.9487x + 147.4216$ $R^2 = 0.98346$	$y = 947917.8133x^3 - 281117.8789x^2 + 26232.8967x - 631.465$ $R^2 = 0.99651$

4. CONCLUSIONS

Based on the obtained results, the following conclusions were drawn:

- The use of a diamond tool led to a significant improvement in surface quality. Although the greatest differences were observed for the roughness parameter Ra, the results of the parameters Rz and RSm clearly differed as well.
- For both tested tools, the use of variable cutting parameters had a similar effect on the surface roughness results yet with different intensity. Although the diamond tool was more

susceptible to changes in the machining conditions, its use allowed to control the machining effect to a greater extent.

- Regardless of the cutting tool type, lower surface roughness parameters were obtained when the milling process was conducted with the highest cutting speed and the lowest feed per tooth.
- The use of variable cutting speed had a similar effect on the changes in the cutting force components for both tested cutting tools. The exception was the milling process conducted with the diamond tool and $v_c = 300$ m/min where an increase in the values of these components was observed.

- The impact of variable feed per tooth depended significantly on the cutting speed. When the milling process was conducted with a cutting speed of 300 m/min, the cutting force components increased linearly as a result of the feed per tooth increase, while the use of a cutting speed of 900 m/min caused the changes to occur in a non-linear manner. Nevertheless, regardless of the cutting tool and cutting speed applied, the lowest values of the cutting force components were obtained when the milling process was conducted with low feed values.
- Regardless of the machining conditions, the highest values were obtained for the F_x component, i.e. in the direction perpendicular to the movement of the cutting tool. While the values of F_y and F_z depended on the cutting parameters.
- No clear relationship was observed between the obtained surface roughness parameters and the cutting force. This makes it difficult to optimize machining both in terms of process stability and workpiece quality. The correlation between the two indicators became evident mainly when the milling process was conducted with the cutting speed $v_c = 300$ m/min, where the cutting force components and the surface roughness parameters increased linearly with increasing the feed per tooth.

In future works, it is planned to extend the research conducted so far with additional indicators, such as: tool wear (especially at high speed cutting), vibrations, cutting temperature or tool deflection. These are phenomena that also have a significant impact on the course of machining and its effects. Analysis of additional parameters will allow for a better understanding of the processes occurring during milling of this group of materials. The research will also be continued for other aluminum alloys.

REFERENCES


1. Balon P, Rejman E, Kielbasa B, Smusz R. Using HSM Technology in Machining of Thin-Walled Aircraft Structures. *Acta Mech Autom.* 2022;16(1):27–33.
2. Yeganefar A, Ali Niknam S, Songmene V. Machinability study of aircraft series aluminium alloys 7075-T6 and 7050-T7451. *Trans Can Soc Mech Eng.* 2020;44(3):427–39.
3. Santos MC, Machado AR, Sales WF, Barrozo MAS, Ezugwu EO. Machining of aluminum alloys: a review. *Int J Adv Manuf Technol.* 2016;86(9–12):3067–80.
4. Soren TR, Kumar R, Panigrahi I, Sahoo AK, Panda A, Das RK. Machinability behavior of aluminium alloys: A brief study. *Mater Today Proc.* 2019;18:5069–75.
5. Pimenov DY, Kiran M, Khanna N, Pintaude G, Vasco MC, da Silva LRR, et al. Review of improvement of machinability and surface integrity in machining on aluminum alloys. Vol. 129, *International Journal of Advanced Manufacturing Technology*. Springer London. 2023; 4743–4779.
6. Yuazhi Z, Guozheng Z. Prediction of surface roughness and optimization of process parameters for efficient cutting of aluminum alloy. *Adv Mech Eng.* 2024;16(1):1–12.
7. Pham TH, Luyen TT, Nguyen DT. Investigating the correlation between surface roughness and degree of chip segmentation in A7075 aluminum alloy milling across varied cutting speeds. *Sadhana - Acad Proc Eng Sci.* 2024;49(2):1–16.
8. Tahmasbi A, Mougomo JBM, Samuel AM, Zedan Y, Songmene V, Samuel FH. Role of Li and Sc Additions and Machining Conditions on Cutting Forces on Milling Behavior of A7075-Based Alloys. *J Manuf Mater Process.* 2024;8(2).
9. Ping Z, Yue X, Shuangfeng H, Ailing S, Baoshun L, Xiao Y. Experiment and simulation on the high-speed milling mechanism of aluminum alloy 7050-T7451. *Vacuum.* 2020;182:109778.
10. Habrat W, Lisowicz J, Tymczyński J, Skroban A. Simulation and Experimental Study of the Thermo-Mechanical Effect of the Milling Process of 7075 Aluminium Alloy. *Adv Sci Technol Res J.* 2024;18(3): 58–66.
11. Sethupathy A, Shanmugasundaram N. Prediction of cutting force based on machining parameters on AL7075-T6 aluminum alloy by response surface methodology in end milling. *Materwiss Werksttech.* 2021 Aug 16;52(8):879–90.
12. Bhirud NL, Dube AS, Patil AS, Bhole KS. Multi-objective optimization of cutting parameters and helix angle for temperature rise and surface roughness using response surface methodology and desirability approach for Al 7075. *Int J Interact Des Manuf.* 2023;
13. Ikhries II, Al-Shawabkeh AF. Novel methods for optimizing CNC aluminum alloy machining parameters in polymer mold cavities. *Int J Light Mater Manuf.* 2024;7(4):507–19.
14. Żyłka Ł, Flejszar R, Krupa K, Lajmert P. Redefinition of precision in finishing milling: Exploring the influence of tool margin and edge micro-radius on surface roughness. *Manuf Lett.* 2024;41:52–8.
15. Schönecker RIE, Baumann J, Garcia Carballo R, Biermann D. Fundamental Investigation of the Application Behavior and Stabilization Potential of Milling Tools with Structured Flank Faces on the Minor Cutting Edges. *J Manuf Mater Process.* 2024;8(4).
16. Kuczmazewski J, Łogin W, Pieško P, Zawada-Michałowska M. Assessment of the Accuracy of High-Speed Machining of Thin-Walled EN AW-2024 Aluminium Alloy Elements Using Carbide Milling Cutter and with PCD Blades. In: *Advances in Manufacturing Lecture Notes in Mechanical Engineering*. 2018; 671–80.
17. Teicher U, Pirl S, Nestler A, Hellmich A, Ihlenfeldt S. Surface roughness and its prediction in high speed milling of aluminum alloys with PCD and cemented carbide tools. *MM Sci J.* 2019;3136–41.
18. Chen X, Tang J, Ding H, Liu A. Experimental study on the evolution of chip morphology, chip formation, and surface topography with cutting parameters, and their relationships in dry milling of cast aluminum alloy with PCD inserter. *J Mech Sci Technol.* 2021;35(4):1651–62.
19. O'Toole L, Fang F. Experimental study on efficient micro-milling of Alumina with PCD and cBN micro-milling tools. *nanoMan 2022 AETS 2022 - 2022 8th Int Conf Nanomanufacturing 4th AET Symp ACSM Digit Manuf.* 2022;1–6.
20. Davim JP, Maranhão C, Jackson MJ, Cabral G, Grácio J. FEM analysis in high speed machining of aluminium alloy (Al7075-0) using polycrystalline diamond (PCD) and cemented carbide (K10) cutting tools. *Int J Adv Manuf Technol.* 2008;39(11–12):1093–100.
21. Bourlet C, Fromentin G, Harika E, Crolet A. Analysis and modeling of burr formation during the plane milling of cast aluminum alloy using polycrystalline diamond tools. *J Manuf Sci Eng Trans ASME.* 2016;138(8):081010.
22. Karolczak P, Kołodziej M, Kowalski M. Effectiveness of Diamond Blades in the Turning of Aluminium Composites. *Adv Sci Technol Res J.* 2020;14(4):262–72.
23. Horváth R, Czifra Á, Drégelyi-Kiss Á. Effect of conventional and non-conventional tool geometries to skewness and kurtosis of surface roughness in case of fine turning of aluminium alloys with diamond tools. *Int J Adv Manuf Technol.* 2015;78(1–4):297–304.
24. Fraga da Silva T, Soares RB, Jesus AMP, Rosa PAR, Reis A. Simulation Studies of Turning of Aluminium Cast Alloy Using PCD Tools. *Procedia CIRP.* 2017;58:555–60.
25. Soares RB, de Jesus AMP, Neto RJL, Chirita B, Rosa PAR, Reis A. Comparison Between Cemented Carbide and PCD Tools on Machinability of a High Silicon Aluminum Alloy. *J Mater Eng Perform.* 2017;26(9):4638–57.
26. Soares RB, de Jesus AMP, R.J.L. N, Rosa PAR, Machado M, Reis A. Machinability of an Aluminium Cast Alloy Using PCD Tools for Turning. In: *Materials Design and Applications Advanced Structured Materials*. 2023; 329–46.
27. Aslantas K, Hascelik A, Çiçek A. Performance evaluation of DLC and NCD coatings in micro-milling of Al7075-T6 alloy. *J Manuf Process.* 2022;81:976–90.
28. Tamiloli N, Venkatesan J, Raja Raghu Vamsi Krishna P, Sampath Kumar T. Time domain and frequency domain of coated milling inserts


- using FFT spectrum. *Mater Manuf Process.* 2022; Dec 10;37(16):1882–92.
29. Pittalà GM, Linguanotto S. A study of machinability of Al7075-T6 with solid carbide end mills. *Procedia CIRP.* 2022;115:148–53.
 30. Silva FJG, Martinho RP, Magalhães LL, Fernandes F, Sales-Contini RCM, Durão LM, et al. A Comparative Study of Different Milling Strategies on Productivity, Tool Wear, Surface Roughness, and Vibration. *J Manuf Mater Process.* 2024;8(3):1–26.
 31. Burhanudin, Margono, Suryono E, Triatmoko N, Zainuddin. The Effect of Finishing Allowance and Milling Method on Surface Roughness in the Finishing Process of Al5052 and Al7075. *Key Eng Mater.* 2022;935:63–71.
 32. Tzotzis A, Korlos A, Verma RK, Kyratsis P. Ann-Based Surface Roughness Modelling of Aa7075-T6 Slot Milling: Cutting Technique Evaluation. *Acad J Manuf Eng.* 2023;21(4):27–35.
 33. Sivalingam V, Liu H, Tiwari S, Kumar PG, Sun M, Kai G, et al. Effect of reinforced particles on the machinability of Al alloy under MQL, cryogenic, and hybrid lubrication. *Int J Adv Manuf Technol.* 2024;132(7–8):3349–61.
 34. Tran CC, Luu VT, Nguyen VT, Tran VT, Vu HD. Multi-objective Optimization of CNC Milling Parameters of 7075 Aluminium Alloy Using Response Surface Methodology. *Jordan J Mech Ind Eng.* 2023;17(3):393–402.
 35. Yapan YF, Türkeli K, Emiroğlu U, Bahçe E, Uysal A. Machining and Sustainability Performance Comparison for the Milling Process of Al6082 Alloy Under Various Minimum Quantity Lubrication Conditions. *Int J Precis Eng Manuf - Green Technol.* 2024;12(2):409–30.
 36. Guntreddi B, Ghosh A. High-speed machining of aluminium alloy using vegetable oil based small quantity lubrication. *Proc Inst Mech Eng Part B J Eng Manuf.* 2023;237(13):1999–2014.
 37. Bayat M, Amini S. Distortion analysis in axial ultrasonic assisted milling of Al 7075-T6. *Int J Light Mater Manuf.* 2024;7(5):678–87.
 38. Baraya M, Yan J, Hossam M. Improving and Predicting the Surface

Roughness and the Machining Accuracy in Ultrasonic Vibration-Assisted Milling. *J Vib Eng Technol.* 2024;12:127–40.

39. Ali MN, Khalil H, El-Hofy H. Analytical modeling of cutting force in vibration-assisted helical milling of Al 7075 alloy. *J Manuf Process.* 2024;119:372–84.

Research work co-financed from the state budget under the programme of the Minister of Science and Higher Education Republic of Poland called 'Polish Metrology II', project number PM-II/SP/0040/2024/2, amount of funding: 968,000.00 PLN, total value of the project: 968,000.00 PLN. Project title: "Multisensory system for measuring thermos-mechanical interactions with comprehensive condition analysis".

Jarosław Korpysa:  <https://orcid.org/0000-0002-5833-7074>

Magdalena Zawada-Michałowska:  <https://orcid.org/0000-0003-3330-6340>

Paweł Pieśko:  <https://orcid.org/0000-0002-4152-5159>

Witold Habrat:  <https://orcid.org/0000-0002-9010-8175>

Joanna Lisowicz:  <https://orcid.org/0000-0002-9467-721X>



This work is licensed under the Creative Commons BY-NC-ND 4.0 license.

SUSTAINABLE INNOVATIONS: MECHANICAL AND TRIBOLOGICAL ADVANCEMENTS IN CARBON AND KEVLAR REINFORCED EPOXY COMPOSITES

Mohamed K. HASSAN^{*/**}, Muneef H. ALAMERI^{*}, Sufyan AZAM^{*/},
Somia ALFATIH M.S.^{***}, Mohammed Y. ABDELLAH^{****/****}

^{*}Mechanical Engineering Department, College of Engineering and Architecture, Umm Al-Qura University, Makkah 21955, Saudi. Arabia

^{**}Production Engineering and Design Department, Faculty of Engineering, Minia University, Minia 61111

^{***}Mechanical engineering department, College of Engineering, Alasala College, King Fahd Bin Abdulaziz Rd., Dammam 31483, Saudi Arabia

^{****} Mechanical Engineering Department, Faculty of Engineering, South Valley University, Qena, 8323, Egypt

mkorany@msn.com, s44280569@uqu.edu.sa, sufyan441@yahoo.com, somia.alfatih@alasala.edu.sa, mohamed_abdalla@eng.svu.edu.eg

received 20 January 2025, revised 14 April 2025, accepted 23 April 2025

Abstract: The study of technical textiles and their composites is crucial for material selection in performance-driven applications. This research investigates the mechanical and abrasion behavior of plain-woven Kevlar and carbon fiber fabrics and their epoxy-based composites under various environmental conditions. Tensile tests and Martindale abrasion tests were performed in warp and weft directions, following ASTM D3039, ISO 105-E04:2013, and ISO 12947-3:1998 standards. Samples were tested in dry conditions, after immersion in water, and in a salt solution simulating human sweat. Dry fabrics exhibited the highest tensile strength, with Kevlar fabric outperforming carbon fabric due to its denser weave and resistance to moisture-induced degradation. However, carbon/epoxy composites showed superior mechanical properties, owing to better fiber–matrix adhesion and stiffness. Hybrid Kevlar-carbon composites offered a balanced mechanical response, particularly in the warp direction. Abrasion tests revealed lower mass loss in Kevlar fabrics compared to carbon, with damage intensifying under wet conditions especially in sweat simulations due to salt-induced weakening. This behavior is linked to fiber structure, fiber–matrix bonding, and abrasive wear mechanisms. Sweat simulation testing reflects realistic service conditions found in protective clothing and aerospace applications. The results support the development of durable, lightweight composites for environments involving moisture or salt exposure. While statistical consistency was ensured using sample averaging, future studies will include detailed statistical analyses. To mitigate wet-condition degradation, future work will explore the use of surface treatments or coatings. This study contributes to sustainable material design by enabling longer service life, reduced material waste, and optimized hybrid fiber configurations. Further research will explore bio-based matrices and nano-enhanced hybrids to expand eco-friendly performance solutions.

Key words: tensile testing, martindale test, abrasion resistance, sustainable, kevlar textiles, carbon textiles

1. INTRODUCTION

Fabrics have become an integral part of everyday life and are used for clothing, upholstered furniture and technical textiles. Kevlar and carbon fabrics are particularly important. Kevlar, a synthetic para-aramid fiber, is known for its high strength, tensile strength-to-weight ratio, stiffness, heat resistance and abrasion resistance. Carbon fibers, which consist of thin, strong crystalline carbon filaments, are characterized by a high strength-to-weight ratio, stiffness and resistance to temperature and corrosion. Composites of Kevlar and carbon fibers combined with resins such as epoxy offer exceptional strength, stiffness and light weight, making them ideal for applications in the automotive, aerospace and protective clothing industries. Analyzing the mechanical properties of these materials, such as strength, stiffness and elongation, provides insight into how composition affects mechanical behavior. Many researchers have studied the mechanical properties of Kevlar and carbon composites and their hybrids. Rajesh et al. [1] investigated the tensile strength of a four-ply Kevlar composite produced by hand lay-up and found it to have high tensile strength, making it suitable for various engineering applications. Suthan et al. [2] studied Kevlar fiber-epoxy composites, focusing on their tensile and flexural properties, and found them to be superior to aluminum composites.

Yeung et al. [3] examined Kevlar-49 reinforced composites with different thermoplastic matrices and found that composites with a SAN matrix exhibited higher tensile strength than those with ABS, polyester, and polyethylene matrices. Agarwal et al. [4] compared the mechanical, wear, and thermomechanical properties of epoxy composites reinforced with glass, Kevlar, and carbon fabrics. They found that increasing the fabric content initially improved the properties, but excessive loading reduced them. Carbon fabric composites performed better overall than glass and Kevlar composites. Al-Qrimli et al. [5] investigated carbon/epoxy fabric composites produced by hand lay-up and found that they exhibited good elastic properties, with similar behavior in both warp and weft directions, and comparable shear and Poisson's ratios. Channabasavaraju et al. [6] studied the tensile and flexural properties of polymer composites reinforced with glass, graphite, and Kevlar fibers and concluded that both the type and thickness of the fiber affect these properties, with greater thickness leading to improved performance. Hybrid composites are materials made by combining different types of fibers or materials to achieve improved properties. They can be developed using synthetic, natural, and metallic fibers, resulting in enhanced strength, stiffness, and a high strength-to-weight ratio [6]. Furthermore, Kumar et al. [7] investigated the effects of hybridization on the properties of synthetic fibers using 3 mm thick laminates:

Kevlar49-E-glass, pure Kevlar49, and Kevlar49-carbon. The Kevlar-E-glass hybrid retained 90% of the strength of Kevlar, the carbon-Kevlar hybrid exhibited higher strength, and Kevlar showed higher impact strength. In another study, Hashim et al. [8] examined the tensile properties of carbon/Kevlar hybrids with different fiber orientations (0° , 45° , and 90°). The highest tensile strength was observed when the fibers were oriented in the direction of the carbon fibers (0°). Recently, Khaddour et al. [9] studied carbon, glass, and Kevlar fabrics, as well as epoxy hybrid composite laminates. Increasing the number of carbon layers increased the modulus of elasticity and tensile stress while reducing the elongation at break. The stacking sequence had no significant effect, except for a central Kevlar layer, which reduced the tensile properties. Priyanka et al. [10] also found that the hybridization pattern and the orientation of the carbon yarn in the carbon-Kevlar hybrid fabric significantly affected the modulus and strength, while the weaving pattern had no effect on mechanical performance. Plain woven fabrics resulted in stiffer laminates under loading. In addition, Hossain et al. [11] showed that CK/epoxy composites exhibited better mechanical properties compared to other matrices. Furthermore, Karthik et al. [12] investigated the tensile properties of hybrid composites with different stacking sequences and found that the carbon-Kevlar-carbon (C-K-C-C-C) sequence exhibited the highest tensile strength. Recent advancements in composite materials have emphasized sustainability, durability, and performance optimization under variable environmental conditions. Studies have explored the development of eco-friendly and high-strength polymer composites using bio-fillers, hybrid reinforcements, and water treatment applications to enhance material performance and longevity [13-16]. Innovations in textile-reinforced composites, including the integration of carbon and Kevlar fibers, have shown promising results in mechanical and tribological improvements [17-20]. Moreover, the role of surface treatments, hybrid stacking, and environmental resistance has been critically examined to address durability challenges in aggressive environments [20].

This study focuses specifically on plain-woven technical textiles, as woven fabrics are commonly used in structural composite applications due to their predictable mechanical behavior. The study hypothesizes that the mechanical and abrasion properties of Kevlar and carbon fiber fabrics, as well as their composites, are significantly influenced by environmental conditions, fiber type, and fabric orientation. It is expected that dry conditions will enhance tensile strength and reduce material loss during abrasion testing, while wet conditions, including exposure to water and salt solutions, will negatively affect performance. Additionally, hybrid composites combining Kevlar and carbon fibers are anticipated to provide balanced mechanical behavior by utilizing the strengths of both materials. The main objective of this research is to investigate the mechanical response of these fabrics and their composites under varying environmental conditions. The study includes tensile and abrasion testing of the materials in both dry and wet states, and compares the performance of Kevlar, carbon, and hybrid composites considering fiber orientation and stacking sequence. The findings aim to inform material selection for sustainable, high-performance applications in fields such as aerospace, automotive, and protective equipment.

2. MATERIALS AND METHODS

In this research, two types of fabrics were used: plain weave Kevlar fabric (0.24 mm thickness, 200 g/m² surface density) and

plain weave carbon fabric (0.28 mm thickness, 200 g/m² surface density). In this experimental study, the fabrics and their composites were tested under various conditions using tensile and abrasion tests. Tensile tests were carried out on a Universal Testing Machine for both the fabrics and the composites, while abrasion tests were conducted using a Martindale Abrasion Tester.

2.1. Tensile Test on Fabrics

The most common mechanical test performed on textiles is the tensile strength test. It measures how a fabric responds when subjected to a stretching force along its length. The test works on the basic principle of holding the sample at two or more points and pulling it until it breaks [21]. In this study, tensile tests were carried out on fabric samples under different conditions: dry, after being soaked in water for 24 hours, and after being soaked in a saltwater solution for 24 hours to simulate human sweat. According to ISO 105-E04:2013 [22], the artificial sweat solution consists of 5 grams of sodium chloride (NaCl) dissolved in 1 liter of distilled water. All tests were conducted in both the warp and weft directions to examine any differences in performance under each condition. The samples, made of Kevlar and Carbon fabrics, measured 25 mm × 250 mm and were cut using a laser cutting machine. Aluminum plates (25 × 50 mm) were attached to the ends of each sample and bonded with epoxy to ensure smooth tensile loading and to prevent slipping from the jaws of the testing machine. The tensile strength tests were performed using a Zwick Roell Z600 tester with hydraulic grips, operating at a speed of 2 mm/min.

2.2. Tensile Test on Composite Fabrics

A tensile test is a widely used method for evaluating the mechanical properties of materials, including composite fabrics. These fabrics consist of two or more components—typically reinforcing fibers and a matrix material. In this study, three types of composite materials were prepared: Kevlar/epoxy, Carbon/epoxy, and a hybrid Kevlar-Carbon/epoxy composite. The Kevlar and Carbon specimens each contained six layers of fabric (referred to as 6K and 6C, respectively), while the hybrid composite was made by alternating three layers of Kevlar and three layers of Carbon in a KCKCKC sequence. The epoxy resin and hardener were mixed in a recommended weight ratio of 10:6. The composites were then fabricated using the hand layup method, by layering fabric and resin alternately in an open mold. The samples were left to cure at room temperature for at least 24 to 48 hours to ensure the resin dried completely. Tensile tests were carried out using a Zwick Roell Z600 material testing machine in accordance with the ASTM D3039 standard [23], at a test speed of 2 mm/min for all composite samples. Three specimens were prepared for each fabric type in both the warp and weft directions, with dimensions of 250 mm × 25 mm, a thickness between 2.0 and 2.5 mm, and a gauge length of 150 mm. The average values of the results were recorded. Samples were cut using an abrasive water jet machine. To ensure a smooth tensile process and prevent slippage from the grips of the testing machine, aluminum tabs (25 mm × 50 mm) were securely bonded to the ends of each specimen using epoxy. Tensile loading was applied in both the warp and weft directions. Mechanical properties such as tensile strength, tensile modulus, elongation at break, and maximum force were evaluated.

2.3. Abrasion test on Fabrics

The wear behavior of fabrics involves examining how different materials respond to mechanical stress and environmental conditions over time. This includes evaluating their resistance to abrasion, pilling, tearing, and other types of wear. Abrasion testing is one of the key methods used to assess the durability and wear resistance of fabrics. Abrasion refers to the mechanical damage caused by rubbing the fabric against another surface. Over time, this can lead to the loss of performance properties—especially strength—and negatively affect the fabric's appearance [24]. Abrasion resistance is evaluated by measuring changes such as loss of mass, reduction in strength, increased air or light permeability, decrease in thickness, and alterations in surface structure (e.g., broken yarns or holes). These surface changes often reflect modifications in the fabric's physical properties and internal structure [25]. Several techniques are used to test abrasion resistance. All of them involve rubbing the sample fabric against an abrasive surface, another fabric, or emery paper, either for a set duration or a certain number of strokes, often following a Lissajous pattern of movement [18]. The Martindale abrasion test is the most commonly used method. In this test, circular fabric samples are rubbed against a standard abradant under a specific load. One advantage of the Martindale test is that it exposes the sample to wear from multiple directions. Common abrasives used in the test include silicon carbide paper or woven worsted wool [26].

In the current study, abrasion tests were conducted on 100% Kevlar and 100% Carbon fabrics using a Martindale abrasion tester (Fig. 1). Three types of sandpaper with different grit levels were used: Silicon Carbide Paper P1000 and P500 from STRUERS, and Micro Cloth Paper P1200 from BUEHLER. Tests were carried out for 25, 50, and 75 cycles. The abrasion resistance was evaluated based on ISO 12947-3:1998, which outlines the procedure for determining fabric mass loss using the Martindale method [27]. While this standard served as a reference, the testing conditions were adapted to suit different scenarios, but all procedures were conducted in a consistent and controlled manner. Experiments were performed under both dry and wet conditions for each cycle count and sandpaper type. Three fabric samples were tested for each case, and the average mass loss was recorded. Samples were cut into 80 mm diameter circles using a laser cutting machine, ensuring each circular piece included both warp and weft yarns. All samples were labeled and coded for clarity, with "S" referring to Kevlar and "C" to Carbon samples. Figure 2: Kevlar and Carbon fabric samples cut into 80 mm diameter circles using a laser cutter, shown placed in holders prior to abrasion testing using the Martindale abrasion tester. Each sample includes both warp and weft yarns to ensure uniform exposure to abrasion during testing. The wet condition tests were conducted using two methods: immersion in pure water and immersion in a simulated sweat solution. The sweat solution, based on ISO 105-E04:2013 [22] contained 5 grams of sodium chloride (NaCl) dissolved in 1 liter of water. Samples were soaked in each solution for 24 hours before testing and were weighed on a precision scale both before and after abrasion testing. In all test cases, the samples were abraded against sandpaper using the Martindale abrasion tester. The process began under dry conditions, with tests conducted using P500 sandpaper for 25, 50, and 75 cycles. After each cycle set, the samples were carefully removed from the holder to prevent damage or displacement of the yarns, then weighed to calculate mass loss. This procedure was repeated for the 50- and 75-cycle tests. The same sequence was followed for the tests conducted under pure water and simulated sweat

conditions.

All tests were carried out under consistent conditions, with the sandpaper replaced at each stage—whether in dry or wet testing. Abrasion resistance was determined by calculating the mass loss of each sample before and after each test cycle (25, 50, and 75), and the results were expressed as percentages for comparison.



Fig. 1. Martindale abrasion tester

3. RESULTS AND DISCUSSIONS

3.1. Fabric Tensile Test Results and Discussions:

Tensile strength is a key mechanical property of woven materials, representing the force required to break multiple yarns simultaneously in either the warp or weft direction. It measures the fabric's ability to withstand tension or pull forces without breaking or tearing. Table 1 presents the average tensile strength and maximum force for two fabrics—Kevlar and Carbon—in both warp and weft orientations, tested under three conditions: dry, immersion in water, and immersion in a water-and-salt solution to simulate human sweat. "K" refers to Kevlar fabric samples, while "C" refers to Carbon fabric samples.

It is well known that woven fabrics exhibit different mechanical properties depending on direction and environmental conditions. As shown in Figures 2a and 2b, the tensile strength in the warp direction is greater than in the weft direction. This is because warp threads are typically under higher tension during the weaving process, which tightens and aligns the yarns, making them more resistant to stretching or breaking in the longitudinal direction. In contrast, weft threads, which interlace with the warp yarns, experience less tension during weaving and generally exhibit lower tensile strength in the transverse direction. When comparing tensile strength across different conditions, the dry samples consistently showed higher strength than those immersed in water or the sweat solution. For Kevlar fabric (Figure 3a), the ultimate tensile strength (UTS) in the warp direction reached approximately 548.21 MPa, 546.44 MPa, and 527.45 MPa for the dry, water-immersed, and sweat-immersed samples, respectively—each surpassing their corresponding weft-direction values. A similar trend was observed for the Carbon fabric, where the warp direction generally exhibited higher UTS than the weft direction. However, an exception was noted in the C3 warp-direction sample, which reached 359.68 MPa—higher than the dry and sweat-condition samples. Further inspection revealed that this sample had more burned edges due to laser cutting, which may have increased its resistance compared to the other samples. It was also observed that tensile strength is

influenced by multiple factors beyond yarn strength. These include the type of fiber or fiber blend, the degree and direction of twist, the number of yarns, the spinning system, the yarn's bending behavior, its frictional properties, as well as the fabric's geometry, thread density, and weave pattern. Additionally, testing conditions—such as temperature, humidity, loading duration, applied force, jaw spacing, and the specific testing procedures—can significantly affect fabric strength [28].

Tab. 1. Average results of Tensile test for Kevlar and Carbon fabric on different conditions

Average Results in Dry Conditions			
Fabric Code	Thickness (mm)	Tensile strength (MPa)	Fmax (N)
K1 (Warp)	0.24	548.21	3289.25
K2 (Weft)	0.24	512.19	3073.14
C1 (Warp)	0.28	340.33	2382.33
C2 (Weft)	0.28	149.38	1045.69
Average Results with Water Conditions			
K3 (Warp)	0.24	546.44	3278.64
K4 (Weft)	0.24	510.57	3063.43
C3 (Warp)	0.28	359.68	2517.74
C4 (Weft)	0.28	29.78	208.48
Average Results with Sweat Conditions			
K5 (Warp)	0.24	527.45	3164.71
K6 (Weft)	0.24	507.50	3045.01
C5 (Warp)	0.28	326.22	2283.51
C6 (Weft)	0.28	116.14	812.95

It has been observed that fabric strength is highest in the dry state compared to wet conditions. Furthermore, fabric submerged in water retains more strength than when submerged in a saltwater solution. In the dry state, fiber remains tightly packed and well-aligned, allowing them to bear loads and resist deformation more effectively. In wet conditions, fibers absorb moisture, which causes swelling and reduces their mechanical performance. When immersed in a saltwater solution, the presence of salt ions causes additional swelling and interacts with the fiber surface, disrupting intermolecular forces. These ionic interactions weaken the bonding between fibers, resulting in decreased overall textile strength. Salt ions interact with the fibre surface and interfere with intermolecular bonding, increasing the degree of fiber swelling and reducing structural cohesion. This leads to a greater reduction in tensile strength compared to pure water exposure. Due to differences in composition and structure, Kevlar fabric demonstrates more durable and consistent performance than Carbon fabric. Kevlar threads are more tightly interwoven, while the threads in Carbon fabric may not bind as effectively, leading to fiber separation or release. This contributes to greater variability and fluctuations in the performance of Carbon fabric, making it less reliable as a structural textile compared to Kevlar. Sweat simulation led to greater fabric mass loss than pure water immersion, indicating that salt content accelerates degradation.

3.2. Composites Fabric Tensile Test Results and Discussions:

The tensile test is a vital evaluation method for composite materials, offering critical insights into their mechanical performance

under stress. It measures key properties such as strength, stiffness, and elongation by applying an axial load to a specimen until failure occurs. These data are essential for informed material selection and sustainable technical design in sectors such as aerospace, automotive, construction, and advanced manufacturing, where durability, performance, and resource efficiency are priorities. In this study, tensile tests were performed on three types of composite materials—Kevlar/Epoxy, Carbon/Epoxy, and a Kevlar-Carbon hybrid/Epoxy composite. Mechanical properties including tensile strength, Young's modulus (tensile modulus), elongation at break, and maximum force were determined to assess the structural integrity and performance potential of each material configuration.

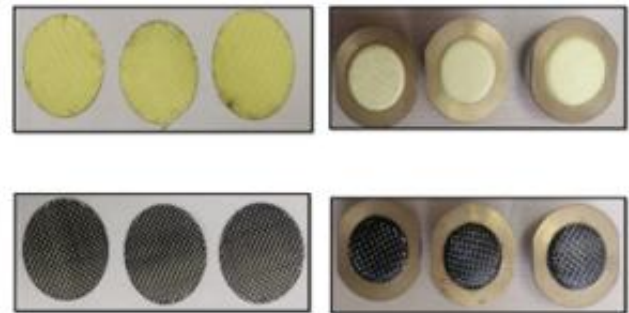


Fig. 2. Kevlar and Carbon fabrics samples after cutting in 80mm diameter from fabrics and in holders before test

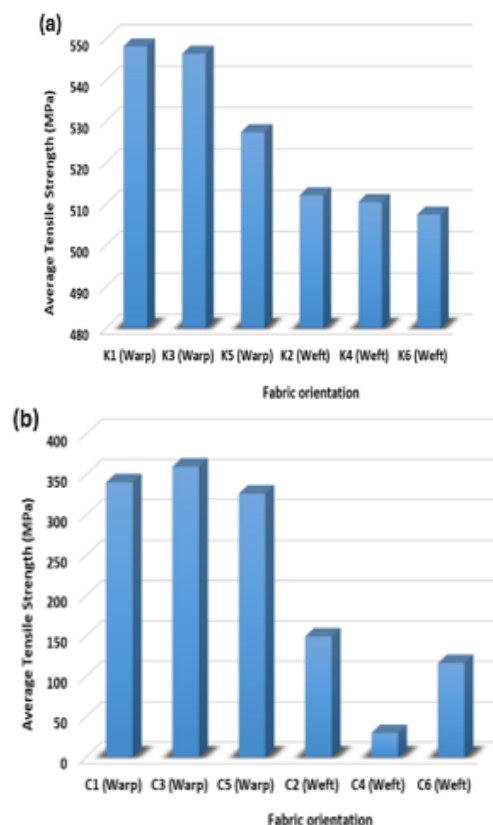


Fig. 3. Average results of Tensile strength in dry and wet cases for: a) Kevlar fabric , b) Carbon

Table 2 and Figures 4a and 4b present the average mechanical results for the different composite types in both warp and weft orientations. The data reveal that Kevlar/Epoxy composites exhibit

high tensile strength and strain in both directions, with notably higher Young's modulus and tensile strength in the warp direction. Similarly, Carbon/Epoxy composites demonstrate superior tensile strength and modulus in the warp direction, although with reduced strain compared to Kevlar/Epoxy. This indicates that Carbon composites offer higher stiffness and load-bearing capacity, while Kevlar composites provide more flexibility. The hybrid Kevlar-Carbon/Epoxy composites combine the mechanical advantages of both fiber types. In the warp direction, these hybrid materials show a balanced performance, with tensile strength and modulus values between those of pure Kevlar and Carbon composites. In the weft direction, however, the hybrid composites exhibit a compromise—lower tensile strength than either of the individual fiber composites, but a higher modulus than Kevlar/Epoxy, suggesting improved stiffness with some trade-off in strength.

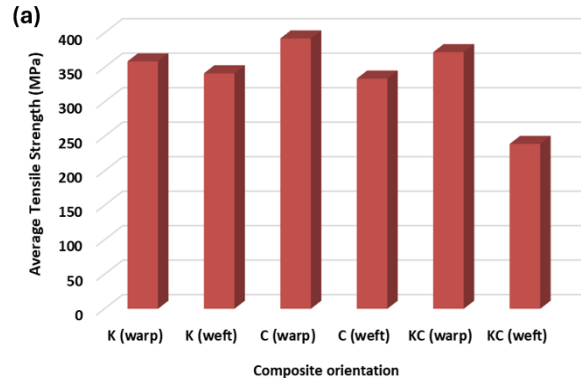
Tab. 2. Average results of Tensile test for Kevlar and Carbon fabric on different conditions

for (Kevlar/Epoxy, Carbon/Epoxy, and K-C hybrid/Epoxy) in warp and weft directions					
Code	Thick-ness (mm)	Max Strain %	Tensile strength (MPa)	Fmax (kN)	E-Mod (GPa)
K (warp)	2.25	4.03	358.63	19.72	8.39
K (weft)	2.13	4.56	341.28	18.20	6.77
C (warp)	2.30	2.09	391.85	23.13	21.64
C (weft)	2.37	1.65	333.68	19.13	22.20
KC (warp)	2.17	2.31	372.04	20.06	16.07
KC (weft)	2.30	1.84	238.97	13.73	11.96
for both directions (warp & weft) for each composite (Kevlar/Epoxy, Carbon/Epoxy, and K-C hybrid/Epoxy)					
K	2.19	4.30	349.95	18.96	7.58
C	2.33	1.87	362.77	21.13	21.92
KC	2.23	2.08	305.51	16.89	14.01

As illustrated in Figure 4a, Kevlar/Epoxy composites in the warp direction achieve a tensile strength of 358.63 MPa, slightly lower than Carbon/Epoxy composites, which reach 391.85 MPa. This indicates that Carbon-based composites offer enhanced tensile strength compared to Kevlar-based ones. In the weft direction, the tensile strengths of Kevlar/Epoxy (341.28 MPa) and Carbon/Epoxy (333.68 MPa) are closely matched, suggesting that both materials perform comparably in the transverse orientation [29-31]. The Kevlar-Carbon hybrid composite in the warp direction achieves a tensile strength of 372.04 MPa—higher than Kevlar/Epoxy but still lower than Carbon/Epoxy. This demonstrates that the inclusion of Carbon fibers enhances the tensile properties of the hybrid compared to Kevlar alone, though not to the level of pure Carbon/Epoxy. In the weft direction, the hybrid composite shows a tensile strength of 238.97 MPa, which is lower than both Kevlar/Epoxy (341.28 MPa) and Carbon/Epoxy (333.68 MPa). This suggests that hybridization in the weft direction may lead to weaker fiber interactions and reduced load transfer efficiency, which impacts tensile strength. The hybrid composite achieved 372.04 MPa in warp direction, compared to 358.63 MPa for Kevlar/Epoxy, indicating improved tensile strength due to the reinforcing contribution of carbon layers. Overall, the results provide valuable data for the development of high-performance, fiber-reinforced composites with applications in sustainable design and lightweight structural components. Hybrid composites may offer a strategic balance between

performance and material efficiency, contributing to the broader goals of sustainability through optimized resource use and extended material life cycles. Figure 4b illustrates that Carbon/Epoxy composites exhibit significantly higher Young's moduli in both the warp (21.64 GPa) and weft (22.20 GPa) directions compared to Kevlar/Epoxy composites, which recorded values of 8.39 GPa and 6.77 GPa in the warp and weft directions, respectively. These findings confirm that Carbon fibers impart superior stiffness and rigidity to composite materials. However, the hybrid Kevlar-Carbon composites demonstrate intermediate Young's moduli—16.07 GPa in the warp direction and 11.96 GPa in the weft direction—indicating a reduction in stiffness relative to pure Carbon/Epoxy composites, yet an improvement over Kevlar/Epoxy composites. This highlights the trade-off introduced by blending fibers: while Kevlar fibers enhance other properties such as flexibility, they reduce the overall stiffness of the hybrid composite. In terms of strain behavior, Kevlar/Epoxy composites display greater ductility compared to Carbon-based composites. Specifically, Kevlar/Epoxy composites exhibit strain values of 4.03% in the warp direction and 4.56% in the weft direction, compared to Carbon/Epoxy composites, which show 2.09% and 1.65% strain in the warp and weft directions, respectively. These results suggest that Kevlar-based composites can endure higher deformation under tensile loading, making them more suitable for applications where flexibility and impact resistance are critical. For the hybrid Kevlar-Carbon composites, strain in the warp direction is 2.31%, and in the weft direction, 1.84%. These values lie between those of the Kevlar and Carbon composites, indicating a synergistic behavior that combines some flexibility from Kevlar with the rigidity of Carbon. This behavior suggests the hybrid structure could offer a balanced mechanical response, which is advantageous for applications requiring a compromise between stiffness and flexibility.

As summarized in Table 2, the comparative performance of the composite types shows that Carbon/Epoxy composites consistently demonstrate higher tensile strength and stiffness, but lower strain, compared to Kevlar/Epoxy and hybrid composites. These characteristics may result from stronger interfacial bonding between the Carbon fibers and the epoxy matrix, which contributes to more efficient load transfer and improved mechanical performance. In contrast, Kevlar/Epoxy composites exhibit lower tensile strength and stiffness, likely due to weaker adhesion between the Kevlar fibers and the resin, but benefit from greater strain capacity. The hybrid Kevlar-Carbon composites exhibit a combination of the properties found in the individual materials, offering a viable compromise for multifunctional applications. From a sustainability perspective, such hybridization can contribute to material efficiency by optimizing mechanical performance while reducing dependency on high-cost or resource-intensive components like pure Carbon fibers.



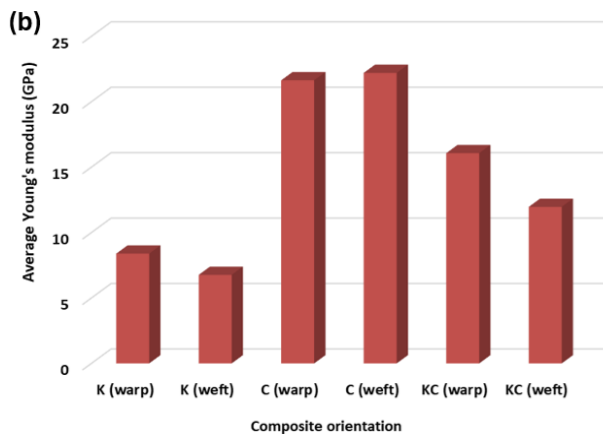


Fig. 4. Average mechanical properties for (Kevlar/Epoxy, Carbon/Epoxy, and K-C hybrid/Epoxy) in warp and weft directions for; a) Tensile strength, b) Young's modulus

These findings also reinforce the well-documented anisotropic nature of fiber-reinforced composites, in which mechanical properties vary depending on the direction of applied stress relative to fiber alignment. This directional dependence is a fundamental design parameter in sustainable composite engineering. By carefully selecting fiber types, orientations, and matrix combinations, designers and engineers can tailor composite materials to meet performance requirements while optimizing resource use and minimizing environmental impact. In summary, the results underscore the critical role of fiber selection, orientation, and material hybridization in achieving desirable mechanical performance and advancing sustainable material development for structural and engineering applications. The stress-strain curves of the composite materials, evaluated in both the warp and weft directions, exhibit an initial linear response up to the point of ultimate failure, which occurs suddenly and without significant plastic deformation. However, slight nonlinear behavior is observed prior to fracture, primarily due to matrix cracking and micro-damage accumulation, which introduces minor fluctuations in the curves, as illustrated in Figures 5a, 5b, and 5c. It is important to note that several factors influence the mechanical performance of composite materials. These include the fabrication technique, the type and quality of the matrix, fiber grade, thermal processing conditions, chemical treatments related to performance enhancement, and the degree of fiber-matrix interfacial adhesion. Optimizing these factors is essential not only for improving mechanical properties but also for advancing the development of more durable, resource-efficient, and sustainable composite systems [32-34].

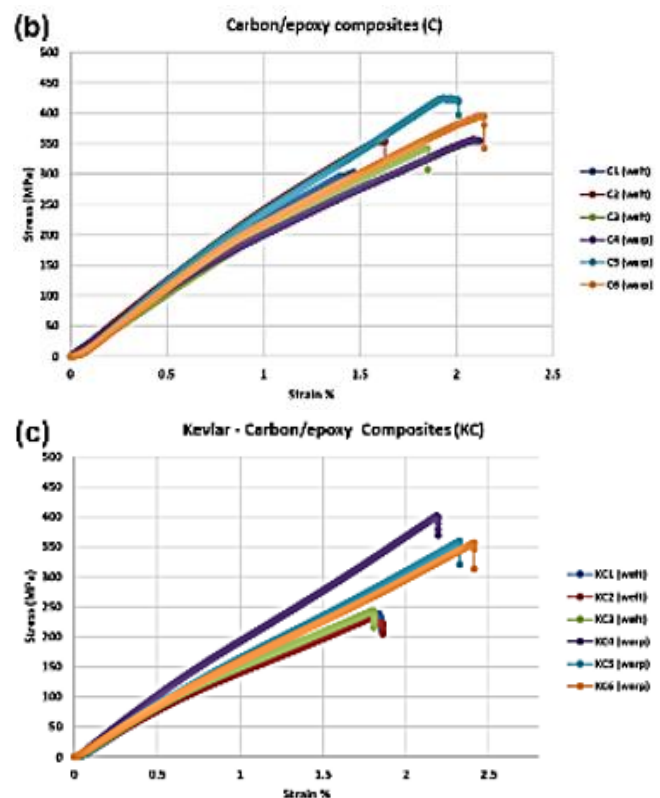
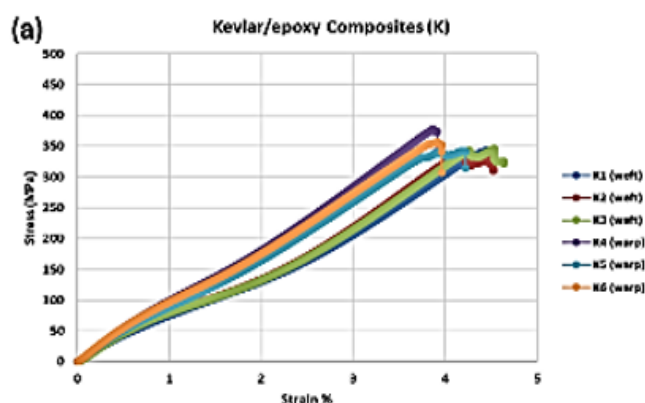


Fig. 5. Stress-Strain curve composites in warp and weft directions of: a) Kevlar/epoxy, b) Carbon/epoxy and c) Kevlar – Carbon /epoxy

Figure 6a illustrates the failure modes of the composite materials in both the warp and weft directions. As observed, the failures occur at the length of the specimens. The failure strength of a composite typically falls between the failure strengths of its fibers and matrix, with some fibers breaking at various points and others pulling out at regions where matrix-fiber adhesion fails [35, 36]. In Kevlar/epoxy composites, failure initiates with matrix cracking, where the epoxy resin matrix begins to crack under stress. This is followed by fiber/matrix interface debonding and fiber pull-out, indicating that the epoxy matrix is unable to effectively distribute and absorb the applied load, leading to localized failure. This failure mode is a critical consideration when designing composites for sustainability, as improving matrix-fiber bonding could enhance the longevity and durability of materials, reducing the need for frequent replacements and minimizing waste. For Carbon/epoxy composites, a simultaneous and complete cutting of both the matrix and Carbon fibers was observed. This suggests a strong interaction and bonding between the matrix and Carbon fibers, enhancing the material's stiffness and strength. The failure near the grips may be attributed to stress concentration at these points, but the efficient load transfer between matrix and fibers contributes to improved overall mechanical performance. The strong fiber-matrix bonding in Carbon composites also has sustainability implications, as it potentially leads to longer-lasting materials with lower environmental impact over their lifecycle. This anisotropy is attributed to the weaving process, where warp threads are subjected to higher tension, resulting in better alignment, tighter packing, and enhanced load transfer capabilities. In hybrid composites, consisting of both Kevlar and Carbon fibers in an epoxy matrix, a combination of failure modes is observed. Carbon layers exhibit complete cutting or failure, whereas Kevlar layers initially fail in the matrix, followed by fiber failure. Additionally, delamination between the Kevlar and Carbon layers occurs. This

delamination suggests mismatched properties or interactions between the two materials, implying imperfect adhesion or bonding. Such issues are important in the context of sustainability, as delamination can reduce the overall strength and lifespan of the composite, leading to more frequent material replacement. Future efforts to optimize the adhesion and compatibility of hybrid materials could improve their performance and sustainability, contributing to the development of more efficient and environmentally friendly composite materials. While Kevlar fabric exhibits higher tensile strength than carbon fabric in isolation, the superior fiber–matrix adhesion and stiffness of carbon fibers enable carbon/epoxy composites to outperform Kevlar/epoxy composites overall.

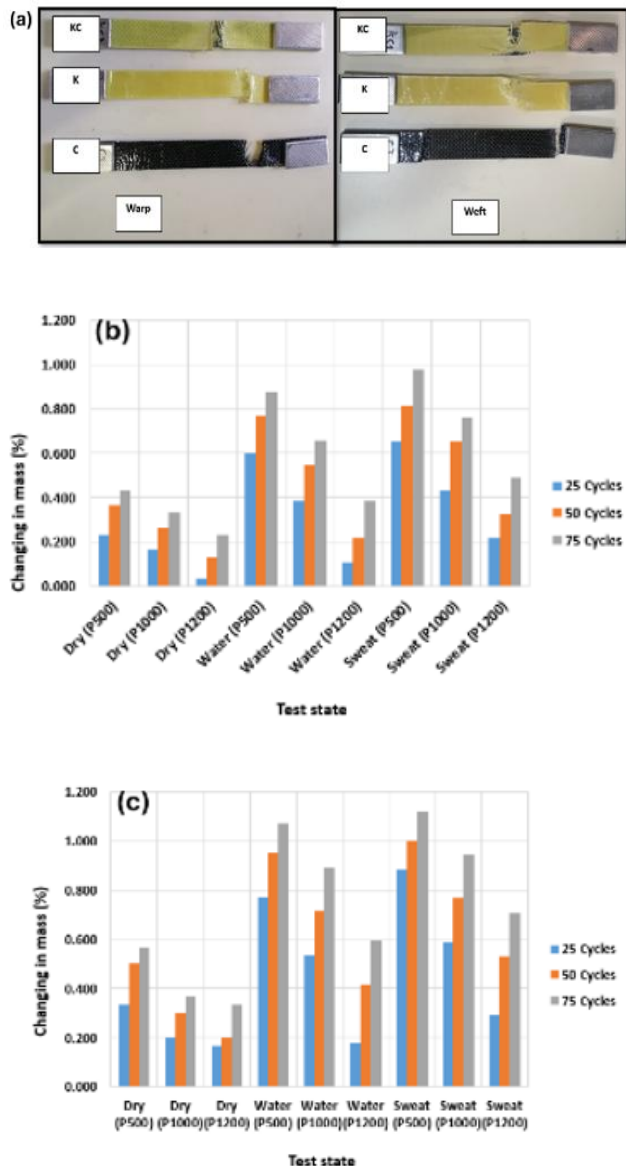


Fig. 6. The failures of the composite; a) (Kevlar/Epoxy, Carbon/Epoxy, and K-C hybrid/Epoxy), b) Kevlar fabric against sandpapers, c) Carbon fabric against sandpapers in warp and weft directions

3.3. Fabric Abrasion Test Results and Discussion

Fabric abrasion resistance was evaluated using the Martindale test, a widely recognized method for assessing textile durability. The results of abrasion resistance for the fabrics, tested against

three types of sandpaper (P500, P1000, and P1200), are presented in Table 3 and expressed as a percentage of mass loss. Figures 6b and 6c illustrate the percentage of mass loss for all fabric specimens based on the number of abrasion cycles and different test conditions (dry and wet). These figures represent the average results of three samples evaluated for each abrasion cycle, where each sample was tested for each cycle against a sandpaper, and the average was computed. The abrasion testing results at 25, 50, and 75 cycles revealed varying levels of mass loss among the fabric samples under different sandpaper grits and test conditions (dry and wet). In dry conditions, Kevlar fabric exhibited less mass loss at all testing cycles against all sandpapers when compared to Carbon fabric, as shown in Figures 6b and 6c. For instance, under dry conditions with an abrasion cycle of 25 and sandpaper P500, Kevlar fabric experienced a mass loss of 0.2333%, whereas Carbon fabric exhibited a mass loss of 0.333%. As the number of abrasion cycles increased, the mass loss intensified, reaching 0.366% and 0.433% for Kevlar fabric at 50 and 75 cycles, respectively. Similarly, Carbon fabric demonstrated a mass loss of 0.5% at 50 cycles and 0.5667% at 75 cycles, as shown in Table 3. This trend persisted when testing with sandpapers P1000 and P1200, although the magnitude of mass loss varied depending on the sandpaper grit. The superior strength and endurance of Kevlar allow it to better withstand abrasion and wear than Carbon fabric. Moreover, the molecular structure of Kevlar provides remarkable tensile strength and toughness, making it highly resistant to abrasion and friction damage. In contrast, Carbon fabric, despite its strength, is less resistant to abrasion compared to Kevlar. The increased mass loss in carbon fabric is likely due to lower resistance to fiber breakage under mechanical abrasion, as well as differences in yarn bonding. Kevlar's high crystallinity and hydrogen bonding provide better abrasion resistance.

Tab. 3. Average results for Abrasion test samples in different conditions in Dry case for Kevlar and Carbon fabrics

Cy- cles	P500				P1000				P1200			
	Fabric code	Mass be- fore (g)	Mass af- ter (g)	%	Fabric code	Mass be- fore (g)	Mass af- ter (g)	%	Fabric code	Mass be- fore (g)	Mass af- ter (g)	%
25	S1	1	0.997	0.23	S4	1	0.998	0.16	S7	1	0.999	0.03
50	S2	1	0.996	0.36	S5	1	0.997	0.26	S8	1	0.998	0.13
75	S3	1	0.995	0.43	S6	1	0.996	0.33	S9	1	0.997	0.23
25	C1	1	0.996	0.33	C4	1	0.998	0.20	C7	1	0.998	0.16
50	C2	1	0.995	0.50	C5	1	0.9970	0.30	C8	1	0.9980	0.20
75	C3	1	0.994	0.56	C6	1	0.9963	0.36	C9	1	0.9967	0.33
with pure water case for Kevlar and Carbon fabrics												
25	S10	1.829	1.82	0.60	S13	1.83	1.82	0.38	S16	1.828	1.826	0.1094
50	S11	1.829	1.82	0.77	S14	1.83	1.82	0.55	S17	1.828	1.824	0.22
75	S12	1.828	1.81	0.88	S15	1.83	1.82	0.66	S18	1.828	1.821	0.38
25	C10	1.682	1.67	0.77	C13	1.68	1.67	0.54	C16	1.682	1.679	0.18
50	C11	1.682	1.67	0.95	C14	1.68	1.67	0.71	C17	1.682	1.675	0.42
75	C12	1.682	1.66	1.07	C15	1.68	1.67	0.89	C18	1.682	1.672	0.59
sweat simulation case for Kevlar and Carbon fabrics												
25	S19	1.841	1.829	0.6518	S22	1.841	1.833	0.4346	S25	1.841	1.837	0.2173
50	S20	1.839	1.824	0.8157	S23	1.841	1.829	0.6518	S26	1.840	1.834	0.3261
75	S21	1.841	1.823	0.9777	S24	1.841	1.827	0.7605	S27	1.841	1.832	0.4889
25	C19	1.698	1.683	0.8834	C22	1.698	1.688	0.5890	C25	1.698	1.693	0.2945
50	C20	1.698	1.681	1.0012	C23	1.697	1.684	0.7661	C26	1.698	1.689	0.5300
75	C21	1.698	1.679	1.1190	C24	1.698	1.682	0.9423	C27	1.698	1.686	0.7067

The observations indicate that the fabric's mass loss is greater in wet conditions (both pure water and sweat simulation) than in dry conditions for both Kevlar and Carbon textiles. As seen in the

figures, the percentage of mass loss during water tests, using sandpaper P500 and an abrasion cycle of 25, was 0.6014% for Kevlar fabric and 0.7729% for Carbon fabric. Notably, as the number of cycles increased, a significant divergence between the two fabrics became apparent under identical water test conditions, as shown in Table 3. Furthermore, the mass loss percentage in the sweat simulation cases exceeded that observed in the water test. For instance, with sandpaper P500 and an abrasion cycle of 25, the mass loss for Kevlar fabric was recorded as 0.6518%, while Carbon fabric exhibited a higher mass loss of 0.8834%, as shown in Table 3. Additionally, the degree of mass loss increased with the number of abrasion cycles. Comparing the two wet test conditions, it is clear that the pure water test resulted in lower mass loss than the sweat simulation in all samples tested, including Kevlar and Carbon fabrics. This difference is attributed to the presence of particles such as salt in sweat, which can act as abrasive agents, increasing friction and accelerating the wear on the fabric surface. As a result, fibers exposed to the sweat solution experience more abrasion-induced mass loss than those exposed to pure water.

The difference in mass loss between wet and dry conditions can be attributed to the weaker and more brittle connections between the fabric's threads when exposed to moisture or immersed in water or sweat solutions, compared to their stronger bonds in dry conditions. In the dry state, the fibers and threads are typically tightly bound, creating resilient connections that provide structural integrity and strength. However, when exposed to wet or damp conditions, these connections weaken, making textiles more prone to breakage and distortion. Consequently, the threads and fibers become more susceptible to separation, breakage, or pull-out from the fabric surface, resulting in increased mass loss. Additionally, moisture absorbed by the fabric contributes to its weight, further increasing the overall mass loss. Visual comparisons of the fabric's appearance before and after testing reveal significant differences in mass loss, as shown in Figures 7(a, b, c, d, e, and f). These images display the fabric's state before and after 75 cycles of abrasion testing under various conditions, including dry and wet states, using different grades of sandpaper. Based on the images, it is evident that Carbon fabric experiences greater mass loss compared to Kevlar fabric. The images also illustrate the extent of damage and deterioration on the surface of the Carbon fabric in contrast to the Kevlar fabric. Furthermore, it is worth noting that mass loss is larger in the wet state compared to the dry state, with sweat testing resulting in higher mass loss than water testing. It should be emphasized that the abrasion resistance of textile materials is a complex phenomenon influenced by various factors, including fiber, yarn, fabric features, and finishing techniques. Some of these factors impact the fabric's surface, while others affect its internal structure [37].

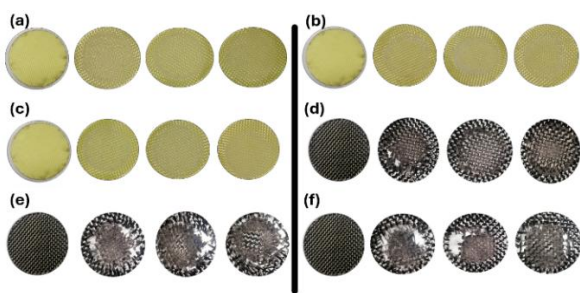


Fig. 7. The failure modes before and after 75 abrasion cycles for a) Kevlar dry, b) Kevlar pure water, c) Kevlar sweat, d) carbon dry, e) carbon pure water, f) carbon sweat

It has been observed that fabric samples tested with P500 sandpaper exhibited higher mass loss compared to those tested with P1000 and P1200, indicating increased abrasion damage. The higher mass loss observed with P500 sandpaper can be attributed to its coarser grit size. Coarser grits contain larger abrasive particles, which cause more fiber damage and material loss during the abrasion cycle. Conversely, finer grits (P1000 and P1200) have smaller abrasive particles, resulting in a gentler abrasion process with less fiber breakage and material loss. When comparing the differences in mass loss with the number of abrasion cycles, it is evident that the samples experience greater mass loss as the cycles increase. Cycles 50 and 75 show more mass loss than cycle 25, with cycle 75 showing the highest mass loss.

4. CONCLUSION

This study emphasizes the importance of understanding material behavior for advancing sustainability in industries such as aerospace, automotive, and protective clothing, where high-performance textiles are crucial. The results from tensile tests revealed that material orientation and environmental conditions significantly influence tensile strength. Specifically, dry conditions consistently yielded better results than wet conditions. For composite materials, Carbon/Epoxy exhibited superior strength and stiffness, with a tensile strength of 391.85 MPa in the warp direction, compared to Kevlar/Epoxy, which showed a tensile strength of 358.63 MPa in the same direction. Hybrid Kevlar-Carbon composites demonstrated a balanced performance, with a tensile strength of 372.04 MPa in the warp direction, combining the strengths of both Kevlar and Carbon fibers, making them suitable for applications requiring both strength and flexibility. Sweat simulation reflects realistic operational environments in applications such as military uniforms, firefighting suits, and aerospace seat structures, where body perspiration or saline air can degrade fabric integrity.

Furthermore, abrasion tests indicated that wet conditions led to increased mass loss for both fabric types. Under pure water conditions, Kevlar fabric showed a mass loss of 0.6014% at 25 abrasion cycles with P500 sandpaper, while Carbon fabric exhibited a higher mass loss of 0.7729% under the same conditions. In sweat simulation tests, the mass loss increased further, with Kevlar fabric showing a loss of 0.6518% and Carbon fabric 0.8834%. Kevlar consistently outperformed Carbon in terms of abrasion resistance, particularly in wet conditions, due to its superior strength and durability.

These findings highlight the importance of careful material selection and the consideration of environmental conditions in optimizing performance characteristics such as strength, stiffness, flexibility, and durability. Future research should focus on further exploring the impact of different environments, fabric structures, and textile treatments to enhance the sustainability and performance of materials across various applications, aiming to improve long-term material lifespan and reduce the environmental footprint of textile production and use. While triplicate samples were used to ensure consistency, further statistical analysis (e.g., ANOVA) will be applied in future studies to validate differences across environmental conditions. Future work should explore the use of hydrophobic coatings, fibre sizing agents, or nano-fillers to enhance moisture resistance and reduce the performance drop observed under wet conditions.

REFERENCES

- Rajesh S, Ramnath BV, Elanchezian C, Abhijith M, Rijju RD, Kishan KK. Investigation of tensile behavior of Kevlar composite. *Mater Today Proc.* 2018; 5: 1156-1161.
- Suthan R, Jayakumar V, Madhu S. Evaluation of mechanical properties of kevlar fibre epoxy composites: an experimental study. *Int. J. Veh. Struct. Syst.* 2018; 10: 389-394.
- Yeung KH and Rao K. Mechanical properties of Kevlar-49 fibre reinforced thermoplastic composites. *Polym Polym Compos.* 2012; 20: 411-424.
- Agarwal G, Johri N. Experimental investigations on mechanical properties and abrasive wear response of glass, kevlar and carbon fabric reinforced composites. *Mater Today Proc.* 2021; 46: 7966-7972.
- AL-Qrimli HF, F. A. Mahdi FA, Ismail FB. Carbon/epoxy woven composite experimental and numerical simulation to predict tensile performance. *Adv Mater Sci.* 2015; 4:33-41.
- Channabasavaraju S, Shivanand H, Santhosh K. Evaluation of tensile and flexural properties of polymer matrix composites. *Int J Mod Eng Res.* 2013; 3: 3177-3180.
- Prabhuram T, Somurajan V, Prabhakaran S. Hybrid composite materials in *Front Automot Mech Eng.* 2010; 27-31.
- Hashim N, Abdul Majid DL, Zahari R, Yidris N. Tensile properties of woven Carbon/Kevlar reinforced epoxy hybrid composite in *Mater Sci Forum*; 2017; 20-23.
- Al Khaddour S, Ibrahim MB. Experimental Investigation on Tensile Properties of Carbon Fabric-Glass Fabric-Kevlar Fabric-Epoxy Hybrid Composite Laminates. *J Compos Adv Mater*; 2021; 31.
- Priyanka P, Mali HS, Dixit A. Carbon-Kevlar intraply hybrid fabric polymer composites: mechanical performance. *Iran Polym J.* 2023; 32: 633-645.
- Hossain MM, Khan M, Khan R, Siddiquee MAB, Islam T. Carbon/Kevlar reinforced hybrid composite: impact of matrix variation, in *Proceedings of the Int Conf Mech Eng Renew Energy Chittagong. Bangladesh*; 2015.
- Karthik K, Rajamani D, Manimaran A, Udayaprakash J. Evaluation of tensile properties on Glass/Carbon/Kevlar fiber reinforced hybrid composites, *Mater Today Proc.* 2021; 39:1655-1660.
- Lakshmaiyana N, Surakasi R, Nadh VS, Srinivas C, Kaliappan S, Ganesan V et al. Tanning wastewater sterilization in the dark and sunlight using Psidium guajava leaf-derived copper oxide nanoparticles and their characteristics. *ACS Omega.* 2023; 8: 39680-39689.
- Velmurugan G, Chohan JS, Babu K, Paramasivam P, Maranan R. Biosynthesis of SiO₂ nanoparticles from bamboo leaves for tanning wastewater treatment and mechanical properties of HMPc-SiO₂ nanocomposite, *Clean Technol Environ Policy.* 2024; 1-20.
- Natrayan L, Janardhan G, Nadh VS, Srinivas C, Kaliappan S, Velmurugan G. Eco-friendly zinc oxide nanoparticles from Moringa oleifera leaf extract for photocatalytic and antibacterial applications. *Clean Technol Environ Policy.* 2024; 1-13.
- Velmurugan G, Chohan JS, Paramasivam P, Maranan R, Nagaraj M, Green marvel: Harnessing spinach leaves' power for enhanced photodegradation of various effluents with biogenic ZnO nanoparticles. *Desalin Water Treat.* 2024; 319: 100566.
- Velmurugan G, Chohan JS, Babu K, Nagaraj M, Velumani A. Exploring the efficacy of biosynthesized cupric oxide nanoparticles from Jasminum Sambac flower extract in wastewater treatment: experimental investigations and potential applications. *Desalin Water Treat.* 2024; 319: 100570.
- Velmurugan G, Chohan JS, Paramasivam P, Maranan R. Green synthesis of silver nanoparticles from southern Eucalyptus globulus: Potent antioxidants and photocatalysts for rhodamine B dye degradation. *Desalin Water Treat.* 2024; 320: 100687.
- Natrayan L, Jayakrishna M, Shanker K, Muthu G, Kaliappan S, Velmurugan G. Green synthesis of silver nanoparticles using lawsonia inermis for enhanced degradation of organic pollutants in wastewater treatment. *Glob NEST J.* 2024; 26:10.30955.
- Ganesan V, Shanmugam V, Alagumalai V, Kaliyamoorthy B, Das O, Misra M. Optimisation of mechanical behaviour of Calotropis gigantea and Prosopis juliflora natural fibre-based hybrid composites by using Taguchi-Grey relational analysis. *Compos C Open Access.* 2024; 13: 100433.
- Jahan I. Effect of fabric structure on the mechanical properties of woven fabrics. *Adv Res Text Eng.* 2017; 2:1018.
- ISO B. Textiles—tests for color fastness. Part E04: Colour fastness to perspiration; 2013 (BS EN ISO, 105-E04: 2013).
- International A. Standard test method for tensile properties of polymer matrix composite materials: ASTM Int; 2007.
- Kaynak HK, Topalbekiroğlu M. Influence of fabric pattern on the abrasion resistance property of woven fabrics. *Fibres Text East Eur.* 2008; 16: 54-56.
- Radmanovac N, Ćirković N, Šarac T. The importance of the resistance to wear in the choice of fabrics for protective garments. *Adv Technol*; 2017; 6:81-87.
- Özdil N, Kayseri GO, Mengüç GS. Analysis of abrasion characteristics in textiles. *Abrasion Resist Mater.* 2012; 2:119-146.
- ISO E. Textiles—Determination of the Abrasion Resistance of Fabrics by the Martindale Method—Part 2: Determination of Specimen Breakdown; 1998.
- Hossain MM, Datta E, Rahman S. A review on different factors of woven fabrics' strength prediction. *Sci Res.* 2016; 4: 88-97.
- Abdellah MY, Alharthi H. Stress Analysis and Strength Prediction of Carbon Fiber Composite Laminates with Multiple Holes Using Cohesive Zone Models. *Polym.* 2025;17(1):124.
- Mohamed AF, Abdellah MY, Hassan MK, Backar R. Advanced Prediction and Analysis of Delamination Failure in Graphite-Reinforced Epoxy Composites Using VCCT-Based Finite Element Modelling Techniques. *Polym.* 2025; 17(6): 771.
- Sadek MG, Abdellah MY, Abdel-Jaber GT. A review on properties, applications and feasibility study of date palm fiber-reinforced polymer composites. *SVU Int J Eng Sci Appl.* 2024; 5: 50-61.
- Mohammed Y, Hassan MK, Hashem A. Finite element computational approach of fracture toughness in composite compact tension specimen. *Int J Mech Mechatron Eng.* 2012; 12: 57-61.
- Gamal M, Abdellah MY, Alharthi H, Abdel-Jaber G, Ahmed H. Backar, Characteristic Properties of Date-Palm Fibre/Sheep Wool Reinforced Polyester Composites, *J Bioresour Bioprod.* 2023, 8(4): 430-443.
- Fahmy HS, Abdellah MY, Abdel-Jaber G, Hashem AM. Characteristic Properties of Glass Fiber Reinforced Sugarcane Bagasse Medium Density Fiber Board. *Cienc Tecnol Mater.* 2017; 29: 97-105.
- Gelany A, Abdellah MY, Mohamed AF, Khoshaim AB, Protection of limestone Coated with Different Polymeric Materials. *Am J Mech Eng.* 2017; 5.
- Abdellah MY, Hagag AAE, Marzok W, Hashem AF. Tensile and Fracture Properties of Chemically Treatment Date Palm Tree Fibre Reinforced Epoxy. *Int J Mech Mechatron Eng IJMME-IJENS.* 2019; 4: 40.
- Fouad H, Moura AHI, Alshammari BA, Hassan MK, Abdellah MY, Hashem M. Fracture toughness, vibration modal analysis and viscoelastic behavior of Kevlar, glass, and carbon fiber/epoxy composites for dental-post applications. *J Mech Behav Biomed Mater.* 2020; 101: 103456.

Mohamed K. Hassan:  <https://orcid.org/0000-0002-5353-3578>

Sufyan Azam:  <https://orcid.org/0000-0001-8084-0955>

Somia Alfatih M.S.:  <https://orcid.org/0009-0009-0032-2265>

Mohammed Y. Abdellah:  <https://orcid.org/0000-0003-2538-3207>



This work is licensed under the Creative Commons BY-NC-ND 4.0 license.

NATURAL FREQUENCIES OF FUNCTIONALLY GRADED SANDWICH PLATES RESTING ON AN ELASTIC FOUNDATION USING CHEBYSHEV FINITE ELEMENT METHOD

Hoang Lan TON-THAT^{*}

^{*}Department of Civil Engineering, HCM city University of Architecture, 196 Pasteur, District 3, Ho Chi Minh, Vietnam

lan.tonthathoang@uah.edu.vn

received 21 January 2025, revised 16 April 2025, accepted 02 May 2025

Abstract: In this study, the article uses a finite element method based on Chebyshev polynomials to calculate the natural frequencies of functionally graded sandwich (FGS) plates with hard-core (HC) or soft-core (SC) resting on an elastic foundation. Chebyshev polynomials are a series of orthogonal polynomials defined recursively, and the value of them belongs to the range $[-1, 1]$ as well as vanishes at Gauss points. More clearly, the novelty of this article is to use the high-order shape functions that satisfy the interpolation condition at the points based on Chebyshev polynomials to build the flat quadrilateral element for analysis of FGS plates. On the other hand, these plates are composed of two functionally graded skins and a hard or soft core. The elastic foundation with a two-parameter as a spring stiffness (α_1) and a shear layer stiffness (α_2) are used. Comparative examples are presented to validate the effectiveness of the current approach.

Key words: functionally graded sandwich plate, frequency, Chebyshev polynomial, finite element method, elastic foundation

1. INTRODUCTION

Nowadays, sandwich plates are common and important components of engineering structures consisting of two skins integrated with a core. These structures stand out for their outstanding bending stiffness, low mass density, efficient noise cancellation, and thermal insulation. They could be widely applied in many fields of engineering and defense technology. However, they also exhibit shortcomings, such as susceptibility to damage due to stress concentration or material discontinuities. Therefore, studying their mechanical behavior is necessary and has practical significance in engineering. Some typical deformation theories proposed and applied to analyze sandwich structures are the first-order shear deformation theory [1-3], the higher-order shear deformation theory [4-7], or the quasi-3D theory [8, 9], and many refined theories [10-17]. Furthermore, readers can find some results on sandwich structure analysis as well as composite structures in available documents [15-24]. For example, in the document [1], the authors presented analytical solutions for free vibration analysis of moderately thick rectangular plates, which were composed of functionally graded materials and supported by either Winkler or Pasternak elastic foundations. Based on the first-order shear deformation plate theory, the analysis procedure solved the exact equations of motion and captured the fundamental frequencies of the functionally graded rectangular plates resting on an elastic foundation. Theoretical formulation, Navier's solutions of rectangular plates, and finite element models based on the third-order shear deformation plate theory were presented in [2] for the analysis of through-thickness functionally graded plates. A refined trigonometric higher-order plate theory as in [3] was presented for bending analysis of simply supported functionally graded ceramic-metal sandwich plates. The effects of transverse shear strains as well as the

transverse normal strain were taken into account. The number of unknown functions was only four, as opposed to six or more in the case of other shear and normal deformation theories. A general third-order plate theory that accounts for geometric nonlinearity and two constituent material variations through the plate thickness (i.e., functionally graded plates) was presented using the dynamic version of the principle of virtual displacements. The formulation was based on power-law variation of the material through the thickness and the von Kármán nonlinear strains. The governing equations of motion derived herein for a general third-order theory with geometric nonlinearity and material gradation through the thickness were specialized to the existing classical and shear deformation plate theories in the literature. Analysis of functionally graded material plates was studied using higher-order shear deformation theory with some special modifications in conjunction with finite element models [4-7]. Furthermore, the vibrational or thermomechanical bending behaviors of functionally graded sandwich plates were also presented in the documents [8-10]. Quasi-3D plate theories considering shear and normal deformations were incorporated to estimate the final results. In the papers [11, 12], the bending and the free flexural vibration behavior of sandwich functionally graded material plates were investigated based on higher-order structural theory. This theory accounted for the realistic variation of the displacements through the thickness. A multi-layered shell formulation was developed in the paper [13] based on a layerwise deformation theory within the framework of isogeometric analysis. The high-order smoothness of non-uniform rational B-splines offered the opportunity to capture the structural deformation efficiently in a rotation-free manner. The derivation also followed a layerwise theory, which assumed a separate displacement field expansion within each layer and considered the transverse displacement component as C0-continuous at layer interfaces, thus resulting in a layerwise

continuous transverse strain state. In the paper [14], the authors derived a higher-order shear deformation theory for modeling functionally graded plates accounting for extensibility in the thickness direction. The explicit governing equations and boundary conditions were obtained using the principle of virtual displacements under Carrera's Unified Formulation. The static and eigenproblems were solved by collocation with radial basis functions.

In recent years, the study of structures embedded in foundations has drawn a lot of attention amongst researchers. To express the interaction between foundation and plate, various hypotheses of foundation models have been introduced [15]. The oldest and simplest hypothesis of elastic medium models, which has only one coefficient substrate reaction, is known as Winkler elastic foundation [16]. Despite its ease of implementation, the Winkler model is defective in providing continuity in the foundation due to separate springs [17]. This hypothesis was improved by the Pasternak model [18] via adding a shear layer over springs. The Pasternak model, including two-parameter substrate (spring and shear layer), is widely used to explain the mechanical interactions of soft plates with different distributions of material properties. In the Kerr foundation [19], nonconcentrated reactions do not occur due to an upper spring layer. It means that, in the Kerr model, a shear layer is surrounded by upper and lower spring layers. From there one can see more related documents. The thermodynamic behavior of functionally graded sandwich plates resting on Winkler/Pasternak/Kerr foundations with various boundary conditions was studied in [20] by using a refined 2D plate theory. The displacement field contained undetermined integral forms and involved only four unknowns to derive. The plate was considered to be subject to a time-harmonic sinusoidal temperature field across its thickness. Three types of foundations were studied. Each was described by a mathematical model. Different boundary conditions were used to study the thermodynamic behavior of sandwich plates on elastic foundations. These models gave an incredible concurrence with the accessible literature. The research [21] investigated the free vibration analysis of advanced composite plates, such as functionally graded plates resting on two-parameter elastic foundations, using a hybrid quasi-3D (trigonometric as well as polynomial) higher-order shear deformation theory. The theory, which did not require a shear correction factor, accounted for shear deformation and thickness stretching effects by a sinusoidal and parabolic variation of all displacements across the thickness. The governing equations of motion for the plates were derived from Hamilton's principle. The closed-form solutions were obtained by using the Navier technique, and natural frequencies were found for simply supported plates by solving the results of eigenvalue problems. The research [22] analyzed the natural frequencies of the imperfect functionally graded sandwich plate comprised of porous face sheets made of functionally graded materials and an isotropic homogeneous core resting on the elastic foundation. To accomplish this, the material characteristics were taken to be changed incessantly along the thickness direction based on the volume fraction of constituents expressed by the modified rule of the mixture, which included porosity volume fraction with three diverse kinds of porosity distribution models. Furthermore, to describe the two-parameter elastic foundation's response on the imperfect plates, the medium was supposed to be linear, homogenous, and isotropic, and it had been modeled using the Winkler-Pasternak model. Moreover, in the kinematic relationship of the imperfect plate resting on the Winkler-Pasternak foundation, third-order shear deformation theory was used, and the motion equations were set up employing Hamilton's principle. A buckling analysis of functionally graded plates of a complex form resting on

an elastic foundation and subjected to an in-plane nonuniform loading was performed by the R-functions method as in [23]. The mathematical formulation of the problem was presented within the framework of the classical laminate plate theory. The approach proposed and the software developed consider the heterogeneous subcritical state of the plates. To solve the problems, the Ritz method combined with the R-functions theory was used, etc.

Another aspect: the finite element method was first introduced in 1960 with the basic idea of dividing the entire problem domain into discrete components with simple geometry. Within each element, the representation of dependent variables is accomplished through shape functions. Structural analysis using the finite element method will be more accurate with higher-order shape functions. Nowadays, applying the finite element method to structural analysis has become popular and shows outstanding benefits compared to analytical methods, especially for structures with complex shapes and arbitrary boundary conditions. The study [24] focused on establishing the finite element model based on a new hyperbolic shear deformation theory to investigate the static bending, free vibration, and buckling of the functionally graded sandwich plates with porosity. The novel sandwich plate consisted of one homogeneous ceramic core and two different functionally graded face sheets, which could be widely applied in many fields of engineering and defense technology. The discrete governing equations of motion were carried out via Hamilton's principle and the finite element method. Besides, Chebyshev polynomials play a significant role in approximation theory. They constitute a sequence of orthogonal polynomials defined recursively. Their absolute value in the interval $[-1, 1]$ is bounded by 1. Based on this ideal, the authors [25, 26] proposed a finite element method associated with Chebyshev polynomials of the first kind for the analysis of plate/shell structures. In this approach, Gauss points were employed to formulate the shape functions grounded in Chebyshev polynomials. Consequently, the code was introduced to overcome shear locking and eliminate spurious zero energy modes.

There are different approaches to analyzing this type of structure, and in this article, the finite element method based on Chebyshev polynomials is first used to study the free vibration of FGS plates with HC or SC resting on an elastic foundation. The reliability of this method is verified through numerical examples related to the effects of geometrical parameters, materials, and foundation. Furthermore, increasing the degree of the Chebyshev polynomial will increase the total number of degrees of freedom of the structure, leading to increased computational costs. However, the survey in this paper shows that it is possible to control the degree of the polynomial sufficiently to obtain the required approximate results. Some other advantages of the proposed method, although not explicitly verified in this article, are that the obtained results are not affected by mesh distortion or, although the Chebyshev interpolation polynomial is established in the form of the Lagrange interpolation, Runge's phenomenon [27] does not occur; therefore, it can be used as an original finite element method for solving PDEs with high accuracy.

This article is organized as follows. The formulation is presented in Sect. 2. To highlight the reliability of the element, some numerical examples are thoroughly studied in Sect. 3. Finally, conclusions are drawn in Sect. 4.

2. FORMULATION

Considering rectangular FGS plates with HC or SC resting on an elastic foundation as shown in Fig. 1. A group of $h_1 - h_2 - h_3$

represents the ratio of thicknesses.

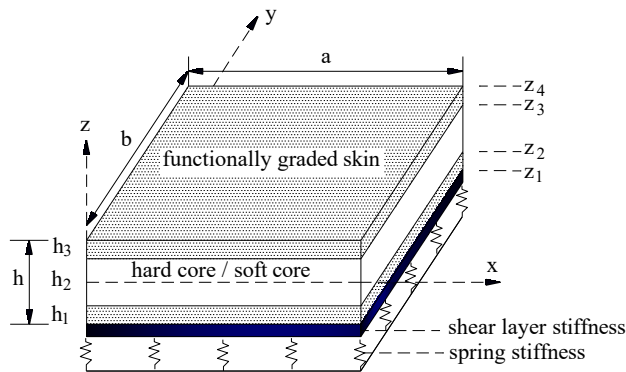


Fig. 1. The model of an FGS plate resting on an elastic foundation

The volume fraction $V_c^{(i)}$ of the ceramic phase of each layer is formulated by [3]

+ For FGS plate with HC (FGS-HC):

$$\begin{cases} V_c^{(1)} = \left(\frac{z-z_1}{z_2-z_1}\right)^n & z \in [z_1, z_2] \\ V_c^{(2)} = 1 & z \in [z_2, z_3] \\ V_c^{(3)} = \left(\frac{z-z_4}{z_3-z_4}\right)^n & z \in [z_3, z_4] \end{cases} \quad (1)$$

+ For FGS plate with SC (FGS-SC):

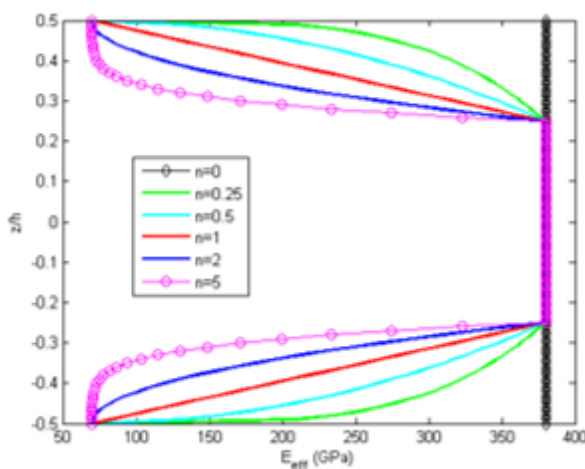
$$\begin{cases} V_c^{(1)} = 1 - \left(\frac{z-z_1}{z_2-z_1}\right)^n & z \in [z_1, z_2] \\ V_c^{(2)} = 0 & z \in [z_2, z_3] \\ V_c^{(3)} = 1 - \left(\frac{z-z_4}{z_3-z_4}\right)^n & z \in [z_3, z_4] \end{cases} \quad (2)$$

The effective material properties of FGS plates are determined by

$$M^{(i)}(z) = M_c V_c^{(i)} + M_m (1 - V_c^{(i)}), \quad i = 1, 2, 3 \quad (3)$$

Here $M^{(i)}(z)$ stands for the material characteristics of each layer.

a) FGS-HC



b) FGS-SC

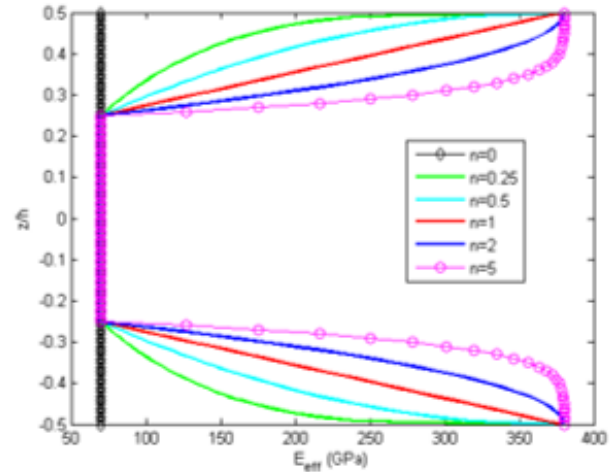


Fig. 2. The effective elastic modulus against the thickness of $(Al/Al_2O_3)_{FGS(1-2-1)}$ plates

The mechanical characteristics of the ceramic and metal are used in this article as Al_2O_3 ($E = 380$ GPa, $\rho = 3800$ kg/m³, $\nu = 0.3$); Al ($E = 70$ GPa, $\rho = 2707$ kg/m³, $\nu = 0.3$); and ZrO_2 ($E = 151$ GPa, $\rho = 3000$ kg/m³, $\nu = 0.3$). In addition, Fig. 2 plots the effective elastic modulus versus the thickness of $(Al/Al_2O_3)_{FGS(1-2-1)}$.

The elastic foundation is modeled with two parameters (α_1, α_2). The foundation reaction is given as a function of the deflection and its Laplacian. The reaction-deflection relation of this foundation is defined by

$$\mathcal{R} = \alpha_1 w - \alpha_2 \left(\frac{\partial^2 w}{\partial x^2} + \frac{\partial^2 w}{\partial y^2} \right) \quad (4)$$

The Chebyshev polynomials as in [25, 26] is given

$$C_p(x) = C_p(\cos \varphi) = \cos p\varphi, \quad x = \cos \varphi \in [-1, 1] \quad (5)$$

$$\cos(p+1)\varphi = 2 \cos \varphi \cos p\varphi - \cos(p-1)\varphi \quad (6)$$

or

$$C_{p+1}(x) = 2xC_p(x) - C_{p-1}(x), \quad p = 0, 1, 2, \dots \quad (7)$$

The Chebyshev polynomial $C_p(x)$ with $p \geq 2$ will equals 0 at the Gauss points x_i

$$x_i = -\cos[(2i-1)\pi/2p], \quad i = 1, 2, 3, \dots \quad (8)$$

The most important of ideas involves the approximation process of an unknown function $f(x)$ by Lagrangian interpolation polynomial $\mathfrak{N}(x)$ through these known points $(x_k, f(x_k))$ based on Chebyshev polynomials as described

$$f(x) \approx \mathfrak{N}(x) = \sum_{i=0}^{p-1} a_i C_i(x) \quad \text{and} \quad f(x_k) = \mathfrak{N}(x_k) \quad (9)$$

On the interval $[-1, 1]$, Chebyshev polynomials have the orthogonal property so the unknown coefficient a_i may be calculated by

$$a_i = \sum_{k=1}^p f(x_k) C_i(x_k) / \sum_{k=1}^p C_i^2(x_k) \quad (10)$$

Hence

$$\mathfrak{N}(x) = \sum_{k=1}^p \sum_{i=0}^{p-1} [(C_i(x_k) C_i(x)) / \sum_{j=1}^p C_i^2(x_j)] f(x_k) \quad (11)$$

with $x = \cos(\pi/2p) \xi$

$$\mathfrak{N}(\xi) = \sum_{k=1}^p N_k(\xi) f(x_k) \quad (12)$$

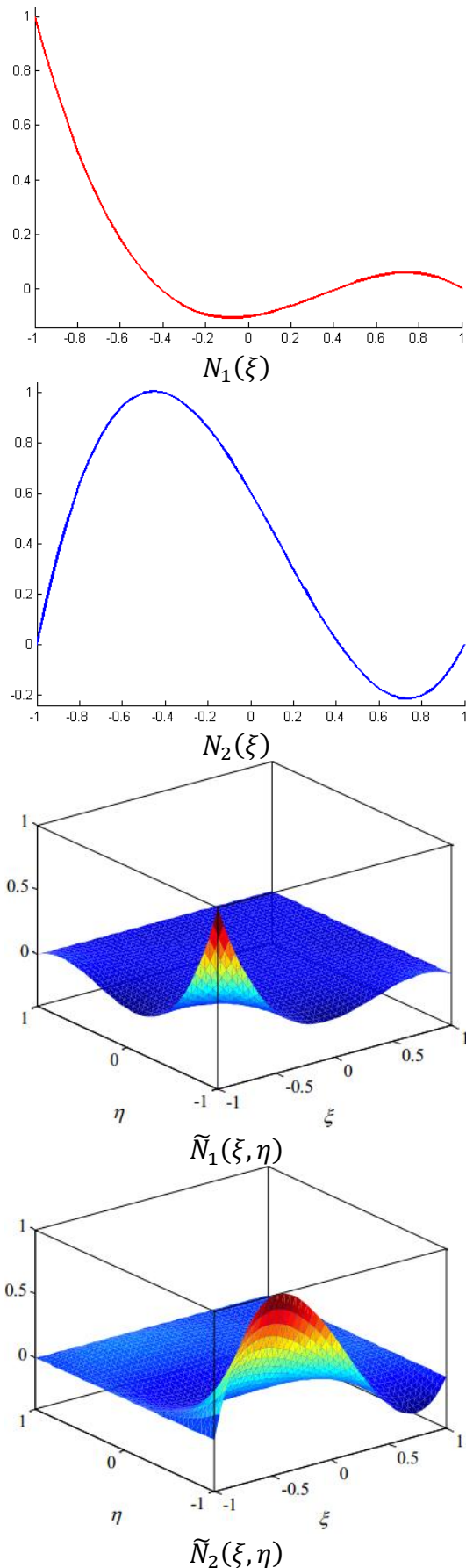


Fig. 3. The third-order shape functions in 1D & 2D

where $N_k(\xi)$ are called the 1D shape functions defined as

$$N_k(\xi) = \sum_{i=0}^{p-1} \left[\frac{C_i(\cos(\pi/2p) \xi_k) C_i(\cos(\pi/2p) \xi)}{\sum_{j=1}^p C_i^2(\cos(\pi/2p) \xi_j)} \right] \quad (13)$$

$$\xi_i = -\cos[(2i-1)\pi/2p] / \cos(\pi/2p) \quad i = 1, 2, \dots, p \quad (14)$$

In 2D problems, $(\xi, \eta) \in [-1, 1] \times [-1, 1]$, the shape functions associated with node $K(\xi_i, \eta_j)$

$$\tilde{N}_K(\xi, \eta) = N_i(\xi) N_j(\eta) \quad (15)$$

with $N_i(\xi)$ or $N_j(\eta)$ is 1D p -order shape functions related to the set $\xi \in [-1, 1]$ or the set $\eta \in [-1, 1]$ respectively. Fig. 3 gives some third-order shapes functions related to the Chebyshev polynomials in 1D space and 2D space.

The finite element formulation related to Chebyshev polynomials is established as in [25, 26]. The plate is divided by the quadrilateral elements with five degrees of freedom in each node of an element. These components can be approximated through the displacement components at node K

$$\begin{aligned} u &= \{u_o \quad v_o \quad w_o \quad \beta_x \quad \beta_y\}^T = \\ &= \sum_{K=1}^{(p+1)(q+1)} \tilde{N}_K(\xi, \eta) \{u_{oK} \quad v_{oK} \quad w_{oK} \quad \beta_{xK} \quad \beta_{yK}\}^T = \\ &= N_K d_K \end{aligned} \quad (16)$$

with

$$N_K = \tilde{N}_K \text{diag}(1, 1, 1, 1, 1),$$

$$d_K = \{u_{oK} \quad v_{oK} \quad w_{oK} \quad \beta_{xK} \quad \beta_{yK}\}^T$$

are nodal displacement vector associated node K . Based on the first-order shear deformation theory, the kinematics of the plate is calculated through five displacement components u_o , v_o , w_o , β_x and β_y in the mid-surface

$$\begin{aligned} u(x, y, z) &= u_o(x, y) + z\beta_x \\ v(x, y, z) &= v_o(x, y) + z\beta_y \\ w(x, y, z) &= w_o(x, y) \end{aligned} \quad (17)$$

with u_o , v_o , w_o are three displacement components, and β_x , β_y are the rotations related to the x - and y - axes. The in-plane strain vector and the transverse shear strain vector are shown

$$\begin{aligned} \varepsilon &= \begin{bmatrix} \varepsilon_{xx} \\ \varepsilon_{yy} \\ \gamma_{xy} \end{bmatrix} = \underbrace{\begin{bmatrix} u_{o,x} \\ v_{o,y} \\ u_{o,y} + v_{o,x} \end{bmatrix}}_{\varepsilon^m} + z \underbrace{\begin{bmatrix} \beta_{x,x} \\ \beta_{y,y} \\ \beta_{x,y} + \beta_{y,x} \end{bmatrix}}_{\varepsilon^b} \\ &= \varepsilon^m + z\varepsilon^b \end{aligned} \quad (18)$$

$$\varepsilon^s = \begin{bmatrix} \gamma_{xz} \\ \gamma_{yz} \end{bmatrix} = \begin{bmatrix} \beta_x + w_{o,x} \\ \beta_y + w_{o,y} \end{bmatrix} \quad (19)$$

The constitutive relation for functionally graded plate can be defined as below

$$\begin{Bmatrix} \sigma_{xx} \\ \sigma_{yy} \\ \tau_{xy} \\ \tau_{xz} \\ \tau_{yz} \end{Bmatrix} = \begin{bmatrix} Q_{11} & Q_{12} & 0 & 0 & 0 \\ Q_{21} & Q_{22} & 0 & 0 & 0 \\ 0 & 0 & Q_{66} & 0 & 0 \\ 0 & 0 & 0 & Q_{55} & 0 \\ 0 & 0 & 0 & 0 & Q_{44} \end{bmatrix} \begin{Bmatrix} \varepsilon_{xx} \\ \varepsilon_{yy} \\ \gamma_{xy} \\ \gamma_{xz} \\ \gamma_{yz} \end{Bmatrix} \quad (20)$$

with the material constants are given by

$$\begin{aligned} Q_{11} &= Q_{22} = E(z)/[1 - \nu^2(z)], \\ Q_{12} &= Q_{21} = \nu(z)E(z)/[1 - \nu^2(z)], \\ Q_{44} &= Q_{55} = Q_{66} = E(z)/2[1 + \nu(z)] \end{aligned} \quad (21)$$

By applying the Hamilton's principle, the weak-form for free vibration analysis can be presented by

$$\int_{\Omega} \delta \bar{\epsilon}^T D_b^* \bar{\epsilon} d\Omega + \int_{\Omega} \delta \bar{\gamma}^T D_s^* \bar{\gamma} d\Omega + \int_{\Omega} \Re w d\Omega = \int_{\Omega} \delta u^T m \ddot{u} d\Omega \quad (22)$$

where

$$\bar{\epsilon} = \{\epsilon^m, \epsilon^b\}^T, \quad \bar{\gamma} = \{\epsilon^s\}^T \quad (23)$$

and $m = \begin{bmatrix} I_1 & I_2 \\ I_2 & I_3 \end{bmatrix}$ with the mass inertia terms $I_i (i = 1, 2, 3)$ are given by

$$(I_1, I_2, I_3) = \int_{-h/2}^{h/2} \rho(z) (1, z, z^2) \begin{bmatrix} 1 & 0 & 0 \\ 0 & 1 & 0 \\ 0 & 0 & 1 \end{bmatrix} dz \quad (24)$$

Besides, D_b^* and D_s^* , the material matrices, are written by

$$D_b^* = \begin{bmatrix} A & B \\ B & D \end{bmatrix}, \quad D_s^* = A^s \quad (25)$$

with

$$\begin{aligned} (A, B, D) &= \int_{-h/2}^{h/2} (1, z, z^2) \begin{bmatrix} Q_{11} & Q_{12} & 0 \\ Q_{21} & Q_{22} & 0 \\ 0 & 0 & Q_{66} \end{bmatrix} dz, \\ A^s &= \frac{5}{6} \int_{-h/2}^{h/2} \begin{bmatrix} Q_{55} & 0 \\ 0 & Q_{44} \end{bmatrix} dz \end{aligned} \quad (26)$$

The discretized systems for free vibration analysis may be given as

$$(K - \omega^2 M)d = 0 \quad (27)$$

where K is the global stiffness matrix including the plate and elastic foundation, M is the global mass matrix, respectively. Furthermore, the Gauss quadrature rule is taken on the integration through a set of $(p+1)(q+1)$ Gauss points, in which p and q are the orders of $N_i(\xi)$ and $N_j(\eta)$. The total numbers of Gauss points and degrees of freedom per each element are $(p+1)(q+1)$ and $5(p+1)(q+1)$. The values of p and q are set to 3 for all numerical examples by following [16]. The BCs are given by

Clamped (C): $u_0 = v_0 = w_0 = \beta_x = \beta_y = 0$ at all edges.

Simply supported (S): $u_0 = w_0 = \beta_x = 0$ at $y = 0$ & $y = b$ and $v_0 = w_0 = \beta_y = 0$ at $x = 0$ & $x = a$.

In order to clarify how the proposed technique is incorporated into a finite element code, a numerical implementation is briefly presented as follows.

- Discretize the domain into quadrilateral elements and form the matrices of node coordinates (*coord*) and element connections (*nodes*).
- Declare the order p, q of the Chebyshev polynomials. The Gauss quadrature rule is taken on the integration through a set of $(p+1)(q+1)$ Gauss points.
- Calculate and assemble element matrices to build the system matrices.
- Assign boundary conditions.
- Solve the system of equations to obtain results.

3. NUMERICAL RESULTS AND DISCUSSIONS

The normalized parameters in this study are expressed by

$$\begin{aligned} k_1 &= \alpha_1 a^4 / D_m, \quad k_2 = \alpha_2 a^2 / D_m, \\ D_m &= E_m h^3 / 12 / (1 - \nu_m^2), \\ \bar{\omega} &= \left(\frac{\omega a^2}{h} \right) \sqrt{\frac{\rho_o}{E_o}}, \\ \rho_o &= 1 \text{ kg/m}^3, \quad E_o = 1 \text{ GPa} \end{aligned} \quad (28)$$

Firstly, the free vibration analysis of thin ($h = a/200$) and thick ($h = a/10$) square plates with two boundary conditions, SSSS and CCCC, is considered. The Young's modulus $E = 200$ GPa, Poisson ratio $\nu = 0.3$, and mass density $\rho = 8000$ kg/m³ are the material properties. The first four normalized frequencies of these structures $\omega^* = [12\omega\rho a^4(1 - \nu^2)/(Eh^2)]^{1/4}$ are presented in Table 1 and Fig. 4. These results are also compared with other results of MITC4 element [28] and exact solutions [29].

Tab. 1. The first four normalized frequencies of square plate ($h = a/10, a/200$)

Mode	a/h = 10, (SSSS)		
	[28]	Article	[29]
1	4.403	4.366	4.37
2	6.940	6.744	6.74
3	6.940	6.744	6.74
4	8.608	8.354	8.35
Mode	a/h = 10, (CCCC)		
	[28]	Article	[29]
1	5.808	5.703	5.71
2	8.226	7.876	7.88
3	8.226	7.876	7.88
4	9.731	9.325	9.33
Mode	a/h = 200, (SSSS)		
	[28]	Article	[29]
1	4.481	4.443	4.443
2	7.252	7.025	7.025
3	7.252	7.025	7.025
4	9.200	8.885	8.886
Mode	a/h = 200, (CCCC)		
	[28]	Article	[29]
1	6.124	5.998	5.999
2	9.060	8.567	8.568
3	9.060	8.567	8.568
4	11.019	10.403	10.407

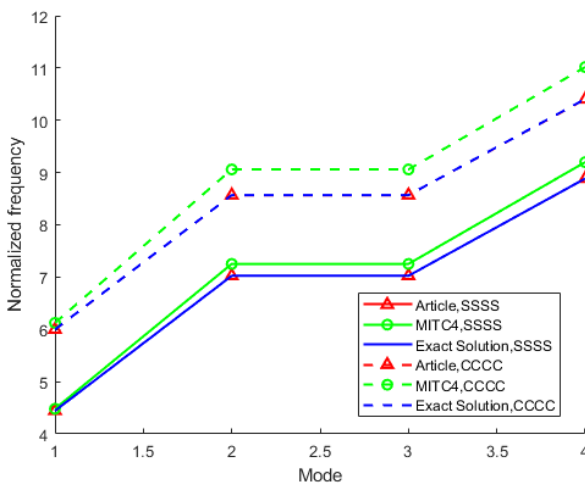
Tab. 2. The first frequency of FGM plates resting on the elastic foundation with $n = 1$ and $h = a/20$

(k_1, k_2)	Method	$p=q$	Meshing		
			4 x 4	6 x 6	8 x 8
(100,100)	Article	1	0.0662	0.0510	0.0474
		2	0.0398	0.0397	0.0396
		3	0.0396	0.0396	0.0396
		4	0.0396	0.0396	0.0396
	[30]		0.0388		
	[31]		0.0386		

Tab. 3. The dimensionless frequencies of the FGS-HC plate resting on the elastic foundation.

a/h	n	(k_1, k_2)	(2-1-2)		(1-1-1)		(2-2-1)	
			Article	[32]	Article	[32]	Article	[32]
10	0	(0,0)	1.29918	1.29692	1.29918	1.29692	1.29918	1.29692
		(10,10)	1.61828	1.61603	1.61828	1.61603	1.61828	1.61603
		(100,100)	3.32217	3.31161	3.32217	3.31161	3.32217	3.31161
	10	(0,0)	0.93921	0.93742	0.95419	0.95372	0.98414	0.98239
		(10,10)	1.37299	1.37067	1.38093	1.37733	1.40154	1.39522
		(100,100)	3.30716	3.29462	3.30545	3.2805	3.30531	3.28023
100	0	(0,0)	1.34067	1.34038	1.34067	1.34038	1.34067	1.34038
		(10,10)	1.65962	1.65899	1.65962	1.65899	1.65962	1.65899
		(100,100)	3.36947	3.36942	3.36947	3.36942	3.36947	3.36942
	10	(0,0)	0.96026	0.96023	0.97591	0.97582	1.00790	1.00620
		(10,10)	1.39691	1.39670	1.40294	1.40285	1.42311	1.42192
		(100,100)	3.34844	3.34801	3.33422	3.33315	3.33346	3.33266

a) Thin plate



b) Thick plate

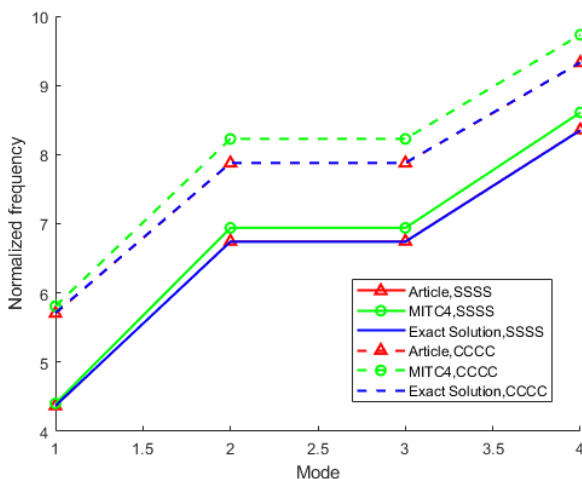


Fig. 4. The comparison of the first four normalized frequencies of square plate

Secondly, consider the SSSS square (Al/Al_2O_3) FGM plate resting on an elastic foundation. The dimensionless frequency is normalized by

$$\omega^{**} = (\omega h) \sqrt{\rho_b / E_b}.$$

Observing that the obtained results converge at a mesh size of 4×4 with the order of shape functions $p = q = 3$ and are in good agreement with those of solutions using quasi-3D theory [30] and third-order shear deformation theory [31], as given in Table 2. An error of about 2% compared to the results from quasi-3D theory is acceptable when using only coarse meshes.

Next, the SSSS square (Al/ZrO_2) FGS-HC plate is considered. The first normalized frequencies $\bar{\omega}$ are provided in Table 3. It can be observed that the obtained results are completely consistent with the results of [32], employing a closed-form solution based on the hyperbolic shear deformation theory. Moreover, it is clear from the table that the natural frequencies are increasing with the existence of the elastic foundation. Clearly, the natural frequencies are increasing with the increasing values of two parameters: spring stiffness and shear layer stiffness. Table 3 also shows that, as the volume ratio of ceramic in the sandwich plate increases, the natural frequencies of the plate increase.

Continuously, the dimensionless frequencies of the square (Al/ZrO_2) FGS plates with different values of the power-law index, ratio of thicknesses, and BCs are listed in Table 4 and Table 5. From these tables, it can be seen that when the power-law index n increases, the frequencies of the FGS-HC plates decrease while the frequencies of the FGS-SC increase. The reason is that as n increases, the volume fraction of ceramic decreases for the FGS-HC plate, leading to a decrease in the FGS-HC plate stiffness; so the frequency of the FGS plate decreases. The frequency of FGS-HC plates with $n = 0$ is highest, because when $n = 0$, FGS-HC plates become homogeneous ceramic plates. On the other hand, when n increases, the frequencies of the FGS-SC plates increase, because when n increases, the volume fraction of the ceramic components increases, and the FGS plate stiffness increases. Besides, when $n = 0$, the FGS-SC plates become homogeneous metal plates, so the frequency of FGS plates is the smallest. In addition, the thicker ceramic core results in a stiffer FGS-HC plate, causing the frequency of the FGS plate to increase. This is in contrast to the FGS-SC plate, when the thicker metal core leads to a softer FGS-SC plate, so the frequency of the FGS plates reduces.

Tab. 4. The dimensionless frequencies of square FGS plates with $a/h = 15$, $k_1 = 10$, $k_2 = 10$

BCs	Plate	n	Ratio of thicknesses			
			(1-0-1)	(1-1-1)	(1-2-2)	(1-6-1)
SSSS	FGS-HC	0	1.9543	1.9543	1.9543	1.9543
		0.5	1.5924	1.6596	1.6907	1.8175
		1	1.4114	1.5053	1.5556	1.7477
		2	1.2580	1.3579	1.4278	1.6794
		5	1.1721	1.2350	1.3213	1.6209
		10	1.1662	1.1949	1.2819	1.6067
	FGS-SC	0	1.1769	1.1769	1.1769	1.1769
		0.5	1.7605	1.6906	1.6537	1.4641
		1	1.8992	1.8417	1.7978	1.5740
		2	1.9714	1.9446	1.8989	1.6657
		5	1.9852	2.0037	1.9611	1.7343
		10	1.9733	2.0155	1.9776	1.7504
SSCC	FGS-HC	0	2.5957	2.5957	2.5957	2.5957
		0.5	2.0944	2.1903	2.2334	2.4092
		1	1.8388	1.9751	2.0455	2.3131
		2	1.6161	1.7658	1.8655	2.2194
		5	1.4846	1.5889	1.7125	2.1385
		10	1.4699	1.5283	1.6548	2.1181
	FGS-SC	0	1.4774	1.4774	1.4774	1.4774
		0.5	2.3060	2.2035	2.1516	1.8838
		1	2.5018	2.4142	2.3537	2.0374
		2	2.6067	2.5587	2.4952	2.1638
		5	2.6317	2.6435	2.5834	2.2584
		10	2.6188	2.6624	2.6087	2.2805
SCSC	FGS-HC	0	2.7507	2.7507	2.7507	2.7507
		0.5	2.2165	2.3197	2.3655	2.5530
		1	1.9420	2.0896	2.1641	2.4509
		2	1.7015	1.8651	1.9717	2.3510
		5	1.5573	1.6737	1.8071	2.2649
		10	1.5398	1.6082	1.7447	2.2430
	FGS-SC	0	1.5457	1.5457	1.5457	1.5457
		0.5	2.4340	2.3225	2.2671	1.9804
		1	2.6444	2.5476	2.4825	2.1437
		2	2.7581	2.7025	2.6345	2.2782
		5	2.7871	2.7944	2.7302	2.3788
		10	2.7747	2.8154	2.7575	2.4024
CCCC	FGS-HC	0	3.3663	3.3663	3.3663	3.3663
		0.5	2.7033	2.8327	2.8898	3.1229
		1	2.3590	2.5461	2.6399	2.9967
		2	2.0540	2.2641	2.3985	2.8727
		5	1.8669	2.0222	2.1906	2.7658
		10	1.8407	1.9381	2.1113	2.7389
	FGS-SC	0	1.8436	1.8436	1.8436	1.8436
		0.5	2.9587	2.8163	2.7473	2.3877
		1	3.2223	3.0967	3.0158	2.5904
		2	3.3669	3.2904	3.2055	2.7581
		5	3.4070	3.4069	3.3268	2.8827
		10	3.3937	3.4346	3.3620	2.9119

Tab. 5. The first four frequencies of square FGS plates (1-4-1) with $a/h = 45$, $k_1 = 50$, $k_2 = 15$

BCs	Plate	n	Normalized frequencies			
			$\bar{\omega}_1$	$\bar{\omega}_2$	$\bar{\omega}_3$	$\bar{\omega}_4$
SSSS	FGS-HC	0	2.0351	4.8527	4.8527	7.6586
		0.5	1.8611	4.3877	4.3877	6.9055
		1	1.7707	4.1436	4.1436	6.5090
		2	1.6811	3.8982	3.8982	6.1097
		5	1.5964	3.6633	3.6633	5.7257
		10	1.5643	3.5740	3.5740	5.5797
	FGS-SC	0	1.3185	2.7594	2.7594	4.1886
		0.5	1.6503	3.7252	3.7252	5.7897
		1	1.7741	4.0725	4.0725	6.3581
		2	1.8764	4.3540	4.3540	6.8179
		5	1.9566	4.5755	4.5755	7.1788
		10	1.9831	4.6487	4.6487	7.2979
SSCC	FGS-HC	0	2.7052	5.9047	5.9266	8.9704
		0.5	2.4566	5.3292	5.3484	8.0838
		1	2.3269	5.0266	5.0448	7.6161
		2	2.1970	4.7216	4.7382	7.1440
		5	2.0732	4.4288	4.4437	6.6894
		10	2.0261	4.3177	4.3323	6.5166
	FGS-SC	0	1.6225	3.2659	3.2746	4.8327
		0.5	2.1214	4.4804	4.4956	6.7338
		1	2.3039	4.9129	4.9301	7.4055
		2	2.4527	5.2635	5.2827	7.9484
		5	2.5692	5.5387	5.5590	8.3744
		10	2.6083	5.6297	5.6504	8.5155
SCSC	FGS-HC	0	2.8756	5.3557	6.7353	9.1380
		0.5	2.6076	4.8374	6.0736	8.2344
		1	2.4671	4.5654	5.7249	7.7575
		2	2.3264	4.2913	5.3733	7.2769
		5	2.1921	4.0284	5.0346	6.8132
		10	2.1416	3.9287	4.9057	6.6368
	FGS-SC	0	1.6935	2.9985	3.6657	4.9129
		0.5	2.2376	4.0841	5.0755	6.8517
		1	2.4353	4.4723	5.5750	7.5362
		2	2.5967	4.7870	5.9794	8.0896
		5	2.7231	5.0344	6.2970	8.5240
		10	2.7652	5.1161	6.4020	8.6677
CCCC	FGS-HC	0	3.5315	7.1179	7.1179	10.4331
		0.5	3.1928	6.4172	6.4172	9.3997
		1	3.0152	6.0476	6.0476	8.8533
		2	2.8367	5.6747	5.6747	8.3016
		5	2.6652	5.3157	5.3157	7.7691
		10	2.6004	5.1788	5.1788	7.5661
	FGS-SC	0	2.0033	3.8544	3.8544	5.5549
		0.5	2.7066	5.3520	5.3520	7.7846
		1	2.9595	5.8820	5.8820	8.5694
		2	3.1644	6.3109	6.3109	9.2038
		5	3.3258	6.6474	6.6474	9.7021
		10	3.3789	6.7588	6.7588	9.8669

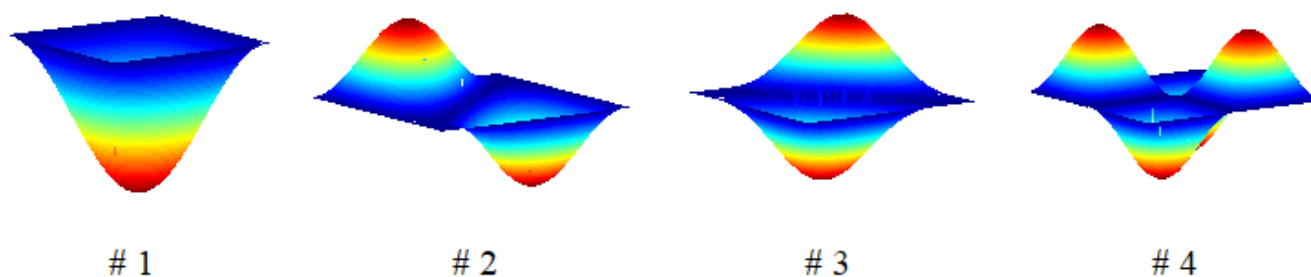


Fig. 5. The first four mode shapes of (SSSS) FGS-HC plate with $a/b = 1$, $a/h = 20$, $k_1 = 10$, $k_2 = 5$, $n = 1$, ratio of thicknesses (1-1-1)

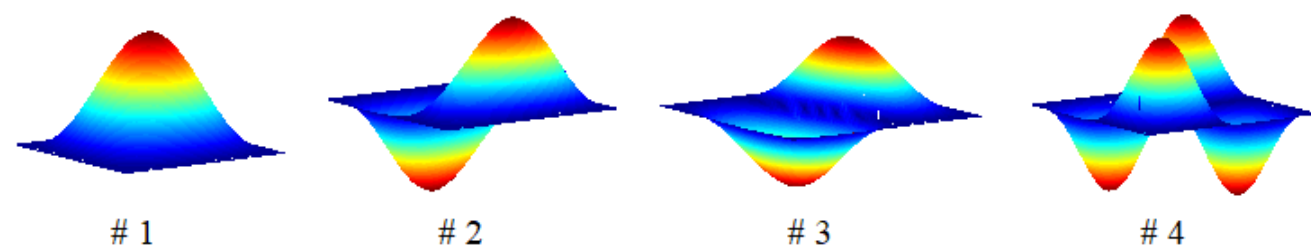


Fig. 6. The first four mode shapes of (CCCC) FGS-SC plate with $a/b = 1$, $a/h = 25$, $k_1 = 15$, $k_2 = 10$, $n = 2$, ratio of thicknesses (1-2-1)

Figs. 5 and 6 present the first four modeshapes of FGS plates. Observing that the 2nd and 3rd eigenmodes are the same as each other, owing to the FGS plates under the same “S” or “C” boundary conditions at the edges.

4. CONCLUSIONS

The article aims to conduct the frequency analysis of FGS plates resting on an elastic foundation by using a finite element method based on Chebyshev polynomials. The idea of this element is to use the high-order shape functions that satisfy the interpolation condition at the points based on Chebyshev polynomials as well as to use the full Gauss quadrature rule for the establishment of the stiffness matrix and mass matrix. Numerical examples and comments are made to illustrate in detail the influence of geometric parameters and material properties on the free vibrations of the FGS plates. According to the numerical outcomes, some important observations are summarized as follows: i. The effectiveness of using the finite element method based on Chebyshev polynomials in the analysis of free vibrations of FGS plates on the elastic foundation. ii. Elastic foundation increases the frequency of FGS plates, as expected. More specifically, the natural frequencies are increasing with the existence of an elastic foundation. The natural frequencies are increasing with the increasing values of two parameters: spring stiffness and shear layer stiffness. iii. While increasing the value of the power-law index leads to the decreasing value of the natural frequency for hardcore sandwich plates, the natural frequency increases with increasing value of the power-law index for softcore sandwich plates. In conclusion, it is evident that the elastic foundation has a significant effect on the mechanical behavior of sandwich plates.

The obtained results can be useful for extended calculation, design, and fabrication of FGS plates working under various conditions. In the near future, the proposed method will continue to demonstrate the stability of the results when meshing distortion. In addition, although the Chebyshev interpolation polynomial is established in the form of Lagrange interpolation, the Runge phenomenon does not occur, so it can be used as an original finite element

method to solve PDEs with high accuracy. Besides, the task of non-linear analysis of plate/shell structures will be developed. Last but not least, the computational cost for complex structures will also be considered to help readers have a specific view of the advantages and disadvantages of this proposed method.

REFERENCES

1. Hosseini HS, Taher HRD, Akhavan H, Omid M. Free vibration of functionally graded rectangular plates using first-order shear deformation plate theory. *Appl. Math. Model.* 2010;34(5):1276-91. Available from: <https://doi.org/10.1016/j.apm.2009.08.008>
2. Reddy JN. Analysis of functionally graded plates. *Int. J. Numer. Methods Eng.* 2000;47:663-84.
3. Zenkour AM. Bending analysis of functionally graded sandwich plates using a simple four unknown shear and normal deformations theory. *J. Sandw. Struct. Mater.* 2013;15:629-56. Available from: <https://doi.org/10.1177/1099636213498886>
4. Reddy JN. A general nonlinear third-order theory of functionally graded plates. *Int. J. Aerosp. Lightweight Struct.* 2011;1:1-21. Available from: <https://doi.org/10.3850/S201042861100002X>
5. Talha M, Singh BN. Static response and free vibration analysis of FGM plates using higher order shear deformation theory. *Appl. Math. Model.* 2010;34:3991-4011. Available from: <https://doi.org/10.1016/j.apm.2010.03.034>
6. Zenkour AM. Generalized shear deformation theory for bending analysis of functionally graded materials. *Appl. Math. Model.* 2006;30(1):67-84. Available from: <https://doi.org/10.1016/j.apm.2005.03.009>
7. Yaghoobi H, Fereidoon A. Mechanical and thermal buckling analysis of functionally graded plates resting on elastic foundations: An assessment of a simple refined nth-order shear deformation theory. *Compos. B: Eng.* 2014;62:54-64. Available from: <https://doi.org/10.1016/j.compositesb.2014.02.014>
8. Sobhy M, Al-Mukahal FH. Magnetic control of vibrational behavior of smart FG sandwich plates with honeycomb core via a quasi 3D plate theory. *Adv. Eng. Mater.* 2023;25(13):2300096. Available from: <https://doi.org/10.1002/adem.202300096>
9. Zarga D, Tounsi A, Bousahla AA, Bourada F, Mahmoud SR. Thermo-mechanical bending study for functionally graded sandwich plates using a simple quasi-3D shear deformation theory. *Steel Compos. Struct.*

- 2019;32(3):389-410.
Available from: <https://doi.org/10.12989/scs.2019.32.3.389>
10. Alibeigloo A, Alizadeh M. Static and free vibration analyses of functionally graded sandwich plates using state space differential quadrature method. *Eur. J. Mech. A/Solids*. 2015;54:252-66. Available from: <https://doi.org/10.1016/j.euromechsol.2015.06.011>
 11. Natarajan S, Manickam G. Bending and vibration of functionally graded material sandwich plates using an accurate theory. *Finite Elem. Anal. Des.* 2012;57:32-42.
Available from: <https://doi.org/10.1016/j.finel.2012.03.006>
 12. Li Q, Lu VP, Kou KP. Three-dimensional vibration analysis of functionally graded material sandwich plates. *J. Sound Vib.* 2008;311:498-515.
Available from: <https://doi.org/10.1016/j.jsv.2007.09.018>
 13. Liu N, Jeffers AE. Isogeometric analysis of laminated composite and functionally graded sandwich plates based on a layerwise displacement theory. *Compos. Struct.* 2017;176(15):143-53. Available from: <https://doi.org/10.1016/j.compstruct.2017.05.037>
 14. Neves A, Ferreira A, Carrera E, Cinefra M, Roque C, Jorge R, Soares CM. Static, free vibration and buckling analysis of isotropic and sandwich functionally graded plates using a quasi-3D higher-order shear deformation theory and a meshless technique. *Compos. B: Eng.* 2013;44:657-74.
Available from: <https://doi.org/10.1016/j.compositesb.2012.01.089>
 15. Wang Y, Tham L, Cheung Y. Beams and plates on elastic foundations: a review. *Prog Struct Eng Mat.* 2005;7:174-82. Available from: <https://doi.org/10.1002/pse.202>
 16. Winkler E. Die Lehre von der Elastizität und Festigkeit (The Theory of Elasticity and Stiffness), H. Dominicus, Prague, Czechoslovakia. 1867.
 17. Kolahchi R, Safari M, Esmailpour M. Dynamic stability analysis of temperature-dependent functionally graded CNT-reinforced visco-plates resting on orthotropic elastomeric medium, *Compos. Struct.* 2016;150:255-65.
Available from: <https://doi.org/10.1016/j.compstruct.2016.05.023>
 18. Pasternak P. On a New Method of Analysis of an Elastic Foundation by Means of Two Foundation Constants, Gosudarstvennoe Izdatel'stvo Literaturi po Stroitel'stvu i Arkhitekture, Moscow. 1954.
 19. Kneifati MC. Analysis of plates on a Kerr foundation model. *J. Eng. Mech.* 1985;111:1325-42.
 20. Mohamed M, Samir B, Abdelkader M, Abdelouahed T, Abdelmoumen AB, Mahmoud SR. Thermodynamic behavior of functionally graded sandwich plates resting on different elastic foundation and with various boundary conditions. *J. Sandw. Struct. Mater.* 2021;23(3):1028-57.
Available from: <https://doi.org/10.1177/1099636219851281>
 21. Guerroudj HZ, Yeghnem R, Kaci A, Zaoui FZ, Benyoucef S. Eigenfrequencies of advanced composite plates using an efficient hybrid quasi-3D shear deformation theory. *Smart Struct. Syst.* 2018;22(1):121-32.
Available from: <https://doi.org/10.12989/sss.2018.22.1.121>
 22. Lazreg H, Mehmet A, Nafissa Z. Natural frequency analysis of imperfect FG sandwich plates resting on Winkler-Pasternak foundation. *Mater. Today: Proc.* 2022;53(1):153-60.
Available from: <https://doi.org/10.1016/j.matpr.2021.12.485>
 23. Kurpa L, Shmatko T, Linnik A. Buckling Analysis of Functionally Graded Sandwich Plates Resting on an Elastic Foundation and Subjected to a Nonuniform Loading. *Mech. Compos. Mater.* 2023;59:645-58. Available from: <https://doi.org/10.1007/s11029-023-10122-w>
 24. Pham VV, Le QH. Finite element analysis of functionally graded sandwich plates with porosity via a new hyperbolic shear deformation theory. *Def. Technol.* 2022;18(3):490-508.
Available from: <https://doi.org/10.1016/j.dt.2021.03.006>
 25. Dang TH, Yang DJ, Liu Y. Improvements in shear locking and spurious zero energy modes using Chebyshev finite element method. *J. Comput. Inf. Sci. Eng.* 2019;19:011006.
Available from: <https://doi.org/10.1115/1.4041829>
 26. Ton-That HL, Nguyen-Van H, Chau-Dinh T. A novel quadrilateral element for analysis of functionally graded porous plates/shells reinforced by graphene platelets. *Arch. Appl. Mech.* 2021;91:2435-66. Available from: <https://doi.org/10.1007/s00419-021-01893-6>
 27. Fornberg B, Zuev J. The Runge Phenomenon and Spatially Variable Shape Parameters in RBF Interpolation. *Comput. Math. Appl.* 2007;54(3):379-98.
Available from: <https://doi.org/10.1016/j.camwa.2007.01.028>
 28. Lee SJ. Free Vibration Analysis of Plates by Using a Four-Node Finite Element Formulated With Assumed Natural Transverse Shear Strain. *J. Sound Vib.* 2004;278(3):657-84.
Available from: <https://doi.org/10.1016/j.jsv.2003.10.018>
 29. Abassian F, Haswell DJ, Knowles NC. Free Vibration Benchmarks. National Agency for Finite Element Methods and Standards, Glasgow, UK. 1987.
 30. Shahsavari D, Shahsavari M, Li L, Karami B. A novel quasi-3D hyperbolic theory for free vibration of FG plates with porosities resting on Winkler/Pasternak/Kerr foundation. *Aerosp. Sci. Technol.* 2018;72:134-49.
Available from: <https://doi.org/10.1016/j.ast.2017.11.004>
 31. Baferani AH, Saidi A, Ehteshami H. Accurate solution for free vibration analysis of functionally graded thick rectangular plates resting on elastic foundation. *Compos. Struct.* 2011;93(7):1842-53.
Available from: <https://doi.org/10.1016/j.compstruct.2011.01.020>
 32. Akavci S. Mechanical behaviour of functionally graded sandwich plates on elastic foundation. *Compos. B: Eng.* 2016;96:136-52.
Available from: <https://doi.org/10.1016/j.compositesb.2016.04.035>

Hoang Lan TON-THAT:  <https://orcid.org/0000-0002-3544-917X>



This work is licensed under the Creative Commons BY-NC-ND 4.0 license.

ANALYSIS OF CONVECTIVE INSTABILITY IN DUSTY FERROMAGNETIC FLUIDS WITH MAGNETIC FIELD-DEPENDENT VISCOSITY UNDER FLUID-PERMEABLE MAGNETIC BOUNDARIES

Awneesh KUMAR^{*}, Pankaj KUMAR^{*}, Abhishek THAKUR^{*}, Mandeep KAUR^{*}

^{*}Srinivasa Ramanujan Department of Mathematics, Central University of Himachal Pradesh, Kangra, Himachal Pradesh, India, 176206

ranaawneesh@gmail.com, pankajthakur28.85@hpcu.ac.in, abhishekthakur665@gmail.com, mandeepinspire2013@gmail.com

received 28 December 2024, revised 16 April 2025, accepted 03 May 2025

Abstract: The subject under consideration finds manifold applications across various disciplines, including biological, industrial, and environmental sectors. Therefore, this study aims to analytically investigate the onset of convective instability in a dusty ferromagnetic fluid layer, influenced by magnetic field-dependent viscosity and fluid-permeable magnetically active boundaries, when subjected to a uniform transverse magnetic field. The eigenvalue problem is formulated through the utilization of linear stability theory followed by normal mode analysis. To address this problem, a single-term Galerkin method is employed, followed by a numerical calculation of the critical magnetic Rayleigh number. It is investigated numerically and graphically that $(N_c)_{Free} \leq (N_c)_{Permeable} \leq (N_c)_{Rigid}$. It has been observed that as the dust particle parameter h_1 increase, the critical Rayleigh number decreases, indicating the destabilizing nature of h_1 . On the other hand, the viscosity parameter δ and magnetic susceptibility χ and permeability parameter Da_s demonstrate a stabilizing effect on the system. Initially, measure of nonlinearity of magnetization M_3 exhibits a destabilizing effect, but beyond a certain threshold, it switches to a stabilizing effect within the system.

Key words: magnetic field-dependent viscosity, dust particles, ferrofluid, thermal convection, fluid-permeable magnetic boundaries

1. INTRODUCTION

Ferrofluids are unique types of fluids that exhibit both fluidic and magnetic properties. They are composed of stable colloidal suspensions of single-domain ferromagnetic or ferrimagnetic nanoparticles dispersed in a suitable liquid medium. The magnetic particles typically consist of ferromagnetic metals such as iron, nickel, and cobalt, or ferrimagnetic oxides like magnetite (Fe_3O_4) and spinel-type ferrites. Common carrier liquids include water, ethylene glycol, and various oils. The specific combination of magnetic particles and carrier fluid is chosen based on the intended application of the ferrofluid. Ferrofluids are widely used in sealing, damping, heat transfer, bearings, and sensors. They act as coolants in systems like loudspeakers and transformers, and enhance heat transfer in devices such as heat exchangers. Their use in exclusion seals helps protect sensitive components, making them valuable in robotics, textiles, electronics, and machinery [1, 2].

Due to their vast practical applications, researchers have conducted numerous experimental and theoretical studies on ferrofluids. These studies cover areas such as synthesis and characterization, heat transfer and thermal properties, theoretical modelling and simulation, and industrial applications [3, 4, 5]. Discussing the thermal stability of ferrofluids is equally important as examining their other properties. Understanding thermal stability ensures that ferrofluids can be effectively and safely utilized in current and future technologies.

Thermal stability of ferrofluid in the existence of a vertical magnetic field has been investigated by Finlayson [6]. Schwab et al. examined experimentally the Finlayson's problem [7]. Thermal

stability of ferrofluid depends upon many factors such as density of ferrofluid, gravity acting on ferrofluid, medium of ferrofluid, Coriolis force on ferrofluid and hydrodynamic boundary conditions of ferrofluid. The influence of viscosity variation with magnetic field on thermal convection of ferrofluid has been explored by Sunil et al. [8]. whereas the viscosity variation with temperature field on thermal convection of ferrofluid for general boundary conditions has been investigated by Dhiman and Sharma [9, 10]. The porous medium plays a crucial role in directing geophysically detectable liquids into specific zones for imaging, controlled placement, or chemical treatment. Hence, analyzing the thermal stability of ferrofluids within a saturated porous layer is equally important. Vaidyanathan et al. [11] explored thermoconvective instability in a ferromagnetic fluid saturating a porous medium under the influence of a vertical magnetic field. Since rotation can significantly affect the thermal stability of a fluid layer, Venkatasubramanian and Kaloni [12] examined the impact of rotation on thermo-convective instability in a ferrofluid layer. Many authors have made remarkable contributions to exploring the impact of various parameters on ferrofluid convection (see references [13, 14, 15, 16, 17]).

There are many practical situations where ferrofluids may contain suspended particles. For instance, in industrial settings, ferrofluids are sometimes used as lubricants for machinery, particularly in high-precision equipment like bearings, seals, and pumps. However, in such environments, it is common for the ferrofluid to become contaminated with suspended particles. Therefore, studying ferrofluids with dust particles is equally important. Thermal stability of ferrofluid in the existence of dust particles is studied by Sunil et al. [18]. Sunil et al. [19] explored the impact of viscosity variation

with magnetic field on the thermal convection of dusty ferrofluids for the case of free-free boundaries. Sunil et al. [20] conducted a theoretical study on how magnetic field-dependent (MFD) viscosity influences thermal convection in a ferromagnetic fluid saturated porous medium containing dust particles. Sharma and Kumar [21] carried out a theoretical analysis of the combined influence of MFD viscosity and rotation on ferroconvection in a dusty fluid exposed to a uniform transverse magnetic field, whereas Kumar et al. [22] explored the impact of viscosity variation with temperature on the thermal convection of dusty ferrofluids of permeable boundaries. For a detailed understanding of thermal convection in dusty ferrofluids under various effects, one may refer to references [23, 24, 25, 26]. For further insights into related studies involving fluid systems containing dust particles and their significant effects, readers are referred to references [27, 28, 29, 30, 31].

The thermal stability of the liquid is determined by the thermal and hydrodynamic conditions at the surfaces that border it. In past works, fluid boundaries have been mainly either free-free or rigid-rigid. However, in many cases boundaries are neither purely free-free nor purely rigid-rigid. For instance, porous structures are used in cooling systems of electronic devices so as to facilitate ferrofluid movement and controlled heat transfer. Magnetic seals in rotating machinery consist of field-permeable membranes that maintain fluid position while allowing for fluid exchange and pressure fluctuations. For example, targeted drug delivery and hyperthermia treatment require ferrofluids to pass through semi-permeable biological membranes. Also heat exchangers, magnetic field-controlled filtration systems, ferrofluid-based microfluidic devices and aerospace thermal management all rely on boundary permeability for effective thermal convection. Siddheshwar [32] has documented the convective instability of ferromagnetic fluids confined by fluid-permeable and magnetically active boundaries. More recently, Nanjundappa et al. [26] explored penetrative ferro-thermal convection (FTC) driven by internal heating in a porous layer saturated with ferrofluid, considering various temperature, velocity, and magnetic potential boundary conditions. Additionally, Surya [33] examined convective instability of a liquid layer with permeable boundaries under the influence of variable gravitational force.

To the best of our knowledge, no prior studies have examined the combined effects of viscosity variation with magnetic fields and fluid-permeable magnetic boundary surfaces on the thermal convection of ferrofluids containing dust particles. This research is motivated by this gap in the literature. The study will provide different insights on how thermal convection can be optimized for various engineering applications such as electronics cooling, aerospace systems, biomedical technologies and environmental engineering through dust particles effects on it and variation of viscosity with magnetic field and fluid – permeable magnetic boundaries.

2. RESEARCH METHODOLOGY

The analytical investigation of convective instability in a dusty ferromagnetic fluid layer considering magnetic field-dependent viscosity and fluid-permeable, magnetically active boundaries under a uniform transverse magnetic field follows a structured approach aligned with the objectives of the study. A brief overview of the methodology is presented below as per the defined sections.

2.1. Fundamental Equations of the Problem

This phase includes recognizing and developing the core

equations that govern the problem. These equations may be based on physical laws or derived from mathematical models.

2.2. Basic State

After establishing the fundamental equations, the system's basic state is identified. The system is considered to be in this basic state when there is no fluid motion in its initial condition.

2.3. Perturbation

Perturbations refer to small disturbances or deviations from the basic state that are introduced into the system. These disturbances enable the examination of the system's stability and behavior under different conditions [34].

2.4. Linear Analysis

To identify the instability threshold for an dusty ferromagnetic fluid during thermal convection, linear analysis specifically using normal mode analysis as described by Chandrasekhar [34] to create an eigenvalue problem offers valuable insights into the fundamental physics of thermal convection.

2.5. Normal Mode Analysis

Normal mode analysis is utilized to reduce the system of partial differential equations into an eigenvalue problem, which allows for a systematic examination of the stability of the system.

2.6. Non-dimensionalize the System of Equations

The governing equations of the system are non-dimensionalized to simplify the analysis and eliminate any reliance on specific units of measurement. Scaling factors are used to non-dimensionalize the perturbed equations.

2.7. Method of solution

The Galerkin method is employed to solve the eigenvalue problem, transforming it into a solvable system of algebraic equations. This method approximates the solution by selecting trial functions that satisfy the boundary conditions.

2.8. Result and discussion

Identify the effects of different parameters on the systems for different bounding surfaces, and interpret the results graphically.

3. MATHEMATICAL MODELLING

Consider a static layer of ferromagnetic fluid with a finite vertical thickness d and an infinite horizontal extent, heated from below, and containing dust particles. This fluid layer is subjected to a uniform vertical magnetic field \mathbf{H} and experiences a gravitational force

represented by g and this system is confined between two horizontal fluid-permeable magnetic boundaries (as depicted in Fig. 1)

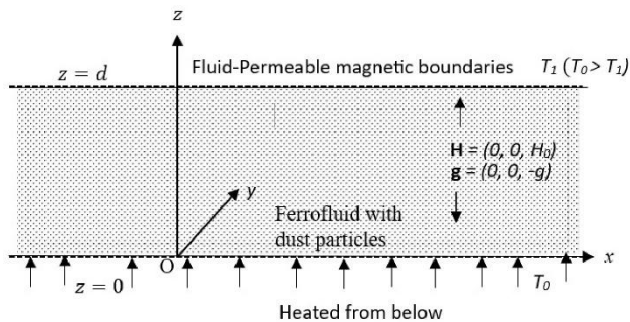


Fig. 1. Geometrical Configuration

We assume the fluid is incompressible, electrically non-conductive, and has a viscosity depend upon the magnetic field, expressed as $\mu = \mu_1 (\delta \cdot \mathbf{B} + 1)$ [35]. The fluid's viscosity when the magnetic field is zero is μ_1 , the isotropic coefficient of viscosity change is δ , and the magnetic induction is represented by \mathbf{B} . For the model described, the governing equations under the Boussinesq approximation are provided by [6, 19]:

$$\nabla \cdot \mathbf{q} = 0, \quad (1)$$

$$\rho_0 \left(\mathbf{q} \cdot \nabla + \frac{\partial}{\partial t} \right) \mathbf{q} - \rho g + \nabla p = \mu \nabla^2 \mathbf{q} + \nabla \cdot (\mathbf{H} \mathbf{B}) - K N_d (\mathbf{q} - \mathbf{q}_d), \quad (2)$$

$$m N_d C_{pt} \left(\frac{\partial}{\partial t} + \mathbf{q}_d \cdot \nabla \right) T - \left[\mu_0 \mathbf{H} \cdot \left(\frac{\partial \mathbf{M}}{\partial T} \right)_{H,V} - \rho_0 C_{H,V} \right] \frac{DT}{Dt} + \mu_0 T \left(\frac{\partial \mathbf{M}}{\partial T} \right)_{H,V} \cdot \frac{D\mathbf{H}}{Dt} = K_1 \nabla^2 T. \quad (3)$$

The equation of state for density is

$$\rho = \rho_0 [1 + \alpha (T_0 - T)], \quad (4)$$

In the aforementioned equations: \mathbf{q} represents the ferrofluid's velocity, \mathbf{q}_d indicates the dust particles' velocity, p pertains to pressure, ρ corresponds to density, N_d signifies the number density of the dust particles, \mathbf{M} stands for magnetization, \mathbf{B} represents magnetic induction, T is the temperature, $C_{H,V}$ characterizes the specific heat at constant magnetic field and volume, C_{pt} indicates the specific heat of dust particles, K_1 designates the thermal conductivity, α represents the coefficient of thermal expansion, and $K = 6\pi\mu r$ signifies the Stokes drag coefficient, where r represents the radius of the dust particle. Additionally, ρ_0 and μ_0 correspond to the density and magnetic permeability at the reference temperature.

The buoyant force acting on the dust particles is neglected [18, 23, 26]. It is further assumed that the spacing between the particles is much larger than their diameters, allowing inter-particle interactions to be disregarded. The influence of gravity, pressure, and viscous forces on the particles is assumed to be negligibly small and is thus omitted from consideration. An additional force term with this opposite direction must be included in the particles' equation of motion, because the force applied by the ferrofluid on the dust particles is equal in magnitude but opposite in direction to the force exerted by the dust particles on the ferrofluid. Let mN_d denote the mass of dust particles per unit volume; the motion and continuity equations for the dust particles, under these assumptions, are given as follows

[19, 22]:

$$m N_d \left(\mathbf{q}_d \cdot \nabla + \frac{\partial}{\partial t} \right) \mathbf{q}_d = -N_d K (\mathbf{q}_d - \mathbf{q}), \quad (5)$$

$$\nabla \cdot (N_d \mathbf{q}_d) + \frac{\partial N_d}{\partial t} = 0. \quad (6)$$

Due to assumption that fluid is electrically non-conductive, the equations of Maxwell in the case where displacement current is absent for a non-conductive fluid can be stated as follows [6]:

$$\nabla \times \mathbf{H} = 0, \quad \nabla \cdot \mathbf{B} = 0, \quad (7)$$

and

$$\mathbf{B} = \mu_0 (\mathbf{M} + \mathbf{H}). \quad (8)$$

Thus, from equations (7) and (8), we get

$$\nabla \cdot (\mathbf{M} + \mathbf{H}) = 0. \quad (9)$$

The alignment of magnetization is governed by both the magnetic field's strength and temperature, resulting in the following relationship

$$\mathbf{M} = \left(\frac{\mathbf{H}}{H} \right) M(H, T), \quad (10)$$

and

$$M = M_0 + K_2 (T_0 - T) - \chi (H_0 - H), \quad (11)$$

Where M_0 is the magnetization when temperature is T_0 and magnetic field is H_0 , while

$$K_2 = - \left(\frac{\partial M}{\partial T} \right)_{T_0, H_0}, \quad \chi = \left(\frac{\partial M}{\partial H} \right)_{T_0, H_0}$$

represents the pyromagnetic coefficient and magnetic susceptibility respectively.

Equations (1) to (11) are solved for zero flow at base state and thus the basic state solutions are given by

$$\begin{aligned} \rho &= \rho_b(z), \quad p = p_b(z), \quad \mathbf{q}_d = (\mathbf{q}_d)_b = \mathbf{0}, \quad \mathbf{q} = \mathbf{q}_b = \mathbf{0}, \\ T &= T_0 - \beta z = T_b(z), \quad \beta = \frac{T_0 - T_1}{d}, \quad (N_d)_b = N_d = N_0, \\ H_0 + M_0 &= H_0^{ext}, \quad \mathbf{H}_b = \left(H_0 - \frac{\beta K_2}{\chi + 1} z \right) \hat{\mathbf{k}}, \quad \mathbf{M}_b = \left(M_0 + \frac{\beta K_2}{\chi + 1} z \right) \hat{\mathbf{k}}. \end{aligned} \quad (12)$$

Further following Finlayson [6] perturbations are added to initial basic state as:

$$\begin{aligned} \rho &= \rho_b(z) + \rho', \quad p = p_b(z) + p', \quad \mathbf{q}_d = (\mathbf{q}_d)_b + \mathbf{q}_d', \quad \mathbf{q} = \mathbf{q}_b + \mathbf{q}', \\ T &= T_b(z) + \theta', \quad N_d = (N_d)_b + N', \quad \mathbf{M} = \mathbf{M}_b(z) + \mathbf{M}', \quad \mathbf{H} = \mathbf{H}_b(z) + \mathbf{H}'. \end{aligned} \quad (13)$$

Where the variables

$$\rho', p', \mathbf{q}' = (u', v', w'), \quad \mathbf{q}_d' = (l', r', s'), \quad \theta', \mathbf{M}' \text{ and } \mathbf{H}'$$

represent infinitesimal disturbances in density, pressure, velocity of ferrofluid, velocity of dust particles, magnetic field intensity, magnetization and temperature, respectively.

On introducing equation (13) into equations (1) to (11) and applying the basic state solutions, we derive the linearized perturbation equations in the form.

$$\frac{\partial u'}{\partial x} + \frac{\partial v'}{\partial y} + \frac{\partial w'}{\partial z} = 0, \quad (14)$$

$$\begin{aligned} [L_0 \rho_0 + m N_0] \frac{\partial u'}{\partial t} &= L_0 \left[\mu_0 (M_0 + H_0) \frac{\partial H'_1}{\partial z} + \mu_1 [1 + \delta \mu_0 (M_0 + H_0)] \nabla^2 u' - \frac{\partial p'}{\partial x} \right], \end{aligned} \quad (15)$$

$$[L_0\rho_0 + mN_0] \frac{\partial v'}{\partial t} = L_0 \left[\mu_0(M_0 + H_0) \frac{\partial H'_2}{\partial z} + \mu_1 [1 + \delta\mu_0(M_0 + H_0)] \nabla^2 v' - \frac{\partial p'}{\partial y} \right], \quad (16)$$

$$[L_0\rho_0 + mN_0] \frac{\partial w'}{\partial t} = L_0 \left[\mu_0(M_0 + H_0) \frac{\partial H'_3}{\partial z} + \mu_1 [1 + \delta\mu_0(M_0 + H_0)] \nabla^2 w' - \frac{\partial p'}{\partial z} + \rho_0 g \alpha \theta' - \mu_0 K_2 \beta H'_3 + \frac{\mu_0 K_2^2 \beta}{(\chi+1)} \theta' \right], \quad (17)$$

$$L_0 \left[(\rho C_1 + N_0 m C_{pt}) \frac{\partial \theta'}{\partial t} - K_1 \nabla^2 \theta' - \mu_0 T_0 K_2 \frac{\partial}{\partial t} \left(\frac{\partial \phi'}{\partial z} \right) \right] = L_0 \left[\beta \left(\rho C_1 - \frac{\mu_0 T_0 K_2^2}{\chi+1} \right) w' \right] + N_0 m \beta C_{pt} w', \quad (18)$$

Here $\rho C_1 = \mu_0 H_0 K_2 + \rho_0 C_{H,V}$, $L_0 = \left(\frac{m}{K} \frac{\partial}{\partial t} + 1 \right)$, also,

$$\frac{\partial}{\partial x} (M'_1 + H'_1) + \frac{\partial}{\partial y} (M'_2 + H'_2) + \frac{\partial}{\partial z} (M'_3 + H'_3) = 0, \quad \nabla \phi' = \mathbf{H}', \quad (19)$$

where ϕ' is the perturbed magnetic potential, and

$$M'_3 + H'_3 = H'_3(\chi + 1) - K_2 \theta', \quad M'_i + H'_i = \left(1 + \frac{M_0}{H_0} \right) H'_i \quad (i = 1, 2).$$

Here we have considered that $\beta d K_2 \ll (\chi + 1) H_0$. (Finlayson [6]).

Now, eliminating p' , u' , v' between equations (15)-(17) using equation (14), we get

$$[L_0\rho_0 + mN_0] \frac{\partial}{\partial t} (\nabla^2 w') - L_0 \mu_1 [1 + \delta\mu_0(M_0 + H_0)] \nabla^4 w' = L_0 \left(\rho_0 g \alpha + \frac{\mu_0 K_2^2 \beta}{(\chi+1)} \right) (\nabla_1^2 \theta') - L_0 \mu_0 K_2 \beta \nabla_1^2 \frac{\partial \phi'}{\partial z}, \quad (21)$$

where

$$\nabla_1^2 = \frac{\partial^2}{\partial x^2} + \frac{\partial^2}{\partial y^2}, \quad \nabla^2 = \nabla_1^2 + \frac{\partial^2}{\partial z^2}.$$

Also, from equations (19) and (20), we have

$$(\chi + 1) \frac{\partial^2 \phi'}{\partial z^2} + \left(\frac{M_0}{H_0} + 1 \right) \nabla_1^2 \phi' - \frac{\partial \theta'}{\partial z} K_2 = 0. \quad (22)$$

Now, following normal mode analysis assuming that all quantities characterizing the perturbation depend on t, x, y , and z in the form

$$(w', \phi', \theta')(t, x, y, z) = e^{[nt + i(xk_{x1} + yk_{y1})]} [w^*(z), \phi^*(z), \theta^*(z)]. \quad (23)$$

In this context, we have wave numbers represented as k_{x1} and k_{y1} for the x and y directions, respectively. Additionally, n denotes the growth rate, and k is defined as the magnitude of the resultant wave number, calculated as the square root of the sum of the squares of k_{x1} and k_{y1} and using non dimensional parameters:

$$z_* = \frac{z}{d}, \quad D_* = \frac{\partial}{\partial z_*}, \quad a = kd, \quad \omega = \frac{nd^2}{\nu}, \quad w_* = \frac{d}{\nu} w^*, \quad t_* = \frac{\nu}{d^2} t, \\ \theta_* = \frac{K_1 a \sqrt{R}}{\rho C_1 \beta d \nu} \theta^*, \quad \phi_* = \frac{(\chi+1) K_1 a \sqrt{R}}{k_2 \rho C_1 \beta \nu d^2} \phi^*, \quad k_{1*} = \frac{k_1}{d}, \quad \delta_* = \delta \mu_0 H (\chi + 1), \quad \nu = \frac{\mu_1}{\rho_0}, \quad P_r = \frac{\nu \rho C_1}{K_1}, \quad \tau = \frac{mv}{K d^2}, \quad R = \frac{g \alpha \beta d^4 \rho C_1}{K_1 \nu},$$

$$M_1 = \frac{\mu_0 K_2^2 \beta}{(\chi+1) \alpha \rho_0 g}, \quad M_2 = \frac{\mu_0 T_0 K_2^2}{(\chi+1) \rho C_1}, \quad M_3 = \frac{1 + \frac{M_0}{H_0}}{(\chi+1)}, \quad f = \frac{m N_0}{\rho_0}, \\ L_{0*} = \left(\tau \frac{\partial}{\partial t_*} + 1 \right), \quad h = \frac{m N_0 C_{pt}}{\rho C_1},$$

in equations (18), (21) and (22), we obtained the non-dimensional linearised equations as

$$(D^2 - a^2) [(\omega \tau + 1) \{ (M_3 \delta + 1) (D^2 - a^2) - \omega \} - f \omega] w = (\omega \tau + 1) [(M_1 + 1) \theta - M_1 D \phi] a \sqrt{R}, \quad (24)$$

$$(\omega \tau + 1) \{ P_r M_2 \omega D \phi + (D^2 - a^2 - (1 + h) \omega P_r) \theta \} = -[h + (\omega \tau + 1) (1 - M_2)] a \sqrt{R} w, \quad (25)$$

$$(D^2 - a^2 M_3) \phi = D \theta. \quad (26)$$

A real independent variable z in the range $0 \leq z \leq 1$ is used in the aforementioned equations. Here, the square of the wave number is represented by a^2 , while differentiation with respect to z is shown by $D = \frac{d}{dz}$. The variables P_r, R, M_1, M_2 and M_3 correspond to the Prandtl number, Rayleigh number, magnetic number, a non-dimensional parameter, and measure of nonlinearity of the magnetization parameter, respectively. The parameters h and f are related to dust particles. The complex constant $\omega = \omega_r + i\omega_i$ signifies the complex growth rate, where ω_i and ω_r are real constants. The variables, $w(z) = w_i(z)\iota + w_r(z)$, $\phi(z) = \phi_i(z)\iota + \phi_r(z)$, and $\theta(z) = \theta_i(z)\iota + \theta_r(z)$, are all complex functions of the real variable z , while $w_r, w_i, \phi_r, \phi_i, \theta_r, \theta_i$, are the real components of these functions.

From a physical standpoint, equations (24) to (26) define an eigenvalue problem for R , which governs ferromagnetic convection within a ferrofluid layer containing dust particles. In these equations, w represents the vertical velocity, θ indicates the temperature, and ϕ denotes the amplitude of the magnetic potential. Since M_2 is of a very small magnitude (on the order of 10^{-6}) [6], its influence is negligible for further analysis, allowing equation (25) to be simplified as.

$$(\omega \tau + 1) (D^2 - a^2 - \omega P_r (1 + h)) \theta = -[1 + \omega \tau + h] a \sqrt{R} w. \quad (27)$$

For the scenario of stationary convection, setting $\omega = 0$ simplifies the eigenvalue problem into the following form:

$$(1 + M_3 \delta) (D^4 - 2a^2 D^2 + a^4) w = [(M_1 + 1) \theta - M_1 D \phi] a \sqrt{R}, \quad (28)$$

$$(-a^2 + D^2) \theta = -[h + 1] a \sqrt{R} w, \quad (29)$$

$$(D^2 - a^2 M_3) \phi = D \theta. \quad (30)$$

Since the ferrofluid layer is confined between two thermally conducting and fluid-permeable magnetic surfaces. Hence, we use the following fluid-permeable magnetic boundaries condition as proposed by ([6, 32, 36, 37]):

$$-(D a_s) D w + D^2 w = w = 0, \text{ at } z = 0 \text{ and } (D a_s) D w + D^2 w = w = 0, \text{ at } z = 1,$$

$$-a \phi + (1 + \chi) D \phi \text{ at } z = 0 \text{ and } a \phi + (1 + \chi) D \phi \text{ at } z = 1, \\ \theta = 0 \text{ at } z = 0 \text{ and } z = 1, \quad (31)$$

where $D a_s$ is the slip-D'Arcy number and χ is the magnetic susceptibility.

4. MATHEMATICAL ANALYSIS

The non-dimensionalized linear ODEs (28) to (30) along with boundary conditions (31) form the eigen value problem with R as Rayleigh number. To determine the Rayleigh number for the given boundary conditions (31), we will employ a single-term Galerkin method. Let's consider a single term in the expansions of w , θ , and ϕ as follows:

$$w = A_{11}w_1(z), \theta = B_{11}\theta_1(z), \phi = C_{11}\phi_1(z), \quad (32)$$

Here, A_{11} , B_{11} , and C_{11} are constants, and $w_1(z)$, $\theta_1(z)$, and $\phi_1(z)$ are appropriately selected trial functions that satisfy the necessary boundary conditions (31). By replacing w , θ , and ϕ with their respective expressions in equations (28) to (30), then multiplying each resulting equation by $w_1(z)$, $\theta_1(z)$, and $\phi_1(z)$ accordingly, and integrating by parts the necessary number of times while applying the boundary conditions, we derive three homogeneous equations in A_{11} , B_{11} , and C_{11} . The coefficients of these equations are expressed as definite integrals. This system can be expressed in matrix form as follows:

$$\begin{pmatrix} (M_3\delta + 1)A_2 & -a\sqrt{R}(1 + M_1)A_3 & a\sqrt{R}M_1A_5 \\ (1 + h_1)a\sqrt{R}A_3 & -A_1 & 0 \\ 0 & A_4 & A_6 \end{pmatrix} \begin{pmatrix} A_{11} \\ B_{11} \\ C_{11} \end{pmatrix} = \begin{pmatrix} 0 \\ 0 \\ 0 \end{pmatrix}$$

were,

$$\begin{aligned} A_1 &= \int_0^1 [(D\theta)^2 + a^2\theta^2] dz, \\ A_2 &= \int_0^1 [(D^2w)^2 + 2a^2(Dw)^2 + a^4(w)^2] dz + \\ &\quad (Da_s) [(Dw(0))^2 + (Dw(1))^2], \\ A_3 &= \int_0^1 w\theta dz, \\ A_4 &= \int_0^1 \phi D\theta dz, \\ A_5 &= \int_0^1 wD\phi dz, \\ A_6 &= \int_0^1 [(D\phi)^2 + a^2M_3\phi^2] dz + \frac{a}{\chi+1} [\phi(0)^2 + \phi(1)^2]. \end{aligned}$$

For simplicity, the subscript 1 is omitted, and the functions $w_1(z)$, $\theta_1(z)$, and $\phi_1(z)$ are henceforth denoted as w , θ , and ϕ respectively.

For a non-trivial solution to occur, the determinant of the coefficient matrix must be zero. This results in the following expression, which establishes a first-order relationship between the Rayleigh number R and the wave number a .

$$R = \frac{(M_3\delta + 1)A_1A_2}{a^2(1+h)A_3\{(M_1+1)A_3 + \frac{M_1A_4A_5}{A_6}\}}. \quad (33)$$

Let us now select the following trial functions that satisfy the specified boundary conditions.

$$w = \frac{2}{2+Da_s}z + \frac{Da_s}{2+Da_s}z^2 - 2z^3 + z^4, \theta = z - z^2, \phi = -\frac{1}{2} + z. \quad (34)$$

The initially proposed trial function for the magnetic potential, denoted by ϕ , does not meet the boundary conditions given in equation (31). To resolve this inconsistency, the boundary residual method, as described by Finlayson [6], is applied to the function ϕ .

By applying these trial functions to the integrals A_1 through A_6 , we derive the following formula for Rayleigh number as

$$R = \frac{5880(M_3\delta + 1)(\chi + 10) \left[\frac{6\sqrt{\chi}}{1+\chi} + 12 + \chi M_3 \right]}{\left[\left(\frac{4}{5} + 4P \right) + \left(\frac{P^2}{30} + \frac{P}{70} + \frac{1}{630} \right) \chi^2 + 2 \left(\frac{P^2}{3} + \frac{2P}{15} + \frac{2}{105} \right) \chi \right]} \frac{h_1\chi(3+14P)}{\{(M_1+1)(3+14P) \left(\frac{6\sqrt{\chi}}{1+\chi} + 12 + \chi M_3 \right) - 28(1+5P)M_1\}} \quad (35)$$

where $P = \frac{2}{2+Da_s}$, $h_1 = h + 1$ and $\chi = a^2$.

Using MATLAB R2023a software, the square of the critical wave number χ_c is determined by finding the positive roots of the equation $\frac{dR}{d\chi} = 0$. Additionally, the associated critical Rayleigh number R_c is numerically calculated.

Also, we have the following formula for the magnetic Rayleigh number N for significantly large values of M_1 derived from expression (35) utilizing Finlayson [6] analysis.

$$N = \frac{5880(M_3\delta + 1)(\chi + 10) \left[\frac{6\sqrt{\chi}}{1+\chi} + 12 + \chi M_3 \right]}{\left[\left(\frac{4}{5} + 4P \right) + \left(\frac{P^2}{30} + \frac{P}{70} + \frac{1}{630} \right) \chi^2 + 2 \left(\frac{P^2}{3} + \frac{2P}{15} + \frac{2}{105} \right) \chi \right]} \frac{h_1\chi(3+14P)}{\{(M_1+1)(3+14P) \left(\frac{6\sqrt{\chi}}{1+\chi} + 12 + \chi M_3 \right) - 28(1+5P)M_1\}} \quad (36)$$

which stand for the magnetic mechanism that functions when buoyancy effects are not present.

5. RESULTS AND DISCUSSION

This study explores the convective instability of a dusty ferro-magnetic fluid, incorporating the effects of viscosity that depend on the magnetic field. The system is analyzed within a Rayleigh-Bénard configuration, where the fluid is contained between permeable boundaries that are also magnetically active. Additionally, the setup is subject to a uniform transverse magnetic field. Given the complexity of the boundary conditions, the Galerkin method was employed to calculate the critical eigenvalue. These findings can contribute to better control of instability in engineering systems and enhance the efficiency of applications where stability and precise thermal regulation are essential.

In the present analysis, the nonlinearity of the magnetization parameter M_3 is considered to vary from 0 to 25, as suggested by Finlayson [6]. The MFD viscosity parameter δ ranges from 0 to 0.09, as per the work of Prakash et al. [14]. The dust particle parameter h_1 is taken to vary between 1 and 9, following the suggestion of Sunil et al. [18]. Furthermore, the magnetic susceptibility of boundaries χ and the permeability parameter of boundaries Da_s are assumed to range from 10^0 to 10^6 and from 0 to ∞ , respectively, as suggested by Siddheshwar [32].

First, we discuss the accuracy of the results presented in this study. For the case of ordinary fluid, in the absence of a magnetic parameter ($M_1 = 0$ and $M_3 = 0$), $\chi \rightarrow \infty$ and without dust particles ($h_1 = 1$), the critical Rayleigh number (R_c) and wave number (a_c^2) are found to be $R_c = 664.5251$ at $a_c^2 = 4.9594$ for free boundaries. This closely matches to $R_c = 657.551$ at $a_c^2 = 4.9328$ as obtained by Surya [33]. Additionally, for rigid boundaries, we have $R_c = 1750.0$ at $a_c^2 = 9.7127$, which closely matches $R_c = 1715.070$ at $a_c^2 = 9.6969$, as reported by Surya [33].

Also, Tab. 1 provide a qualitative comparison of the numerical results computed at $\chi \rightarrow \infty$, without dust particle ($h_1 = 1$), $M_3 = 10$, $M_1 = 1.5$ for the case of free-free and rigid-rigid boundaries

with Dhiman [10]. The table clearly shows that our results align exceptionally well with previously published data, confirming the accuracy of our numerical procedure.

Tab. 1. Comparison of Values from the Present Study with Existing Studies

	Free-Free		Rigid-Rigid	
	Present Study	Dhiman [10]	Present Study	Dhiman [10]
	$R_c(a_c^2)$	$R_c(a_c^2)$	$R_c(a_c^2)$	$R_c(a_c^2)$
$M_1 = 1$	360.0088 (5.4644)	342.52 (5.174)	913.1268 (10.2291)	889.15 (9.921)
$M_1 = 5$	126.5677 (5.8260)	116.49 (5.319)	313.1211 (10.5816)	299.56 (10.06)

Tab. 2. Variation of critical magnetic Rayleigh numbers N_c with M_3 , χ and δ at fixed $h_1 = 3$ and $Da_s = 1$

$h_1 = 3$		Critical Magnetic Rayleigh Number $N_c(a_c^2)$ at				
χ	M_3	$\delta = 0.01$	$\delta = 0.03$	$\delta = 0.05$	$\delta = 0.07$	$\delta = 0.09$
1	1	412.4400 (7.7909)	420.6071 (7.7909)	428.7742 (7.7909)	436.9413 (7.7909)	445.1085 (7.7909)
	5	333.0876 (7.0576)	364.8102 (7.0576)	396.5328 (7.0576)	428.2554 (7.0576)	459.9781 (7.0576)
	10	321.2218 (6.6092)	379.6257 (6.6092)	438.0297 (6.6092)	496.4336 (6.6092)	554.8376 (6.6092)
	15	323.9978 (6.3847)	408.5190 (6.3847)	493.0402 (6.3847)	577.5614 (6.3847)	662.0825 (6.3847)
	20	331.3287 (6.2498)	441.7716 (6.2498)	552.2144 (6.2498)	662.6573 (6.2498)	773.1002 (6.2498)
10	1	494.4820 (8.9375)	504.2737 (8.9375)	514.0654 (8.9375)	523.8572 (8.9375)	533.6489 (8.9375)
	5	342.8150 (7.3292)	375.4640 (7.3292)	408.1130 (7.3292)	440.7621 (7.3292)	473.4111 (7.3292)
	10	324.5245 (6.7147)	383.5290 (6.7147)	442.5334 (6.7147)	501.5379 (6.7147)	560.5423 (6.7147)
	15	325.7133 (6.4415)	410.6820 (6.4415)	495.6507 (6.4415)	580.6194 (6.4415)	665.5881 (6.4415)
	20	332.4015 (6.2855)	443.2020 (6.2855)	554.0025 (6.2855)	664.8030 (6.2855)	775.6035 (6.2855)
10^3	1	525.1702 (9.3988)	535.5696 (9.3988)	545.9690 (9.3988)	556.3685 (9.3988)	566.7679 (9.3988)
	5	345.3312 (7.4019)	378.2199 (7.4019)	411.1086 (7.4019)	443.9972 (7.4019)	476.8859 (7.4019)
	10	325.3216 (6.7407)	384.4710 (6.7407)	443.6204 (6.7407)	502.7697 (6.7407)	561.9191 (6.7407)

10^5	15	326.1164 (6.4551)	411.1902 (6.4551)	496.2641 (6.4551)	581.3379 (6.4551)	666.4118 (6.4551)
	20	332.6499 (6.2938)	443.5332 (6.2938)	554.4166 (6.2938)	665.2999 (6.2938)	776.1832 (6.2938)
	1	525.5497 (9.4046)	535.9567 (9.4046)	546.3636 (9.4046)	556.7705 (9.4046)	567.1774 (9.4046)
	5	345.3597 (7.4027)	378.2512 (7.4027)	411.1426 (7.4027)	444.0340 (7.4027)	476.9254 (7.4027)
	10	325.3305 (6.7410)	384.4815 (6.7410)	443.6325 (6.7410)	502.7835 (6.7410)	561.9345 (6.7410)
10^5	15	326.1209 (6.4552)	411.1959 (6.4552)	496.2709 (6.4552)	581.3459 (6.4552)	666.4209 (6.4552)
	20	332.6527 (6.2939)	443.5369 (6.2939)	554.4212 (6.2939)	665.3054 (6.2939)	776.1896 (6.2939)

Tab. 2 presented the numerical values of critical magnetic Rayleigh number (N_c) and square of critical wave number (a_c^2) for different combination of δ , M_3 , χ at fixed $h_1=3$ and $Da_s = 1$. Tab. 4 presented the numerical values of critical magnetic Rayleigh number (N_c) and square of critical wave number (a_c^2) for different combination of h_1 , Da_s and M_3 at fixed $\delta=0.03$ and $\chi = 10$.

Fig. 2 depict the variation of critical magnetic Rayleigh numbers N_c versus χ with different values of M_3 and fixed values of δ , h_1 and Da_s . From Fig. 2 and numerical values of critical magnetic Rayleigh numbers N_c presented in Tab. 3 we can observe that critical magnetic Rayleigh numbers increases for increasing values of χ , which yields that χ has stabilizing effect on the system. This stabilizing effect of χ directly depend upon M_3 . χ has strong stabilizing effect for smaller values of M_3 as compare to larger values of M_3 . Also from Tab.3 we can observe that the critical wave number increases as χ increases which indicate that χ reduces the size of convection cell.

Fig.3 depict the variation of critical magnetic Rayleigh numbers N_c versus Da_s with different values of δ and fixed values of M_3 , h_1 and χ . From Fig. 3 and numerical values of critical magnetic Rayleigh numbers N_c presented in Tab. 4 we can observe that critical magnetic Rayleigh numbers increases for increasing values of Da_s , which yields that Da_s has stabilizing effect on the system. Also we can conclude that $(N_c)_{Free} \leq (N_c)_{Permeable} \leq (N_c)_{Rigid}$. Because $(N_c)_{Free}$ and $(N_c)_{Rigid}$ can be acquired from $(N_c)_{Permeable}$ in the limit $Da_s \rightarrow 0$ and ∞ respectively. Therefore the equality sign in $(N_c)_{Free} \leq (N_c)_{Permeable} \leq (N_c)_{Rigid}$ is understandable. This analysis effectively demonstrates the connection between the results for free-free and rigid-rigid boundary conditions. This behavior arises because free boundaries impose minimal resistance to fluid motion near the surfaces, allowing the temperature gradient to drive convection more easily. As a result, the fluid becomes more responsive to instabilities, leading to a lower critical magnetic Rayleigh number and an earlier onset of convection compared to the case with rigid boundaries. Further, it is evident from Tab.4 that the critical wave number increases as Da_s increases which indicate that Da_s reduces the size of convection cell.

Fig. 4 depict the variation of critical magnetic Rayleigh numbers N_c versus δ with different values of M_3 and fixed values of χ , h_1

and Da_s . From Fig. 3, Fig. 4, Fig. 5, Fig. 7 and numerical values of critical magnetic Rayleigh numbers N_c presented in Tab.3 we can observe that critical magnetic Rayleigh numbers increases for increasing values of δ , which yields that δ has stabilizing effect on the system. This is consistent with the physical understanding that higher viscosity suppresses disturbances and restricts fluid movement, resulting in a delayed onset of convection. Also, it is noted from table Tab.3 that the critical wave number has no influence of MFD viscosity δ , i.e. size of convection cell is independent of MFD viscosity δ .

Tab. 3. Variation of critical magnetic Rayleigh numbers N_c with h_1 , M_3 and Da_s at fixed $\chi = 10$ and $\delta = 0.03$

$\chi = 10$		Critical Magnetic Rayleigh Number $N_c(a_c^2)$ at				
M_3	h_1	$Da_s = 0$	$Da_s = 10$	$Da_s = 10^2$	$Da_s = 10^3$	$Da_s = 10^5$
3	1	1058.2 (7.1019)	1713.5 (10.3132)	2257.1 (11.8650)	2371.8 (12.1002)	2385.8 (12.1272)
	3	352.7195 (7.1019)	571.1730 (10.3132)	752.3706 (11.8650)	790.5888 (12.1002)	795.2814 (12.1272)
	5	211.6317 (7.1019)	342.7038 (10.3132)	451.4224 (11.8650)	474.3533 (12.1002)	477.1689 (12.1272)
	7	151.1655 (7.1019)	244.7884 (10.3132)	322.4445 (11.8650)	338.8238 (12.1002)	340.8349 (12.1272)
	9	117.5732 (7.1019)	190.3910 (10.3132)	250.7902 (11.8650)	263.5296 (12.1002)	265.0938 (12.1272)
5	1	998.5998 (6.5835)	1660.7 (9.6886)	2210.0 (11.1916)	2325.7 (11.4193)	2339.9 (11.4454)
	3	332.8666 (6.5835)	553.5690 (9.6886)	736.6527 (11.1916)	775.2371 (11.4193)	779.9737 (11.4454)
	5	199.7200 (6.5835)	332.1414 (9.6886)	441.9916 (11.1916)	465.1422 (11.4193)	467.9842 (11.4454)
	7	142.6571 (6.5835)	237.2439 (9.6886)	315.7083 (11.1916)	332.2445 (11.4193)	334.2744 (11.4454)
	9	110.9555 (6.5835)	184.5230 (9.6886)	245.5509 (11.1916)	258.4124 (11.4193)	259.9912 (11.4454)
10	1	1010.8 (5.9857)	1734.0 (9.0216)	2332.5 (10.4899)	2458.4 (10.7120)	2473.8 (10.7375)
	3	336.9392 (5.9857)	578.0082 (9.0216)	777.4880 (10.4899)	819.4643 (10.7120)	824.6157 (10.7375)
	5	202.1635 (5.9857)	346.8049 (9.0216)	466.4928 (10.4899)	491.6786 (10.7120)	494.7694 (10.7375)
	7	144.4025 (5.9857)	247.7178 (9.0216)	333.2092 (10.4899)	351.1990 (10.7120)	353.4067 (10.7375)
	9	112.3131 (5.9857)	192.6694 (9.0216)	259.1627 (10.4899)	273.1548 (10.7120)	274.8719 (10.7375)
15	1	1077.7 (5.7151)	1875.3 (8.7376)	2534.0 (10.1969)	2672.5 (10.4175)	2689.5 (10.4428)
	3	359.2290 (5.7151)	625.0951 (8.7376)	844.6717 (10.1969)	890.8388 (10.4175)	896.5038 (10.4428)
	5	215.5374 (5.7151)	375.0570 (8.7376)	506.8030 (10.1969)	534.5033 (10.4175)	537.9023 (10.4428)
	7	153.9553 (5.7151)	267.8979 (8.7376)	362.0022 (10.1969)	381.7881 (10.4175)	384.2159 (10.4428)
	9	119.7430 (5.7151)	208.3650 (8.7376)	281.5572 (10.1969)	296.9463 (10.4175)	298.8346 (10.4428)

The behavior of the critical magnetic Rayleigh number N_c as a function of M_3 is illustrated in Fig. 6 for several values of χ , while keeping M_3 , h_1 and δ constant. Similarly, Fig. 7 depicts the relationship between N_c and M_3 for different values of δ , with h_1 , M_3 , and χ held fixed. The critical magnetic Rayleigh number N_c initially decreases for increasing values of M_3 , but after a certain value of M_3 , it increases for increasing values of M_3 , as shown by Fig. 2,

Fig. 4, Fig. 6, Fig. 7 and Tab. 2 as well as Tab. 3. This destabilizing or stabilizing effect of M_3 varies upon the value of δ . The destabilizing effect range of M_3 is larger for small values of δ than it is at large values of δ . From Tab. 2 and Tab. 3 it is observed that critical wave number reduces with raise in M_3 which means that M_3 increases the size of convection cell.

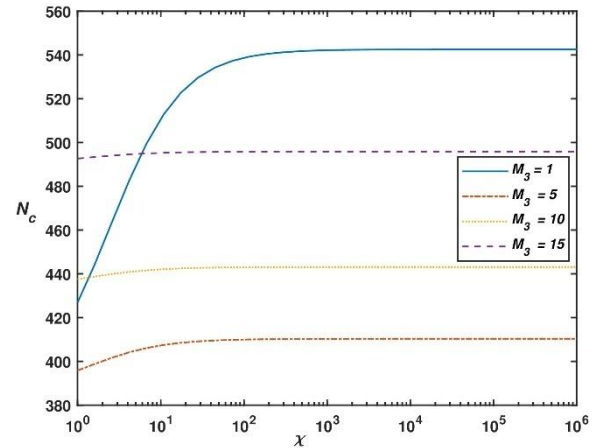


Fig. 2. Graph between N_c vs χ at $\delta = 0.05$, $h_1 = 3$ and $Da_s = 1$

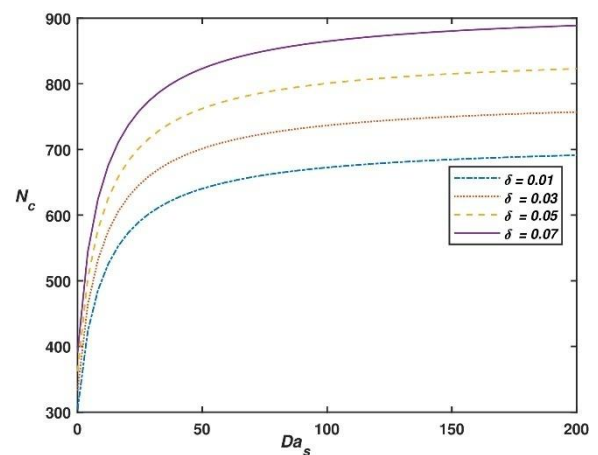


Fig. 3. Graph between N_c vs Da_s at $h_1=3$, $\chi = 10$ and $M_3 = 5$

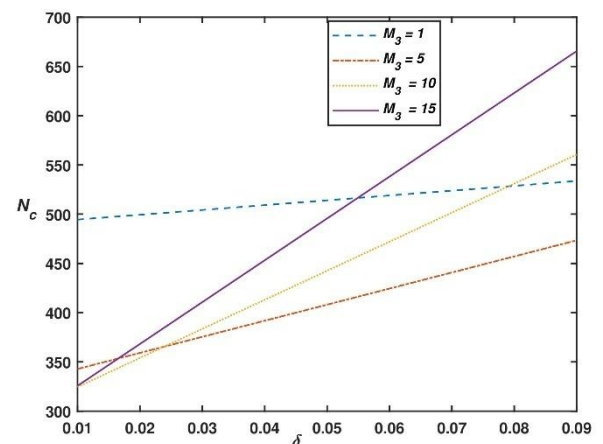


Fig. 4. Graph between N_c vs δ at $\chi = 10$, $Da_s = 1$ and $h_1 = 3$

The behavior of the critical magnetic Rayleigh number N_c as a function of dust particles parameter h_1 is illustrated in Fig. 5 for

several values of δ , while keeping h_1 , M_3 , and χ constant. From Fig. 2 and numerical values of critical magnetic Rayleigh numbers N_c presented in table Tab. 2 we can observe that critical magnetic Rayleigh numbers decreases for increasing values of h_1 , which shows that h_1 has destabilizing effect on the system as the overall heat capacity of the fluid increases due to the additional contribution from the dust particles. Moreover Tab. 2 demonstrates that the critical wave number does not depend on the parameter h_1 of dust particles, meaning that the size of the convection cell is not affected by dust particles parameter h_1 .

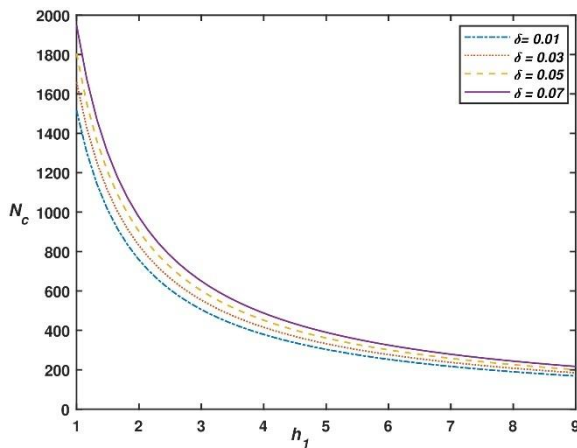


Fig. 5. Graph between N_c vs h_1 at $Da_s = 10$, $\chi = 10$ and $M_3 = 5$

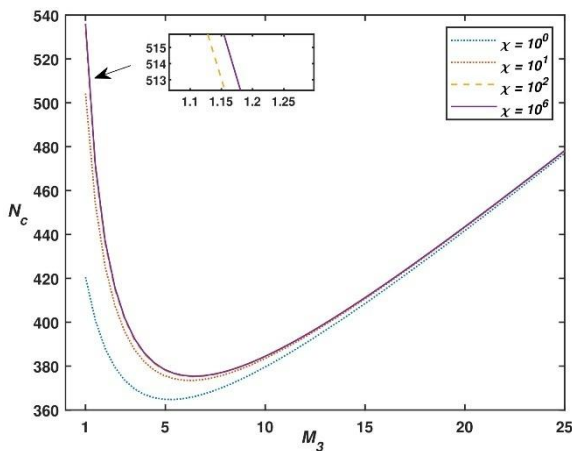


Fig. 6. Graph between N_c vs M_3 at $\delta = 0.03$, $Da_s = 1$ and $h_1 = 3$

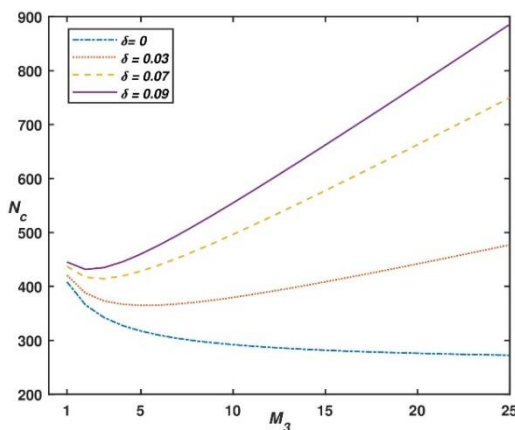


Fig. 7. Graph between N_c vs M_3 at $\chi = 1$, $Da_s = 1$ and $h_1 = 3$

6. CONCLUSION

For a Rayleigh-Bénard situation between fluid-permeable, magnetic boundaries, we investigate the impact of dust particles and viscosity variation with magnetic field on the convective instability of a ferro magnetic fluid layer using the single term Galerkin technique for stationary mode of convection. The main conclusion from our research can be summarized as follows:

- The parameters of fluid permeable, magnetic boundaries and MFD viscosity parameter delay the initiation of onset of convection which indicate their stabilizing effect.
- Dust particles parameter h_1 initiate the initiation of onset of convection which indicate their destabilizing effect.
- Measure of nonlinearity of magnetization M_3 exhibits a destabilizing effect, but beyond a certain threshold, it switches to a stabilizing effect within the system.
- The size of cells formed at the initiation of convection narrows with a raise in the parameter of permeable magnetic boundaries.
- The size of cells formed at the initiation of convection widens with a raise in the measure of nonlinearity of magnetization M_3 .
- The dust particles parameter and MFD viscosity has no effect on the size of cell formed at the initiation of convection.

These discoveries advance our knowledge of the variables affecting convection of ferrofluid and offer useful data for a number of disciplines, including fluid dynamics and geophysics. Additional investigation in this field may clarify our understanding of convection phenomena and examine the practical consequences of these results.

Nomenclature

Symbol	Explanation
d	Depth of the ferromagnetic fluid layer (m)
t	Time variable (s)
T	Temperature (K)
T_0, T_1	Reference temperatures at $z = 0$ and $z = d$ respectively (K)
r	Radius of a dust particle (m)
m	Mass of a dust particle (kg)
N_d	Number density of dust particles (particles/m ³)
N'	Disturbance to number density of dust particles (particles/m ³)
C_{pt}	Heat capacity of dust particles (kJ/m ³ K)
$C_{H,V}$	Specific heat at constant magnetic field and volume (kJ/m ³ K)
K_1	Thermal conductivity ($\frac{W}{mK}$)
K_2	Pyromagnetic coefficient = $-\partial M / \partial T$ at (T_0, H_0) (A/mK)
K	Stokes drag coefficient (kg/s)
Da_s	Darcy number accounting for velocity slip
p	Fluid pressure (psi)
p'	Pressure perturbation (psi)
q	Velocity of the ferrofluid (m/s)
$q' = (u', v', w')$	Velocity perturbation of the fluid (m/s)
q_d	Dust particle velocity (m/s)
$q_d' = (l', r', s')$	Dust velocity disturbance (m/s)

g	Gravitational acceleration, $g = (0, 0, -g) (m/s^2)$
D/Dt	Convective (material) derivative (s^{-1})
k_{x1}, k_{y1}	Horizontal wave numbers in x and y directions (m^{-1})
k	Overall wave number, $k = \sqrt{(k_{x1}^2 + k_{y1}^2)} (m^{-1})$
\hat{k}	Unit vector in the vertical (z) direction
\mathbf{H}	Magnetic field vector (A/m)
H, H^0, H^{ext}	Magnitude of field, reference field, and external magnetic field (A/m)
\mathbf{H}'	Magnetic field perturbation (A/m)
\mathbf{B}	Magnetic flux density (T)
B	Magnitude of magnetic induction (T)
\mathbf{M}	Magnetization (A/m)
\mathbf{M}'	Magnetization disturbance (A/m)
M_0	Magnetization at (H_0, T_0) (A/m)
b	Subscript indicating base (equilibrium) state
Greek Symbols	
α	Thermal expansion coefficient (K^{-1})
β	Constant thermal gradient $ dT/dz (K/m)$
ν	Kinematic viscosity (m^2/s)
μ	Dynamic viscosity ($kg/m \cdot s$)
μ_1	Dynamic viscosity under ambient magnetic field ($kg/m \cdot s$)
μ_0	Magnetic permeability of vacuum (H/m)
ρ	Fluid density (kg/m^3)
ρ_0	Reference density at T_0 (kg/m^3)
ρ'	Density perturbation (kg/m^3)
θ'	Temperature fluctuation (K)
ω	Rate of growth of disturbances (s^{-1})
χ	Magnetic susceptibility = $\partial M / \partial H$ at (T_0, H_0)
∇	Gradient (del) operator (m^{-1})
ϕ'	Perturbation in magnetic scalar potential (A)

REFERENCES

- Scherer C, Figueiredo Neto AM. Ferrofluids: properties and applications. Braz J Phys. 2005;35(3A):718–727. <https://doi.org/10.1590/S0103-97332005000400018>
- Kole M, Khandekar S. Engineering applications of ferrofluids: A review. J Magn Magn Mater. 2021;537:168222. <https://doi.org/10.1016/j.jmmm.2021.168222>
- Genc S, Derin B. Synthesis and rheology of ferrofluids: a review. Curr Opin Chem Eng. 2014;3:118–124. <https://doi.org/10.1016/j.coche.2013.12.006>
- Alsaady M, Fu R, Li B, Boukhanouf R, Yan Y. Thermo-physical properties and thermo-magnetic convection of ferrofluid. Appl Therm Eng. 2015;88:14–21. <https://doi.org/10.1016/j.applthermaleng.2014.09.087>
- Ivanov AO, Kantorovich SS, Reznikov EN, Holm C, Pshenichnikov AF, Lebedev AV, et al. Magnetic properties of polydisperse ferrofluids: A critical comparison between experiment, theory, and computer simulation. Phys Rev E. 2007;75(6):061405. <https://doi.org/10.1103/PhysRevE.75.061405>
- Finlayson BA. Convective instability of ferromagnetic fluids. J Fluid Mech. 1970;40(4):753–767. <https://doi.org/10.1017/S0022112070000423>
- Schwab L, Hildebrandt U, Stierstadt K. Magnetic Bénard convection.

- J Magn Magn Mater. 1983;39(1–2):113–114. [https://doi.org/10.1016/0304-8853\(83\)90412-2](https://doi.org/10.1016/0304-8853(83)90412-2)
- Sunil, Sharma A, Sharma D, Kumar P. Effect of magnetic field-dependent viscosity on thermal convection in a ferromagnetic fluid. Chem Eng Commun. 2008;195(5):571–583. <https://doi.org/10.1080/00986440701707719>
- Dhiman J, Sharma N. Thermal instability of hot ferrofluid layer with temperature-dependent viscosity. Int J Fluid Mech Res. 2018;45(5):389–398. <https://doi.org/10.1615/InterJFluidMechRes.2018016842>
- Dhiman JS, Sharma N. Effect of temperature dependent viscosity on thermal convection in ferrofluid layer. J Theor Appl Mech. 2021; 51:3–21.
- Vaidyanathan G, Sekar R, Balasubramanian R. Ferroconvective instability of fluids saturating a porous medium. Int J Eng Sci. 1991;29(10):1259–1267. [https://doi.org/10.1016/0020-7225\(91\)90029-3](https://doi.org/10.1016/0020-7225(91)90029-3)
- Venkatasubramanian S, Kaloni PN. Effects of rotation on the thermo-convective instability of a horizontal layer of ferrofluids. Int J Eng Sci. 1994;32(2):237–256. [https://doi.org/10.1016/0020-7225\(94\)90004-3](https://doi.org/10.1016/0020-7225(94)90004-3)
- Chand P, Bharti PK, Mahajan A, et al. Thermal convection in micropolar ferrofluid in the presence of rotation. J Magn Magn Mater. 2008;320(3–4):316–324. <https://doi.org/10.1016/j.jmmm.2007.06.006>
- Prakash J, Manan S, Kumar P. Ferromagnetic convection in a sparsely distributed porous medium with magnetic field dependent viscosity revisited. J Porous Media. 2018;21(8). <https://doi.org/10.1615/JPorMedia.2018018832>
- Prakash J, Kumar P, Manan S, Sharma K. The effect of magnetic field dependent viscosity on ferromagnetic convection in a rotating sparsely distributed porous medium-revisited. Int J Appl Mech Eng. 2020;25(1):142–158. <https://doi.org/10.2478/ijame-2020-0010>
- Kumar P, Kaur M, Thakur A, Bala R. On estimating the growth rate of perturbations in Rivlin-Ericksen ferromagnetic convection with magnetic field dependent viscosity. Tech Mech. 2024;44(1):1–13. <https://doi.org/10.24352/UB.OVGU-2024-0512024>
- Kaur M, Kumar P, Manan S, Kumar A. Combined effect of magnetic field dependent viscosity and fluid-permeable, magnetic boundaries on convective instabilities in a hot ferrofluid layer. J Taibah Univ Sci. 2025;19(1):2464462. <https://doi.org/10.1080/16583655.2025.2464462>
- Sunil, Sharma A, Sharma D, Sharma R. Effect of dust particles on thermal convection in a ferromagnetic fluid. Z Naturforsch A. 2005;60(7):494–502. <https://doi.org/10.1515/zna-2005-0705>
- Sunil, Sharma A, Shandil R. Effect of magnetic field dependent viscosity on ferroconvection in the presence of dust particles. J Appl Math Comput. 2008;27:7–22. <https://doi.org/10.1007/s12190-008-0055-2>
- Sunil, Divya, Sharma R. The effect of magnetic-field-dependent viscosity on ferroconvection in a porous medium in the presence of dust particles. J Geophys Eng. 2004;1(4):277–286. <https://doi.org/10.1088/1742-2132/1/4/006>
- Sharma A, Kumar P et al. Effect of magnetic field dependent viscosity and rotation on ferroconvection in the presence of dust particles. Appl Math Comput. 2006;182(1):82–88. <https://doi.org/10.1016/j.amc.2006.03.037>
- Kumar P, Kumar A, Thakur A. Effect of viscosity variation with temperature on convective instability in a hot dusty ferrofluid layer with permeable boundaries. Numer Heat Transf B. 2024;1–18. <https://doi.org/10.1080/10407790.2024.2380755>
- Mittal R, Rana U. Effect of dust particles on a layer of micropolar ferromagnetic fluid heated from below saturating a porous medium. Appl Math Comput. 2009;215(7):2591–2607. <https://doi.org/10.1016/j.amc.2009.08.063>
- Singh B. Effect of rotation on a layer of micro-polar ferromagnetic dusty fluid heated from below saturating a porous medium. Int J Eng Res Appl. 2016;6(3):4–28.
- Kumar S, Pundir R, Nadian PK. Effect of dust particles on a rotating

- couple-stress ferromagnetic fluid heated from below. *Int J Sci Eng Appl Sci*. 2020.
26. Nanjundappa C, Pavithra A, Shivakumara I. Effect of dusty particles on Darcy-Brinkman gravity driven ferro-thermal-convection in a ferrofluid saturated porous layer with internal heat source: influence of boundaries. *Int J Appl Comput Math*. 2021;7:1–20. <https://doi.org/10.1007/s40819-020-00948-6>
 27. Khan D, Rahman AU, Ali G, Kumam P, Kaewkhao A, Khan I. The effect of wall shear stress on two phase fluctuating flow of dusty fluids by using Lighthill technique. *Water*. 2021;13(11):1587. <https://doi.org/10.3390/w13111587>
 28. Khan D, Ali G, Kumam P, Rahman AU. A scientific outcome of wall shear stress on dusty viscoelastic fluid along heat absorbing in an inclined channel. *Case Stud Therm Eng*. 2022;30:101764. <https://doi.org/10.1016/j.csite.2022.101764>
 29. Khan D, Hussien MA, Elsiddieg AM, Lone SA, Hassan AM. Exploration of generalized two phase free convection magnetohydrodynamic flow of dusty tetra-hybrid Casson nanofluid between parallel microplates. *Nanotechnol Rev*. 2023;12(1):20230102. <https://doi.org/10.1515/ntrev-2023-0102>
 30. Kumam P, Kumam W, Suttiarporn P, Rehman A, et al. Relative magnetic field and slipping effect on Casson dusty fluid of two phase fluctuating flow over inclined parallel plate. *S Afr J Chem Eng*. 2023;44:135–146. <https://doi.org/10.1016/j.sajce.2023.01.010>
 31. Khan D, Kumam P, Wathayu W, Jarad F. Exploring the potential of heat transfer and entropy generation of generalized dusty tetra hybrid nanofluid in a microchannel. *Chin J Phys*. 2024;89:1009–1023. <https://doi.org/10.1016/j.cjph.2023.10.006>
 32. Siddheshwar PG. Convective instability of ferromagnetic fluids bounded by fluid-permeable, magnetic boundaries. *J Magn Magn Mater*. 1995;149(1–2):148–150. [https://doi.org/10.1016/0304-8853\(95\)00358-4](https://doi.org/10.1016/0304-8853(95)00358-4)
 33. Surya D, Gupta A. Thermal instability in a liquid layer with permeable boundaries under the influence of variable gravity. *Eur J Mech B Fluids*. 2022;91:219–225. <https://doi.org/10.1016/j.euromechflu.2021.10.010>
 34. Chandrasekhar S. Hydrodynamic and hydromagnetic stability. 10th ed. Basingstoke: Courier Corporation; 2013.
 35. Prakash J, Kumar R, Kumari K. Thermal convection in a ferromagnetic fluid layer with magnetic field dependent viscosity: A correction applied. *Stud Geotech Mech*. 2017;39(3):39–46. <https://doi.org/10.1515/sgem-2017-0028>
 36. Beavers GS, Joseph DD. Boundary conditions at a naturally permeable wall. *J Fluid Mech*. 1967;30(1):197–207. <https://doi.org/10.1017/S0022112067001375>
 37. Kumar P, Thakur A, Kaur M, Kumar A. Numerical investigation of the impact of magnetic field dependent viscosity on darcy-brinkman ferromagnetic convection with permeable boundaries. *Special Topics & Reviews in Porous Media: An International Journal*. 2025;16(4). <https://doi.org/10.1615/SpecialTopicsRevPorousMedia.2024054589>

Awneesh Kumar:  <https://orcid.org/0009-0001-2934-8487>

Pankaj Kumar:  <https://orcid.org/0000-0002-2938-1033>

Abhishek Thakur:  <https://orcid.org/0009-0005-0027-708X>

Mandeep Kaur:  <https://orcid.org/0009-0000-1512-6798>



This work is licensed under the Creative Commons BY-NC-ND 4.0 license.